NNT : 2017SACLC061

Thèse de doctorat de l'Université Paris-Saclay et du Politecnico di Milano préparée à CentraleSupélec

Ecole doctorale n°*ED*579
Sciences mécaniques et énergétiques, matériaux et géosciences
Scuola di Dottorato di Ricerca
Spécialité de doctorat : Génie Civil
Structural, Seismic and Geotechnical Engineering

par

M. Filippo Gatti

Analyse physics-based de scénarios sismiques «de la faille au site»: prédiction de mouvement sismique fort pour l'étude de vulnérabilité sismique de structures critiques.

Thèse présentée et soutenue à Paris, le 25 Septembre 2017.

Composition du Jury :

M.	Raul Madariaga	Professeur émérite Ecole Normale Supérieure	(Président du jury)
M.	Etienne Bertrand	Directeur de Recherche CEREMA, Seismic risk team	(Rapporteur)
M.	Hiroshi Kawase	Professeur Kyoto University	(Rapporteur)
Mme	Evelyne Foerster	Ingénieur de Recherche Commissariat a l'Energie Atomique (CEA)	(Examinatrice)
M.	Kyriazis PITILAKIS	Professeur Aristotle University Thessaloniki (AUTH)	(Examinateur)
M.	Fernando LOPEZ-CABALLERO	Maître de Conférence/LRU CentraleSupélec	(Co-directeur de thèse)
M.	Roberto PAOLUCCI	Professeur Politecnico di Milano	(Directeur de thèse)
M.	Didier CLOUTEAU	Professeur CentraleSupélec	(Directeur de thèse)

université PARIS-SACLAY
ÉCOLE DOCTORALE
Sciences mécaniques et énergétiques, matériaux et géosciences (SMEMAG)

Titre : Analyse physics-based de scénarios sismiques «de la faille au site»: prédiction de mouvement sismique fort pour l'étude de vulnérabilité sismique de structures critiques.

Mots clefs : seismologie, génie parasismique numérique, mouvements sismiques forts, modélisation physics-based, vulnerabilité sismique, quantification d'incertitude

Résumé : L'ambition de ce travail est la prédiction du champ d'onde incident réalistique, induit par des mouvement forts de sol, aux sites d'importance stratégique, comme des centrales nucléaires. À cette fin, un laboratoire virtuel efficace et multi-outil est développé et exploité pour simuler les aspects différents d'un phénomène complexe comme un tremblement de terre: le mécanisme de source, la propagation dans la croûte terrestre, l'interaction avec les interfaces géologiques et l'effet des couches de sol hétérogènes et non-linéaires. La plate-forme numérique aide non seulement à l'approfondissement de l'aperçu et la compréhension du tremblement de terre lui-même, mais permet aussi la quantification d'incertitude de bases de données sismiques, des outils de prédiction traditionnels, des procédures de conception et des paramètres cruciaux définissant le scénarios sismique de mouvement fort. Ce cadre computationnel multi-échelle fait face à la nature diversifiée d'un tremblement de terre par approche *holistique* local-régionale: la réponse de site localement observée est premièrement caractérisé dans les détails pour la commuter à réponse-cible pour une analyse à plus grande échelle. L'outil principal est représenté par un logiciel très performant pour résoudre le problème d'équation d'onde basé sur la Méthode des Éléments Spectrales. Ce code, appelé SEM3D, est conçu pour tourner efficacement sur des architectures parallèles multi-core. SEM3D est intégré par un générateur parallèle de champs aléatoires à grande échelle pour représenter l'hétérogénéité des propriétés de sol, avec un solveur non-linéaire efficace pour simuler le comportement hysteretic de sols. Un cas d'étude complexe est choisie à cette fin: le tremblement de terre M_W6.6 Niigata-Ken Chūetsu-Oki, qui a endommagé la centrale nucléaire de Kashiwazaki-Kariwa. Les effets de site non-linéaires observés, la nature impulsive des signaux et l'incohérence spatiale du mouvement de sol enregistré sont à premier examinés et caractérisés. Dans la suite, le modèle physics-based 3D «de la faille au site» est construit et employé pour prédire le mouvement sismique dans une bande de fréquence de 0-7 Hz. L'effet de la structure géologique pliée au-dessous du site est quantifié en simulant deux chocs d'intensité modérée et en évaluant la variabilité spatiale des spectres de réponse aux différents endroits dans le site nucléaire. Le résultat numérique souligne le besoin d'inclure la structure géologique syncline-anticline dans le modèle, pour obtenir une réponse de site amplifiée par rapport à l'hypothèse classique d'un demi-espace par couches parallèles. De plus, l'analyse comparative reproduit l'incohérence remarquable des signaux observés dans les enregistrements, mettant en évidence le besoin d'une description plus détaillée et spécifique à site du champ d'onde incident utilisé comme paramètre d'entrée dans la conception structurel antisismique de réacteurs nucléaires et des installations. Dans une deuxième temps, l'effet de rupture de la faille est testé et calé. Finalement, la bande de fréquences des signaux synthétiques obtenues comme résultat des simulations numériques est agrandie en exploitant la prédiction stochastique des ordonnées spectrales à courte période fournies par des Réseaux Artificiels de Neurones. Les synthétiques sont spectral-matched sur ces simulations.

Title : Forward physics-based analysis of "source-to-site" seismic scenarios for strong ground motion prediction and seismic vulnerability assessment of critical structures

Keywords : engineering seismology, computational earthquake engineering, strong ground motion earthquake, physics-based modelling, seismic vulnerability, uncertainty quantification

Abstract : The ambition of this work is the prediction of a synthetic yet realistic broad-band incident wave-field, induced by strong ground motion earthquakes at sites of strategic importance, such as nuclear power plants. To this end, an effective multi-tool virtual laboratory is developed and exploited to simulate the different aspects of the complex phenomenon an earthquake embodies: the source mechanism, the wave propagation path through the Earth's crust, the interaction with the shallow geological interfaces and the effect of the non-linear heterogeneous softer soil deposits. The platform not only helps in deepening the insight and the understanding of the earthquake itself, but also permits the uncertainty quantification of seismic databases, traditional predictive tools, design procedures and crucial parameters defining strong ground shaking scenarios. This multi-scale computational framework copes with the manifold nature of an earthquake by a *holistic* local-to-regional approach: the locally observed site-response is at first characterized in details to switch to target response for a larger-scale analysis, in a second instance. The core tool is represented by a high-performance software to solve the wave-equation problem based upon the Spectral Element Method. This code, called SEM3D, is taylored to effectively scale on multi-core parallel architectures. SEM3D is featured by a large-scale random-field parallel generator to represent the heterogeneity of the soil properties, along with an effective non-linear solver to simulate the hysteretic soil behaviour. A complex case study is chosen to this end: is the M_W6.6 Niigata-Ken Chūetsu-Oki earthquake, which damaged the Kashiwazaki-Kariwa nuclear power plant. The observed non-linear site-effects, the pulse-like wave-motion and the spatial incoherence of the recorded ground motion are at first investigated and characterized. In the following, the 3D source-to-site physics-based model is constructed and employed to provide reliable input ground motion, for a frequency band of 0-7 Hz. The effect of the folded geological structure underneath the site is quantified by simulating two aftershocks of moderate intensity and by estimating the spatial variability of the response spectra at different locations within the nuclear site. The numerical outcome stresses the need to include the syncline-anticline geological structure within the model, so to picture the amplified site-response in contrast with the classical assumption of a layered half-space. Moreover, the comparative analysis reproduces the remarkable incoherence of the ground motion time-histories observed in the recordings, highlighting the need for a more detailed and site-specific description of the incident wave-field used as input parameter in the antiseismic structural design of nuclear reactors and facilities. In a second time, the effect of extended fault rupture is tested and tuned. Finally, the frequency band of the time-histories obtained as outcome of the numerical simulations is enlarged by exploiting the stochastic prediction of short-period response ordinates provided by Artificial Neural Networks. The synthetics are spectral-scaled upon those provisions.

Université Paris-Saclay
Espace Technologique / Immeuble Discovery
Route de l'Orme aux Merisiers RD 128 / 91190 Saint-Aubin, France

Contents

List of Figures

List of Tables

1

Strong Earthquake Ground Motion Prediction: tools and methods to build realistic seismic scenarios

"It is not light that we need, but fire; it is not the gentle shower but thunder. We need the storm, the whirlwind, and the earthquake."

– Frederick Douglass

The concept of earthquake-related *risk* embodies the possibility of disastrous effects (in terms of human and economic losses) that are likely to occur in the future, due to the occurrence of a ground shaking. The definition of *risk* of natural disasters was traditionally inflected into physical *hazard*, *vulnerability* and *exposition*. Therefore, the hazard event is not the sole driver of risk, since the degree of adverse effects is prevalently determined by its intricate combination with vulnerability and exposure of societies and social-ecological systems (Cardona et al., 2012).
Recently, strong ground motion earthquakes have been widely documented and studied. For instance, between 2010 and 2016, a sequence of devastating earthquakes struck several places all over the world. Figure 1.1 shows a selection of strong motion earthquake (M_W >6.5) occurred all over the world in the last 10 years. As a matter of fact, economic losses quickly raised to billion dollars in this period. For instance, comparing the 1995 Kobe and the 2011 Tohoku earthquakes, the loss statistics shows a factor 3 increase for the economic loss (Paolucci et al., 2014). This trend appears intrinsically related to population dynamics and growth, along with multiple and variegate demands for location, comfort and energy which, in turns, leads to the gradual decrease in the availability of safer lands, along with an increased susceptibility to excessive damage and low resilience, i.e. an inevitable increase of potentially dangerous places (Lavell, 2003). Where exposure to events is impossible to avoid, land use planning and location decisions can be accompanied by other structural or non-structural methods for preventing or mitigating risk (Cardona et al., 2012).
From a modern conceptual point of view, earthquakes (such as other natural disasters) mainly represent an un-managed risk or series of risks, whose detonator is the physical event itself. As things stand, the procedures and methods for post-earthquake disaster management, seismic vulnerability and hazard assessment started to be re-thought, so to include the identification of critical structures and infrastructures, their vulnerability evaluation, control and financing along with the traditional predictive framework (Paolucci et al., 2014). The aim is twofold: on one side, to improve the *preparedness* and *response*, predominantly based on engineering schemes; on the other, to consider *prevention* and *mitigation* as major efforts in reducing the overall risk. Unfortunately, the latter aspect has been widely disregarded in the past, and even so governments and society were mostly devoted to the modification of hazards using structural engineering measures or sporadic relocation of commu-

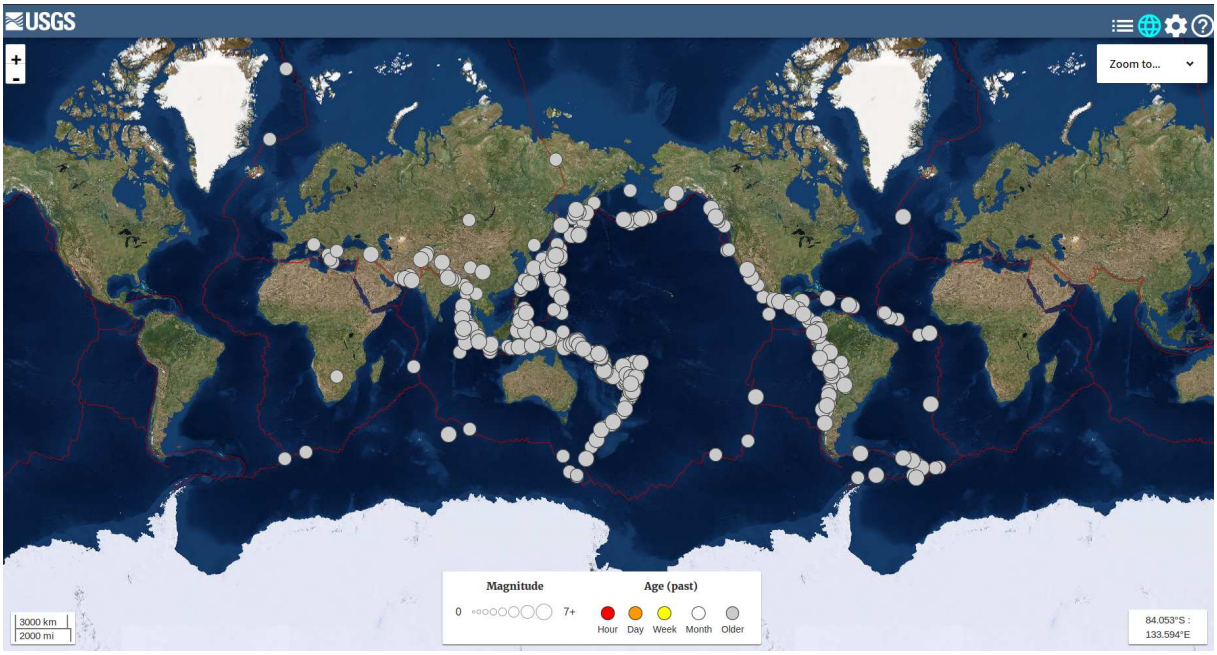

Figure 1.1: Map of strongest earthquakes that struck several regions all around the world in the last 10 years (source: https://earthexplorer.usgs.gov/).

nities located in risk zones (Lavell, 2003). From early 1990s up to now, however, the good practice of risk mitigation through intervention prior to earthquake disasters took place, enforced by the devastations caused by those ruthless natural disasters. Specifically, vulnerability and exposure to earthquake disasters were revisited, so to better assess and estimate the severity of the impact of extreme and non-extreme ground shaking. In this sense, one of the hot tasks to cope with is the seismic design of critical structures, such as highways, bridges, all major lifelines and energy power plants, such as nuclear ones. The latter aspect is doubly important, due to the associated primary disaster potential and to the indirect damage and losses due to their scarce resilience. Understanding the multiple shades of vulnerability and exposure of those structures to earthquakes disasters steers the path to design and implement effective adaptation and disaster risk management strategies (Cardona et al., 2012).
Bearing in mind the ultimate goal of risk mitigation, the performance-based earthquake engineering methodology evolved accordingly. For instance, the Pacific Earthquake Engineering Research (PEER), proposed a brand new methodology which unravels in four stages (Porter, 2003):

1. the hazard analysis in which one of several intensity measure (IM) parameters are identified
2. the structural analysis in which the response to the earthquake is represented by the engineering demand parameter (EDP)
3. the damage analysis in which the probability of failure is quantified (e.g. by drawing realistic fragility curves)
4. the loss analysis, which requires the estimation of the decision based on the cost and maintenance of the project

The listed items may be arranged into a pyramidal scheme: the database of observed and/or synthetic ground motion parameters (item 1) bare the whole framework, since it provides realistic input motion to perform structural analyses (item 2), it feeds probabilistic models (item 3) by defining marginal distributions of several IM and they constrain macro-seismic intensity maps that steer loss analysis

(item 4). Following this framework, this work places itself into the first stage, as it aims to provide reliable yet synthetic earthquake ground motion estimations so to feed the whole PEER work chain. In doing so, strong ground motion observations are employed to tune the constructed seismological model.

1.1 The Earthquake Ground Motion Prediction framework

On of the main ingredients of the seismic hazard assessment resides into the Earthquake Ground Motion Prediction (EGMP) framework. Its ultimate goal is the *prediction* of a parameter related to the severity of earthquake ground motion, given a set of basics information as magnitude, distance, faulting style etc. First and foremost, quantitative EGMP requires the definition of an Intensity Measure (IM). Traditionally, earthquake intensity and ground acceleration are two parameters which express the degree to earthquake ground shaking. In this sense, EGMP outcome has a twofold nature since it may be intended as (1) full time-histories and/or as some ground motion peak value (typically Peak Ground Acceleration, PGA, or the Peak Ground Velocity, PGV), or (2) as an *macro-seismic intensity measure*. The former interpretation better describes the incident wave field and the physical process underlying the earthquake, whereas macro-seismic intensity measures generally quantify the effects of earthquakes on structures on a observational basis. The general problem when working with macro-seismic intensity data is that intensities are assigned relative to various scale and within certain cases, a considerable portion of personal judgment (Sørensen et al., 2010). However, when observed at larger scale and over a large number of points, intensity parameters show a quite regular pattern that may be controlled by radiation properties of the seismic source (Panza et al., 1997).

In a broad sense, EGMP may be portrayed as an operational framework that encompasses different methods and tools (both probabilistic and deterministic) and takes advantage of large databases of ground motion recordings. It is worth to mention that, due to the major intrinsic uncertainties that resides within each earthquake scenarios (mainly due to the general poor understanding of the physical process underlying an earthquake, inherited from the difficulty to handle the naturally multi-scale problem and to quantify each aspect one apart from the other), each estimation must be supplied with a measure of the level of confidence or of the safety margins. A traditional conceptual scheme (widely used in seismology to help unravelling EGMP) asserts that a given earthquake *intensity measure* Y can be estimated at a generic site by the following convolution product (Boore, 2003):

$$Y\left(M;R;f\right)=E\left(M;f\right)*P\left(R;f\right)*G\left(f\right)*I\left(f\right) \tag{1.1}$$

with:

- E: the Earthquake source mechanism
- P: the propagation Path effect
- G: the soil Site effect
- I: instrument or type of motion

where M is alternatively the seismic moment M_0 (firstly introduced by Kanamori and Anderson, 1975) or the moment magnitude, R and f are source-to-site distance and frequency respectively. Figure 1.2 schematically portrays a Source-to-Site earthquake scenario, highlighting some of the features characterizing the source, the propagation multi-pathing and the site effects. In the following paragraphs, each of the components of a complete Source-to-Site analysis are described into details, keeping in mind that an exhaustive EGMP requires the whole of them to be convolutely coupled together.

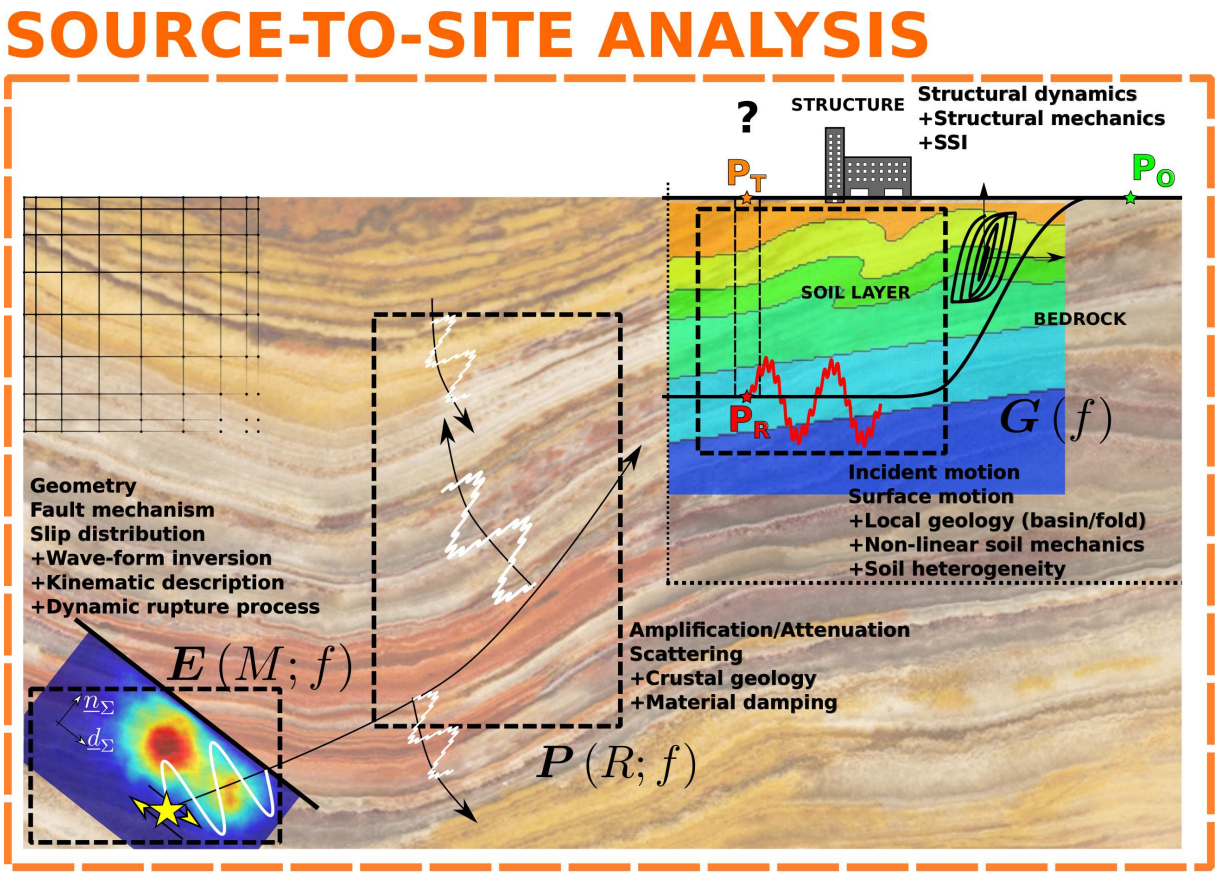

Figure 1.2: Scheme of the forward deterministic EGMP. Three main items (source $E(M;f)$, path $P(R;f)$ and site-effect $G(f)$) are highlighted in dashed black boxes meaning they may be characterized as standalone features. The external dashed orange line indicates the all-embracing Source-to-Site framework, to highlight its multi-scale nature. Next by each of dashed box, a set of keywords concerning the highlighted feature is listed.

Earthquake Source $E(M;f)$

The ground shaking originates along active rupture fronts inside crustal rocks, the dimensions of which may range from few km (e.g. M_W5-M_W6) up to hundreds of km (e.g. M_W8-M_W9). Intuitively, the source is interpreted as a discontinuity in the Earth's crust, whose sides slip one with respect to another at a certain rupture velocity and along a certain rupture path, releasing and dissipating energy due to complex frictional mechanisms. As a matter of fact, the complete characterization of the seismic source process requires, along with the knowledge of the geometry, the 3D orientation and the structure of the fault system, the knowledge of spatio-temporal distribution of the forces acting on the discontinuity interface (Bizzarri, 2014), and the respective nonuniform distribution of those physical properties. Forward analysis may be performed by translating the inverted slip distribution/stress drop into equivalent dynamic forces that excite the computational model. Nowadays, the kinematic approach is widely adopted to describe the seismic source, which is represented as a set of force couples, denoted by their *seismic moment* (Madariaga et al., 2013). It has been widely observed that the amplitude of the source Fourier's spectrum scales with the earthquake magnitude, according to a *similarity condition* firstly outlined by Aki (1967). As a matter of fact, earthquakes of higher magnitude are prone to generate longer period wave-field. Conventional scaling relations for the fault parameters, such as the fault length and average slip on the fault based on the seismic magnitude, are mostly estimated with the help of wave-form inversion techniques exploiting from surface offsets

and using teleseismic/geodetic measurements (Tarantola, 1988). Those observations characterize the long-period part of the motion, thus being insufficient to picture the broad-band near-source ground motion effects at periods less than 1 s, which are of major concern for engineers (Miyake et al., 2003). In determining the spectral and spatial limits of high-frequency wave propagation, the rupture propagation schemes cannot be overlooked however.

Propagation Path $P\left(R;f\right)$

The wave-field radiated from slipping interfaces propagates to the Earth's surface through complex geological configurations. It is well known that Earth's crust has statistically a stratified nature. However, the tectonic stress state generated complex folded structures with regional scale extension. From a smaller scale point of view, crustal material happens to be rather heterogeneous and anisotropic. The latter issues cause wave scattering and dispersion, along with the radiative damping due to the large distances (within a radius of interest of 50-100 km approximately) travelled by the wave-front. Moreover, the heterogeneous nature of the bedrock material induces scattering phenomena which address the radiated wave-forms at higher frequencies. Therefore, the physics-based approach models the propagation effect by describing the mechanical behaviour of the Earth's crust and of the regional geological interfaces. The pre-existent tectonic stress state should be taken into consideration as well.

Site-effects $G\left(f\right)$

The very final objective of any EGMP is the provision of the so-called *incident ground motion* that excites the structural components. The site specific conditions (i.e. within a distance $\approx$ 100-1000 m in the site surroundings) have huge impact on the ground motion propagating from deep crustal rock conformation towards the surface. This is mainly due to the *impedance contrast* between shallow softer soil deposits and the stiffer bedrock, combined with the presence of complex geological interfaces and the heterogeneous non-linear rheology characterizing sandy and clayey layers beneath the surface. The latter factors play competitive roles in modifying the input motion (Kramer, 1996): the impedance contrast (softer-over-stiffer layer) tends to amplify the ground motion and steer it along the vertical direction, whereas the non-linear rheology lead the soil deposits to absorb seismic energy damping the incoming ground motion (hysteresis loops in Figure 1.2). Moreover, the wave scattering/dispersion due to the heterogeneity of soil media is contrasted by the wave focalization due to the *basin*-type geology (often observed at shallow depths, due to the diagenesis process).
When assessing the seismic site-effects, the eventual presence of the structure must not be disregarded. *Soil-Structure-Interaction* (SSI) represents the direct application of EGMP: the predicted ground motion excite the structural resonance modes, implying the structure to modify the incident seismic wave-field by radiating seismic energy back to the soil.

1.1.1 Classical EGMP: tools and approaches

A huge variety of approaches for EGMP has been proposed in the past four or five decades, relying on different information detail associated to different outputs (Figure 1.3). The most intuitive approach consists into casting all the aspects within an empirical Ground Motion Prediction Equation (GMPE). The latter is usually calibrated upon instrumental observations from real earthquakes, in terms of average prediction and standard deviation. A compilation by Douglas (2011) has reported about 300 of such equations to estimate peak ground acceleration (PGA) since 1964, and about 200 to estimate the response spectral ordinates. As reported, for instance, by Boore et al. (2013) and by Douglas et al. (2014), the empirical GMPE tool represented so far a valid substitute of more efficient numerical

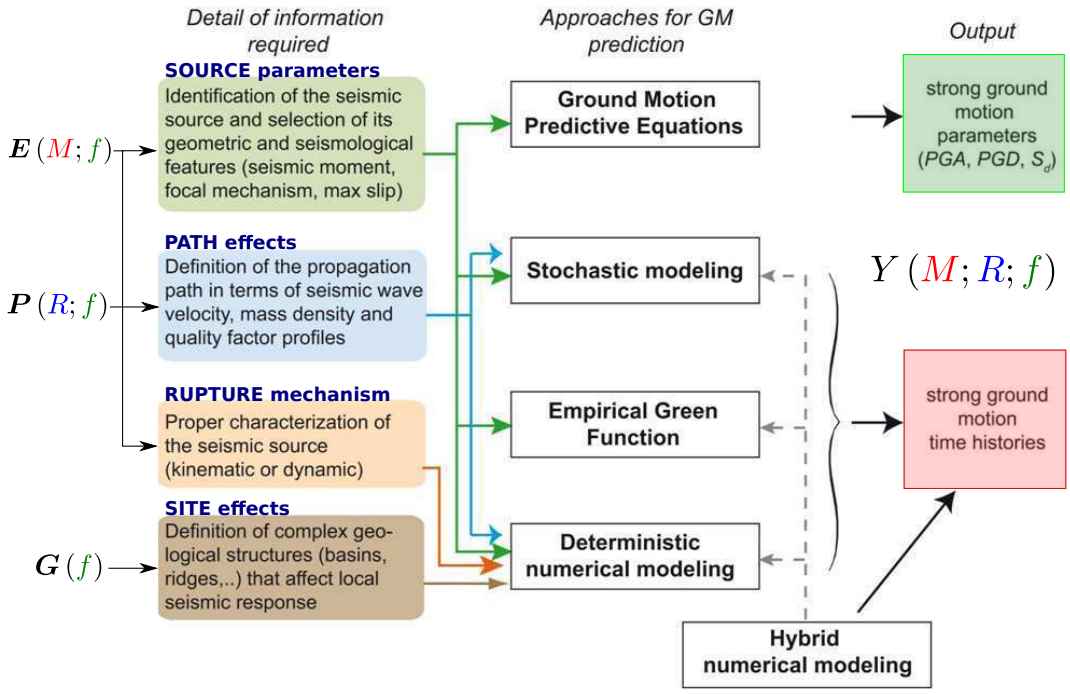

Figure 1.3: Scheme of the principal EGMP methods, with relative inputs required and provided outcomes. Reprinted from Paolucci et al. (2014).

tools and an intensive statistical processing of available records (whose quality and associated metafiles are continuously increasing, however). Peak values predicted through GMPEs may be also obtained by a *stochastic* approach (Hanks and McGuire, 1981; Boore, 1983, among others). However, one of the major improvement due to the stochastic approach resides in its capability of generate time-histories. The idea beneath is rather simple: the earthquake ground motion is interpreted as a non-stationary time-varying stochastic process. The synthetic spectrum is generally expressed as white-noise spectrum opportunely scaled by the source amplitude spectrum (frequency modulating functions). Alternatively, time-varying autoregressive moving average (ARMA) models are employed (Liu, 1970; Lin and Yong, 1987). For instance, the stochastic method proposed by Boore (1983) filters a suite of randomly generated windowed time series, whose average amplitude spectrum matches the specified one. Originally developed for a point-source, the stochastic method has been extended to finite-fault simulations by Motazedian and Atkinson (2005).
It is worth to remark that despite the reduced number of parameters required, those approaches are still data-driven. Moreover, the main parameters affecting the ground motions (i.e. source, path, and site) are still cast into simple functional forms. As a matter of fact, certain magnitude-distance ranges or specific site conditions remain poorly covered. This inevitably leads to major approximations, especially in complex near-fault conditions or when non-linear site-effects are observed. During the last decades, some authors proposed to use GMPEs calibrated on a combination of both empirical and numerically simulated ground motion data to overcome the limitation related to available observed data (Abrahamson and Silva, 2007). Despite its undoubted advantages, the classical EGMP suffers of major drawbacks, namely:

- the fundamental unresolved dichotomy between *simple* casting equation and the degree of complexity of the phenomenon;
- the scarce adaptability to different site conditions and seismic scenarios (due to their regression coefficients, issued from limited databases Lee and Han, 2002);

- the difficulty to employ those equations to estimate reliable broad-band full time-histories (since peak values or IM are generally provided);

- the unrealistic spatial variability of the synthetic ground motion.

1.1.2 Physics-based EGMP: history, development and new horizons

In recent years, the transient evolution of the incident motion and structural response has become more ease to handle and study, thanks to the technological and computational enhancement. A great interest has been given to deterministic numerical simulations of seismic scenarios, the so called forward Physics-Based Simulations (PBS). The ever increasing computational power (e.g. massively parallel supercomputers) made a 3D numerical simulations of the source-to-site seismic wave propagation at local, regional or global scale relatively fast and efficient. For this reason, PBS is rapidly becoming one of the leading tool to simulate ground shaking scenarios for future earthquakes. The method encompasses (1) the detailed description of the rupture process (kinematic or dynamic), along with (2) the detailed 3D description of the geological profile, topography and eventually (3) non-linear site effects. Physics-based modelling already proved in the past decades to be well suited for global (Graves, 1996; Wald and Graves, 1998; Pitarka et al., 1998; Komatitsch and Tromp, 2002a,b) and regional scale simulation (Bao et al., 1998; Olsen, 2000; Dumbser and Käser, 2006; Day et al., 2008; Tsuda et al., 2011; Smerzini and Villani, 2012; Taborda and Bielak, 2013; Villani et al., 2014; Paolucci et al., 2015; Chaljub et al., 2015), challenging the dynamic problem from the source of earthquake up to the structures in an omni-comprehensive computational model. In this context, the idea behind a modern EGMP physics-based platform is to build up a *virtual laboratory* for better understanding of the physical process and for the assessment of the epistemic uncertainty on the physical parameters. Ground motions can be simulated for arbitrary conditions and model parameters, that can be varied systematically to assess sensitivity to input specification and safety margins (conforming to a performance-based approach). Physics-based simulations are integrated to the current seismic hazard analysis, used to constrain empirical ground motion predictions in circumstances not well-constrained by observations (Abrahamson et al., 2013).
Although very powerful, to run a reliable physics-based simulation represents a delicate task, fundamentally due to its multi-physics (i.e., fluid and solid mechanics), multi-mechanism (e.g. rupture dynamics, wave-propagation in non-linear heterogeneous media), multi-scale (from extended seismogenic fault structures at depth towards the surface throughout coarser to finer geological deposits) nature. Although all those features are extremely appealing, tribute must be payed to the higher modelling complexity, to the increasing computational costs (therefore most of the simulations have been so far restricted to relative low-frequency range, i.e. hardly overcome the limit of 4.0 Hz), not to mention to the deep knowledge of the area under investigation required. The great theoretical and technological progresses made so far widened the horizon of fancy analyses, that unfortunately slams into the hinder represented by the need for preservation of physical sense to correctly interpret the observations. A classical example is provided by the source modelling: typical studies on wave-form inversion characterize the slip patch along a fault plane up to 1.0-2.0 Hz. Therefore, even if the computation model was capable to accurately propagate wave-fields at frequencies higher than 2.0 Hz, the energy sourced into the the system do not cover a broad band. The higher frequencies eventually observed in the synthetic time-histories are generated by other mechanism, only due to the propagation path and to the site effects, due to lack of information on the source process. At a first glance, those analyses are more than compatible with the results of wave-form inversions performed to characterize seismic sources. However, a further effort in enlarging the radiated spectrum is required so to provide plausible realizations of an earthquake occurrence on both a regional and local scales for a multi-shaded estimation of the risk associated, the costs implied and the emergency plans.

Two strategies are possible to obtain reliable broad-band synthetics, by leaning on physics-based simulations: (1) to produce them by directly refining the computational model, so to reduce the numerical dispersion due either to the poor spatial/time discretizations and (2) by applying stochastic methods to low-frequency deterministic simulations (Seyhan et al., 2013).
Concerning the first option, several issues must be tackled to build-up a complete broad-band model. The latter must handle complex and large geometries (regional topography, bathymetry, coastlines, geological structures), detailed mechanical models for material behaviours (viscous, non-linear and heterogeneous soil materials, fluid-solid interaction) and a refined description of the source mechanisms in a more refined manner, including its time-evolution from nucleation to post-event settlement. In this sense, it must be mentioned the great contribution provided by the Southern California Earthquake Center (SCEC) group, which launched in 1991 a vast research program (still ongoing) explicitly targeting the study of the earthquake phenomenon under different point of views, integrating seismology, tectonic geodesy, earthquake geology, and computational science. The major concern the SCEC group tackles is the need to synthesize the huge amount of information provided by the mentioned study fields (in terms of observations, laboratory experiments and numerical analyses) into a multitasking and multipurpose platform to produce reliable and physics-based ground shaking scenarios. For instance, the CyberShake project[1] was intended to entirely replace the GMPEs with simulation-based ground motion predictions (Baker et al., 2014). This great effort aimed to extend the frequency band and to enable PBS to be used with confidence in engineering applications (e.g.: seismic hazard analysis and structural or geotechnical dynamic analysis). To this end, the SCEC started promoting the Broadband Platform (BBP), an open-source software distribution that contains physics based ground motion models capable of calculating earthquake ground motions at frequencies up to 10 Hz across regional distances [2]. Moreover, SCEC is currently exploring the feasibility of using almost entirely physics-based, 3D deterministic methods (the *High-F Project* [3], moving deterministic simulations up to 10 Hz within the next decade. High-F will benefit from recent results in realistic characterization of earthquake source complexity, as well as statistical description of small-scale heterogeneities of the surrounding media.
Concerning the earthquake nucleation, major efforts are intended into obtain reliable description of the complex time-evolving rupture patterns, primarily responsible of broad-band (i.e. 0.0-20.0 Hz) energy radiation. The complex phenomenon span multiple spatial and temporal scales. From a spatial point of view, the SCEC group is striving to obtain a multi-scale spatial description capable to depict both the lithospheric strain rates (inferred from far-field motion of plate boundaries) and the slip distributions along active faults. A multi-physics approach is sought, which encompasses the low-temperature elastic-plastic mechanisms along with the viscous creep at high temperature. To this end, the stress transfer across the elastic upper crust and flowing mantle is taken into account (Takeuchi and Fialko, 2012), since the processes that determine frictional resistance and its evolution during co-seismic slip are critical to understanding earthquake behavior (how, when, and where ruptures initiate, propagate, and stop, Lapusta et al., 2000; Noda and Lapusta, 2013). Short term dynamics is mainly related to brittle rheology but it must however be coupled with a model for the long-term ductile fracture propagation, which is fundamental to assess the tectonic stress distribution along the whole earthquake and post-event phase. It appears evident that the SCEC group is marching beyond kinematic models to a fully coupled dynamic modelling of the fault offset along the rupture segments. Nonetheless, correlations between slip and rupture velocity fluctuations linked to the fault geometry, open up to new pseudo-dynamic approaches. Realistic simulations require the consideration of off-fault plasticity and damage, co-seismic fault weakening due to shear heating and

[1] a SCEC research project developing a PSHA-oriented Probabilistic Seismic Hazard Analysis
[2] http://scec.usc.edu/scecpedia/Broadband_Platform
[3] http://scec.usc.edu/scecpedia/High-F

pore pressure evolution (Goldsby et al., 2014), fault roughness, and large-scale complexities (Proctor et al., 2014). Moreover, a stochastic approach is foreseen to perform some sort of *stress-test* on the system response to different realization of dynamic rupture configurations, and quantify the tectonic stress confidence margins at which earthquakes are likely to occur (Lapusta et al., 2000). Several realizations of rough fault simulations (with different rupture styles, e.g. sub-Rayleigh vs. supershear, slip pulse vs. crack) populate the pool of response on which perform solid uncertainty quantification. Another source of high-frequency energy that the SCEC project is investigating is related to the inelastic and heterogeneous nature of the Earth's crust. Scattering by small-scale heterogeneities contributes significantly to the apparent attenuation of high-frequency pulses in near-field condition and leads to incoherence in the wave-field important to ground-motion predictions. Fine-scale material heterogeneities represent spatially correlated random perturbations of the mean velocity models (characterized by data from well-logs, seismic reflection surveys, and dense seismic arrays) and they significantly alter the high-frequency part of the simulated ground motion (>2 Hz Withers, 2016). Moreover, it becomes therefore necessary to alter intrinsic attenuation used in simulations by making the quality factor Q dependent on both frequency and depth. The non-linear soil behaviour and the site response of thin geotechnical layers as well, are involved into the scattering and damping mechanisms of the wave-field (Roten et al., 2016, see for instance).
This great effort towards broad-band forward physics-based simulations was made possible by the SCEC's vision of a *center-without-walls* (SCEC, 2017), based on collaboration and sharing of data and tools. This interdisciplinary community-centered approach is embodied by the so called *Community Models* (CXM, see Figure 1.4) on specific areas in the Southern California, as the high-resolution 3D Velocity model (CVM, Tape et al., 2010; Lee et al., 2014), the Community Fault Model (CFM, Plesch et al., 2007), these two integrated from countless investigations of the California crust into the Unified Structural Representation of the southern California crust and upper mantle (Shaw et al., 2015). During SCEC4 (research plan 2012-2016), investigators initiated a Community Geodetic Model (CGM Jordan, 2015), gathering GPS and InSAR datasets to improve maps of inter-seismic strain rates at the surface and a Community Stress Model (CSM, http://sceczero.usc.edu/projects/CSM), to describe the current knowledge about the stress state of the San Andreas fault system. These developments have motivated considerable research on the prediction of strong ground motions from the large, as of yet unobserved fault ruptures that will someday occur. Empirical ground motion prediction equations (GMPEs) can potentially be improved by supplementing the direct observations of ground motions with simulation data that use the physics of wave propagation to extrapolate to unobserved conditions (Baker et al., 2014). Continuous improvements to these community models, sustained by

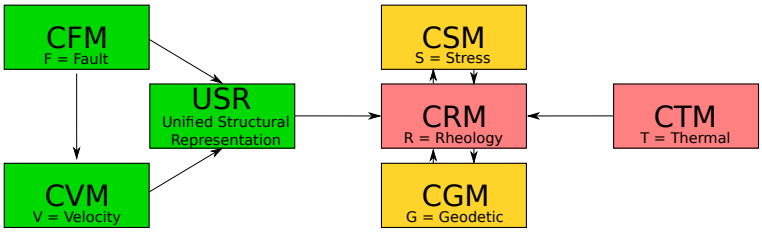

Figure 1.4: Sketch of the Community Models constructed by the SCEC group. Reprinted from SCEC (2017)

SCEC, have led to a boom in physics-based hazard modeling of Southern California. One major goal in the multi-objective research proposal of the SCEC group for 2017-2022 (SCEC5) is explicitly the improvement of high-fidelity ground-motion simulations, in terms of high-frequency accuracy (in the engineering band, up and beyond 10.0 Hz). The construction of two new Community Models have been planned, (1) the Community Rheology Model (CRM) providing the constitutive properties essential for understanding active tectonics and the cyclical deformation of tectonic stress accumulation

and earthquake stress release, along with non-elastic rheologies (mineralogy, grain size, and fluid content) and conditions (temperature, stress, and fluid pressure) that vary in space and time; (2) the Community Thermal Model (CTM), which will estimate the temperature structure of the Southern California lithosphere.
Inspired by the SCEC project, the SINAPS@ project financed the development of a high-performance numerical code conceived to perform the numerical simulation of the 3D wave propagation in large heterogeneous and non-linear geological domains. The code, called SEM3D, is based on the Spectral Element Method (Patera, 1984; Mayday et al., 1989), originally developed for fluid mechanics and then extended and widely employed in computational seismology (please refer to the original contributions of Faccioli et al., 1997; Komatitsch, 1997; Komatitsch and Vilotte, 1998). SEM3D tackles the computational burden by running on parallel computer architectures. I contributed to its development, both in terms of its effective vectorization so to improve the scalability on multi-core supercomputers and by implementing a non-linear constitutive relationship to be able to reproduce the energy adsorption due the hysteretic cyclic behaviour of the shallow soil layers. The final goal, however, is the SEM3D exploitation towards the construction of high-fidelity and broad-band earthquake ground shaking scenarios. In this thesis, my major effort was to produce a realistic regional-scale numerical model of the site response of a nuclear site, accurate in frequency range of 0.0-7.0 Hz. The focus was pointedly set on the effect of complicated 3D geological configurations, so to test the performance of SEM3D as *propagator tool*. Therefore, conceptually speaking, this work may be ascribed to the study of the Propagation Path $P\left(R;f\right)$.

Although the described *brutal force* approach is very appealing, the mentioned forward deterministic strategy will still take some years in the making, mainly due to the burdensome computational costs required to shatter the 10.0 Hz frequency barrier and produce synthetics wave-forms with realistic Fourier's spectra up to 30.0 Hz (for major engineering applications). Besides, a major conceptual gap has to be bridged: the high-frequency part of the earthquake ground motion is still poorly constrained by physics-based model, since it is the result of a complex convolution process encompassing the source mechanism, the dispersive and scattering effects due to the propagation throughout the Earth's crust, the non-linear interaction between the incident wave-field and the softer shallow soil layers and the growth of intricate surface wave-fields, mainly due to the presence of irregular geological and topographical geometries. As a matter of fact, regardless the frequency band reached by the *propagator tool*, the seismological models traditionally split the low-frequency content from the high-frequency one when describing real records. The former is considered as the deterministic part of the wave-motion and it is mainly due to the source mechanism and to the propagation path throughout the Earth's crust. It results fairly constrained and reproducible via physics-based simulations for frequencies $f < 3.0$ Hz. For what concern the higher-frequency part of the seismic records ($f > 3.0$ Hz), major difficulties arises when trying to discriminate the different factors that can eventually affect it. A crucial aspect resides in the hinder of reproducing reliable near-field synthetics, given the extreme directivity effects which usually take place in the epicentre's surroundings, along with the impulsive nature of the seismic observation in the forward direction of the rupture propagation, the permanent displacement due to the fault offset and the complex interaction between the rise and the rupture times (Mai and Beroza, 2003). Traditional GMPEs may be confidently employed for large source-to-site distances; numerical simulations, on the other hand, require a huge amount of parameters, often unavailable. Therefore, major uncertainties on the high-frequency content of the radiated wave-field have traditionally been condensed into a probabilistic framework, somehow capable of mimicking the observations. This assumption helps, in a sense, to overcome the intrinsic difficulty of *understanding* the physical mechanisms that lead to such recordings, although, the mentioned stochastic framework should be accurately formulated and calibrated upon available observations.
In this piece of research, I provide a deeper insight of an interesting hybrid approach, which couples the low-frequency content obtained by forward deterministic analyses and high-frequency predictions

made through of Artificial Neural Networks (ANN). The latter represent a fringe computational tool and they are widely employed in several scientific fields nowadays. They are particularly appreciated since they reproduce the biological learning process, but in a fictive but accelerated trial and error learning session. They are endowed with *intelligent* predictive capability, once repeatedly trained. Therefore, the idea behind their employment in constructing a broad-band seismic scenario is to predict short period spectral ordinated upon feeding the ANN with long-period synthetics produced by physics-based simulations.

1.2 Motivation and credits: the SINAPS@ project

The PhD thesis presented hereafter places itself within the framework of the French research project SINAPS@ (*Séisme et Installations Nucléaires, Améliorer et Pérenniser la Sûreté*). The latter has been conceived to rethink all the EGMP work-chain (along with the vulnerability and risk assessment procedures) employed to assess the seismic vulnerability of nuclear facilities. This ambitious research project was launched by the members of the SEISM Institute[4] and it stemmed from the nuclear disaster occurred in March 2011 in Japan, at the Fukushima nuclear power plant. The French government has reacted immediately after, by publishing a call (50M €) to enhance the scientific background in the area of the nuclear safety and radiation protection. Specifically, the call targeted the following issues:

- to deepen the knowledge of the circumstances that led to major nuclear accidents, taking into consideration initial findings and Ratings Supplemental Security implemented by the Nuclear Safety Authority;
- to investigate the different ways of managing all major nuclear accidents;
- to study the impact of these incidents on the environment on the release of radioactive materials, their impact on health and the environment and conditions for recovery of contaminated territories;
- to apply the gathered knowledge to France's nuclear facilities, both for present and future approach to increase reliability, resilience and effectiveness of their emergency mechanism, in case of extreme events.

SINAPS@ represents the engineering seismology facet of this scientific context: it was conceived to assess the uncertainties of databases, methods and procedures adopted at each and everyone of the steps required for a detailed seismic hazard analysis. All of these aspects target the ultimate goal of a better understanding of the whole physical phenomenon which entails earthquake-related nuclear disasters. In this sense, a modern risk mitigation approach has been followed: the main objective is to identify or quantify the seismic margins resulting from every assumption made in the design process, from the definition of the IM to the selection of the structural demands, taking into account the uncertainties related to conservative choices and design strategies. Figure 1.5 sketches the main work-packages of the SINAPS@ project. The SINAPS@ work-packages cover SINAPS@ main aims can be listed as follows:

- to explore uncertainties inherently to available databases;
- to increase knowledge of physical processes, design methods at each step of seismic hazard evaluation and structural vulnerability;

[4]CEA, EDF, École Normale Supérieure de Saclay, CentraleSupélec, http://www.institut-seism.fr/en/about-us/

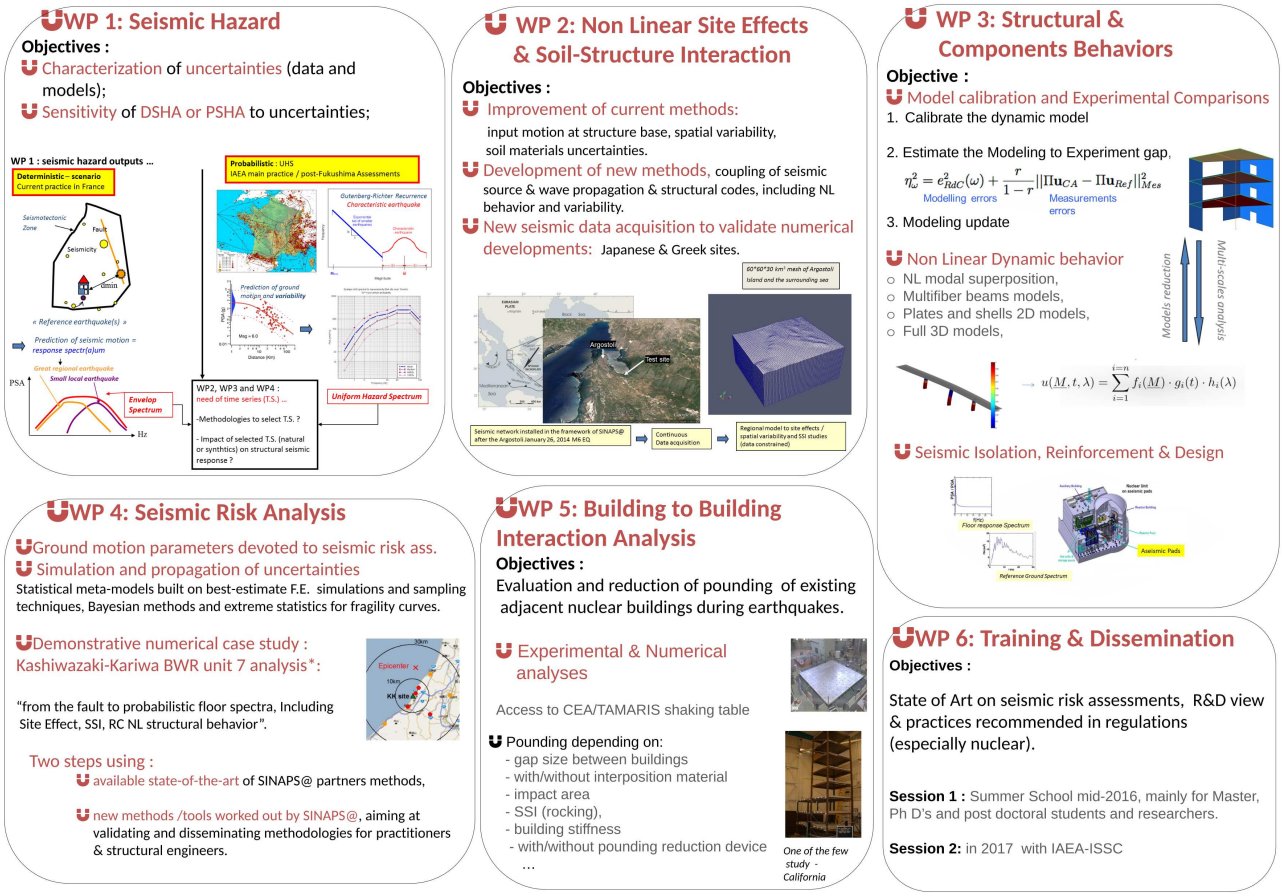

Figure 1.5: Work packages of the SINAPS@ project.

- to identify or quantify the seismic margins related to the assumptions made (selection of seismic design level and strategies).

SINAPS@ project will help to address safety issues highlighted following the Fukushima accident and French studies additional security, especially with regard to seismic safety margins.

KARISMA numerical benchmark

The great computational power reached in engineering seismology widened the horizon of the predictive exercise. Most of the modelling simplified assumptions, inherited from an obsolete engineering practice, constrained by a poor technology, incapable to follow the evolution of complexity of the mathematical and physical models, may be carefully dropped today. However, the increased complexity granted by the ease in handling and solving huge computational burdens, entailed the need for comparison with certified traditional models. That is why it became of great interest to run numerical benchmarks, so to compare and validate the computational resources in blind tests issued from canonical cases or either from real case studies.
In this sense, my research activity can be considered a follow up of the KARISMA numerical benchmark (KAshiwazaki-Kariwa Research Initiative for Seismic Margin Assessment), which took place between 2011 and 2013 and which targeted the Kashiwazaki-Kariwa Nuclear Power Plant and its seismic response during the *Niigata-Ken Chūetsu-Oki* . Indeed, the core part of the thesis covers the topics encapsulated in Work Package 4, since a demonstrative case was taken into consideration (see Chapters 2). KARISMA exercise included benchmarking on the analytical tools and numerical sim-

ulation techniques for predicting seismic response of NPP structures (in linear and non-linear range), site response, soil-structure interaction (SSI) phenomena, seismic response of piping systems, sloshing in the spent fuel pool and buckling of tanks. The benchmark is primarily based on data provided by Tokyo Electric Power Company (TEPCO). It is not linked to seismic re-evaluation of KKNPP which was carried out by TEPCO itself (IAEA, 2014).

1.3 Outline of the report

This work tackles the problem of defining reliable and exploitable earthquake intensity measures. The major outcome is the provision of realistic yet synthetic input ground motion for further vulnerability studies. Specifically, I focused on the multiple aspects required to picture realistic seismic scenarios at a regional scale, which aid in defining the realistic IM values and corresponding time-histories. The main scope is to contribute to reach the *ultimate dream* represented by a multi-tool computational platform which can quickly and reliably estimate ground shaking effects over wide urban areas or at specific sites of economic and human relevance. A huge effort was made in grouping and linking all the tools and the methods employed at different stages of a seismic analysis, trying to effectively compute the convolution of all the factors (i.e. investigate the importance of including 3D basin effects on ensemble averaged long-period ground motions, comparing ground motions computed in 1D and 3D crustal models) affecting the level of shaking at the site, i.e. radiating source, path effect and local site-effects. An omni-comprehensive (or *holistic*) approach has been followed, consisting in characterizing each factor that may have an impact on the wave-field radiated from the fault and propagating towards the site. An vulnerability-oriented critical review of the common IM employed in engineering seismology is discussed, stressing the importance of the assumption made in their definition compared to the more stringent and less characterized near-source conditions. The ultimate goal of this piece of research is to assess the uncertainty related to each modelling assumption when it comes to understand and reproduce complex phenomena as strong ground motion scenarios, serving as solid foundation for further vulnerability studies on critical structures, such as nuclear power plants. In doing so, I took advantage of a series of new generation numerical tools, employed at different stage of the analysis, and widely described. This work can be placed partially within Work Package 1 and Work Package 2, in terms o uncertainty quantification of seismic databases (described in Chapter 2) and assess non-linear site-effects from a engineering point of view (described in Chapter 2 and partially in Chapter 3). This part of the thesis aims to provide a deeper insight on the uncertain determination of dynamic soil properties and geological profile, due to the epistemic contribution related to the possible inaccuracy of the site investigation method. Those issues are widely discussed, highlighting the difficulties arising when assessing near-field site response from an engineering point of view. From another perspective, a closer view of those site-effects is provided, by investigating the contribution of either the non-linear soil behaviour and the aleatory contribution of small-scale random variability of the soil properties. The working approach follows the SCEC philosophy to explore and to validate the effects of empirical and statistical models of velocity heterogeneities of Central California upon past earthquake scenario, so to estimate the the significance of the lowest (S-wave) velocities as frequencies increase along with the significance of progressively including geotechnical layers.

2

Seismic Site Response at Kashiwazaki-Kariwa Nuclear Power Plant in 2007 Chuetsu-Oki Earthquake

"The only people who see the whole picture are the ones who step outside the frame."
– Salman Rushdie, The Ground Beneath Her Feet

2.1 Summary

The aim of this chapter is to clarify some aspects concerning the seismic site effects that took place at the Japanese nuclear site of Kashiwazaki-Kariwa (KK), during the 6.6 *Niigata-Ken Chūetsu-Oki* earthquake (July, 16th 2007). Due to the relative small source-to-site distance and shallow hypocenter depth, the mentioned seismic scenario is extremely complex to be characterized, although very appealing due to the consistent seismic record database available. The site characterization presented herein targeted two down-hole arrays of strong motion accelerometers, installed within the nuclear site. Those recordings allowed to track the seismic wave path (origin and direction of propagation towards the surface) and they were studied to outline the site response dependency on the direction of motion. Moreover, those records were to check the two V_S profiles (estimated by in situ PS logging), by applying borehole interferometry technique. In one case, an improved agreement with the empirical amplification functions was obtained using a smoothed V_S profile. The main non-linear features highlighted by signal processing were globally reproduced by means of equivalent linear analyses. The strong influence of the considered motion direction was assessed.
Parts of this chapter has been object of a paper in an international conference proceeding (Gatti et al., 2015) and of a scientific paper recently submitted to the *Bulletin of Earthquake Engineering*.

2.2 Introduction

Seismic site effects represent the modification (in amplitude, direction and frequency content) that the shallow Earth's layers induce on the radiated wave field while travelling from the nucleation point on the seismic fault to the considered site. In the last few decades, complex 3D non-linear site-effects have been extensively observed and studied (e.g. during the 1985 Mexico City, 1994 Northridge, 1995 Hyogoken-Nanbu (Kobe) and the more recent 2011 Tōhoku earthquake). Local soil conditions within the upper part of the Earth's crust plays a crucial role in the seismic design of building's foundation, since they dramatically increase the destructive power of seismic ground motion on structural

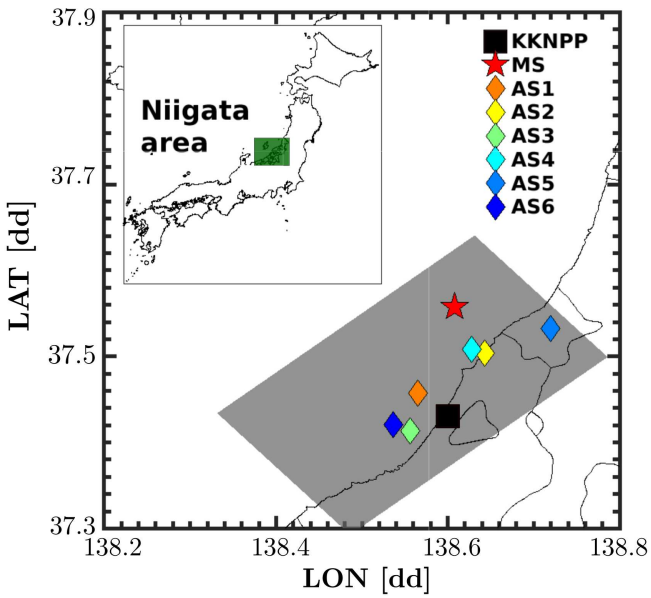

Figure 2.1: Map of the area in the surroundings of the KK-NPP. Epicentres of main shock (MS) and selected aftershocks (AS) are depicted; grey shaded area axes represents the fault projection. Small axes: map of Japan highlighting the region of Niigata (west Japan).

components (Faccioli and Vanini, 2003; Regnier et al., 2013). Namely, the main features to be assessed are (1) the (de-) amplification due to soil layering, (2) the scattering caused by interactions with geological interfaces and topographical surfaces, (3) the time-dependent non-linear stiffness decay of geomaterials, triggered at relative small strain magnitudes (Hashash and Groholski, 2010). In near-source conditions, uncertain faulting mechanisms and propagation path add further complexity to the problem. In such a case, addressing seismic hazard evaluation should be re-examined carefully, especially relatively to critical structures as nuclear power plants.

In this context, strong ground motion recordings represent a great source of information in order to calibrate numerical models for site-specific seismic response analyses. For this purpose, arrays of seismometers deployed down-hole, till the depth of the *engineering bedrock*, provide an additional relevant evidence on the effect of shallow geology on the seismic motion. Signal processing techniques unravel the non-linear evolution of soil properties, as well as some major features of ground motion in near-source conditions (e.g. the possible impulsive nature of velocity records). Nevertheless, the exploitation of record databases is not always straight-forward and the interpretation of results can be difficult.

In this chapter, borehole recordings were processed to characterize the seismic site effects observed during the M_W6.6-6.8 *Niigata-Ken Chūetsu-Oki* (NCO) earthquake, occurred on July, 16th 2007 (10:13 UCT) off the coast of the Niigata prefecture (Japan). The NCO earthquake affected an area of approximately 100 km of radius along the coastal line of South-West Niigata prefecture, till a maximum depth of 17 km (Pavlenko and Irikura, 2012). The seismic sequence (see further details in Table 2.1) caused the shut down of the Kashiwazaki-Kariwa Nuclear Power Plant (KK-NPP), located close to the epicentre location (see Figure 2.1). The site (composed by 7 generators and whose map is presented in Figure 2.2) is located on the hanging wall of the mentioned fault, above a region of relatively high slip (Ozawa, 2008). The strong motion sensors indicated that during the earthquake the site experienced nearly twice the ground shaking (in terms of Peak Ground Acceleration,) that was considered in the plant design. The rather high variability of PGA values within the area of the plant is representative of directivity features of the source radiation (Pavlenko and Irikura, 2012). Accord-

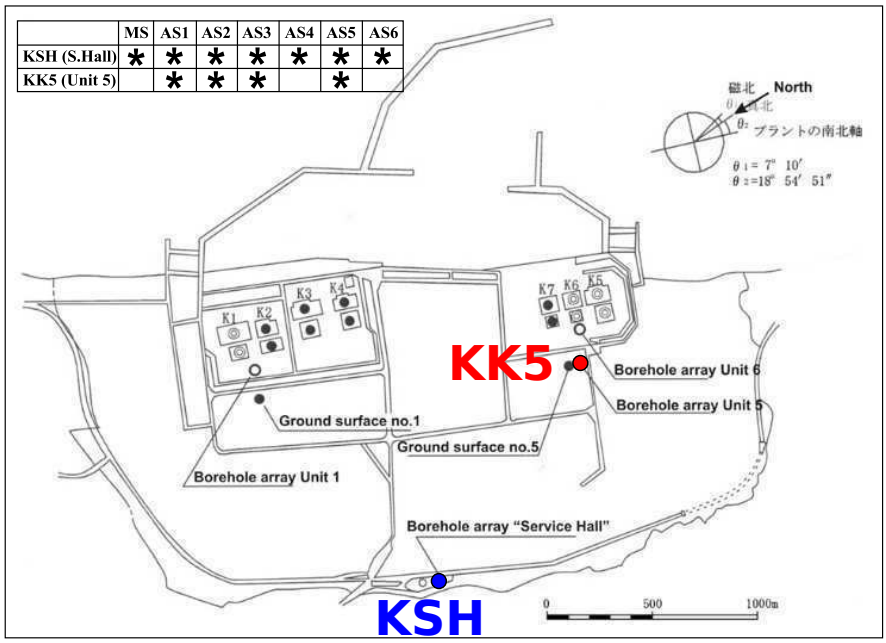

Figure 2.2: Georeferenced and scaled map of the Kashiwazaki-Kariwa Nuclear Power Plant (courtesy of TEPCO (2008)). The site has 7 units, with four units (Units 1-4) at south side of the site and the other three units (Units 5-7) only about 1.5 km away from Units 1-4.

ing to Kokusho and Suzuki (2008), the acceleration spectral response is unexpectedly high at long period. Pavlenko and Irikura (2012) made an extensive study to assess the non-linear site response at KK-NPP. They performed one-dimensional analyses on representative soil columns (i.e. horizontally layered models and shear wave vertical propagation). They subdivided the soil layers into three groups (e.g. by classifying them according to their values) characterized by batch normalized stress-strain relationship. For each group of layers, they generated 250 different stress-strain relations, from which they selected the curves showing the best-fit approximation to the observed records (the main shock or the aftershocks) at the depths of locations of the recording devices. They performed their calculations using the method proposed by (Joyner, 1975). The reduction of the shear moduli estimated in the upper softer layers was about 30-35% during the main shock and about 1.5-3% during the aftershocks.

Another extensive work on the seismic characterization of the Kashiwazaki-Kariwa Nuclear Power Plant during the NCO earthquake was performed by Yee et al. (2011). The authors focused on the simulation of site response recorded free-field at the Service Hall. They compared equivalent linear and full non-linear soil column models, adjusting input parameters (i.e. $\frac{G}{G_{max}} - \gamma - D$ curves) according to *in situ* and laboratory tests on soil samples from KK-NPP. They assessed the non-linear site response during the NCO main shock, in an extensive study which encompasses a liquefaction analysis.

Hereafter, further investigations on the geotechnical seismo-induced site effects at the KK-NPP are performed. First of all, this study aims to assess the features of near-source ground motion and to describe the variability of seismic response within the KK-NPP. To this end some representative locations were selected on the base of the quantity and quality of the available seismic records. On the other hand, performance of standard numerical approaches (based on 1D soil column models and the equivalent linear approach), as well as their applicability, are tested in such complex scenario. This is a crucial step before any further 3D model involving complicated surface geology and faulting mechanism. In Section 2.3 a general overview on the main features of the incident wave motion is presented, by proving its quasi-vertical propagation as well as its impulsive nature (symptomatic of

near-fault conditions). Besides, some insight is presented both on the directivity effects registered and on the borehole de-amplification. In the following (Section 2.4) the estimated geological configuration beneath the surface is checked by means of seismic interferometry. The latter technique is suitable to assess the non-linear evolution of V_S values during shock. Finally, in Section 2.5 the results obtained via equivalent linear analyses on 1D soil columns are compared to the recorded response, for both the aftershock and the main shock.
In Table 2.1 the ensemble of seismic events considered herein is listed. PGA and PGV values registered at two borehole stations are reported.

Table 2.1: List of the earthquake considered in the chapter (courtesy of TEPCO, 2007). M_{JMA} is magnitude according to the Japanese Meteorological Agency, R represents the epicentral distance in km. - and - represents the Peak Ground Acceleration/Velocity on the Horizontal and Vertical directions respectively. SG1 and G51 denote the surface stations of boreholes KSH and KK5 respectively. Not available values (due to data loss) are reported as -.

	M_{JMA}	[km]	PGA_H[cm/s^2]		PGA_V[cm/s^2]		PGV_H[cm/s]		PGV_V[cm/s]	
			SG1	G51	SG1	G51	SG1	G51	SG1	G51
MS	6.8	16	433	-	583	-	123	-	44	-
AS1	3.7	5	36	23	42	20	1	1	0.7	0.4
AS2	5.8	10	189	275	188	88	25	22	9	4
AS3	4.2	4	50	42	36	23	2	2	0.8	0.4
AS4	4.4	10	70	-	65	-	2	-	1	-
AS5	4.8	17	77	101	50	27	5	5	2	1
AS6	3.2	6	34	-	26	-	1	-	0.5	-

2.3 Overview on seismic site response at KK-NPP

The *Niigata-Ken Chūetsu-Oki* earthquake occurred as a result of a buried reverse-slip motion nucleated at the estimated hypocenter depth of 8 km and causing no significant surface rupture (Aochi et al., 2013a). Despite the dense observation network in operation (considering Kik-Net records as well) and the extensive number of seismological studies, the faulting mechanism remains uncertain (see for instance Aoi et al., 2008; Kato et al., 2008). Moreover, the distance of the nuclear site of Kashiwazaki-Kariwa to the surface projection of the fault (i.e. Joyner-Boore distance) is =0 km, whereas the rupture distance is =16 km (Yee et al., 2011).
By the time the 2007 NCO earthquake occurred, KK-NPP was instrumented with an older and a more recent systems of accelerometers. The horizontal recording devices (EW and NS respectively) are oriented with respect to the Plant North (see Figure 2.2). The *Tokyo Electric Power Company* (TEPCO) provided the azimuthal deviation of some seismometers due to their installation down-hole. Ground motion at 33 locations were registered by the new system, although the recordings of the old system obtained at other 66 locations (including two free-field down-hole arrays and most structural arrays) were lost with the exception of the peak values (Kayen et al., 2009).
In this study, the attention is focused on the seismic response occurred at two down-hole arrays, installed respectively at Unit 5 (KK5 set) and at the Service Hall (KSH set), to characterize the site response in the structure's surroundings and in the assumed free-field conditions. In Figure 2.2 the locations of those two sites are illustrated along with the KK-NPP planimetry: KK5 is located nearby the north-east group of reactors, while KSH is placed at the entrance, on the south. The distance

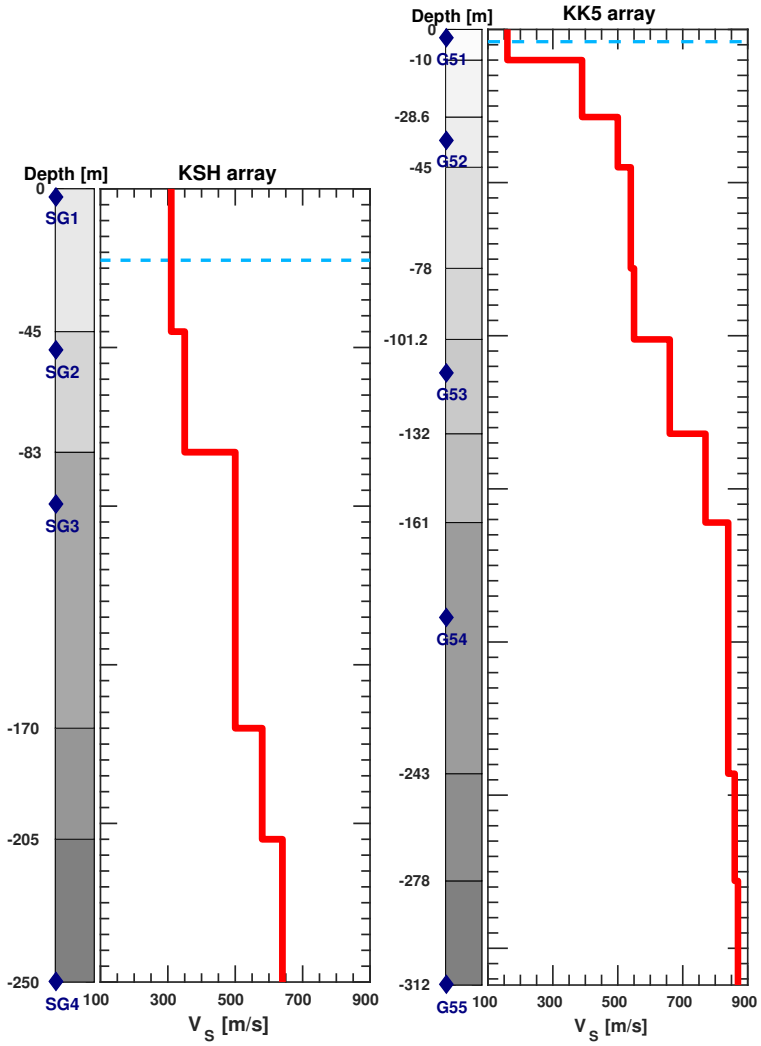

Figure 2.3: V_S profiles and seismometers locations at (a) array KSH (Service Hall) and (b) KK5 (Unit 5).

between the boreholes is relatively large (approximately 1 km) and the geology and topography quite complicated. Strong motions accelerometers are installed and PS-logging V_S profiles were provided by TEPCO, as well as reference $\frac{G}{G_{max}} - \gamma - D$ curves for four different soil layers (where and are initial and secant shear moduli, the shear distortion and the hysteretic damping). Figure 2.3 shows the mentioned V_S profiles.

The available records revealed that during the NCO earthquake the nuclear site experienced nearly two times the plant design shaking intensity (in terms of PGA). For instance, recorded accelerations reached up to 6.80 m/s^2 (EW component) at the basement of Unit 1, largely above the design specification for safe shutdown, i.e. 4.50 m/s^2 and well above the rapid restart specification for key equipment in the plant, i.e. 2.73 m/s^2. At the reactor basements of Unit 2, 3 and 4 (located on the southwest part of the plant), accelerations of 6.06, 3.84, and 4.92 m/s^2 respectively were recorded (EW component), whereas at Unit 5, 6 and 7 (located on the northeast part of the site) PGA were slightly lower (4.42, 3.22, and 3.56 m/s^2 respectively). Besides, ground motion exceeded 0.5 g on outcropping bedrock.
Concerning the acceleration response spectra (Sa), Figure 2.4 shows the recorded at the Unit 7 reactor building basemat (along the EW and NS directions), compared to the design spectrum employed by the TEPCO (IAEA, 2014). As confirmed by many authors (Kokusho and Suzuki, 2008, among oth-

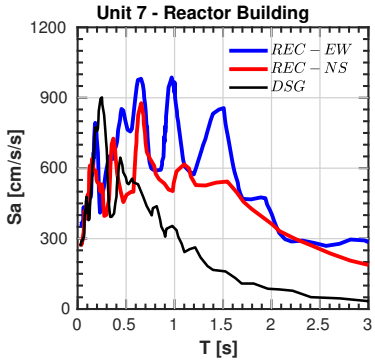

Figure 2.4: Pseudo-acceleration response spectrum Sa at Unit 7 reactor building basemat. Blue and red lines refer to the recorded response spectrum during the NCO main shock, along the EW and NS direction respectively. Black line refers to the design spectrum for the reactor building basemat (TEPCO).

ers), the recorded ground motion entailed a rather amplified low period component, which exceeded the design response. However, post-seismic site inspections reported minor structural damages to the Kashiwazaki-Kariwa Nuclear Power Plant . Kayen et al. (2009) observed a discrepancy between the measured and the design PGA, along with the apparent absence of structural damage. They attributed this occurrence to the conservative design in the equivalent static design procedure used in Japan, i.e. redundant structures with large *over-strength*, large *importance factor* (≈ 3).

2.3.1 Predominant vibration period

From the point of view of ground motion amplitude, the discrepancy between recorded and design response can be explained by considering not only the great PGA values but also the corresponding Peak Ground Velocities (PGV). Figure 2.5 shows the relationship between PGA and the inverse of the *predominant harmonic period* , recorded at KK-NPP during the NCO cluster:

$$\frac{1}{T_{V\backslash A}} = \frac{\alpha^{PGA}_{(\xi=5\%)}}{\alpha^{PGV}_{(\xi=5\%)}} \frac{PGA}{2\pi PGV} \tag{2.1}$$

Eq. (2.1) (proposed by Green and Cameron (2003) and Kawase (2011)) is based on the assumption that ground motion is dominated by the harmonic component corresponding to the intersection between the constant spectral acceleration and velocity regions of a 5% damped Newmark-Hall type spectrum constructed using the actual PGA-PGV values (Green and Cameron, 2003). In this sense, and are the median spectral amplification factors for horizontal motion proposed by Newmark and Hall (1982) for the constant velocity and constant acceleration regions of 5% damped response spectra. Green and Cameron (2003) suggest values of $\alpha^{PGA}_{(\xi=5\%)} \cong 2.12$ and $\alpha^{PGV}_{(\xi=5\%)} \cong 1.65$.
Black dashed lines in Figure 2.5a represent respectively iso-PGA (i.e. 800-2700 cm/s^2) and iso-PGV lines (i.e. 100-250 cm/s), the latter with a slope from left-down side to right-up side. Based on the observations in 1995 Kobe earthquake, those lines delimit the region above which major damages are expected (Kawase, 2011), and roughly correspond, according to the relationship between the Modified Mercalli Intensity (IMM) and PGV/PGA values proposed by Wald et al. (1999), to IMM $\cong$X. As shown in Figure 2.5b, a few points range within the polygonal area included between the mentioned black dashed lines. Such points refers to the main shock (MS) and to devices placed on (1) the turbines at the basement level (1T2, 2T2 and 3T2, on turbines at Units 1,2 and 3 respectively), (2) on the reactor of Unit 1 at first floor (1R1) and (3) at the ground surface nearby Unit 1 (point 1G1).

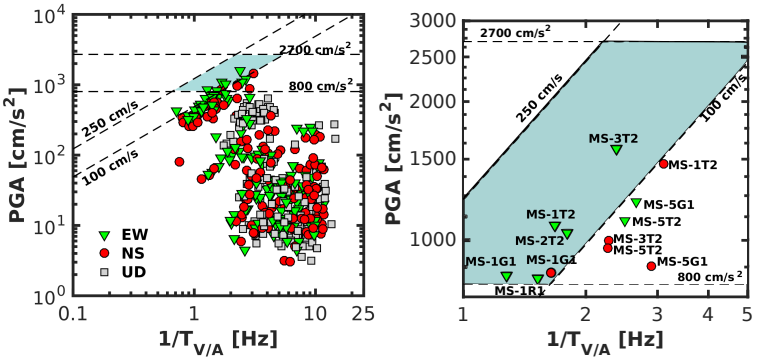

(a) (b)

Figure 2.5: PGA values with respect to the inverse of the *equivalent harmonic dominant period* $\frac{1}{T_{V\backslash A}}$ for all the record database provided by TEPCO.(a) all the values in the two directions (EW-NS); (b) zoom on the area delimited by the dashed lines representing the PGA-PGV limit values and suggested by (Kawase, 2011), after Kobe earthquake.

Figure 2.5 is in agreement with the evidence highlighted by site inspections (see for example IAEA, 2014), i.e. that the large ground deformations damaged Unit 3 (although with no particular safety significance).

2.3.2 Directivity and *hanging wall* effects

Although not exhaustive, $T_{V\backslash A}$ is a significant and intuitive index of the severity of the ground motion, but waveforms should be analyzed carefully too. The velocity pulse coupled with a corresponding large peak displacement considerably enhance the damage potential (Cox and Ashford, 2002). Therefore artificial *spectrum-compatible* ground motions are generated based on recorded motions selected as *seeds*, modified to possess not only PGA but also duration, velocity and displacement similar to those of the target design seismic event. Intuitively, a large displacement imposed at low velocity does not have a significant damaging potential since the structure adapts itself in a *quasi-static* way (Cox and Ashford, 2002). In near-field, large velocity pulses incorporate the cumulative effect of most of the seismic radiation from the fault dislocation (Bolt, 2004). A ground shaking characterized by strong velocity pulses exerts an extreme demand on the structural components as proved by several studies (e.g. Mavroeidis and Papageorgiou, 2003; Mavroeidis et al., 2004; Luco and Cornell, 2007). Therefore, the selected seed motions should have phase spectra that entail a definite velocity pulse. As a matter of fact, several authors argued the pulse-like shape of some velocity time-histories recorded at KK-NPP. For instance, (Uetake et al., 2008) observed three significant pulses at KSH array (i.e. Service Hall), possibly associated to the three major asperities identified on the fault plane, via waveform inversion. In this context, the occurrence of velocity pulses at the Kashiwazaki-Kariwa Nuclear Power Plant was verified considering the borehole records available and by classifying them as according to the ranking criterion proposed by Baker (2007) (excluding late arrivals and small events). Figure 2.6 schematically presents the results of the above-mentioned classification. The Pulse Indicator (PI) proposed by Baker (2007) (see Eq. (2.2)) is based on two predictor variables: the Peak Ground Velocity (PGV) of the residual record - obtained by subtracting the extracted pulse from the as-recorded time-history - divided by the original record's PGV (i.e. PGV-ratio, reported along the x-axis in Figure 2.6b) and the energy of the residual record divided by the original record's energy (i.e. the Energy-ratio, reported along the y-axis in Figure 2.6c and computed by dividing the Cumulative

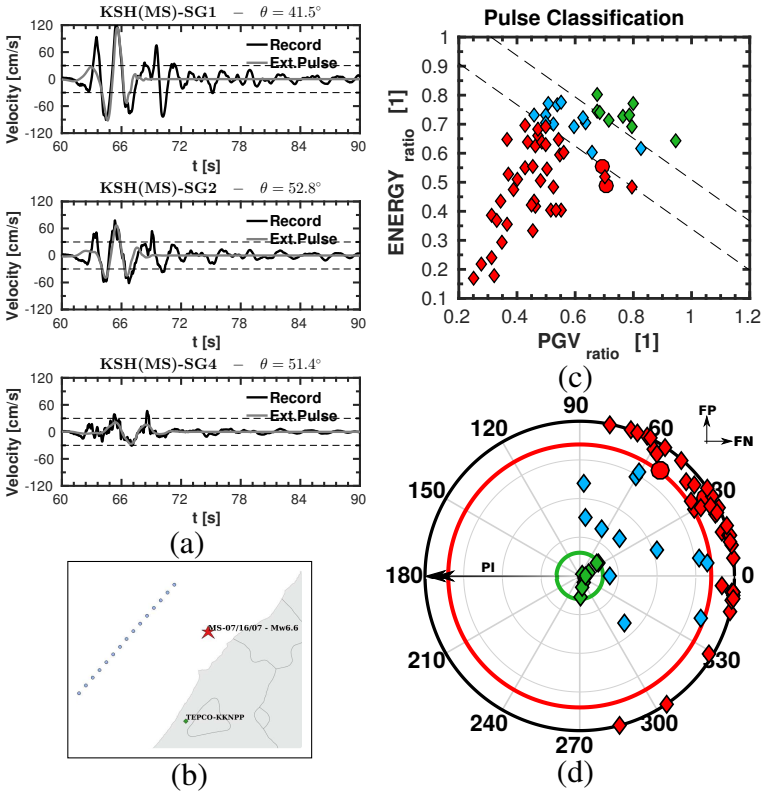

Figure 2.6: Pulse classification for borehole records at KK-NPP (horizontal components). (a) Comparison between recorded velocity signals and extracted pulses. (b) Map of the surrounding of the KK-NPP with the causative fault trace and NCO earthquake main shock. (c) Pulse classification according to Energy-ratio and PGV-ratio. Red and green points represent respectively pulse-like and non-pulse-like signals, whereas light-blue points cannot be clearly classified automatically (according to predictor factor proposed by (Baker, 2007)). Circles indicate the extracted pulse fulfils criteria CT1 and CT2 (mentioned in this paragraph). (d) Polar plot portraying the angles at which pulses were extracted, with respect to the fault-normal (FN) and fault-parallel directions (FP). The angle corresponds to the one that provides the highest PI.

Squared Velocity(CSV) of the residuum by the original record's CSV).

$$PI = \frac{1}{1 + e^{-23.3+14.6PGV_{ratio}+20.5Energy_{ratio}}} \tag{2.2}$$

Records with PI scoring above 0.85 and below 0.15 were classified as pulses (red circles in Figure 2.6b and Figure 2.6c) and non-pulses respectively (green diamonds in Figure 2.6b and Figure 2.6c). The remaining time-histories cannot be classified since they do not comply the seismological criteria mentioned above (i.e. light-blue diamonds in Figure 2.6b and Figure 2.6c). In pulse identification, recorded components were rotated by 5 different angles to check the preferential direction they mostly come from (with respect to fault normal (FN) and fault parallel (FP) directions, corresponding to $0°$ and $90°$ in Figure 2.6c). In Figure 2.6c each point corresponds to the direction at which the greatest pulse-like wave form has been extracted. The pulse-like wave field is not oriented along a preferential direction although most of the extracted pulses come from a $+30°$ angle with respect to the FN direction, approximately along the site-to-epicentre direction. Since the KK-NPP is located on the fault hanging wall of a buried reverse-slip fault, wave pulses were also observed on the vertical component, although not shown here for brevity. High PGA values along the vertical direction are in agreement with the rapid uplift of the ground during the fault slip, caused by elastic rock rebound effects (Bolt, 2004). This result is typical when forward directivity condition is met. Further studies on

the so called *hanging wall effect* for this earthquake may be found in Spudich et al. (2013). Although the followed procedure does not discriminate the mechanism originating the pulse-like recordings, it helps in quantifying the near-field effects for engineering purposes, barely described by traditional tools (such as the pseudo-spectral acceleration response).

2.3.3 Verticality of the propagation of wave motion

Another crucial step prior the construction of a realistic ground motion scenario is the detection of wave field incidence. When simplified 1D analyses are performed, one must ensure the input signals to have a quasi-vertical incidence. To this end a polarization analysis of the records was carried out, consisting into a linear transformation of the three components of motions into the principal ones (e.g. vertical and radial/transverse projections with the respect to the source-to-site direction). In fact, those components are associated to the eigenvectors/values of the cross-correlation matrix (at zero lag time) between the three components. The azimuth angle AZ and the angle of apparent incidence IN (e.g. angle of deviation from the vertical) were estimated within a time-window sliding along the whole record duration. Those parameters defines the wave trajectory along the whole records length, considering time window of 0.1-0.5 s and low-pass filtering up to 2.5-5 Hz to get stable results. In Figure 2.7 stereo-net projections summarize the average wave incidence computed at P-wave arrival time (northern axis refers to local KK-NPP's one). Signals drift vertically towards the surface, as

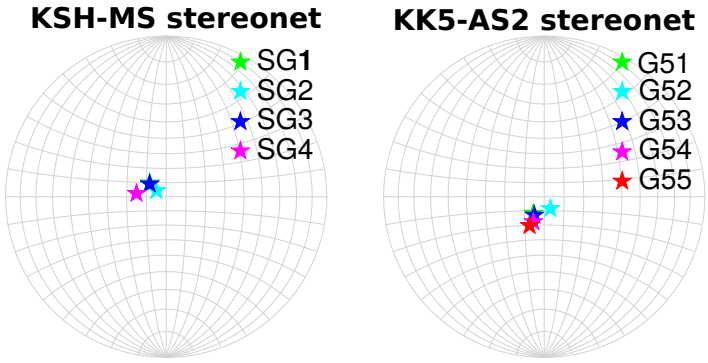

(a) (b)

Figure 2.7: Wulff projections indicating wave-field incidence at each accelerometers' location.(a) Stereo-net referring to main shock recorded at KSH; (b) stereo-net referring to aftershock 2 (the most intense) at KK5.

outlined by Gatti et al. (2015). Nevertheless, such rectilinearity decays in time. Concerning the azimuth, it must be noted that the focal mechanism is still uncertain (Aochi et al., 2013a). This is due to the difficulties in deconvolving the source mechanism from the effects of 3D geological structures. Two potential fault planes have been proposed so far: a NW dipping plane striking at 215° and a SE dipping one at 49° strike. Which of these two planes is associated with the main shock rupture is unresolved (see Aoi et al., 2007; Miyake et al., 2010). Aftershock locations fell along both planes, although the majority of the aftershocks were located along the SE dipping plane (strike 49° Kayen et al., 2009; Aochi et al., 2013a). Estimated azimuth values are coherent with the observed tectonic mechanisms. The quasi-vertical propagation of the incident wave field, maintained along the whole borehole length, supports modelling the problem by a 1D soil-column analysis, due to small influence of spurious waves impinging the borehole at sub-horizontal incidence.

2.3.4 Horizontal principal axes of the ground motion

Once vertical incidence has been proven (see previous paragraph), standard 1D soil column analyses may be carried out, assuming one horizontal component of the motion at time. This shortcoming can be resolved by finding preferential direction of motions, e.g. the two components associated to maximum and minimum energy release. For instance, Penzien and Watabe (1975) defined the principal axes of ground motion as the directions along which the three components of motions are statistically independent. They assumed projected time series uncorrelated, although uncorrelated variables are not *a priori* statistically independent. Along the *major principal axis*, the motion amplitude, measured for instance as Arias intensity (Rezaeian and Der Kiureghian, 2012), is the highest. The major principal axis is assumed horizontal and pointing towards the direction of the earthquake source (Penzien and Watabe, 1975). However, this hypothesis appears not to be always verified, especially in a near field regime (as further recent investigations by (Rezaeian and Der Kiureghian, 2012) proved). Assuming quasi-vertical ground motion and the vertical component as the less intense, the second horizontal principal component is denoted as the *intermediate principal component* (int) (Rezaeian and Der Kiureghian, 2012; Penzien and Watabe, 1975). Figure 2.8 shows the mentioned cross-correlation coefficient varying with the in-plane rotation angle for two selected records at SG1 (for KSH site) and at G51 (for KK5 site). Penzien and Watabe (1975) examined the correlation coefficient ρ_{XY} for

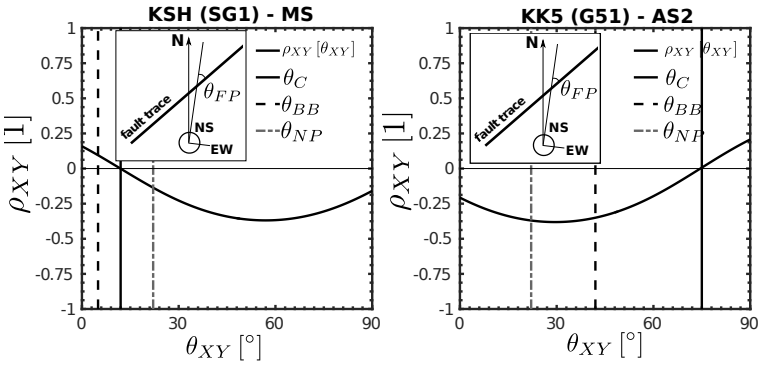

(a) (b)

Figure 2.8: Cross-correlation coefficient ρ_{XY} varying with rotation angles angle at SG1/G51. makes the ρ_{XY}=0 at the considered depth. θ_{BB} (black dashed line) represents the angle corresponding to ρ_{XY}=0 for accelerometers (a) SG4 and (b) G55 respectively. θ_{NP} (grey dotted line) is the angle between the strike directions of the fault and the seismometers' reference system.

a number of recorded ground motions, varying the angle θ_{XY} by which the in-plane components are rotated. They did not observe a significant time-dependence so that ρ_{XY} was computed for the entire length of the record. For each signal, the *correction angle* θ_C refers to the in-plane rotation angle at which ρ_{XY} vanishes, thus defining major and intermediate axes at that depth. Such an angle (the solid black line in Figure 2.8) was compared to and to , where θ_{BB} corresponds to the correction angle computed at the deepest sensor in the array (SG4 and G55 respectively), whereas θ_{NP} is measured between seismometers and fault plane strike directions (see the miniature in Figure 2.8b). For the main shock (Figure 2.8a) θ_C values calculated for array KSH are coherent with the those estimated by Pavlenko and Irikura (2012). They corrected the orientations of the sensors based on the recorded low-frequency (0.01-0.2 Hz) trajectories within a 3s-wide window located just after the first wave arrival time. They obtained correction angles θ_C of 6°, 8°, 4° for sensors SG2, SG3 and SG4 respectively. θ_C and θ_{BB} are close to θ_{FP} when considering the main shock, confirming somehow a dominant direction of the motion (i.e. towards the fault asperities). In this sense, maj-int directions align to the FN/FP ones. This is not true for the aftershocks sequence, e.g. for aftershock 2 (see

Figure 2.8b), where the three mentioned angles differ one from each other.
However, the fact that $\theta_C \neq \theta_{BB}$ in both cases may be due to the local geological conditions that deviate the principal axes of motions from down-hole towards the surface (see Section 2.4).

2.3.5 Rotation independent horizontal response spectra

Ground Motion Prediction Equations (GMPEs) are usually formulated exploiting some sort of measure of the as-recorded site response. To this end, the signals recorded along the two horizontal components are combined into a single measure of shaking intensity, usually by computing the geometric mean of their related response spectra (Somerville et al., 1999), sometimes with a correction of the standard deviation of the predicted motions to approximate a randomly chosen component of ground motion (Boore et al., 2006; Boore and Joyner, 1997). Although the geometric mean reduces the aleatory uncertainty in ground-motion prediction equations (Boore et al., 2006), a fundamental drawback holds: geometric mean is not invariant to the orientation of the sensors. Therefore, in the ideal case of noise-free, linearly polarized ground motion, the component along the direction of polarization would give the maximum spectral response, whereas on the orthogonal direction it would be zero (and so the geometric mean), regardless of the amplitude of the polarized ground motion.
Figure 2.9 shows the pseudo-acceleration spectra (PSA) at SG1 and SG4 (array KSH, at the Service Hall of KK-NPP site) for the two horizontal components rotated by an angle θ_{BB} (see Section 2.3.4) compared to their geometric mean GM (green line in Figure 2.9). The former angle makes the horizontal time-series at SG4 uncorrelated (i.e. maj-int components), but signals rotated by the same angle at SG1 are generally correlated (see Figure 2.8a). The difference between the single-component PSAs and their geometric mean (GM) is more significant for SG4 (uncorrelated signals) rather than for SG1 (correlated time-series), as stated by (Boore et al., 2006). This trend attenuates close to the surface (e.g. at SG1, as depicted in Figure 2.9b). At SG4 major (X) and intermediate (Y) PSA values are visibly different over the period range between 0.1 and 2 s. The proximity of the source is predominant. Non-linear effects attenuates this trend at surface (SG1, Figure 2.9b). Despite the benefit of reducing the discrepancy between the two directions and the geometric mean, the de-amplification leads to higher PSAs along the intermediate direction for some periods. This proves that although major and intermediate directions are usually related to stronger and weaker components of motions in terms of time series, it might not be always the case when considering spectral ordinates at different periods.

2.4 Identification of non-linear site-effects

2.4.1 Borehole (de-) amplification

The aim of this section is the identification of those features of recorded ground motions, both during the main shock and the aftershocks, that may support the evidence of non-linear soil response. A first hint of non-linearity taking place is given by plots in Figure 2.10, where a spectral amplification function (SAF) is introduced as the ratio of PGA at ground surface with respect to the corresponding PGA at depth (). Site Amplification Factors were computed at KSH and KK5 by considering two couples of seismometers each: (1) SG1-SG2 at GL-2.4 m and GL-50.8 m and SG2-SG4 at GL-50.8 m and GL-250 m respectivelyat KSH; (2) G51-G52 at GL-2.7 m and GL-36 m and G52-G55 at GL-36 m and GL-312 m respectively for KK5. In the case of linear response, the trend of SAF would be constant, independent of PGA_R, supposed not to be affected by non-linearity. As a matter of fact, on one side the KK5 array shows this trend, having recorded only the aftershocks (Figures 2.10c- 2.10d), while, on the other side, KSH shows a clear tendency to a decreased SAF for increasing PGA_R beyond about 0.1 g (Figures 2.10a- 2.10b), which is often considered as the threshold for significant

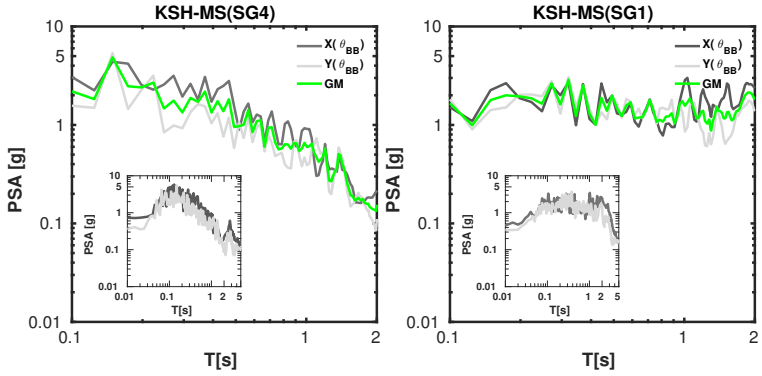

(a) (b)

Figure 2.9: Pseudo Spectral Horizontal Acceleration spectra (PSA) for NCO main shock recorded at the KK-NPP Service Hall (KSH). (a) PSA for signal recorded at GL-250 m (SG4); (b) PSA for signal recorded at GL-2.4 m (SG1). Small axes show the spectra for a larger band of natural periods. Dark grey and light grey lines refer to the rotated components X and Y, by the angle θ_{BB} at which the two as-recorded horizontal components EW-NS at SG4 (base of the borehole) are uncorrelated. Main axes represent a zoom between 0.1 and 2 s. Green line represents the geometric mean of the X-Y components.

non-linear response in soft soils (Kramer, 1996, e.g.). The latter tendency is observed not only when considering the shallowest instrument (SG1), but also when considering SG2, placed at GL-50.8 m, meaning that non-linear effects may have occurred below this depth. The presented results agree with the results presented by Pavlenko and Irikura (2012). The authors concluded that the motion at the Service Hall was de-amplified during its propagation to the surface from the depth of 250 m because of the non-linearity of the soil response. At the same time, at Unit 5 the ground motion was amplified on the surface if compared to the motion at 200-300 m, indicating that the seismic waves resonant amplification prevailed.

2.4.2 Validation of shear-wave velocity profile

The entity of recorded seismic site-effects strongly depends on the initial, small strain shear wave velocity values and on the spatial distribution of geological layers. To this end, *in situ* measurements represent a good estimation of the initial V_S profiles. Down-hole methods (such as PS-logging) are generally considered the most accurate and direct (invasive) measurement of the shear wave velocity, but their estimation may be biased by the soil disturbance (as observed by Thompson et al., 2009). Moreover, the upward propagating wave motion alters the mechanical properties of shallow sediments, reducing their stiffness and increasing their damping capacity. Those alterations may be irreversible sometimes. For this reasons, the first investigation consisted into estimating V_S variation along the strong motion duration. A *seismic interferometry* technique was applied to the available records (Curtis et al., 2006). Briefly, this technique consists of computing the wave travel-times between two adjacent sensors, estimated as the lag-time at which the seismic interferogram attains its peak. In 1D Earth-like models, only a single wave source is considered to construct those seismic interferograms (cross-correlation between two recorded signals in function of lag-time) between any source-receiver pair, including sources or receivers placed on the free surface (Curtis et al., 2006). A sliding time window of 4-6 s (with 50% of overlap) was selected. Base line correction and Hanning tapering (5%) were performed on the windowed signals.

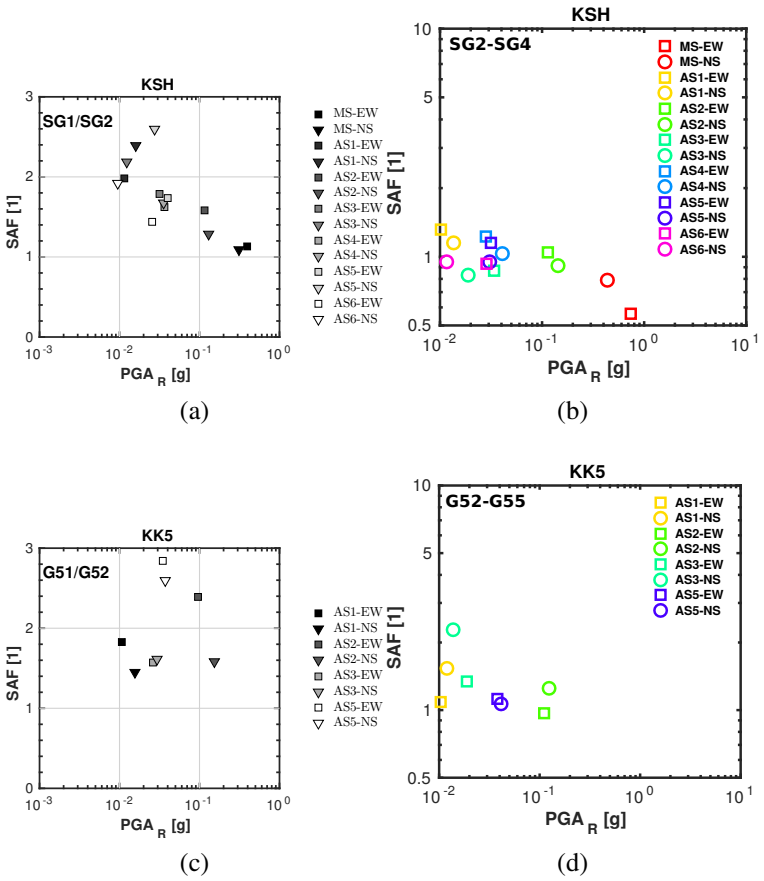

Figure 2.10: Site Amplification Factors (SAF) computed on PGA at KSH (a-b) and KK5 (c-d) array, with respect to the PGA recorded at bedrock. (a) SAF considering SG1/SG2 ratio (KSH); (b) SAF considering SG2/SG4 ratio; (c) SAF considering G51/G52 ratio (KK5); (d) SAF considering G52/G55 ratio (KK5).

Figure 2.11 presents V_S values varying with time, at Service Hall and Unit 5 respectively. At shallow depths (i.e. within the first 50 m under the surface, which is the distance from instruments SG1 and SG2) a consistent V_S reduction may be observed after the main shock arrival (array KSH). Values are substantially lower than the minimum V_S value at SG1 ($\cong$ 310 m/s), especially along the NS direction (probably due to a non-linear anisotropic soil behaviour and to the ground motion incoherence due to near-field conditions). Shear wave velocity does not seem to retrieve its original value within the first meters under the surface, at least for the first 150 s of MS (Figure 2.11a). On the other hand, the most intense aftershock did not cause a significant degradation of shear modulus, as we can notice in Figure 2.11b. A reduction at *intermediate* depths can be observed too at KSH (in the strata between SG2 and SG3's depths, Figure 2.11c), whereas no reduction occurred at KK5 (Figure 2.11d). Reduction could be neglected for stiffer sediments. In Figure 2.12, estimated V_S profiles are compared to PS-logging estimations provided by the TEPCO. Results from the aftershocks overestimate PS-log V_S profile: this is probably due to scarce resolution of the method for ground motions of weak intensity. Aftershock 2 seems not to degrade significantly the soil mechanical properties. However, borehole interferometry analysis is limited by the coarse distribution of recording devices along depth. Suspension logging measurements performed at KSH by Yee et al. (2011) also revealed V_S values between 130-240 m/s within the first 16 m depth, followed by values ranging between 240-390 m/s till 70 m depth finally the bedrock materials have velocities increasing from 330-450 m/s (between 70-83 m) to 400-600 m/s (for depths greater than 83 m). Seismic interferometry revealed a stiffness reduction

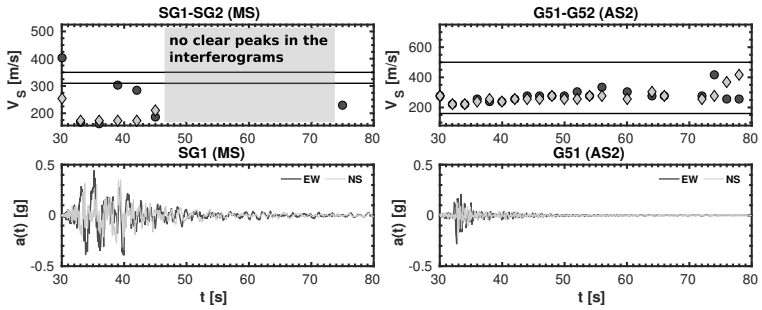

(a) (b)

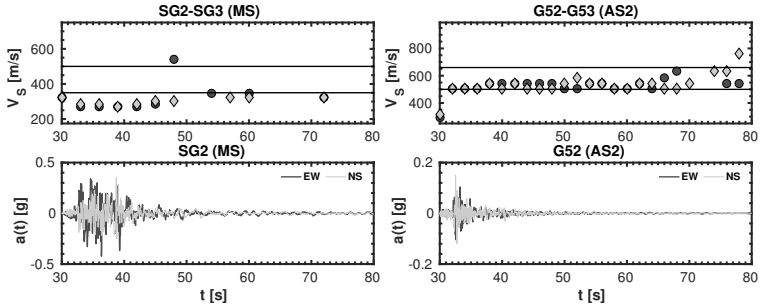

(c) (d)

Figure 2.11: V_S values estimation by borehole interferometry (along the EW-NS directions, dark grey circles and light grey diamonds, respectively); solid black lines indicate average V_S values (from PS-log) at the two devices' locations. The EW-NS time-histories are shown along side, for (a) main shock at KSH (seismometers SG1-SG2); (b) aftershock 2 at KK5 (seismometers G51-G52); (c) main shock at KSH (seismometers SG2-SG3); (d) aftershock 2 at KK5 (seismometers G52-G53).

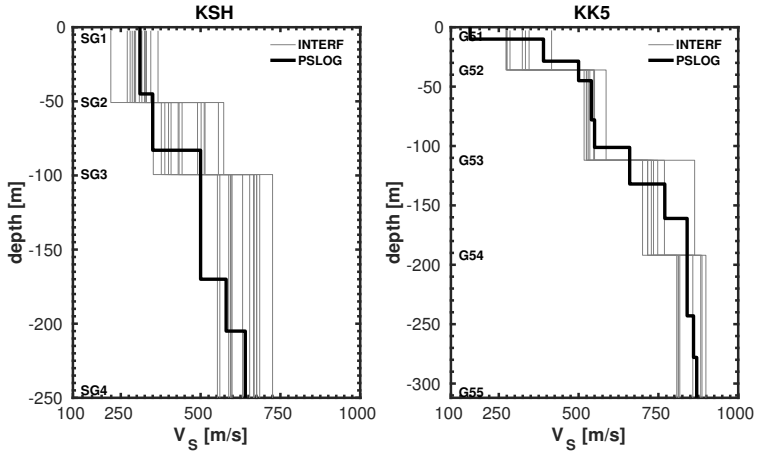

(a) (b)

Figure 2.12: V_S profile obtained by averaging EW-NS results from borehole interferometry analysis on the two arrays KSH (instruments SG1 to SG4 at depths GL-2.4, -50.8, -99.4 and -250 m respectively) and KK5 (instruments G51 to G55 at depths GL-2.7, -36, -112, -192 and -312 m respectively). Computed profiles are compared with the PS-logging one (black line) provided by TEPCO (2008).

within the shallowest soil layers for main shock at KSH, while computed and measured shear wave values are similar at KK5. Tokimatsu and Arai (2008) back-calculated the shear wave velocity values

by coupling genetic algorithms with the equivalent linear method. Their findings showed shear wave velocities at depths smaller than about 70 m significantly smaller than the PS-logging measures (even for small aftershocks). In contrast, those at deeper depths for the three events are almost identical. Those results make the PS-logging profiles questionable. The estimated V_S profiles may be used as simplified geology configuration for numerical models. The described behavior was remarked by several authors. For instance, Pavlenko and Irikura (2012) estimated a $\cong$ 30-35% reduction of the shear modulus within the first 42 m down-hole, during the main shock. Mogi et al. (2010) estimated temporal changes of S-wave velocity by using Normalized Input-Output Minimization (NIOM) method based on the vertical array records observed during the main shock and the events before and after it and found that the S-wave velocity in the layers (0-50 m) and (50-100 m) decreased significantly during the principal motion of the main shock (indicating non linear behaviour), whereas nearly linear behaviour was observed in the bedrock layer (below 100 m). In Section 2.3.4 the deflection of major-intermediate direction was referred to as a possible consequence of soil heterogeneity. Therefore, results coming from interferometry technique were used to verify the latter occurrence. Moreover, in traditional analysis of 1D soil columns the lateral isotropy is assumed by default. Thus the validity of this hypothesis should be verified. To this end, V_S values computed in the EW and NS directions (by borehole interferometry) are reported in Figure 2.13. Values estimated herein follow the 1:1 line, proving an overall lateral isotropy.

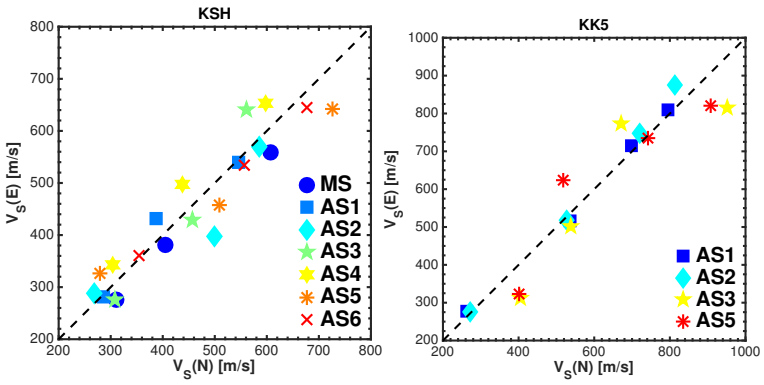

Figure 2.13: On the x-axis V_S values computed by borehole interferometry along NS direction; on the y-axis the values computed considering EW records.

2.5 1D numerical simulations of soil response

As stated in Section 2.4, non-linear de-amplification occurred in the high-frequency part of ground motion (especially in terms of PGA) during the 2007 Chuetsu-Oki main shock strong motion earthquake, whereas aftershock sequence caused negligible degradation of soil stiffness. To complete the site characterization, 1D numerical simulations were performed in two stages: (1) verification of the stratified geological profile and site seismic response at small strains (i.e. analyses on the aftershocks sequence); (2) validation of available $\frac{G}{G_{max}} - \gamma - D$ curves by standard equivalent linear approach (EQL). The first stage of the analysis aims to compare the discontinuous shear modulus profiles released by TEPCO (PS-logging measures plotted in Figure 2.3) with modified ones, in terms of empirical borehole spectral ratio (BHSR). In both cases the wave equation is solved in the frequency domain, but in the EQL formulation the shear modulus and damping ratio are iteratively adjusted as a function of an effective measure of shear strain (Kramer, 1996).

The two soil column models defined for KSH and KK5 respectively, reach the depth at which sensors SG3 and G52 were installed, i.e. GL-99.4 m for KSH and GL-36 m for KK5 (see Figure 2.3 and Figure 2.14). For this purpose, two real accelerograms are available to compare the result of

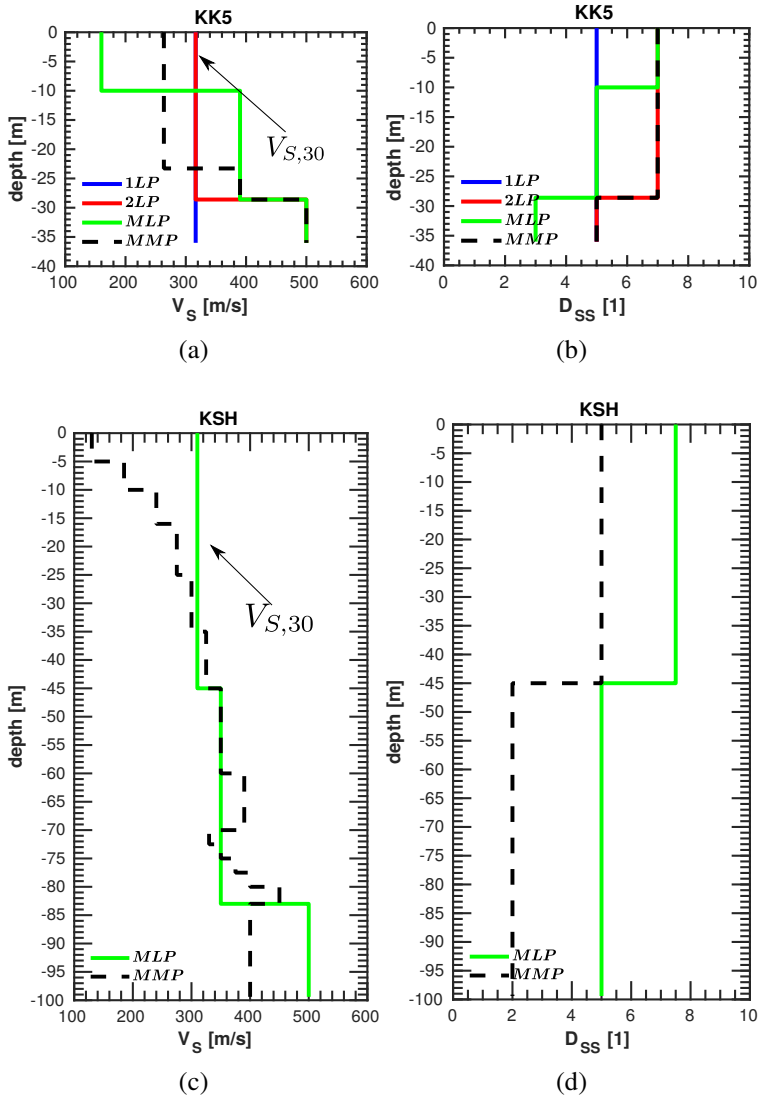

Figure 2.14: Simplified V_S and small-strain damping (D_{SS}) profiles used in the analysis herein. (a) V_S profiles for KK5 and KSH soil column models; (b) small strain damping D_{SS} for KK5 and KSH soil column models. 1LP and 2LP are a mono- and bi-layer profiles respectively. MLP profiles corresponds to the PS-logging measurements provided by TEPCO (2008). MMP are the adjusted profiles adopted in the further sections for equivalent linear analysis.

numerical simulation. Furthermore, EQL formulation is generally suitable to characterize the seismic response at shallow depths, where the hypothesis of quasi-vertical propagation of the seismic input holds approximately (see Section 2.3.3). Real base-line corrected recordings were introduced, under the assumption of *inside input motions* (Dobry, 2013). To overcome the limitation of 1D numerical analyses to be dependent on the input motions and therefore to tackle the dependence of the observed site response on the direction considered (see Section 2.3), results were post-processed by applying common averaging techniques used in seismology. For instance, theoretical borehole spectral ratios are compared to the geometric mean (called , see Eq. (2.3)) of the ensemble of spectral

ratios computed for N_θ different in-plane rotations of the two horizontal components (by an angle $\theta_n \in [0°; 180°]$), namely

$$\text{EMP-GM}\,(f) = \prod_{n=1}^{N_\theta} \sqrt[n]{\left(\frac{O_X\,(f,\theta_n)}{I_X\,(f,\theta_n)}\right)\left(\frac{O_Y\,(f,\theta_n)}{I_Y\,(f,\theta_n)}\right)} \tag{2.3}$$

where $O_X\,(f,\theta_n)$,$O_Y\,(f,\theta_n)$ represent the Fourier ordinate of recordings at shallowest depth at frequency , considering two horizontal orthogonal directions X and Y respectively, obtained by a rotation of angle θ_n of the as-recorded EW-NS components. $I_X\,(f,\theta_n)$,$I_Y\,(f,\theta_n)$ refer to deepest recording station.
In equivalent linear analyses, numerical results depend on the different rotation angles θ at which the input motion were injected at the soil-column base. Therefore, the response spectra geometric mean between each couple of rotated components X-Y obtained numerically (one couple for each θ) is first computed. Then, geometric mean (called GM-EQL) and 16$^{\text{th}}$-84$^{\text{th}}$ percentiles of $Sa_{GM}\,(\theta)$ are compared to the Sa obtained from original records (EW/NS components) at the shallowest stations in the arrays (SG1 and G51 for KSH and KK5 respectively).

2.5.1 Seismic response at KK5

Seismic response in small strain regime

In the surroundings of Unit 5, *in situ* measurements found a shallow subsurface layer of over-consolidated clay overlying the engineering bedrock. Gatti et al. (2015) observed some discrepancies when using the PS-logging measurements (provided by TEPCO) at shallow depths, at Unit 5 array. They compared empirical transfer functions with the theoretical ones, comparing the original V_S profile, provided by TEPCO, and called *Multi-Layer Profile* (MLP) with two simplified profile, *Two-Layers Profile* (2LP) obtained by *smoothing* the two shallow layers of MLP (i.e. replacing them with $V_{S,30}$ value) and *One-Layer Profile* (1LP), with $V_{S,30}$ uniform value. Those findings have been extended hereafter, by introducing a further modified profile (MMP) (black solid lines in Figures 2.14a- 2.14b). In Figure 2.15, theoretical transfer functions (called *borehole spectral ratios*, BHSR) are compared to the empirical geometric mean (orange thick line labelled as EMP-GM) and to the 16$^{\text{th}}$-84$^{\text{th}}$ percentiles. Results presented in Figure 2.15 show the achieved effect due to the adjustment of the provided V_S profile. Profile MMP seems to be the best compromise, at least for the weakest aftershocks such as AS1 and AS3 (Figure 2.15a- 2.15c): the related theoretical transfer function matches satisfactorily the first two peaks of the EMP-GM transfer function. This result supports the importance of the impedance contrast between the deepest stiff layer (V_S =500m/s) and the shallowest ones. However, slight discrepancies between simulated and recorded soil response are still pronounced as provided in Figure 2.15b where it can be seen that the simulated spectral ratios fit rather well the recorded ones in two cases (AS1 and AS3), while in the other ones (AS2 and AS5) the observed spectral ratio peaks stand at lower frequencies than the simulated ones. On one side, it may be argued that the shift of the observed peak towards lower frequencies may be due to the onset of significant non-linear effects (as a matter of fact, AS2 is the most intense aftershock). On the other side, other factors may affect the position and amplitude of the peaks of seismic response for weak motions, such as the frequency dependence of damping (e.g. Miura et al., 2000), which is commonly considered constant in the 1D equivalent linear simulations. In the present case, a satisfactory match with observed spectral ratios was found using hysteretic damping ratio of about 7% (see Figure 2.14b), which is substantially larger than expected at small strain. This implies the underestimation of higher modes.

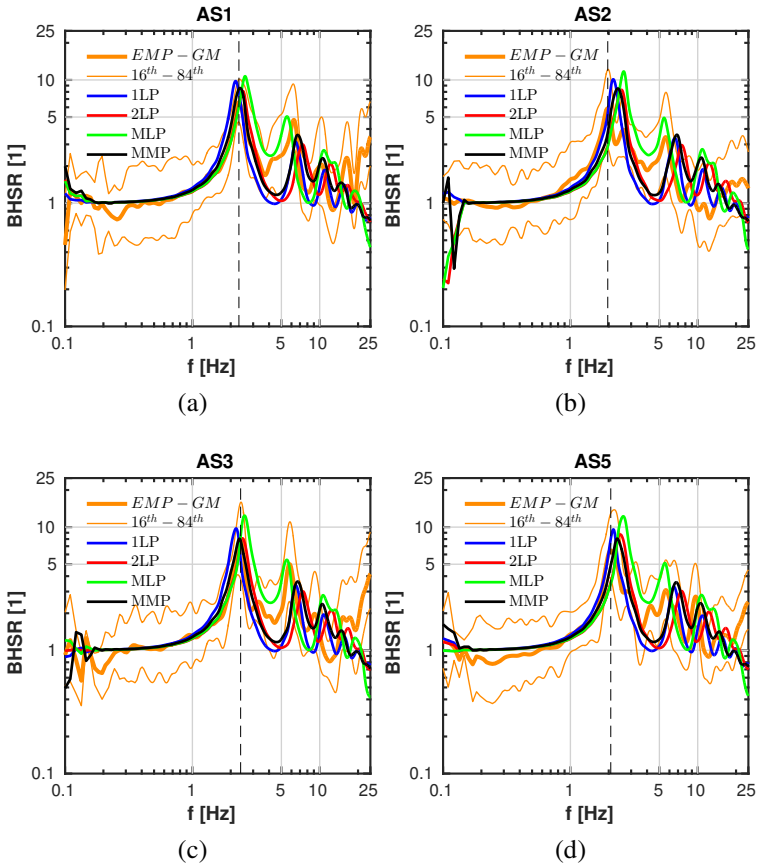

Figure 2.15: Theoretical transfer function for borehole KK5, compared to the Empirical ones along the generic X-Y directions for (a) aftershock 1, (b) aftershock 2, (c) aftershock 3 and (d) aftershock 5. EMP-GM represents the geometric mean transfer function on different in-plane rotation angles $\theta \in [0°; 180°]$. 16^{th}-84^{th} percentiles of Empirical borehole spectral ratios are plotted as thin orange lines.

Equivalent Linear analysis

For borehole KK5 two aftershocks are considered to reproduce non-linear site effects (i.e. AS2 and AS5), since they exhibited period lengthening (as mentioned in previous subsection), with respect to the linear visco-elastic approach. Unfortunately, records of NCO main shock went lost.
A few information on the dynamic properties of the soil deposits at this site were released by the TEPCO, namely: (1) a set of normalized secant shear modulus reduction and damping curves for the shallower clayey deposits (curve *Clay Ref.* in Figure 2.16) and (2) a set of curves referring to the so called *engineering bedrock* (curve *Rock* in Figure 2.16). As observed by many authors (e.g. Vardanega and Bolton, 2013; Darendeli, 2001) the cyclic behaviour of over-consolidated clays is affected by the confining pressure to some extent. TEPCO did not specify the reference confinement pressure at which the non-linear model curves were issued, so a conventional value of 100 kPa was assumed and a stress-wise correction was applied consequently. The latter was inspired by Pecker (2011), who proposed the variation of the dynamic non-linear properties to the effective overburden vertical stress . For instance, they presented two new sets of curves, referring respectively to σ'_{V0} =75-125 kPa and portrayed in Figure 2.16, under the tag *Clay 75 kPa* and *Clay 125 kPa*. Figure 2.16 compares the mentioned experimental curves with the set of curves selected in the equivalent linear analysis, performed on MMP V_S model (see Figure 2.14). The stress-wise correction unwraps into two steps:

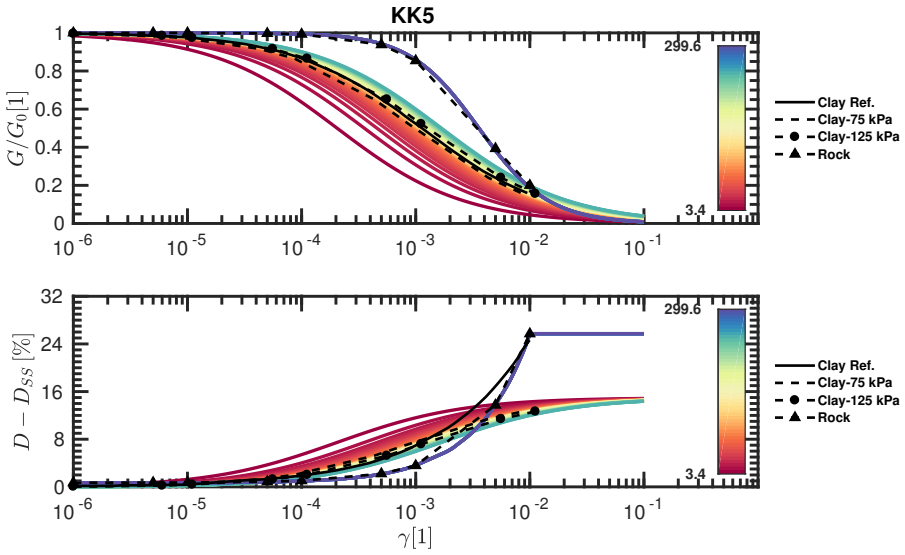

Figure 2.16: $\frac{G}{G_{max}} - \gamma - D$ curves for KK5 site. Experimental data from laboratory tests (*Clay Ref.* and *Rock*, courtesy of TEPCO) are compared to curves used in equivalent linear analysis (MMP V_S profile). Damping values are discounted from the small strain critical damping relative to each layer and taken from MMP model. The color bar refers to the vertical stress state estimated along the borehole depth.

(1) interpolating the experimental points of the reference curve by employing the backbone curve model proposed by Nakagawa and Soga (1995); (2) correcting the calibrated parameters by a factor $\sqrt{\sigma'_{V0}/p_{atm}}$, according to Pecker (2011) (with σ'_{V0} being evaluated at the middle of each soil layer and the atmospheric pressure). In details, the shear modulus degradation curve is casted into the following bi-parametric equation:

$$\frac{G}{G_{max}} = \frac{1}{1 + \alpha \left(\gamma \sqrt{\frac{p_{atm}}{\sigma'_{V0}}}\right)^{\beta}} \tag{2.4}$$

Stress dependency was also assumed for the non-linear evolution of critical damping ratio as follows:

$$\mathrm{D}\left(\sigma'_{V0}\right) = D_{SS} + D_{LS}\left(1 - \frac{G}{G_{max}}\left(\sigma'_{V0}\right)\right) \tag{2.5}$$

where D_{SS} and indicate small- and large- strain damping ratios respectively (set respectively to 5% and 15%). The corrected hysteretic damping at large strain was forced to saturate, in agreement with the adjustments proposed by Darendeli (2001). were obtained by logarithmic interpolation of the reference curve released by TEPCO (*Clay ref.*). The modified $\frac{G}{G_{max}} - \gamma - D$ curves were associated to the first 25 m of the MLP model (over-consolidated clays). The deepest layer (defined by V_S of 500m/s) was associated to the *Rock* degradation curve (Figure 2.16), interpolated over the experimental data. Numerical prediction and recorded response are compared in Figure 2.17 in terms of acceleration time-histories and in Figure 2.18 in terms of elastic response spectra in acceleration Sa. An overall good agreement is observed between simulated time-histories and the recorded ones for AS2 and AS5. In terms of spectral ordinates however, EQL analysis provides a slightly damped Sa spectrum, compared to the recorded one (Figure 2.18b). This might be due to the recovered stiffness of the clayey deposits at shallow depths. The chosen stress correction may play a major role as well. For AS2, some discrepancies at shorter periods can be noticed, e.g. the peak at approximately 0.3 s along the EW direction in Figure 2.18a. As a matter of fact, EQL simulations well captured the dependency of the spectral ordinates on the rotation angle of the input motion only for periods longer than 0.4 s.

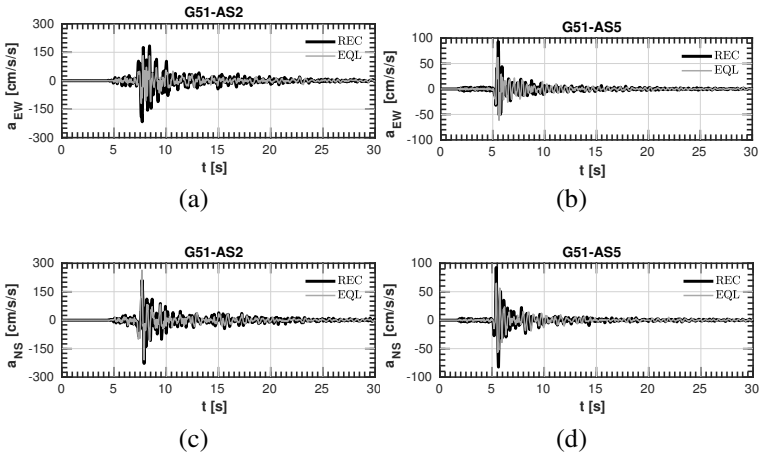

Figure 2.17: Comparisons between acceleration time-histories recorded and simulated (by equivalent linear analyses and angle θ=0°) time-histories for AS2 (a-c) and AS5 (b-d) at KK5 site.

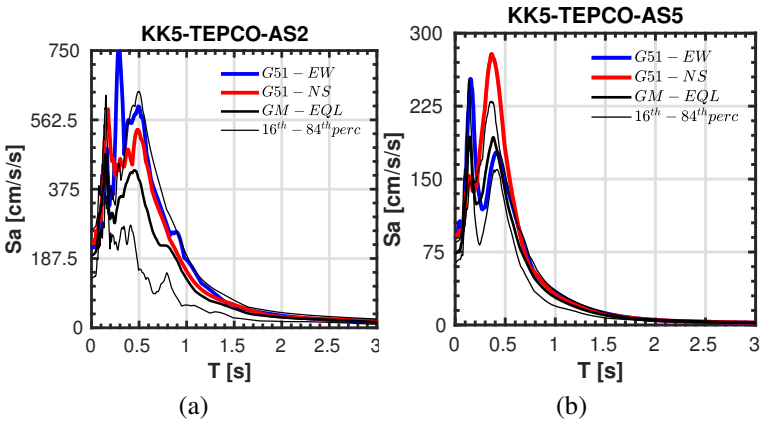

Figure 2.18: Elastic response spectrum in acceleration Sa (conventional damping 5%) referring to AS2 (a) and AS5 (b) at KK5 site. Thick solid black lines (GM-EQL) refers to the results from equivalent linear analyses, being the geometric mean of all the $Sa_{GM}(\theta)$. Finer solid black lines represent the 16$^{\text{th}}$-84$^{\text{th}}$ percentiles of $Sa_{GM}(\theta)$ distribution. Blue and red lines refer to the recorded EW-NS response accelerations.

2.5.2 Seismic response at KSH

Seismic response in small strain regime

The site response at the Service Hall was simulated according to the same approach as for KK5 site. The TEPCO V_S profile (MLP, portrayed by the green lines in Figures 2.14c- 2.14d), based on an earlier suspension logging campaign, was compared to the estimation made by Yee et al. (2011)(MMP, portrayed by the dashed black lines in Figures 2.14c- 2.14d), obtained by integrating new PS-logging measurement with Standard Penetration Tests performed by the Tokyo Soil Research in 2009 at the Service Hall site. The soil deposits is composed of unsaturated and poorly graded sands till 70 m. Below this depth, for both the geological models, the unit weights at different depths were retrieved from *in situ* and laboratory results performed by Yee et al. (2011). The MLP layered geological model is poorly refined at shallow depths, compared to the MMP model, which is also featured by a velocity inversion below 70 m. As expected from the interferometry results (Section 2.4.2 and Figure2.12) the MMP model looks more adequate in reproducing the empirical borehole transfer

function (Figure 2.19), both in terms of the main natural frequency peak for weaker (AS3) and more intense aftershocks (AS2). Higher models are well reproduced by the MMP layering configuration,

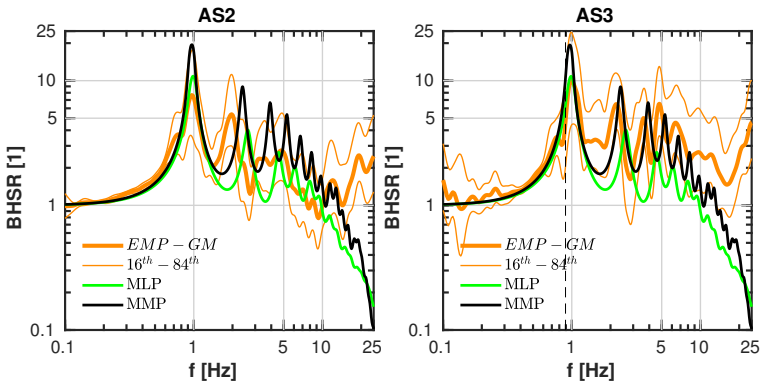

(a) (b)

Figure 2.19: Theoretical transfer function for borehole KSH, compared to the Empirical ones along the generic X-Y directions for (a) aftershock 2 and (b) aftershock 3. EMP-GM represents the geometric mean transfer function on different in-plane rotation angles $\theta \in [0°; 180°]$. 16$^{\text{th}}$-84$^{\text{th}}$ percentiles of Empirical borehole spectral ratios are plotted as thin orange lines.

although de-amplification and shift towards the lower frequencies is observed for AS2. For MLP, the critical damping values provide a decrease of the frequency peaks much larger than observed. However, the D_{SS} values employed represent the *best* compromise for MLP profile to match the first mode. As a matter of fact, Yee et al. (2011) highlighted that the as-provided model-data (from the previous studies performed by TEPCO) showed some over-prediction of motions at GL-2.4 m (device SG1), which they addressed as an underestimation of damping ratios (ranging between 1-4%), which they also observed in their resonant column tests. Thus, they slightly increased D_{SS} to 2-5%. However, results does not clearly support either a preferential choice on MLP or MLP, probably due to the greater depth reached by the soil column model (i.e. GL-99.4 m) where recording device SG3 is installed and to some residual modification of the soil properties, due to the strong main shock that struck the site.

Non-linear site response at KSH

The borehole array KSH, installed at the KK-NPP Service Hall, recorded the NCO main shock. Nonetheless, according to Yee et al. (2011), prior to the 2011 Tohoku Japan earthquake, the KSH array recorded the strongest motions for a vertical array in soil, without exhibiting liquefaction. Therefore, this location is suitable to study the non-linear site response in the surroundings, via 1D soil column analyses. Main shock (MS) and aftershock 2 (AS2) are considered herein.
The TEPCO released a degradation curve for sand layer (*Sand ref.* in Figure 2.20). Those values were assumed to refer to an *in situ* confining pressure state of 100 kPa. The stress correction described in Section 2.5.1 was judged incompatible with the experimental results obtained by Yee et al. (2011) (curves tagged as *Yee et al.*, in Figure 2.20). A more accurate description of the effect of the overburden pressure was proposed by Yee et al. (2011), so to fit the laboratory results. The authors adopted a classical hyperbolic model (Hartzell et al., 2004), in the form of:

$$\frac{G}{G_{max}} = \frac{1}{1 + \left(\frac{\gamma}{\gamma_r(p'_0)}\right)^{\beta(p'_0)}} \tag{2.6}$$

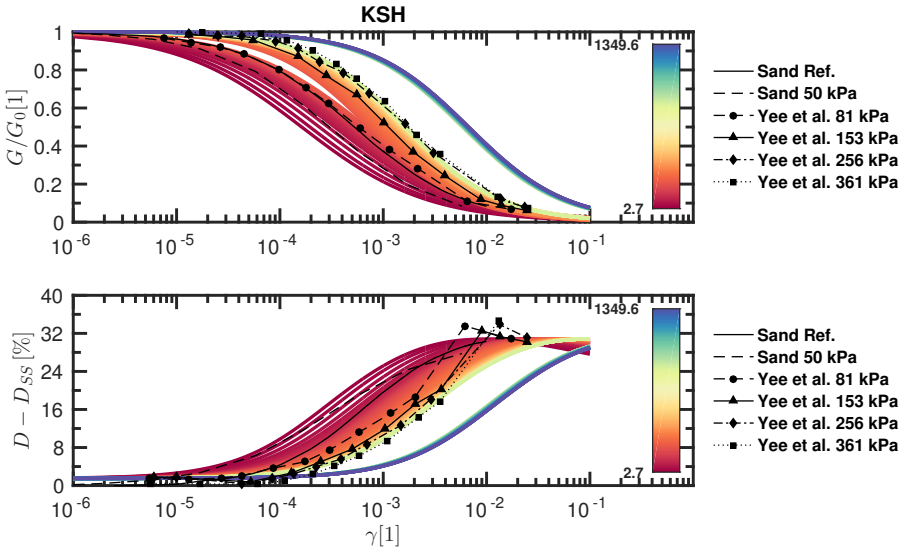

Figure 2.20: $\frac{G}{G_{max}} - \gamma - D$ curves for KSH site. Experimental data from laboratory tests conducted by the Tokyo Soil Research (Yee et al., 2011) and by TEPCO are compared to curves used in equivalent linear analysis (MLP V_S profile), obtained by applying the overburden stress correction proposed by Yee et al. (2011).

where represents the pseudo-reference shear strain and the mean effective confining pressure at depth. Based on the previous parametric studies performed by Menq (2003) on the dynamic properties of cohesionless granular soils, they adjusted the provided empirical relations by proposing the following stress dependencies for γ_r and β:

$$\gamma_r\left(p_0'\right) = \gamma_{r,1}\left(\frac{p_0'}{p_{atm}}\right)^n \tag{2.7}$$

$$\beta\left(p_0'\right) = \beta_1 + \beta_2 \log\left(\frac{p_0'}{p_{atm}}\right) \tag{2.8}$$

are regression coefficients, which have been tuned upon the experimental results for the unsaturated sandy deposit above 70 m (approximately corresponding to a confining pressure $p_0' = 6.75$ atm), whereas at higher depths they assume the empirical values obtained for clays by Darendeli (2001). However, the inherent uncertainty on those regression coefficients reported by Yee et al. (2011) was solved by a trial and error adjustment, at each depth. Figures 2.21a-2.21b portray the comparison between the adopted values of γ_r and β with varying confining pressure (referred as to $Y - mod.$) along with the models proposed by Yee et al. (2011) (average value $Y - \mu$ and confidence limits $Y - \mu + / - \sigma$). Figure 2.21 highlights the two main major adjustments adopted herein: (1) γ_r deviates from the Yee et al. (2011) exponential model at small confining pressures (i.e. $p_0' < 2$ atm) so to better capture the experimentally measured pseudo-reference strain; (2) β values generally range across the lowest curve ($Y - \mu - \sigma$).

Thanks to those quite simple expedients, the simulated time-histories (see Figure 2.22) are rather well reproduced, despite the higher frequency content *polluting* the simulations and mainly due to the limitations of the equivalent linear method with intrinsic hysteretic assumption of a frequency-constant damping (Miura et al., 2000, among others). In Figure 2.23 simulated site response for MS is strongly dependent on the direction along which the motion is projected. The MS recorded response spectra are well replicated for natural periods greater than 2.0 s, EQL results show high variability depending on the input motion angle considered at shorter periods. On the other hand, for AS2 the simulated response ranges within a narrow confidence band across GM-EQL (Figure 2.23b). Those

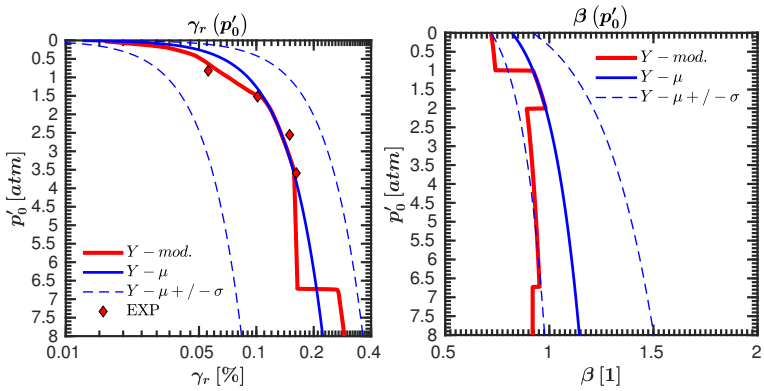

(a) (b)

Figure 2.21: Values of γ_r (a) and β (b) with varying confining pressure p'_0. Red lines referred as to $Y - mod.$ indicate the stress correction employed in this study. Blue lines refer to the average $(Y - \mu)$ values and confidence limits $(Y - \mu+)$ of the regression coefficients according to Yee et al. (2011). The red symbols in Figure 2.21a indicate the laboratory results reported by Yee et al. (2011).

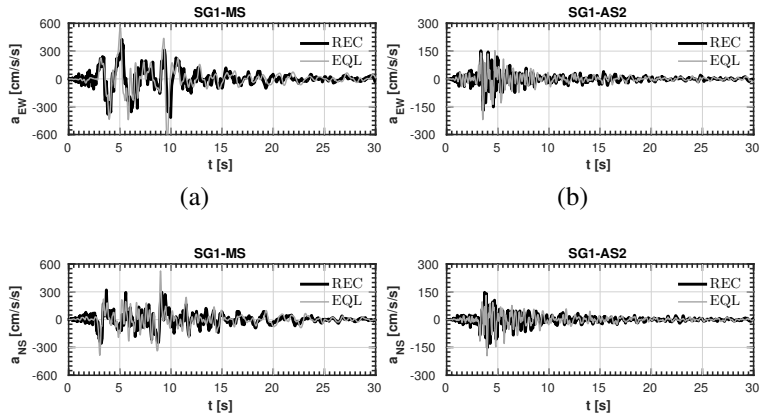

(a) (b)

(c) (d)

Figure 2.22: Comparisons between acceleration time-histories recorded and simulated (by equivalent linear analyses) for MS (a-c) and AS2 (b-d) at KSH site.

effects are related to the proximity of the seismic source since the motion intensity and direction change drastically the response. Moreover, those discrepancies highlight the shortcomings of EQL analysis when large strains occur.

2.6 Conclusions

The *Niigata-Ken Chūetsu-Oki* earthquake affected the Kashiwazaki-Kariwa Nuclear Power Plant causing limited damage to the nuclear installments. Non-linear site effects were observed. The case study was very interesting either from a seismological point of view, either from an engineering one. In this study, some crucial features of the global seismic response of KK-NPP were tackled, with an engineering approach.

First of all, since the design seismic capacity has been exceeded during the main shock, a correlation between the recorded peak values (i.e. PGAs) and the dominant harmonic periods of the ground motion was established, proving the potential damage occurrence at some locations within the site.

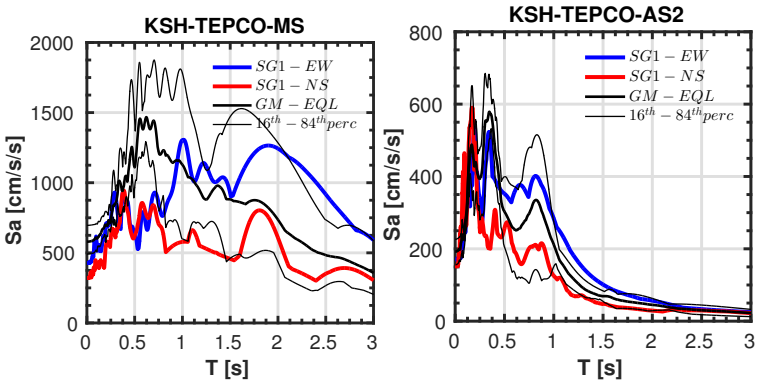

(a) (b)

Figure 2.23: Elastic response spectrum in acceleration Sa (conventional damping 5%) referring to MS (a) and AS2 (b) at KSH site. Thick solid black lines (GM-EQL) refers to the results from equivalent linear analyses, being the geometric mean of all the $Sa_{GM}(\theta)$. Fine solid black lines represent the 16$^{\text{th}}$-84$^{\text{th}}$ percentiles of $Sa_{GM}(\theta)$ distribution. Blue and red lines refer to the as-recorded EW-NS response accelerations.

In the following, the impulsive response of the incoming wave field was assessed. *Hanging wall* and *directivity* effects were judged as responsible of such a response, due to the small source-to-site distance. This characteristics of the seismic scenario prevent the recognition of preferential direction of motion, i.e. making the site response strongly dependent on the considered horizontal direction at each location.
The consistent number of recordings available was exploited to check whether non-linearity took place. Wave motion de-amplifies towards the surface, as expected during the main shock and non-linear stiffness degradation is observed at shallow depths, thanks to seismic interferometry applied to borehole arrays of seismometers. Thus, PS-logging measurements referring to this specific site are poorly adequate and they may lead to an underestimation of the of the structural response of both the reactor building and other structural components in nuclear facilities. V_S values measured *in situ* may overestimate the real soil stiffness during transient analyses. This is confirmed by the equivalent linear calculations presented in Section 2.5: predicted transfer functions provide a reasonable match to the shape and resonant frequencies of the observed ones, although the data is clearly too limited to establish statistically significant empirical trends for small-strain site response. Original mechanical properties may have not been recovered during the aftershock cluster, preventing the use of weak motions as input for calibration of non-linear soil models. On the other hand, limitations of the 1D models may alter the predictions (e.g. the frequency dependence of the damping, the wave motion deviation from the vertical, the spurious wave content and the destructive interference). However, none of those factors can generally be dealt exhaustively with 1D models. Care should be paid in near-field conditions, where the strong dependency on the orientation of the input motion may alter dramatically the results of numerical simulations. In this case, consideration of the different components of the motion is strongly recommended to obtain more stable results.
It is clear that the present case of study needs for complex 3D numerical models since complex geology underlies the site, as reported by several authors (Aochi et al., 2013a; Tsuda et al., 2011). Due to the near-field conditions, the seismological model should also include the faulting mechanism to be able to model the impulsive nature of seismic records.

3

Numerical tools

"In the beginning there was nothing, which exploded."

– Terry Pratchett, Lords and Ladies

In recent years, classical seismological models have been successfully improved so as to explain the observed waveforms in sedimentary basins Graves and Wald (2004) or at the global scale Komatitsch and Tromp (2002a). The computation of high-quality synthetic seismograms and their comparison with actual recordings at the stations, steer an ever improving knowledge of the deep geological models and earthquake parameters (Liu, 2006). It is well known the role of the geological site conditions as one of the dominant factors controlling the spatial variation of the ground shaking (Olsen, 2000, for instance). Historically, synthetics have been computed via numerous techniques, like ray tracing or normal mode summation (Cupillard et al., 2012). For many purposes, those techniques resulted very convenient but with major shortcomings (low-frequency approximation, limitation to weak lateral heterogeneities, etc.). To this end, the three-dimensional (3D) source-to-site numerical simulation of strong ground motion earthquakes has become the leading and most reliable tool Paolucci et al. (2014). Large scale simulations comprehend the regional geology and topography. The incident wave-field is naturally radiated from a kinematic description of the fault mechanism.
The available numerical methods used in seismology are able to simulate 3D seismic wave propagation in complex geological media at large scale with increasing resolution (Maufroy et al., 2015; De Martin, 2011). Among the direct numerical solutions investigated, the Finite Difference Method (FDM) has widely employed to solve the wave equation (Alterman and Karal, 1968; Boore, 1972; Virieux, 1986; Moczo et al., 2007, among others). Although its undoubted major advantages compared to analytical and semi-analytical methods, the FDM suffers of intrinsic shortcomings, such as dealing with complex geometries (typically the basin edges and the bathymetry), with unstructured computational grids sometimes required to mesh huge physical domains and its cumbersome numerical solution and memory requirement. The Finite Element Method is more flexible and does not suffer of the problems above mentioned. However it is traditionally featured by low-degree polynomial approximation and therefore not indicated for this kind of analysis, due to high numerical dispersion and inaccuracy (Lysmer and Drake, 1972; Marfurt, 1984; Cupillard et al., 2012). In the plethora of numerical methods used in engineering seismology, the Spectral Element Method (SEM, i.e. a high-order version of the FEM) has recently become predominant due to its accuracy and straight-forward extension to parallel implementation (Göddeke et al., 2014), and it is well known to provide an accurate solution of the elasto-dynamic problem in highly heterogeneous media (Seriani, 1998; Komatitsch and Tromp, 1999). This high-order numerical method is based on the pioneering works in fluid dynamics performed by (Patera, 1984; Korczak and Patera, 1986; Maday et al., 1987; Mayday et al., 1989). The Spectral Element (SE) formulation (extensively detailed in appendix A) bares on a non-isoparametric piecewise polynomial approximation of the wave-field. The key-point

of this powerful numerical tool resides in the use of orthogonal Lagrangian polynomials, sampled at the Gauss-Lobatto-Legendre (GLL) quadrature points. The accuracy of the solution can be arbitrarily increased by simply enhancing the polynomial approximation degree (Mazzieri et al., 2013). The first seismology-oriented application of the SEM can be found in Priolo et al. (1994); Seriani et al. (1995). Large scale 3D wave-propagation ($\approx 10^9$ degrees of freedom) in visco-elastic media has been successfully performed using the SEM, both at local and regional scales (Faccioli et al., 1997; Komatitsch and Vilotte, 1998, among others).
However, to model the spatial variability of seismic incident field (due to its significant effect on the structural response), the heterogeneous composition and the non-linear behaviour of soil deposits must be taken into account. Non-linear soil behaviour was integrated into 2D Spectral Element codes in the recent years (see, for instance, Stupazzini and Zambelli, 2005; di Prisco et al., 2007; Stupazzini et al., 2009; Oral, 2016)).

The physics-based simulation of realistic earthquake scenarios requires a reliable estimation of several different parameters, related to the source mechanism, to the geological configuration and to the mechanical property of the soil layers and crustal rocks. Due to the enormous extension of those regional scale scenarios, the degree of uncertainty associated to the whole earthquake process (from fault to site) is extremely high. Another drawback resides on the computational effort required to routinely solve the wave propagation on such huge domains and over such a great number of DOFs. An extensive parametric study on each and everyone of the parameters involved is rather complicated. At this point, it appears necessary to build up a multi-tool *virtual laboratory* to construct and calibrate the seismological model. The different physical mechanisms encompassed (mainly the source mechanism and the propagation into non-linear heterogeneous soil layers) are firstly calibrated by means of simplified analyses (e.g. semi-analytical methods), each one focusing on an aspect of the earthquake scenario. All the contributions are finally convolved together in a large scale simulation. To this end, three main issues must be tackled:

- mesh the domain of interest, its geological conformation (bedrock to sediment geological surfaces), the topographical surface and the bathymetry (if present)
- represents the material rheology (i.e., elastic, viscous-elastic, non-linear hysteretic)
- describe the natural heterogeneity of the soil properties, at different scales (i.e., regional geology, local basin-type structures and heterogeneity of granular materials)

Among the tools employed, the main wave propagation solver is herein represented by a software called SEM3D, an High-Performance code tailored to efficiently solve the SE numerical approximation of wave propagation at the regional scale[1]. Among the advantages of SEM3D, two main aspects must be stressed, namely (1) its efficient and cost-effective massively parallel implementation (by Message Passing Interface, MPI) on large super-computers and (2) its ability to accurately take into account 3D discontinuities such as the sediment-rock interface. The original core of the SEM3D software (written in Fortran 90/C/C++ routines) allowed to solve the wave propagation problem in any velocity model, including anisotropy and intrinsic attenuation. However, within the framework of the SINAPS@ project, the software has been equipped with an external library to effectively generate scalar random fields at the regional scale and with a non-linear solver to efficiently integrate the cyclic hysteretic soil rheology (modelled within the elasto-plasticity framework). Moreover, the code makes use of an efficient linear octree finite element mesh generation scheme, called *HexMesh* (Camata and Coutinho, 2013). The latter is capable to generate large scale computational grids by

[1]To clarify, by *regional scale*, it is hereafter assumed an average distance range between about 1 km (local scale) to 90 (continental scale).

extruding the Digital Elevation Model (DEM) provided. To validate the code, results from PRENOLIN international benchmark are employed (Régnier et al., 2016). The PRENOLIN project addressed the numerical simulation of 1D wave propagation in elastic and non-linear soil deposits. Moreover, to test the implementation of the point source double-couple (an *kinematic* approach to simulate fault offsets in computational seismology), large scale simulations were compared to the semi-analytical solution provided by the Wave Number Integration method (WNI) (Hisada, 1994, 1995). All these simulations show the great flexibility of the code at the local and regional scale.

3.1 3D Spectral Element based numerical solver

The extensive formulation of the SEM is presented in the appendix A. The SEM borrowed from the FEM its natural capability to handle both interface and free boundary surface conditions, allowing a good resolution of evanescent interface and surface waves (Cupillard et al., 2012). Given a 3D open domain $\Omega \subseteq \mathbb{R}^3$ and a time interval $\mathbb{I}_t \subseteq \mathbb{R}^+$, the wave propagation problem is governed by the Euler-Lagrange equations (which, in turn, express the conservation of the linear momentum), in the form (Lagrange, 1853):

$$\begin{cases} \underline{\boldsymbol{\nabla}}_x \cdot \underline{\underline{\boldsymbol{\sigma}}} \left(\underline{\boldsymbol{u}} \left(\underline{\boldsymbol{x}}; t \right) \right) + \underline{\boldsymbol{b}} \left(\underline{\boldsymbol{x}}; t \right) = \rho \left(\underline{\boldsymbol{x}}; t \right) \underline{\dot{\boldsymbol{v}}} \left(\underline{\boldsymbol{x}}; t \right) & \forall \left(\underline{\boldsymbol{x}}; t \right) \in \Omega \times \mathbb{I}_t \quad (3.1) \\ \rho \left(\underline{\boldsymbol{x}}; t \right) \underline{\boldsymbol{v}} \left(\underline{\boldsymbol{x}}; t \right) = \rho \left(\underline{\boldsymbol{x}}; t \right) \underline{\dot{\boldsymbol{u}}} \left(\underline{\boldsymbol{x}}; t \right) & \quad (3.2) \end{cases}$$

with and the unknown displacement/velocity wave-field respectively, >0 the unit mass density, the body force density distribution (per unit mass) applied to the medium (e.g. the mass gravity) the Cauchy's stress tensor[2]. The relationship between $\underline{\underline{\boldsymbol{\sigma}}}$ and displacement field $\underline{\boldsymbol{u}} \left(\underline{\boldsymbol{x}}; t \right)$ depends on the chosen rheology. $\dot{\square}$ represents the *material time derivative* $d\square/dt$. Equations 3.2 is supplied with the initial conditions:

$$\begin{cases} \underline{\boldsymbol{u}} \left(\underline{\boldsymbol{x}}; 0 \right) = \underline{\boldsymbol{u}}_0 \left(\underline{\boldsymbol{x}} \right) & \forall \left(\underline{\boldsymbol{x}} \right) \in \Omega \quad (3.3) \\ \underline{\boldsymbol{v}} \left(\underline{\boldsymbol{x}}; 0 \right) = \underline{\boldsymbol{v}}_0 \left(\underline{\boldsymbol{x}} \right) & \forall \left(\underline{\boldsymbol{x}} \right) \in \Omega \quad (3.4) \end{cases}$$

and the following Neumann's boundary condition:

$$\underline{\boldsymbol{t}}_n = \underline{\underline{\boldsymbol{\sigma}}} \left(\underline{\boldsymbol{x}}; t \right) . \underline{\boldsymbol{n}} \left(\underline{\boldsymbol{x}}; t \right) = \underline{\boldsymbol{t}}_{n,0} \left(\underline{\boldsymbol{x}}; t \right) \qquad \forall \left(\underline{\boldsymbol{x}}; t \right) \in \Gamma_T \times \mathbb{I}_t \quad (3.5)$$

with $\Gamma_T \subseteq \partial\Omega$ the surface where the Neumann's conditions are applied. For the sake of simplicity, $\Gamma_T = \partial\Omega$ and a free-surface is assumed (i.e. $=\underline{\mathbf{0}}$).
Due to lack of a closed form solution for complex geometries and source domains, a numerical solution is required. The latter is obtained by first rewriting the Euler-Lagrange Equation 3.2 in its variational formulation (see Section A.4) and then by subdividing the spatial domain $\bar{\Omega}$ into N_e non-overlapping elements $\bar{\Omega}_e$ (generally hexahedral elements) such that $\bar{\Omega} = \cup_{e=1,N_e} \bar{\Omega}_e$ and the intersection between two distinct elements $e^{'}$ and e $\bar{\Omega}_{e'} \cap \bar{\Omega}_e$ is an element's corner, edge or face. The approximate solution of the Euler-Lagrange problem (i.e. the displacement/velocity couple $\left(\underline{\boldsymbol{u}}^h ; \underline{\boldsymbol{v}}^h \right)$) is sought in the space of high-order piece-wise polynomial on the element Ω_e. Specifically, the SEM employs tensorized (and orthogonal) Lagrangian polynomials of order N^d as basis functions (see Section A.5). The tensorial grid features $(N+1)^d$ interpolation nodes of belonging to the Gauss-Lobatto-Legendre (GLL) set (Section A.2). Those GLLs are involved in the Gauss quadrature used to evaluate the integrals in the variational formulation and to discretize the displacement and velocity fields, their derivatives and the external forces. Moreover, the choice of a Lagrangian interpolation associated with the GLL nodes gives the SEM a very interesting convergence property: an increase

[2] the *small strain* and *small displacement* assumptions are considered hereafter

of the polynomial order leads to an exponential diminution of the aliasing error (the so called *spectral precision* Cupillard et al., 2012; Mazzieri et al., 2013). Substituting the piecewise polynomial approximation into the variational counterpart of the Euler-Lagrange equations and approximating the integrals by means of the Gauss quadrature rules (based on the GLL tensorized grid)[3] lead to a system of ordinary differential equations governing the evolution at the global nodal position, which can be written as follows:

$$\begin{cases} \mathbb{M}\dot{\hat{\underline{\boldsymbol{V}}}}_G^h = \mathbb{F}^{ext} - \mathbb{F}^{int}\left(\hat{\underline{\boldsymbol{U}}}_G^h; \hat{\underline{\boldsymbol{V}}}_G^h\right) + \mathbb{F}^{trac}\left(\underline{\boldsymbol{\mathcal{T}}}_G^h\right) & (3.6) \\ \dot{\hat{\underline{\boldsymbol{U}}}}_G^h = \hat{\underline{\boldsymbol{V}}}_G^h & (3.7) \end{cases}$$

with , and the displacement, velocity global DOF vectors and the traction at the global nodes, respectively. is the diagonal mass matrix (an interesting property, in terms of computational effort, inherited from the spectral discretization, and specifically from the orthogonal Lagrange polynomials employed, see Section A.7). The vectors and contain the external and internal forces, respectively, and corresponds to the traction forces (Delavaud, 2007). The natural diagonality of the mass matrix steers the choice of an explicit time-marching scheme, e.g. a second-order accurate *leap-frog* method (belonging to the Newmark's family) which was found to preserve the angular momentum (Simo et al., 1992).

3.2 Meshing regional Earth's chunks

From a practical point of view, keeping in mind the need for large scale (i.e. $\sim$ 10-100 km) computational grids representing chunks of the Earth's crust, an efficient meshing tool must tackle the following difficulties:

- meshing the topographical surface and eventually the coastline and the sea bottom;
- consider geological discontinuities (typically sedimentary basins, folded geological strata, fault segments)
- reach a sufficient refinement close the topographical surface, where slower soil strata are naturally found, so to preserve the maximum frequency propagated by the numerical model

In the following subsections, some of the main aspects concerning the SE meshing tool adopted in this work are explained and detailed, along with some rule of thumbs and practical considerations for a good meshing procedure.

3.2.1 General aspects

Hexahedral meshes are generally less adapted than tetrahedral for meshing geometrically complex structures. However, they feature two major advantages, i.e. (1) the intrinsic tensorization property and (2) the flexibility provided by a non-linear geometric mapping from a master unit cube $\square_\Omega$ to any deformed 8- or 27-node hexahedra element in the physical space (Figure 3.1). The second aspect opens up to the ease of generating unstructured meshes with additional advantage (Cupillard et al., 2012). The high flexibility of the SE discretization allows to handle high number of integration points per minimum wavelength. After Tromp et al. (2008), using 4^{th} or 5^{th} order Lagrange polynomial might provide a best trade-off between accuracy and computational time. However, typically much higher values of N are used in the SEM, e.g. $5 \leq N \leq 10$, and in these cases the spacing of the

[3] The complete mathematical derivation of the Galerkin's formulation

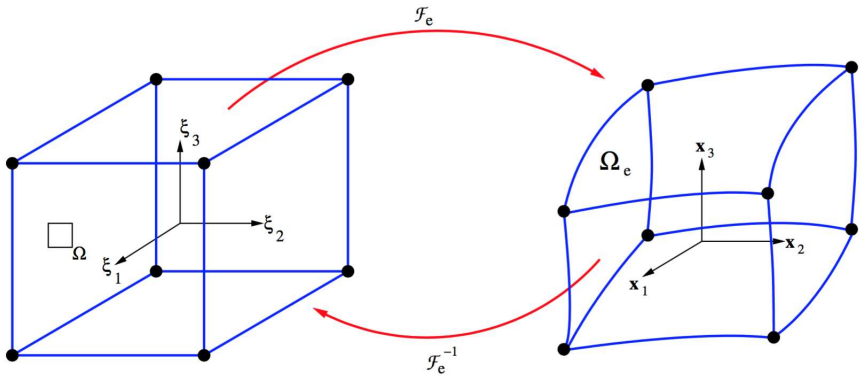

Figure 3.1: 8-node hexahedral reference element and the mapping function (Delavaud, 2007)

nodes is not even: the nodes tend to cluster near the element borders and are rarefied in the interior (Komatitsch, 1997). This means that the size of the elements d and the polynomial order N are both constrained by the shortest wavelength propagated in the medium. This condition can be summarized by the following relation (Cupillard et al., 2012):

$$d \leq \frac{N}{No}\lambda_{min} \tag{3.8}$$

where represents the number of integration point per minimum wave-length, set to either 4 or 5. Moreover, to ensure the stability of the time-marching, the time step Δt of the *leap-frog* scheme has to verify the Courant-Friedrichs-Lewy (CFL) condition (Courant et al., 1967):

$$\Delta t \leq C\Delta t_{min} = C\left(\frac{d}{c_p}\right)_{min} \tag{3.9}$$

where d is the size of an element, n is the order of the polynomial, λ is the minimum wavelength and is the Courant's number which is generally considered to be 0.4 for a 3D modelling.

3.2.2 Parallel implementation of the meshing scheme

As a strict requirement, the meshing tool must be fast, accurate (in terms of multiple levels of refinement/coarsening) and cost-effective. Although many solvers have been recently adapted to parallel supercomputers, grid generators did not. As a matter of fact, most of the numerical solver (as SEM3D) exploits an efficient domain partitioning scheme featured by a mapping sub-domain $\rightarrow$ target parallel system (Camata and Coutinho, 2013). For instance, the Metis library[4], for instance, is widely used to roughly partition the computational nodes/elements in equal parts (among the processors involved), such that the number of edges connecting vertices in different parts is minimized (Karypis and Kumar, 1995). Moreover, for direct application in engineering seismology, one would desire the mesher to handle complex surfaces, such as the regional topography, the ocean bathymetry and the coastline. All the mentioned requirements are met by *HexMesh*[5], a software tailored to extrude a given Digital Elevation Model (DEM)[6] down to a certain depth so to obtain an unstructured hexaedral mesh (with

[4]source: http://www.cs.umn.edu/~karypis

[5]source: https://github.com/jcamata/HexMesh.git

[6]See for instance, the Shuttle Radar Topography Mission (SRTM) data sets, result from a collaborative effort by the National Aeronautics and Space Administration (NASA) and the National Geospatial-Intelligence Agency (NGA), as well as the participation of the German and Italian space agencies, to generate a near-global digital elevation model (DEM) of the Earth using radar interferometry. Source: https://dds.cr.usgs.gov/srtm/version2_1.

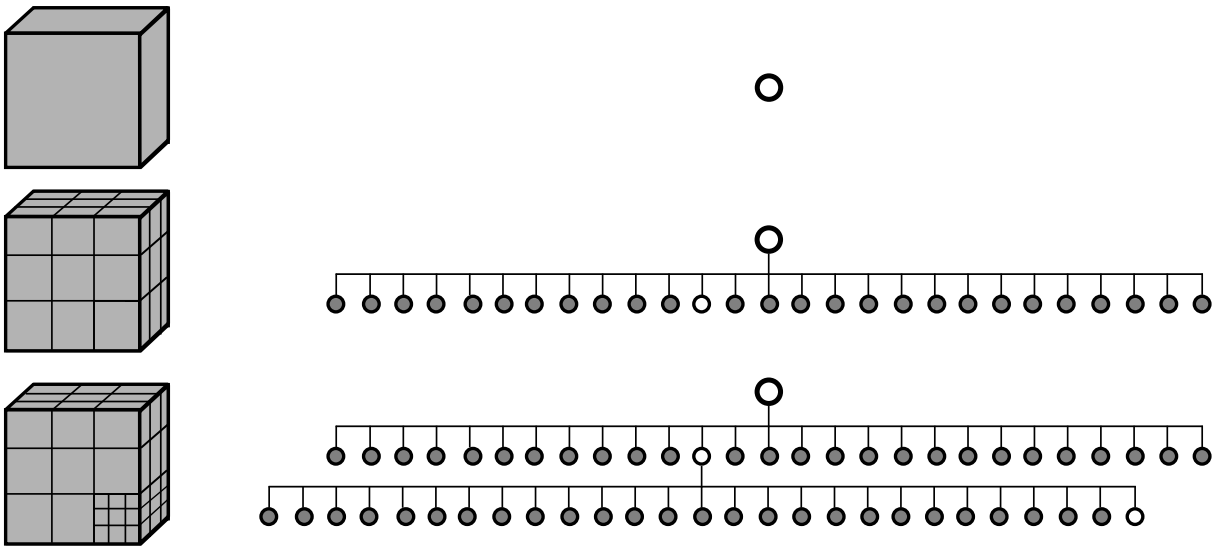

Figure 3.2: 27-tree definition scheme.

a 3:1 balance refinement from down to top) spanning up to 100 km size. The mesher portability is granted by its parallel implementation (MPI based) and by its 27-tree based axis-aligned hierarchical data structures. A 27-tree is a *tree* data structure composed by nodes each one with exactly 27 children and finite volume associated with it. The generation algorithm starts from a *root* node 0 taken to be the smallest axis-aligned cube V^0 fully enclosing the domain (Camata and Coutinho, 2013). The *parent* volume V^0 is then subdivided into 27 smaller and equal-size *child* sub-cubes $V_i^1, i = 1, ..., 27$ (also called *cells*) obtained by simultaneously dividing V^0's edges along each of the coordinate axes (x_1, x_2, x_3) in three. This parent $\rightarrow$ children decomposition strategy is recursively applied till the tree reaches a maximum *depth* (the refinement depth of a node from the root is called *level*) or the cubes getting smaller than some preset minimum size. Nodes that have no children are called *leaf nodes*. Figure 3.2 shows a 27-tree domain decomposition and its tree representation. Considering that the maximum permissible depth of 27-tree is fixed a priori and that each node has exactly 27 nodes, the whole hierarchical data structure can also be represented with a complete list of leaf nodes, arranged in a linear array, instead of the tree data structure. Each cell is encoded with a bijective scalar key called *locational code* (Camata and Coutinho, 2013), treated as a binary scalar value and containing information about position and level of the cell in the tree. The leaf nodes are therefore sorted according to their locational codes, being the storing order univocal determined from the preorder traversal of the 27-tree (Camata and Coutinho, 2013). The location code is generated by generating $3^n \times 3^n \times 3^n$ indivisible cells in the 3D Cartesian coordinate space. n is the maximum possible depth. Any 27-tree can be identified by an integer triplet representing its lower left corner coordinates and its levels in the tree (Camata and Coutinho, 2013). The mesh is refined from depth to the surface, by interposing transition elements (see small panel in Figure 3.3). Once the reference cube has been generated and appropriately refined, the nodes belonging to the free surface are slightly adjusted according to the DEM of the meshed region. Figure 3.3 shows a 27-tree based mesh which encompass the topography and the bathymetry, along with the coastline. HexMesh handles arbitrary surfaces pretty easily: those surfaces are generally parametrized by a triangulation, which typically is obtained from CAD packages via STL files. The cells intersected by those complicated surfaces are smartly detected by testing the overlap between object *bounding volumes* encapsulating one or more objects of more complex nature.

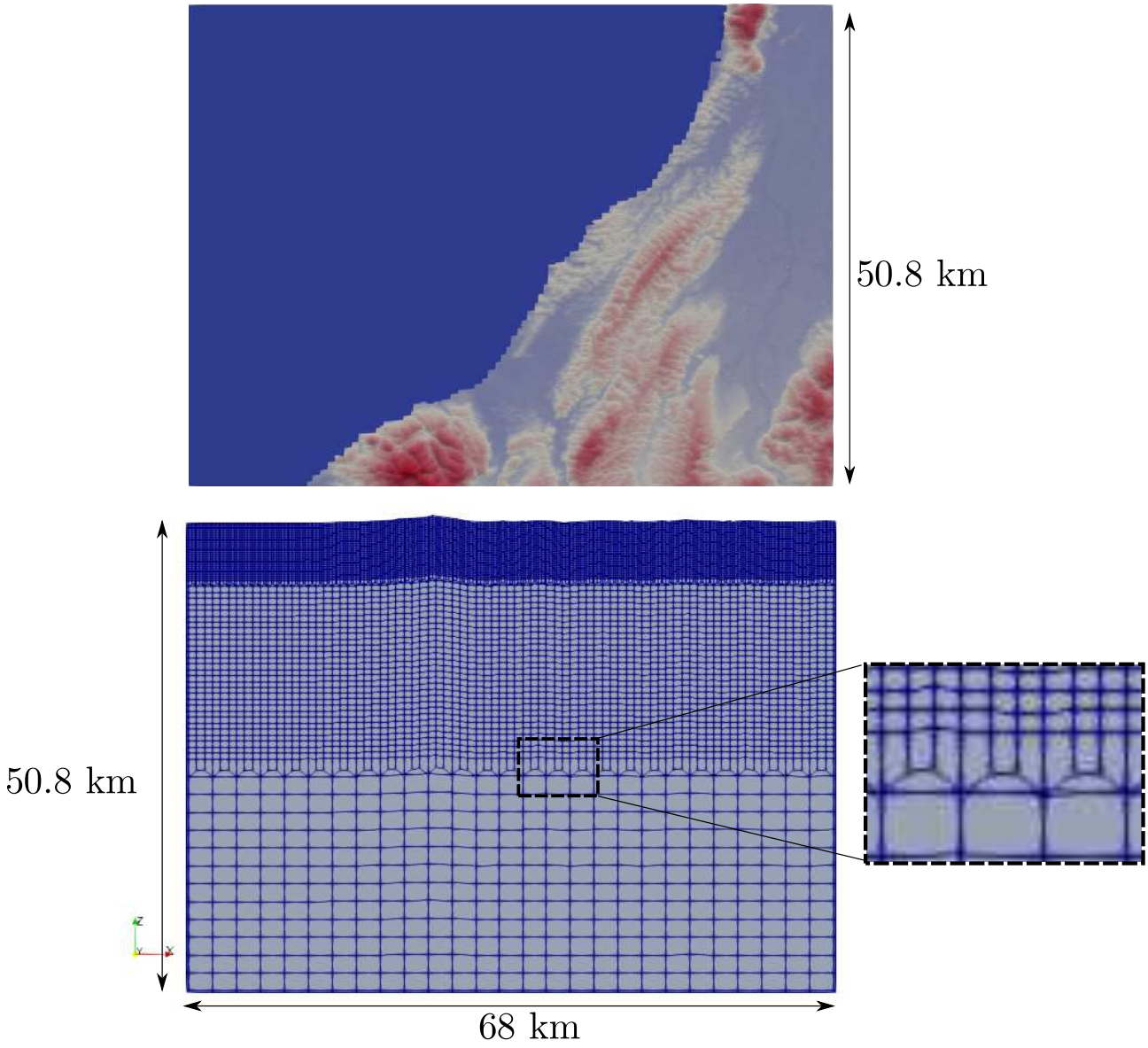

Figure 3.3: Sketch of large scale ($60 \times 50.8 \times 50.8$ km) mesh generated by 27-tree algorithm, for the Niigata region, Japan. Small panel: detail on the 3:1 refinement. The Digital Elevation Model is portrayed on the top panel: the bathymetry and the coastline of the Japan Sea were meshed as well.

3.2.3 Handling complex geology and discontinuity

The accuracy of the wave-propagation numerical solutions is strongly sensitive to the smoothness of the velocity model, or, in other words, on the level of accuracy the discontinuous material properties are modelled and the interfaces discretized. An improper discrete representation of the interfaces can cause inaccurate numerical modelling of surface waves (Chaljub et al., 2015). According to Moczo et al. (2002), the transverse anisotropy (i.e. the canonical case of a layered half-space) is the correct representation of a planar material interface consistent with the boundary conditions in the long wavelength approximation, i.e. Assuming a welded interface, the boundary condition implies the continuity of the displacement (or particle-velocity) and traction vector along it. However, one cannot infer a stress/strain continuity from this boundary conditions. Therefore, in traditional Finite Element and Finite Difference Schemes, the mesh must theoretically *honour* the spatial distribution of the geological discontinuities (i.e. sediments, folds, basins, fault disconituies) so to effectively benefit of the high degree of accuracy of the method. However, a *not honouring* approach is worth considering as well: the mesh does not model the geometrical discontinuities, but different mechanical properties are attributed to the GLL points across the discontinuity, by employing the SEM interpolating shape functions. In Figure 3.4a, a numerical example is sketched, for a bi-layered domain, with a planar material discontinuity and an impedance factor of V_{S2}/V_{S1} = 2. The impact of different modelling

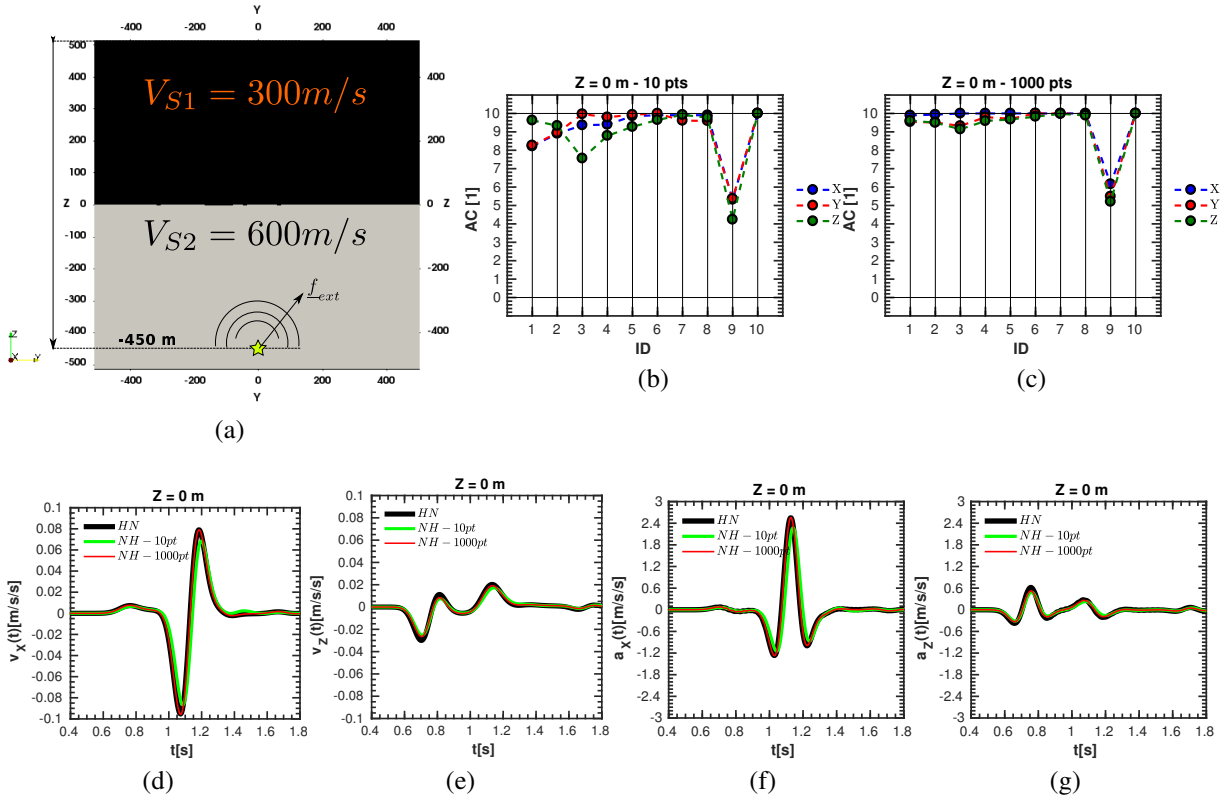

Figure 3.4: (a) Example of bi-layered domain. (b-c) Anderson's criteria values for the three components of motion simulated at the material discontinuity (Z=0 m): the honouring approach is compared to the not-honouring one, with 10 points (b) and 1000 points (c) of discretization respectively. Velocity (d-e) and Acceleration (f-g) time-histories obtained at the interface between layers 1 and 2, by employing an *honouring* (HN, black line) and *not-honouring* (coarse $NH - 10pt$, green line, and fine $NH - 1000pt$, red line) approach respectively.

strategies to handle the material heterogeneity is assessed herein: synthetic wave-forms for an honouring (black line) and not-honouring (green and red lines) are shown in terms of the velocity and

acceleration time-histories in Figures 3.4d-3.4g respectively. For the not-honouring approach, the profile was discretized by means of 10 (coarse) and 1000 points (fine), to test the impact on the synthetic wave-form. As a matter of fact higher number of GLL integration points (deployed along the element face/edges, including their corners) entail a satisfactory approximation of the heterogeneous nature of the Earth's crust, as the overall good ranking in terms of Anderson's criteria between the honouring and coarse (Figure 3.4b) and fine (Figure 3.4c) not-honouring cases show. A not-honouring approach with coarser discretization, i.e. smoother material profile, might be however poorly accurate.

3.3 Non-linear modelling in explicit dynamics

One major objective of my PhD thesis was the choice, the calibration and the numerical implementation in SEM3D of a non-linear hysteretic constitutive behaviour for soils. Hereafter, a brief summary of the main ingredients required to realistically model the soil cyclic behaviour is presented, along with some hints on the computational effort required for the numerical implementation in a 3D wave-propagation code. The choice of the elastic-plastic non-linear model was steered by the sake of its *simplicity*: a few number of parameters to be calibrated and a rather ease of implementation. To this end, one may argue that the renowned complexity of the soil cyclic behaviour is barely reproduced by a *simple* model, due to the peculiarities (such as, for instance, the shear-volumetric elastic-plastic coupling). However, I chose to privilege a less sophisticated hysteretic for two reasons, one chained to another: (1) the types of physics-based numerical analyses I performed (presented in Chapter 5) consider large scale regional domains (i.e. an area of $\approx$ 50 km of diameter) whose level of detailing and resolution seem poorly compatible with the inherent peculiarities of the soil behaviour at the laboratory scale; (2) since SEM3D was originally conceived for a visco-elastic heterogeneous rheology (i.e. for the Earth's crust) and speeded-up accordingly, a simple elastic-plastic model (that normally requires an iterative stress correction and the need to store internal variables to reproduce the path-dependent rheological behaviour) would hopefully contain the extra computational cost and have a limited impact on the overall code performance. The latter statement applies specifically to the classical type of analyses run by SEM3D: the non-linear behaviour is typically spatially restrained to the shallow soil layers (i.e. of $\approx$ 200 m of thickness), whereas the rest of the computational domain may be considered as visco-elastic. In the context of a massively parallel implementation of SEM3D, the use of sophisticated non-linear model, requiring complex iterative procedures to solve the path-dependent stress-strain relationship and several internal variables to be calibrated and stored, would eventually jeopardize the overall computational balance among the cores. The situation that is likely to avoid is the case of some MPI cores dealing with the non-linear soil behaviour of shallow layers and over-charged of floating operations, while the rest of the MPI cores is waiting. Those topics require a sophisticated analysis, which however have not been made object of this study.

3.3.1 An *excursus* on soil rheology

The main issue concerning non-linear finite element analysis is represented by the time-integration of the local constitutive relationships and to subsequently assemblage of the internal force vector $\mathbb{F}^{int}\left(\underline{\hat{\boldsymbol{U}}}_G^h; \underline{\hat{\boldsymbol{V}}}_G^h\right)$. The latter is issued from the SE semi-discretized form[7] of the following expression:

$$\sum_e^{N_e} \int_{\Omega_e} \underline{\boldsymbol{w}}_e^h \otimes_S \underline{\boldsymbol{\nabla}}_x : \underline{\underline{\boldsymbol{\sigma}}}\left(\underline{\boldsymbol{u}}_e^h\right) dV_x \tag{3.10}$$

[7]The semi-discrete counter part is expressed in Equation A.71. See Section A.6 for all the mathematical development of the mentioned semi-discretized formulation.

where Ω_e is the single element volume, $\underline{\boldsymbol{w}}_e^h$ is the SE piece-wise polynomial trial test function employed in the SE variational formulation and $\underline{\boldsymbol{u}}_e^h$ is the SE piece-wise polynomial approximation of the displacement wave-field. It is important to stress the key role that the *rheology* in bonding the internal force evolution with the displacement/velocity field, within a displacement-based mechanical problem. The rheology translates into the action of the stress operator $\underline{\underline{\boldsymbol{\sigma}}}(\cdot)$. In the following, three of the main rheologies commonly used in seismology and geotechnics are briefly described.

Elasticity

The internal force vector linearly depend on the displacement field gradient when elasticity is solely considered. For an elastic isotropic material, the rheological model reads:

$$\underline{\underline{\boldsymbol{\sigma}}}\left(\underline{\boldsymbol{u}}\left(\underline{\boldsymbol{x}};t\right)\right) = \lambda\left(\underline{\boldsymbol{x}}\right) Tr\left(\underline{\underline{\boldsymbol{\varepsilon}}}_x\left(\underline{\boldsymbol{u}}\left(\underline{\boldsymbol{x}};t\right)\right)\right) + 2\mu\left(\underline{\boldsymbol{x}}\right)\underline{\underline{\boldsymbol{\varepsilon}}}_x\left(\underline{\boldsymbol{u}}\left(\underline{\boldsymbol{x}};t\right)\right) \tag{3.11}$$

with are the so called Lamé coefficients, and the linear operator is the small strain tensor, defined as:

$$\underline{\underline{\boldsymbol{\varepsilon}}}_x\left(\underline{\boldsymbol{u}}\left(\underline{\boldsymbol{x}};t\right)\right) = \underline{\boldsymbol{u}} \otimes_s \underline{\boldsymbol{\nabla}}_x\left(\underline{\boldsymbol{x}};t\right) \tag{3.12}$$

being the symmetric gradient operator. The Lamé coefficients are usually casted into the so called *elasticity* 4^{th} *tensor* , that reads:

$$\mathbb{D}^{el}\left(\underline{\boldsymbol{x}}\right) = \lambda\left(\underline{\boldsymbol{x}}\right)\underline{\underline{\boldsymbol{I}}} \otimes \underline{\underline{\boldsymbol{I}}} + \mu\left(\underline{\boldsymbol{x}}\right)\mathbb{I}, \quad \underline{\underline{\boldsymbol{\sigma}}}\left(\underline{\boldsymbol{u}}\left(\underline{\boldsymbol{x}};t\right)\right) = \mathbb{D}^{el} : \underline{\underline{\boldsymbol{\varepsilon}}}_x\left(\underline{\boldsymbol{u}}\left(\underline{\boldsymbol{x}};t\right)\right) \tag{3.13}$$

with the 2^{nd} order identity tensor and the 4^{th} order identity tensor. When one considers an anisotropic material, $\mathbb{D}^{el}\left(\underline{\boldsymbol{x}}\right)$ has 21 independent coefficients.

Viscoelasticity

In a more general sense, the stress state in attenuating media is determined by the functional:

$$\underline{\underline{\boldsymbol{\sigma}}}\left(\underline{\boldsymbol{x}};t\right) = \int_{-\infty}^{t} \mathbb{D}^{el}\left(\underline{\boldsymbol{x}};t-\tau\right)\underline{\underline{\boldsymbol{\varepsilon}}}_x\left(\underline{\boldsymbol{u}}\left(\underline{\boldsymbol{x}};\tau\right)\right) d\tau \tag{3.14}$$

In seismology, the quality factor is generally observed to be approximately constant over a wide range of frequencies (see Section B.2 for further details).

Elastoplasticity

The classical theory of rate-independent plasticity is effectively described by means of strain-stress rate (i.e. infinitesimal increments). The reason behind this approach is that it allows to follow the path-dependent material response at each step by solving a set of ordinary differential equations (ODEs). As confirmed by experimental evidence, non-linear modelling is based on the assumption that the total strain rate is the sum of a recoverable and an irrecoverable strain ones (*elastic-plastic split*):

$$\dot{\underline{\underline{\boldsymbol{\varepsilon}}}}_x\left(\underline{\boldsymbol{x}};t\right) = \dot{\underline{\underline{\boldsymbol{\varepsilon}}}}^{re}\left(\underline{\boldsymbol{x}};t\right) + \dot{\underline{\underline{\boldsymbol{\varepsilon}}}}^{ir}\left(\underline{\boldsymbol{x}};t\right) \tag{3.15}$$

where $\dot{\underline{\underline{\boldsymbol{\varepsilon}}}}_x\left(\underline{\boldsymbol{x}};t\right) \in \mathbb{S}$ represents the small-strain rate tensor for a generic REV positioned at point $\underline{\boldsymbol{x}}$ in space at time t; $\dot{\underline{\underline{\boldsymbol{\varepsilon}}}}^{re}\left(\underline{\boldsymbol{x}};t\right)$ and $\dot{\underline{\underline{\boldsymbol{\varepsilon}}}}^{ir}\left(\underline{\boldsymbol{x}};t\right)$ are the recoverable and irrecoverable strain rates respectively. In the elastic-plastic framework, the recoverable strain rate is called *elastic* one (), whereas the entire irrecoverable part is purely plastic (). Irrecoverable strain increments take place *instantaneously*, coherently with the rate-independent plasticity theory. As mentioned in subsection B.1, the non-linear cyclic material behaviour is modelled by considering a set of *hidden internal variables*, noted

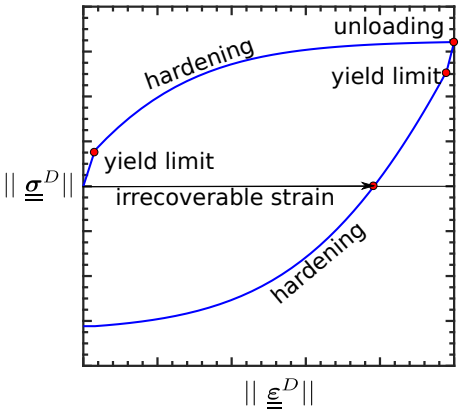

Figure 3.5: Typical non-linear strain-stress curve.

as . The hidden variables keep track of the loading path, by influencing the stress response at each time. For instance, a typical stress-strain curve for a simple-shear test is shown in Figure 3.5. The stress-strain relationship remains linear as long as the stress state does not exceed a certain threshold (indicated as *yield limit* in Figure 3.5). At this stage, all the strain cumulated is entirely recoverable and the set of hidden variables does not evolve since strain and stress states are directly related through the incremental linear (hyper-) elastic Hooke's law, which reads:

$$\dot{\underline{\underline{\boldsymbol{\sigma}}}}\left(\underline{\boldsymbol{x}};t\right)=\mathbb{D}^{el}\left(\underline{\boldsymbol{x}};t\right):\left(\dot{\underline{\underline{\boldsymbol{\varepsilon}}}}_{x}\left(\underline{\boldsymbol{x}};t\right)-\dot{\underline{\underline{\boldsymbol{\varepsilon}}}}_{x}^{pl}\left(\underline{\boldsymbol{x}};t\right)\right) \tag{3.16}$$

The Hooke's law is valid within the so called *initial elastic domain* (Simo and Hughes, 1998). As general assumption, the stress state and the set of hidden variables must lie at all the time within the an *admissible* domain referred as to the *instantaneous elastic range* (that can be seen as a non-linear evolution of the initial one). Its boundary is called the *yield locus* (defined by means of a convex *yield function* =0): in an elastic-plastic framework, the stress-strain relationship is perfectly linear and elastic before crossing $\partial\mathbb{E}_{\sigma\chi}$, and $\underset{\sim}{\boldsymbol{\chi}}$ remains constant. The yield locus constrains the admissible stresses within a closed interval (i.e. the $\mathbb{E}_{\sigma\chi}$ is a closed convex set, Simo and Hughes, 1998). It has been experimentally proven that plastic flow develops as long as the the stress state is equal or exceeds the so called *yield limit* ($f = 0$). Plastic strains develop according to the so called *flow rule*, whereas the yield function f evolves along with the plastic flow according to the appropriate *hardening-rule* (see Section B.3.3). The whole process of elastic-plastic loading/unloading may be formulated as a constrained evolution problem and solved by translating those constrains into some non-linear programming conditions. Traditionally, the plastic flow activation and evolution are ruled by the manifold *Karush-Kuhn-Tucker condition* (KKT) (Simo and Hughes, 1998). The KKT approach generalizes the method of Lagrange multipliers (limited to equality constraints) and they translate mathematically the experimental evidence that when the applied stress is less than the flow stress, no irrecoverable strain is developed and the instantaneous response of the device is elastic (the so called *plastic consistency*). The inadmissible stress state therefore lies outside the yield locus. Moreover, the consistency condition requires a complementary condition to ensure the *persistency* of the plastic flow, which assures the stress state to be confined within the evolving yield locus. When plastic flow occurs, the set of ruling equations can be reformulated in the following time-marching computational problem, arising by splitting the loading path into N sub-steps $\Delta t_n = (t_n; t_{n+1})$ of the total time interval $\mathbb{I}_t = \cup_{n=0}^{N} \Delta t_n$:

Given the state of the material $\left(\underline{\underline{\boldsymbol{\sigma}}}_n, \underset{\sim}{\boldsymbol{\chi}}_n\right)$ *at* $t = t_n$*, and the evolution equations of the Elastic-*

Plastic model:

$$\mathcal{EP}\left(\underline{\underline{\boldsymbol{\sigma}}}, \underset{\sim}{\underline{\underline{\boldsymbol{\chi}}}}\right) : \begin{cases} \dot{\underline{\underline{\boldsymbol{\sigma}}}} = \mathbb{D}^{ep}\left(\underline{\underline{\boldsymbol{\sigma}}}; \underset{\sim}{\underline{\underline{\boldsymbol{\chi}}}}\right) : \dot{\underline{\underline{\boldsymbol{\varepsilon}}}}_x, & \text{elastoplastic CE} \quad (3.17) \\ \dot{\underset{\sim}{\underline{\underline{\boldsymbol{\chi}}}}} = \dot{p}\underset{\sim}{\boldsymbol{h}}\left(\underline{\underline{\boldsymbol{\sigma}}}; \underset{\sim}{\underline{\underline{\boldsymbol{\chi}}}}\right) = \mathbb{H}\left(\underline{\underline{\boldsymbol{\sigma}}}; \underset{\sim}{\underline{\underline{\boldsymbol{\chi}}}}\right) : \dot{\underline{\underline{\boldsymbol{\varepsilon}}}}_x, & \text{hardening law} \quad (3.18) \end{cases}$$

find:

$$\begin{cases} \underline{\underline{\boldsymbol{\sigma}}}_{n+1} = \underline{\underline{\boldsymbol{\sigma}}}_n + \int_{t_n}^{t_{n+1}} \mathbb{D}^{ep}\left(\underline{\underline{\boldsymbol{\sigma}}}; \underset{\sim}{\underline{\underline{\boldsymbol{\chi}}}}\right) : \dot{\underline{\underline{\boldsymbol{\varepsilon}}}}_x d\tau & (3.19) \\ \underset{\sim}{\underline{\underline{\boldsymbol{\chi}}}}_{n+1} = \underset{\sim}{\underline{\underline{\boldsymbol{\chi}}}}_n + \int_{t_n}^{t_{n+1}} \mathbb{H}\left(\underline{\underline{\boldsymbol{\sigma}}}; \underset{\sim}{\underline{\underline{\boldsymbol{\chi}}}}\right) : \dot{\underline{\underline{\boldsymbol{\varepsilon}}}}_x d\tau & (3.20) \end{cases}$$

and that respect the KKT conditons $\mathcal{K}$ (Equation B.29).

is the so called *elastic-plastic* tensor (depending on the current stress state and on the strain increment). represents the plastic hardening modulus and is the plastic multiplier (Sloan et al., 2001). The system of Equations 3.18 rarely has a closed form solution. Therefore, the stress state/plastic flow integration at the current time-step is numerically obtained by means of either *implicit* (or *backward Euler*) algorithm or *explicit* (or *forward Euler*).

3.4 Numerical integration of the elastic-plastic stress state

During a typical step or iteration of an elastic-plastic finite element analysis, the external forces $\mathbb{F}^{ext}$ are applied in increments and the corresponding nodal displacement $\underline{\boldsymbol{u}}$ and velocities $\underline{\boldsymbol{v}}$ are predicted from the global stiffness equations. Those quantities are obtained by computing the internal forces, which are the expression of the strain-energy stored by the body and which are derived from the strain increment $\dot{\underline{\underline{\boldsymbol{\varepsilon}}}}_x$ and the induced stress increment $\dot{\underline{\underline{\boldsymbol{\sigma}}}}$. In the context of fast transient dynamics (e.g. the regime induced by a strong ground motion), strain increments are computed (at each integration point, within each element) by exploiting the *velocity-wise* approach proposed by Joyner (1975), that reads:

$$\dot{\underline{\underline{\boldsymbol{\varepsilon}}}}_x = \underline{\boldsymbol{v}} \otimes_s \underline{\boldsymbol{\nabla}}_x \quad (3.21)$$

The stress state can be computed by exploiting the desired constitutive relationship, expressed by a generic functional form $\mathcal{F}$ (see Section 3.5, for further details). In SEM3D an explicit multi-step integration scheme was adopted. A simple and fast iterative procedure is introduced to obtain final stress and hardening states, so to check whether they comply with the plastic consistency conditions within an accepted tolerance (see Section B.3.2). In a fully implicit scheme, non-linear ODEs linearized and solved by iterative minimization of the residuals. Implicit methods solve the set of ODEs at the final step, leading to resulting stress and hardening states intrinsically satisfy the plastic consistency. In explicit methods, an artificial drifting correction must be applied to fulfill those conditions. Although generally more accurate, the great disadvantage of implicit methods resides in the fact that their complex algebraic formulation requires the second derivatives of the yield function and plastic potential to be computed at each sub-iteration, dramatically slowing the solver down and leading to cumbersome computational costs. Explicit schemes just involve first order derivatives. Another crucial aspect is that implicit schemes do not require the intersection with the yield surface to be found, whereas the explicit ones do. SEM3D was featured by the general explicit elastic-plastic integrator with automatic sub-stepping and error control proposed by Sloan et al. (2001). This adaptive procedure is based on the pioneering work of Sloan (1987), so to improve the solution accuracy. The latter *sub-stepping algorithm* was implemented in SEM3D due to the important enhancements to improve their accuracy,

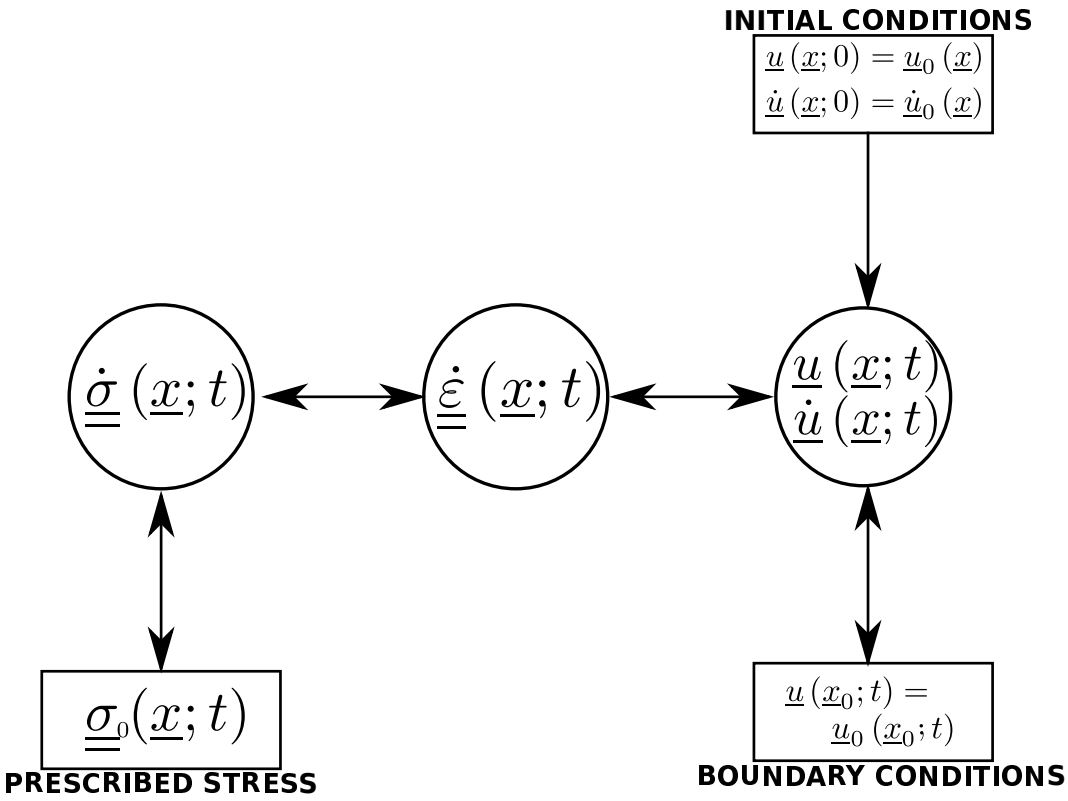

Figure 3.6: Sketch of the usual time marching algorithm used in non-linear dynamics.

efficiency and robustness. In such a way, the error on the final stress is automatically limited and stress state which does not comply with the yield criterion is automatically *drifted* onto the yield surface. The main drawback of such methods is that they bare on the knowledge of the stress state that intersects the yield surface: spurious intersections may appear when fast cyclic loading is concerned, but they are effectively avoided as explained in Section B.3.4.

3.4.1 Cyclic behaviour of geo-materials

Inelastic straining of geo-materials induces many complex phenomena which have to be described separately or simultaneously. The elastic behaviour does not allow for plastic (permanent) strains, resulting inadequate to describe the unloading and reloading stress-strain curves observed experimentally. Masing was able to produce a simple model to reproduce the hysteretic behaviour and the stress reversals (Masing, 1923, 1926). Such simplified approach (sometimes referred as to *deformational plasticity*) is based upon the assumption of a *backbone* strain-stress curve featured by arbitrary loading, unloading and reloading shear moduli which have to respect the so called *generalized Masing rules* (Vucetic, 1990; Kramer, 1996, among others). This mathematical interpretation of the hysteresis behaviour is phenomenological. Several models of backbone curves have been proposed so far: the Ramberg-Osgood, the hyperbolic and the logarithmic models are among the most popular ones (e.g. Ishihara et al., 1985; Kramer, 1996; Beresnev and Wen, 1996). Modified versions may be found in Hashash and Groholski (2010); Hashash and Park (2001). Non-linear stress-strain functions, in combination with the Masing rules, allow for a simplified equivalent-linear analysis of shear wave propagation in soils, which is an important component of many seismic and dynamic geotechnical problems (Puzrin, 2012). However, the proper way to model both the non-linearity and the irreversibility of the small and large strain behaviour is within the framework of the plasticity theory. Compared to elastic-plastic models, the deformational plasticity approach is however more

cost-effective, since neither internal variables need to be stored, nor their evolution has to be described. Traditionally, the cyclic behaviour has been described by means of an internal *back stress* as state variables, which changes sign according to the corresponding stress-strain cycle, taking the form of a hysteresis loop (Armstrong and Frederick, 1966; Frederick and Armstrong, 2007). The conventional elastic-plastic constitutive model assumes that a purely-elastic behaviour takes place at small strain (Drucker, 1988). However, the latter is therefore incapable of describing the plastic strain rate due to the rate of stress inside the yield surface (Hashiguchi, 2015). Starting from the late 60s, lot of research has been done on unconventional elastic-plastic constitutive models aiming at describing the progressive plastic strain development even inside the yield surface. To effectively model the non-linear path-dependence of soil materials, several mathematical models have been formulated in the past. For instance, the multi-yield surface plasticity model was proposed by Iwan (1967) and Mroz (1967), then applied by Prevost to soil mechanics (for instance, Prevost, 1977, 1978). The model is an extension of classical $J2$ (or Von Mises) elastic-plastic behaviour, featured by a series of N nested yield surfaces to reproduce the soil non-linear hysteretic behaviour by means of a piecewise linear approximation based on the contributions of each plastic moduli. The i^{th} yield surface is associated to a linear-kinematic hardening rule, defining a sub-regions (in the stress space) of constant plastic shear moduli (computed considering the active plastic mechanisms). A pure deviatoric kinematic hardening rule is employed to capture the Masing-type hysteretic cyclic response behavior of clays under undrained shear loading conditions. Another efficient model was proposed by Aubry et al. (1982), who developed it at *École Centrale Paris* (ECP). The ECP model was then improved by Hujeux (1985) and applied to seismic wave propagation (e.g., Aubry and Modaressi, 1992; Lopez-Caballero et al., 2007; Lopez-Caballero and Modaressi-Farahmand-Razavi, 2010; Montoya-Noguera, 2016, among others). The ECP model can take into account a large range of deformations due to its decomposition into pseudo-elastic, hysteretic and mobilized domains. According to the critical-state concept, the macroscopic behavior of sands and clays is similar and is related to the proximity of its initial state to the critical state or steady-state rather than to the absolute measurements of density (Jeffries and Been, 2006; Ishihara et al., 1985). Three hardening evolutions are used for the different mechanisms. For monotonic mechanisms: (1) the deviatoric, which is based on the plastic strain and is dependent on deviatoric and volumetric strains, and (2) the isotropic, where only volumetric strains are involved; and for cyclic loading: (3) the kinematic hardening that relies on the state variables at the last load reversal (Montoya-Noguera, 2016).

The reality is that in many practical geotechnical problems only a relatively small volume of soil experiences large deformations. The strains in the remaining part are very small. In assessing a strong ground motion earthquake scenarios at the regional scale, the analysis is not intended to estimate the settlements of shallow deposits, but rather the overall influence of the non-linear material behaviour on the incident wave field in terms of absorbed energy and frequency content. As the problem size scales up, the small strain contribution can be quite insignificant to depict the overall geotechnical-seismic response. Moreover, the computational cost associated to a detailed dynamic analysis of the highly non-linear nature of soils rapidly blows up due to the required spatial refinement of the computational grids.

3.5 Modelling hysteretic soil non-linearity

The deformation behaviour of geo-materials is very hard to be described. The main reason resides in the high path-dependency of soil behaviour, that restricts the predictive efficiency of any mathematical formulation, despite its degree of complexity, mainly due to the poor generalization. Specifically, in soil dynamics, the behaviour of soils under dynamic loading is mainly characterized by (1) the elastic or maximum-stiffness represented by the shear modulus (μ_0); and (2) the degradation of the

secant shear modulus (G) and the evolution of damping (D) with respect to the shear distortion (γ), known as the *non-linearity curves*. The decrease of μ involves the decrease of the shear wave velocity (V_S) and hence a shift to low frequencies, as shown earlier. Additionally, the increase in D causes a deamplification of the amplitude of the propagating motion. Finally at high levels of strain, other phenomena appear related to the evolution of volume change and of pore water pressure generation, in the case of saturated media. Two resisting/dissipative mechanism usually take place, i.e. the frictional (displacement proportional) and viscous one (velocity proportional).

As a matter of fact, a suitable non-linear model for soil dynamics should meet a few requirements (Prevost, 1982; Pisanò and Jeremić, 2014):

1. a *complete* multi-axial formulation: the behaviour must be captured when soil undergoes a general stress-strain path instead of being limited to a few classes of paths (e.g. axial symmetry or pure shear);

2. a good compromise between *ease of calibration* a *sufficient* description of the physical process: a simpler model is desirable, since it would require less samples and less tests to be calibrated, until it does reproduce the major of observed phenomena

3. a fair reproduction of the *dynamic stiffness reduction* and *damping*: it should be verified over a wide strain range, as well as frictional failure and irreversible deformation. Dilatancy would be desirable as well, to describe volumetric behaviour.

For instance, numerous formulations have been proposed in the past for quasi-static loading conditions. For many specific experimental tests, those existent constitutive relationships resulted to be very accurate, yet hardly applicable to different *in situ* loading conditions (such as in earthquake engineering applications). The model should fit some experimental curves, but preserving its applicability to a larger dataset and loading conditions. In this perspective, a *good* material model should be able to first determine correctly the stress-strain behaviour in the specific experimental test conditions and then predict the observed behaviour in a blind prediction. In this work, the hysteretic material behaviour was modelled within the context of a J_2-plasticity framework, i.e. characterized by a von Mises failure criterion and a non-linear Armstrong-Frederick (AF) kinematic hardening rule (also called Chaboche's model) (Armstrong and Frederick, 1966; Chaboche, 1989). The yield locus is identified as the von Mises cylinder, i.e. the norm of the deviatoric stress, expressed as:

$$f = \sqrt{\frac{3}{2}\left(\underline{\underline{\boldsymbol{S}}}^{\sigma} - \underline{\underline{\boldsymbol{X}}}\right) : \left(\underline{\underline{\boldsymbol{S}}}^{\sigma} - \underline{\underline{\boldsymbol{X}}}\right)} - \sigma_{yld} \tag{3.22}$$

where $\underline{\underline{\boldsymbol{S}}}^{\sigma}$ denotes the deviatoric stress tensor:

$$\underline{\underline{\boldsymbol{S}}}^{\sigma} = \underline{\underline{\boldsymbol{\sigma}}} - \underline{\underline{\boldsymbol{\sigma}}} : \underline{\underline{\boldsymbol{I}}} \tag{3.23}$$

and (called *back-stress tensor*) denotes the center of the yield surface ($f = 0$) in the deviatoric stress space (grey circle in Figure 3.7a). embodies the size the yield surface ($\frac{3}{2}$ times the yield surface ratio). The plastic potential function reads:

$$g = f + \frac{3}{4}\frac{\kappa_{kin}}{C_{kin}}\underline{\underline{\boldsymbol{X}}} : \underline{\underline{\boldsymbol{X}}} \tag{3.24}$$

with being the two parameters that rule the non-linear evolution of the kinematic hardening. The isochoric flow-rule derived from Equation 3.24 is expressed as:

$$\underline{\underline{\dot{\boldsymbol{\varepsilon}}}}_x^{pl} = \underline{\underline{\dot{\boldsymbol{\varepsilon}}}}^{pl} = \langle \dot{p} \rangle \underline{\underline{\boldsymbol{\nabla}}}_{\sigma} g \tag{3.25}$$

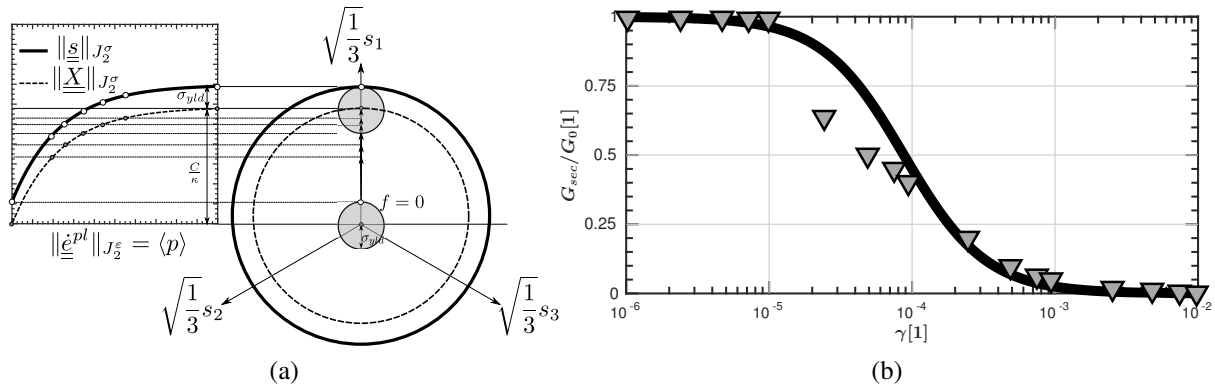

(a) (b)

Figure 3.7: (a) Norm of the deviatoric stress and back-stress (black dashed line) as a function of the plastic-strain norm, according to the AF hardening rule. (b) Normalized decay curve obtained with the AF model, used to model the non-linear soil behaviour.

where $\langle \dot{p} \rangle = \max(0, \dot{p})$ is the plastic multiplier ($\langle \dot{p} \rangle = \|\underline{\underline{\dot{\varepsilon}}}_x^{pl}\|_{J_2^\varepsilon}$), $\underline{\underline{\nabla}}_\sigma g$ is the gradient of the plastic potential g with the respect to the deviatoric stress tensor and the deviatoric plastic strain rate. Despite the non-associative flow rule ($f \neq g$), plastic flow is normal to the yield locus in the deviatoric plane. The plastic strain increment is non-negative and it undergoes the KKT complementary conditions. The extra term $\frac{3}{4}\frac{\kappa_{kin}}{C}\left(\underline{\underline{\boldsymbol{X}}} : \underline{\underline{\boldsymbol{X}}}\right)$ represents the model's *fading memory*. Finally, the hardening rule for the kinematic internal variable $\underline{\underline{\boldsymbol{X}}}$ reads:

$$\underline{\underline{\dot{\boldsymbol{X}}}} = -\frac{2}{3}C_{kin}\dot{p}\underline{\underline{\nabla}}_X g = \frac{2}{3}C_{kin}\underline{\underline{\dot{\varepsilon}}}_x^{pl} - \frac{3}{2}\kappa_{kin}\underline{\underline{\boldsymbol{X}}} \tag{3.26}$$

The latter expression describes the shift in the deviatoric plane of the yield locus's center $\underline{\underline{\boldsymbol{X}}}$: the critical state (i.e. hardening saturation) is achieved when the stress point lies both on $f = 0$ and on the yield limit surface (black solid line in Figure 3.7a). With the respect to the classic linear kinematic hardening rule, the Armstrong-Frederick model states the back-stress increment along with the plastic flow, but adding a *recall* term $-\frac{3}{2}\kappa_{kin}\underline{\underline{\boldsymbol{X}}}$ that makes the back-stress evolution non-linear. In this context, C_{kin} represents the *initial hardening modulus*, i.e. the slope of the stress-plastic strain curve, when $k_{kin} = 0$. In such a case, the model is a bilinear one, with classic linear kinematic hardening. The second parameter k_{kin} represents the rate at which the hardening modulus decreases with increasing plastic strain.
The inelastic response of a material model develops under different loading conditions, typically when the material undergoes monotonic or cyclic excitation, applied in a quasi-static or dynamic manner. Figure 3.8 shows the performance of the AF model, in terms of two normalized stress paths (red lines) developed accordingly, under cyclic strain-controlled loading (blue line). In Figures 3.8b- 3.8d, it can be noticed the different stress response between a symmetric and non-symmetric straining paths. Features such as inclination or breadth of the hysteresis loops strongly depend on both soil stiffness and damping.

3.5.1 Application of AF model in soil dynamics

It has been widely observed that when a clayey soil undergoes fast dynamic loading (for instance, a seismic excitation), it attains an undrained behaviour. This assumption entails the possibility of a total stress analysis, since no the water over-pressure corresponds to the volumetric load increment at each time step under isochoric conditions. This property inherited from the undrained assumption couples with the pressure-independent failure criterion usually adopted, in total stress, when describing the

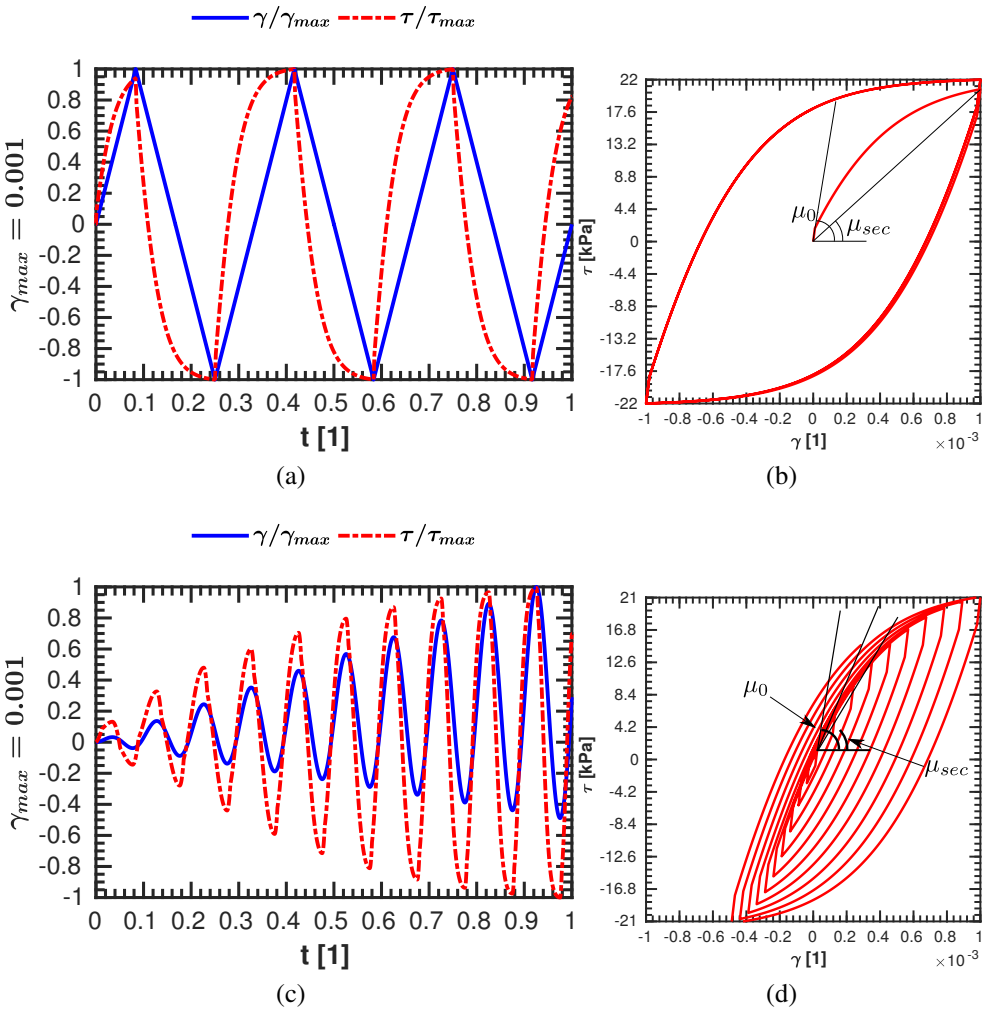

Figure 3.8: Shear stress-strain curves $\gamma - \tau$ for a typical saw-tooth (a-b) and rising sinus (c-d) strain paths. On the left, the time evolution of the normalized strain-stress paths id portrayed. On the right, the stress-strain hysteresis loops are depicted instead.

plastic behaviour of clays. In this sense, the AF model presented in the section above suits the basic requirements to describe the inelastic and hysteretic behaviour of cohesive soils under shear loading. This statement translates into being capable to display a non-linear decay of the secant shear modulus (also indicated as G, in an engineering notation), along with increasing shearing distortion γ, as portrayed in Figure 3.7b. The loops portrayed in Figures 3.8b- 3.8d indicate the non-linear evolution of the secant modulus with increasing shear distortion. The secant shear modulus may be taken as an average shear stiffness of the soil. Given that the cyclic behaviour of the soil is nonlinear as well as hysteretic, it becomes clear that stiffness together with the damping (computed upon the calculation of the loop's area) are strain dependent. Therefore, a series of cyclic tests should be performed with varying strain levels such that the collection of results, in terms of stiffness, lead to the normalized modulus reduction curves. One key parameter is the shear modulus at small strains, also known as small-strain shear modulus, μ_0 (also indicated as G_0, in an engineering notation) because it plays a significant role in the elaboration of the normalized modulus reduction curves. As the name itself describes it, G_0 serves the normalization of the cyclic tests stiffness outcome as being the maximum value the material can experience. One other key parameter, damping ratio represents a material property related to the friction between soil grains, strain rate effects and inelastic stress-strain response. Each hysteresis loop describes the dissipation of energy during a loading cycle; the post-processing

of data leads to the damping ratio as it depends both on the energy dissipated during a complete loading cycle at a given strain amplitude and maximum retained strain energy. Moreover, the decrease in shear strain translates into decrease in dissipated energy, thus the area of the loop will suffer a reduction as well. Similarly, the damping ratio curves are defined collecting different nonlinear soil responses based on increasing strain amplitude. However, the trend is opposite, as in the nonlinearity of the soil results in an amplification of dissipated energy, thus in the damping ratio, with increasing strain magnitude.
In this study, the mentioned decay curve is employed to define the non-linear soil behaviour, independently from its elastic properties (represented herein by the initial elastic shear modulus μ_0).

3.6 Numerical Verification: the PRENOLIN test case

SEM3D was verified by running some of the canonical cases proposed within the framework of the PRENOLIN international benchmark (*PREdiction of NOn-LINear soil behavior*) (Régnier et al., 2016). The principal scope of the PRENOLIN project was to assess and verify the response of several numerical codes in predicting non-linear seismic site response with various constitutive models. Several recommendations were provided, concerning some good practices in the numerical simulation of 1D seismic site-effects. Another major achievement of this numerical benchmark was represented by the uncertainty quantification performed on the major geotechnical parameters (e.g. elastic modulus, shear strength), on the interpretation of laboratory and *in situ* experimental results and on the way to inject the incident wave motion at the sediment-substratum inter- face (that is via an elastic base, and via a rigid base respectively).
The PRENOLIN benchmark involved 21 teams and 23 different computational codes. Most of them solve the SH-wave propagation equation by considering a mono-dimensional layered half-space (trimmed at the *engineering bedrock*), featured by elastic/visco-elastic/equivalent linear/non-linear soil rheology. However, some of the codes involved are based on the two-dimensional (2D) version of the wave-propagation problem and were effectively re-adapted to reproduce a plane shear wave field propagating vertically towards the free surface. SEM3D has not been conceived to simulate 1D seismic site response, but rather to study the propagation of the regional wave-field radiated from seismic source. In this sense, a major effort has been pursued to re-adapt a full 3D numerical code to a mono-dimensional boundary problem. In this sense, this section aims to highlight the capability to approximate the ideal conditions assumed in this benchmark and effectively reproduce the non-linear site-effects. Keeping that goal in mind, the main results of the verification phase portrayed in the following sections refer to the simplest test cases previewed in PRENOLIN. Although not fully exhaustive, the analyses performed highlight a few major features of the SEM3D code, namely:

1. its capability to approximate the incident plane wave-front, by means of a set of in-phase point-sources deployed all over an horizontal plane

2. its satisfactory performance in reproducing the site amplification in elastic/visco-elastic cases

3. the predicted non-linear site response, according to the implemented AF elastic-plastic model

3.6.1 Canonical test case P1

The simplest test case proposed to the participants of the PRENOLIN projects is the Profile 1 (P1, Figure 3.9), a 20 m thick homogeneous soil layer presenting a significant velocity impedance ratio at rock, with amplification in the intermediate frequency range (2-10 Hz). The P1 geology was modelled in SEM3D by considering a 130 m$\times$130 m$\times$25 m (see Figure 3.10). The numerical model was enveloped by Perfectly-Matched-Layers (PML), required to dampen the incident waves at the lateral boundaries, so to simulate the ideal half-space conditions.

3.6.2 Approximation of the incident plane wave-motion

A simple Ricker pulse (RCP) input motion was tested (Figure 3.11). As far as the input motion is concerned, SEM3D is featured by point force/moment, widely employed in computational seismology to introduce a dynamic excitation into the computational model. The far-field approximate solution of the elasto-dynamic problem for an elastic isotropic and homogeneous material and a point source

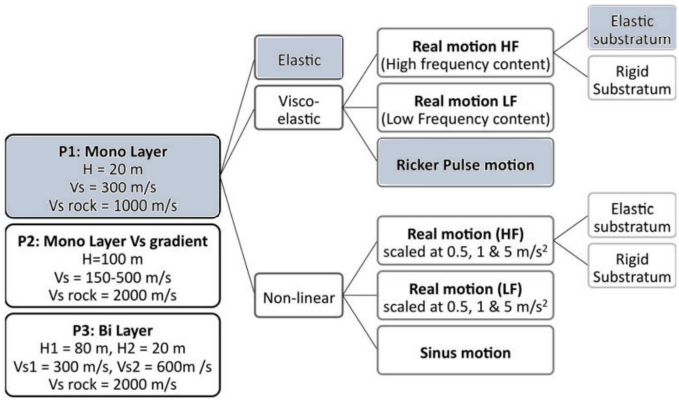

Figure 3.9: The three simple idealized profile cases studied here (P1-P3), for the elastic and nonelastic domains, and for a rigid and elastic soil-bedrock base, using a Ricker pulse and three accelerations of different peak ground acceleration (PGA) and frequency contents

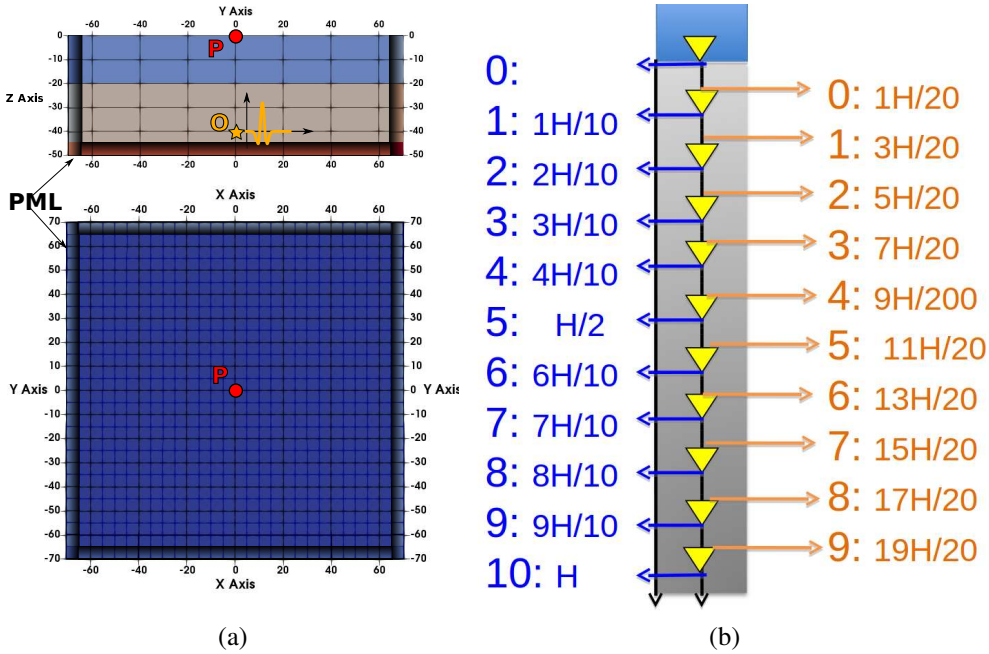

(a) (b)

Figure 3.10: (a) SEM3D model for the P1 case. (b) Scheme of the recording stations along the soil column.

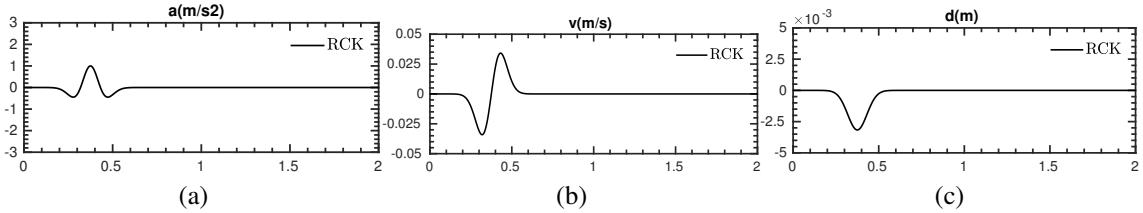

(a) (b) (c)

Figure 3.11: Ricker pulse acceleration

$\underline{\boldsymbol{f}} = \delta\left(\underline{\boldsymbol{x}} - \underline{\boldsymbol{x}}_O\right)\underline{\boldsymbol{a}}$ reads:

$$\underline{\boldsymbol{u}}^G\left(\underline{\boldsymbol{x}}, \underline{\boldsymbol{x}}_O, \underline{\boldsymbol{a}}; t\right) = \frac{\left(\underline{\boldsymbol{e}}_r.\underline{\boldsymbol{a}}\right)\underline{\boldsymbol{e}}_r}{4\pi\rho c_P^2 r}\delta\left(t - \frac{r}{c_P}\right) + \frac{\underline{\boldsymbol{a}} - \left(\underline{\boldsymbol{e}}_r.\underline{\boldsymbol{a}}\right)\underline{\boldsymbol{e}}_r}{4\pi\rho c_S^2 r}\delta\left(t - \frac{r}{c_S}\right) \tag{3.27}$$

being the Dirac's function, the P-wave and S-wave velocities, ρ the crust density and with $r = \|\underline{\boldsymbol{x}} - \underline{\boldsymbol{x}}_O\|$, and $\underline{\boldsymbol{e}}_r = \left(\underline{\boldsymbol{x}} - \underline{\boldsymbol{x}}_O\right)/r$ the radial unit vector (in spherical coordinates). The elasto-dynamic solution for a generic time-varying source function is represented by the convolution product $\underline{\boldsymbol{u}}^G\left(\underline{\boldsymbol{x}}, \underline{\boldsymbol{x}}_O, \underline{\boldsymbol{a}}; t\right) * f\left(t\right)$. Therefore, any arbitrary incident wave motion can be *a priori* generated by a spatial distribution of point-wise forces, keeping in mind that the elasto-dynamic Green's function is the superposition of a P-wave (first term in Equation 3.27) and a S-wave (second term in Equation 3.27). For instance, if one considers a plane Σ and a point force $\underline{\boldsymbol{f}}^\Sigma\left(\underline{\boldsymbol{x}}_0; t\right) = f^\Sigma\left(t\right)\delta_{\underline{\boldsymbol{x}}_0}\underline{\boldsymbol{e}}_\Sigma$[8] located at a distance d from a plane Σ and tangent to it (Figure 3.12), the resulting wave-field $\underline{\boldsymbol{u}}^\Sigma\left(\underline{\boldsymbol{x}}; t\right)$, impinging the plane Σ can be written as:

$$\begin{aligned}&\underline{\boldsymbol{u}}^\Sigma\left(\underline{\boldsymbol{x}}, \underline{\boldsymbol{x}}_O, \underline{\boldsymbol{e}}_\Sigma; t\right) = \underline{\boldsymbol{u}}^G\left(\underline{\boldsymbol{x}}, \underline{\boldsymbol{x}}_O, \underline{\boldsymbol{e}}_\Sigma; t\right) * f^\Sigma\left(t\right) = \\ &\frac{\left(\underline{\boldsymbol{e}}_r.\underline{\boldsymbol{e}}_\Sigma\right)\underline{\boldsymbol{e}}_r}{4\pi\rho c_P^2 r} f^{SH}\left(t - \frac{r}{c_P}\right) + \frac{\underline{\boldsymbol{e}}_\Sigma - \left(\underline{\boldsymbol{e}}_r.\underline{\boldsymbol{e}}_\Sigma\right)\underline{\boldsymbol{e}}_r}{4\pi\rho c_S^2 r} f^{SH}\left(t - \frac{r}{c_S}\right)\end{aligned} \tag{3.28}$$

It is clear from Equation 3.28 that the plane Σ is impinged by asynchronous P- and S-waves arrivals.

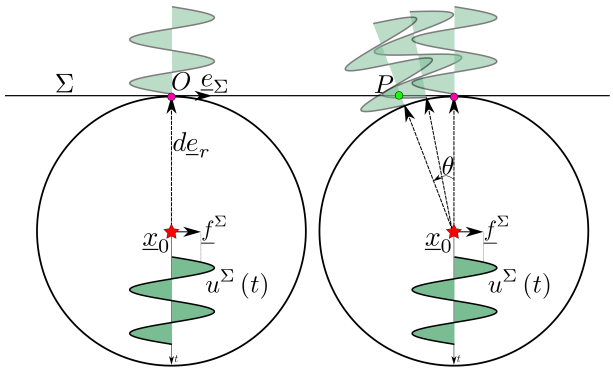

Figure 3.12: Sketch of the plane wave-front composed by spherical waves (Huygen's principle).

In addition to the normal incidence ray-path, there are other rays not quite vertical which constructively interfere with the normal ray to generate the total response (non-specular rays) (Liner, 2004). A plane-wave field at Σ requires multi-point sources to be generated. The idea stems from the *Huygen's principle*, which states that the wave-front at any later instant may be regarded as the envelope of secondary spherical waves placed along the earlier wave-front. Therefore, it becomes of primary importance to chose a sufficiently small lag-distance ℓ between each point source, so to vanquish the disturbance of non-specular rays, by letting them constructively interfere to obtain a planar in-phase wave-field. The numerical simulation of the Huygens' principle is rather complicated to reproduce however, due to the intricate interference patterns created by the spherical wave-fields. Moreover, the single source amplitude should be calibrated so to obtain a quasi-plane wave-field at the soil-to-bedrock interface with the desired incident amplitude. To this end, a first trial & error numerical experiment was performed on an 3D column (Figure 3.10) so to simulate the wave-propagation from depth up to the soil layer throughout the bedrock. An homogeneous bedrock material was considered at this stage and the free surface was distanced from the desired interface to avoid reflected waves travelling backwards to pollute the incident ground motion. Figure 3.13 shows the good fit between the reference input motion and the SEM3D simulation at point O in Figure 3.10.

[8] $\underline{\boldsymbol{e}}_\Sigma$ represents unit vector parallel to the plane Σ

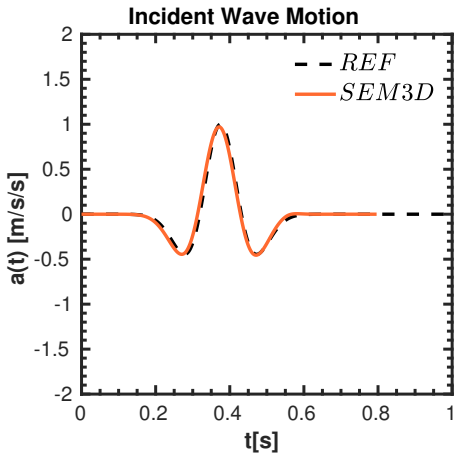

Figure 3.13: Incident wave motion at the soil-bedrock interface (point O in Figure 3.10): reference motion (REF, dashed black line) and synthetic wave motion generated by SEM3D (orange line).

The incident wave motion was generated by a distribution of equally spaced point sources (ℓ=20 m) aligned on an horizontal plane (distanced 20 m from point the point O).

3.6.3 Site amplification in linear elastic regime

Despite some minor discrepancies due to the handmade implementation of the plane-wave input motion, SEM3D was effectively employed to reproduce the ground motion amplification due to shallow softer sediments, in a classical soil-over-bedrock configuration (portrayed in Figure 3.10). The incident wave-motion calibrated in Subsection 3.6.2 was injected in the model as *outcrop* motion (i.e. by dividing its amplitude by a factor 2) and the synthetics accelerogram obtained at surface was compared to the reference one, obtained from the Haskell-Thomson analytical solution (see Figure 3.14a Haskell, 1953; Thomson, 1950). The site amplification by uniform layer on elastic bedrock is shown in Figure 3.14b: SEM3D effectively reproduce the theoretical response for a soil column. Minor discrepancies appear to be due to the 3D wave-propagation effect, with some spurious interference between the spherical waves employed as sources

3.6.4 Site de-amplification and stiffness degradation due inelastic behaviour

As far as the inelastic soil response is concerned, the AF model implemented in SEM3D was tested by gradually increment the input motion amplitude so to study the transition from moderate to strong non-linearity. In Figure 3.15, some interesting aspects of the non-linear modelling are pictured. Either for weak and strong non-linearity, late wave-form arrival is observed (Figures 3.15a- 3.15b), along with a consistent de-amplification. Moreover, the stress-strain curves produced at different depths show consistent hysteresis for strong non-linearity, symptom of to consistent material damping taking place along the soil column.

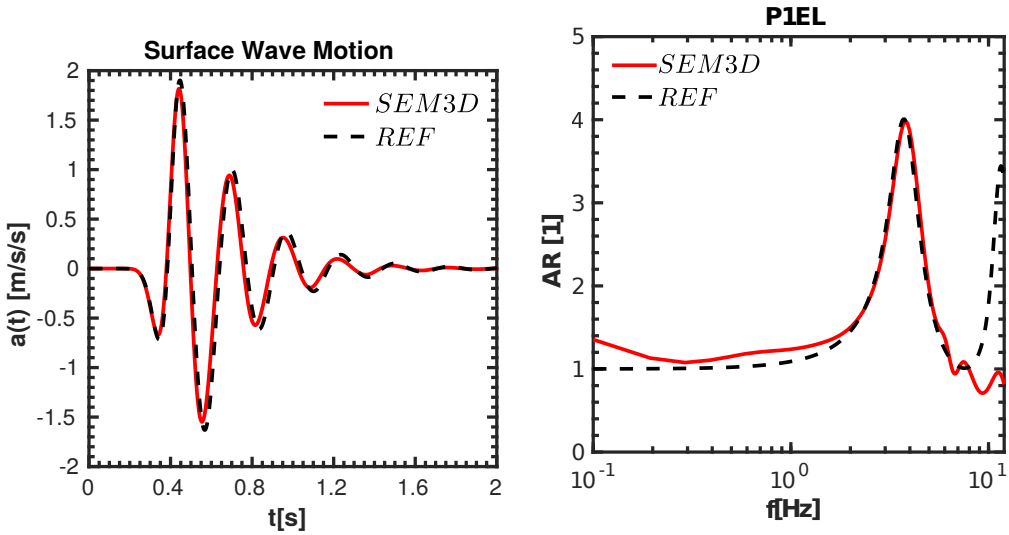

(a) (b)

Figure 3.14: (a) Wave motion at the free-surface (point P in Figure 3.10): reference motion (REF, dashed black line) and synthetic wave motion generated by SEM3D (red line); (b) Amplification Ratio (AR) for the soil layer in Figure 3.10

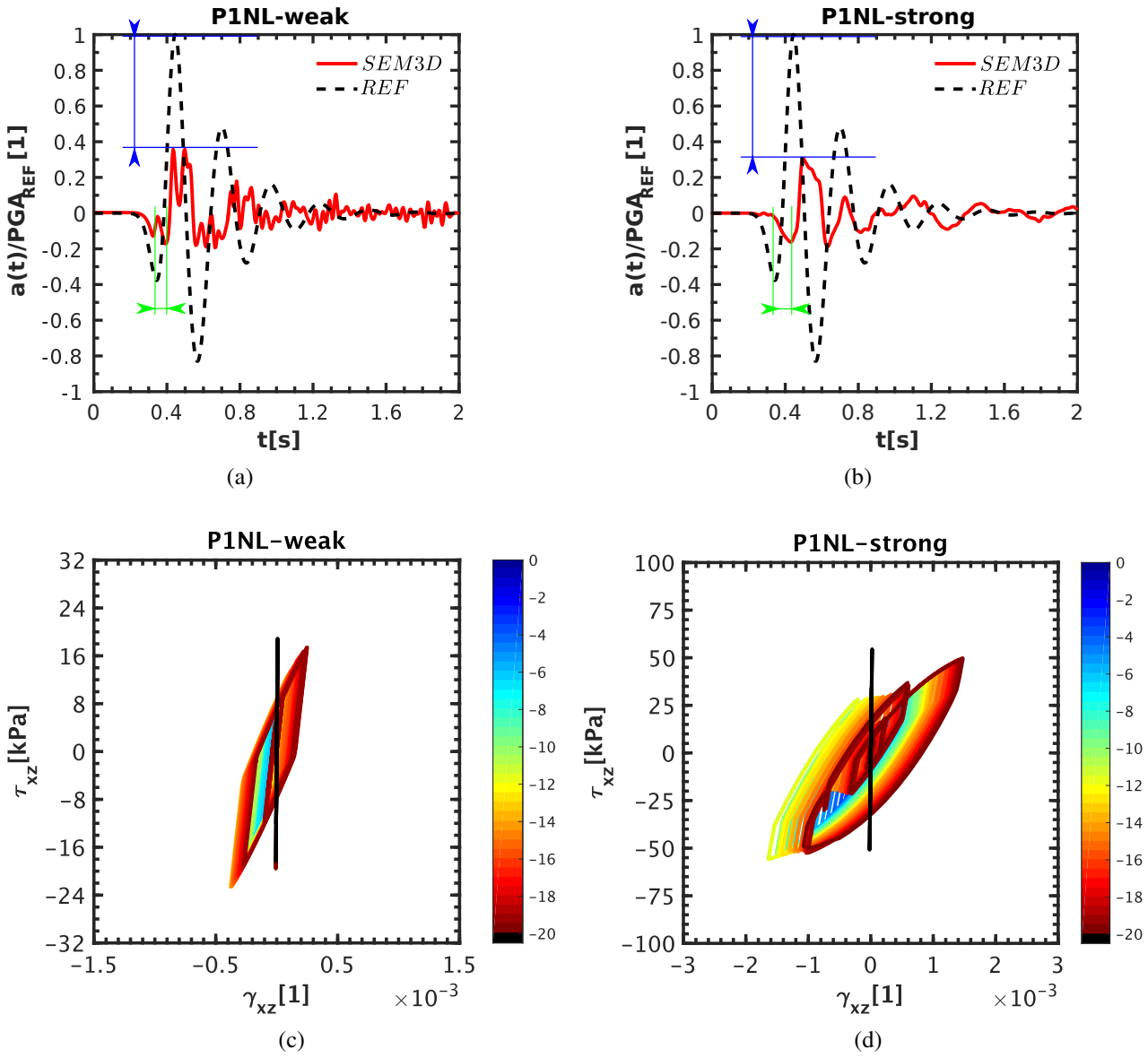

Figure 3.15: Wave motion at the free-surface (point P in Figure 3.10) for weak (a) and strong (b) non-linearity: reference motion (REF, dashed black line) and synthetic wave motion generated by SEM3D (red line) for non-linear case (with AF model). Time-histories are normalized by the maximum value of the elastic response (REF, dashed black line), so to highlight the de-amplification. Stress-Strain hysteresis cycles obtained with AF model implemented in SEM3D at different depths along the soil layer, for weak (c) and strong (d) non-linearity. The black straight line represents the elastic bedrock response.

3.7 Modelling soil heterogeneity by means of random field

A strategy to model heterogeneous media consists in considering the mechanical properties as one stationary random field (featured at least by its average and its auto-covariance model). The latter is then sampled at N_p integration points in the computational domain Ω: in the SEM, those are the Gauss-Lobatto-Legendre (GLL) integration points, at which both mass matrix and internal force vectors are computed. A realization of $\theta(\mathbf{x})$ is obtained by generating a Gaussian random field $G(\mathbf{x})$, whose Cumulated Distribution Function (CDF) is mapped point-wise ((e.g., via the non-linear Rosenblatt transform Rosenblatt, 1952) to the desired first-order marginal density (e.g. log-normal).Modelling soil heterogeneity in large scale domains implies a major computational effort: despite its characteristic dimension ($\approx 10^4$ m) the computational grid must resolve both the wavelength and the heterogeneity correlation length ($\approx 10^2$ m). To generate our random samples an open-source library ScaRL was used (Paludo et al., 2015). It uses the spectral representation technique (Shinozuka and Deodatis, 1991). In this method the random field is generated as a sum of $N_\phi = N_x N_y N_z$ cosines with random phases, namely:

$$G(\underline{\boldsymbol{x}}) = \sum_{n \leq N_\phi} \sqrt{2\mathcal{S}(\underline{\boldsymbol{k}}_n)|\Delta\mathbf{k}|}\cos(\underline{\boldsymbol{k}}_n \cdot \mathbf{x} + \phi_n) \tag{3.29}$$

Following this approach, the wave-number domain spanned by is discretized over a regular grid of size $\underline{\boldsymbol{N}} = [N_x, N_y, N_z]^T$, indexed by $\underline{\boldsymbol{n}} = [n_x, n_y, n_z]^T$. $\mathcal{S}(\underline{\boldsymbol{k}}_n)$ represents the power spectral density of the random field, whereas $|\Delta\mathbf{k}|$ is the unit volume in the spectral domain and the random variables ϕ_n are the independent elements of a $\underline{\boldsymbol{N}}$-dimensional random variable with uniform density over $[0, 2\pi]$. The Fast Fourrier Transform can be used to bring the complexity of this generation method to $\mathcal{O}(N_\phi \log N_\phi)$) (Shinozuka and Deodatis, 1991) but it requires an uniform grid. Since the GLL points are not uniformly distributed in space, the random field must then be interpolated to the N_p GLL nodes.

When dealing with large domains ($L \gg \ell_{c\theta}$) ScaRL has a strategy to overcome the scalability issue. It generates realizations of $G(\mathbf{x})$ over the entire domain as superposition of I smaller independent realizations $G_i(\mathbf{x})$ supported on overlapping subdomains Ω_i of Ω (Paludo et al., 2015):

$$G(\mathbf{x}) = \sum_{i \in I} \sqrt{\psi_i(\mathbf{x})} G_i(\mathbf{x}) \,. \tag{3.30}$$

where the set of functions $\psi_i(\mathbf{x})$ forms a partition of unity of Ω (that is to say $\sum_{i \in I} \psi_i(\mathbf{x}) = 1$ for any $\mathbf{x} \in \Omega$), supported by the set of subdomains Ω_i. Using this approach, the complexity becomes $\mathcal{O}(n_p \log(n_p))$ where $n_p = N_\phi/\mathrm{P}$ and P is the number of processors. Essentially, this means that the scheme is $\mathcal{O}(1)$ when we consider a constant number of GLL nodes per processor. The overlapping Eq. (3.30) involves an approximation that does not alter the average and variance of the resulting field $G(\mathbf{x})$ (Paludo et al., 2015). The influence on the correlation structure depends on the overlap, relative to the correlation length and has been studied in Paludo et al. (2015).

3.7.1 Strategy to couple heterogeneous and non-linear soil behaviour

In this study, the initial shear modulus is represented by a random field $G_0(\underline{\boldsymbol{x}}) = \rho V_S(\underline{\boldsymbol{x}})^2$, where ρ is the homogeneous soil unit weight and $V_S(\underline{\boldsymbol{x}})$ its shear wave velocity. Despite the local variation of the shear modulus, the set of parameters σ_{yld}-C-κ ruling the FA hardening rule (i.e. the back-stress evolution) were adjusted to follow the same normalized decay curve $G_{sec}(\underline{\boldsymbol{x}})/G_0(\underline{\boldsymbol{x}})$. The corresponding decay-curves of secant shear modulus G_{sec} are depicted in Figure 3.16b and they correspond to the normalized decay curve in Figure 3.7b. Figure 3.16a shows the stress-strain relationship ($\tau - \gamma$) issued from the FA model for randomly generated G_0 values. Hysteresis loops have the same shape but different amplitudes. From a practical point of view, a random field representing

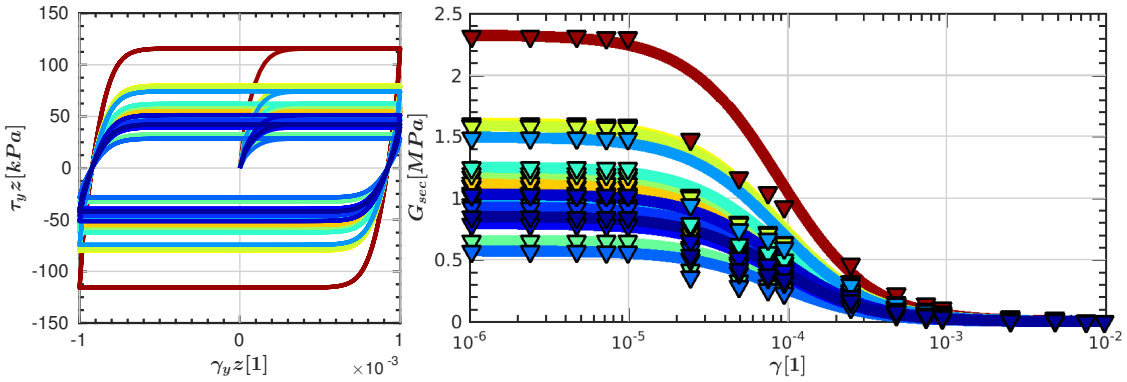

(a) (b)

Figure 3.16: (a) Example of 20 cyclic shear stress-strain relationships ($\tau - \gamma$) for the Fredrick-Armstrong model, with randomly generated elastic shear modulus G_0. (b) 20 secant shear modulus decay curves according to the Fredrick-Armstrong model, corresponding to the $\tau - \gamma$ curves in (a). If normalized by the initial elastic shear modulus G_0, the decay curves in (b) correspond to the prototype curve in Figure 3.7b

shear-wave velocities $V_S\left(\underline{\boldsymbol{x}}\right)$ (at GLL points) was generated at first, with the approach outlined in Sect.3.7. $V_S\left(\underline{\boldsymbol{x}}\right)$ was assumed to follow a log-normal distribution and the isotropic correlation length was set as ℓ_{C-Vs}=30m. $G_0\left(\underline{\boldsymbol{x}}\right)$ was computed accordingly and $C\left(\underline{\boldsymbol{x}}\right)$ was set to be equal to $G_0\left(\underline{\boldsymbol{x}}\right)$ to assure a smoother elastic-to-plastic transition (since C represent the value of the hardening module at first yield and zero plastic strain). As consequence, σ_{yld} and κ remain to be defined: the first is fixed as $\sqrt{3}\rho V_S^2\left(\underline{\boldsymbol{x}}\right)\gamma_{el}$ (with γ_{el} being the shear-distortion at first yield, set equal to 10^{-5}). Considering an analogical 1D shear-test, the critical state is reached when the back-stress saturates (at large strains). The maximum shear stress τ_{max} is attained at this point and it is expressed as $\sqrt{3}\tau_{max} = \sigma_{yld} + C/\kappa$. From the latter expression, the local value of κ is straightforward determined, by either knowing τ_{max} values (for clays, it can be referred as as the Ultimate Strength Su) or estimating it upon correlation relationships with G_0 (see for instance Vardanega and Bolton (2013)).

3.7.2 Limitations of the Armstrong-Fredrerick model

As stated by Pisanò and Jeremić (2013), the singularity at the elastic/elastic-plastic transition prevents the G/G_{max} curves to follow the concavity exhibited by the experimental curves (Darendeli, 2001). The main reason behind this resides in the fact that the non-smooth elastic-plastic implies an abrupt decay of the secant shear-modulus, as soon as the yield strain γ_{el} is reached. The inconsistent fit of the experimental decay curves (over the usual strain range for soil dynamics) is pathologically linked to the decrease of the yield strain. Reasonable fit is achieved, however, for medium/large values of the yield strain. Different trends may be obtained by varying at the same time both k_{kin} and C_{kin}, but this would in general modify the prescribed shear strength.
However, it is in the belief of the author that, at the regional scale of application this model is intended to, such peculiar shortcomings might be of a lesser importance. The idea behind the choice of the model was the ease of implementation, along with the reduced number of parameters required.

3.8 Effect of the soil non-linearity and heterogeneity on the earthquake ground motion coherency

Large scale 3D wave-propagation ($\approx 10^9$ dofs, with 10 points per minimum wavelength) in visco-elastic media has been successfully performed using the SEM, both at local and regional scales Faccioli et al. (1997); Komatitsch and Vilotte (1998). However, to model the spatial variability of seismic incident field (due to its significant effect on the structural response), the heterogeneous composition and the non-linear behaviour of soil deposits must be taken into account. Section 3.7 discusses the efficient generation of 3D Gaussian scalar random-fields to represent the natural heterogeneity of the soil mechanical properties. Section 3.7.1 proposed a strategy to couple the AF non-linear model with the soil heterogeneity. In this section, the results of an extended version of the SEM to handle both non-linear and heterogeneous rheologies, to reproduce the ground motion incoherence. The test case considered is a seismic wave propagation problem within a 3-layer half-space (see Section 3.8.1). The uppermost soil layer is either modelled as elastic homogeneous, elastic heterogeneous, elasto-plastic homogeneous and elasto-plastic heterogeneous. The simulated wave-field at the surface is studied by comparing the synthetic time-histories, in terms of both ground motion coherency curve and soil layer spectral ratio.

3.8.1 Canonical wave-propagation test case

A classical case study is considered herein: a seismic wave generated by a point-wise non-spherical source (i.e. a double-couple representing a pure-shear dislocation, indicated as SRC in Figure 3.17e) propagating towards the surface throughout a 3-layered domain is studied. The two deepest layers are considered homogeneous (HOM) linear-elastic (EL) materials. Due to the propagation in the layered substratum, the spherical wave-field radiated from SRC transforms into a planar incident wave impinging the lower soil layer interface. With this configuration, four simulations were performed and compared, by either considering the top-layer as (1) homogeneous linear-elastic (HOM-EL), (2) heterogeneous linear-elastic (HET-EL), (3) homogeneous non-linear (HOM-NL) and (4) heterogeneous non-linear (HET-NL) material. The domain is enveloped by Perfectly Matched Layers (PML), acting as absorbing boundary conditions. The effect of soil non-linearity and heterogeneity is at first described at three recording stations, namely: SRF1, SRF2 (at the surface) and INT (at the interface). Figure 3.17a-3.17d show the velocigrams obtained at SRF1 and SRF2 (base-line corrected and high-pass filtered at 20 Hz): the two time-histories coincide in the homogeneous cases, as expected due to is plane and coherent wave-field. Typical *coda*-waves appear in the heterogeneous cases instead (Figure 3.17b-3.17d). Those late arrivals are symptomatic of an incoherent wave-field at SRF1 and SRF2. Clear de-amplification of the incident wave motion is presented for the two non-linear cases (Figure 3.17c-3.17d). The pseudo-acceleration response spectra Sa at point SRF1 (shown in Figure 3.17f) is highly influenced by the non-linear soil behaviour (depicted in terms of shear stress-strain relationship $\tau_{yz} - \gamma_{yz}$ in Figure 3.17g) at short period. Heterogeneity plays a minor role for the elastic case ($\approx$25% of PGA reduction), whereas the short-period and peak Sa ordinates are remarkably de-amplified for HET-NL, with the respect to HOM-NL ($\approx$21% of PGA reduction). This result is in accordance with the $\tau_{yz} - \gamma_{yz}$ curves in Figure 3.17g, where the HET-NL hysteresys loop is wider than HOM-NL, indicating the greater amount of energy dissipated. Another interesting aspect is the analysis of the ground motion coherency at the surface. The latter is a fundamental requirement for advanced seismic structural analysis. Coherency curves were computed for three different lag-distances (10, 20 and 30 m respectively), by applying a 11-point Hamming smoothing window Abrahamson et al. (1991). For each lag-distance, the bin set were constructed by considering 40×40 points (i.e. 40 per direction). The mean of the log of the coherency curves was finally computed

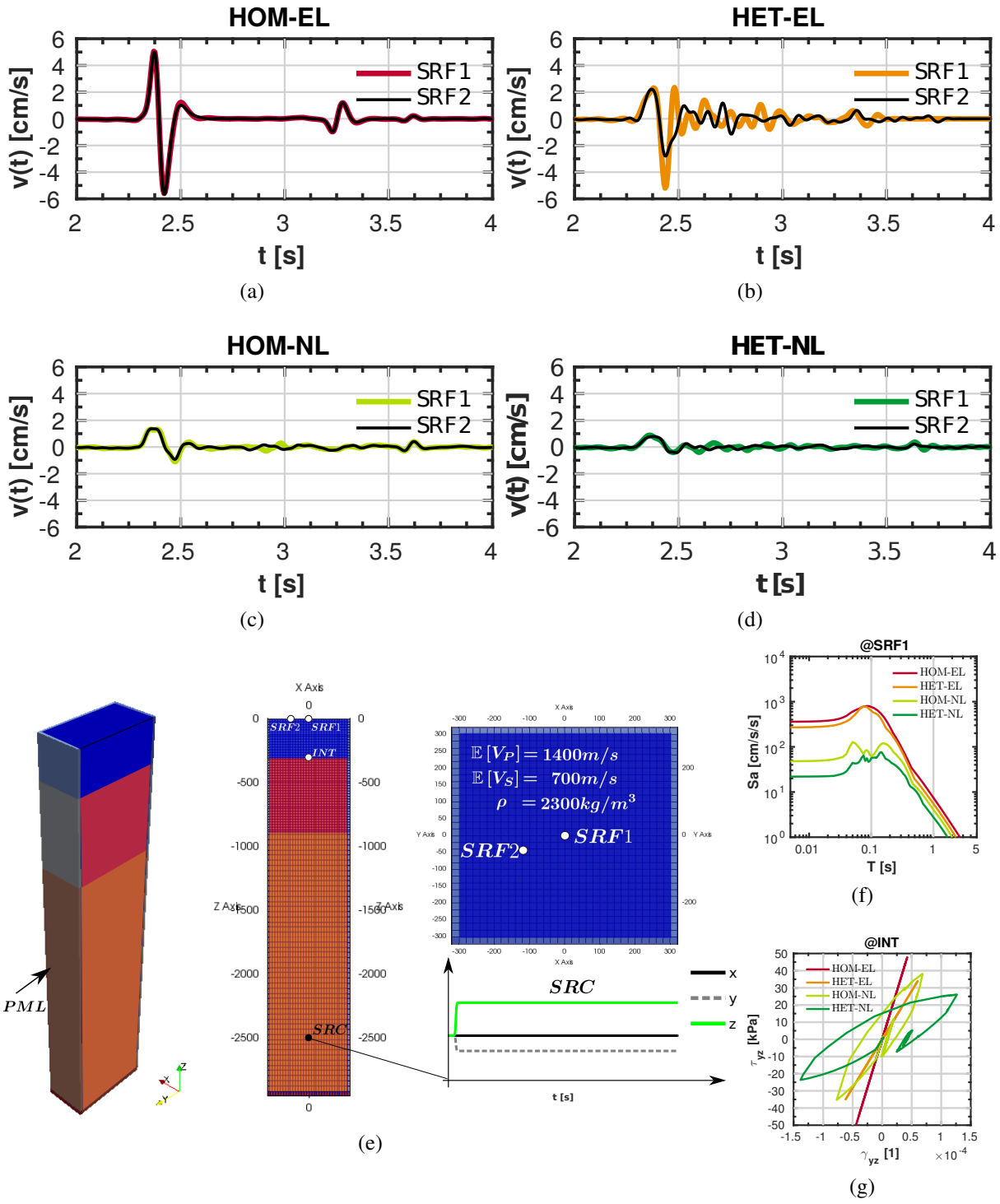

Figure 3.17: (a-d) Synthetic velocigrams obtained at the surface for the four rheological models considered for the uppermost soil layer (HOM-EL, HET-EL, HOM-NL, HET-NL). (e) Clip and front/top views of the domain considered in the test case. The input displacement time-history at SRC is shown. SRF1, SRF2 and INT are employed as reference points. (f) Pseudo-Acceleration reponse spectra Sa at point SRF1. (g) Shear stress-strain relationship $\tau_{yz} - \gamma_{yz}$ at INT point.

and shown in Figure 3.18. Figure 3.18a-3.18e show the lagged coherency for the four rheological models (HOM-EL, HET-EL, HOM-NL and HET-NL), at different lags. The homogeneous cases resulted to be coherent over a broad-band frequency range as expected, whereas the heterogeneous

cases show the loss of coherency in the lower frequency band, decreasing after 10 Hz. The impact of the soil heterogeneity on the ground motion incoherence is clear even at small frequency and it appears more pronounced in the elastic case (Figure 3.18b) with respect to the non-linear one (Figure 3.18d). For HET-EL, the coherency loss is evident event at small lag-distance (i.e. coherency amplitude $|\gamma(\bar{f})|$ ≈0.9 for lag-distance of 10 m) and $|\gamma(\bar{f})|$ drops to values ≈0.6 for lag-distance of 30 m (comparable to ℓ_{C-V_S}). For a non-linear rheological model (HET-NL), $|\gamma(\bar{f})|$ stabilizes at above 0.75 between 0-10 Hz.

3.8.2 Partial Conclusions

In this study, a parametric large scale numerical simulation of the seismic wave propagation in a non-linear-heterogeneous soil layer is presented, by exploiting the The Spectral Element Method. Numerical analyses are featured by the generation of soil heterogeneous mechanical properties by an efficient large random field generator. Moreover, a modified non-linear solver is employed to solve the dynamic equilibrium equation for elasto-plastic materials. The soil non-linearity mostly affects the ground motion de-amplification, whereas the soil heterogeneity produces incoherent ground motion at the surface. However, the non-linear decay of the shear modulus values seems to counteract the loss of coherency due to wave scattering. For the sake of brevity, a moderate source amplitude was considered herein. The effect of an increasing amplitude on the synthetics at the surface is interesting to be investigated (especially for a non-linear material behaviour). The preliminary parametric analysis presented herein may be extended also to the case of anisotropic correlation lengths of the shear-wave velocity (or other mechanical properties), which are estimated geological surveys and influence the recorded motion at the surface. In doing so, higher degrees of mesh refinement should be considered so as to capture the extended frequency band of the surface signal, due to the wave-scattering effect.

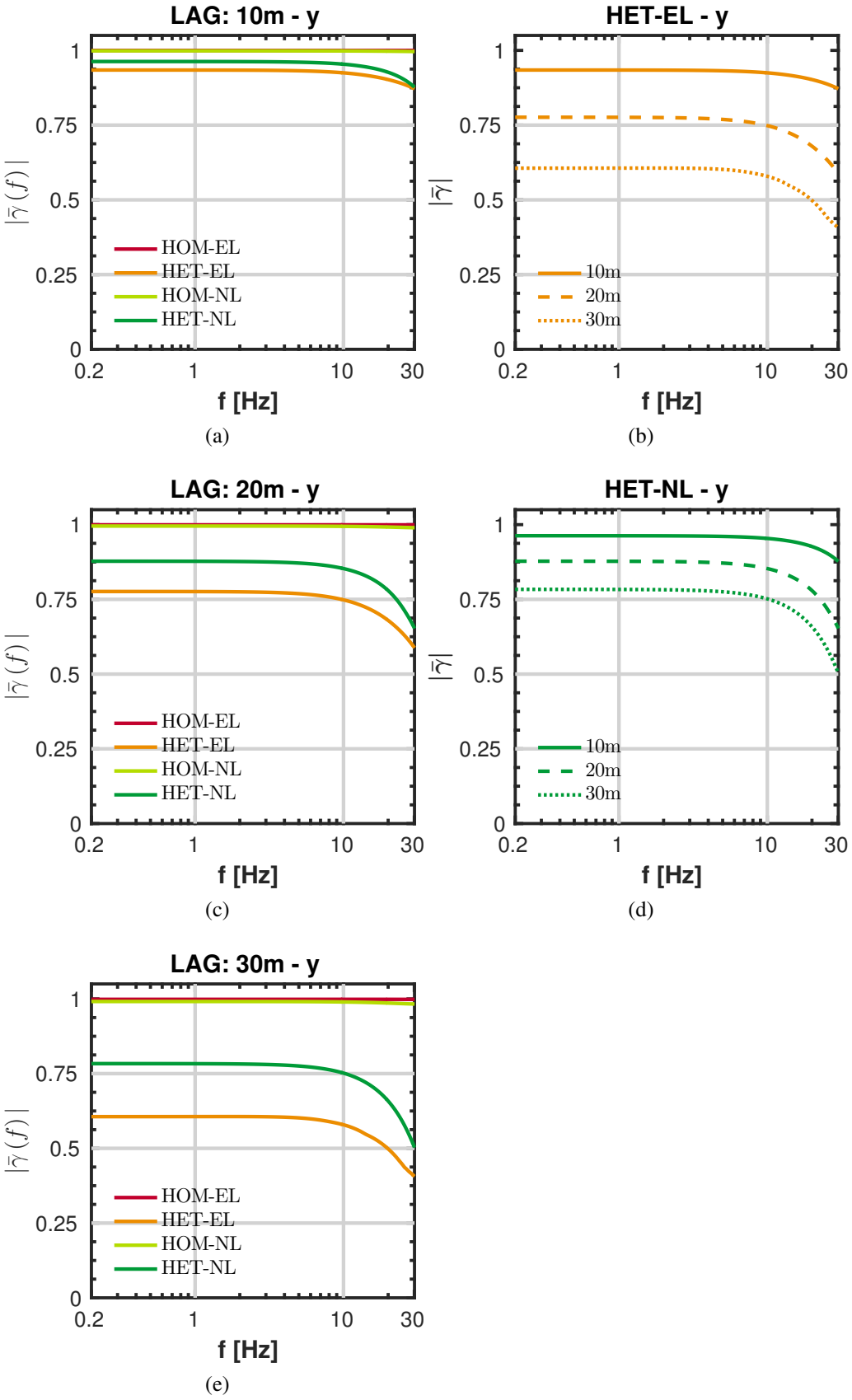

Figure 3.18: Lagged coherency curves at the surface, for different lag-distances: (a) 10 m (c) 20 m (e) 30 m. $|\bar{\gamma}(f)|$ represents the absolute value. In each plot, four coherency curves are depicted, one for each rheological models considered (HOM-EL, HET-EL, HOM-NL and HET-NL) for the uppermost soil layer. Lagged coherency curves for the HET-EL and HET-NL cases are depicted, one for each lag-distance considered (10 m, 20 m and 30 m), in (b) and (d) respectively.

3.9 Numerical modelling of seismic sources

3.9.1 Basic concepts

Seismic observations of strong ground motions proved that earthquakes originate along seismogenic faults, i.e. major fractured discontinuities within the Earth's crust. Blocks of crust on either side of the fault surface moves relative to one another parallel to the fracture. A fault is addressed as *active* whether an earthquake is likely to occur sometime in the future. Faults are commonly considered to be active if they have moved one or more times in the last 10.000 years (USGS glossary). They are located either along the major tectonic plate boundaries (Japan, California, Turkey) or inside these plates (Alps). Earthquakes are generated from the dynamic stress-release along the fault's edges. At this occurrence, the cumulated strain energy of crustal materials is partially released inducing ground motions. This failure mechanism is described in details in Section D.1. Increasing deformation is accumulated during the very slow relative motions of the plates at a speed of a few centimeters per year. Depending on the tectonic context, the faults' depth ranges from 10 to 200 km. The strongest ground shaking generally occurs close to an earthquake fault rupture because geometric spreading reduces ground shaking amplitudes as distance from the fault increases.
The conceptual and theoretical framework of the modern seismic source modelling was built starting from the pioneering works of Eshelby (1957), who studied the perturbation of the elastic field due to an ellipsoidal inclusion. Burridge and Knopoff (1964) derived an explicit expression for the body force to be applied in the absence of a dislocation, which produces radiation identical to that of the dislocation. Haskell (1964) rigorously derived the equivalence between relative displacement on rectangular shear fault to a distribution of double-couple point sources over the fault plane. Madariaga (1978) deepen this study, focusing on the near-field generated by Haskell's rectangular fault model used extensively to interpret seismic data. Aki (1968) and Haskell (1969) developed provided theoretical considerations on the elastic displacements in the near-field of a propagating fault. In the following, Brune (1970) proposed an earthquake model, by considering the effective stress available to accelerate the sides of the fault, describing for near- and far-field displacement-time functions and spectra (also including the effect of fractional stress drop).
A common belief among seismologists is that the strong motion earthquakes are primarily caused by the slipping upon the heterogeneities on the fault plane, namely *asperities*, defined as regions of the fault plane that have larger slip rate relatively to the average one on the rupture area (Somerville et al., 1999). In this sense, one of the first numerical method developed to deconvolve complex body waves into a multiple shock sequence was developed by Kikuchi and Kanamori (1982), by employing the Haskell (1964) asperity model and with a superposition of point dislocations with identical fault orientation and depth. Another original interpretation contribution was provided by Papageorgiou and Aki (1983), who constructed an earthquake source model from a specific form of the *barrier model* proposed by Das and Aki (1977), i.e. the fault surface is visualized as composed of an aggregate of circular cracks which represent areas of localized slip, and the strong motion is assumed to be generated by the stationary occurrence of these localized ruptures as the rupture front propagates.

As a matter of fact, it is well known that the source processes are difficult to be fully determined, due to the lack of a complete panorama of specific information about this complex phenomenon. Irikura and Miyake (2010) outlined the main information required to predict and simulate strong ground motion (see Figure 3.19). Strong motion observations do not represent an exhaustive information when studying the strong motion earthquake initiation. For instance, data collected from monitoring activity on active faults (i.e. GPS data referring to the fault trace onto the surface) are extremely useful in assessing the fault mechanism and reproduce it. They steer the definition of three sets of parameters, (1) outer (defining the *size* of the strong ground motion, such as rupture area and

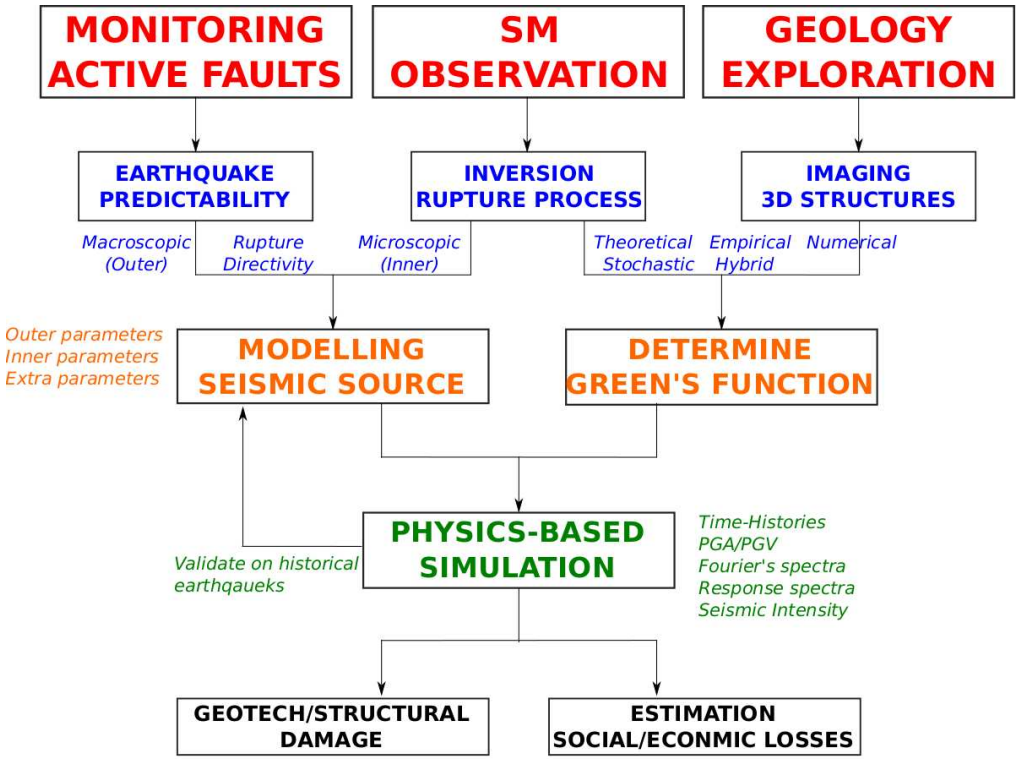

Figure 3.19: Predicting framework for strong ground motion scenarios, proposed by Irikura and Miyake (2010).

seismic moment), (2) inner (e.g. slip heterogeneities, asperity areas and their stress drops) and (3) extra parameters (related to the definition of rupture paths, e.g. nucleation and termination points). A seismogram may contain information relevant to all of the above parameters but it is extremely difficult to be interpreted in this sense. Moreover, each seismogram must be corrected for distortion by the instrument and the Earth and for dynamic properties of the source and faulting main direction. The magnitude was the first quantitative measure of the strength of an earthquake, issued from observed seismograms. Although still widely used, this parameter has some intrinsic shortcomings. Among all, it is poorly related to other source characteristics such as strain energy release, fault offset, stress drop, source dimension, moment and radiated seismic energy. Although in some cases the rise time, or source-time function, can be determined from the seismogram, the information usually available is the amplitude at some frequency (the magnitude). A spectral description of the seismic source is therefore desirable to relate the faulting parameters to the magnitude. Such a description is inferred from a complete time-space description of the faulting mechanism (or stress release mechanism). Techniques of waveform inversion of strong motion data are widely used to estimate the rupture process. When the observed body waveforms are relatively simple, the modeling can be alternatively done by using inverse methods, as originally shown by Langston (1976) and Burdick and Mellman (1976) that used a time-domain inversion method to determine some of the complexities of the source time function. Another seminal contribution was provided by Madariaga (1977), in terms of the implications of stress-drop models for the inversion of seismic observations.

3.9.2 Self-similarity of the seismic sources

Several studies (Kanamori and Anderson, 1975, among others) show the systematic scaling of inner and outer fault parameters with the earthquake magnitude. Moreover, it was historically observed that

the dimensions of fault asperities scale with the source intensity (measured in terms of seismic moment) and the area of strong motion generation usually coincides with asperities area (i.e. the rupture area, where the largest stress concentration releases at first Irikura and Miyake, 2010). Conventional scaling relations for the fault parameters (see, for instance Aki, 1967), such as the fault length and average slip on the fault based on the seismic magnitude, are mostly measured from surface offsets and from forward source modelling, using teleseismic and geodetic data. A dynamic description of the faulting process is employed to derive the relationship. These scaling relations are important for establishing general rules for developing source models for simulating strong ground motions.
The basic property of a self-similar system is that events of different sizes cannot be distinguished except by a scale factor. The simplest scaling relationship is a *self-similar* one in which the basic properties of the slip models, and of the asperities that they contain, remain scale invariant. When considering an uniform failure with a constant slippage Δu along a given surface S in an elastic medium with a rigidity (*shear modulus*) μ, one can defines the *seismic moment* as[9]:

$$M_0 = \mu \Delta u S \tag{3.32}$$

The scalar seismic moment M_0 may be seen as a measure of the earthquake intensity, and it is the product of a force times a displacement, thus it can be compared to a work or an energy. Nevertheless, M_0 is referred as *moment* since μ is a shear modulus and not the actual stress. On the contrary one can define the released energy as the mechanical work dissipated on the fault:

$$E = \tau \Delta u S \tag{3.33}$$

with τ the mean shear stress on the fault during the earthquake. The above relationship $E \approx 10^{-4} M_0$ suggests that the fault rupture occurs for shear strains reaching 10^{-4}. The expression of the static moment (in Equation 3.32) represents a basic self-similar scaling law: an increase in seismic moment occurs by proportionately equal changes in the average slip Δu or in the surface extension S (e.g., for a rectangular fault plane, the fault length L and fault width W), considering a constant stress drop (proportional to the ratio of Δu to L or W). Stress-drop $\Delta\tau$ and fault length are directly related to the seismic moment. According to Kanamori and Anderson (1975), the relation between $\log S$ and $\log M_0$ is remarkably linear (slope $\approx 2/3$), corresponding to stress drops $\Delta\tau$ of 30, 100, 60 bars for inter-plate, intra-plate and *average* earthquakes. Although the static and dynamic study of such a relationship is out of the scope of this study, developments in fracture mechanics lead to the following general expression to relate the stress drop to a fault characteristic length $\tilde{L}$ (Aki, 1967; Kanamori and Anderson, 1975; Madariaga, 1977):

$$\Delta\tau = C \frac{\mu \Delta u}{\tilde{L}} \tag{3.34}$$

where μ represent a measure of the rigidity, and C is a non-dimensional shape factor. The characteristic dimensions of the fault are the radius R for circular faults, the length L and width W for rectangular ones. For instance, for a penny-shape crack with diameter $2R$ in a purely elastic material, Eshelby (1957) proposed the following relationship:

$$\Delta\tau = \frac{7\pi}{16} \mu \frac{\Delta u}{2R} \tag{3.35}$$

[9] in a more general way, the slip displacement may be time-varying (i.e. $\Delta u\,(t)$). If one considers the average displacement offset $\langle \Delta u \rangle$ on the total fractured area at the end of the seismic process $A \subseteq S$, the scalar seismic moment may be expressed as:

$$M_0\,(t) = \mu \langle \Delta u \rangle\,(t)\, A = \mu \langle \Delta u_{tot} \rangle s\,(t)\, A \tag{3.31}$$

with $\langle \Delta u_{tot} \rangle$ the total average slip on the rupture area. The *source time-function* STF $s\,(t)$ can be expressed as $\frac{\langle \Delta u \rangle (t)}{\langle \Delta u_{tot} \rangle}$

This leads to the following approximate expression for the seismic moment as a function of the fault length:

$$M_0 \approx \frac{L^3}{4}\Delta\tau, \quad 3 \text{ MPa} \leq \Delta\tau \leq 10 \text{ MPa} \tag{3.36}$$

showing that the seismic moment is proportional to the length to the power 3. This means that an increase of the active length by one order of magnitude corresponds to a thousand time the original seismic moment. This lead to a linear relationship between the slippage and the fault length

$$\Delta u = \frac{16}{7\pi}\frac{\Delta\tau}{\mu}L \approx 10^{-4}L \tag{3.37}$$

roughly observed in practice when the fault reaches the free surface (Eshelby, 1957). At last it is worth to notice that the corresponding released energy reads:

$$E = \tau\Delta u S = \frac{\tau}{\mu}M_0 \approx \frac{\Delta u}{L}M_0 \tag{3.38}$$

Also, the duration of slip on the fault τ increases in proportion to Δu, or equivalently to L or W, so that the slip velocity (expressed as the ratio $\frac{\Delta u}{\tau}$) remains constant. In this self-similar model, the size of asperities in relation to L (and W) remains constant, their average slip in relation to Δu (slip contrast) remains constant, and the number of asperities remains constant. The self-similar model is convenient to use, and in many instances its use can be justified because it provides a reasonably good description of nature. For example, Tanioka et al. (1997) found that the teleseismic source time functions of large earthquakes are compatible with a self-similar scaling model.

3.9.3 Modelling strong ground motion via Green's functions

The ground motions produced at any site by an earthquake are the result of seismic radiation associated with the dynamic faulting process *convolved* to the *path-effects* that influence the way the seismic energy propagates from fault's nucleation points to the site of concern. Based on the self-similarity principle, seismologists defined a commonly adopted procedure to produce synthetic waveforms for large seismic events developing along extended fault segments. This technique was proposed by Hartzell (1978) and then modified by Irikura (1983) based on a scaling law of fault parameters for large and small events (Kanamori and Anderson, 1975) and the omega-squared source spectra (Aki, 1967). A common assumption made states that the fault rupture initiates at some point on the fault (the hypocenter) and proceeds outward along the fault surface. For the sake of simplicity, each fault's segment maybe approximated to a 2D plane. The latter is commonly discretized into finite sub-faults, each one considered as a radiating source (see Figure 3.20). Using the representation theorem (see Section D.2.2 Spudich and Archuleta, 1987),the ground velocity $\underline{\boldsymbol{v}}(\underline{\boldsymbol{x}};t)$is the convolutive tensor-product between the *slip-time functions* $\dot{s}_{ij}(t)$ of each sub-fault ($i = 1, ..., m$ and $j = 1, ..., n$ are row and column indexes in the along-depth and along-width directions of the fault plane, as shown in Figure 3.20) and the *impulsive response functions* $\underline{\boldsymbol{u}}^G_{ij}(\underline{\boldsymbol{x}};t)$defined by means of site Green's functions:

$$\underline{\boldsymbol{v}}(\underline{\boldsymbol{x}};t) = \sum_{i,j}^{m,n} \underline{\boldsymbol{v}}^G_{ij}(\underline{\boldsymbol{x}};t)\,\dot{s}_{ij}(t) \tag{3.39}$$

The site Green's $\underline{\boldsymbol{v}}^G_{ij}$ function is computed by considering the corresponding $i \times j$ sub-fault as a impulsive source point and it takes the form of the time-derivative of Equation D.17. By taking the

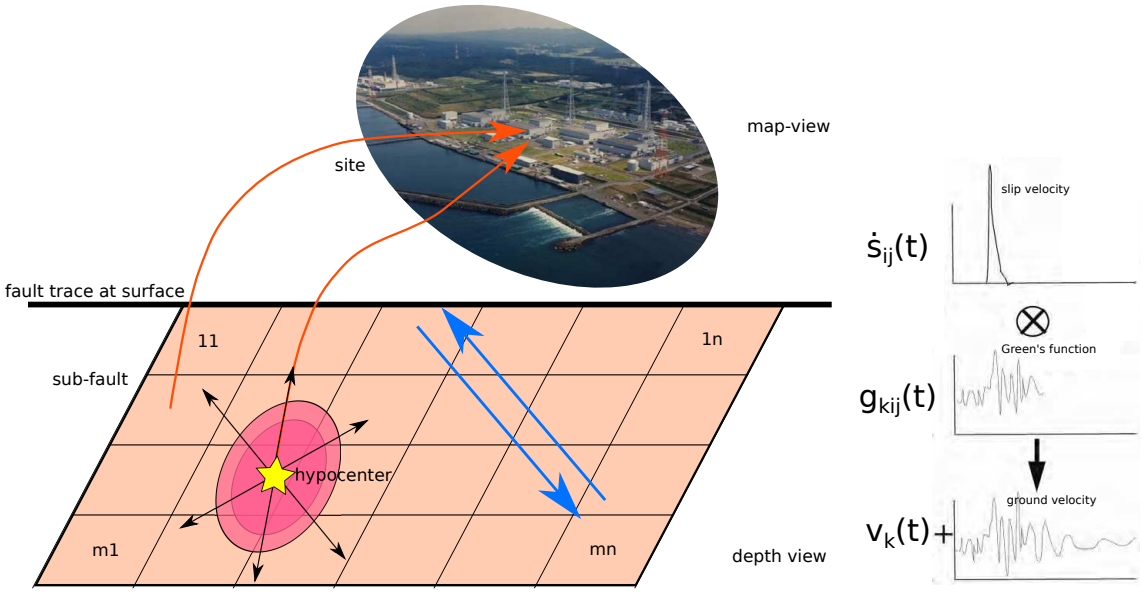

Figure 3.20: Schematic diagram of finite-fault discretization scheme. Rings and arrows emanating from the hypocenter represent the time evolution of the rupture. Large blue arrows denote fault slip orientation (after O'Connell et al., 1984).

Fourier transform with respect to time of Equation 3.39, one gets the following expression:

$$\begin{cases} \widehat{\underline{\boldsymbol{v}}}\left(\underline{\boldsymbol{x}};\omega\right) = \sum_{i,j}^{m,n} \widehat{\underline{\boldsymbol{v}}_{ij}^{G}}\left(\underline{\boldsymbol{x}};\omega\right)\hat{s}_{ij}\left(\omega\right) & (3.40) \\ \widehat{\underline{\boldsymbol{V}}}\left(\underline{\boldsymbol{x}};\omega\right)\exp\left(i\omega\phi_{v}\left(\omega\right)\right) = \sum_{i,j}^{m,n} \widehat{\underline{\boldsymbol{V}}_{ij}^{G}}\left(\underline{\boldsymbol{x}};\omega\right)\exp\left(i\omega\phi_{G}\left(\omega\right)\right)\hat{\dot{S}}_{ij}\left(\omega\right)\exp\left(i\omega\phi_{s}\left(\omega\right)\right) & (3.41) \end{cases}$$

where capital letters indicate the Fourier's transform amplitude, while ϕ is the frequency-dependent phase.

This approach cannot be performed without knowing the system response at each pulse-wave radiated from small sources, disregarding the delay and directivity effects due to the rupture path but just focusing on the propagation path effect, i.e. the impact of 3D geological structure. The latter response is referred as to the system *Green's function*. From a mathematical standpoint, defining and tuning a Green's function is an extremely hard task, due to the complexity of the propagative domain (i.e. geometry, boundary and radiation conditions, material mechanics). Therefore, seismologists traditionally employed the seismic observations from real small aftershocks as *empirical Green's function*. As a matter of fact, their limited size leads to approximate those events as point-sources, so to assume the recorded waveforms unaffected by the complex rupture mechanisms. A Green's function $\widehat{\underline{\boldsymbol{v}}^{G}}\left(\underline{\boldsymbol{x}};t\right)$ (or its counterpart in the frequency domain, $\widehat{\underline{\boldsymbol{v}}^{G}}\left(\underline{\boldsymbol{x}};\omega\right)$) is mainly influenced by the following parameters (O'Connell et al., 1984):

- Amplitude $\widehat{\underline{\boldsymbol{V}}^{G}}\left(\underline{\boldsymbol{x}};\omega\right)$
  - *Geometrical spreading* : Body waves decrease with $1/r, 1/r^2, 1/r^4$ (with strong influence on higher frequency) and $1/\sqrt{r}$ for surface waves
  - *Large-Scale Velocity structure* : Horizontal/Vertical velocity gradients affect amplitudes and durations; Low-velocity basins amplify the motion+basin-edge effects

- *Near-Surface sediments* : Coupled interface modes can amplify and extend durations of ground motions
- *Non-Linear site response* : Dynamic non-linear soil properties and pore pressure influence decrease intermediate/high frequency amplitudes and amplify low/high and extend/reduce duration of large amplitudes
- *Frequency independent attenuation* Q: Linear hysteretic behavior that reduces amplitudes
- *High-frequency attenuation* κ: Strong attenuation of high-frequencies in the shallow crust
- *Scattering* : It tends to reduce amplitudes on average
- *Anisotropy* : It complicates shear-wave amplitudes and modifies radiation pattern amplitudes; It introduce frequency-dependent amplification based on direction of polarization.
- *Topography* : It can produce amplification near topographic highs and introduces an additional sources of scattering

- Phase ϕ_G
  - *Geometrical spreading* : It introduce frequency-dependent time-delays
  - *Large-Scale Velocity structure* : Horizontal/Vertical velocity/density gradients produces frequency-dependent phase-shifts
  - *Near-Surface sediments* : Interactions of shear-wave arrivals of varying angles of incidence and directions produce frequency-dependent phase shifts.
  - *Non-Linear site response* : Depending on the dynamic soil properties and pore pressure responses, it can increase/reduce phase dispersion.
  - *Frequency independent attenuation* Q: It produces frequency-dependent velocity dispersion that produces frequency dependent phase variations.
  - *Scattering* : It determines propagation distances required to randomize the phase of shear-waves as a function of frequency
  - *Anisotropy* : It complicates shear-wave polarizations; It modifies radiation pattern polarization
  - *Topography* : It complicates phase as a function of topographic length scale and near-surface velocities.

The Wave Number Integration method for extended seismic source simulation

The Earth's crust has been traditionally approximated as a layered half-space, for the sake of simplicity (see Figure 3.21). Within the limits of this rude approximation, however, one can take advantage of a semi-analytical expression of the Green's function. For instance, the Wave-Number Integration (Hisada, 1994, 1995, 2008, WNI,) is a semi-analytical method that simulates the complete 3D wave propagation field radiated from an extended kinematic seismic source in an extended half-space. This approach is based on the computation of static and dynamic Green's functions of displacements and stresses for a visco-elastic horizontally layered half-space. It takes advantage of two main ingredients, namely (1) the stress discontinuity representation for boundary and source conditions and (2) an analytical form derived from the generalized Reflection/Transmission coefficients (R/T) method (which is numerically stable up to very high frequencies) to asymptotically solve the Green's function integrands (Hisada et al., 2012). The analysis computes the Green's functions by means of a truncated wave-number series, with high accuracy even when sources and receivers located are located at equal or nearly equal depths. The fault plane is subdivided into rectangular sub-faults at constant

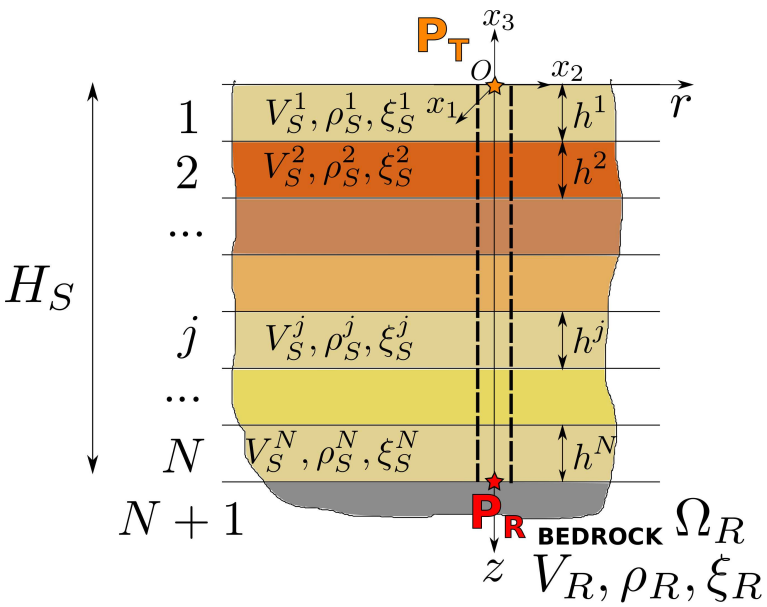

Figure 3.21: Green's function in cylindrical coordinates for layered half-space (Luco and Apsel, 1983a,b).

slip and rake angle and their contribution is then convolved to obtain the waveforms at each receiver's location.
In this work, the WNI method (implemented by Y. Hisada in FORTRAN77 code) is extensively used. Although the numerical tool suffers of major shortcoming (1D layered geology, long-period limitation, deterministic approach), it helps in a preliminary stage of the source modelling, steering more complicated and physics-based analyses. Some further insight about the WNI method may be found Section D.3.

A verification study concerning the synthetic wave-field generated by means of the WNI method is presented hereafter, so to check its efficacy. A canonical test case is borrowed from the SISMOWINE platform[10], a long-term interactive web interface for verifying numerical-modeling methods in seismology, and developed by the Comenius University Bratislava. SISMOWINE is a continuation of the original SPICE Code Validation interface established within the 6^{th} Framework Programme project SPICE[11]. The test case WP1-HSP1 was chosen which consists into a point-wise double-couple within an infinite homogeneous and isotropic elastic medium. First of all, the analytical solution presented in the Subsection D.2.5 is implemented in a Matlab code and tested against the solution found in the literature (e.g. De Martin et al., 2007; De Martin, 2010) and with the *reference* solution uploaded on the SISMOWINE website. The verified analytical solution is used as reference to test the WNI semi-analytical solution. This approach allows investigating the effects of source, fling step, rupture directivity and strong motion in near-fault conditions, which may play a relevant role in the ground shaking prediction. Finally, analytical and semi-analytical solutions are compared. To assess the goodness of fit (GoF), the Anderson's criteria are employed (Anderson, 2004, listed in Table 3.1). Both theoretical and numerical wave forms were opportunely band-pass filtered between 0.05-5 Hz, so to consider a good signal-to-noise ratio. Figure 3.22 shows the comparison between theoretical (orange traces) and WNI wave-field (black traces) at some monitors placed in both near and far field. On the other side, the results of the Anderson's Criteria applied to the analytical and semi-analytical

[10] source: http://www.sismowine.org/
[11] http://www.spice-rtn.org

Table 3.1: Goodness of fit parameters

Number	Symbol	Similarity of:
C1	SDa	Arias duration
C2	SDe	Energy duration
C3	SIa	Arias Intensity
C4	SIv	Energy Integral
C5	Spga	Peak Acceleration
C6	Spgv	Peak Velocity
C7	Spgd	Peak Displacement
C8	Ssa	Response Spectra
C9	Sfs	Fourier Spectra
C10	C*	Cross Correlation

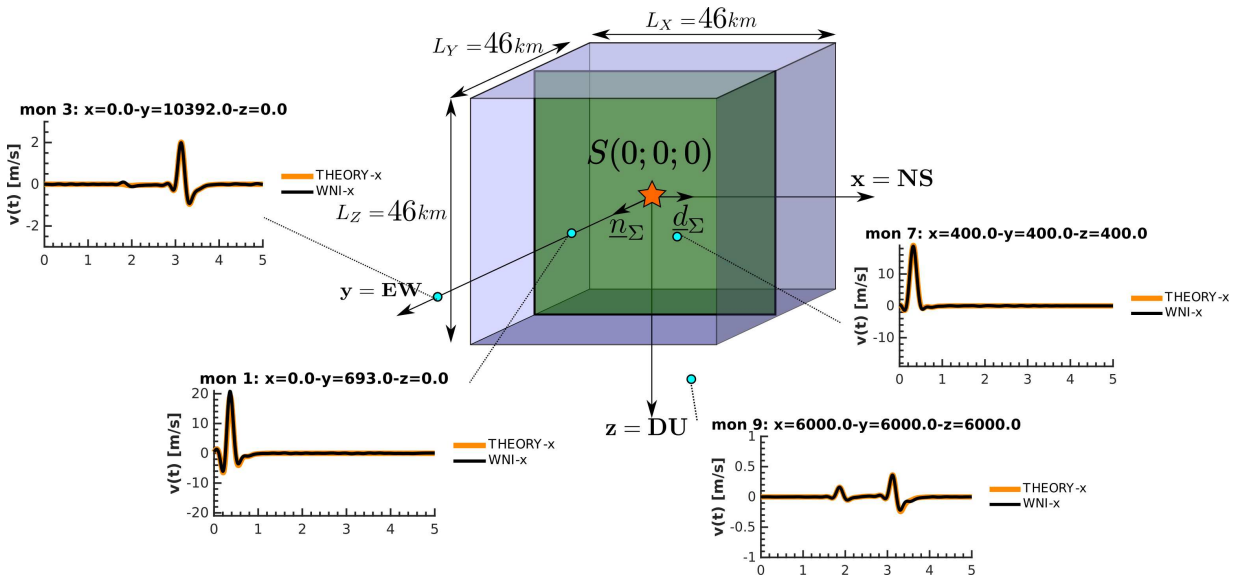

Figure 3.22: Comparison between theoretical and semi-analytical (WNI method) solution obtained for the WP1-HSP1 test case. The fault strikes at 0° and dips at 90°, with a rake angle of 0°.

solutions are portrayed in Figure 3.23, considering the slipping direction x (NS). The results of the verification benchmark certified the accuracy of the WNI method, in the frequency range of applicability.

3.9.4 SEM numerical modelling of the fault mechanism

The bottleneck represented by the extreme difficulty in deriving the Green's function for complex geometries, material interfaces and properties has been broken through by developing numerical methods (such as the SEM) capable to propagate the radiated wave field from source to site. Those methods are usually based on the variational formulation of the wave-equation in solid/fluid domains, supplied by the opportune boundary and initial conditions (see Sections 3.1 and A). However, a mechanical representation of the dynamic source radiating energy into the computational domain is required, in the guise of *external forces*. In computational seismology, the external forces are commonly generated by either point-wise forces, double-couple (see Section D.2.5) or extended kinematic fault planes (Aki and Richards, 1980). For the first two cases, the analytical expression of point-wise force/couple

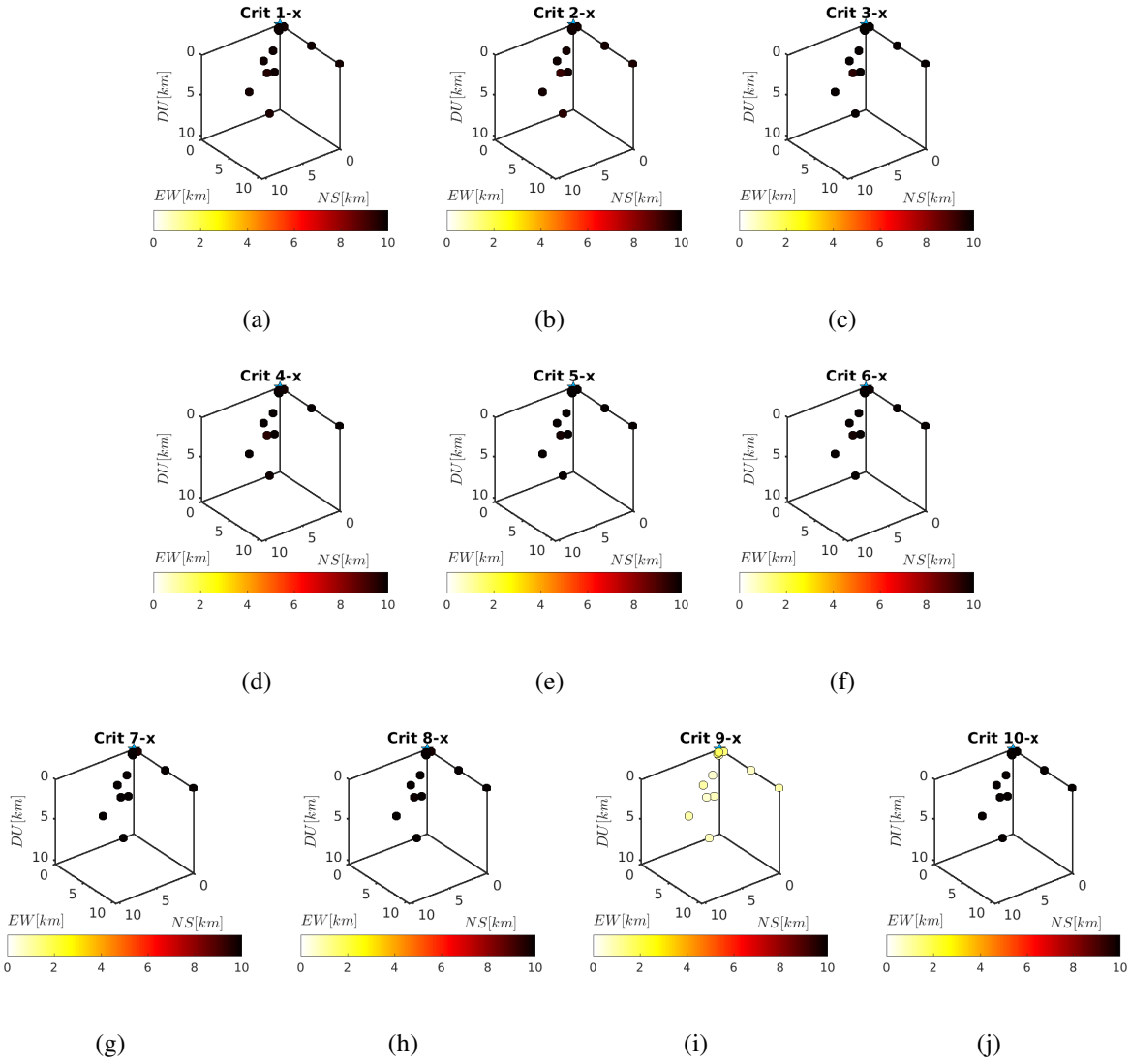

Figure 3.23: Comparison between theoretical and semi-analytical (WNI method) solution in terms of Anderson's Criteria, obtained for the WP1-HSP1 test case.

placed at point $\underline{\boldsymbol{x}}_0$ reads (Faccioli et al., 1997; Madariaga, 1989):

$$\underline{\boldsymbol{b}}\left(\underline{\boldsymbol{x}};t\right) \equiv \begin{cases} \sum_{i=1}^{d} A_i \delta\left(\underline{\boldsymbol{x}}-\underline{\boldsymbol{x}}_S\right) f\left(t\right) \underline{\boldsymbol{e}}_i, & \text{point-wise force} \quad (3.42) \\ -\underline{\boldsymbol{\nabla}}_x . \underline{\underline{\boldsymbol{m}}}\left(\underline{\boldsymbol{x}};\underline{\boldsymbol{x}}_S\right) f\left(t\right), & \text{point-wise double couple} \quad (3.43) \end{cases}$$

with A_i is the amplitude of the point-wise force along the i^{th} direction, δ the Dirac's delta, $\underline{\boldsymbol{x}}_S$ the source point and $\underline{\underline{\boldsymbol{m}}}\left(\underline{\boldsymbol{x}};t\right)$ the seismic moment tensor density and $\underline{\underline{\boldsymbol{m}}}\left(\underline{\boldsymbol{x}}\right) = \underline{\underline{\boldsymbol{m}}}_0 \delta\left(\underline{\boldsymbol{x}}-\underline{\boldsymbol{x}}_S\right)$. To translate the analytical formulation of the point-wise forces, let first $\underline{\boldsymbol{x}}_S$ coincide for simplicity with one of the GLL nodes. Then the body force numerical counterparts $\underline{\boldsymbol{b}}^N\left(\underline{\boldsymbol{x}};t\right)$ may be written as:

$$\underline{\boldsymbol{b}}^N\left(\underline{\boldsymbol{x}};t\right) \equiv \begin{cases} \sum_{i=1}^{d} A_i \delta^N\left(\underline{\boldsymbol{x}}-\underline{\boldsymbol{x}}_S\right) f\left(t\right) \underline{\boldsymbol{e}}_i, & \text{point-wise force} \quad (3.44) \\ -\underline{\boldsymbol{\nabla}}_x . \left[\underline{\underline{\boldsymbol{m}}}_0 \delta^N\left(\underline{\boldsymbol{x}}-\underline{\boldsymbol{x}}_S\right)\right] f\left(t\right), & \text{point-wise double couple} \quad (3.45) \end{cases}$$

δ^N is the numerical counterpart of the Dirac's delta. According to the quadrature formulas and Lagrangian interpolation employed in the SE discretization, δ^N is the N^{th} order Lagrangian shape function Ψ^L/ω_L (with $L = \mathcal{I}_d(r,s,t)$ the multi-index corresponding to the GLL point coordinated by the indexes r,s,t on a 3D master element) that vanishes at all GLL points $I \neq L$ within the element, except at $\underline{\boldsymbol{x}}_S\left(\underline{\boldsymbol{\xi}}^L\right)$, where it is equal to $1/\omega_L$ (the GLL weight associated to $\underline{\boldsymbol{\xi}}^L$ in quadrature formula on Ω_e). Note that the integral $\int_{\Omega_e}\delta^N dV_x = 1$ according to the GLL quadrature formulas employed. Therefore, the Galerkin's formulation of the external force on an element e (and according to the local reference system $\underline{\boldsymbol{x}}_e$) reads:

$$\left(\underline{\boldsymbol{w}}_e^h\left(\underline{\boldsymbol{x}}_e\right), \sum_{i=1}^{d} A_i \delta^N\left(\underline{\boldsymbol{x}}_e - \underline{\boldsymbol{x}}_{eS}\right) f(t)\, \underline{\boldsymbol{e}}_i\right)_{\Omega_e}^h = f(t)\sum_{i=1}^{d} A_i w_{e_i}\left(\underline{\boldsymbol{x}}_{eS}\right) \tag{3.46}$$

for a point-wise force. Concerning the double-coupe source, a convenient representation of the seismic moment tensor density was originally formulated by Aki and Richards (1980), in the following fashion:

$$\underline{\underline{\boldsymbol{m}}}\left(\underline{\boldsymbol{x}};\underline{\boldsymbol{x}}_S\right) = \underline{\underline{\boldsymbol{m}}}_0\delta\left(\underline{\boldsymbol{x}} - \underline{\boldsymbol{x}}_S\right) = \frac{M_0}{V}\left(\underline{\boldsymbol{d}}_\Sigma \otimes_S \underline{\boldsymbol{n}}_\Sigma\right)\delta\left(\underline{\boldsymbol{x}} - \underline{\boldsymbol{x}}_S\right) \tag{3.47}$$

with $\underline{\boldsymbol{d}}_\Sigma$ and $\underline{\boldsymbol{n}}_\Sigma$ the slip and normal vector defining the spatial disposition of the fault offset; M_0 is the total seismic moment (see Section 3.9.2) and V the source elementary volume (Faccioli et al., 1997). The seismic moment[12] translates into the equivalent body force distribution proposed in Equation A.79. Hence, the application of the divergence theorem to the variational formulation of Equation A.81, gives:

$$\begin{aligned}
&\left(\underline{\boldsymbol{w}}_e^h\left(\underline{\boldsymbol{x}}_e\right), -\underline{\boldsymbol{\nabla}}_x\cdot\left[\underline{\underline{\boldsymbol{m}}}_0\delta^N\left(\underline{\boldsymbol{x}} - \underline{\boldsymbol{x}}_S\right)\right] f(t)\right)_{\Omega_e}^h = \\
&= \left(\underline{\underline{\boldsymbol{m}}}_0\delta^N\left(\underline{\boldsymbol{x}} - \underline{\boldsymbol{x}}_S\right) f(t), \underline{\boldsymbol{w}}_e^h \otimes_S \underline{\boldsymbol{\nabla}}_x\right)_{\Omega_e}^h = \\
&= \frac{1}{2}\sum_{i,j=1}^{d} f(t)\, m_{0_{ij}}\left(\frac{\partial w_{e_i}^h}{\partial x_j} + \frac{\partial w_{e_j}^h}{\partial x_i}\right)\omega_L = \\
&\frac{1}{2}\sum_{i,j=1}^{d} f(t)\, m_{0_{ij}}\left(\frac{\partial \Phi_i^L}{\partial x_j} + \frac{\partial \Phi_j^L}{\partial x_i}\right)
\end{aligned} \tag{3.48}$$

From Equation A.84, it appears that the right-hand member vanishes if L is associated to any of the nodes outside the sub-domain e containing the source, whereas it is different from zero for those L associated to each of the nodes inside e (except at $\underline{\boldsymbol{x}}_S$). Thus, due to the discretization into subdomains of finite size, the virtual internal work associated to the source is spread over e . As a consequence, the numerical method can accurately portray a double couple point source provided the size (Faccioli et al., 1997).

With the intent to verify the accuracy of SEM3D in reproducing the wave-field radiated from a point source double-couple, the SISMOWINE benchmark is used again as reference.
The structured computational grid was designed with an average element size of 346 m, and 7 GLL points per direction. The model was enclosed into PML domain all along its external surface, so to absorb the spurious waves coming from artificial reflection at the computational boundaries. The model runs over 216 MPI cores: 2 hours (CPU-time) are required to simulate up to 5 s of wave propagation.
According to the results of the verification case (portrayed in Figures 3.24 and 3.25), SEM3D is well suited to reproduce the near and far wave-field generated by a concentrated double-couple.

[12]The seismic moment tensor is symmetric. Its traces vanishes for pure slip condition, i.e. when $\underline{\boldsymbol{d}}_\Sigma.\underline{\boldsymbol{n}}_\Sigma = 0$.

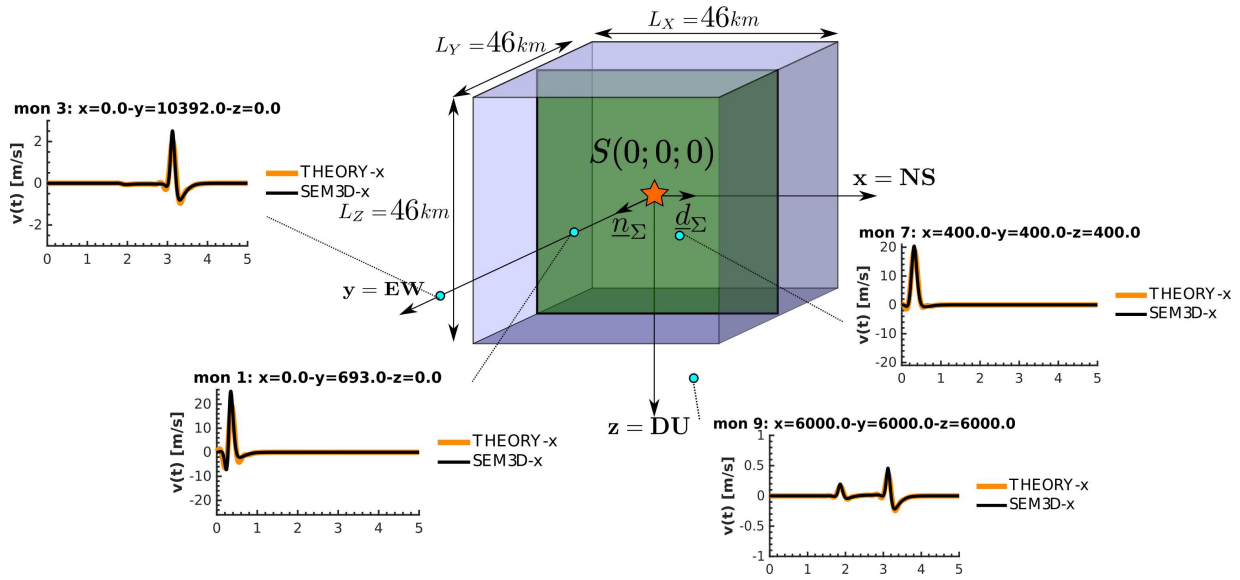

Figure 3.24: Comparison between theoretical and numerical (SEM3D) solution obtained for the WP1-HSP1 test case. The fault strikes at 0° and dips at 90°, with a rake angle of 0°.

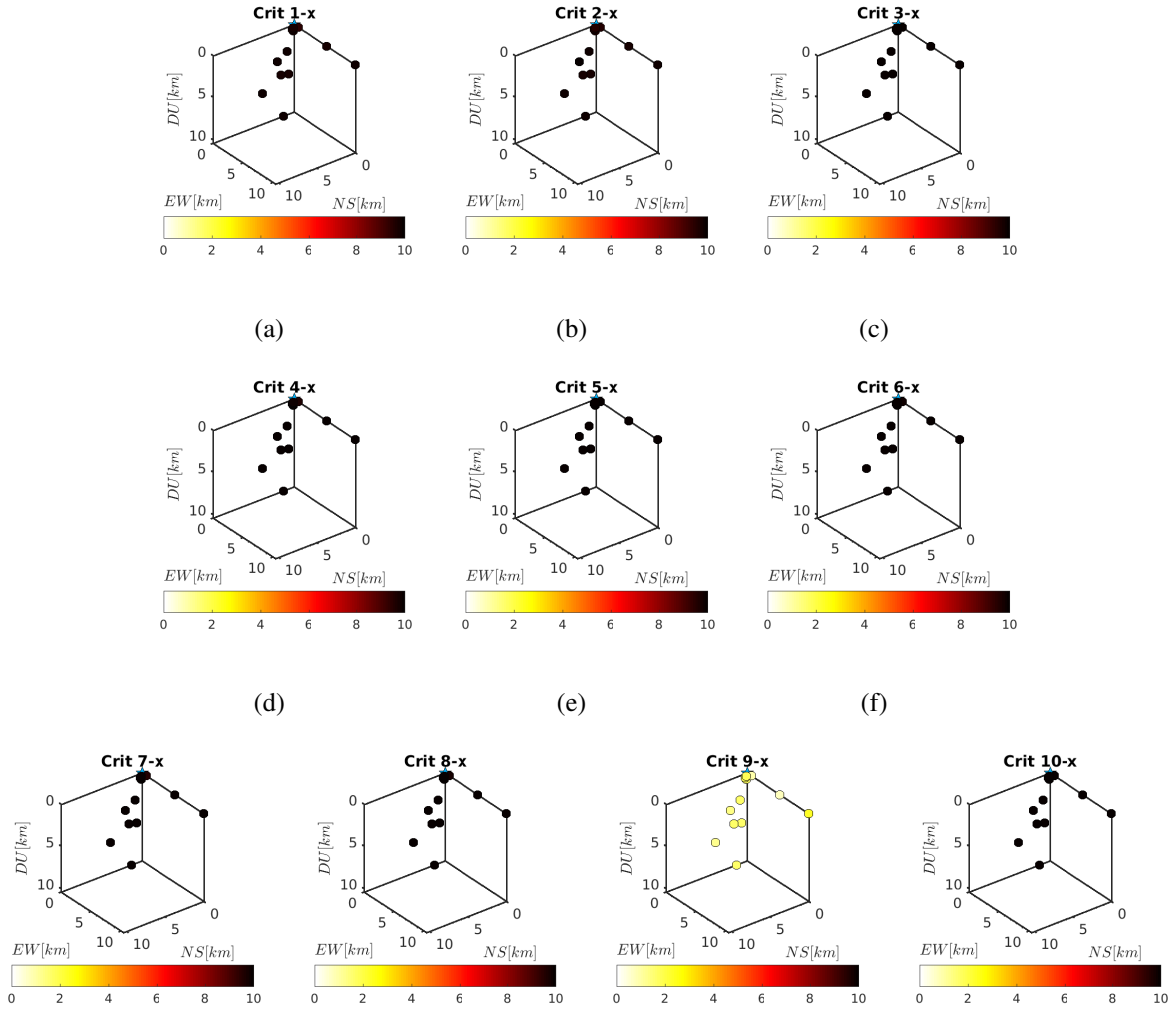

Figure 3.25: Comparison between theoretical and numerical (SEM) solution in terms of Anderson's Criteria, obtained for the WP1-HSP1 test case.

4

Coupling physics-based numerical simulations and Artificial N. N. to generate realistic broadband earthquake ground motions

"Maybe the only significant difference between a really smart simulation and a human being was the noise they made when you punched them."

– Terry Pratchett, The Long Earth

4.1 Introduction

As mentioned in Chapter 1, recent developments in physics-based earthquake ground motion simulation are intended to produce broad-band synthetic seismograms, to be confidently used in structural seismic design. This aspect has been a primary goal of Engineering Seismology ever since, and the need for broad-band synthetics to be exploited for engineering purposes has been progressively approached by several authors in the past. The path was steered by the seminal works of Hartzell (1978) and Irikura (1983), who first proposed to sum the recordings from small aftershocks to reproduce larger ones. This concept lead to the Empirical and Semi-Empirical Green's function method. However, Green's functions are not always available for different focal mechanisms sufficient signal to noise ratio at low frequencies Zeng et al. (1994). Boore (1983) extended the original concept by considering stochastic source and path effects (the methods goes under the name *stochastic point-source*, SPS, indeed). The author considered the transient earthquake wave-motion as a stationary scalar random field, possibly obtained by filtering a suite of windowed stochastic time histories (typically white noise with zero mean), whose spectrum is then scaled to a specified one, leaving the phase untouched. Noticeably, the method produce reasonable broad-band synthetics (up to 15.0 Hz), covering all the essential aspects of high-frequency ground motions for earthquakes over a very large magnitude range. However, Zeng et al. (1994) observed that this approach only generates an S-wave pulse, generate three-component seismograms with poor physically expected coherency. Moreover, phases of arrivals, such as dispersed surface waves, cannot be simply included. Somerville et al. (1991) developed a procedure to produce synthetic acceleration time histories of large sub-duction earthquakes and have tested it against the recorded strong ground motions of the M_W = 8.0 Michoacan, Mexico, and Valparaiso, Chile, earthquakes of 1985. The response spectra of the simulated motions have little or no significant bias in the period range of 0.05 to 2 sec for both earthquakes, and the peak accelerations, durations, and envelope shapes of the time histories are in good agreement with the recorded motions.

Such models for wave propagation have represent the ground motion as a convolution of a slip function on the fault with a synthetic Green's function (Aki and Richards, 1980), although appropriate source descriptions are hardly obtained. To cope with this shortcoming, Zeng et al. (1994) presented a composite source model for the convolution with synthetic Green's functions, in order to synthesize strong ground motions due to a complex rupture process of a large earthquake. Sub-events with a power-law distribution of sizes are located randomly on the fault. Each sub-event radiates a displacement pulse with the shape of a Brune's pulse in the far field, at a time determined by a constant rupture velocity propagating from the hypocenter. They produced hihg-quality broad-band synthetics up to 10.0 Hz. Exploiting the SPS, Saikia and Somerville (1997) combined the deterministic low-frequency wave-forms with stochastic high-frequency ones, granting a classical ω^{-2} spectral decay for far-field displacement seismograms. Combining the deterministic and semi-empirical results, the authors obtained no significant bias in the frequency range of 0.2 to 30.0 Hz. However, an atypical behaviour was observed at the corer frequency where the low-frequency and high-frequency spectra are intended to be *sewed*: if amplitude spectra are easily matched, a phase mismatch usually occurs at the hybridization step. Mai and Beroza (2003) solved this problem by constructing the hybrid broad-band synthetic wave-form filtering the two components with smooth weighting functions defined in the Fourier's domain, mirrored upon the corner frequency ($f \sim 1.5$ Hz) and that sum to unity at each frequency. This approach is similar to the *simultaneous deconvolution approach* proposed by Harvey and Choy (1982). In their study, Mai and Beroza (2003) generated a *decimated* low-wavenumber filtered dislocation model to generate low-frequency displacements (by employing the discrete-wavenumber/finite element method proposed by Olson et al. (1984), opportunely extended to finite-fault sources by Spudich and Archuleta (1987) and Spudich and Xu (2002)). The high-frequency ray-theory seismograms were instead computed by employing the isochrone integration method proposed by Spudich and Frazer (1984) and Spudich and Xu (2002), applied to a finer fault grid, capable of take into consideration near-source effects. Being the background dislocation model employed the same, no significant phase shift was observed. With this technique, they produced reliable synthetics up to a frequency of 10.0 Hz. Beresnev and Atkinson (1997) and Motazedian and Atkinson (2005) extended the SPS method to extended fault mechanisms (SFS method): the fault is divided in a certain number of sub-faults, whose contribution to the total wave-field is computed one modelled as a point source can be calculated as suggested by Boore (2003) and then summed at the observation point, with a proper time delay. This permits to control the local frequency corner at each sub-fault as a function of time. The rupture begins with a high corner frequency and progresses to lower corner frequencies as the ruptured area grows. Thus, the hybrid models cover a broad frequency range, from about 0.1 to 20 Hz. However, hybrid methods may not necessarily provide Green's functions that satisfy both the amplitude and phase information in the important intermediate frequency range from 0.5 to 2.0 Hz; the source processes generating the 0.5 to 2.0 Hz motions are not adequately resolved by either low or high-frequency models (Motazedian and Atkinson, 2005). Hartzell et al. (2005) compared kinematic models based on the summation of a fractal distribution (Irikura and Kamae, 1994) of sub-event sizes with a dynamic model based on the slip-weakening friction law proposed by Ida (1972). Kinematic modeling is performed for the frequency band 0.2 to 10.0. Hz, dynamic models are calculated from 0.2 to 2.0 Hz, instead. Source models were propagated to the far field by convolution with 1D and 3D theoretical Green's functions. Because the knowledge of the velocity structure is often poor, however, theoretical Green's functions may be poorly realistic for frequencies higher than 1.0 Hz. Broad-band (0.0-20.0 Hz) synthetic seismograms were generated by Frankel (2009), for finite-fault sources with constant stress drop with seismic moment. They were obtained by combining deterministic synthetics for plane-layered models at low frequencies with stochastic synthetics at high frequencies. The deterministic synthetics were calculated using an average slip velocity, and hence, dynamic stress drop, on the fault that is uniform with magnitude (exploiting the frequency-wavenumber integration proposed by Zhu and Rivera (2002), to generate synthetic Green's functions for a plane-layered model). The

stochastic part of the broad-band synthetics was generated by employing the SPS (Boore, 2003). The spectral accelerations at 0.2, 1.0, and 3.0 sec periods from the synthetics generally agreed with those from the set of Next Generation Attenuation (NGA) relations for M_W 5.5-7.5 for distances of 2-100 km. At distances of 100-200 km some of the NGA relations for 0.2 sec spectral acceleration were substantially larger than the values of the synthetics for M_W 7.5 and M 6.5 earthquakes because these relations do not have a term accounting for quality factor Q. At 3 and 5 sec periods, the synthetics for M 7.5 earthquakes generally had larger spectral accelerations than the NGA relations, although there was large scatter in the results from the synthetics. The synthetics showed a sag in response spectra at close-in distances for M 5.5 between 0.3 and 0.7 sec that is not predicted from the NGA relations. Pulido and Dalguer (2009) generalized the dynamic high-frequency model of a suddenly stopping circular crack Madariaga (1977) to the radiation from a general 3D rupture in a planar fault, where HF content is radiated during gradual changes of rupture velocity at the rupture front. Their simulations of the 2000 Tottori (Japan) earthquake by inverting observed near-source acceleration envelopes of the earthquake were reliable up to 10.0 Hz. Their simulated near-source strong ground motions of the Tottori earthquake are also able to reproduce the ω^{-2} radiation theoretically predicted in 2D dynamic fault rupture models.

All the mentioned studies produce satisfactory broad-band synthetics. However, they suffer the lack of an accurate propagator tool. Moreover, the dynamic models are poorly constrained at high-frequencies, due to the paucity of observations. As a matter of fact, most modern broadband procedures use analytical Green's functions to model low-frequency path effects, including the effects of sedimentary basins. However, the development of high-fidelity physics-based simulations of the low-frequency content of the seismic wave-motion has been widely exploited as a basis to generate hybrid broad-band records. Graves and Pitarka (2004) combined the physics-based simulations (valid up to 1.0 Hz, with a kinematic description of fault rupture, featured by a model of heterogeneous slip distribution, rupture velocity and rise time) with a stochastic approach at high-frequencies (proposed by Beresnev and Atkinson, 1997), for moderate and larger crustal earthquakes. The broadband response (up to 10.0 Hz) was obtained by summing the separate responses in the time domain using matched filters centered at 1.0 Hz for ground motion time histories. The authors restricted both the velocity models for low- and high- frequencies to a computational velocity model with the same average near-surface shear wave velocity. In this manner, frequency-dependent non-linear site amplification factors were applied to efficiently include a detailed site-specific geologic information in the ground motion estimates. Validation studies of the simulation methodology using ground motions recorded during the 1989 Loma Prieta and 1994 Northridge earthquakes. Liu et al. (2006) improved this technique by introducing a spatial correlation structure between slip amplitude, rupture velocity, and rise time, as suggested by dynamic fault modeling. To produce more accurate high-frequency amplitudes and durations, the 1D synthetics were corrected with a randomized, frequency-dependent radiation pattern. The 1D synthetics were further corrected for local site and nonlinear soil effects by using a 1D nonlinear propagation code and generic velocity structure appropriate for the site's National Earthquake Hazards Reduction Program (NEHRP) site classification. The entire procedure is validated by comparison with the 1994 Northridge, California, strong ground motion data set. Graves et al. (2008) simulate a broadband (0.0-10.0 Hz) ground motions for three M_W 7.8 rupture scenarios of the southern San Andreas fault, using the high-performance computing resources of the Southern California Earthquake Center. The hybrid physics-based and semi-stochastic method was employed. Graves and Pitarka (2010) improved their previous work by changing the correlation of random distributions of parameters such as slip and rupture velocity slip, by including a magnitude dependent scaling; the correlation structure for rise-times adopted was proposed by Aagaard et al. (2008b,a). The long period ground motion (up to 1.0 Hz) was obtained by Finite Difference Method (FDM), whereas the high-frequency is generated via Stochastic Finite Source method (Beresnev and Atkinson, 1997). Aagaard et al. (2010b) and Aagaard et al. (2010a) simulated broadband (f_{max} =

10.0 Hz) for 39 scenario earthquakes involving the Hayward, Calaveras, and Rodgers Creek faults. They considered the effects of creep on co-seismic slip using two different approaches, both of which reduce the ground motions, compared with neglecting the influence of creep. The Finite Element Method (FEM) was exploited. An important parameter in the overall slip distribution they adopted was heterogeneity length scale that defines the crossover between the background distribution and the stochastic distribution. Selecting too short length scale for the crossover results in only very short length-scale heterogeneity. This leads to excessive energy radiated at long periods and a deficiency of energy radiated at shorter periods. On the other extreme, selecting a too long length scale for the crossover results in ruptures that do not have the desired dimensions due to large regions with zero slip. To choose a reasonable crossover length scale, they generated broadband ($T > 0.1$ s) synthetics for a simple 1D velocity structure and a suite of 50 sites ranging from 2 km to 70 km from the rupture, with the goal of minimizing the overall residual in spectral acceleration with respect to NGA ground-motion prediction models. These simulations use the hybrid broadband ground motion simulation methodology of Graves and Pitarka (2004) with a 1D seismic velocity model based on the generic rock profile of Boore and Joyner (1997), deterministic ground motion calculations at periods longer than 1.0 s, and stochastic ground-motion calculations for periods 0.10-1.0 s. As a result, they selected to crossover from the background slip distribution to the stochastic slip distribution at a length scale equal to one-half of the rupture length. More recently, Taborda and Bielak (2013) simulated the M_W 5.4 Chino Hills earthquake for a maximum frequency up to 4 Hz and a minimum shear-wave velocity down to 200 m/s, with a Finite Element code for anelastic wave propagation in heterogeneous media. A validation study was performed comparing data obtained from seismic networks with simulation synthetics on more than 300 recording stations. The source model corresponds to that of an independent inversion study, and the material model used is a community velocity model (CVM) developed by the Southern California Earthquake Center (SCEC). Despite the lower frequency solved by their analysis, from a regional perspective, the simulation starts to deviate from the data at frequencies above 1 and 2 Hz. At particular locations or station clusters, however, the synthetics yield very good results, even at frequencies between 2 and 4 Hz. The best results are obtained between 0.1 and 0.25 Hz over the entire region and up to 1 Hz within the major basins. However, the interesting aspect of this study, is the inclusion of a very soft soil deposits. Last but least, in order to address the multi-resolution problem that arises from the inclusion of the earthquake source at a regional scale and the building models at a local scale, and to be able to vary the system configuration during repeated simulations, the Domain Reduction Method (DRM) introduced by Bielak et al. (2003a) has been widely used (Quinay et al., 2013; Isbiliroglu et al., 2015). The methods subdivides the original problem into two simpler ones: (1) an auxiliary problem that simulates the earthquake source and propagation path effects with a model that encompasses the source and a background structure from which the localized feature has been removed and (2) a problem to model local site effects (source of high-frequency enrichment of the incident wave-field). Its input is a set of equivalent localized forces derived from the first step. These forces act only within a single layer of elements adjacent to the interface between the exterior region and the geological feature of interest. This enables to reduce the domain size in the second step. If the background subsurface structure is simple, one can replace the finite-element method in the first step with an alternative efficient method.

Table 4.1 summarizes (in chronological order) the principal research works intended to produce broad-band synthetic wave-forms.

In this chapter, an alternative strategy for the physics-based generation of broad-band synthetics is presented. As a matter of fact, instead of pushing physics-based simulations to higher frequencies by employing a stochastic description to handle fault complexity and crustal structure (one of the main objectives of the SCEC5 research plan for 2017-2021), the described approach targets the ultimate design tool, i.e. the design spectrum. The enhancement strategy suggested goes under the acronym

Table 4.1: Summary of the principal studies to produce broad-band synthetic wave-forms for earthquake ground shaking scenarios. E-GF = Empirical Green's function Irikura (1991); SE-GF = Semi-Empirical Green's Functions (Irikura, 1983; Somerville et al., 1991; Zhu and Rivera, 2002); SPS = Stochastic Point Source method (Boore, 1983); DW-FE = Discrete-Wavenumber/Finite Element method (Olson et al., 1984; Spudich and Archuleta, 1987); ISI = ISochrone Integration (Spudich and Frazer, 1984; Spudich and Xu, 2002); SFS = Stochastic Finite Source method (Beresnev and Atkinson, 1997; Motazedian and Atkinson, 2005); SE-GF (F) = Semi-Empirical Green's Function with Fractal sub-event distribution (Irikura and Kamae, 1994); FLD = Friction-Law Dynamics (Ida, 1972, for instance); FDM = Finite Difference Method; FWI = Frequency-Wavenumber Integration

Author(s)	f_{max} [Hz]	Method(s)
Hartzell (1978)	?	E-GF
Irikura (1983)	5.0	SE-GF
Boore (1983)	15.0	SPS
Somerville et al. (1991)	20.0	E-GF
Zeng et al. (1994)	10.0	SE-GF
Saikia and Somerville (1997)	30.0	SPS + SE-GF
Mai and Beroza (2003)	10.0	DW-FE + ISI
Graves and Pitarka (2004)	10.0	FDM + SFS
Motazedian and Atkinson (2005)	20.0	SFS
Hartzell et al. (2005)	10.0	SE-GF (F)
Hartzell et al. (2005)	2.0	FLD
Liu et al. (2006)	20.0	FDM + SFS
Pulido and Dalguer (2009)	10.0	FLD
Frankel (2009)	20.0	FWI + SPS
Miyake et al. (2010)	10.0	E-GF
Graves et al. (2008)	10.0	FDM + SFS
Graves and Pitarka (2010)	10.0	FDM + SFS
Aagaard et al. (2010b)	10.0	FEM + SFS
Taborda and Bielak (2013)	4.0	FEM

ANN2BB, since it is based on the combination of physics-based simulation with Artificial Neural Networks (ANN). An ANN is a data-processing algorithm (or an actual hardware) designed upon biological neural networks. In other words, it can be regarded as a statistical-computational framework set up to artificially reproduce the predictive capability of interconnected logic units (i.e. neurons). A neural network is constructed by organizing sets of interconnected neurons in layers to estimate or approximate non-linear functions that usually depends on a large number of inputs. Due to their adaptive interconnection, the neurons learn from examples, and exhibit some structural capability for generalization. Moreover, neural networks normally have great potential for parallelism, since the computations of the components are independent of each other. An ANN has the following basic features: it contains sets of adaptive weights, i.e. numerical parameters that are tuned by a learning algorithm and it is capable of approximating non-linear functions of their inputs. The adaptive weights can be thought of as connection strengths between neurons, which are activated during the training phase (upon a set of data, compatible with the expected outcome) and exploited during the prediction phase. In this context, ANNs are trained upon exemplary strong ground motion database, taking LP spectral ordinates as input data (once a corner period has been arbitrarily chosen). Applying the trained ANN upon the synthetic time-histories provided by deterministic numerical simulations (PBS or hybridized), one gets two response spectra, exactly coincident at long-period, but diverging at short-periods. Therefore, by scaling the synthetic response spectrum upon ANN prediction at short

periods, one gets broad-band synthetics whose response spectrum is predicted by ANN constrained by deterministic analysis of the earthquake scenario. ANN2BB was conceived to try to solve the uncertainty related to system-specific PBS and contribute to the overall understanding of earthquake predictability. This goal is worldwide shared by the scientific community, as for instance it is indicated in the SCEC5 provisional proposals.
In Section 4.2, the ANN training procedure is described in detail. The design of the training workflow is presented at first: neural networks are constructed by testing their regression performance on validation sets. In the following, two crucial aspects are discussed: the sensitivity to the site-class of the training dataset and the predictive performance with respect to the vertical component of motion. Section 4.3 outlines the recipe to produce broad-band strong ground motions from 3D physics-based numerical simulations, following the workflow depicted in Figure 4.1). Some applications of the methodology are also presented in the following. Specifically, two Italian strong ground motion earthquakes are considered, namely: (1) the 2009 M_W6.3 L'Aquila earthquake, Central Italy and (2) M_W6.0 2012 May 29 earthquake in the Po Plain, Northern Italy. Recording stations nearby the epicentres were considered in this study, since they experienced an intense ground shaking in near-field conditions.

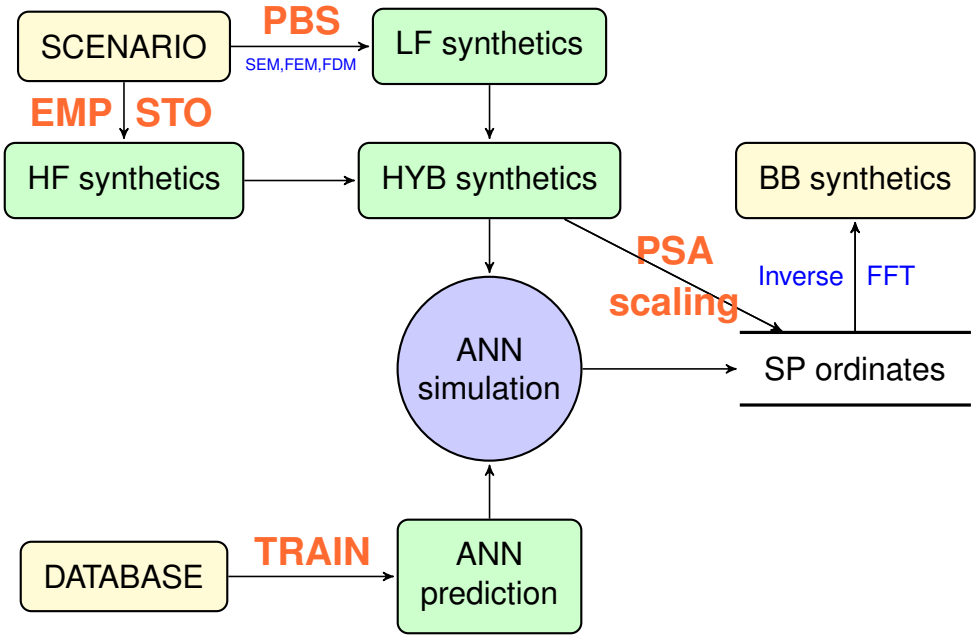

Figure 4.1: Outline of the proposed strategy to generate broad-band(BB) synthetics. Low-frequency (LF) synthetics are obtained by numerical physics-based simulations (PBS) (e.g. by exploiting the Finite Difference Method (FDM), the Spectral Element Method (SEM) or the Finite Element Method (FEM)). The high-frequency (HF) part of the ground motion is preliminary generated independently, for instance by Empirical (EMP) or Stochastic (STO) methods (e.g. the one proposed by Sabetta and Pugliese (1996) or by Boore Boore (1983)). A classical hybrid coupling is performed at first to obtain hybrid (HYB) records. The latter are spectral scaled upon the short-period (SP) spectral ordinates obtained by applying an Artificial Neural Network (opportunely trained on a trial set of records). The spectral-matching technique is applied iteratively by exploiting the direct and inverse Fast Fourier Transform (FFT) to finally obtained BB synthetics, once the original HYB spectrum matches the ANN prediction.

The content of this chapter has been object of a submitted publication to the *Bulletin of Seismological Society of America*.

4.2 Correlation of long and short period spectral ordinates, through an ANN based on a strong motion dataset

4.2.1 Design and train of an ANN

It is commonly assumed that any physical quantity can be obtained by summing a deterministic function (depending on the set of input parameters) to a stochastic contribution (Bishop, 1995). The deterministic function is often described by a *model* (analytical or numerical) of the problem. Nevertheless, in some cases the complexity of the problem is increased by the undetermined nature of the input, such as the seismic slip distribution along the fault, and by the poor control of the model parameters, such as the large scale geological models involved in PBS, due to insufficient detailed information and possible non-linear soil response. In most cases, Artificial Neural Networks are used to estimate the non-linear relationship between a vector of input variables (e.g. the LP spectral ordinates obtained via numerical simulation) and the output target (e.g. the SP Sa). As a matter of fact, under mild mathematical conditions, any problem involving a continuous mapping between vector spaces can be approximated to arbitrary precision (i.e. within an error tolerance) by *feed-forward* ANNs which is the most often used type (Cybenko, 1989). Especially, ANNs are very effective in generalizing output predictions when facing problems tolerant to some errors, featured by a highly populated input database, but to which hard and fast rules can not easily be applied. ANNs with a proper architecture can be therefore considered statically consistent estimators. Our purpose is to establish through the ANN a correlation between N_{Sa}^{LP} response spectral ordinates selected for $T \geq T^{\star}$, being $T^{\star}$ the corner period corresponding to the range of reliability of PBS, with N_{Sa}^{SP} response spectral ordinates for $T \leq T^{\star}$. A strong ground motion dataset (Smerzini et al., 2014) was used as teaching set. The dataset consists of N_{db}=501 three components high-quality accelerograms, spanning a range of Moment Magnitude from 5 to 7.4 and epicentral distances less than 40 km. Two ANNs are considered, one referring to the geometric mean of the horizontal components and one to the vertical one. As long as the database is enriched, the procedure can be ideally extended by training different ANNs separately, for different homogeneous datasets (such as for different soil classes) and/or for different components of motion (such as fault normal and fault parallel). In our case, the neural network is designed as a two-layers (i.e. nodes are grouped in layers) feed-forward (i.e. the arcs joining nodes are unidirectional, and there are no cycles) neural network with N_n^h sigmoid hidden neurons (the so called *activation functions*) and a linear output neuron. The number of nodes in the input layer N_n^i equals the number of input variables N_{Sa}^{LP}. The number of nodes in the output layer N_n^o equals the number of target values N_{Sa}^{SP}. With this kind of configuration, the ANN takes the name of Multi Layer Perceptron (Bishop, 1995; Bishop and Roach, 1992). The *backpropagation of error* was used in the training phase (McClelland et al., 1986). The idea is to propagate error signal, computed in single teaching step, back to all connected neurons.Back-propagation needs a *teacher* that knows the correct output for any input (*supervised learning*) and uses gradient descent methods (e.g. the Levenberg-Marquardt algorithm (Levenberg, 1944; Marquardt, 1963)) on the error to train the weights. The neural network fitting tools (`nftool`) implemented in `Matlab` was employed at this stage. A sketch of the ANN training process for the problem at hand is shown in Figure4.2a. The N_{Sa}^{LP} input parameters are $\{Log_{10}[Sa(T_j)]\}_{j=1}^{N_{Sa}^{LP}}$, where Sa is the pseudo-acceleration response spectral ordinates at period T_j, ranging from the corner period $T^{\star}$ to 5 s. The outputs are N_{Sa}^{SP} ground motion parameters, specifically, $\{Log_{10}[Sa(T_k)]\}_{k=1}^{N_{Sa}^{SP}}$, at periods T_k = 0 (PGA = Peak Ground Acceleration), up to $T^{\star}$ (depicted as red dots in Figure4.2b). Typically, the entire set of N_{db} input-output data is divided into three subsets: a training (input/output) data set, used to calibrate the adjustable ANN weight; a validation (input/output) data set made of patterns different from those of the training set and thus used to monitor the accuracy of the ANN model during the training procedure; a test (in-

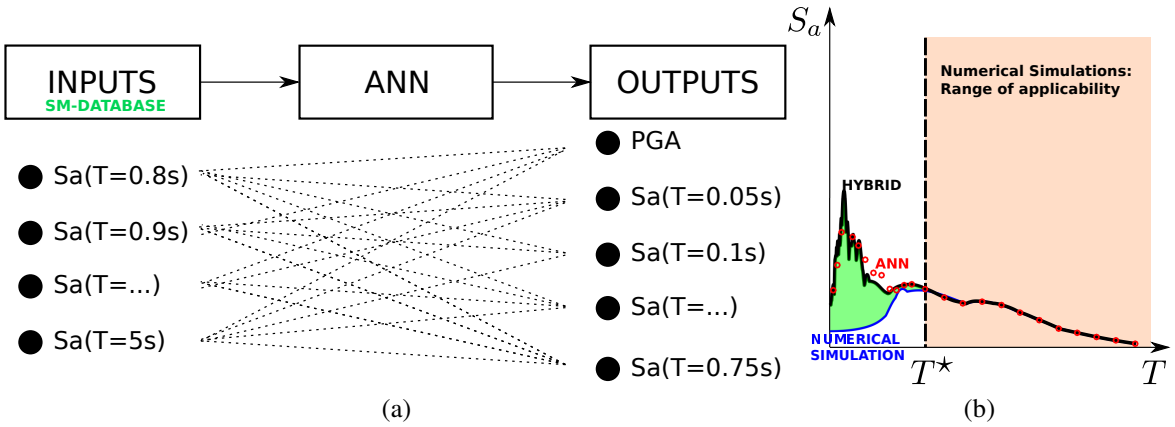

Figure 4.2: (a) Logic scheme of the ANN training patterns: the LP spectral ordinates represents the *teaching inputs*, whereas the SP ones are the biased output predicted by the ANN. (b) Sa spectrum obtained by numerical simulations (blue line), compared to ANN prediction (red dots). The black line represents the response spectrum of hybrid records obtained by coupling PBS with broad-band wave-forms generated by empirical/stochastic methods.

put/output) data set, not used during ANN training and validation, but needed to evaluate the network capability of generalization in the presence of new data. This distinction helps to avoid the problem of *overfitting*, which is a well known shortcoming of ANN design. As a matter of fact, even though the error on the training set is driven to a very small value, the network may fail in generalizing the learned training patterns if the patterns of the training set do not sufficiently cover the variety of new situations. Therefore, an *early stop* criterion was adopted to stop the training phase when the error on the validation set starts growing. Moreover, it is common practice to randomly divide the set of data into training, validation, and test. As a matter of fact, the `nftool` package resets the initial weights and biases at each training session: different starting sets lead to different solutions. Therefore, the N_{train}=50 neural networks were trained upon the 95% of the total data available. The *best* (i.e. most performant) ANN was chosen among those N_{train}, as the one that provided the lowest mean square error on the remaining 5% of the dataset. Another issue to be solved is the choice of the number of neurons composing the network. As a matter of fact, Figure 4.3 shows the poor increase in terms of prediction of six different ANNs trained with an increasing number of connected neurons (i.e. N_n^h varying from 30 to 180). The error bars refer to train set (blue in Figure 4.3), validation set (green in Figure 4.3) and test set (red in Figure 4.3) corresponding to the *best* at each iteration to find the *best* ANN (over the N_{train} trained). Despite the increased computational cost associated to the higher number of neurons employed at hand, no significant improvement were achieved along the whole sets of target periods. Therefore, N_n^h was kept as low as possible (since a too small network may not have enough power to fit the data), due to lack of data and to reduce the chance of *overfitting* (Hagan et al., 1996). As a matter of fact, the number of parameters in the network is much smaller than the total number of points in the training set, then there is little or no chance of *overfitting*.

In the following subsections, the ANN sensitivity to different choices of $T^\star$ is tested, on both the horizontal and vertical components of motion. Moreover, the response of different ANNs trained on subsets of records selected by site-class is presented. The trained ANNs were tested to the time-histories recorded during recent earthquakes, such as the 2016 M_W7.1 Kumamoto (KMM2016) earthquake (Japan) and the two seismic sequences that stroke central Italy in August (M_W6.2) and October (M_W6.5) 2016 (referred as to CIT2016).

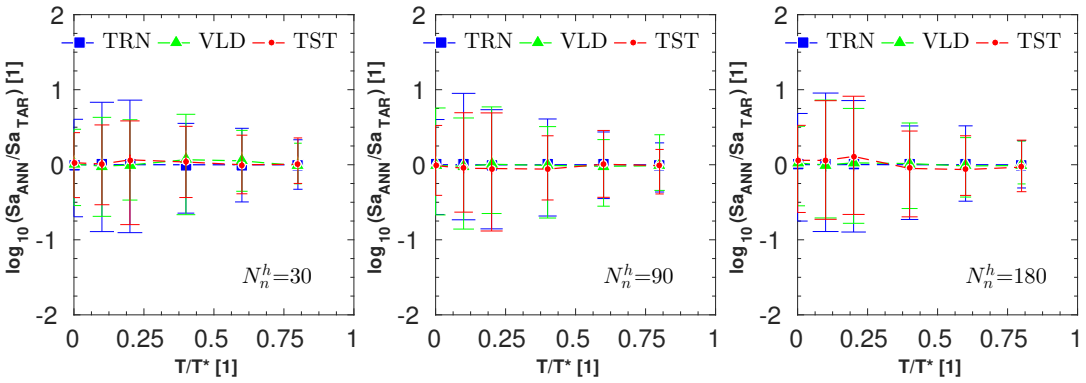

(a) (b) (c)

Figure 4.3: ANN performance in the training phase, expressed in terms of estimated/target Sa. The performance is estimated at each target natural period T, here normalized by the corner period $T^\star$=0.5 s. Three ANNs were trained by changing the number of hidden neurons N_n^h from 30 (a), to 90 (b) and to 180 (c) respectively.

4.2.2 Testing the ANN performance on the horizontal component

Effect of the corner period $T^\star$

The choice of the corner period $T^\star$ is allegedly delicate. One may expect that as smaller $T^\star$ becomes as much more accurate will be the neural network prediction. In practice, a smaller $T^\star$ means to feed the neural network with a greater number of input values and to reduced number of outcomes accordingly. However, the risk of over-fitting the data in the training phase may increase. Moreover, the level of confidence on the LP spectrum raise to higher frequency content. Since the physics-based simulations (at which we aim to apply this procedure) loose reliability in the SP region, reducing $T^\star$ translates into an increased confidence in the PBS carrier spectrum, which would require high computational effort to be produced. To clarify the effect of the corner period onto the ANN prediction, three different ANNs were trained upon the ensemble of records available (N_{db}=501) but considering a corner period $T^\star$ of 0.5, 0.75 and 1 s respectively. Their performances were tested for the CIT2016 (Figure 4.4) and KMM2016 (Figure 4.5) strong ground motions respectively.
The ratio between estimated (Sa_{ANN}) and recorded (Sa_{REC}) spectral values at SP are presented in the top rows of both Figure 4.4 and Figure 4.5. The synoptic comparisons between the recorded and estimated spectra are depicted along the bottom row. The geometric mean spectra of the two horizontal components is depicted for comparisons. The Accumuli (ACC) and Norcia (NRC) stations were considered for CIT2016, whereas stations KMMH16 and KMMH14 stations were studied for KMM2016. It seems clear that the neural network prediction is highly sensitive to the corner period selected. For instance, in Figures 4.4e and 4.4b, the choice of $T^\star$= 1 s seems quite inappropriate. This hypothesis is backed by KMM2016 spectra (Figure 4.5b, 4.5e). Although it is not possible to distinguish the spectral region where the deterministic nature of the seismic scenario plays a major role on the spectral shape, the ANN trained ad $T^\star$ = 1 s seems poorly constrained, thus indicating that the purely stochastic component of the input motion dominates the spectral shape at lower periods. On the other hand, the prediction becomes more accurate starting from $T^\star$ = 0.75 s (see Figures 4.4a, 4.4d 4.5a,4.5d). Generally speaking, although for one-peak-shaped spectra (such as the ACC one, in Figure 4.4d), the three tested ANNs are very precisely reproducing the SP spectral content, for more complicated spectral shapes, both $T^\star$ = 0.75 s and $T^\star$ = 0.5 s look suitable for an accurate estimation rather than $T^\star$ = 1.0 s.

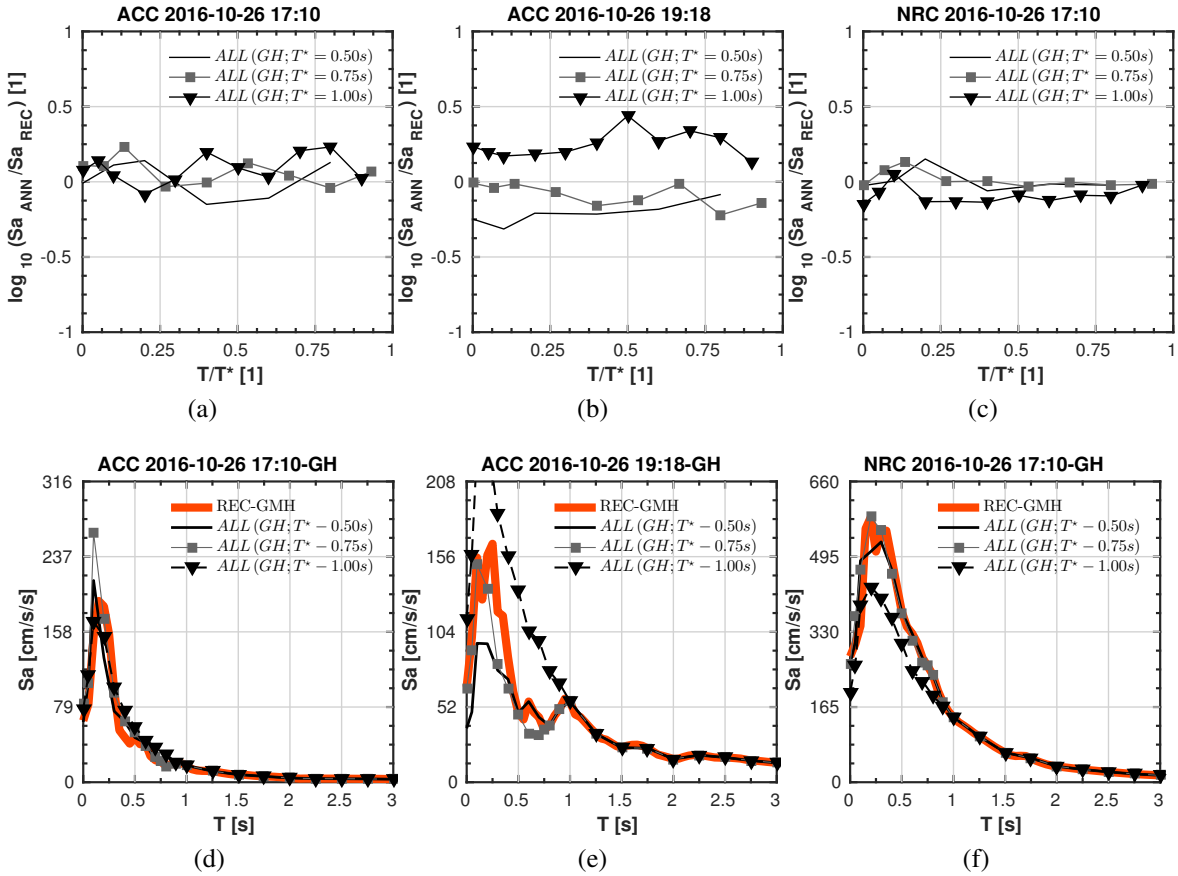

Figure 4.4: ANN performance for different training corner periods $T^{\star}$, expressed in terms of estimated/target Sa (a-c). (d-f) estimated Sa spectra compared to the recorded ones (thick orange line). The recordings at two stations (ACC and NRC) for the CIT2016 earthquake are shown. Thin solid black line refers to an ANN trained at $T^{\star}$=0.5s; thin solid grey line with squared markers refers to an ANN trained at $T^{\star}$=0.75s and solid black line with triangle markers refers to an ANN trained at $T^{\star}$=1.0s.

Effect of the site class

Another characteristic of the SP spectral shape the ANN have desirably to predict is the effect of the non-linear site response onto it. In particular, soft soils exhibit lower Sa values at short periods since the high-frequency content of the input motion is damped out due to a viscous mechanism (taking place for weak shear-strain amplitudes, γ $<10^{-5}$) and to the soil non-linear hysteresis (γ $>10^{-5}$). In this sense, one expects the neural network trained upon a set of time-histories recorded on soft rock or stiff soil to be prone to estimate lower Sa values, whereas higher response-spectral ordinates are likely to be predicted if the teaching set refers to stiffer sites (e.g. rock). To prove the latter assumption, a set of three different ANNs is considered herein, called respectively AB, CD and ALL. Those networks have been selectively trained upon sub-sets of the original database, formed by time-histories recorded at the same *site class* (classically defined based on the shear wave velocity of the top 30 m of the soil, $V_{S,30}$, according to *EuroCode 8* (EC8)). As a matter of fact, very firm soil and soft rock sites (classes C and D) have similar amplitudes, distinctively different from the ones on rock and firm rock sites (classes A and B). Thus, AB and CD refer to classes A-B ($V_{S,30} > 760$ m/s) and C-D (180 m/s $< V_{S,30} <$ 760 m/s) respectively. ALL has been trained without taking into account the site classification. To study the effect of the site-class filter applied to the training database, the three ANN were tested on two stations of class A-B (i.e. ACC and NRC, during the CIT2016 earthquake

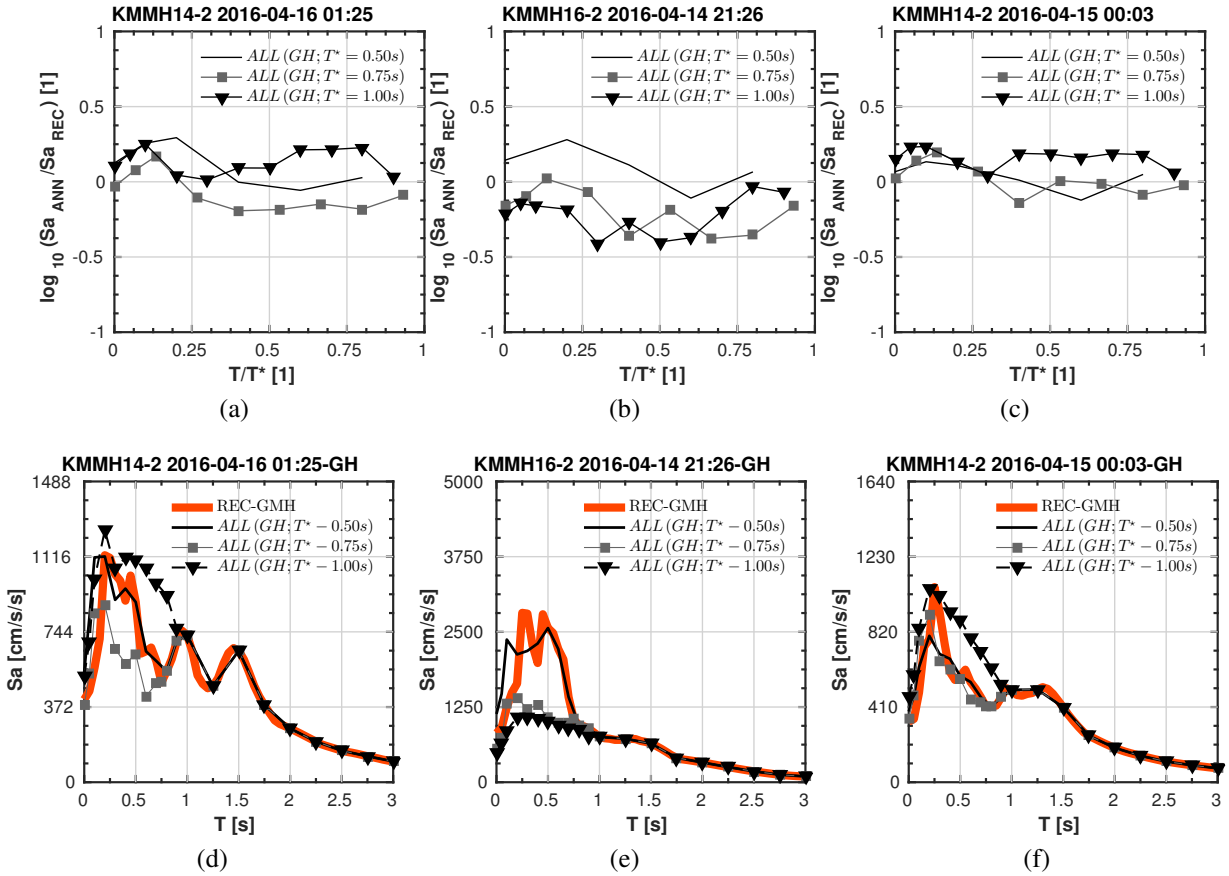

Figure 4.5: ANN performance for different training corner periods $T^\star$, expressed in terms of estimated/target Sa (a-c). (d-f) estimated Sa spectra compared to the recorded ones (thick orange line). The recordings at two stations (KMMH14 and KMMH16) for the KMM2016 earthquake are shown. Thin solid black line refers to an ANN trained at $T^\star$=0.5s; thin solid grey line with squared markers refers to an ANN trained at $T^\star$=0.75s and solid black line with triangle markers refers to an ANN trained at $T^\star$=1.0s.

- see Figure 4.6) and two stations classified as C-D sites (i.e. KMMH14 and KMMH16, during the KMM2016 earthquake - see Figure 4.7).
AB predicts higher SP-Sa values compared to CD, whereas ALL stands in the middle. In the case of KMMH16, the CD artificial network has the best performance: relatively low SP amplitudes (due, at large magnitudes and short distances, to non-linear site effects) are correctly reproduced. One may argue that the greatest differences in horizontal ground motion among the four EC8 site categories occur at long periods on firm rock sites, which have significantly lower amplitudes due to an absence of sediment amplification (Campbell, 2008). In our analysis, we did not take into account this difference since all the three ANN tested have the been fed with the same LP-Sa.
The neural network application to the horizontal ground motion revealed the scarce importance of the site class upon the final prediction whereas it highlighted the importance of the choice of the corner period.

4.2.3 ANN performance on ground motion vertical component

Another interesting point we investigated herein is the ANN performance on the vertical component of the ground motion. According to Campbell (Campbell, 2008), the vertical strong ground motion

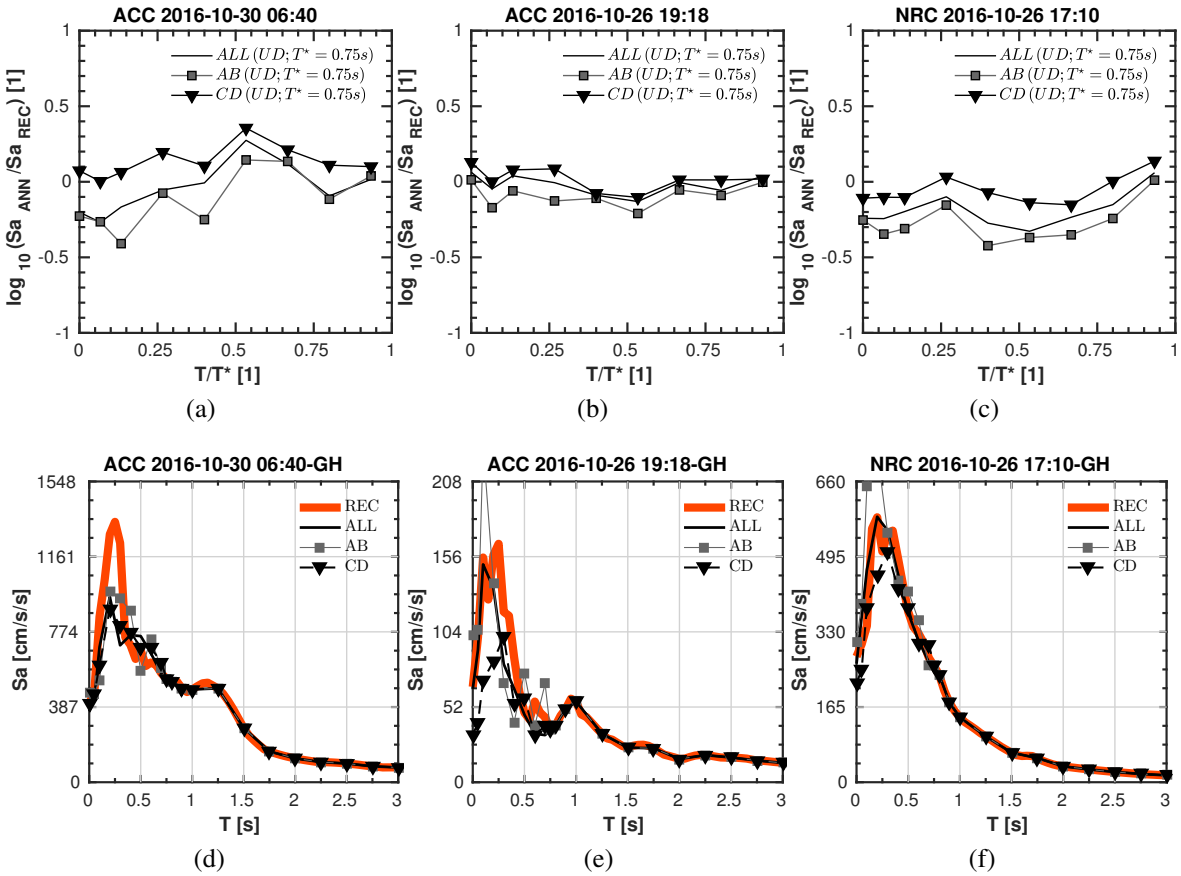

Figure 4.6: ANN performance for different EC8 site classes, expressed in terms of estimated/target Sa (a-c). (d-f) estimated Sa spectra compared to the recorded ones (thick orange line). The recordings at two stations (ACC and NRC) for the CIT2016 earthquake are shown. Thin solid black and grey lines with square markers refers to an ALL and AB respectively; solid black line with triangle markers refers to CD.

component exhibits similar behaviour to the horizontal ones for firm rock sites (class A) at long periods, but has relatively higher short-period amplitudes at short distances on firm soil (class C) sites due to a lack of non-linear site effects, less anelastic attenuation, and phase conversions within the upper sediments. Figures 4.8 shows the pseudo-spectral acceleration response predicted by AB, CD and ALL respectively for $T^{\star}$ = 0.75 s. The latter are compared to the recorded Sa spectrum. No significant differences may be noticed in the ANN predictions.

4.3 Recipe to produce broad-band strong ground motions from 3D physics-based numerical simulations

4.3.1 ANN-based broad-band response spectra

According to the procedure described hereafter, the construction of broad-band synthetics cannot part with the physics-based analysis of the seismic scenario. The latter serves as a background deterministic milestone, to which routinely apply the ANN prediction. The seismological/geotechnical model usually spans several tens of kilometres in the surroundings of the epicentral area, so to encompass the regional geology and the rupture area. However, common numerical methods barely solves

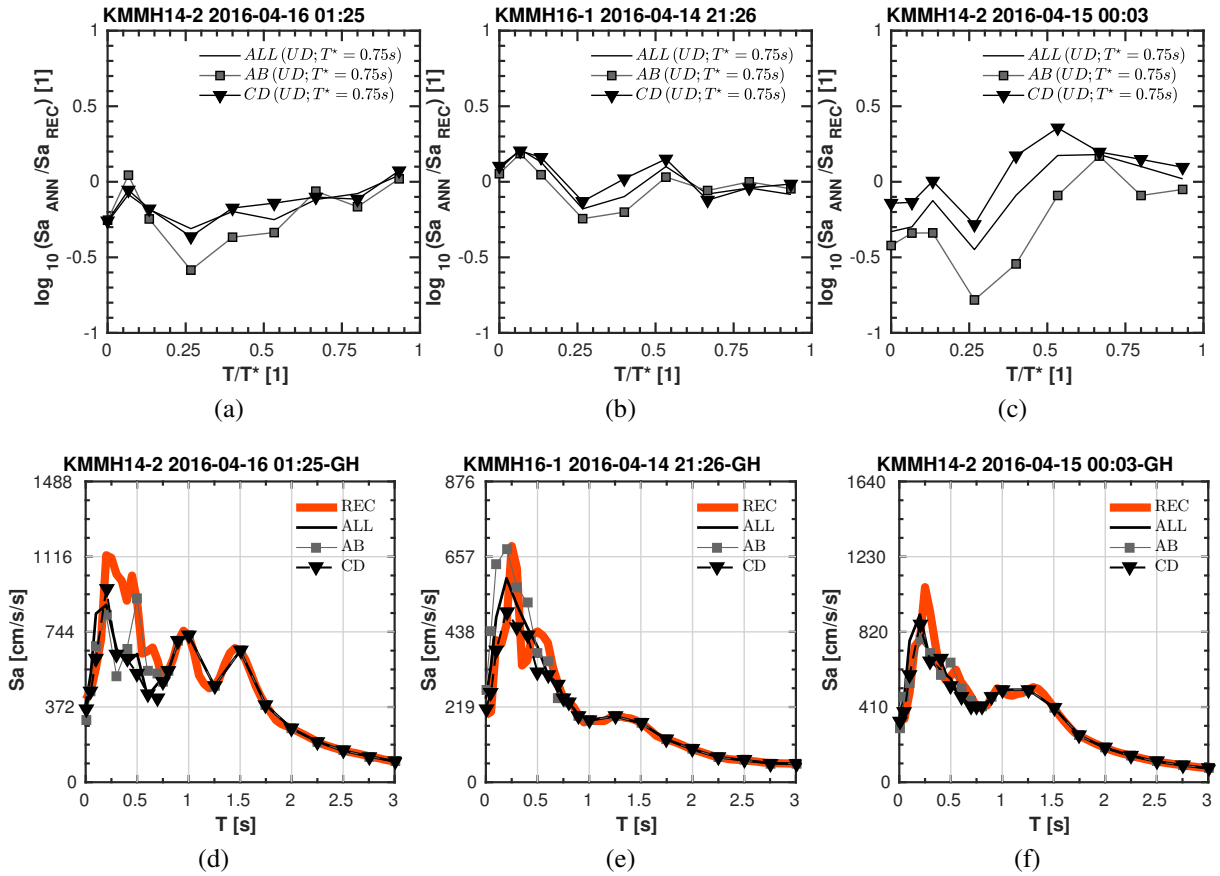

Figure 4.7: ANN performance for different EC8 site class, expressed in terms of estimated/target Sa (a-c). (d-f) estimated Sa spectra compared to the recorded ones (thick orange line). The recordings at two stations (KMMH14 and KMMH16) for the KMM2016 earthquake are shown. Thin solid black and grey lines with square markers refers to an ALL and AB respectively; solid black line with triangle markers refers to CD.

the intermediate-to-high frequency range with sufficient accuracy, unless an ever-increasing computational burden is accepted (see, for instance, Paolucci et al., 2015; Chaljub et al., 2015). Herein, numerical analyses were performed by using SPEED - Spectral Elements in Elastodynamics with Discontinuous Galerkin (http://speed.mox.polimi.it), an innovative high-performance computer code to solve seismic wave-propagation problems in heterogeneous media at local and regional scales. This tool is based on the Discontinuous Galerkin Spectral Element Method (DGSEM), a non-conforming version of the classical SEM formulation firstly proposed by Patera (1984). Earlier applications in computational seismology can be found in Seriani et al. (1995); Faccioli et al. (1997); Komatitsch and Vilotte (1998); Komatitsch et al. (1999). Fast and accurate solutions can be achieved by using the SEM (as shown by Mayday et al., 1989), also due to its relatively easy parallel implementation on large supercomputers (Göddeke et al., 2014). SPEED has been efficiently developed on parallel architectures, exploiting the Multi Passing Interface (MPI) algorithms. In other words, the SEM accuracy can be improved by either decreasing the mesh-size h or, alternatively, by increasing the polynomial order p of the approximated displacement field. The possibility to address discontinuous approximations (Käser and Dumbser, 2006) conducted to an efficient strategy to build up complex and large meshes on the DG version of the method (as explained in Antonietti et al. (2012)). The global mesh is thus the result of the assemblage of a set of sub-meshes, each one with its own ele-

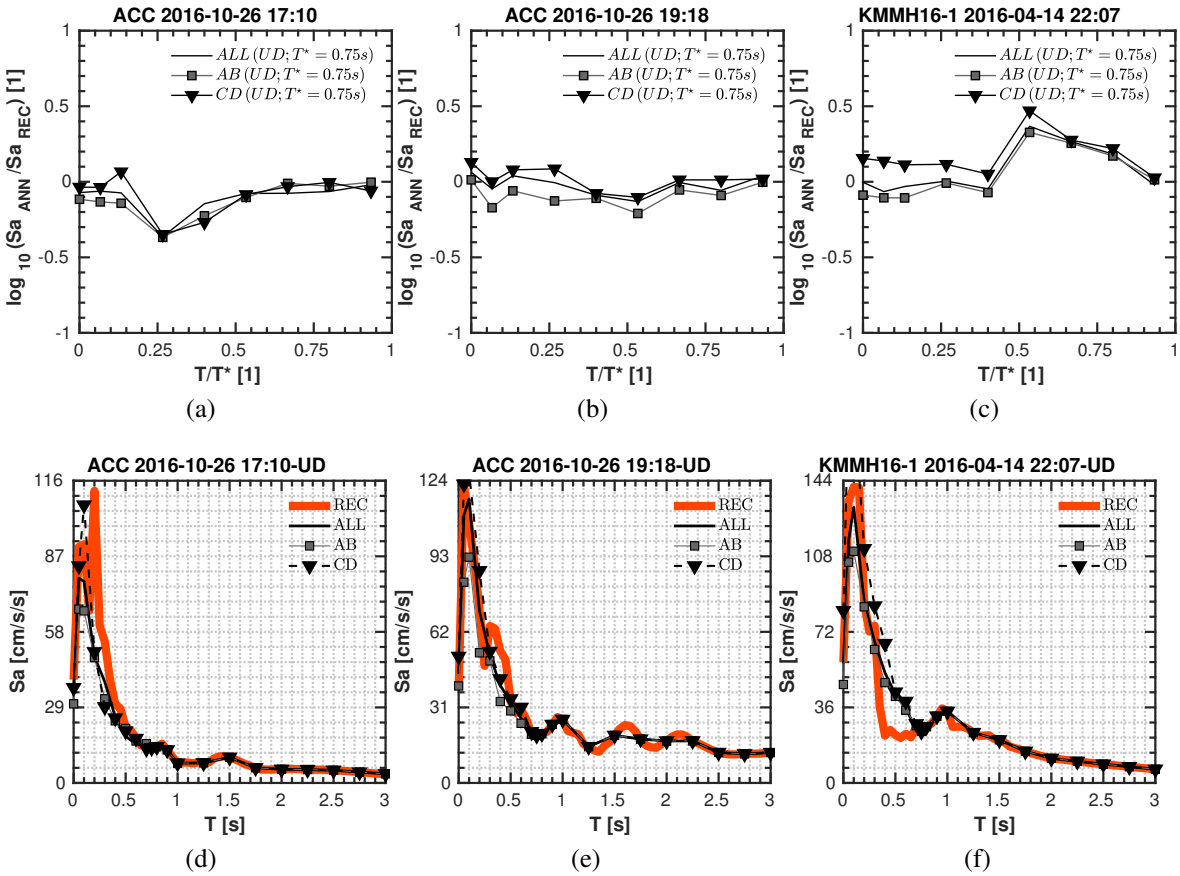

Figure 4.8: ANN performance for different training corner periods $T^{\star}$, expressed in terms of estimated/target Sa (a-c). (d-f) estimated Sa spectra compared to the recorded ones (thick orange line). The recordings at ACC station for the CIT2016 earthquake and at KMMH16 station for KMM2016 earthquake are shown. Thin solid black and grey lines refers to an ANN trained at $T^{\star}$=0.5s and at $T^{\star}$=0.75s respectively; thin dashed black line with triangle markers refers to an ANN trained at $T^{\star}$=1.0s.

ment size and polynomial degree, according to the required detail. This represents a flexible meshing technique, capable to tackle complicated 3D geological discontinuities and topographies as well as to better describe the local wave-field, due to selective finer approximations.
The source mechanism is numerically reproduced in SPEED by exploiting a kinematic description of the fault rupture. The set of required parameters is calibrated upon inverted slip models, based on observed co-seismic deformations. Some enhancements of the slip distribution are eventually possible, by making it compatible with a k^2 model (using the approach developed by Herrero and Bernard, 1994, ,for instance). Nevertheless, the mesh size and the poor description of the fault mechanism reduced so far the range of confidence of LF-synthetics up to 1.5-2 Hz (Smerzini and Villani, 2012; Paolucci et al., 2015, ,among others). Numerical dispersion is usually observed above the design frequency. Due to the mentioned features, SPEED represents a flexible numerical tool for several applications in engineering seismology. For instance, Paolucci et al. (2015) studied the anatomy of complex strong ground motion events and the seismic risk scenarios in large urban areas for reinsurance evaluations (Paolucci et al., 2014). SPEED was exploited as well to quantify the city-site interaction effects related to the dynamic response of large infrastructures (Mazzieri et al., 2013). Following the parametric study on the ANN performance presented in Section 4.2, the trained neural networks are now tested on the LF synthetics provided by the PBS analysis. The broad-band synthet-

ics are finally obtained by scaling the original PBS Sa to the ANN prediction. From Figure 4.2b), it is clear that the forward deterministic model (blue line in Figure 4.2b) fails in predicting short-periods Sa, as expected. Preliminary tests conducted on such synthetics showed major difficulties and poor effectiveness when trying to match their SP spectrum to ANN prediction. We repeatedly observed that the numerical dispersion polluting PBS time-histories at high-frequencies impoverishes the quality of the final broad-band synthetics. Therefore, instead of applying the spectral-scaling technique to PBS synthetics, a classical hybridization mid-step was introduced. The latter combines the LF wave-forms with independently generated HF synthetics. For instance, hybrid accelerations a^{HYB} at a given site are generated by first computing an empirical/stochastic realization a_d^{HF} for each ground motion component d. The a_d^{LF} and a_d^{HF} are aligned in time, by matching their respective $t_{5\%}$, the time-step corresponding to a normalized Arias intensity I_a = 5%. Finally, LF and HF waveforms are convolved together into $a_d^{HYB}(t)$ by applying a Butterworth's *match filter* in the frequency domain. This double filter is defined as follows (see Figure 4.9):

$$\mathcal{A}\left[a_d^{HYB}\right](f) = w^{LF}(f)\,\mathcal{A}\left[a_d^{LF}\right](f) + w^{HF}(f)\,\mathcal{A}\left[a_d^{HF}\right](f) \tag{4.1}$$

where the $\mathcal{A}[\square](f)$ operator stands for the Fourier's amplitude spectrum applied to the $\square$ acceleration wave-form and w^{LF}, w^{HF} represent the LF and HF weight of the double filter respectively. $w^{LF}(f)$ and $w^{HF}(f)$ are low-pass and high-pass Butterworth's filters of order 3 respectively, with the same frequency corner f_C (Figure 4.9). In this study, a_d^{HF} are routinely generated by following

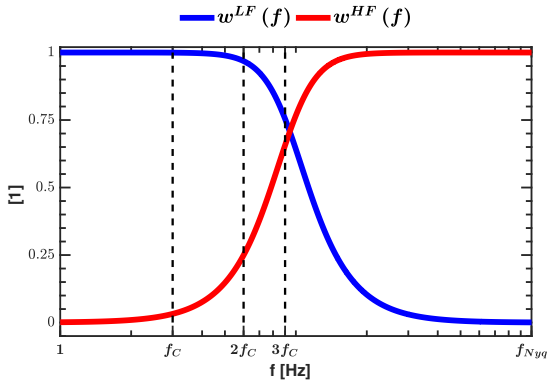

Figure 4.9: Fourier's spectrum of the Butterworth's low-pass (LF) and high-pass (HF) match filter, used for hybrid scheme.

the empirical recipe proposed by Sabetta and Pugliese (1996). The latter consists in generating synthetic wave-forms extending the spectral moments theory to the non-stationary case. Input parameters are easily correlated with earthquake magnitude, source distance, and soil conditions. The resulting ground motion has realistic earthquake intensity indices (PGA, PGV, Arias intensity), Fourier's spectra and response spectra (Sabetta and Pugliese, 1996). Even though the mentioned approaches usually encapsulate the physics of the earthquake process and wave propagation into simple equation forms (Boore, 2003), they are particularly useful for our purpose, since they are simply exploited to increase the effectiveness of spectral matching technique, without affecting the LF reliable part of the strong motion.

4.3.2 Scaling synthetics to the broadband response spectrum

At this point, the hybrid response spectrum (the black line in Figure 4.2b) is iteratively matched to ANN one at short-periods. In detail, the spectral-match is performed in five steps, iteratively repeated

to achieve a satisfactory convergence. At each k^{th}-iteration, the procedure (1) computes the pseudo-spectral acceleration and Fourier's spectrum of the input record $a_d^k(t)$ (with $a_d^0(t) = a_d^{HYB}(t)$), namely $Sa\left[a_d^k\right](T)$,$\mathcal{F}\left[a_d^k\right](f)$; (2) the spectral ratio $Ra_D\left[a_d^k\right](T) = Sa\left[a_d^k\right]/Sa_d^{ANN}$ is computed, defined as the ratio (at a discrete set of oscillation periods T) between the hybrid spectrum and the target one (estimated by ANN simulation); (3) a $Ra_D\left[a_d^k\right](T)$ linear interpolation over the desired frequency range (typically till 40 Hz) is carried out along with a change of variable from period to frequency, obtaining $Ra_I\left[a_d^k\right](f)$; (4) the input Fourier's spectrum $\mathcal{F}\left[a_d^k\right](f)$ is scaled by a factor $1/Ra_I\left[a_d^k\right](f)$ and finally (5) its inverse Fourier's transform is taken to get a new wave-form $a_d^{k+1}(t)$. The described spectral-matching technique applies in the frequency domain, thus causing the well-known displacement distortions. When time domain spectral-matching procedures are employed, displacement drifts are unlikely to appear, due additivity of the scaled wavelet functions. Extra displacement arises when the matching is performed in the frequency domain with a multiplicative scale function applied to the Fourier spectrum. Figure 4.10 portrays schematically the iterative procedure to spectral-match the hybrid spectrum to the ANN prediction at short period. Improved velocity and

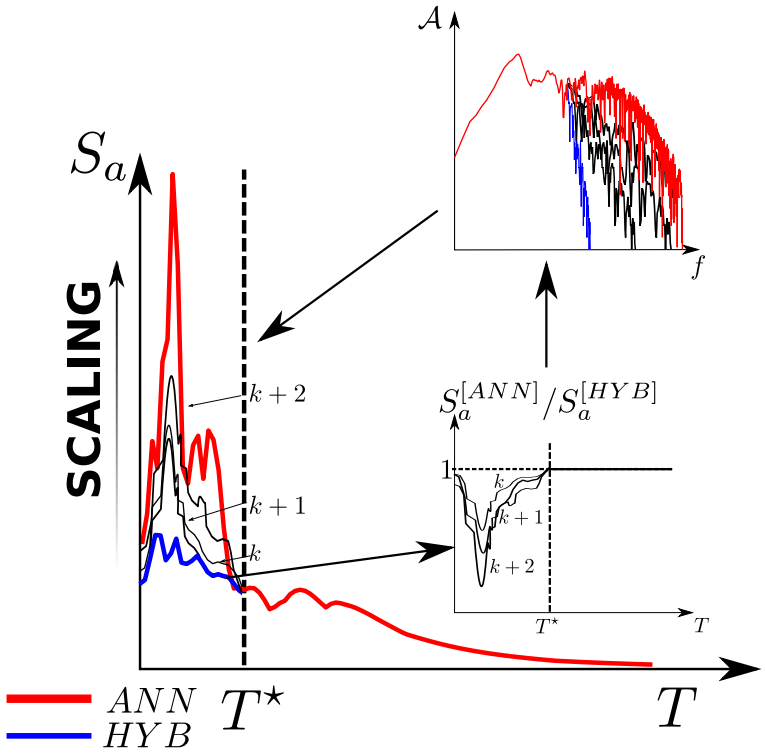

Figure 4.10: Sketch of the Sa spectral matching iterative procedure.

displacement time-histories where obtained by applying the corrective factor proposed by Shahbazian and Pezeshk (2010). A further improvement is performed by generating a set of trial hybrid waveforms and select the best one in terms of goodness of fit of the target ANN spectrum.

4.3.3 Two applicative exercises

To test the described recipe for generation of broad band time-histories, two test cases were investigated, namely (1) the 2009 April 6 M_W6.3 L'Aquila (AQE2009) and (2) the 2012 May 29 Po Plain earthquakes (PPE2012). In particular, we refer to the work of Smerzini and Villani Smerzini and Villani (2012) for the former and to Paolucci et al. Paolucci et al. (2015) for the latter. In both cases, the numerical simulations were performed by means of the Spectral Element code SPEED. In both

cases the authors addressed the seismic risk analysis in large urban areas and they focused on the effects of near-fault conditions and of complex geological settings. The results were compared with the recordings provided by relatively dense seismographic networks around the epicentre areas.

4.3.4 The 2009 M_W6.3 L'Aquila Earthquake

The 2009 L'Aquila earthquake (AQE2009) one of the largest event recorded by accelerometric stations in Italy. Furthermore, it is one of the best instrumentally documented strong ground motion in the Italian catalogue. Smerzini and Villani (2012) reconstructed the seismic scenario of the AQE2009, by building up a numerical model of the by epicentral area. The parametric study they performed revealed that (1) the assumed simplified local geology had minor influence on estimated synthetics and (2) that main discrepancies with the available recordings were most likely due to the poor kinematic description of the causative fault (i.e. the *Paganica fault*), unveiling a more complex rupture process. The authors improved their source model through the definition of stochastically (but realistically) varying kinematic source parameters that may play a relevant role in propagating high-frequency. With this stratagem, the synthetics fitted reasonably well the strong-motion recordings up to 2.5 Hz (see, for instance, the results at AQK in Figure 4.11). To improve the numerical results in

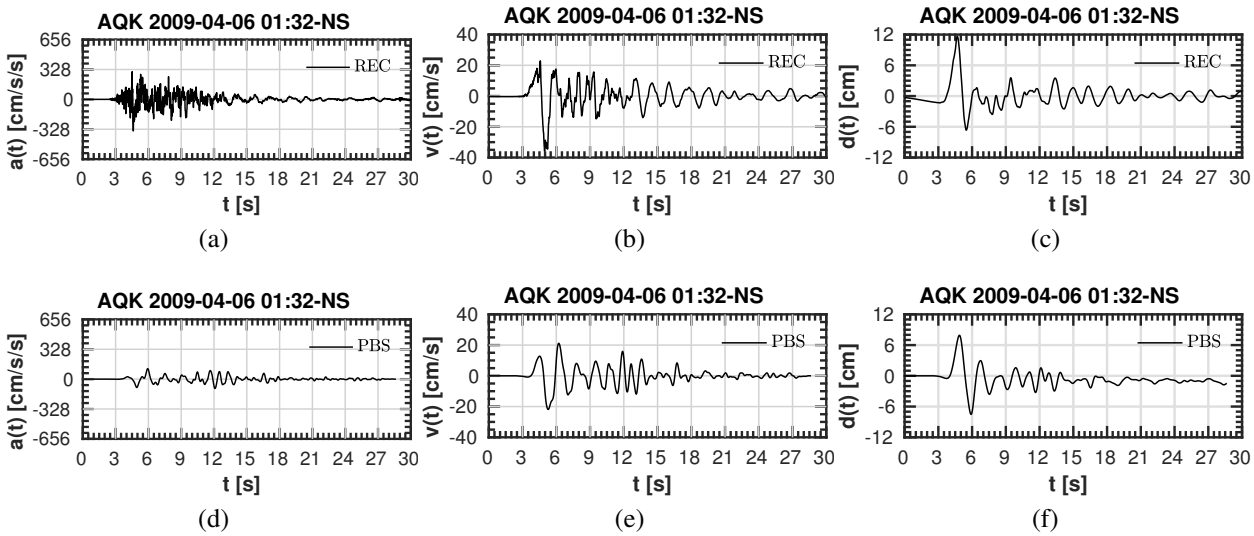

Figure 4.11: AQK time-histories in NS direction: (a-c) Recorded (REC) time-histories; (d-f) Physics-Based Simulated (PBS) time-histories.

a post-process phase, the LF synthetics were enriched at high-frequency, by exploiting the proposed methodology. The hybrid scheme considers a corner frequency f_C = 3 Hz. Moreover, the Artificial Neural Network was trained on SIMBAD database and it refers to the geometric mean of the two horizontal ground motion components, with corner period $T^{\star}$= 0.75s. Hybrid (HYB-SP96) and Spectral Matched (SPM) time-histories are portrayed in Figure 4.12. Both the hybrid and the spectral-matched wave-form are enriched at high-frequency, although HYB-SP96 accelerograms look quite spiky. As a matter of fact, the employed ANN provides better estimation of the shape of the Sa spectrum at SP, both on the horizontal (Figure 4.13b) and on the vertical (Figure 4.13c) components, the SPM spectrum is closer to the recorded one, with the respect to the HYB-SP96 one, which looks mono-peaked and it reaches unrealistic Sa values. However, the limits of the procedure are highlighted in Figure 4.13a, where a worse fit of the recorded spectral shape is portrayed. The physics-based simulations failed in reproducing the spectral peak at intermediate periods (i.e. 1-3 s) probably due to

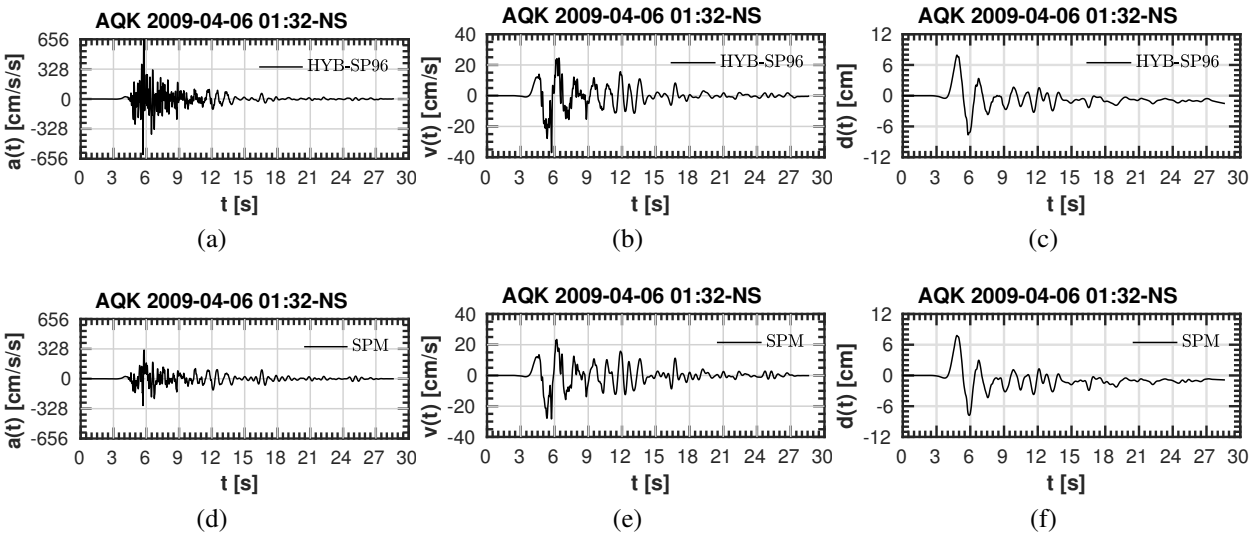

Figure 4.12: AQK time-histories in NS direction: (a-c) Hybrid (HYB-SP96) time-histories (obtained employing Sabetta and Pugliese (1996) technique); (d-f) Spectral-Matched (SPM) time-histories.

surface waves, thus the ANN is less effective. However, the Peak Ground Acceleration (PGA) (i.e. $Sa\,(T = 0s)$) of the SPM wave-forms is closer to the recorded one. Moreover, Figures 4.13d- 4.13f clarify the broad-band nature of the synthetic wave-forms. The synthetic high-frequency falloff (red line) is realistic and in good agreement with the observations, whereas the hybrid one (green line) shows an high-frequency peak which is unlikely to occur.

The 2012 M_W6.0 Po Plain Earthquake

In 2012, Northern Italy was interested by a sequence of strong ground motions, caused by a thrust-fault focal mechanism. Although it is an area of moderate seismicity, huge damages occurred in the Emilia-Romagna region, in a densely populated urban area residing on a very deep sedimentary structure such as the Po Plain. The seismic sequence had two major events: a first M_W6.1 event on May 20th and a second relevant shock (M_W6.0) on May 29th. A large database of high-quality recordings covering the epicentral area was released: the second event (hereby referred to as PPE2012) was the best documented in terms of strong-motion records and it presented some unique features, the most important being (1) the complex geological setting of a deep and large sedimentary basin such as the Po Plain, with sharp variability of sediment thickness, from a few tens of metres to about 8 km and (2) the availability of a nearly unique near-fault strong ground motion data set on deep and soft sediments in the context of a region of moderate seismicity. Those characteristics resulted into peculiar near-source strong-motion records and spatial variability of damage distribution. Paolucci et al. (2015) designed a 3D numerical model of the interested portion of the Po Plain to depict the PPE2012 anatomy. An overall good agreement between their numerical simulations and strong-motion records was achieved, especially along the NS direction (see for instance the comparison at MIR08 in Figure 4.14). The inverted kinematic fault model was adjusted accordingly to the records, as well as rapidly varying thickness of Quaternary sediments in the epicentral area, based on the arrival time of the observed waveforms. Preliminary investigations (i.e. the analysis of a wide set of near-source records, the calibration of an improved kinematic seismic source model) resulted to be crucial in this sense. The satisfactory reproduction of the LF content achieved by PBS is observable in velocity and displacement traces (e.g. Figures 4.14e-4.14f). Synthetic accelerograms are however poorly consistent at high frequencies. Therefore, to improve the numerical results, we firstly hybridize the LF

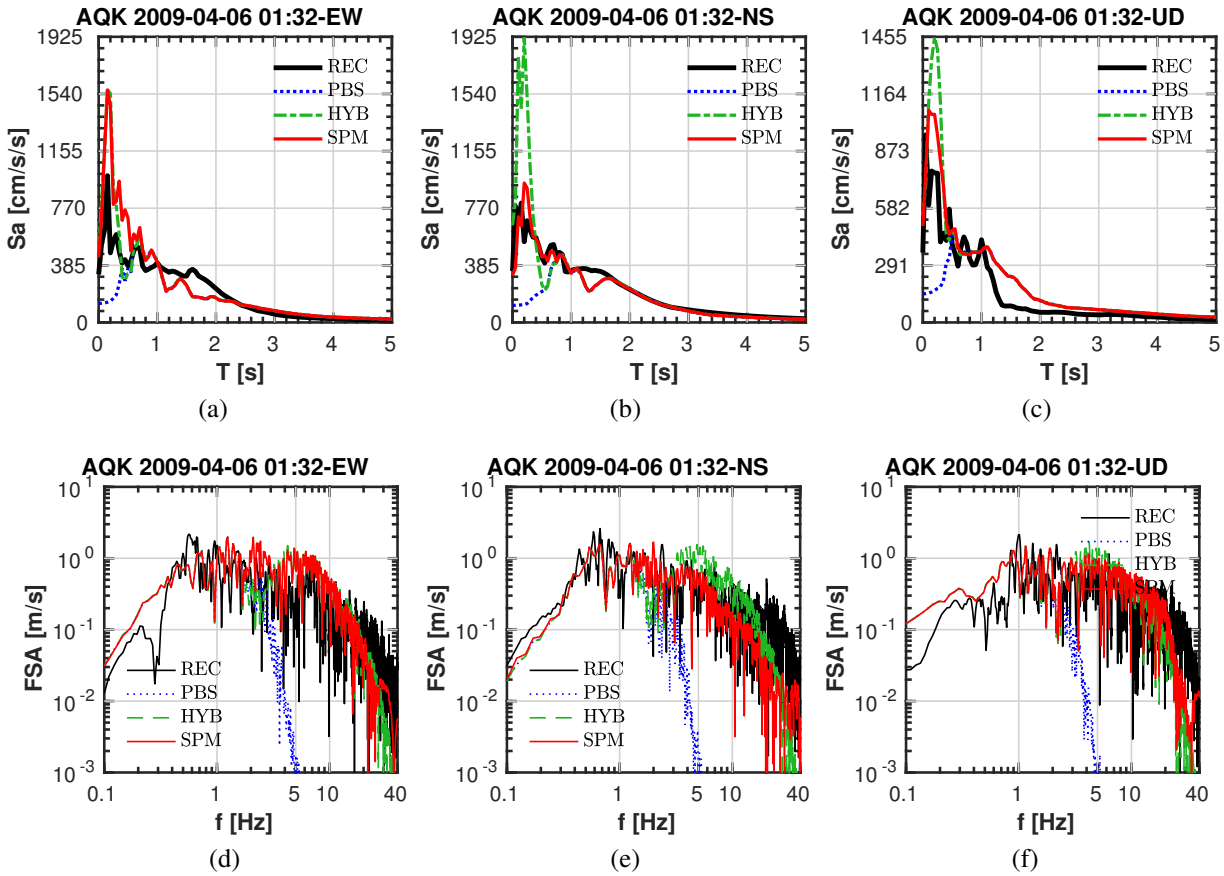

Figure 4.13: (a-c) AQK response spectra. (d-f) AQk Fourier's spectra. Black solid lines represent the recorded (REC) wave-forms, the blue dotted lines the Physics-Based Simulations (PBS), the green dashed lines the hybrid synthetics (HYB-SP96) and the red solid lines the Spectral Matched synthetics (SPM).

synthetics with HF wave-forms in a post-process phase (see the wave-forms in Figures 4.15a- 4.15c). Although no significant difference is appreciable between HYB-SP96 and SPM synthetics, their respective Sa spectra have rather assorted shapes: once again the HYB-SP96 response spectra are too much spiky at SP (green dashed lines in Figure). The latter features is unrealistic and it highlights the great improvement made by spectral matching the hybrids upon the ANN predictions. In this range of vibration periods, LF synthetics show high numerical dispersion, being therefore unreliable. However, our methodology goes beyond this step, by applying a trained Artificial Neural Network to the hybrid wave-forms. The ANN refers to the geometric mean of the two ground motion horizontal components and it is trained upon the SIMBAD strong motion database (presented by Smerzini et al. (2014)). A corner period $T^{\star}$=0.75 s was chosen and reasonable SP-Sa values were found by employing all the SIMBAD database in the training phase. An overall improvement of the hybrid broad-band synthetics is obtained by applying ANN2BB to the original PBS traces, both in terms of Sa spectra (Figures 4.16a-4.16c) and Fourier's spectra (Figures 4.16d-4.16f), both on the horizontal and vertical components. Unexpectedly, the ANN is capable of distinguish between the peak-shaped spectra typical of vertical components, with the respect to the flatter one for horizontal components.

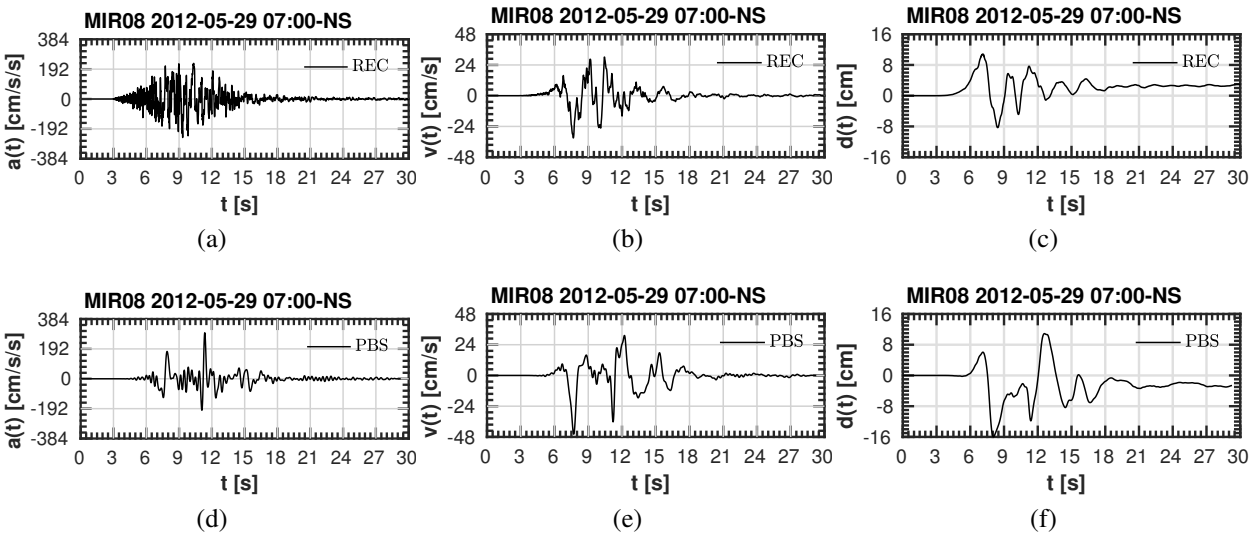

Figure 4.14: MIR08 time-histories in NS direction: (a-c) Recorded (REC) time-histories; (d-f) Physics-Based Simulated (PBS) time-histories.

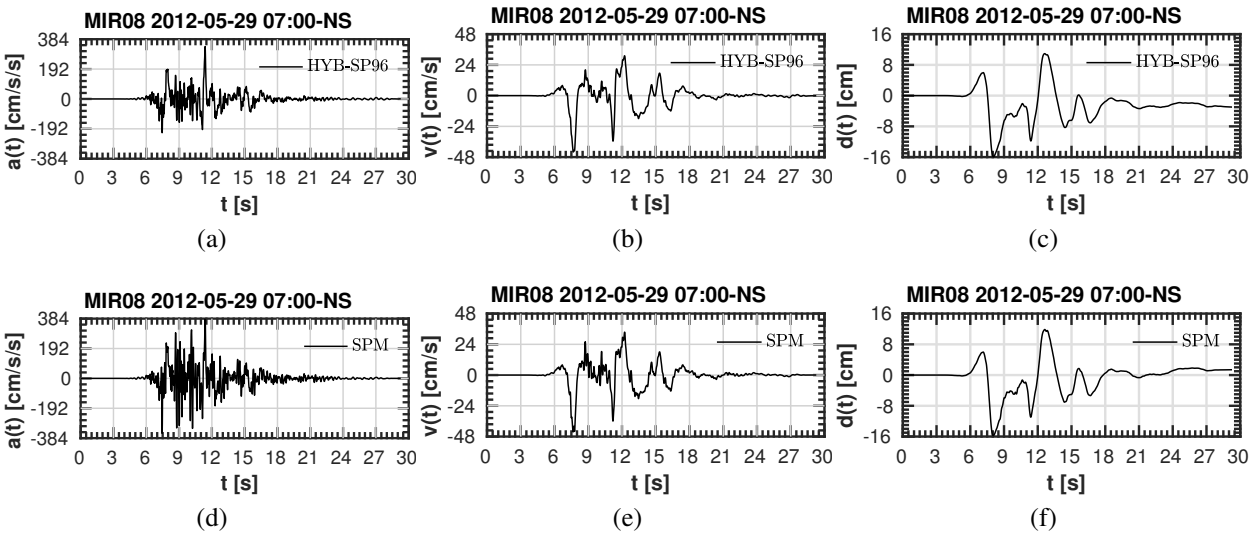

Figure 4.15: MIR08 time-histories in NS direction: (a-c) Hybrid (HYB-SP96) time-histories (obtained employing Sabetta and Pugliese, 1996, technique); (d-f) Spectral-Matched (SPM) time-histories.

4.4 Partial conclusions and perspectives

ANN2BB has been proven as highly effective alternative strategy to generate broad-band synthetic seismograms, out of low-frequency physics-based analyses. This meta-modelling technique looks very promising for a point wise estimation of realistic wave-motion. However, one of the near future tests foreseen is the assessment of ANN2BB performance in depicting the spatial variability of the earthquake ground motion at short period, starting from a LP ground shaking scenario.

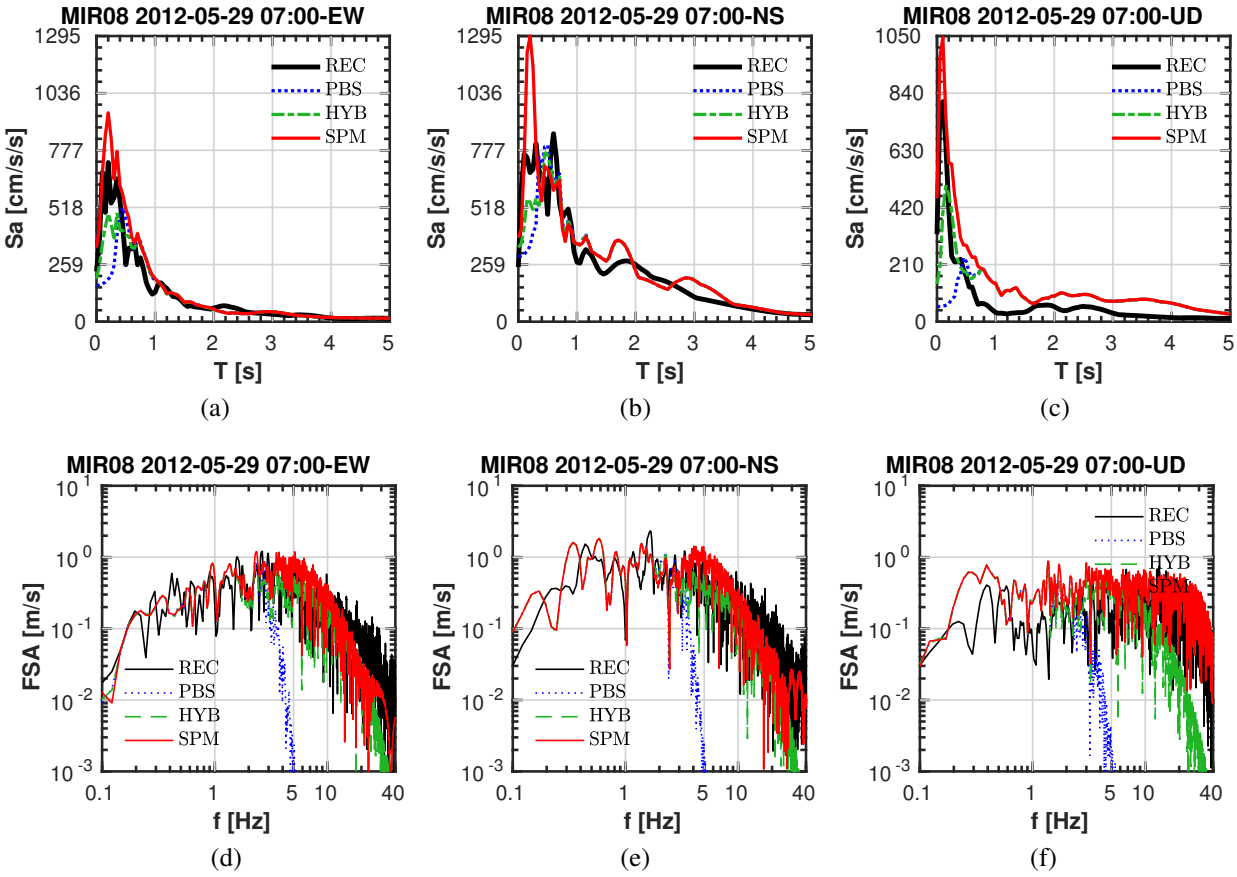

Figure 4.16: (a-c) MIR08 response spectra. (d-f) MIR08 Fourier's spectra. Black solid lines represent the recorded (REC) wave-forms, the blue dotted lines the Physics-Based Simulations (PBS), the green dashed lines the hybrid synthetics (HYB-SP96) and the red solid lines the Spectral Matched synthetics (SPM).

5

Physics-based simulation of the 2007 Niigata-Chuetsu-Oki earthquake

"The only thing that makes life possible is permanent, intolerable uncertainty: not knowing what comes next."

– Ursula K. Le Guin,The Left Hand of Darkness

5.1 The 2007 *Niigata-Ken Chūetsu-Oki* earthquake

The M_W6.6-M_{JMA}6.8 *Niigata-Ken Chūetsu-Oki* (Japan) earthquake (NCOEQ-2007) of the July, 16th 2007 affected a wide area in the surrounding of the Kashiwazaki-Kariwa Nuclear Power Plant . It occurred as a result of a buried reverse-slip motion nucleated at an estimated hypocenter depth of 8 km, and no significant surface rupture was detected (Aochi et al., 2013a). The distance of the Kashiwazaki-Kariwa Nuclear Power Plant to the surface projection of the fault (i.e. Joyner-Boore distance) is R_{JB}=0 km, whereas the rupture distance is R_{rup} = 16 km (Yee et al., 2011, see Figure 5.1). Due to the relative small source-to-site distance and shallow hypocenter depth, this seismic scenario appears very appealing to study and to quantify the effects of the near-field ground motion. Moreover, as proved in Chapter 2, the ground shaking event is fairly well documented (a consistent database of seismic recordings is available, e.g. the Japanese strong ground motion seismograph networks K-NET and KiK-Net, as well as the seismometer network installed at the Kashiwazaki-Kariwa Nuclear Power Plant). In this context, the test-case represents a suitable benchmark for the work-packages of the SINAPS@ project.

The objective of this chapter is to perform realistic physics-based numerical simulation of the NCOEQ-2007 scenario. The tectonic context of the epicentral area is primarily described in Section 5.1.1, followed by an *excursus* upon the different slip distributions proposed in the literature for the NCOEQ-2007 fault plane is presented (see Aoi et al., 2008; Kato et al., 2008, among other), outlined in Section 5.1.2. Those models have been obtained by exploiting several wave form inversion techniques (Virieux and Operto, 2009), by assuming different simplified geological profiles of the Niigata area, which in turn limits their reliability to a narrow low-frequency band (0.1-1 Hz). However, the uncertainty on the rather complicate fault mechanism has still to be solved. A deeper insight on the exceptional spatial variability of the earthquake ground motion recorded at the KKNPP is provided in Section 5.1.3, identifying its possible origin as the along-path focalizing effect exerted by the complex geological conformation lying beneath the site, and described in Section 5.1.4. In this section, the results of several previous investigations performed to assess a suitable geological profile for the Niigata region are discussed.

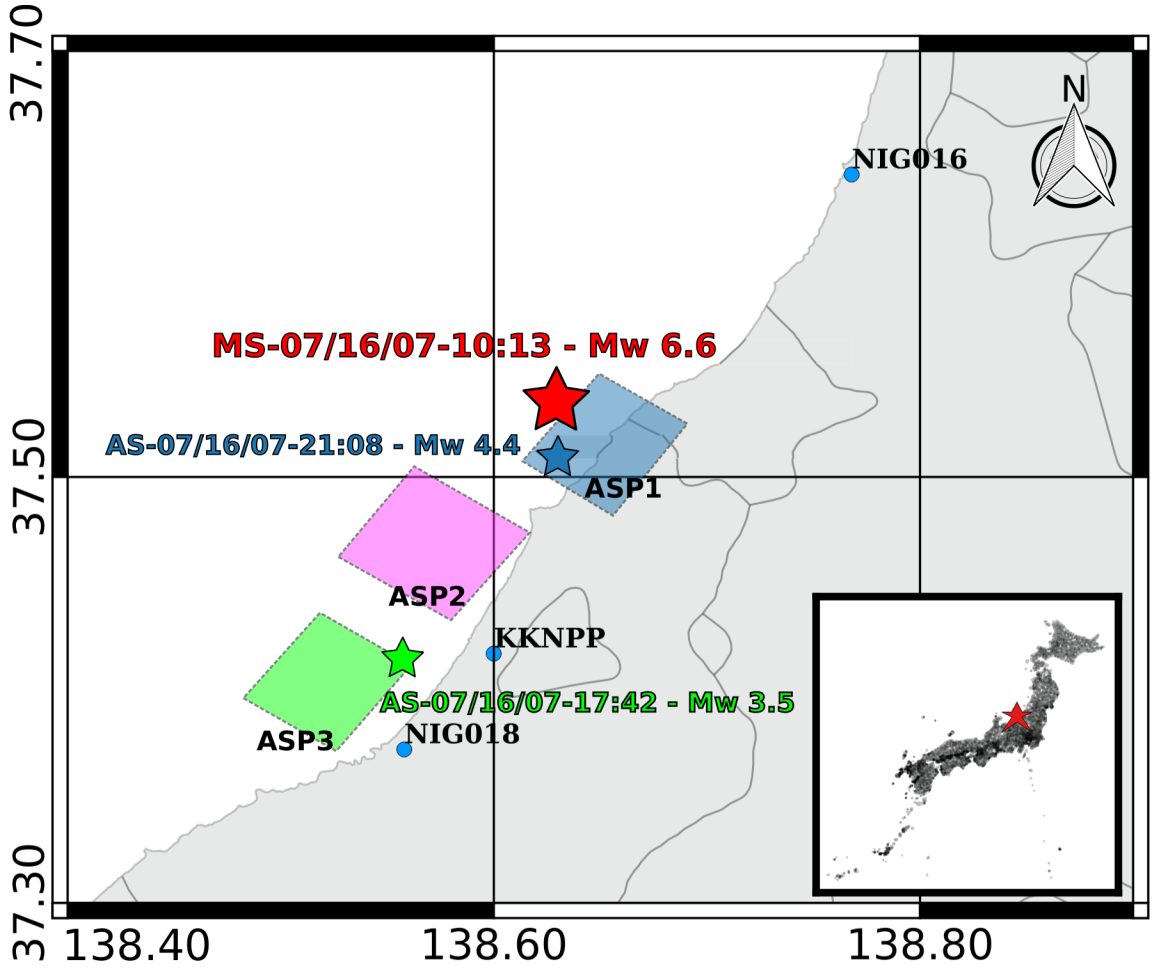

Figure 5.1: Map of the region surrounding the Kashiwazaki-Kariwa Nuclear Power Plant . Some stations belonging to the Japanese strong ground motion seismograph networks K-NET and KiK-Net are shown (blue circles), along with the TEPCO-KKNPP site and the NCOEQ-2007 epicenter (red star).

In the following, Section 5.2 describes the steps to build up and calibrate a high-fidelity seismic scenario, capable to provide a synthetic wave-field at the regional scale, according to an *all-embracing* approach. An accurate source-to-site model of the wave-motion propagation is pursued by (1) assessing a stratified geological model for the Niigata region, (2) checking the topography effect, (3) testing the effect of the source parameters in a kinematic approach (e.g. the rise time and the shape of the Source Time Function). A series of 3D source-to-site numerical simulations of the M_W4.4 NCOEQ-2007 aftershock is therefore carried out with this regard (by means of the Spectral Element Method code, SEM3D). The seismic scenario calibration is aided by the use of the semi-analytical solutions provided by the Wave-Number Integration Method (WNI) and by comparing the synthetics with the recordings at several locations (i.e. the KNET-Kik-Net stations nearby and the KKNPP site). The forward physics-based analysis renders a low-frequency (0.00-3.75 Hz) synthetic wave-field to be exploited in further studies as a reliable regional incident wave-field for the *engineering bedrock*. The latter study has been presented during the 6th International Conference on Computational Methods in Structural Dynamics and Earthquake Engineering, COMPDYN 2017 (Gatti et al., 2017). Based on calibrated regional model, the near-field earthquake scenario of the KKNPP site is constructed by including the local 3D geological structure. Section 5.3 describes the implications due to the inclu-

sion of a shallow syncline-anticline structure: the spatial variability of the broad-band (0.0-7.0 Hz) wave-field within KKNPP is addressed and satisfactorily reproduced by the computational model. Specifically, I focused on the spatially variable amplification of the site-response, clearly due to the folding structure and not pictured when a classical sub-horizontally layered configuration is considered instead. Two aftershocks were simulated, so to discount the outcome from the complex effect of the extended fault mechanism, focusing on the along-path and buried topography effect instead. The results presented at this point were submitted to the *Geophysical Journal International* for a journal publication. An application of the ANN2BB methodology (outlined in Chapter 4) is presented in Section 5.4, based on the physics-based simulations performed on the $M_{\mathrm{W}}4.4$ aftershock, to improve the frequency spectrum of the synthetic seismograms.
Finally, a preliminary investigation on the extended fault rupture is presented in Section 5.5. The NCOEQ-2007 main shock is replicated by means of point-wise double-couples located at each asperity identified by wave-form inversion. Those results have however to be largely improved by the future introduction of a full kinematic description of the fault offset and rupture mechanism.

5.1.1 The tectonic context of the Niigata area

Recent GPS measures performed by the Geographical Survey Institute of Japan revealed that the central coastal area of the Japan Sea - technically named NKTZ (Niigata-Kobe Tectonic Zone) - is subjected to large strain rate, due to subduction of the Pacific and Philippine Sea plates. The NKTZ represents a 500×100 km deformation belt (Figure 5.2). Specifically, the Niigata region is placed within

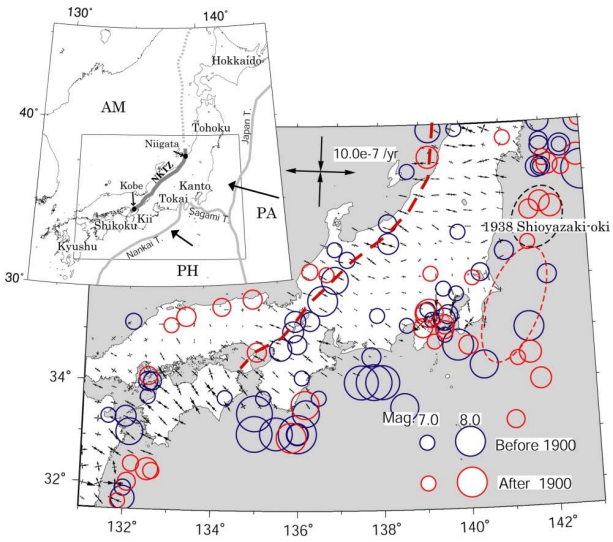

Figure 5.2: Distribution of principal axes of horizontal strain rates deduced from continuous GPS observation (February 1996-June 1999). Historical large ($M_{\mathrm{W}} > 7$) shallow (depth < 60 km) earthquakes in and around southwest and central Japan are also plotted by blue (before 1900) and red (after 1900) circles. The red broken line and the thick gray line in the inset show the high strain rate zone (NKTZ). In the inset, plate tectonic setting in the Japan islands and the district names are also shown, where AM, PA and PH indicates the Amurian, Pacific and the Philippine Sea plate, respectively. The gray lines indicate the major plate boundaries. The rectangle in the inset shows the southwestern and central Japan. Reprinted from Hyodo and Hirahara (2003)

a region of compressional deformation that is associated with the boundary between the Amurian plate and the Okhotsk plate, two relatively small plates that lie between the larger Eurasia and Pacific plates (Kayen et al., 2009; Sagiya et al., 2000). Historically, large earthquakes occurred in and around

the NKTZ. Figure 5.2 and Figure 5.3a show the documented earthquakes in the region, such as the 1964 Niigata (M_W7.5), 1847 Zenkoji (M_W7.4), 1858 Hietsu (M_W7.1), 1961 Kita-Mino (M_W7.0), 1891 Nobi (M_W8.0), and 1995 Kobe (M_W7.2) earthquakes. In the northern extension of NKTZ, although deformation cannot be inferred by land-based GPS, there have been large earthquakes such as 1983 Japan Sea (M_W7.7), 1993 Hokkaido Nansei-Oki (M_W7.8), and 1940 Shakotan (M_W7.5) earthquakes, implying the existence of an active deformation zone. Sagiya et al. (2000) measured large strain rates (0.1 ppm/year) and assumed that two strain rate distributions are going on at two different time scales (2 years and 100 years respectively) but with common features, such as a similar dominant compressive strain along the NW-SE axe of the NKTZ. The northern part of NKTZ is dominated by

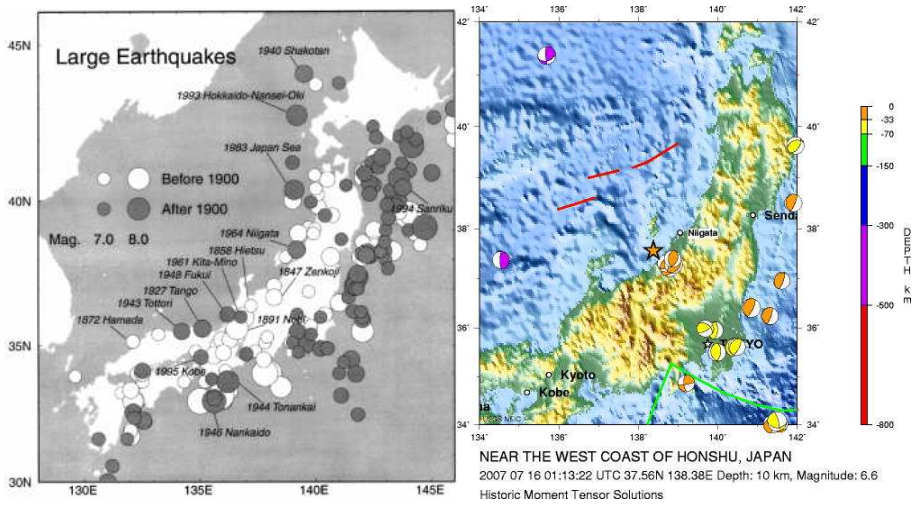

(a) (b)

Figure 5.3: (a) epicentres of past large earthquakes in NTKZ (reprinted from Sagiya et al., 2000); (b) seismicity in NKTZ Region in the last two decades (reprinted from USGS report, 2007). Yellow, green, blue and purple *beach balls* indicate hypocenters related to subducting slab. Orange symbols represent shallow crustal hypocenters of large earthquakes in Japan and NTKZ area.

a large east-west compression, as the 1964 Niigata earthquake witnessed (thrust mechanism with an east-west compression strain regime, dominated by the absolute vertical stress Sagiya et al., 2000). However, the mechanism underlying those strong ground motion earthquakes is not easy to understand. In fact, large earthquakes in the south-western half of NKTZ mainly have strike-slip source mechanisms, being shear strain rates relatively larger than in surrounding regions. Although the heterogeneous structure of the surrounding crustal rocks might explain the sharp contrast in deformation rate, the geological studies indicated that a thick sedimentary basin was formed by a rift structure with a normal fault plane system developed during the extension stage of Japan Sea (Sato, 1994; Nakahigashi et al., 2012). The normal fault system during the rifting stage has been reactivated as a reverse fault system by a change in the tectonic stress from extension to compression. This stress change is estimated to have been caused by a change in the dip angle of the sub-ducting Pacific plate (Nakahigashi et al., 2012). Moreover, several quaternary active faults and folds are placed in this region, comprising a series of anticline structures and reversal faults.

5.1.2 NCOEQ-2007: Fault mechanisms from wave-form inversion

Coherently with the main compressional strain regime in the region, the NCOEQ-2007 occurred as the result of a buried reverse-slip (Kayen et al., 2009) faulting. The main shock (MS) occurred in the

upper crust (although the main fault trace has not been found) with a steeply dipping reverse fault mechanism under the North-West/South-East (NW/SE) compression (the so called Western Nagaoka Basin active fault system Yukutake et al. (2008)). In the MS immediate aftermath, a long aftershock sequence struck the region, lasting for about a month. The largest aftershock's magnitude was estimate as M_{JMA}5.8. The whole scenario was found in accordance with regional tectonic context in the NKTZ (Nakamura et al., 2009). The fault mechanism was estimated by the distribution of the polarity for the P-wave first motion by Hi-net (Obara et al., 2005) and by the moment tensor analysis of F-net data (Okada et al., 2004). The P-axis WNW-ESE direction was consistent with the tectonic maximum compressive stress direction in and around the Mid-Niigata area (Matsumoto et al., 2007; Aoi et al., 2008). Yukutake et al. (2008) relocated the hypocenter using the differential arrival times obtained by both manual picking and wave-form cross-correlation analysis (37.5397N, 138.6091E, and 7.417 km depth). Moreover, they found that the aftershocks extended for approximately 25 km in the direction of N38°E-S38°W (Figure 5.4). The trend of aftershock epicenter distributions in the

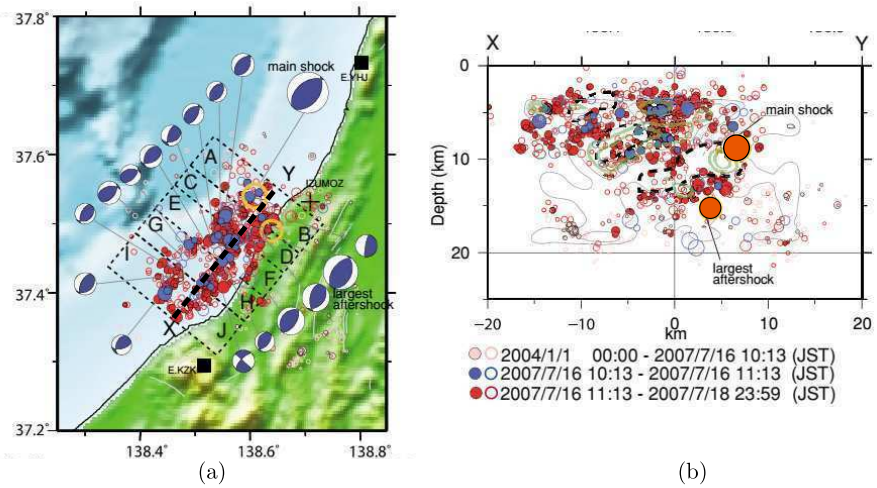

Figure 5.4: (a) Map of the NCOEQ-2007 sequence relocated by Yukutake et al. (2008). XY section is portrayed, corresponding to nodal plane along-strike direction. (b) XY section: orange circles represent the main shock and largest aftershock. Red/blue circles refer to earthquakes occurred in the period between 2004 and the MS.

map view in Figure 5.4 is rather consistent with Plane B, predominantly SE dipping (at $\sim 50°$). The aftershock depth distribution along the nodal plane cross section in Figure 5.4a is deeper (down to approximately 20 km) in the NE part (where the largest aftershock occurred), while it is shallower at the SW part (with an upper limit of approximately 3 km). The ordinary seismic activity before the main shock (i.e. since the 2004 Niigata earthquake, up to the NCOEQ-2007, illustrated by the light red colour in Figure 5.4) was deployed along in the 15-20 km large surroundings of the lower limit of the NCOEQ-2007 aftershock distributions.

The two conjugate fault planes A and B (red and blue plane in Figure 5.5a) were estimated as:

- **Plane A** (Figure 5.5b): ϕ_S=215°, δ=49°, λ=80° (NW dipping)
- **Plane B** (Figure 5.5c): ϕ_S=49°, δ=42°, λ=101° (SE dipping)

However, which of the two fault planes was the effective causative one is still a matter of debate. For this purpose, aftershock spatial distribution poorly steered the choice.

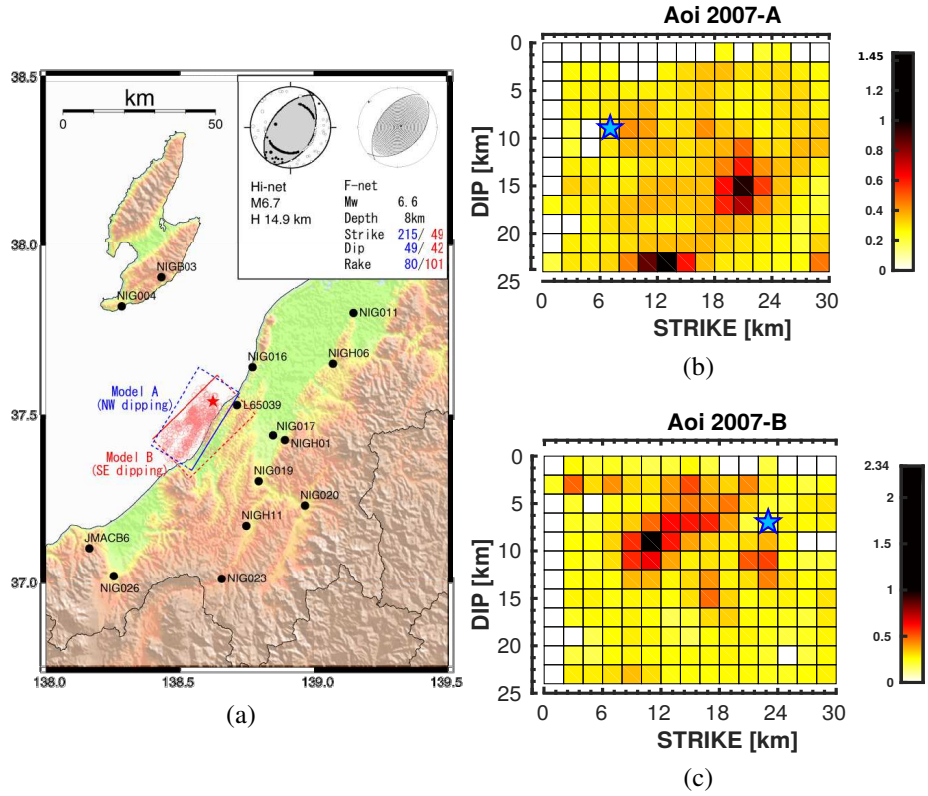

Figure 5.5: (a) Projection of the NCOEQ-2007 conjugate fault planes. (b-c) Fault models (A and B) proposed by Aoi et al. (2008). Open circles are aftershock distribution within 24 hours after the main shock located by manual picking of Hi-net data. (Reprinted from Aoi et al., 2008)

Aoi's models

For wave-form inversion, the Japanese National Research Institute for Earth Science and Disaster Resilience (NIED) assumed a rupture starting point at the same epicenter and 8 km depth (Aoi et al., 2007). They considered a fault plane model of 30 km length by 24 km width to cover the aftershock distribution corresponding to the first 24 hours after the main shock. Both Plane A and Plane B were investigated (Figures 5.5b-5.5c). In the multi-time window linear wave-form inversion procedure, the moment-release distribution was discretized in both space (180 sub-faults, each 2 km $\times$ 2 km) and time (6 smoothed ramp functions with 1.0 sec duration separated by 0.5 sec). Aoi et al. (2008) integrated NIED's analyses and they found that Plane A (NW-dipping fault plane) has a total seismic moment of 1.42E19 Nm (M_W6.7) with a large asperity in the south-west deeper part of the rupture starting point, which is close to the Kashiwazaki-Kariwa Nuclear Power Plant . Plane B (SE-dipping fault plane) has a total seismic moment of 1.62E19 Nm (M_W6.7), with a large asperity in the south-west shallower part of the rupture starting point, which is also close to the Kashiwazaki-Kariwa Nuclear Power Plant . In both models, they detected a small asperity near the rupture starting point and a large asperity approximately 10 km south-westward. The latter has a maximum slip of 2.3 and 2.5 m for Models A and B, respectively. The large asperities fall on to the area with relatively sparse aftershock distribution. The triggering velocities for the first time windows giving the best wave-form fits were 2.5 km/s for Plane A and 2.1 km/s for Plane B. As the difference of the residuals between the observed and synthetic wave-forms for both the models was not significant, Aoi et al. (2008) could not conclude which fault plane more appropriately explains the observations.

Cirella's model

A similar slip-patch was obtained by Cirella et al. (2008). The authors performed a non-linear joint inversion of strong motion and GPS data, retrieving peak slip velocity, rupture time, rise time and slip direction for the SE dipping fault plane (Plane B). This slip model is available at the SRCMOD [1], an online database of finite-fault dynamic rupture models of past earthquakes, developed by Dalguer and Mai (2011). The inferred rupture model contains two asperities: a small patch near the nucleation and a larger one located 10-15 km to the south-west. The maximum slip ranges between 2.0 and 2.5 m and the total seismic moment is 1.6E19 Nm (see Figure 5.6). The inferred rupture history is characterized by rupture acceleration and directivity effects, which are stable features of the inverted models.

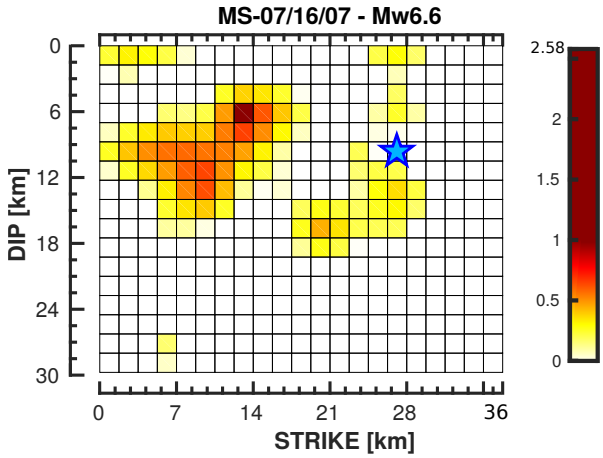

Figure 5.6: NCOEQ-2007 slip patch proposed by Cirella et al. (2008) for the SE dipping plane (Plane B)

Shiba's model

Shiba (2008) inferred a detailed source mechanism for the NCOEQ-2007, from regional strong-motion records. They assumed a south-east dipping (Plane B - ϕ_S=35°-λ=90°-δ=35°) rectangular fault of 29.4 km long and 16.8 km wide, corresponding to the aftershock distribution relocated through the data from ocean bottom seismometers (Shinohara et al., 2008). The distribution of the main fault parameters (e.g., the seismic moment and the rise-time) along the fault plane and their time variation were estimated by coupling a very fast simulated annealing technique (VFSA) with the empirical Green's function method (Irikura, 1991). The Green's functions were tuned upon the M_{JMA}4.4 (occurred on 16th, July 2007 at 21:08). Strong-motion records of two horizontal components from 18 stations (within 50 km from the center of the main shock fault) were employed by the authors for the inversion; the characterized source model was tuned to generation broadband strong motions during the main shock at the Kashiwazaki-Kariwa Nuclear Power Plant stations. Their estimated *optimal* solution is depicted in Figure 5.7. The author recognized three separated asperity areas on the fault plane (Figure 5.7), each one corresponding to a separated pulse-like waveform observed at near-source stations (KKNPP). It is likely that this area also includes the second asperity ASP2, because the distance between the first and second asperities is so small that the inversion of long-period seismograms cannot resolve the zone into separate asperities. The rupture accelerates abruptly on the third asperity which is most distant from the hypocenter, and the local rupture velocity seems to exceed the S-wave velocity. Shiba (2008) assumed a radial rupture propagation, driven by individual rupture speeds at

[1] http://equake-rc.info/SRCMOD/

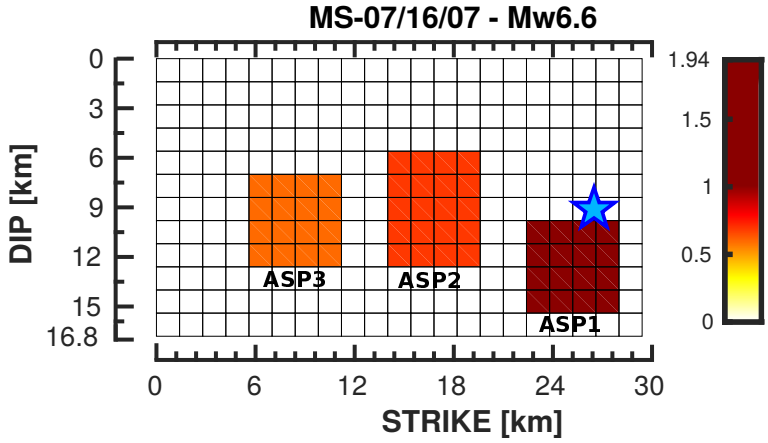

Figure 5.7: Slip patch for the NCOEQ-2007 main shock, proposed by Shiba (2008)

each asperity. The fault plane was subdivided into 21×12 1.4 km × 1.4 km sub-faults. The characterized source model is moreover featured by the effective stress drop on each the asperity, which is roughly distributed between 20-25 MPa (see Table 5.2). The original fault mechanism was updated a few year later (Shiba et al., 2011), by using the empirical Green's functions based on the aftershock distributions newly determined by Shinohara et al. (2008). The distribution changes along the strike direction (modified to 39°, but set to constant), thus leading to an heterogeneous dip angle and slip distribution at each sub-fault (the rake angle λ was set to 90°). Compared to the previous model (Shiba, 2008), the surface of the asperity and effective stress have been changed only for the ASP1. The dip angles were set to 40° for ASP1 and 30° for ASP3, respectively. For ASP2, the rupture area was divided into smaller rectangular sub-faults, deployed at different depths. On ASP2, the dip angle varies linearly from 40° (northernmost side, close to ASP1) to 30° (southernmost side, ASP3).

Hikima & Koketsu model

Another set of source models were proposed by Hikima (2007) and lately integrated by Miyake et al. (2010). The authors performed four kinds of wave-form analyses for determining the source fault plane: point source analysis and finite source inversion of teleseismic records and finite source inversion and empirical Green's function simulation of strong-motion records. Focal mechanism and hypocenter depth of the earthquake were estimated from the moment tensor inversion of teleseismic P-wave motion observed at 34 stations of the International Federation of Digital Seismograph Networks (FDSN). They confirmed that the conjugate fault planes in the Centroid Moment Tensor (CMT) solution were almost equivalent to the two trends identified in the distribution of aftershocks. They then performed finite source inversions of the previously described teleseismic records to determine the detailed geometry and depths of the conjugate fault planes. The best fit of synthetic to observed seismograms was accomplished with strikes/dips of 34°/36° and 214°/54° for the south-east- (Plane B in Aoi et al. (2008)) and north-west-dipping (Plane A in Aoi et al. (2008)) fault planes, respectively, though these teleseismic inversions for the two conjugate fault planes resulted in similar wave-form residuals. They fixed the epicenter of 37.53824N and 138.61744E (Earthquake Research Institute, University of Tokyo; personal communication), and the hypocenter at a depth of 9 km resulted in the smallest degree of variance for the two conjugate fault planes. As the hypocenter is located close to the intersection (see Figure 5.8) of the two trends in the 3D aftershock distribution, they arranged two fault planes of 32 km in length by 24 km in width such that they intersect along a horizontal line at the hypocenter depth of 9 km. The authors recognized the intrinsic difficulty in determining the focal mechanism and the slip distribution, due to the complex velocity structure of the Niigata re-

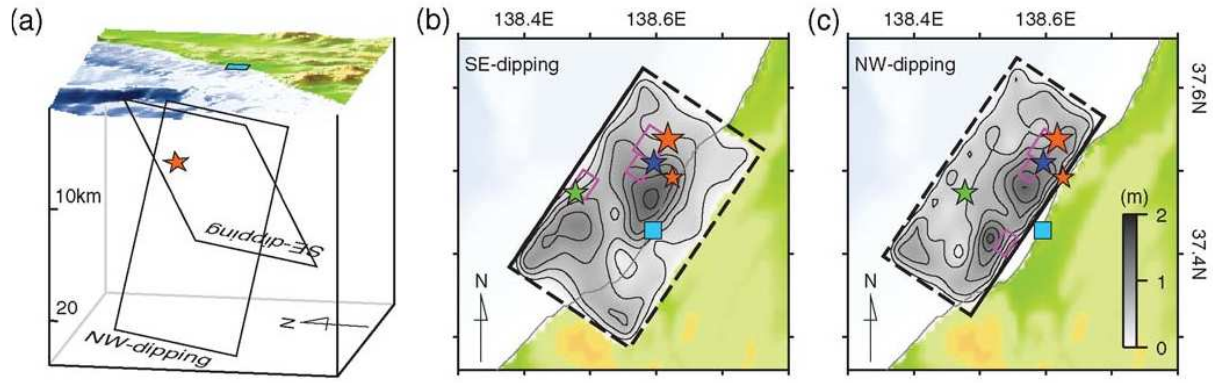

Figure 5.8: (a) Sketch of the conjugated fault planes, intersecting at the hypocenter depth of 9 km (red star). (b-) Slip distributions estimated via wave-form inversion for the SE-NW dipping planes respectively. Blue square represent KKNPP site; the epicenters of the main shock MS and M_{JMA}4.4 aftershock (red stars), and the first (blue star) and third (green star) asperities located by joint hypocenter determination are also shown. (Reprinted from Miyake et al., 2010)

gion. Therefore, adaptive 1D layered velocity profiles were built for each station, by inverting ground motion wave-forms from an M_{JMA}4.4 aftershock with a simple source mechanism (small red stars in Figure 5.8b,c). Using the resulting velocity structure models, they then obtained the slip distribution shown in Figure 5.8b- 5.8c for the south-east-dipping planes and north-west-dipping planes, respectively, from the source inversions of velocity seismograms filtered with a frequency band of 0.03 to 0.5 Hz. The main rupture propagates south-westward along strike with a speed of around 2.6 km/s; however, the inversions performed with the two conjugate planes yielded almost identical wave-form residuals, meaning that inability to determine which plane was the source fault of the NCO earthquake (with seismic moments equal to 1.2E19 Nm and 1.4E19 Nm for the south-east and north-west-dipping planes respectively, corresponding to M_W6.7). In the foregoing, Miyake et al. (2010) used the empirical Green's function method (proposed by Irikura, 1991) to simulate broadband ground motions at KKNPP, where dominant frequencies were generally higher than the upper limit of the frequency band used in their inversion. They estimated the size and stress drop of the three asperities located close to the zones of large slip. The simulated seismograms on the two conjugate planes again show similar performance in comparison with the observed ground accelerations, velocities, and displacements at the KKNPP and other strong motion stations. The overall wave-form analyses previously described proposed that both the fault planes are possible. However, Miyake et al. (2010) finally endorsed the assumption of SE dipping plane as the causative of NCO earthquake due to the additional support provided by (1) the relocation of rupture starting points of asperities using strong-motion pulses, (2) the aftershock observation by ocean-bottom seismometers (OBSs) (Shinohara et al., 2008), and (3) the reflection surveys in the source region. Especially, Shinohara et al. (2008) deployed 32 OBSs in and around the earthquake source region from 25 July to 28 August 2007 to obtain an accurate aftershock distribution. They picked P- and S-waves arrivals and then the aftershock hypocenters were precisely determined using the arrival times with the double-difference method (Waldhauser and Ellsworth, 2000). The obtained seismic profile clearly shows a plane south-east-dipping to a depth of around 13 km. Finally, Miyake et al. (2010) fixed the rupture starting point in the surrounding of the first asperity at a depth of 9 ± 1 km, along with the rupture starting point of the first asperity shown as the blue stars in Figure 5.8 located on both of the two conjugate planes, close to their line of intersection. The rupture starting point of the third asperity at a depth of 7.5 km with an error of within 1 km in depth was located at the position of the green stars to the west of the KKNPP in Figure 5.8. Because

there is no zone of large slip around the green star in Figure 5.8c, the third asperity should be located on the south-east-dipping plane as shown in Figure 5.8b. Seven seismograms observed at the KKNPP were aligned upon the initial P-wave arrivals matching the calculated travel times. This finding indicates that the first asperity, corresponding to the first pulse, is located in a zone of large slip close to the hypocenters shown in Figure 5.8. In contrast to pulse 1, pulse 3 arrived at the seven reactors at similar times. This finding implies that the third asperity is independently related to small zones of large slip in the southern parts of the slip distributions, as the reactors are located at approximately equal distances from each of the zones.

Further slip models from wave-form inversion

Nakamura et al. (2009) confirmed the presence of the two fault plane which form a cross-sectional *V* pattern. They analyzed the kinematic source process for the two fault planes consistent with the aftershock distribution using teleseismic body wave-form data. Their results indicate that the main shock initiated rupture on both faults north-east of their intersection and that the rupture propagated unilaterally south-westward along the south-east-dipping fault. The seismic moments of north-west- and south-east-dipping faults are 8E17 Nm (M_W5.9) and 7.5E18 Nm (M_W 6.5) (see Figure 5.9a). The authors argued that the main shock is composed by those two sub-events which together add up to a total of 8.3E18 Nm (M_W6.6). This value is however slightly different from Aoi's estimation. Nakamura et al. (2009) estimated a strike, dip and rake angles of 40.1, 36.8, 89.8° respectively, for SE-dipping fault plane (slightly different from values retrieved by Aoi et al. (2008)). The forward

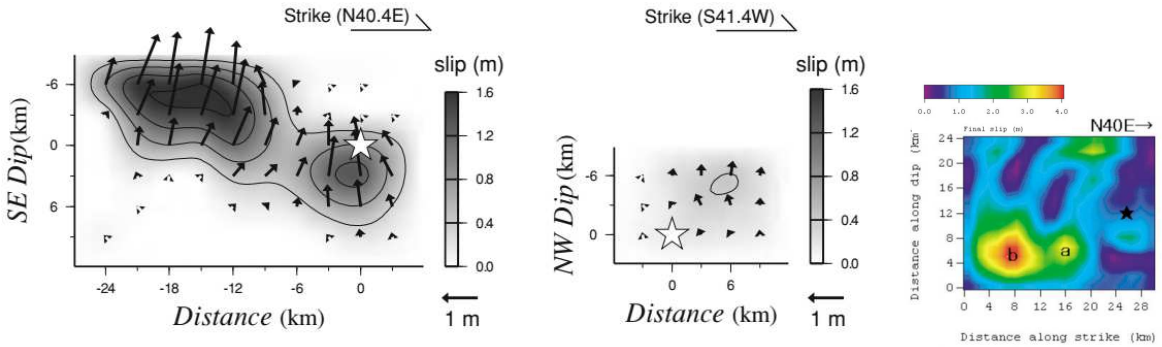

(a) (b)

Figure 5.9: Slip distributions proposed by Nakamura et al. (2009) (Reprinted). Nozu slip proposed for SE-dipping fault plane. The frequency range is 0.2-1.0 Hz. Reprinted from Nozu (2008).

modelling of geodetic displacement from the obtained fault model was found consistent with the GPS and InSAR measurements.

Nozu (2008) performed an inversion analysis based on the SE-dipping plane. Aftershock records were used as empirical Green's functions to avoid uncertainty in subsurface structure in and around the source region for the calculation of Green's functions. To ensure that the path and the site effects are shared between ground motions from the main shock and those from the aftershocks, the main shock fault plane was divided into three domains, each of which was allocated to one of the aftershocks used. Aftershocks were considered as the system response to unit pulses. Based on the results of the inversion, a major distinctive asperity was identified approximately 20 km southwest of the hypocenter, near Kashiwazaki City. A minor, rather obscure asperity was recognizable between the hypocenter and the major asperity (Figure 5.9b). The total estimated seismic moment is 3E19 Nm. Nozu proposed strike, dip and rake to be 40°, 36°, 90°, respectively.

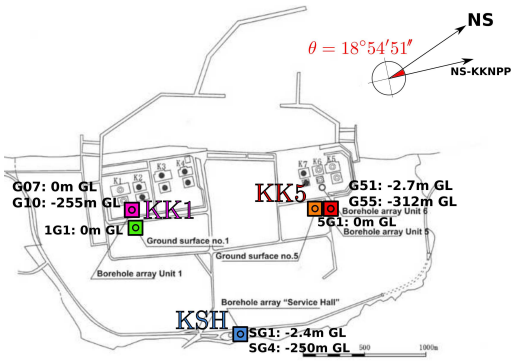

Figure 5.10: Map of the KKNPP site (courtesy of TEPCO, 2007). The three coloured squares indicate the three recording stations which entirely recorded the NCOEQ-2007 main shock. The devices were oriented with the respect to plant North (NS-KKNPP), which differs from the real geodetic North of an angle θ= 18° 54′ 51″. Moreover, some of them suffered of an azimuthal deviation, whose value was provided by TEPCO (2007).

Plane B proposed by Aoi et al. (2008) and the SE dipping model by Miyake et al. (2010) differ in hypocental locations (only about 1 km apart) even though due to differences in strike and dip, the discrepancy between the two fault planes is greater. Both models are analysed using available near-field strong ground motion. The only significant difference is that Hikima and Koketsu used the nearest station data at the Kashiwazaki-Kariwa nuclear power plant, while Aoi et al. (2008) did not. Moreover, Aoi et al. (2008) introduced the moving source effect when calculating their Green's functions semi-theoretically (Aochi et al., 2013a). Aochi et al. (2013a) performed 1D finite difference analysis on the data provided by Aoi et al. (2008) and Miyake et al. (2010). They compared the results at several stations belonging to the Japanese Strong-Motion Network KiK-Net-K-NET. They found that at station NIG016, the synthetic motion from Hikima & Koketsu reproduces the characteristic wave-forms, especially for the vertical component, with time shift of a few seconds. Such a time shift is common in inversions, as the location of the hypocenter and the origin time are not always the same.

5.1.3 Reconnaissance of the earhtquake ground motion spatial variability at KKNPP

The KKNPP site consists of seven Units, grouped into two blocks: (1) Units 1-4, built in the south-west part of the site and (2) Units 5-7 placed approximately 1.5 km away, in the north-east corner. Figure 5.10 shows a sketch of the plant, highlighting the recording devices downhole and at surface. Devices 1G1 (green) and 5G1 (orange) both belong to the most recent (2004) recording network, and they are placed at the surface (G.L. 0 m), respectively close by Unit 1 and Unit 5-7. On the other hand, four devices (SG1-SG4) are deployed along the vertical array KSH (blue) located at the KKNPP Service Hall, up to a depth of 250 m; other five devices are deployed downhole close by Unit 5 (KK5, red), till 312 m of depth; four devices are finally located in the surroundings of Unit 1 (KK1, magenta) with devices G07-G10 reaching 255 m of depth. The three vertical arrays KSH, KK5 and KK1 belong to the oldest recording network, where surface devices 1G1 (Unit 1) and 5G1 (Unit 5) are deployed at surface. It is worth noting that just one (KSH) out of three vertical array entirely recorded the main shock, along with 1G1 and 5G1.
According to Watanabe et al. (2009), the strong motion records at Unit 1 were significantly larger than those in the surrounding of Unit 5. Many authors (e.g. Uetake et al., 2008; Miyake et al., 2010;

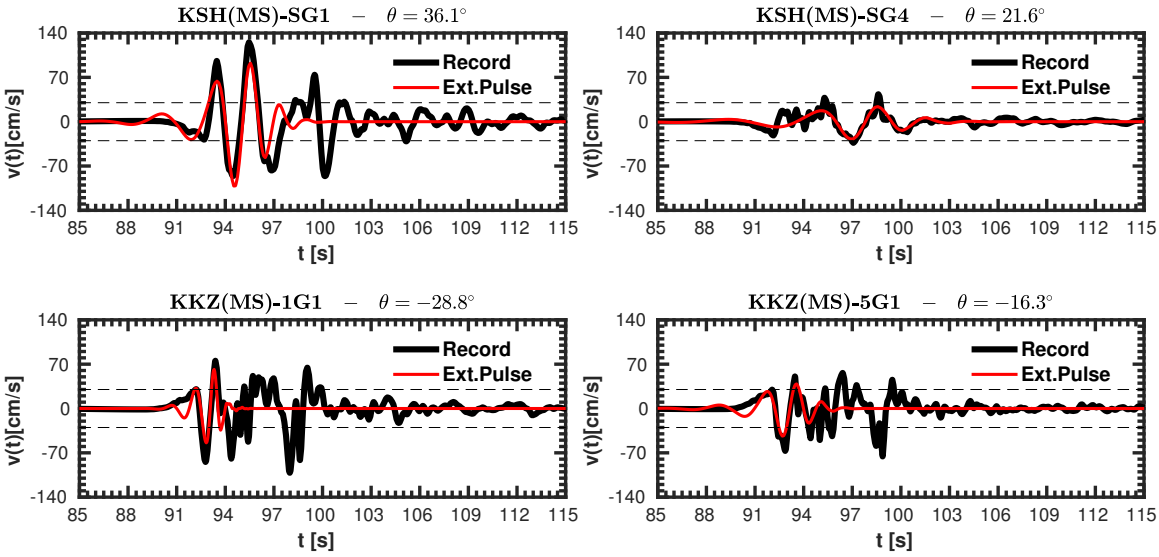

Figure 5.11: Comparison between velocity signal (black traces) and extracted pulses (red traces), according to Baker (2007), for devices SG1 (G.L.-2.4 m, (a)), SG4 (G.L.-250 m, (b)) in the KSH vertical array (Service Hall) and for 1G1 (G.L. 0 m, (c)) and 5G1 (G.L. 0 m, (d)). The in plane azimuthal angle θ at which those pulses were extracted is indicated above the velocigrams.

Tsuda et al., 2011) stressed the impulsive nature of the recorded time-histories. Large velocity pulses are usually observed nearby the fault rupture and coupled with their corresponding large peak displacement, they considerably enhance the structural damage potential (Cox and Ashford, 2002). In the NCOEQ-2007 case, Uetake et al. (2008) first noticed the three significant pulses at KSH array, associating them to the three major asperities identified (via wave-form inversion) on the fault plane. As a matter of fact, velocity pulses may be effectively *extracted* from the time-histories at KSH, 1G1 and 5G1 (i.e. the only devices which entirely recorded the main shock), by employing the ranking criterion proposed by Baker (2007) (excluding late arrivals and small events). Figure 5.11 shows an example of the mentioned pulse-like nature of the velocigrams recorded. The average pulse period ranges around 2.5 s for SG1, SG4 and 5G1, whereas 1G1 identifies with a shorter period pulse (1.5 s). Remarkable differences (in terms of amplitude, period and phase) are evident at a first glance, seemingly indicating an incoherency of the ground motion all around the nuclear facility zone. The observed site response at the surface is definitely more intense at the Service Hall and at Unit 1. It is worth noting that the velocity pulses were identified and extracted at different azimuthal directions (with the respect to the real North) for SG1 (KSH, surface) SG4 (KSH, depth), 1G1 (Unit 1, surface) and 5G1 (Unit 5, surface) respectively, the polarization of the impulsive incident wave-field spatially varies at the site scale, along its travelling path towards the surface. Another interesting aspect resides in the fact that later pulses may be identified at each location, whose nature has been correlated to the progressive fault rupture of the three asperities (Uetake et al., 2008; Miyake et al., 2010). Tsuda et al. (2011) observed that the first two pulses were rather comparable in terms of maximum amplitude, whereas the third one allegedly comes from the third asperity (ASP3, green rectangle in Figure 5.1) are different for two sites: the peak ground velocity on the south side of the KKNPP (KK1) is much larger than that on the north side (KK5) (Tsuda et al., 2011). The exceptional ground motion spatial variability is event more clear when one computes the Anderson's Criteria (Anderson, 2004) for the three station recordings (see Figure 5.12). The difference is remarkably high between SG1 (located at the Service Hall of the KKNPP site) and 1G1-5G1, which are placed nearby the coast of the Japan Sea, 1 km far away from the Service Hall.

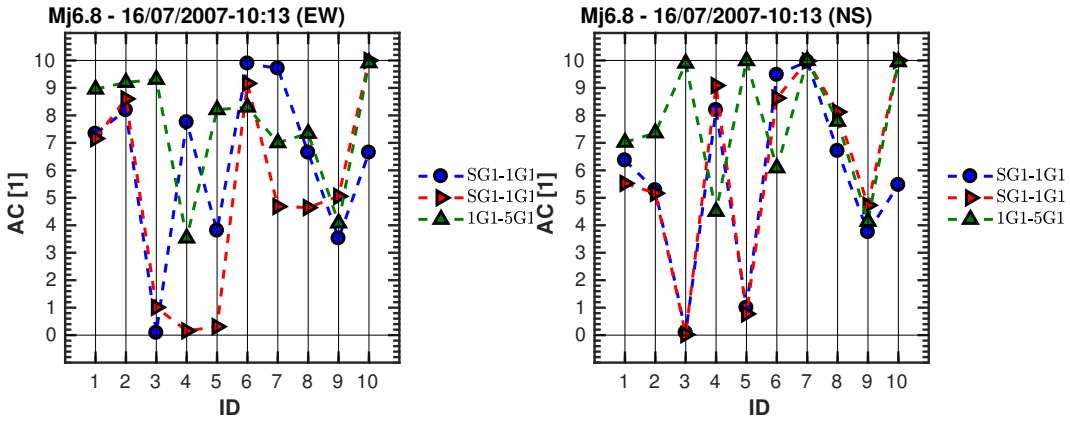

(a) (b)

Figure 5.12: Anderson's criteria for the recordings within the KKNPP site (SG1, 1G1, 5G1, see Figure 5.10).

Table 5.1: Summary of physics-based earthquake ground shaking scenarios of the NCOEQ-2007, targeting the KKNPP. FDM = Finite difference Method; FEM = Finite Element Method; SEM = Spectral Element Method. Fold = Tokumitsu et al. (2009); JNES-2005 = internal report; ERI = Shinohara et al. (2008); Kato et al. (2008, 2009); JNES-2008 = JNES (2008); NIED = Fujiwara et al. (2009); GSJ = Sekiguchi et al. (2009);

Reference	Dimension	Geology	Method	Model Size [km]	f_{max} [Hz]	min (V_S) [m/s]
Watanabe et al. (2009)	2D	Fold	FEM	7.6 × 4.8	5.0	700
Kawabe and Kamae (2010)	3D	JNES-2005	?	?	1.6	700
Ducellier and Aochi (2010)	3D	ERI	FDM	110 × 120 × 30	0.866	866
Tsuda et al. (2011)	3D	JNES-2008 + Fold	FDM	50 × 50 × 20	4.0	700
Aochi et al. (2013b)	3D	ERI/NIED/GSJ	FDM	110 × 120 × 30	0.5	866/350/400
Quinay et al. (2013)	3D	NIED	FEM	110 × 120 × 30	1.0	866/350/400
Aochi and Yoshimi (2016)	3D	GSJ	FDM	110 × 120 × 30	1.0	400

5.1.4 Influence of the geological structure in the Niigata region

The subsurface geological structure underlying the Niigata region has been proven to be rather intricate. Several 1D and 3D models of the velocity structure have been proposed in the past, based on geological and geophysical explorations (see, for instance, Shinohara et al., 2008). The latter set of geological configurations have been tested and tuned by several authors, by exploiting the long aftershock sequence occurred in the main shock aftermath and then exploited to simulate the main shock itself. Table 5.1 resumes the ensemble of physics-based analyses performed on the KKNPP site, during the NCOEQ-2007. Kawabe and Kamae (2010) simulated the wave propagation in a 3D structure model provided by the Japan Nuclear Energy Safety Organization (JNES, internal report, 2005) in a frequency range 0.05-1.6 Hz. Aochi et al. (2013a) and successively Aochi and Yoshimi (2016) performed a complete FDM analysis of the NCOEQ-2007 scenario, comparing three regional velocity models: (1) the model proposed by the Earthquake Research Institute (ERI, University of Tokyo) obtained by P- and S-wave travel time double-difference tomography on the data provided by Shinohara et al. (2008); Kato et al. (2008, 2009), with a grid resolution of 3 km × 5 km × 3 km (vertical) and with a minimum shear-wave velocity V_S of 866 m/s; (2) the model proposed by the National Research Institute for Earth Science and Disaster Resilience (NIED), taken from Fujiwara et al. (2009) from the seismic reflection results and observed H/V spectra (available on the Japan Seismic Hazard Information Station (J-SHIS)[2], with a 1 km × 1 km resolution and minimum V_S equal to 350

[2]source: http://www.j-shis.bosai.go.jp

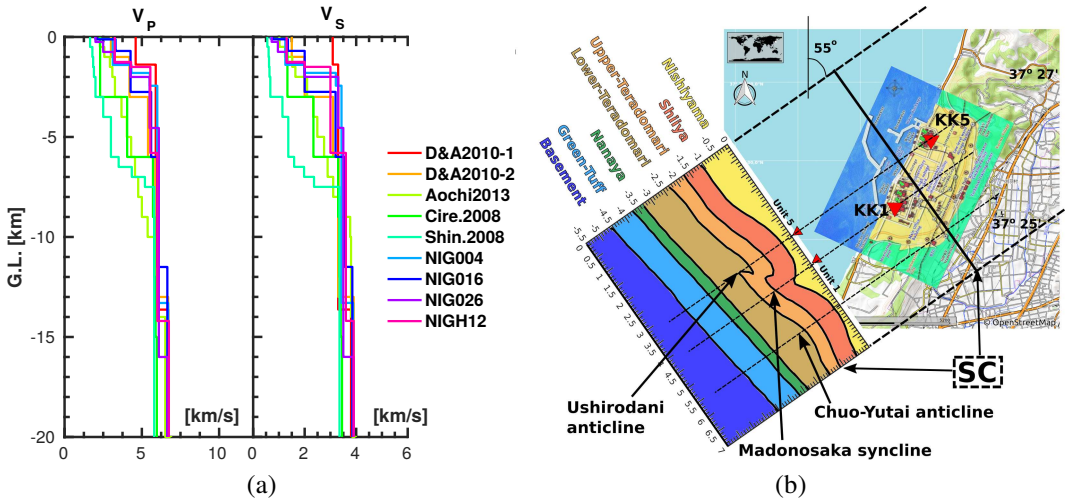

Figure 5.13: (a) Summary of the proposed regional 1D velocity structures (V_P and V_S) for the Niigata region. (b) Sketch of the folded structure lying beneath KKNPP.

m/s; (3) the model proposed by the Geophysical Survey of Japan (GSJ) and found in Sekiguchi et al. (2009), which is an improvement of the NIED velocity structure for the Niigata area (the resolution is 0.5 km $\times$ 0.5 km), carefully tuned upon the regional variation of material parameters (V_{Smin}=400 m/s). The authors concluded that the ERI model was less preferable than the other two in order to reproduce the regional wave field, mainly due to the poor resolution of the shallow deposits and despite the low frequency range of the analyses. Moreover, they argue the use of the JNES model (Kawabe and Kamae, 2010) for the regional-wise purposes, being however more precise around KKNPP. The crust material, topography, and sub-surface data provided by the J-SHIS were used by Quinay et al. (2013) to carry out a complete 3D analysis up to 1.0 Hz, studying the effect of the synthetic wave field on the structural behaviour of one of KKNPP reactor building. Aochi and Yoshimi (2016) improved the previous results by Aochi et al. (2013b) by enlarging the frequency band up to 1.0 Hz and employing the GSJ model, although their study targeted mostly the effect of different seismic source models and numerical implementation.

As a matter of fact, the lowest shear velocities considered in all the mentioned studies varies from 350 m/s to 866 m/s. As a general remark, the velocity models described previously were estimated for low-frequency analyses (i.e. wave-form inversions of the source mechanism), and eventually they are all based on the interpretation of several 1D/2D models, which Aochi et al. (2013a) proved to perform fairly well in reproducing the complex wave-field radiated, although phase shifts must be taken into account, due to modified travel times. Figure 5.13a shows some of the mentioned layered velocity structures available for the Niigata region. *D&A2010-1* and *D&A2010-2* were proposed by Ducellier and Aochi (2010), in their numerical physics-based simulations performed for the NCOEQ-2007 main shock. With the same purposes, Aochi et al. (2013a) provided a simplified 1D profile, tagged as *Aochi2013*. *Cire.2008* velocity values were employed by Cirella et al. (2008) to perform a wave-form inversion of the NCOEQ-2007 source mechanism, whereas *Shino.2008* was obtained by exploiting the data of the seismic survey conducted by Shinohara et al. (2008) and used to relocate the aftershock sequence. Finally, profile indicated as *NIG004*, *NIG016*, *NIG026* and *NIGH12* refer to the namesake K-NET and Kik-Net stations (the NIED strong ground motion networks, covering the Japan territory) and they were estimated by K. Koketsu[3].

[3]source: http://taro.eri.u-tokyo.ac.jp/saigai/chuetsuoki/source/index.html

Despite the good approximation of the regional incident wave motion obtained with simplified 1D and 3D geological configurations in the surroundings of the epicentral area, there is consensus among many researchers (Uetake et al., 2008; Tokumitsu et al., 2009; Watanabe et al., 2009; Hijikata et al., 2010) that none of them is suitable to picture the spatial variability of the ground motion observed at KKNPP. With this regard, Uetake et al. (2008) and Tokumitsu et al. (2009) related this aspect to the presence of a folded structure underneath KKNPP (characterized via boring and seismic reflection surveys, Kobayashi et al. (1995)) and composed by the Madonosaka syncline, interposed between the Ushirodani and Chuo-Yutai anticlines (Gürpinar et al., 2017). The folding cross-section extends for approximately 7 km across the Japanese coastline, up to 2.5 km down depth and with its hinge axes (i.e. the directrixes) strike at N55°E, as shown in Figure 5.13b. The geographical distribution of this peculiar sediment conformation shears through the nuclear facility, with the Ushirodani anticline and Madonosaka syncline placed below KK5 and KK1 respectively. The Chuo-Yatai anticline is indicated as well, which seemingly passes in the Service Hall surroundings (array KSH). A detailed description of the seven strata defining the folding is provided in Section 5.3.1. Watanabe et al. (2009) constructed a 2D FEM model of the syncline-anticline conformation, from boring and seismic reflection survey. Simulation results show good agreement with the observed strong motion records at Unit 1. Tsuda et al. (2011) constructed a 3D model by taking into consideration seven 2D sections across the folding area, and interpolating them. The joined up the folding model with the regional one (the 3D velocity model built by the Japan Nuclear Energy Safety Organization (JNES), which covers broad area including Chuetsu area (JNES, 2008).

5.1.5 Post-event seismic Safety Evaluation at KKNPP

The Tokyo Electric Power Company (TEPCO) and the Japanese Nuclear and Industrial Safety Agency (NISA) performed further studies on the seismic safety and vulnerability of the KKNPP site, after the 2007 *Niigata-Ken Chūetsu-Oki* . Two sets of active faults were judged to be potentially dangerous for the nuclear power plant: one set of inland faults and one set on the ocean side (fault traces are shown in the map in Figure 5.14). The most influential fault segment on the power plant seismic safety were judged to be the F-B fault (approximately 36 km long, located in the sea area) and the Nagaoka Plain Western Boundary fault zone (approximately 91 km in length, in land area). At the continental shelf slope of the Sado basin east edge located the north of the area where the activity of F-B fault (Figure 5.14), the sedimentary layers, normal continental slopes, are growing, but neither the active faults nor active foldings are observed. NISA experts suggest that the northern extension part of F-B fault is further extended to the northern Sado basin east edge. The results of the off-shore ultrasonic survey conducted by NISA showed no deformation in the geologic stratum of late Pleistocene and no activity observed. On the other side, results of the underground exploration revealed that the activity of Kakuta-Yahiko fault contributes to the formation of continental shelf slope in the northern F-B fault. It appears that the Kakuta-Yahiko fault dipping to the west raises the continental shelf slope, the continental shelf, and then Yahiko-yama, contributing to the formation of the asymmetric fold structure (Figure 5.15). The record of the underground exploration shows that there are no fault observed at the east edge of Sado Basin. Moreover, source modelling encompassing Kakuta-Yahiko fault enabled NISA researchers to account for the uplift in the terrace surface. The evaluation of the Nagaoka plain western boundary fault zone by NISA led to define the two following cases should be considered for each of Kakuda-Yahiko, Kihinomiya and Katakai faults, since each fault has a different principal seismicity period, average displacement rate, etc.:

- the case where each fault independently becomes seismically active;
- the case where the section of approx. 91 km formed by grouping three faults simultaneously becomes seismically active in consideration of an uncertainty in the evaluation of the seismic

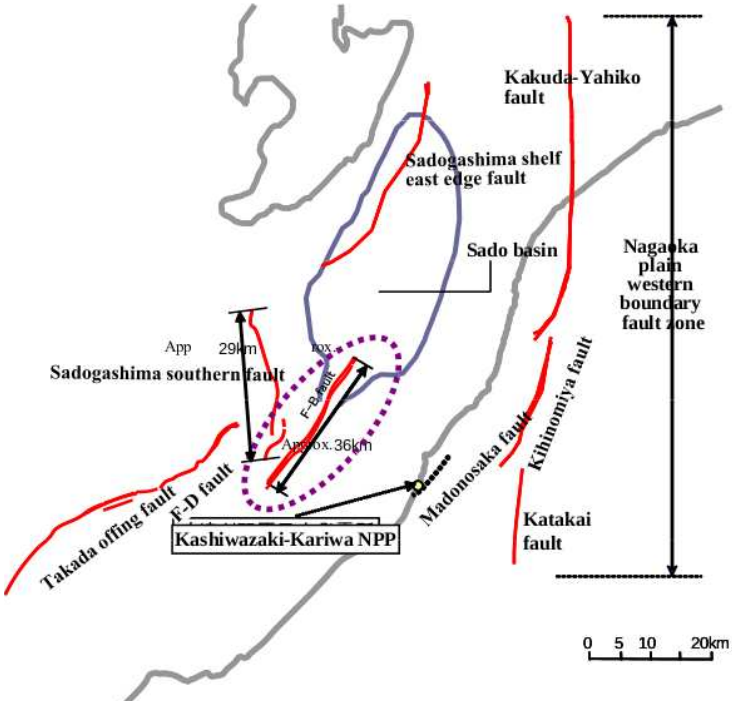

Figure 5.14: Active faults in the Niigata area, to be considered in seismic design of the Kashiwazaki-Kariwa Nuclear Power Station. Reprinted from NISA, personal communication. F-B was judged critical for KKNPP seismic safety.

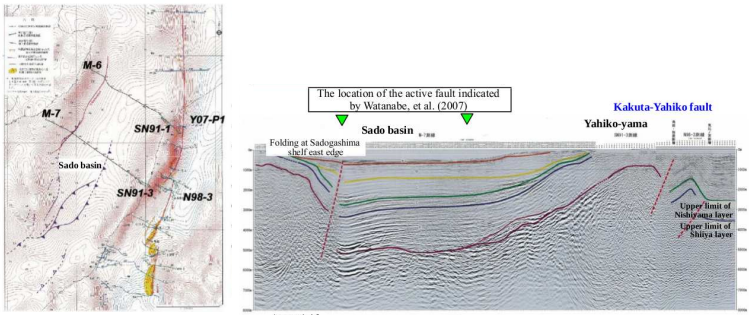

Figure 5.15: Results from TEPCO that independently re-processed and analyzed the data generated by the Japan Petroleum Development Corporation (Present: Japan Oil, Oil Gas and Metal National Corporation) using the refraction seismic survey.

motion.

The event probability of an earthquake of the scale exceeding the standard seismic motion Ss is on average to the extent of once every ten thousand years to a hundred thousand years. NISA confirmed the adequacy of the standard seismic motion formulated by TEPCO and reports to Nuclear Safety Commission. The Special Committee for Seismic Safety Evaluation of Nuclear Safety Commission provided the following instructions:

- A seismic motion for confirmation based on the source model under the following ideas reflecting the 2007 NCO earthquake should be formulated independently of the standard seismic motion Ss to confirm the adequacy of standard seismic motion Ss.

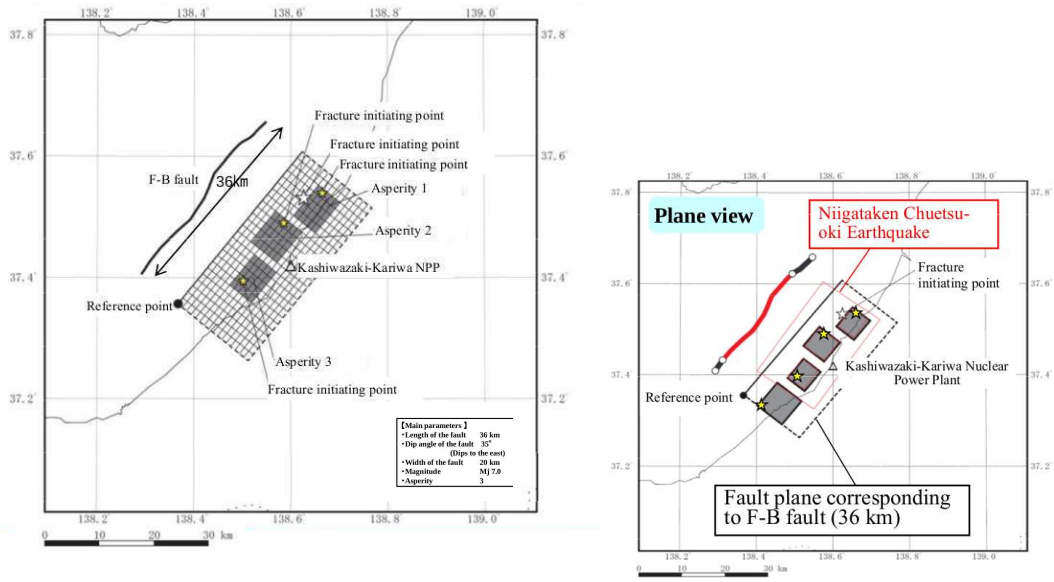

(a) (b)

Figure 5.16: (a) FB fault that originated the NCO earthquake. (b) new fault model proposed by TEPCO to fulfill the recommendations proposed by the Nuclear Safety Commission. A fourth asperity was added, compared to original model proposed by several authors for NCO earthquake model (see e.g. Aoi et al. (2008); Shiba (2008).

- When modelling the F-B fault, the macroscopic and microscopic source parameters should be established based on strong motion prediction recipes of Headquarters for Earthquake Reseach Promotion (2008), with the exception that the number and position of asperity and the stress drop should be established by utilizing maximally the data obtained from the NCO earthquake. Furthermore, the fracture initiating point should be established in consideration of the impact on the premises of the plant, plant because of its uncertainty.

In response to above, TEPCO formulated a seismic motion for confirmation in accordance with the instructions of Nuclear Safety Commission. The size of this seismic motion for confirmation is to the same extent as the standard seismic motion Ss formulated by TEPCO but a fourth asperity was added with the respect to original models proposed for NCO by several authors (see e.g. Aoi's models and Hikima & Koketsu model, described in previous section), and the fracture initiating point of the fourth asperity was set so that the fracture would move to premises of the plant for the evaluation of safety.

5.2 Physics-based simulation of the regional wave-field

Following the logic proposed by Boore (2003), the seismological model of the *Niigata-Ken Chūetsu-Oki* is herein built-up by tuning each feature (source, path, site-effect) stand-alone so to progressively enrich the original *skeleton* model. At any step, a back-verification check is done, so not to spoil the model by progressively dropping simplified assumptions, but to refine it instead.
Another crucial distinction made herein to ease the understanding and modelling of a large broad-band seismic scenario concerns the origin of the synthetic frequency content. Most of the slip distribution estimations available in the literature are derived from longer period ground motions (strong earthquake ground motion time-histories, teleseismic velocity seismograms, GPS and InSar measurements) and therefore valid within a frequency range $\approx$ 0.05-0.50/1.00 Hz. In this long period range,

earthquake ground motion is predominantly deterministic and wave-forms can be usually modelled using simple descriptions of the source and crustal structure. The mentioned WNI method (proposed and numerically implemented by Hisada, 1994, 1995, see Chapter 3) is naturally appropriate to this end, since it couples the need of a relative small amount of parameters with a reduced computational cost to simulate the complete 3D wave propagation field radiated from an extended kinematic seismic source in a layered half-space. Typically, WNI method deterministic analyses are reliable in a 0.05-2.00 Hz frequency band. However, several authors (e.g. Kamae et al., 1998; Hartzell et al., 1996; Somerville et al., 1999) agreed on the fact that despite their modest accuracy, long-period deterministic models are relevant for the simulation of artificial high-frequency signals, since the main uncertainty, both for short- and long-period wave-forms, resides into the methods to characterize the source mechanism (Somerville et al., 1999). For instance, slip models of shallow crustal earthquakes (as the NCOEQ-2007) are characterized by strong spatial variation in slip on the fault surface, including the asperities (Somerville et al., 1999). However, while travelling towards the surface, the wave-field gets enriched at high-frequencies (i.e. 2.0-15.0 Hz) when encountering finer deposits in the shallow part of the Earth's crust and topographical surface (Somerville et al., 1999). This spectral component is predominantly stochastic and it is extremely interesting for structural analysis. Therefore, the numerical model of the NCOEQ-2007 scenario was designed to propagate seismic energy up to 3.75 Hz. SEM3D (see Chapter 3) was employed due to its higher accuracy in solving wave-propagation problems and due its easy and scalable extension to parallel implementation (Göddeke et al., 2014). Moreover, the SEM has been successfully used to simulate 3D seismic wave propagation in complex geological media (and topographical surface) at regional scale with increasing resolution (e.g. Paolucci et al., 2014; Maufroy et al., 2015; De Martin, 2011). However, despite the efficiency of the numerical tool used in this study, the calibration of huge 3D large-scale seismic scenarios was conducted with the aid of a less cumbersome yet simplified semi-analytical/numerical tool (i.e. WNI method). In this way, the initial gross epistemic uncertainty is rapidly trimmed and more refined numerical tools (i.e. SEM3D) are then employed to refine the earthquake scenario.
In particular, this section stresses the methodological approach adopted to construct and calibrate it. The uncertainty quantification mainly targeted the choice of the crustal geology and the topography/-bathymetry effect.
The plan of the performed numerical exercise can be unravelled into the following points:

- to test the influence of different regional geology profiles onto final wave-forms at some location in the surrounding of the NCOEQ-2007 epicentre. Several 1D geological profiles have been tested, either as discontinuous layered geology, or by smoothing it up with a piece-wise linear approximation;
- to perform a sensitivity analysis upon the seismic source time functions (STF), featuring the kinematic description of a point-wise double couple seismic source;
- to test the effect of the topography on the synthetic wave-forms;
- to simulate a broad-band (depending on the source radiated frequency content) synthetic incident wave-field at the *engineering bedrock* issued from 3D forward physics-based numerical simulation

Two numerical tools were employed in this work: (1) the 1D semi-analytical solution provided by the WNI and (2) the SEM3D (Faccioli et al., 1997; Komatitsch and Vilotte, 1998), developed within the framework of the SINAPS@ project (as a collaboration between CentraleSupélec, the *Commissariat à l'énergie atomique et aux énergies alternatives* (CEA) and *Institut de Physique du Globe de Paris*). The former is alternatively employed to find the *most adequate* geological profile (by running a simulation over a M_{JMA}4.4 aftershock, denoted by AS from now on) and the *most adequate* slip

distribution (by running a simulation of the NCOEQ-2007 main shock (MS) featured by the previously chosen geological model). The fairly good comparison between WNI method and the results and recordings is valid between 0.05-0.50 Hz. At this point, SEM3D was adopted to simulate the 3D wave propagation over a broader frequency range (up to $\sim$ 3.75 Hz). In particular, SEM3D was used for manifold purposes, i.e. to test different STFs for a point-wise double couple approximation of the AS earthquake, to test the topography effect on the synthetic wave-forms.

5.2.1 Preliminary Choice of a Suitable 1D Geological Profile

With respect to the *Niigata-Ken Chūetsu-Oki* earthquake, several different stratified geologies (varying station by station) have been calibrated from the aftershocks recordings (Shinohara et al., 2008; Cirella et al., 2008; Aochi et al., 2013b; Miyake et al., 2010). Those 1D profiles are generally obtained by wave-form inversion procedures, performed on narrow time windows ($\sim$ rupture duration) centered on the main phase of S-wave and reaching a maximum frequency of 1.0 Hz. Therefore, in an early stage of the seismic scenario calibration, they are employed to provide a reasonable synthetic wave-field at the *regional engineering bedrock*, supposed underlying the shallow folded sedimentary strata. At this point, it is important to remark that the resolution of those geological profiles is approximately 0.5 km. The large scale model may be equipped with complex 3D geological model (e.g. Kato et al., 2008, 2009; Sekiguchi et al., 2009) in a second instance (Watanabe et al., 2009; Tsuda et al., 2011; Ducellier and Aochi, 2010; Aochi et al., 2013a; Shinohara et al., 2008; Hikima and Koketsu, 2005; Hikima, 2007; Cirella et al., 2008). In this task, some of the mentioned approximated geological profiles were tested. The latter refers to the Niigata region around KKNPP and they are portrayed in Figure 5.13a. The epistemic uncertainty on the geological profile was solved by running a parametric analysis WNI method. The M_{JMA}4.4 aftershock of July 16, 21.08h, was considered, which nucleated near-by one of the three major fault asperities at a depth of 11 km (Tsuda et al., 2011) by detecting the polarity for the P-wave first motion (performed by the Hi-net Obara et al., 2005) and by considering the Centroid Moment Tensor analysis provided by F-net data (Okada et al., 2004). The Kik-Net and KNET recording stations were employed at this point, along with the recorded time-histories at the KKNPP (device KSH-SG4, placed at G.L.-250m at the Service Hall of the nuclear site). The parametric analysis lead to the choice of the soil profile *Aochi2013* in Figure 5.13a and proposed by Aochi et al. (2013b) (although a satisfactory match has been obtained for other soil profiles). Figure 5.17 show a fairly good comparison obtained at several stations in the surroundings of the Kashiwazaki-Kariwa Nuclear Power Plant . A Brune's source model was adopted (see the discussion in Section 5.2.4), with frequency corner f_C= 1 Hz, coherently with the measured magnitude (Geller, 1976). One single unitary sub-fault was considered herein to simulate the small M_{JMA}4.4 aftershock. In accordance with Aochi et al. (2013b), the recordings and the synthetics were band-pass filtered between 0.1-0.5 Hz and aligned at the time-step corresponding to the 1% of the respective Arias intensity. Aochi et al. (2013b) introduced a sequence of softer layers (Figure 5.13a) at shallow depths, with the respect to the crustal models estimated the the KNET/Kik-Net stations (NIG004, NIG016, NIG026, NIGH12). Similar results were however obtained for the crustal models tagged as *Cire.2008* and *Shin.2008*. Despite the local alignment, some phase shift among the simulations and the recordings is still visible for NIG004 and NIGH12, whereas in the near field (cf., NIG018, NIG016) the fit is quite good (probably due to the simple propagation path Aochi et al., 2013b). Finally, from Figure 5.17, it appears that the simulations performed at KKNPP site are satisfactory only along the NS direction, whereas synthetics are de-amplified along the EW direction. This might be a effect of the shallow local geology of the Niigata basin. With that being said, it is well known that the choice of a 1D velocity structure tends to accentuate the ground motion directionality.

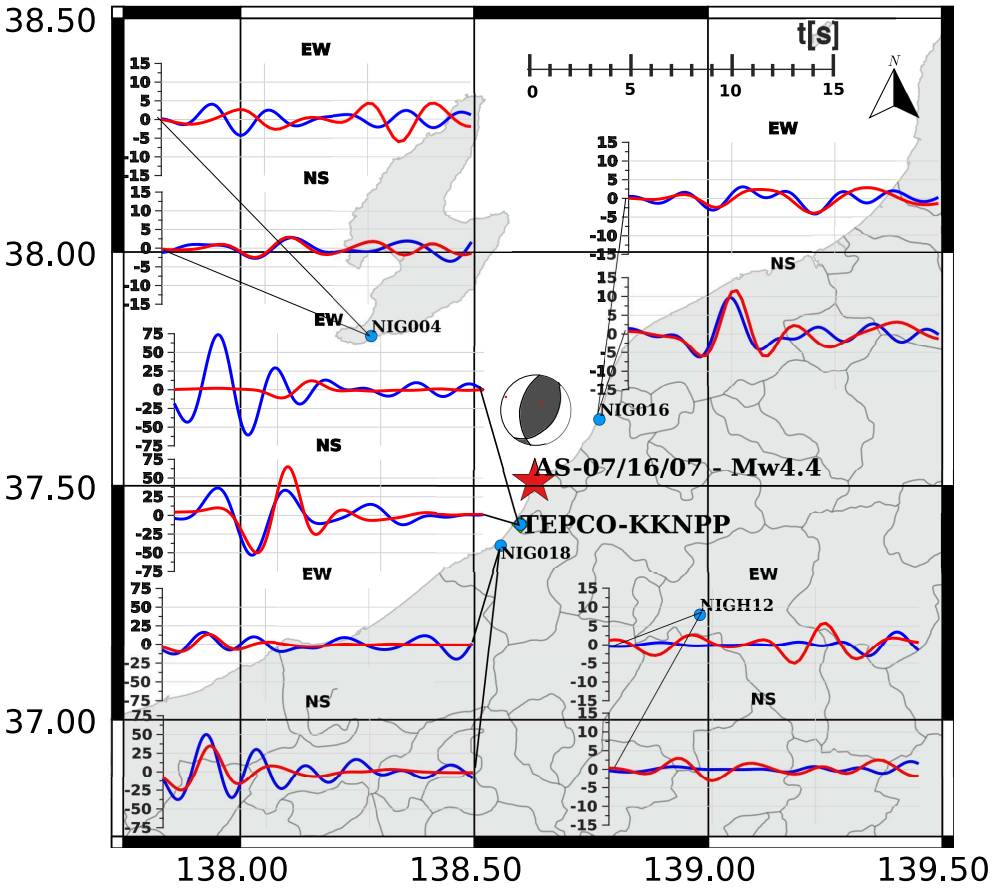

(a)

Figure 5.17: Simulations performed by WNI method of the NCOEQ-2007 M_{JMA}4.4 aftershock of July 16, 21.08h. Blue wave-forms represent the recorded velocigrams, red wave-forms the synthetic ones. Both records and synthetics were base-line corrected and band-passed filtered between 0.1 and 0.5 Hz. Synthetic wave-forms were obtained by considering the soil profile *Aochi2013* (Figure 5.13a). Velocigrams (in cm/s) are herein magnified by a factor 1000 and aligned with respect at the 1% of their Arias intensity.

5.2.2 Test 1D Geological Profile in 3D Large Scale Simulations

The chosen 1D geological model (depicted in Figure 5.18b) was implemented in 3D large scale SEM numerical model (see the sketch in Figure 5.18a). No topography was introduced at first, so to compare the synthetics with WNI results. 5 Gauss-Lobatto-Legendre (GLL) integration nodes were chosen to grant the minimum wave-length ($\approx$ 500m) a satisfactory discretization (i.e. to reach a frequency upper bound of $\approx$ 2 Hz (De Martin, 2011)). The total number of degrees of freedom of the considered mesh is therefore $\approx 1.9 \cdot 10^8$. The SEM3D software was used to solve the wave propagation problem so to verify it with the WNI semi-analytical model tuned in the earlier stages of the parametric analysis (and described in Section 5.2.1).

In the Spectral Element Method formulation, material properties are assigned to each GLL point. Therefore, two strategies were investigated to feature the numerical model with the varying material properties, namely (1) a direct meshing approach that adapts the computational grid to the layer-to-layer interface, so to coherently reproduce the abrupt impedance contrast along it and (2) a *not honouring* approach that associate to the whole independently-meshed domain a space-varying heterogeneous *material map* (in this case, transverse isotropic in the horizontal plane). In this standard

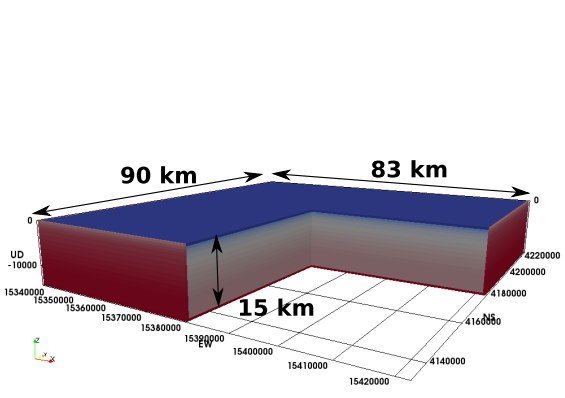

(a)

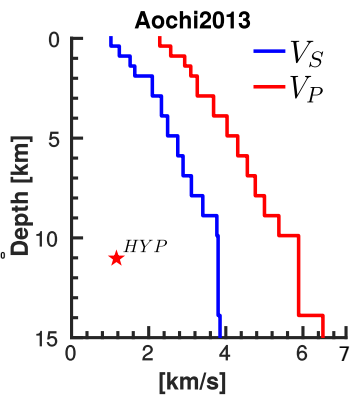

(b)

$z\,[m]$	$Q_P\,[1]$	$Q_S\,[1]$
0.0	200.0	100.0
0.5	228.7	100.0
1.0	257.1	100.0
1.5	293.3	100.0
2.0	309.1	100.0
3.0	325.9	100.0
4.0	368.2	100.0
5.0	403.2	100.0
6.0	430.9	100.0
7.0	455.8	100.0
8.0	476.4	100.0
9.0	500.2	100.0
10.0	537.5	100.0
14.0	588.7	250.0

(c)

Figure 5.18: (a) Sketch of the SEM3D computational domain used designed to simulate a layered half space (without topography). (b) Geology model proposed by Aochi et al. (2013b) for the Niigata area. Blue and red profile refers to V_S and V_P values (in km/s). The red star indicate the depth of the AS hypocenter. The quality factor profile was proposed by Aochi et al. (2013a) and reported in Table 5.18c

test case (i.e. a flat and bounded layered half-space) the second strategy does not seem particularly appealing since the material interfaces are planar and horizontal and a structured mesh was adopted. Although no computational gain is achieved by using one or the other approach at this early stage, the verification test was performed in view of implementing the *not honouring* approach in the non-structured mesh domain portrayed in Figure 5.20, *extruded* at depth from the local Digital Elevation Model.

The numerical back-verification of the model upgrade (WNI→SEM3D) was satisfactory. For instance, Figure 5.19 shows a synoptic comparison between synthetic wave-forms filtered between 0.1 and 1.0 Hz.

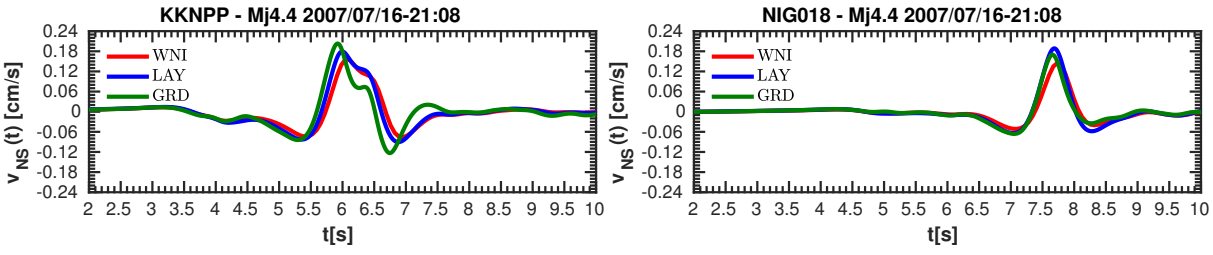

(a) (b)

Figure 5.19: Numerical verification of SEM3D code, against the semi-analytical solution obtained via WNI method. Synthetic acceleration wave-forms obtained at (a) the KKNPP site (KSH-SG4, G.L.-250 m, focal distance 15.1 km) and at (b) the KNET station NIG018 (focal distance of 20.1 km) are portrayed. A good match is achieved between the WNI method (WNI, red line) and SEM3D numerical model equipped either with a layered geology (LAY, blue line) or with a *not honouring* approach (GRD, green line)

5.2.3 Effect of the topographical surface

A further step of the numerical exercise consisted into adding the topographical surface (TOPO) to the previously calibrated flat model (FLAT). Figure 5.20 shows the employed computational grid. The latter was routinely generated on parallel architecture, by exploiting 27-tree data structures (Ca-

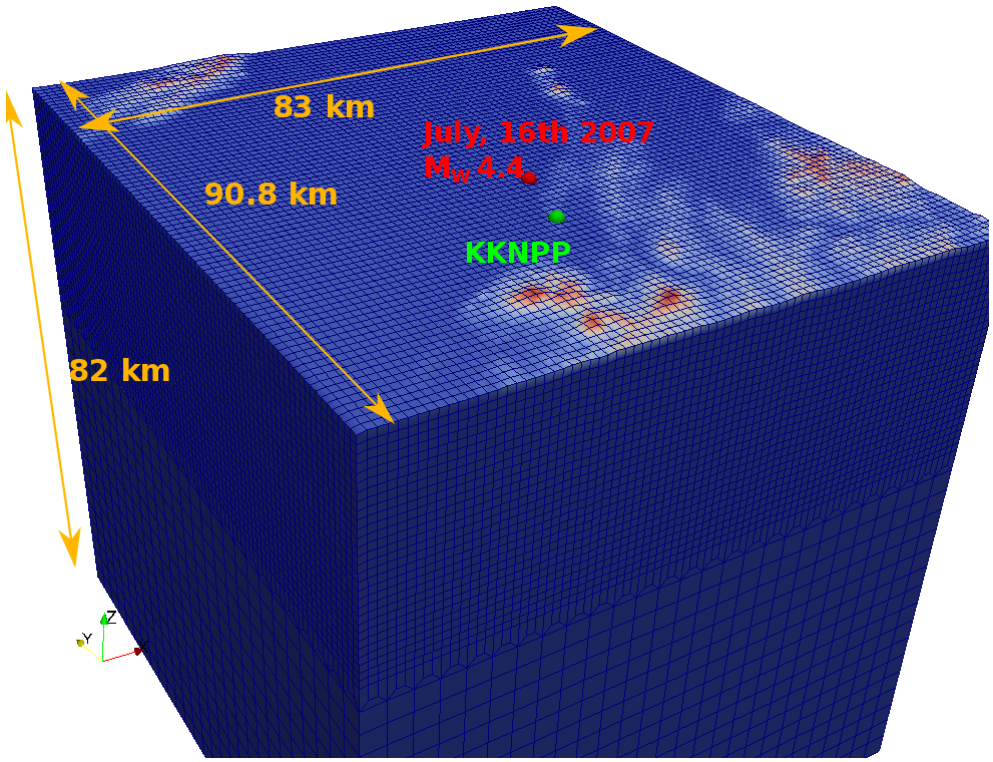

Figure 5.20: Sketch of the numerical model designed for the NCOEQ-2007 scenario. The mesh has been.

mata and Coutinho, 2013, see Section 3.2). A 90 km $\times$ 83 km $\times$ 82 km region in the surrounding of the KKNPP was meshed with 8-nodes tetrahedrons, by extruding the local Digital Elevation Model (DEM), obtained from the SRTM database [4]. The mesh was coarsened along depth (below 15 km of depth). The progressive top-to-down refinement level allowed to enlarge the frequency band propagated by the model. 15 Gauss-Lobatto-Legendre (GLL) integration nodes were chosen to propagate a seismic wave-field up to $\approx$ 3.75 Hz (considering, as reference, a third-order polynomial interpolation, Paolucci et al., 2015). The shear-wave velocity profile (*Aochi2013* model) was implemented via a *not honouring* approach (Figure 5.18b). Constant Q factors of 200 and 100 were chosen for the damping mechanism. The Sea of Japan is not taken into account: a flat solid surface was considered instead. Figure 5.21 shows the comparison between the accelerograms obtained at the ground level at KKNPP site, for the FLAT (red line) and TOPO (blue line) model. The wave-forms were band-pass filtered between 0.05 and 3.75 Hz. Early wave arrivals at higher frequencies are observed when the topographical surface is included in the model, although it does not seem to consistently affect the radiated wave-field. This aspect might be due to the fact that the Japan sea was disregarded. Finally, Figure 5.22 shows the synthetic velocigrams generated by SEM3D physics-based simulation at different locations nearby the Kashiwazaki-Kariwa Nuclear Power Plant . The synthetics wave-forms were band-pass filtered between 0.05 and 3.75 Hz. The typical velocity pulses are visible in the near

[4] source: http://dds.cr.usgs.gov/srtm/version2_1

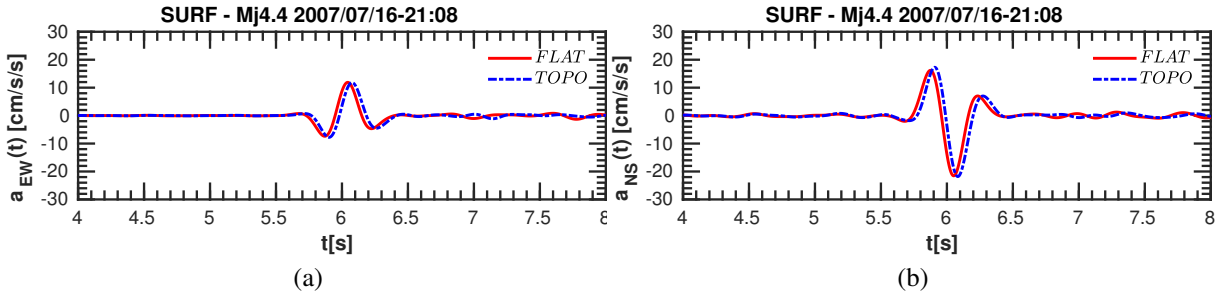

(a) (b)

Figure 5.21: Numerical verification of SEM3D code: effect of the topographical surface. Synthetic wave-forms obtained at KKNPP (at surface) are portrayed: (a) EW component, (b) NS component. Both synthetics were compared in the frequency band 0.05-2 Hz.

field (i.e. KKNPP, NIG018, NIG016), and high-frequency late arrivals may be observed in far field (NIG004 and NIGH12).

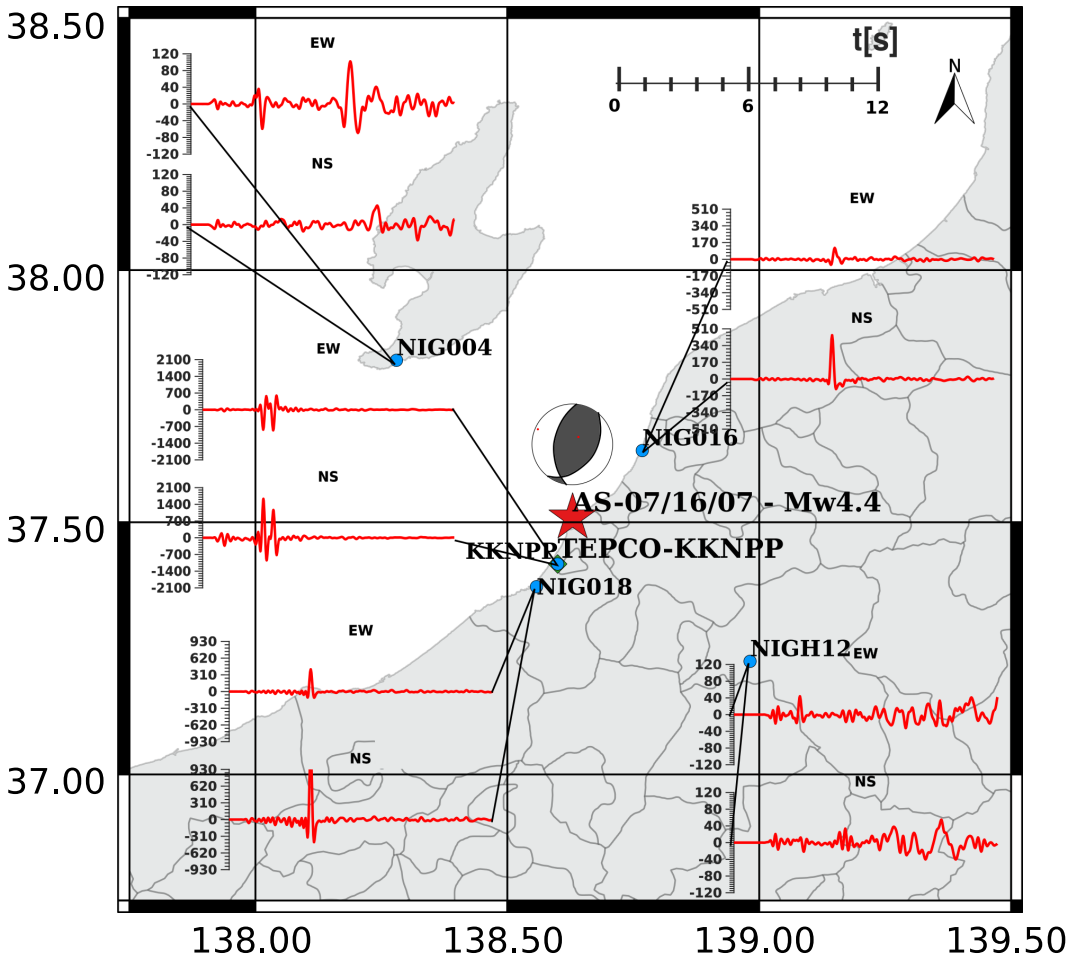

Figure 5.22: Simulations performed by SEM3D analysis of the NCOEQ-2007 M_{JMA}4.4 aftershock of July 16, 21.08h. Synthetic wave-forms were obtained by considering the soil profile *Aochi2013* (Figure 5.13a). Velocigrams (expressed in cm/s) were amplified by a factor 1000 and locally aligned at the time-step corresponding to the %1 of the Arias intensity.

5.2.4 Choice of Source Time Function

Small earthquakes (e.g. aftershocks occurring after a strong ground motion event) have been historically used to replace theoretical Green's functions (Irikura, 1983). This method does not require knowledge of the explicit shape of the slip time function (STF) for the small event. The wave-form for a large event is obtained by summing the contributions of small events, correcting each slip velocity time function (SVF) according to some sort of scaling laws between a large a small event (Miyake et al., 2003). Although this approximation has been proven to be accurate enough to simulate the far-field ground motion component (see for instance Miyake et al., 2003), one may argue that the chosen STF/SVF can influence the synthetic wave-field nearby the source. Moreover, the *a priori* selection of a suitable combination STF/SVF for a point-wise double-couple approximation of the seismic source is not obvious (Bizzarri, 2014). An accurate choice must be done, which in turn is extremely important in the contest of hazard assessment. Therefore, in this section a brief parametric analysis addressing different STFs/SVFs and the respective featuring parameters is presented. SEM3D exploits a kinematic description of the seismic source (Faccioli et al., 1997) which consists in replacing the displacement offset on the point-discontinuity by equivalent body forces (following the approach proposed by Madariaga, 1989).

Several 3D large scale analyses were performed by means of the SEM3D software. The domain geometry considered has been presented in the Section 5.2.3. Two different functions describing the time evolution of the displacement offset have been examined: (1) the so called *Bouchon's ramp* (or *smoothed ramp function* Bouchon, 1981) $u_S^{TNH}(t)$, that writes:

$$u_S^{TNH}(t) = \frac{A}{2}\left[1 + \tanh\left(4\frac{t - t_S}{\tau_R}\right)\right] \tag{5.1}$$

and (2) the source model proposed by Brune (1970), expressed by the following equation:

$$u_S^{EXP}(t) = A\left[1 - \left(1 + \frac{4\,(t - t_S)}{\tau_R}\right)\exp\left(-\frac{4\,(t - t_S)}{\tau_R}\right)\right] H\,(t - t_S) \tag{5.2}$$

The latter is well suited to approximate long-tailed Moment Rate Functions (MRF) (Duputel et al., 2013). Three are the free parameters that tune the shape and the position in time of the two mentioned STFs: the time-shift t_S, the generic *rise time* τ_R and the maximum displacement offset A. $H\,(t - t_S)$ represent the Heaviside function. The maximum slip value A is spontaneously determined by relating it to the scalar seismic moment value (for the M_{JMA}4.4 AS event, the F-net indicated a seismic scalar moment M_0=5.21e15 Nm). The time shift t_S was manually tuned to respect the quiescent past assumption (Aki and Richards, 1980). Among all, the crucial parameter results to be τ_R. Although no explicit definition of the rise time is available neither for $u_S^{TNH}(t)$ nor for $u_S^{EXP}(t)$ (Bizzarri, 2014), τ_R represents the duration of the slip rate pulse (Bizzarri, 2014; De Martin et al., 2007). Besides, τ_R is intrinsically related to the corner frequency of the SVF spectrum f_C (Kanamori and Anderson, 1975; Geller, 1976), which undergoes the empirically scaling laws originally proposed by (Aki, 1967). This aspect is highlighted when one compares the Fourier's spectra of different SVFs. For instance, Figure 5.23 compares three different sources (both in time and frequency domain), tested in the AS simulations performed by exploiting the SEM3D: the red spectrum in Figure 5.23a refers to two Brune's slip rate time evolutions (portrayed in Figure 5.23b), whereas the blue and green lines correspond to the Bouchon's ramp functions. The high-frequency falloff of the two Brune's SVF follows an ω^{-2} decay, whereas Bouchon's ramps steeper decreases for $f > f_C$. Two different values of the free parameter τ_R were tested herein: $\tau_{R1} = 10^{(0.5(M_W - 6.69))}$ (with M_W the moment magnitude, according to Dreger et al., 2007) and $\tau_{R2} = 2 \cdot 1.2 \cdot 10^{-8}\sqrt[3]{M_0}$ (with M_0 representing the scalar seismic moment, in dyne.cm, according to Duputel et al., 2012). The two definition of τ_R (herein τ_{R1}=0.12

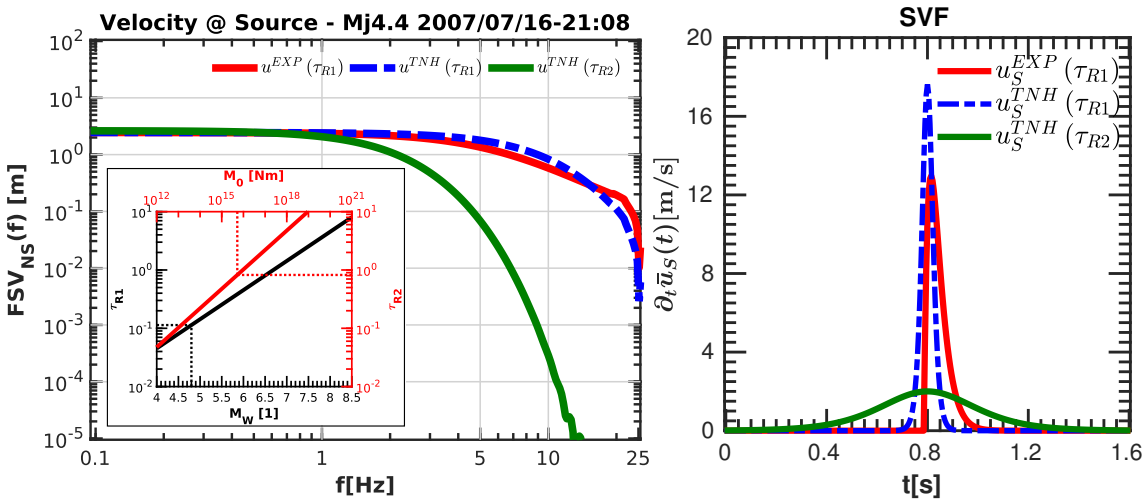

(a) (b)

Figure 5.23: (a) Fourier's spectra of the tested SVFs for the AS simulation (EW component). (b) Time evolution of th source velocity functions tested for a double couple point source in SEM3D. In the captioned sub-axes in (a), two estimations of τ_R are depicted: as a function of the magnitude M_W (black line, according to Dreger et al., 2007); as a function of the seismic moment M_0 (red line, according to Duputel et al., 2012).

s and τ_{R2}=0.82 s) are depicted in black and red lines in the captioned sub-axes in Figure 5.23a. The solution pertaining to the double couple point-wise simulation with the $u_S^{EXP}(t)$ globally has a higher frequency content, compared to the Bouchon's ramps. This result is coherently observed at different free surface receivers (such as KKNPP), although within the frequency band solved by the numerical grid (i.e. f_{max}= 3.75 Hz). In that respect, the synthetic accelerograms generated by SEM3D large scale simulation of the AS event at KKNPP are traced in Figure 5.24. The solution obtained for AS

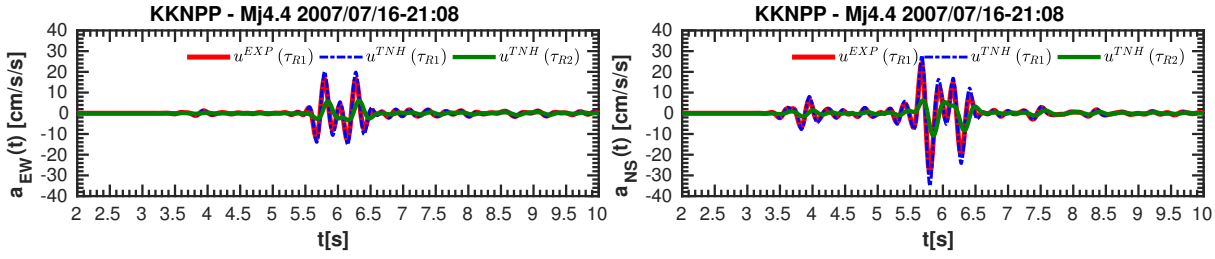

(a) (b)

Figure 5.24: Numerical verification of SEM3D code: effect of the STF parameters (functional form and rise time). Synthetic wave-forms obtained at KKNPP are portrayed: (a) EW component, (b) NS component.

simulation by employing $u_S^{TNH}(\tau_{R2})$ was found to be rather poor at high-frequency and not suitable for this broad band simulation, whereas the synthetic wave-forms obtained by either $u_S^{EXP}(\tau_{R1})$ and $u_S^{TNH}(\tau_{R1})$ are comparable. In the following section, the synthetic peak values were compared to the ones estimated by the Ground Motion Prediction Equations.

5.2.5 Comparison with Ground Motion Prediction Equations

Ground Motion Prediction Equations (GMPEs) are traditional yet very useful tool to estimate strong ground motion parameters. Therefore, they might be employed to check if the outcomes of physics-based numerical simulation are reasonable. For instance, Fukushima (2007) proposed a rather simple GMPE, whose functional form was issued from a probabilistic seismic hazard analysis performed on PGA and PGV. K-NET and KiK-net stations in the Kanto district (Japan) were employed in the regression. The choice of this GMPE is justified by the coherency between the predicted values and AS recordings in the Niigata region. The latter are plotted in Figure 5.25 (in terms of geometric mean of the horizontal PGAs and PGVs) along with the prediction by Fukushima (2007). The Fukushima (2007) GMPE predicts rather well both the recorded mean PGAs and PGVs ($\pm\sigma$), although a slight overestimation may be noticed at larger source-to-site distance. This discrepancy might be due both to the location (the Kanto district is placed south-westward the Niigata prefecture) and to the magnitude (greater or equal to 5.0) to calibrate the GMPE parameters (Cotton et al., 2008). However, Figures 5.25b- 5.25d suggest that the choice of a rise time τ_{R1} (for either u_S^{EXP} or u_S^{TNH}) is the most consistent with the selected GMPE (Fukushima, 2007), so it has been chosen as the suitable STF for the AS analyses. It is worth noticing that the choice of a constant Q factor might affect the peak values, diminishing their values compared to the attenuation relationship.

5.3 Numerical analysis of the near-source wave motion

The numerical model portrayed in Figure 5.20 is considerably large ($\sim$ 90 km) and it is henceforth suitable to quantify (1) the effect of the regional stratified geology, (2) the model sensitiveness to the source parameters (even for a point-wise small aftershock) and (3) the implications of considering or neglecting the topographical surface. This *holistic* approach adopted leads to focus on the coherent methodology to assess all its different tasks. The analysis performed provided reassuring comparisons between the synthetics and the traditional predictive tools (i.e. GMPEs). However, most of the computational tools used in engineering seismology, despite their effectiveness in estimating the far-field part of the wave-field, suffer of major drawbacks when it comes to quantify near-source field. This represent one of the major advantages that a complete and reliable source-to-site strong ground motion scenario must supply with the work-chain and methodology for vulnerability assessment of critical structures. Therefore, a step further is made at this point: the so called *LARGE* model presented in previous sections was improved by extrapolating a smaller yet refined Earth's chunk from within it (see Figure 5.26) and by running new analyses progressively complexifying the computational model. First and foremost, the SMALL model seems to solve the slight numerical dispersion observed in the LARGE model when the topography is considered: the ringing effect seemingly taking place in Figure 5.21 almost disappears when the refined model is considered instead (Figure 5.27). The brand new SMALL model was also featured by the Japan sea at a glance, by running coupled fluid-solid simulations (model called SMALL-W in Figure 5.27, compared to model SMALL-S model, where the Japan sea is replaced by solid Earth's crust). This improvement does not affect much the horizontal components (Figure 5.28a), but seemingly gives rise to late arrivals on the vertical one, as shown in Figure 5.28b.

5.3.1 Effect of the local folding model

The *Aochi2013* velocity model (depicted in Figure 5.27) used so far was found to be suitable to simulate the regional wave-field (Aochi et al., 2013a). However, some major drawbacks prevent it to be reliable for more refined site-specific analysis, namely (1) the coarse stratification (i.e. $H_{min} \sim$ 500 m) and (2) the lack of slower strata ($V_{S,min} \sim$ 1000 m) and foremost the lack of a local folding

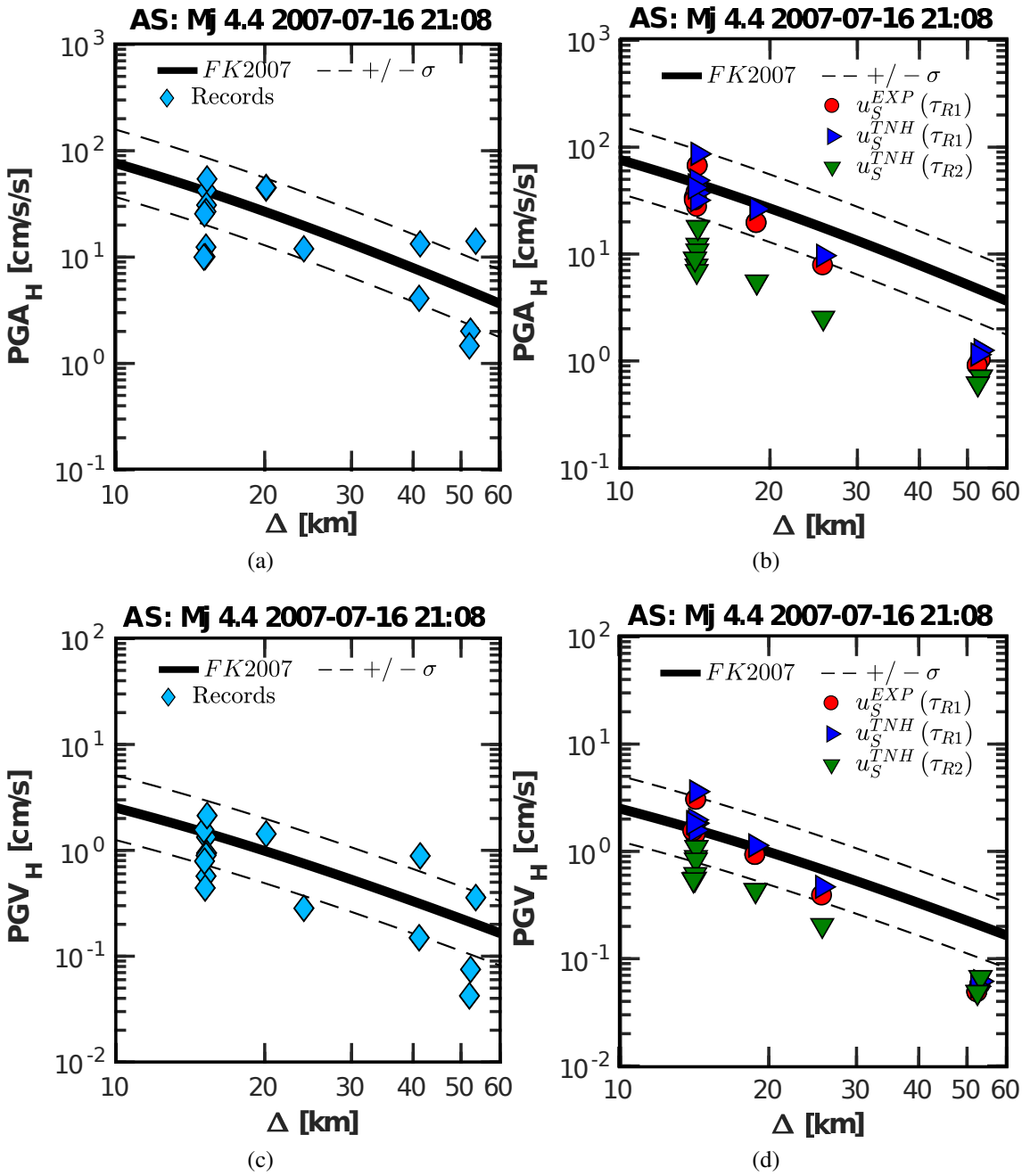

Figure 5.25: Horizontal geometric mean of Peak Ground Acceleration (PGA_H, portrayed in the top row) and Velocity (PGV_H, portrayed in the bottom row) obtained by SEM3D simulations of the M_{JMA}4.4 aftershock event. Synthetic peak ground motion values are compared to the GMPE proposed by Fukushima (2007). (a-c) Recorded peak ground motion values (from Kik-Net, KNET and KKNPP databases); (b-d) SEM3D simulations performed by introducing point-wise double couple source with different SVF: red circles and blue triangles refer to Brune's (u^{EXP}) and a Bouchon's (u^{TNH}) functions respectively, with free-parameter $\tau_R = \tau_{R1} = 0.12s$; green triangles refer to a Bouchon's ramp function with free-parameter $\tau_R = \tau_{R2} = 0.82s$ instead. Thick black line represents the median PGA_H/PGV_H stemming from the chosen GMPE; dashed black lines ($\pm\sigma$) represent the standard deviations.

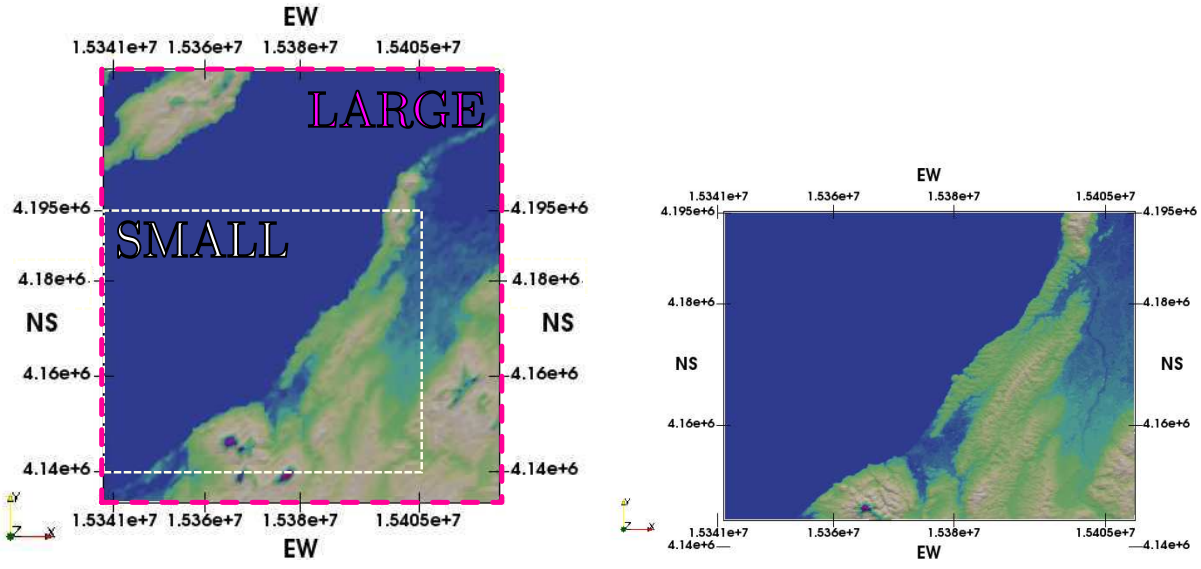

Figure 5.26: Elevation map of the meshed chunk of the Earth's crust. (a) LARGE model of the Niigata region; (b) SMALL model.

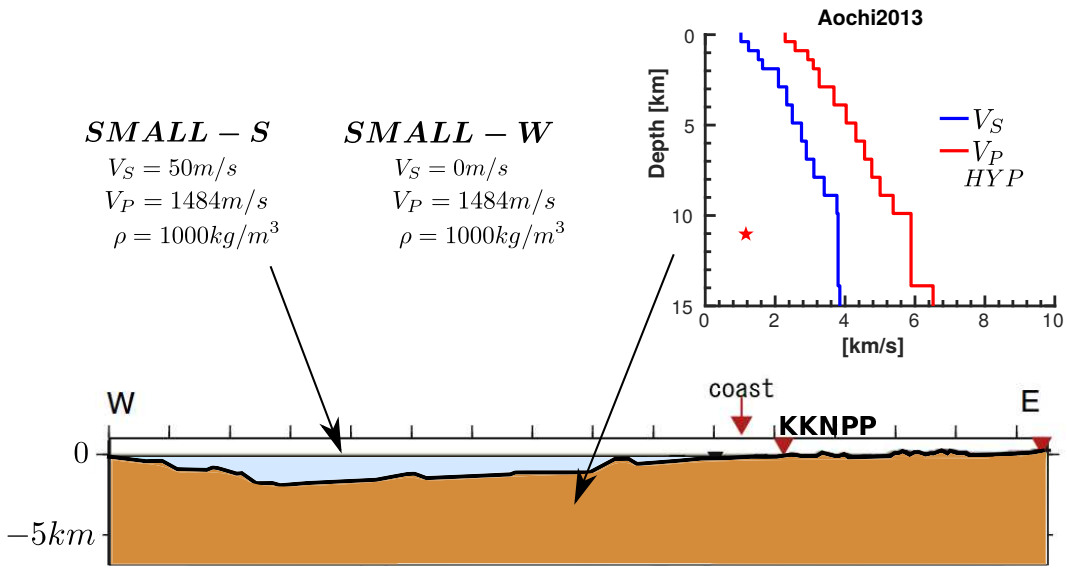

Figure 5.27: Sketch of the refined NCOEQ-2007 scenario. The Japan sea is considered in the smaller model (SMALL-W). Result are compared to the large (LARGE) and small (SMALL-S) model where the sea of Japan is disregarded. Synthetic accelerograms by three different numerical models: large scale model (LARGE, red), small scale solid model (SMALL-S, blue) and small scale solid-fluid model (SMALL-W, green).

structure below the KKNPP site, widely observed and characterized (Watanabe et al., 2009; Tsuda et al., 2011, among others) and constructed from boring and seismic reflection survey. Given the complex geological structure described so far, and with the aim to reproduce the overall regional wave-field, but focusing on a realistic broad-band simulation of the incident ground motion in the KKNPP surroundings, a *hybrid* geological model of the Niigata region was constructed gathering all the available information. Once opportunely calibrated, the regional model has been adjusted so

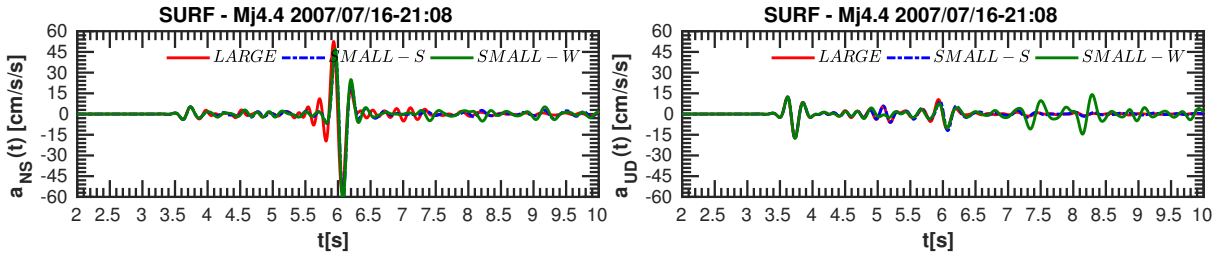

(a) (b)

Figure 5.28: The time-histories portrayed refer to KKNPP site (G.L. 0 m). (a) NS synthetic wave-forms compared; (b) UD synthetic wave-forms compared.

to include a 3D model of the Ushirodani anticline - Madonosaka syncline - Chuo-Yatai anticline, based on the previous work of Tsuda et al. (2011). Geological surveys indicated the folded structure strikes at N55°E, shearing through the nuclear facility, with the Ushirodani anticline and Madonosaka syncline placed below KK5 and KK1 respectively (Figure 5.13b). To clarify, Figure 5.29a portrays a geographical map indicating the estimated extension of the folding area beneath KKNPP. The investigated geological structure, referring to the central cross-section SC, is depicted in Figure 5.29b. The syncline-anticline combination extends up to 7.6 km wide (across the coastline, along SC) and 4.8 km deep. The stratification consists of seven strata, whose mechanical properties are reported in Table 5.29c. The conformation of the soil deposits has a probable continuity of shape in the along-strike direction (N145°E), even outside the KKNPP site. Tsuda et al. (2011) tested a 3D smoothed version of the folded geological structure, obtained by extruding a few cross-sections of it (proposed by Tokumitsu et al., 2009) (and whose geological profile is similar to SC) on either sides along the hinge axis (i.e. till the SE-SW cross-sections in Figure 5.29a have been reached). They adjusted the velocity structure on the boundary area of broad model connecting to the area of local folding model in order to reduce the artificial refracted waves that are generated around the boundary. Inspired by this approach, the representative cross-section SC passing through KKNPP (see its numerical model in Figure 5.30a) was chosen and extruded up to SW (south-westward) and SE (north-eastward), as depicted in Figure 5.30b. A linear smoothing of the folded material discontinuity was applied in so to obtain a quasi-horizontal layered profile at SW and SE (see Figure 5.30b). Due to the asymmetric nature of the folded structural geology, two small aftershocks scenarios were simulated (AS1, M_{JMA}4.4 aftershock of July 16, 21.08h and AS2, M_{JMA}4.2 aftershock of July 16, 17.42h), whose hypocenters were located along the directrix of the Madonosaka syncline, at the two opposite sides with the respect to its planar cross-section passing through the TEPCO facility (see Figure 5.29a). The aim is to characterize the 3D effect of such a complex geology, by spanning different incidence angles of the wave-front impinging the KKNPP. With respect to the LARGE model, the SMALL one, featured by a minimal shear-wave velocity of 700 m/s was designed to accurately propagate up to 5.0 Hz, with a third order polynomial degree.

Except the expected poor reproduction of the late surface wave arrivals, general features of observed records for AS1 and AS2 could be reproduced, as portrayed in Figure 5.31 (AS1, 1G1) and 5.32 (AS2, 5G1). Unfortunately, no recordings for AS1 at 5G1 are in the authors' disposal. The improvement granted by the inclusion of the folded configuration however is evident (red traces in Figures 5.31b-5.31d and in Figures 5.32b-5.32d), compared to the poor fit to the records obtained with a layered geology (green traces in Figures 5.31a-5.31c and in Figures 5.32a-5.32c) For both AS1 and AS2 and for both Unit 1 and Unit 5, the synthetic wave-forms at surface look out of phase with the respect to the records, on one of the two directions FP or FN. This stress the great achievement obtained by including the Madonosaka syncline in the analysis. A more equitable judgment of the wave-form fit

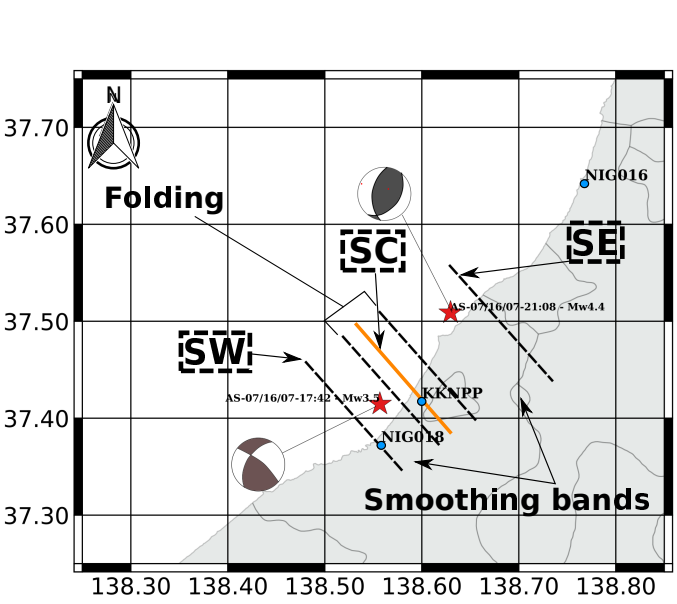

(a)

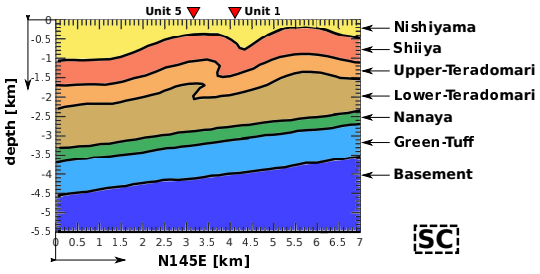

(b)

$\mathbf{V_S}\,[m/s]$	$\mathbf{V_P}\,[m/s]$	$\rho\,[Kg/m^3]$
700	1900	1700
1200	2200	2100
1700	3300	2300
2000	4200	2400
2000	4600	2500
2600	5200	2600
2600->2750	5200	2600

(c)

Figure 5.29: (a) Map of the Niigata region indicating the traces of the geological sections provided by Watanabe et al. (2009); Tsuda et al. (2011) and exploited herein. The two NCOEQ-2007 aftershocks considered at this stage are portrayed, along with their respective focal mechanism. The schematic structural map portrays the series of Ushirodani anticline - Madonosaka syncline, located underneath KKNPP and whose axial planes or hinge axes passes below Unit 1 and Unit 5. The Chuo-Yatai anticline is indicated as well, which seemingly passes in the Service Hall surroundings (array KSH). (b) Folded geological structure at section SC (close by KKNPP site) up to 5 km depth. (c) Mechanical properties of the local folded geology.

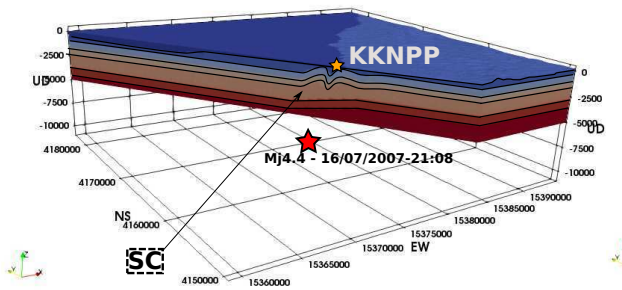

(a)

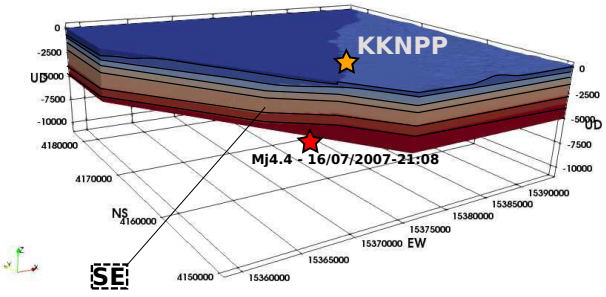

(b)

Figure 5.30: (a) Sketch of Section SC (see Figure 5.29a); (b) Sketch of Section SE (see Figure 5.29a).

is provided by the Anderson's Criteria (Anderson, 2004) in Figures 5.33a 5.33b for AS1 and 1G1, and in Figures 5.33c 5.33d for AS2 and 5G1. For both AS1 and AS2, the complex geological structure seems to influence specifically the FN direction. However, the poor score obtained for both cases for the first four Anderson's Criteria (related to the energy of the wave-form) highlights one major drawback of the model: recordings are more energetic than synthetics, due to late arrivals the model is incapable to reproduce.

In terms of normalized Sa response spectra (with respect to their respective PGA), a suitable mea-

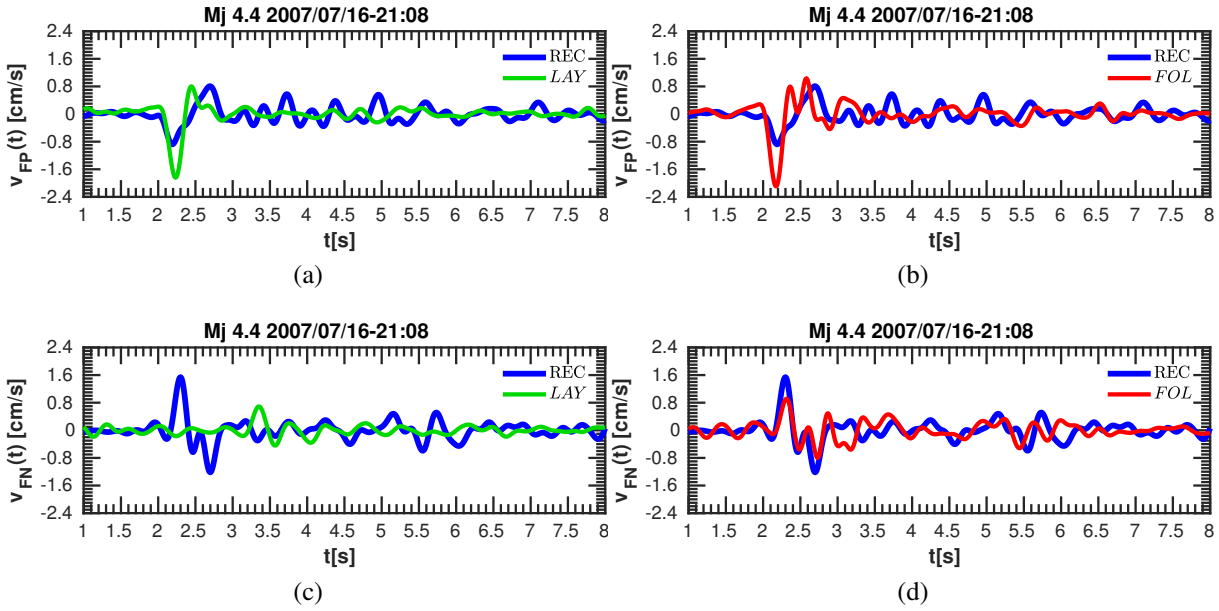

Figure 5.31: Recorded (REC, blue) and synthetic velocigrams for layered (LAY, green) and folded (FLD, red) geology along the fault parallel (FP, top row) and fault normal (FN, bottom row) directions, for AS1, at 1G1.

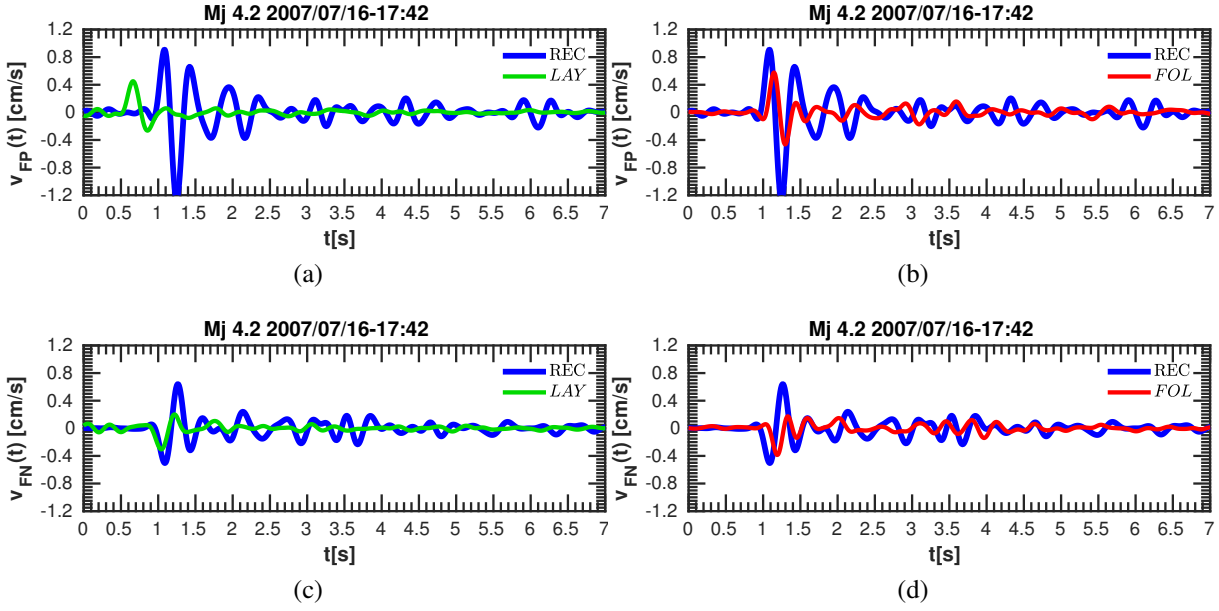

Figure 5.32: Recorded (REC, blue) and synthetic velocigrams for layered (LAY, green) and folded (FLD, red) geology along the fault parallel (FP, top row) and fault normal (FN, bottom row) directions, for AS2, at 5G1.

sure of the goodness of the model is the difference between the natural periods corresponding to the maximum Sa ordinate and referred as to T_P. In Figures 5.34b-5.34d, the focalization of the wavefield due to the syncline causes a shift of T_P towards the observed one, at both SG4 (Service Hall, G.L.-250 m) and 1G1 (Unit 1, G.L. 0 m), compared to the poor fit obtained for a layered geology (see Figures 5.34a- 5.34c). For AS2, the pseudo-spectral acceleration response less sensitive at Unit 5 (Figures 5.35a- 5.35b), where it is improved at 1G1 (Figures 5.35c- 5.35d) Finally, the KKNPP

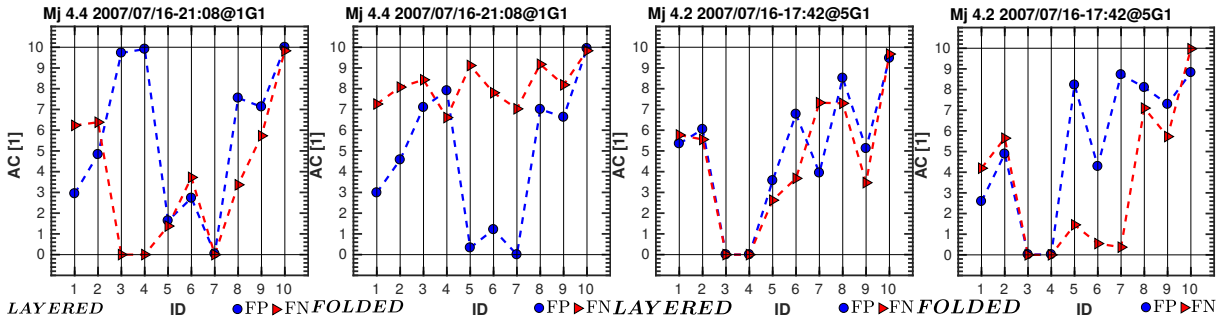

Figure 5.33: Scores of the Anderon's Criteria along the FN/FP directions for AS1 (a-b) and AS2 (c-d).

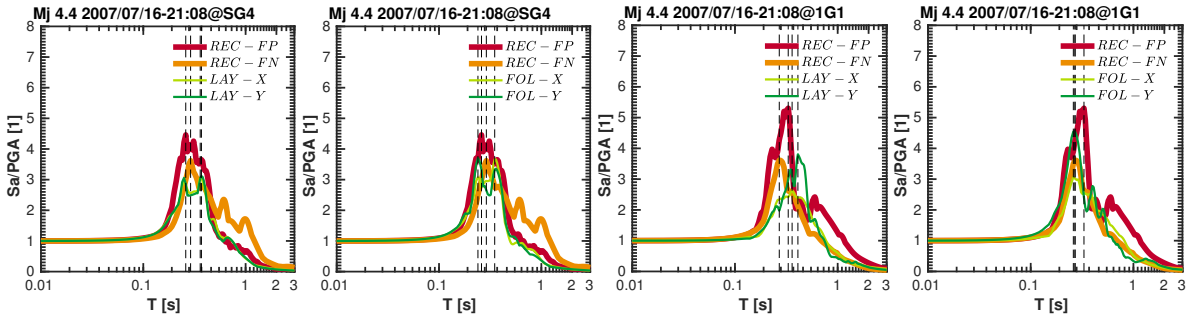

Figure 5.34: Comparison between recorded (REC, red for FP and orange for FN) response spectra Sa for SG4 and 1G1 sites for AS2, compared to synthetic ones. (a-c) Sa spectra for layered geology; (b-d) Sa spectra for folded geology.

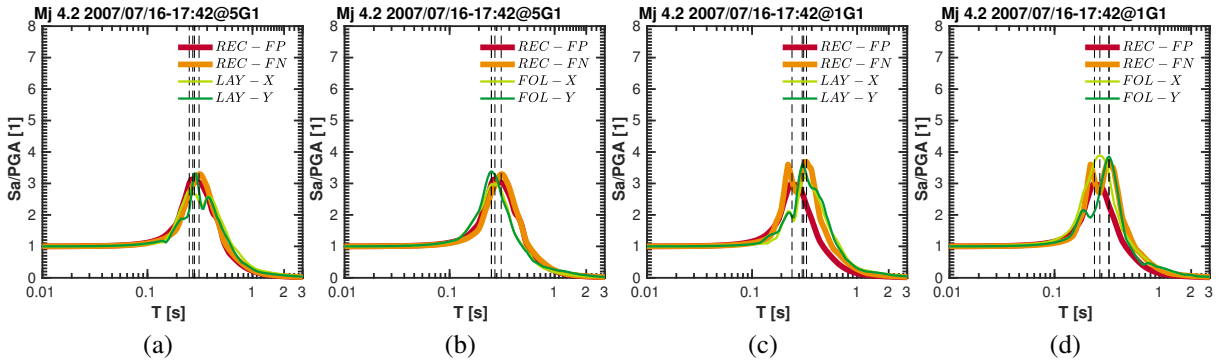

Figure 5.35: Comparison between recorded (REC, red for FP and orange for FN) response spectra Sa for 5G1 and 1G1 sites for AS2, compared to synthetic ones. (a-c) Sa spectra for layered geology; (b-d) Sa spectra for folded geology.

site response estimated by SEM3D analyses for AS1 and AS2 is condensed in the following four figure: Figures 5.36 and Figures 5.37 portray the pseudo-spectral acceleration spectra Sa estimated at KKNPP, for AS1 and AS2 respectively.

Hayakawa et al. (2011) showed that the large amplitude of KK1 site (Unit 1, located on the south-westward part of the KKNPP) comes from the folding structure where KK1 is located on the synclinal axis (Figure 5.13b). In agreement with what proposed in the literature, Figures 5.36- 5.37 indicate

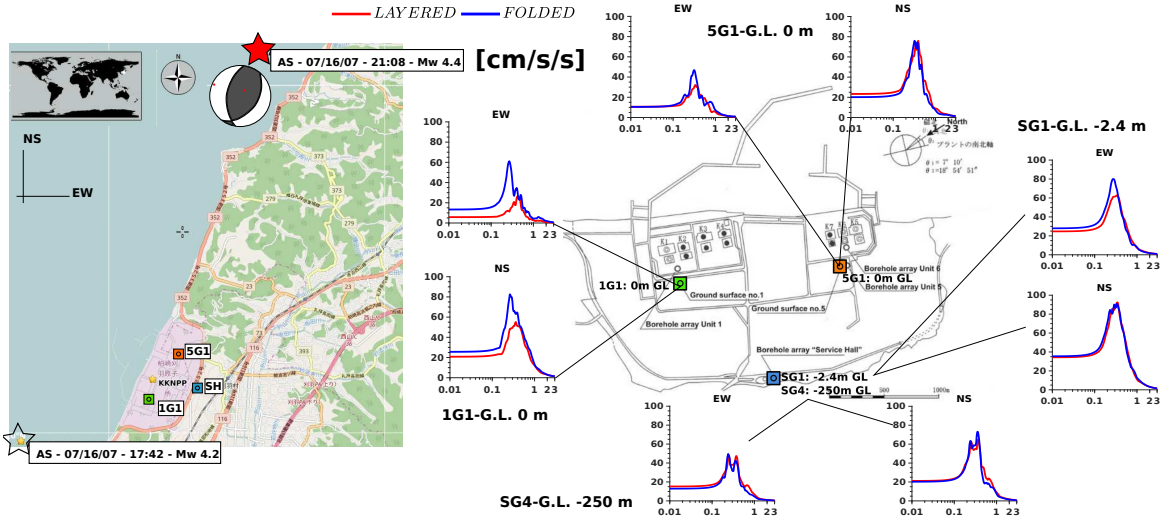

Figure 5.36: Sa response spectra (in cm/s^2) at different location around the KKNPP site. $LAYERED$ (red) and $FOLDED$ geological models were compared for the AS1.

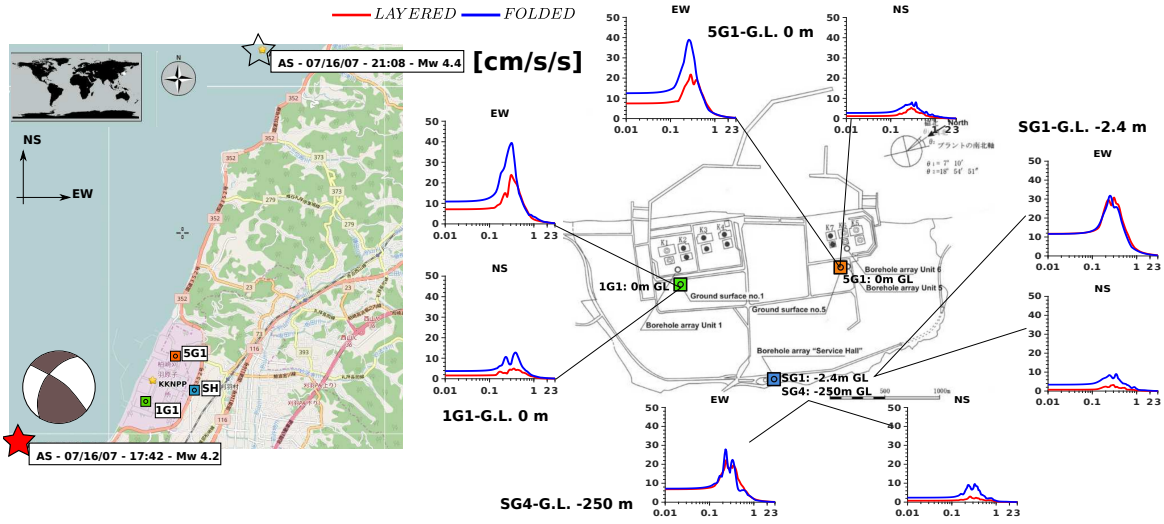

Figure 5.37: Sa response spectra (in cm/s^2) at different location around the KKNPP site. $LAYERED$ (red) and $FOLDED$ geological models were compared for the AS2.

the folded geology as responsible of higher peaks for the response spectra obtained nearby Unit 1, for natural periods T <0.5 s. The site response is seemingly unaltered by the introduction of a complex folding structure beneath KKNPP (at Unit 5 and Service Hall). The minimum shear velocity introduced in the model corresponds to the *engineering bedrock*, justifying that the spatial incoherence of the ground motion recorded at surface and specifically the amplification southwestward are extremely influenced by the syncline-anticline structure, despite the effects due to shallow borehole geology (dispersion, attenuation/amplification) which have been disregarded in the analysis. This strengthens the conviction that the site response at the Service Hall depended mainly on the non-linear site-effects taking place at shallow depths (i.e. G.L.-250 m). The amplification trend occurs independently on the source position, being more accentuated along the EW direction. Watanabe et al. (2009) showed that the Upper Teradomari stratum does not alter the wave-propagation of up-going waves, which tend to focalize at the Madonosaka syncline passing through Shiiya stratum. Site amplification becomes therefore significant at Unit 1. On the other hand, Unit 5 is evidently more sensitive to wave-motion

travelling from South-West to North-East, throughout the folding zone: the pseudo-spectral peaks differs from layered to folded geology only in Figure 5.37, referring to AS2 (nucleated close by the third asperity on the fault rupture plane).

5.3.2 On the accuracy of numerical solution

The *accuracy* of the numerical method employed to solve the 3D elasto-dynamic problem is notoriously a big deal to cope with. Due to inherent spatio-temporal nature of the wave-propagation physical phenomenon, the origins of the observed numerical dispersion are namely (1) the spatial and the (2) time discretization indeed. Usually, a Finite-Difference of Finite-Element spatial semi-discretization is assumed, along with a numerical time-integrator belonging to the Newmark's family. In the SEM, high-order polynomial are employed, sampled at the GLL point on each element. Despite the intrinsic $h-p$ property held by the SEM (leading to finer spatial discretizations and increased accuracy), it is intuitive that the two sources of numerical dispersions are not disconnected: Seriani and Oliveira (2008) stated that low-order time discretizations (such as the 2^{nd}-order accurate Newmark's schemes) deteriorate the high accuracy in space. According to Seriani and Oliveira (2008), P-wave dispersion and polarization errors are less sensitive to the value of Poisson's ratio than the S-wave dispersion error. They confirmed that four grid points per wavelength are sufficient to have the dispersion error below 1% on SE approximations of degree eight with GLL collocation points. Following the indications provided by the modal analysis performed by the mentioned authors, a parametric analysis on the computational model presented in this study for folded geology was performed. The minimum element size Δ_e of the computational grid is $\sim$ 250 m at surface, with $V_{S,min}$=700 m/s and Poisson's ratio ν $\approx$0.4. Three analysis were run therefore, with 5, 7 and 10 GLL points per element edge respectively. According to Seriani and Oliveira (2008) and for the Poisson's ratio considered, the frequencies delimiting the accuracy of the analyses are 2.8, 5.0 and 7.0 Hz respectively. Therefore, the whole set of results of the three-analyses were low-pass filtered at 7.0 Hz, to check whether significant differences emerge. Figure 5.38 show the comparisons (in terms of accelerograms, Fourier's spectrum along FP and FN directions respectively and geometric mean of the horizontal pseudo-spectral acceleration Sa^{GMH}) for 5, 7 and 10 GLL points respectively, at 1G1 (Unit 1, G.L. 0 m). The comparisons are rather explicative, in the following sense:

- the ground motion estimation does not change significantly for 7 or 10 GLL points, whereas it is rather underestimated (see the Sa^{GMH} ordinates in Figure 5.38c) when the computational model is featured by 5 GLL points;

- the response at short periods is amplified by increasing the number of GLL points, granting a certain confidence to the analyses portrayed in the previous section (comparison with layered geology). Increasing the number of GLL points would lead to even more amplified response at both 1G1 and 5G1.

- the computational costs (measured in CPU-time, and plotted in the captioned sub-axes in Figure 5.38c) are growing exponentially with increasing number of GLL points, although no remarkable difference can be found between 7 and 10 GLL. This justify, in a sense, the choice of 7 GLL as an *optimum* solution for the range of frequency of interest;

- the code-to-code numerical error (measured as logarithmic misfit between the log-average response ($\lambda_{Sa^{GMH}}$) of the geometric mean of the horizontal components Sa^{GMH}) on the whole ensemble of analyses, for a frequency corner of 7.0 Hz, is restrained within a narrow band around the average response at short-periods (see Figure 5.39) at both 1G1 and 5G1, with a

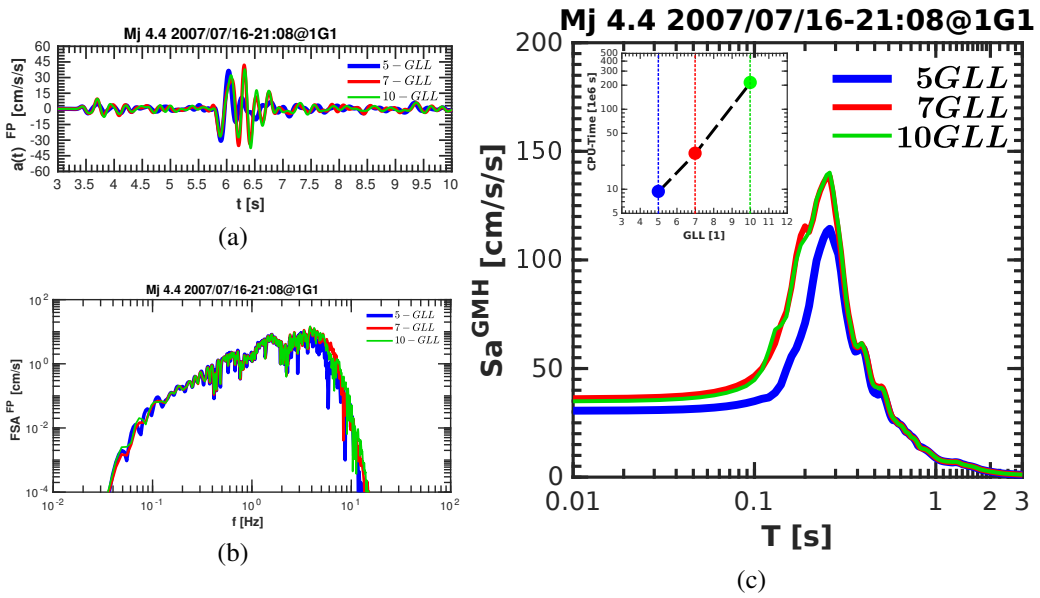

Figure 5.38: Results of the parametric analysis on the SMALL model with folded geology at 1G1. (a) Accelerograms(FP direction), (b) Fourier's spectra (FP direction) and (c) pseudo-spectral acceleration responses (geometric mean of horizontal components) for 5 (blue), 7 (red) and 10 (green) GLL respectively. Synthetics were filtered at 7 Hz. The computational costs of the SEM3D analyses are plotted in the captioned axes in (c).

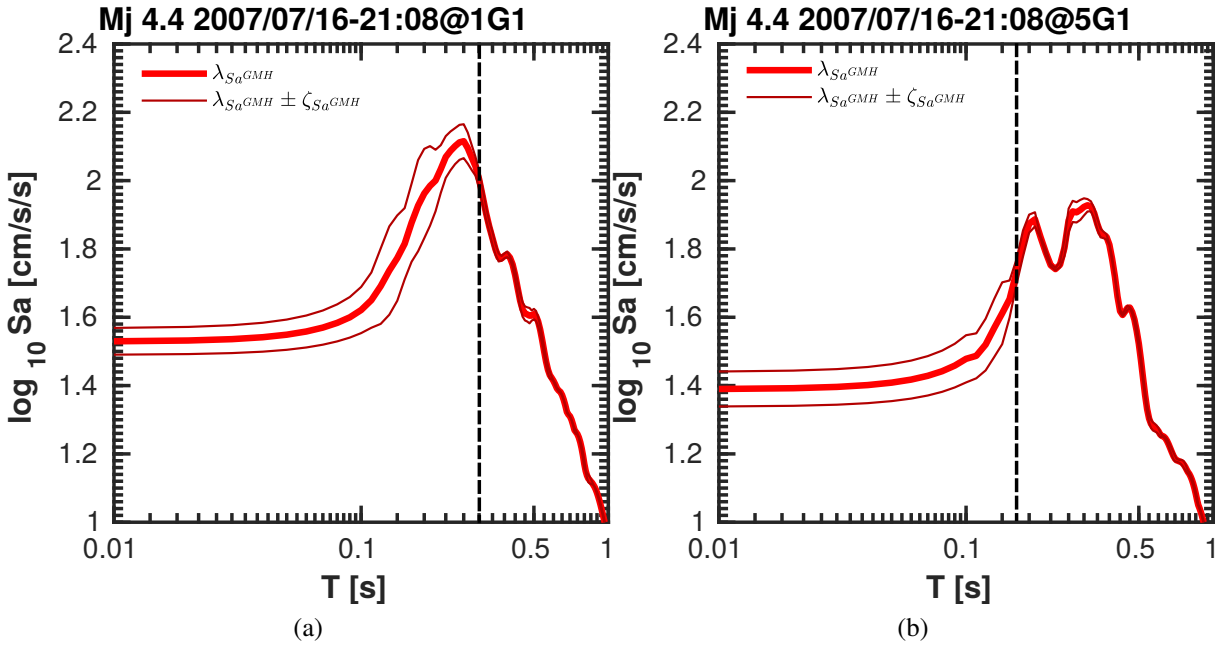

Figure 5.39: Mean λ and relative standard deviations $\lambda \pm \zeta$ of the geometric mean (horizontal components) pseudo-spectral acceleration ordinates Sa^{GMH} at 1G1 (a) and 5G1 (b).

log-standard deviation $\zeta_{Sa^{GMH}}$ attaining a plateau at higher frequencies. The numerical analysis seems therefore quite stable, and the error margins decreasing with increasing number of GLL

5.4 ANN2BB application to SEM3D results

Despite the good fit between the SEM3D numerical simulations and the observations, and the high accuracy obtained at 5.0 Hz, it is interesting to apply the ANN2BB technique to the synthetic time-histories obtained. For the sake of simplicity, AS1 was solely considered. An ANN was trained with corner period T*=0.75 s, and applied to the numerical results obtained either with LAYERED geology and either with FOLDED geology. Figure 5.41 portrays the site response (in terms of Sa) at the KKNPP. The hybrid spectral-matched synthetics (filtered at 25.0 Hz) reproduce the same trend

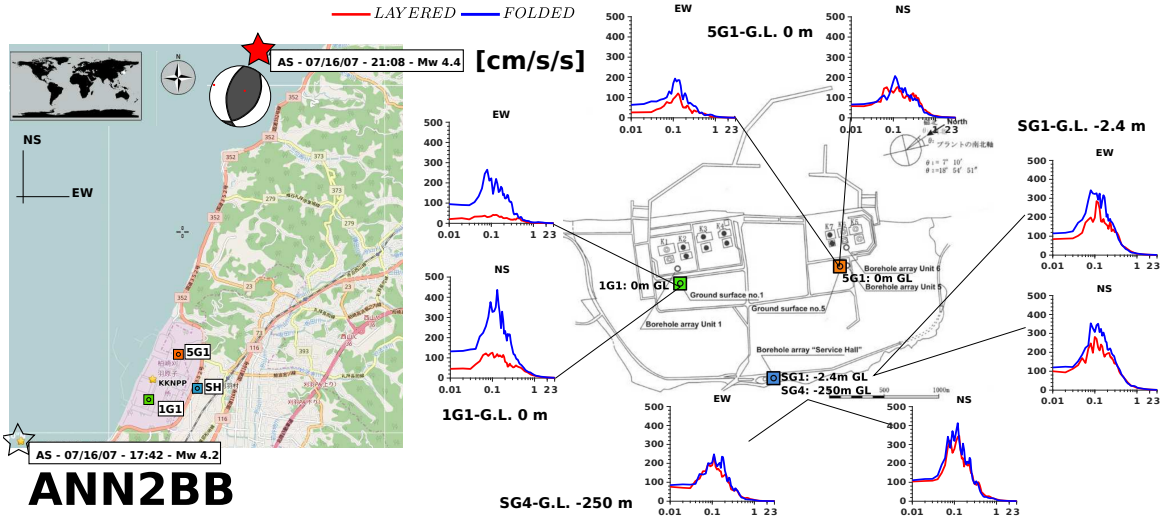

Figure 5.40: Sa response spectra (in cm/s^2) at different location around the KKNPP site, after ANN2BB application. $LAYERED$ (red) and $FOLDED$ geological models were compared for the AS1. Synthetics are filtered at 25.0 Hz.

obtained in the frequency band 0.0-5.0 Hz: the $FOLDED$ model amplifies the response at 1G1 and 5G1, compared to the $LAYERED$ one. This confirms somehow the fact that the broad-band prediction inherits the information concerning spatial distribution of the earthquake ground motion and it propagates it to shorter periods. This is an interesting phenomenon, since it proves the exceptional capability of neural networks to recognize the input pattern and predict the outcome based on the experience gained during the training phase. Finally, the geometric mean spectral ordinates Sa are extremely improved all over the recording stations within KKNPP, as Figures 5.41a- 5.41b portray. The ANN2BB efficacy is highlighted by the improved fit provided at both 1G1 and SG1. Even when SEM3D analyses provided poor fit to the records (probably due to the effect of shallow geotechnical layers, not considered in the numerical analyses), the ANN2BB provides more reasonable spectral ordinates, recommending its utilization to generate realistic broad-band synthetics.
It has to be noted that the ANN employed at this stage were trained upon the SIMBAD database (Smerzini et al., 2014), containing high-quality recordings observed for earthquakes in a magnitude range M_W 5.0-7.5. Despite the fact that AS1 has a magnitude M_W4.4, the satisfactory results obtained ensure somehow the reliability of the ANN predictive capabilities.

5.4.1 Partial Conclusions

In this chapter, a source-to-site numerical model of the NCOEQ-2007 earthquake is constructed, to reproduce the seismic site response observed at KKNPP. Specifically, the aim of this study is to criticize the common simplified assumption of a sub-horizontally layered Earth's crust, inferred from geodetic and geological surveys, stressing the importance of the shallow geological conformation

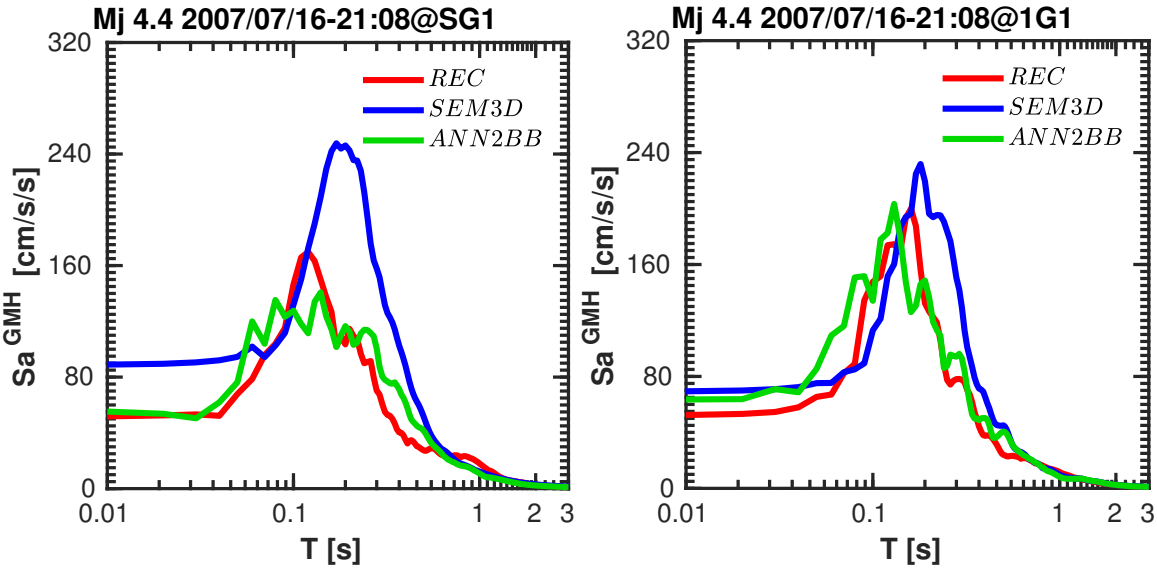

(a) (b)

Figure 5.41: Sa response spectra (in cm/s^2) at SG1 (a) and 1G1 (b) respectively: recorded spectra (REC, blue) are compared to SEM3D analyses (SEM3D, with $FOLDED$geology, red) and to hybrid ones (ANN2BB, green). Recordings and synthetics are filtered at 25.0 Hz.

in altering the incident wave-motion. The case of KKNPP rises as an exemplary benchmark, due to extensively observed near-field effects at the site, such as the ground motion incoherence within a relatively small distance. As a matter of fact, the incident wave-motion resulted amplified in the south-west area, nearby the first group of nuclear reactors and structures (Unit 1-4), compared to the second group of facilities (Unit 5-7), located north-eastward. Two aftershocks belonging to the NCOEQ-2007 sequence were simulated to prove the assumption focusing on the effect of the geological configuration. The dense observation network deployed in the Niigata region and at the KKNPP steered the calibration of two numerical seismic scenarios: one to portrays the regional incident wave-field (in a frequency band 0.1-0.5 Hz) and a second one restricted to the ground shaking pertaining the KKNPP surroundings, but extending the modelling accuracy up to 5 Hz. The paper explains the methodological approach to construct an holistic source-to-site physics-based computational model: LARGE is first calibrated upon the results of semi-analytical solutions, considering a 1D regional geology so to constrain the low-frequency band of the incident wave-field; SMALL is later constructed by trimming a portion of LARGE model and plugging into the 1D regional geology the intricate 3D set of syncline-anticlines, placed right underneath KKNPP. LARGE is used to assess the effect of the source parameters and of the topography, comparing the results with classical GMPEs. SMALL includes the Japan Sea, the bathymetry and the coastline, other than the folding geology. The outcome of the numerical exercise provides a fairly good agreement between the recordings and the synthetics at KKNPP. The effect of the folding clearly improve this fit, compared to the too much simplified sub-horizontally layered profiles. Moreover, the effort of including a complicated geology in the seismological model is worthwhile: the numerical analyses highlight the impact of the syncline laying below Unit 1 in causing an amplification (both in terms of peak ground motions and response spectra) with the respect to the layered geology. The syncline seemingly focalizes the upgoing wave-field, drifting the radiated energy towards Unit 1. This occurrence represents an exception to the current design standards, which traditionally leans towards the assumption of a 1D layered geology in case of lack of further informations concerning the subsurface geology. The case study stresses the importance of the propagation path in drifting and altering (eventually amplifying) the wave-field radiated

even from relatively weak aftershocks. However, the major shortcoming of the analyses presented herein resides in the lack of more refined models of the scattered wave-field in a high frequency range (0.0-10.0 Hz). This is a crucial feature to be taken into consideration in the transition towards a broad-band deterministic modelling of the earthquake phenomenon, along with the a good trade-off between computational cost and sought accuracy. To this end, the performance of SEM3D are particularly promising, as the analyses carried out in this chapter showed. In this specific test-case, for instance, an extra bonus accuracy resides within the chosen size of the computational model, possibly extending their reliability up to 7.0 Hz. As perspective, the inclusion of heterogeneous soil deposits and non-linear hysteretic damping would surely enhance the realism of the final outcome, although it may mislead the understanding of the physical mechanisms taking place, due to the increased number of parameters required. However, satisfactory broad-band synthetic time-histories were obtained by applying the ANN2BB procedure to the PBS outcome. This smart usage of the Artificial Neural Network seems rather attractive, even for weak aftershocks.

Based on these considerations, it can be argued that the current seismic design guidelines for critical structures should require further improvements of site-characterization not only in terms of active faults and local geotechnical conditions, but specifically on the conformation of the Earth's crust (such as the SCEC research plan for the period 2012-2016, focused on specific areas in the Southern California and enhanced the Community Velocity Model (CVM), describing seismic P- and S-wave velocities and densities throughout the southern California region). It is in the authors' belief that the modern procedures for earthquake ground motion prediction for seismic hazard analysis, especially for the low probability events inherent to the seismic design of critical structures, should account for a reliable incident wave-field issued from forward physics-based deterministic analyses. The ever increasing computational power leads to put major efforts to extend the frequency band and to enable PBS to be used with confidence in engineering applications (e.g.: seismic hazard analysis and structural or geotechnical dynamic analysis).

5.5 Preliminary simulation of the extended fault mechanism

Following the same approach outlined in the previous sections, the first and foremost step required to calibrate the $M_{JMA}6.8$ main shock earthquake scenario was the WNI simulation. The two main issues to address are :

1. the fault geometry and orientation
2. the suitable slip patch for a kinematic description of the fault offset

The preliminary WNI numerical analyses were limited to 1.0 Hz. Nevertheless, they steered the choice of a simplified yet reliable kinematic fault model, that was then plugged into the SEM3D computational model for a more detailed broad-band simulation.

The plethora of fault mechanism and related slip patches proposed from 2007 up to now for the NCOEQ2007 main shock (see Section 5.1.2 for the detailed discussion) was sifted to select two models to compare, namely (1) *Cirella2008* (Cirella et al., 2008) and (2) *Shiba2008* (Shiba, 2008). Slip patched are portrayed in Figures 5.42a-5.42b, following the discretization proposed by the authors. The two fault model looks rather different at glance: the *Cirella2008* fault plane is larger than the

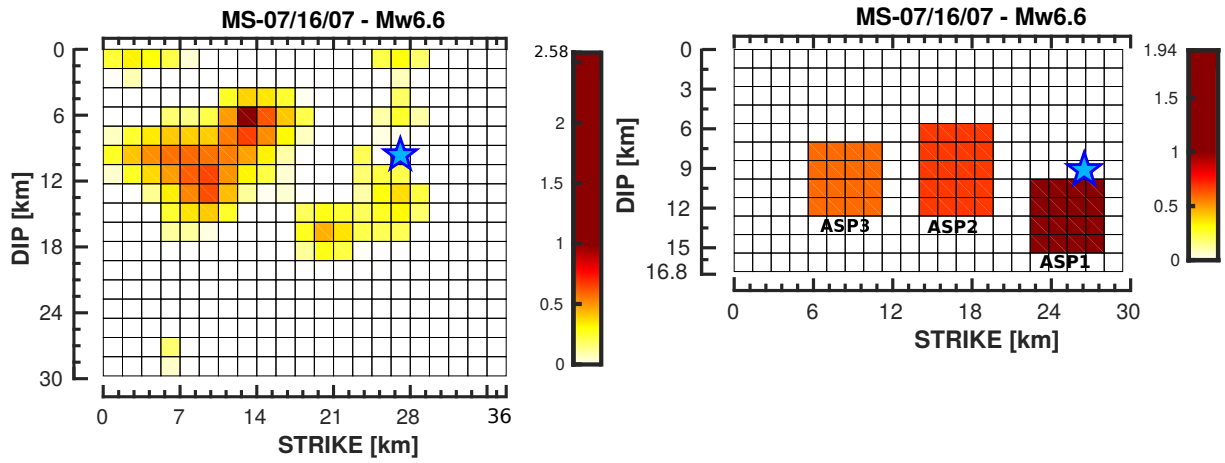

(a) (b)

Figure 5.42: (a) *Cirella2008* model for the SE dipping plane; (b) *Shiba2008* model for the SE dipping plane (Shiba, 2008).

Shiba2008 ones and its peak slip value is higher (2.58 m for *Cirella2008* and 1.94 m for *Shiba2008*). However, the bilobate slip distribution of the *Cirella2008* is shifted NW compared to the three major asperities identified by Shiba (2008).
Cirella et al. (2008) provided the peak slip velocity, rise time and rupture time contours, along with the slip distribution. On the other hand, *Shiba2008* model is featured by the stress-drop $\Delta\sigma$ inferred on three major rectangular asperities (see Table 5.2). Therefore, the average slip values $\bar{S}$ were estimated by means of the following Equation, proposed by Madariaga (1977):

$$\bar{S} = C\frac{\Delta\sigma}{\bar{\mu}}W \tag{5.3}$$

where C represents a shape coefficient (although formally rectangular, sub-faults were assumed to be circular shaped, by considering Madariaga proposition for $C = \frac{16\pi}{7}$). Moreover, the shear modulus of

Table 5.2: Properties of the characterized source model proposed by Shiba (2008) and inferred from the inverted slip source distribution.

	ASP1	**ASP2**	**ASP3**
Effective stress (MPa)	25.5	20.8	19.9
Seismic moment	1.83	2.11	1.43
Fault area (km^2)	5.6×5.6	5.6×7.0	5.6×5.6
Rupture Velocity (km/s)	3.1	2.8	2.5
Rise time (s)	0.4	0.4	0.5

the layers crossing each asperities were averaged along them ($\bar{\mu}$). In this manner, constant slip values were estimated onto each of the three asperities proposed by Shiba (2008). The choice of rectangular definition of asperities facilitates the generation of slip models of future earthquakes using this simple geometry. An asperity is initially defined to enclose fault elements whose slip is more than 1.5 times larger than the average slip over the fault plane. In their inversion analyses, Shiba (2008) exploited displacement records, band-pass filtered till 2.0 Hz.

5.5.1 WNI analysis of NCOEQ2007 earthquake

The WNI analyses performed on the NCOEQ2007 main shock are schematically presented in Figure 5.43 (*Cirella2008*) and Figure 5.44 (*Shiba2008*). Based on the previous results, the *Aochi2013* geology model was considered.
The two models provided rather good comparisons with the recordings, in a frequency range 0.1-0.5 Hz. High frequency content was herein disregarded due to the inherent limitations of the WNI method and to the interest into outlining the low-frequency band radiated from such complicated source mechanism. The best fit was obtained for the KKNPP (G.L.-250 m) and the NIG016 stations. However, there have some major discrepancies for stations collocated far from the hypocenter (NIG004, NIGH12) highlighting the intrinsic difficulties in modelling complex earthquake scenarios at this scale. An interesting aspect is the scarce fit at NIG018: the recorded wave-form is rather underestimated along the NS direction. This might be due to the fact that NIG018 was interested by liquefaction.

5.5.2 Large scale broad-band scenario

By the same token as previously, WNI results were exploited to calibrate large scale SEM3D simulations, once the most suitable fault mechanism has been chosen. The simple slip patch proposed by Shiba (2008) is used in a preliminary analysis, since it requires less parameters and it composes of three well-defined asperities only (see Table 5.2 and Figure 5.45a). Due to the lack of a kinematic model of the extended fault mechanism in SEM3D, most of the assumptions on the rupture path were dropped, in favour of a simplified yet reliable numerical simulation. Keeping this in mind, the slip contour was replaced by equivalent point sources, whose parameters were tuned upon the local stress-drop/seismic moment, rise time and spatial orientation along the fault plane. Each point-wise source triggers asynchronously, according to the rupture time contour picture in Figure 5.45b. The computational model of reference is the SMALL-W one, described in Section 5.3. The *Aochi2013* regional geological profile was considered in a first place.
The choice of a suitable number of point-wise double-couple sources capable of reproducing the continuous and dynamic fault offset is not an easy task. A main issue of debate is represented by the rise-time value. As a matter of fact, the scalar seismic moment is associated to the average cumulative fault slip regardless the approach to generate the extended seismic source (i.e. by either considering

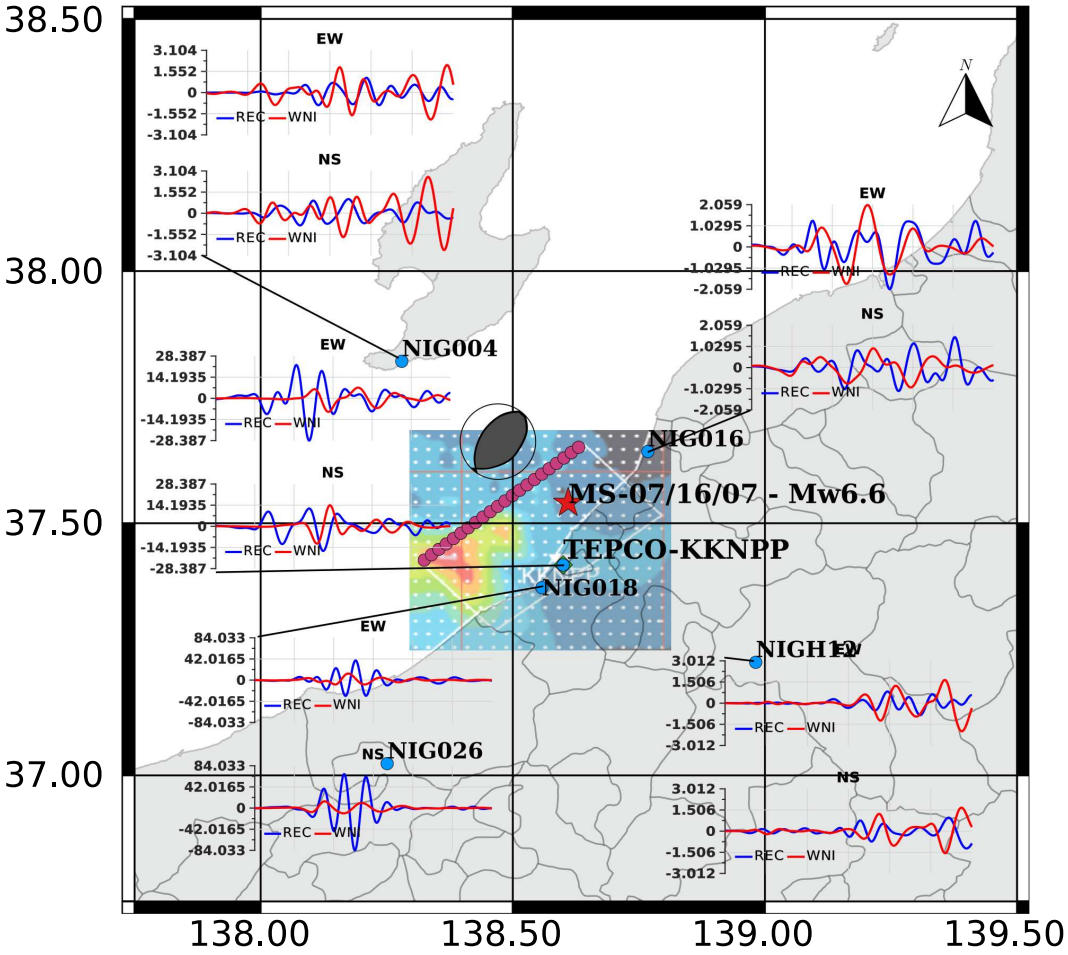

Figure 5.43: WNI simulations of the NCOEQ2007 M_j6.6 main shock of July 16, 10.13h. Blue wave-forms represent the recorded time-histories, red wave-forms the synthetics. Both records and synthetics were base-line corrected and band-passed filtered between 0.1 and 0.5 Hz. Synthetic wave-forms were obtained by either considering the soil profile *Aochi2013* and the source model proposed by Cirella et al. (2008)

a coherent slip patch or approximating it as a series of concentrated double-couples). The value of the time parameter, i.e. the rise time, cannot be straightly scaled from an estimation for a finite fault mechanism to a double-couple point source, due to the effect of the rupture front. Indeed, its empirical estimation is rather polluted by the effect of the propagating rupture and source directivity, along the whole slip duration. For instance, Bizzarri (2012) showed how difficult it is to estimate the rise time from a spontaneous dynamic faulting offset. Therefore, the rise-times provided in Table 5.2 have been found unsuitable for this kind of approach. Instead, a constant value of 1.3 s was estimated from Dreger et al. (2007) and provided to each double-couple representing the set of asperities.

The first trial analysis was performed by employing three double-couple sources, one per asperity. However a very poor fit to the recordings was obtained. At this point, the source model had to be integrated with further information, increasing the level of detail required to correctly describe the rupture path. To this end, a modification of the original *Shiba2008* model released in 2011 (Shiba et al., 2011) was considered. Compared to the previous model, in *Shiba2011* fault mechanism the three asperities, despite striking at the same angle (39°) have slightly different dip angles. The whole seismic source may therefore be seen as originated by a multi-segment fault rupture. The dip angle

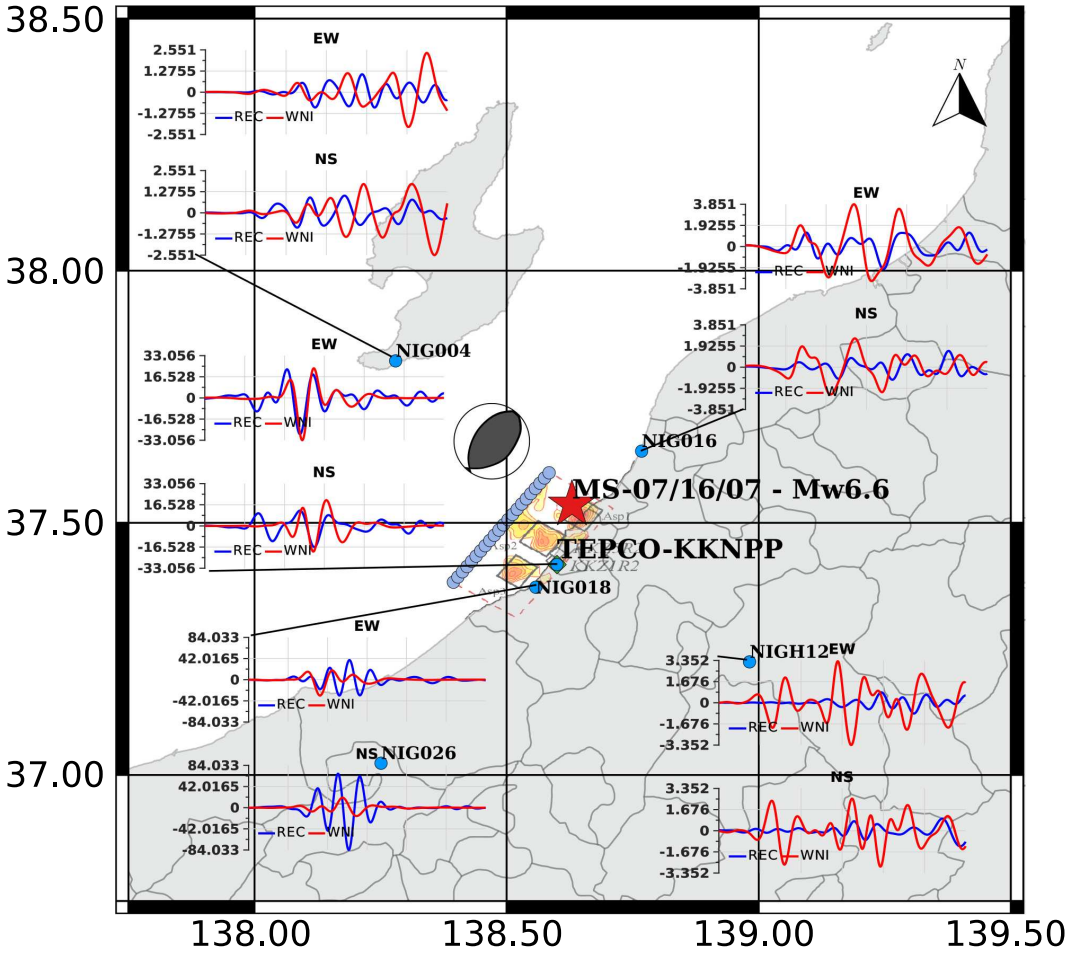

Figure 5.44: Same as Figure 5.43 and the source model proposed by Shiba (2008)

varies from 40° at ASP1 to 30° for ASP3, respectively, through a linear variation along ASP2. The latter was divided into five smaller rectangular sub-faults (i.e. double couples), each one placed at different depth and with dip angles linearly changing from 40° (northward, close to ASP1) to 30° (southward, in the surroundings of ASP3). Table 5.3 lists the newly determined fault parameters of the so called *Shiba2011* model. Stress drops slightly differ from the *Shiba2008* model, along with the seismic moment.

Two multi double-couple models are herein tested: PTS, composed by seven source points, one on ASP1 and ASP3 respectively and five along the NE-SW directrix on ASP2, to depict the assumed-linear dip angle variation (see Figure 5.46a) and GRD, with all three asperities duly discretized by 5×5 grid point each (see Figure 5.46b). The key feature of the PTS and GRD models resides in the fact that the second asperity ASP2 is modelled as multiple point sources instead than one, granting the correct transition from the rupture initiation (on ASP1) to the fault edge (ASP3). This aspect is likely to have been inferred from the fact that the second velocity pulse in KKNPP records was not clearly detected (Miyake et al., 2010). No nucleation times for each asperity was provided, but the point source time shift were set according to the rupture time contour in Figure 5.45b. A fairly good agreement with the recordings is observed, for both PTS and GRD (see the seismograms in Figure 5.47). This is a rather satisfactory result, given the crude assumptions made in the modelling phase. However, one can notice a slight directivity effect for PTS model, due to the location of the sources across ASP2. The energy radiated cumulates at the rupture front, resulting in a long period

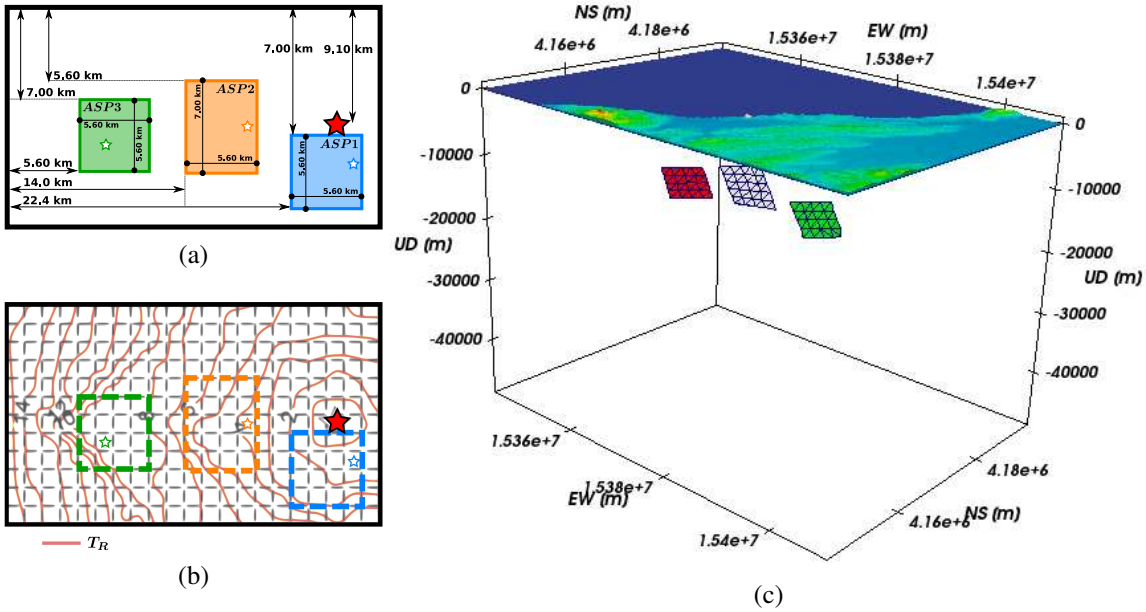

Figure 5.45: Geometry of the fault plane obtained by Shiba (2008). The three asperities ASP1 (blue), ASP2(orange) and ASP3 (green) are indicated (a). In (b) the rupture time T_R contour is shown. (c) Sketch of the SEM3D numerical model including the three asperities proposed by Shiba (2008) and Shiba et al. (2011).

Table 5.3: Properties of the characterized source model proposed by Shiba et al. (2011) and inferred from the inverted slip source distribution.

	ASP1	**ASP2**	**ASP3**
Effective stress (MPa)	23.15	20.84	19.91
Seismic moment (Nm)	1.09	2.11	1.43
Fault area (km^2)	5.6×4.2	5.6×7.0	5.6×5.6
Rupture Velocity (km/s)	3.0	2.8	3.0
Rise time (s)	0.4	0.4	0.4

impulsive wave-form impinging KKNPP, unlikely to occur. This is one of the prior shortcoming related to the simplified assumption made in this preliminary step of the analysis.
In terms of GMPEs, the brand new simulation seems more coherent with the recordings instead of respecting the empirical prediction, both in terms of PGA (Figure 5.48b) and PGV (5.48d). Although GMPEs are a reliable predictive tool, they might be influenced by the sake of generality and fail into estimating local site- and scenario- specific features, such as it is likely to occur herein. Evidently, when high-quality recordings are available, one must confront with real data instead.

5.5.3 Conclusions

This section presents some preliminary results concerning the simulation of the NCOEQ-2007 main shock. The extended fault rupture was first calibrated at low-frequency, by means of a semi-analytical solution. Thereafter, a distribution of point-wise double-couple moment tensors was employed to discretize the fault asperities and reproduce the overall mechanism, by SEM3D broad-band analyses. The results are rather promising, although majors simplified assumptions were introduced in the modelling. This preliminary investigation represents a solid basis for further numerical analysis, en-

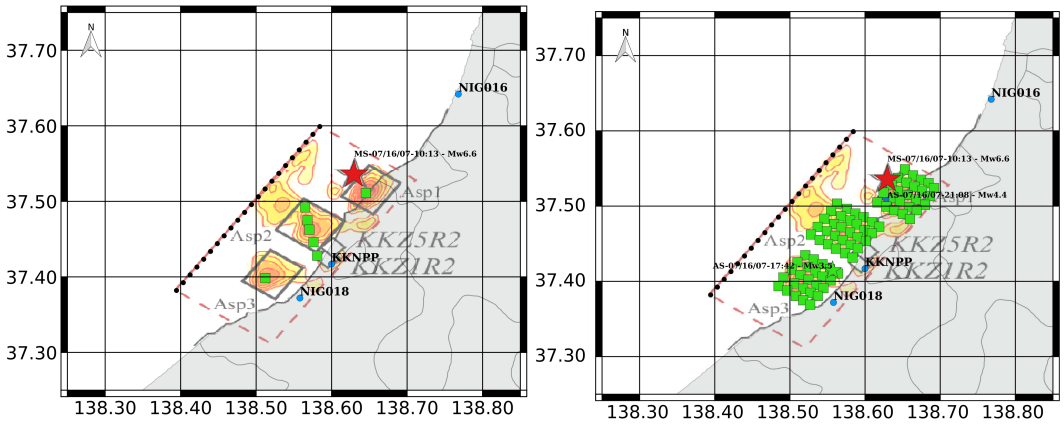

(a) (b)

Figure 5.46: Equivalent point-source model for extended fault mechanism. (a) Simplified model inspired by Shiba et al. (2011) slip contour, with seven double-couple points (PTS). (b) Refined model inspired by Shiba et al. (2011) slip contour, with a grid of double-couple points (GRD).

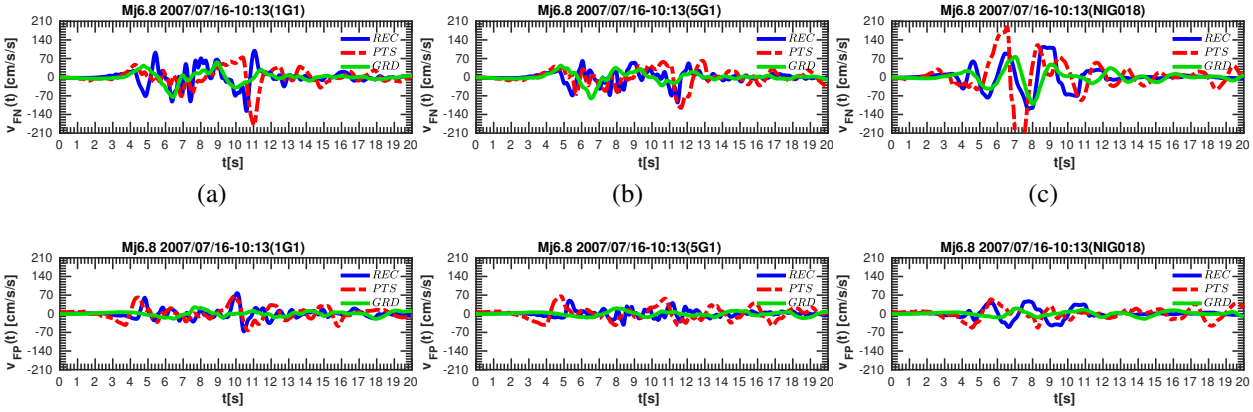

(a) (b) (c)

(d) (e) (f)

Figure 5.47: Synthetic velocity time histories obtained with the multi-point source SEM3D simulation for PTS model (red traces) and GRD model (green traces) compared to NCOEQ2007 recordings (blue traces). Comparisons along the FP/FN direction at recording stations 1G1 (a-d) and 5G1 (b-e), within KKNPP site and at KNET station NIG018 (c-f). Both recordings and synthetics were low-pass filtered at 5.0 Hz.

compassing a reliable kinematic model of the fault offset.

As things stand at present, the numerical implementation of a kinematic model of the fault rupture is being tested in SEM3D. The slip patch provided is obtained by an external software *RIKsrf* [5] (Gallovič, 2016). This software is a slip rate generator for earthquake strong ground motion simulations using an advanced kinematic source model based on the model of Ruiz et al. (2011). Main features of the RIK model are the introduction of randomly distributed overlapping sub-sources with fractal number-size distribution. Their position can be constrained by prior knowledge of major asperities (stemming, e.g., from slip inversions), or can be completely random. This fractal composition of the source model implies that the slip decays as k^{-2} at high wavenumbers k. The rise time is considered to depend on sub-source radius due to the positive correlation between slip and rise time

[5] source: https://github.com/fgallovic/RIKsrf

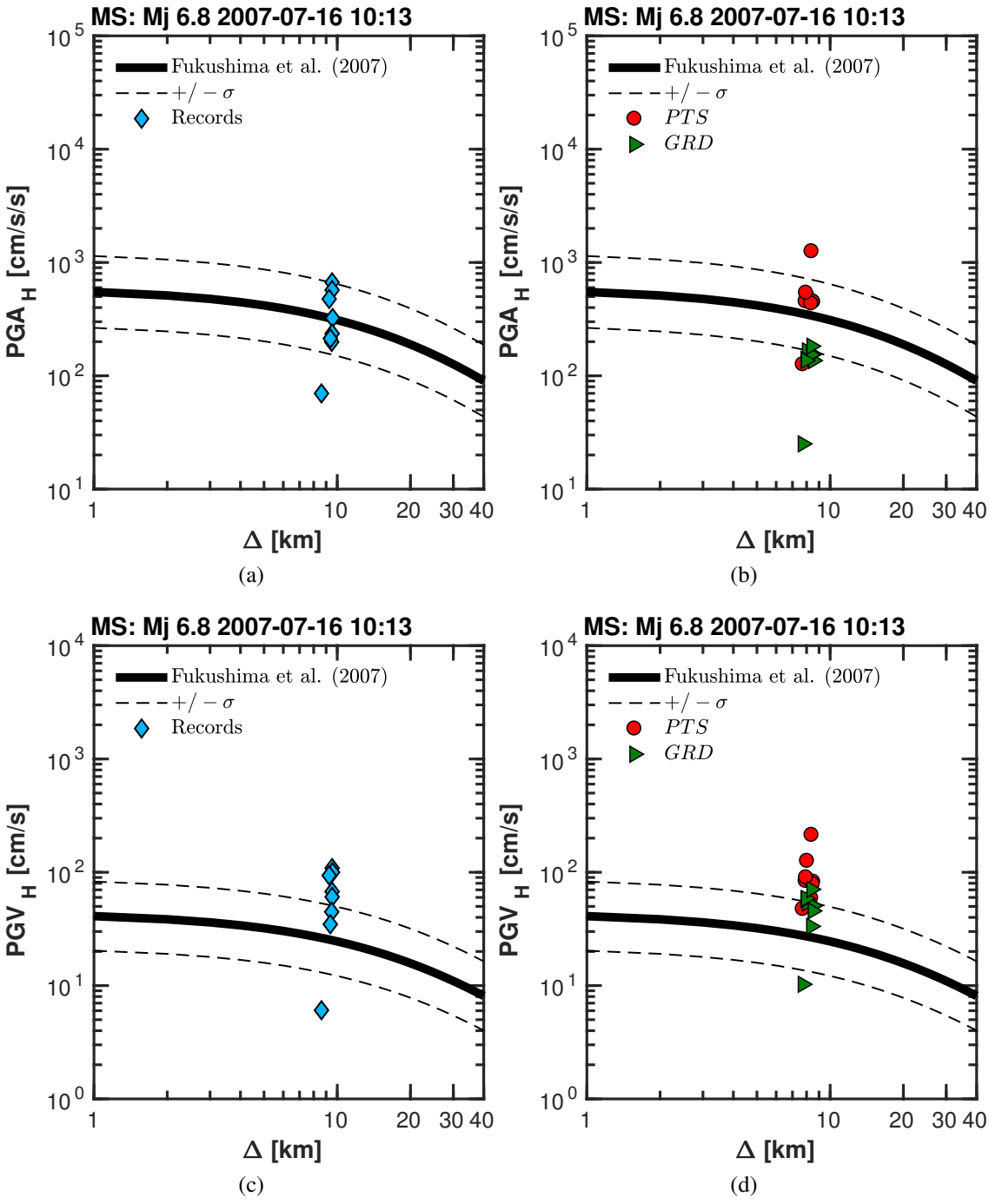

Figure 5.48: Horizontal geometric mean of Peak Ground Acceleration (PGA_H, portrayed in the left column) and Velocity (PGV_H, portrayed in the right column) obtained by SEM3D simulations of the M_j6.8 MS event. Synthetic peak ground motion values from model *Shiba2008* and *Shiba2011* are compared to the GMPE proposed by Fukushima (2007). (a-c) Recorded peak ground motion values (from Kik-Net, KNET and KKNPP database); (b-d) SEM3D simulations performed by introducing three point-wise double couple sources corresponding to the three asperities outlined featuring *Shiba2008* model (red circles) and *Shiba2011* model (green triangles). Thick black line represents the median PGA_H/PGV_H stemming from the chosen GMPE; dashed black lines ($\pm\sigma$) represent the standard deviations.

as observed in dynamic source modeling. The latter two properties ensures ω^{-2} decay of resulting source time function. Rupture velocity and rise time can follow local S-wave velocity profile, so that the rupture slows down and rise times increase close to the surface, avoiding unrealistically strong ground motions. Rupture velocity can be either constant or with have random variations, which results in irregular rupture front while satisfying the causality principle. The generated slip rates can be simply incorporated in any numerical wave propagation code without requiring any cross-over filtering with stochastic Green's functions. RIKsrf provides slip rate functions on a finely discretized source that result in synthetics with the desired ω^{-2} spectral decay in broad-band (up to 10.0 Hz) frequency range.

Another foreseen investigation concerns the role of the soil behaviour on the seismic site response, whose non-linear features have been widely recognized and modelled at the borehole scale (Kayen et al., 2009; Pavlenko and Irikura, 2012; Yee et al., 2011). To this end, a first attempt to perform a source-to-site non-linear site-response analysis was made by Pavlenko and Irikura (2012), using methods of stochastic finite-fault modelling to estimate the input motion to the soil layers during the main shock (recorded by the deepest sensor of the vertical array, e.g. SG4) for f$<$10 Hz. Following the holistic approach presented herein, however, the complete source-to-site analysis must be refined in terms of minimum wave-length solved by the computational model, as well as of topographical detail and, last but least, of shallow geological layers. To this end, the model described in this chapter my be poorly suitable for a so detailed and localized analysis. However, it may be efficiently exploited in the context of the Domain Reduction Method (DRM) proposed by Bielak et al. (2003a) and Bielak et al. (2003b). A first attempt, in this sense, has been made by Quinay et al. (2013), who applied the DRM to the KKNPP case, although their analysis was limited to 1 Hz. However, the proved efficiency of SEM3D in terms of broad-band propagation would surely improve those results. Moreover, SEM3D is already equipped with a non-linear constitutive behaviour (implemented by me, in the framework of the present research study) and a generator of 3D Gaussian random fields to model the soil heterogeneity (see Chapter 3).

6

Conclusions and Perspectives

"If we knew what it was we were doing, it would not be called research, would it?"
– Albert Einstein

The SINAPS@ project, which entirely financed this work, was conceived to gather the information coming from the earthquake engineering and the seismology to integrate them into an omni-comprehensive computational framework. The declared intent is to improve common design practices of critical structures (i.e. nuclear power plants) and revise the existent ones, with an innovative physics-based and source-to-structure slant. To this end, the chosen applicative case all the SINAPS@ workpackages are referring to is the seismic response of the Kashiwazaki-Kariwa Nuclear Power Plant, during the 2007 *Niigata-Ken Chūetsu-Oki* . The latter is a well documented seismic scenario, suitable for deep investigations on the near-field conditions, non-linear site-effects and structural analysis. Moreover, the site has been object of the KARISMA numerical benchmark, which highlighted some critical aspects of the site and structural response.
In this work, I have explicitly focused on some crucial aspects of the physics-based modelling of the NCO earthquake scenario. Inspired by the proposals of SINAPS@, the forging idea of the PhD project was to analyze all (or almost all) the different aspects of the problem, from a holistic point of view, featured by an uncertainty quantification. I avoided to concentrate only on a specific aspect of the whole computational framework, since I see the Engineering Seismology as a multi-disciplinary and multi-objective topic, which requires critical judgment and deep understanding of all the mechanisms influencing the wave-field propagation from the source to the structure. I preferred, instead, to provide a colorful panorama of the tools, methodologies (along with their criticality) current employed in computational earthquake engineering.

The earthquake-induced ground shaking scenario was first investigated and understood by analyzing the available seismic record database, partially referring to the KKNPP site and partially belonging to the K-NET/Kik-Net Japanese strong ground motion network. To this end, Chapter 2 present an extensive review of the consistent (yet hollow) piece of information available on the site. This was intended to pave the way to complex physics-based analyses, helping in understanding the phenomenon and constrain the numerical model. The analysis of the seismic records highlighted the impulsive nature of the wave-motion (typical of near-field conditions) along with the non-linear degradation of the stiffness of the shallow clayey and sandy deposits. The information provided regarding the velocity profile and the degradation curves were revised and modified so to be able to reproduce the site response by means of the Equivalent Linear Method. Further improvements are however possible, running for instance site-specific non-linear 1D and 3D analyses to reproduce the site de-amplification, along with the ground settlements observed (for further acknowledgements, please refer to Yee et al., 2011).

However, the main objective of this work is to quantify the uncertainty related to the practice of simulation-based earthquake predictions, from the source to the site-effects, in accordance with the philosophy of the SINAPS@ project. The second major effort of my thesis has been to produce realistic broad-band time-histories, either by pushing to the limit the accuracy of the deterministic computational models (i.e. $\sim$ 7 Hz), either by coupling them with meta-modelling predictions, such as the Artificial Neural Networks.
The first strategy is intrinsically related to the appropriateness of the earthquake rupture and of the 3D crustal models and rheology. Given the multifaceted nature of the earthquake phenomenon, the construction of realistic seismic scenarios was performed by exploiting different computational tools. Inspired by the SCEC philosophy, I participated into the construction of a HPC (High-Performance-Computing) multi-tool platform, whose main core is represented by a 3D Spectral Element code to solve the wave-propagation problem in viscous non-linear solid and fluid materials on massively parallel supercomputers. The code is featured by a highly scalable random field generator to simulate Earth's crust heterogeneity, along with a high-performance 27-tree based meshing tool to produce numerical model representing Earth's chunks, including topography and bathymetry. In a common context of lack of inherent data, verification and validation against observation are the principal means by which the predictive capability of ground motion simulation methods and their implementation can be assessed. This is the reason why in Chapter 3, the due verification tests have been provided along with the general presentation of the tools of virtual laboratory mentioned earlier. Moreover, a preliminary study on the effect of heterogeneous and non-linear soil deposits on the broad-band wave-motion coherency at the surface is assessed.

The core of this thesis is the physics-based simulation of the KKNPP during the *Niigata-Ken Chūetsu-Oki* . The numerical model was constructed by progressively including further ingredients and back-verifying the upgraded version at each time. The main issue I tackled was the effect of the geology on the regional wave-field. The earthquake source process was investigated as well, although preliminary results were provided. The simulation of two small aftershocks steered the calibration of the geological profiles, i.e. the broader, layered 1D geological structure, suitable for the low-frequency (0.0-0.5 Hz) regional wave-field and the refined 3D folded model to depict the spatial variability at KKNPP (up to 7.0 Hz). The latter analysis unveiled the reason behind the great ground motion incoherence recorded within relative short distances at the nuclear site: the syncline-anticline structure lying below the site caused a wave-motion drift towards Unit 1, where higher amplitude were effectively noticed. This implies the need for an accurate investigation of the deep geological profiles (i.e. up to $\sim$ 5.0 km of depth) when the critical and spatially extended structures are designed, other than the geomechanical characterization of shallower (i.e. up to $\sim$ 500 m of depth) soil deposits, responsible of non-linear site-effects.
Although less significant for slender and elongated structures (such as bridges), the need for broad-band synthetic earthquake seismograms is vital for the design of nuclear facilities, due to the presence of peculiarly rigid structures (such as the nuclear reactors) conceived for safety issues and embedded in the first meters of soil down depth. A critical factor in the numerical solution of the 3D wave equation with comprehensive physics is that the maximum frequency that can be modeled is a function of the model spatial resolution (i.e. grid spacing). Doubling the maximum frequency of the simulation generally results in an increase in computational demands (Bradley et al., 2017). Chapter 4 outlines a new procedure (called ANN2BB) for the hybrid generation of broad-band synthetic time-histories. This strategy bypass the hinder of burdensome computations, slightly deviating from the trending way of improving the earthquake prediction at larger frequency bands by simply constructing more complicated and fancy models. However, ANN2BB bares upon physics-based numerical simulations, by coupling the latter with the outcome (i.e. short-period pseudo-spectral ordinates) of Artificial Neural Networks, opportunely trained on heterogeneous seismic databases. This hybrid approach gravitates

around the need for realistic time-histories, whose response spectrum is compatible to the recorded observations. ANN2BB was applied to some recent Italian earthquake scenarios, with interesting results in terms of site-specific estimated time-histories. It represents a very appealing alternative to fully deterministic analyses, whenever the physical mechanism lying behind the observed records are not easy to be modelled at a certain scale. As immediate perspective, ANN2BB is about to be applied at a regional scale, so to portray reliable shaking maps and to calibrate lagged-coherency functions in a 0.0-20.0 Hz band. With the respect to traditional hybrid approaches (based on empirical or semi-empirical methods), ANN2BB should be able to preserve the ground motion coherency observed at low-frequency. It is in my belief that ANN2BB represents a *smart* meta-modelling technique to effectively cope with the lack of data, of suitable models, of computational resources and, least but last, of a deeper understanding of the earthquake phenomenon.

My PhD thesis represents the conceptual and computational foundation for further developments, intended to improve the multi-tool platform conceived for hybrid physics-based multi-scale simulations. Although not totally exhaustive in all the issues tackled, this document can be seen as a seminal work to be integrated in the very near future with the aspect listed below.

- Despite the argued inadequacy of the Armstrong-Frederick non-linear model to describe the non-linear soil behaviour at a laboratory scale, the key point of this choice the ease of implementation and the paucity of model parameters required. Moreover, the model efficacy was proven, when assessing the effect of the non-linearity on the earthquake ground motion coherency, paired with the description of the soil heterogeneity. Viewed in perspective, however, this choice does not diminish the overall quality of the analyses when considering the scale of the problem (i.e. $\sim$ 100 km). The typical spatial discretization (i.e. element size of $\sim$ 100 m) introduce a major approximation of the propagated wave-field, masking the secondary peculiarities of the cyclic hysteretic model chosen to represent the soil behaviour. However, a more adequate elastic-plastic non-linear model is going to be implemented in the next months, so to provide to SEM3D the necessary flexibility to accurately handle both regional-scale wave-propagation problems and specific site-scale ones. Put in perspective, this further effort is complementary with current parallel developments to couple SEM3D with a structural code (*CodeAster*, developed by EDF) to perform Soil-Structure Interaction studies on nuclear facilities.

- Strong earthquake ground motions are caused by the dynamic rupture of large portions of the Earth's crust, along major active faults. In this study, the complex slip distribution and rupture path was approximated by asynchronous double-couple source points, located in the surroundings of the major fault asperities. However, a numerical implementation of the kinematic finite fault model is being developed in SEM3D. The idea is to discretize the rupture surface by a fine computational grid. Each grid point is treated as a point-wise double-couple seismic source, whose fault offset time-history is provided by an external software, such as RIKsrf [1]. The Ruiz Integral Kinematic (RIK) earthquake source model (Ruiz et al., 2011) provides slip rate functions on a finely discretized source that result in synthetics with the desired ω^-2 spectral decay in full (broad-band) frequency range (f_{max} = 10.0 Hz). Currently, the due canonical verifications are being performed. However, in the very next few months, this tool will stably join the multi-tool platform we are constructing within the framework of the SEISM institute.

- The meshing code employed in this work, *HexMesh*, is currently under development, so to refine the structured mesh issued from the Digital Elevation Model, so to handle complex bathymetries and coastline discontinuities.

[1] https://github.com/fgallovic/RIKsrf

The practice of earthquake ground motion prediction is progressively drifting towards the forward all-embracing numerical simulation of the seismic scenarios. Despite the non-negligible intrinsic difficulties of producing realistic ground shaking simulations, physics-based numerical predictions of past earthquakes have been performed successfully so far. All over the world, seismologists and engineers are striving to increase the accuracy of seismological/geotechnical models along with the computational power of the numerical models required to carry the simulations out. Past and well documented strong-ground motion scenarios improve the understanding of complex phenomena from the source to the site with evident conceptual benefits if compared to empirical ground motion models based on worldwide data from historical earthquakes (Bradley et al., 2017). However, such deterministic approach suffers from great epistemic and aleatory uncertainty, which observations can rarely solve. One of the major problem concerns the detailed modelling of the high-frequency part of the recorded seismograms (see the objectives of the SCEC research plan).
Source-to-site deterministic models capable of portraying all the factors competing and interacting into producing broad-band (0.0-20.0 Hz) time-histories are still poorly constrained. As a matter of fact, a complete analysis should take into consideration the multi-scale thermo-hydro-mechanical processes responsible of the earthquake initiation and evolution, the complex interaction between radiated wave-field and complex 3D geological structures (often poorly described) including attenuation and scattering and, last but least, the site-effect triggered as the wave-fields propagates into the shallow geotechnical layers. If the structural components are included, the soil-structure interaction should be taken into consideration as well. It is evident that this highly non-linear and aleatory problem represent a hard challenge to be tackled with a purely deterministic approach.
Therefore, broad-band seismograms are nowadays routinely produced via hybrid approach, with quite a success. The latter consist in matching the low-frequency part of the signal, obtained by rigorous and well constrained physics-based simulations, with the high-frequency counterpart, obtained by semi-empirical or stochastic approaches. Meta-modelling is another appealing alternative, as for instance the employment of Artificial Neural Networks.
In this optics, the practice hybrid physics-based has become the most attractive tool for a solid Earthquake Ground Motion Prediction. Due to the technological and computational resources demanded to this end, multi-tool platforms have been developing ever since, along with consistent and multipurpose databases (such as the Community Models constructed by the SCEC). Within the framework of the SINAPS@ project, a similar effort has been and will be done, targeting the response of nuclear facilities in France and all over the world.

Forward simulations serve therefore as a solid tool to improve hazard assessment and mitigation of large urban areas from future events. As a matter of fact, this deterministic approach can seal some holes in the databases employed for broad-band Probabilistic Seismic Hazard Analysis (PSHA) and improve its disaggregated output. For instance, PSHA studies in region characterized by low to moderate seismicity, such as continental France, suffer of lack of strong ground motion recorded in near-field conditions. As far as the seismic design of critical structures is concerned (e.g. nuclear facilities), existent seismic scenarios are to be integrated with the outcome of physics-based simulated seismic responses, obtained both in operational and in extreme conditions. The KKNPP embodies a representative test case, in this sense, since it was conceived with a twofold design threshold: an Operating Basis Earthquake (OBE), for which the plant is expected to remain elastic, and the Safe Shutdown Earthquake (SSE), which triggers the shutdown of the facility (Pavlenko and Irikura, 2012). This strategy entails a strong interaction with the Probabilistic Seismic Demand Analysis (PSDA), a performance-based engineering procedure that combines ground motion hazard information with probabilistic structural response, providing a realistic distribution of ground motion intensities contributing to exceedance of a given structural response level. PSDA disaggregation is combined with the PSHA counterpart, so to determine the distribution of Magnitude-Distance pairs entailing the ex-

ceedance of a given structural response level. A typical design tool that PSDA provides is represented by the so called *fragility curves*. Disaggregation procedures with a vector-valued measure of ground motion intensity are available as well (Baker et al., 2005). When the tectonic and geological context is known, the calibrated numerical model can be routinely employed by changing source position and intensity, performing rigorous and detailed *stress-tests* on the seismic response of critical structures. This information provides additional insight to the engineer, and is also useful for verifying that a sufficient range of ground motion levels has been considered the assessment of a structure. Moreover, Operational Earthquake Forecasting and Earthquake Early Warning need for increased high-fidelity predictability, thanks to physics-based forecasting models, conditioning early-warning algorithms (Baker et al., 2005).

Appendices

Appendix A

The Spectral Element Method

A.1 Introduction

Partial Differential Equation (PDE) solutions can be approximated by exploiting different numerical methods. Spectral-type methods are based onto a discrete solution in the form of high-degree polynomial, thus being very accurate when smooth solutions are sought. On the other hand, singularities in the analytical are poorly represented, as well as domains with irregular boundaries are barely handled by those methods (unless domain decomposition methods are considered, Patera, 1984).
The Finite Element Method (FEM) solves PDEs by discrete approximating functions restricted to very small domains (called *elements*), yet exploiting low-degree polynomials. The method is well suited to problems with complex geometries and full non-linearities (both geometric and material-related). Nevertheless, its accuracy is limited by the polynomial degree (Ciarlet, 2002).
Several attempts have been made (see e.g. Patera, 1984; Babuska et al., 1981; Bernardi et al., 1990, among others) to combine the two methods into a unified framework, and thereby obtaining the advantages of both. The main idea consists of a decomposition of the domain into (rather) small regularly shaped sub-domains so as to fit the geometric complexity of the boundary, and then use high-degree polynomials in each sub-domain to approximate the solution. Two different approaches have been proposed: the Spectral Element Method (SEM) and the pFEM. finite element method. The SEM (Patera, 1984; Maday et al., 1987; Mayday et al., 1989) consists of using a spectral algorithm on a fixed number of sub-domains. On the opposite side, the so called p-version of the Finite Element Method exploits the discrete functions in the form of polynomials of fixed high degree on each element. These methods are fundamentally different, first by their origin but also, and mainly, because the bases and quadrature formulas required by the numerical discretization of the methods are completely different. In the Spectral Element Method, the sub-domains have to be curved parallelepipeds; this leads to the use of tensor-bases, so that consistent quadrature rules can be employed to compute the different integrals of the problem. This is not in general the case for the pFEM, and the resulting numerical problems are completely different, even in the number of operations required. The two methods present the same asymptotic behaviour but the operations count for the resolution of the resulting discrete equations is different. The idea presented in (Bernardi et al., 1990) is very different (see also Korczak and Patera, 1986). It consists of dividing the domain where the problem is to be solved in two parts; then, the problem is approximated by a finite element method on one part and by a spectral method on the other. Consequently, the discrete space consists of functions which are piecewise polynomial on one part and a high-degree polynomial of the other, and which satisfy a matching condition on the interface. Two kinds of such matching conditions are presented, analyzed mathematically and compared in (Bernardi et al., 1990): the first kind is a point-wise one, i.e., one requires the functions to be continuous at the nodes of the finite elements of the interface; the second kind is an integral one, where one requires the trace of the FEM function on the interface to be the

L^2 projection of the trace of the polynomial onto the finite element space. Of course, both algorithms are nonconforming in the general case, since it is impossible to match a high-degree polynomial and a piecewise polynomial function on the interface.
The most important conclusion of (Bernardi et al., 1990) is that, whatever the regularity of the exact solution is, better convergence results are obtained in the case of the integral matching condition. For this reason, an integral approach has been adopted herein.

A.2 Spectral Element Method: key points

Consider a PDE problem $\mathcal{P}(u)$ defined over the spatial domain Ω and with suitable boundary and initial conditions. In the Finite Element Method, the domain is subdivided into elements of size h and the solution u is approximated with piecewise polynomials of degree k in each element (usually, the adopted polynomials are of very low degree, being k = 1,2). Then, if u is sufficiently smooth, the approximated solution u_h converges to u as:

$$\lim_{h\to 0} \|u - u_h\|_{L^2(\Omega)} = \lim_{h\to 0} Ch^{k+1} \tag{A.1}$$

where $\|\cdot\|_{L^2(\Omega)}$ represents the L^2 error norm defined as:

$$\|\cdot\|_{L^2(\Omega)} = \left(\int_\Omega |\cdot|^2 dV\right)^{\frac{1}{2}} \tag{A.2}$$

and L^2 the space of square-integrable functions. In the Spectral Element Method, quadrature points are the so called Gauss-Legendre-Lobatto points (GLLs) Dave and Armstrong (1970). The coordinates of those points may be defined as follows. Consider a normalized 1D domain $D := [-1;1] \in \mathbb{R}$ and the N-degree Legendre polynomial $L_N(\xi) : D \to \mathbb{R}$, defined recursively as:

$$\begin{aligned} &L_0(\xi) = 1, L_1(\xi) = \xi \\ &(k+1) L_{k+1}(\xi) = (2k+1)\xi L_k(\xi) - k L_{k-1}(\xi), \quad k \geq 1 \end{aligned} \tag{A.3}$$

The spatial coordinates ξ_N^p of the ensemble of GLL points $\Xi^{N+1} := \{\xi_0^N, \xi_1^N, ..., \xi_N^N\} \in [-1;1]$ correspond to the $N-1$ roots of the L_N first space derivative $L_N'(\xi)$ and the extremes of D, $\{-1;1\}$ (Canuto et al., 1988):

$$\Xi^{N+1} := \{\xi^i \quad | \quad \left(1-\xi^2\right) L_N'(\xi) = 0\}, \qquad i \in [0;N] \cap \mathbb{N} \tag{A.4}$$

The latter set defines the $N+1$ GLL nodes in each space direction.
The spectral solution is then approximated with Lagrange interpolating polynomials $\psi_N^m(\xi) \in l_N(\xi) : D \to \mathbb{R}$ centered at each l GLL point (located at ξ^l):

$$\psi_N^l(\xi) = \prod_{k=1,k\neq l}^{N+1} \frac{\xi - \xi^k}{\xi^l - \xi^k} = -\frac{1}{N(N+1)} \frac{(1-\xi^2) L_N'(\xi)}{(\xi - \xi^l) L_N(\xi^l)} \tag{A.5}$$

The first evident implication of the Lagrange polynomial definition in Equation A.5 is the following:

$$\psi_N^l(\xi^m) = \delta^{lm} \tag{A.6}$$

being δ^{lm}[1] the Kronecker's delta.
In analogy with the FEM, the SEM approximated solution u_N of $\mathcal{P}(u)$ convergence is stated as:

$$\lim_{N\to\infty} \|u - u_N\|_{L^2(\Omega)} = Ce^{-\alpha N} \tag{A.7}$$

[1] apexes corresponds to the nodes at which the function is evaluates

Thus, by comparing Equation A.7 with Equation A.1 one can see that the SEM converges more rapidly than the FEM or, equivalently, it is more accurate for a given number of nodal points, a property known in the literature as *spectral accuracy*. This is the basic reason why spectral elements are being preferred to model the linear part of the domain. Note that for N very low, i.e. $N = 1,2$, the position of the GLL nodes and therefore the shape of the element coincides with the shape of the corresponding Finite Element. After Tromp et al. (2008), using 4^{th} or 5^{th} order Lagrange polynomial might provide a best trade-off between accuracy and computational time. However, typically much higher values of N are used in the SEM, e.g. $3 < N < 10$, and in these cases the spacing of the nodes is not even: the nodes tend to cluster near the element borders and are rarefied in the interior (Komatitsch, 1997). In particular, if h is the distance between the extreme nodes, the grid spacing decrease as $1/h$ at the center, whereas it diminish to $1/h^2$ close to the interval boundaries (Delavaud, 2007). This fact is a potential serious drawback as far as the use of such elements in an explicit time integration context is concerned (Casadei and Gabellini, 1997). In fact, explicit methods are conditionally stable, and the critical integration step is proportional to the minimum intra-nodal distance, as stated by the so called *Courant-Friedrichs-Levy condition* (CFL) (Casadei and Gabellini, 1997). While the FEM usually employs a uniform grid within each element, so that the critical time step $\Delta t_{max} \sim N^{-1}$, in the SEM with GLL grid the dependency is on $\Delta t_{max} \sim N^{-1}$. Thus the use of too fine spectral discretization is rather cumbersome in an explicit context. That is why an efficient parallelization is required (Göddeke et al., 2014). Besides the relative position of the nodes, another relevant practical characteristic of the SEM with the respect to the FEM is the spatial integration rule adopted in order to compute the element's integrals. As a matter of fact, in order to preserve the high accuracy of the SEM approximation, the GLL is used, so to efficiently take into consideration the boundary conditions. In the FEM, the well-known Gauss quadrature rule is exploited, the sampling points ξ^k being internal to the element's domain and the optimal accuracy $o(2N-1)$ with N sampling points (in 1D, Canuto et al., 1988):

$$\begin{cases} \displaystyle\int_{-1}^{1} \phi(\xi)\, d\xi = \sum_{k=0}^{N} \phi\left(\xi^k\right) \omega_k, & \forall \phi \in \mathbb{P}_{2N-1} \qquad \text{(A.8)} \\ \displaystyle\omega_k = \frac{2}{N(N+1)} \frac{1}{L_N(\xi^k)} > 0 & \qquad \text{(A.9)} \end{cases}$$

It turns out that the points at which the unknown variables (displacements, velocities and accelerations) are solved do not coincide with the grid points where the element variables (strains, stresses and material-related quantities) are evaluated. In the SEM, on the other hand, it appears more natural to use the GLL integration rule, because in this way the sampling points coincide with the nodal points. This has a very important practical advantage, in that all the element integrands containing expressions involving the element's shape functions ψ, are easily evaluated at these very points thanks to the properties A.6 (Casadei and Gabellini, 1997).

A.3 Governing equations

Let us consider an elastic medium occupying an open domain $\Omega \subset \mathbb{R}^d$ bounded by a smooth boundary $\partial\Omega$, with the closure $\bar{\Omega} = \Omega \cup \partial\Omega$. Let us call $\mathbb{I}_t = [0, T] \subset \mathbb{R}_+$ the time interval of interest. The displacement and velocity fields are denoted as $\underline{\boldsymbol{u}}(\underline{\boldsymbol{x}}; t) : \bar{\Omega} \times \mathbb{I}_t \to \mathbb{R}^d$ and $\underline{\boldsymbol{v}}(\underline{\boldsymbol{x}}; t) = \dot{\underline{\boldsymbol{u}}}(\underline{\boldsymbol{x}}; t)$ respectively (with $\dot{\square}$ indicating the material time derivative). The Euler-Lagrange equations of elastodynamics can be stated as (Lagrange, 1853):

$$\begin{cases} \underline{\boldsymbol{\nabla}}_x \cdot \underline{\underline{\boldsymbol{\sigma}}}\left(\underline{\boldsymbol{u}}(\underline{\boldsymbol{x}}; t); \underline{\boldsymbol{v}}(\underline{\boldsymbol{x}}; t)\right) + \underline{\boldsymbol{b}}(\underline{\boldsymbol{x}}; t) = \rho(\underline{\boldsymbol{x}}; t)\, \dot{\underline{\boldsymbol{v}}}(\underline{\boldsymbol{x}}; t) & \forall (\underline{\boldsymbol{x}}; t) \in \Omega \times \mathbb{I}_t \qquad \text{(A.10)} \\ \rho(\underline{\boldsymbol{x}}; t)\, \underline{\boldsymbol{v}}(\underline{\boldsymbol{x}}; t) = \rho(\underline{\boldsymbol{x}}; t)\, \dot{\underline{\boldsymbol{u}}}(\underline{\boldsymbol{x}}; t) & \qquad \text{(A.11)} \end{cases}$$

with $\rho(\underline{\boldsymbol{x}};t) = \rho(\underline{\boldsymbol{x}}) > 0$, $\rho(\underline{\boldsymbol{x}}) \in L^{\infty}(\Omega)$ the unit mass density, $\underline{\boldsymbol{b}}(\underline{\boldsymbol{x}};t) \in [L^2(\Omega \times \mathbb{I}_t)]^d$ the body forces, $\underline{\underline{\boldsymbol{\sigma}}}(\underline{\boldsymbol{x}};t) : \bar{\Omega} \times \mathbb{I}_t \rightarrow \mathbb{S} \subset \mathbb{R}^{d \times d}$ the symmetric Cauchy stress tensor. Here $\mathbb{S}$ is the subspace of symmetric second-order tensors of dimension $d(d+1)/2$. The relationship between $\underline{\underline{\boldsymbol{\sigma}}}$ and displacement/velocity fields $\underline{\boldsymbol{u}}(\underline{\boldsymbol{x}};t)$ $\underline{\boldsymbol{v}}(\underline{\boldsymbol{x}};t)$ depends on the chosen rheology, and it will made explicit in the following paragraphs. However, when the solid domain is considered as purely elastic and isotropic, $\underline{\underline{\boldsymbol{\sigma}}}(\cdot)$ is a linear map expressed as follows:

$$\underline{\underline{\boldsymbol{\sigma}}}(\underline{\boldsymbol{u}}(\underline{\boldsymbol{x}};t)) = \lambda(\underline{\boldsymbol{x}})\, Tr\left(\underline{\underline{\boldsymbol{\varepsilon}}}_x(\underline{\boldsymbol{u}}(\underline{\boldsymbol{x}};t))\right) + 2\mu(\underline{\boldsymbol{x}})\, \underline{\underline{\boldsymbol{\varepsilon}}}_x(\underline{\boldsymbol{u}}(\underline{\boldsymbol{x}};t)) \tag{A.12}$$

with $\lambda(\underline{\boldsymbol{x}})$, $\mu(\underline{\boldsymbol{x}})$ are the so called Lamé coefficients, and the linear operator $\underline{\underline{\boldsymbol{\varepsilon}}}_x(\cdot)$ is the small strain tensor, defined as:

$$\underline{\underline{\boldsymbol{\varepsilon}}}_x(\underline{\boldsymbol{u}}(\underline{\boldsymbol{x}};t)) = \underline{\boldsymbol{u}} \otimes_s \underline{\boldsymbol{\nabla}}_x(\underline{\boldsymbol{x}};t) \tag{A.13}$$

being $\underline{\cdot} \otimes_s \underline{\boldsymbol{\nabla}}_x$ the symmetric gradient operator. However, the stress strain relationship is not always linear (see for instance the elasto-plasticity theory). The dependency on the velocity field kicks in when modelling viscosity.
Equations A.11 is supplied with the initial conditions:

$$\begin{cases} \underline{\boldsymbol{u}}(\underline{\boldsymbol{x}};0) = \underline{\boldsymbol{u}}_0(\underline{\boldsymbol{x}}) & \forall(\underline{\boldsymbol{x}}) \in \Omega \quad \text{(A.14)} \\ \underline{\boldsymbol{v}}(\underline{\boldsymbol{x}};0) = \underline{\boldsymbol{v}}_0(\underline{\boldsymbol{x}}) & \forall(\underline{\boldsymbol{x}}) \in \Omega \quad \text{(A.15)} \end{cases}$$

and the following Neumann's boundary condition:

$$\underline{\boldsymbol{t}}_n = \underline{\underline{\boldsymbol{\sigma}}}(\underline{\boldsymbol{x}};t).\underline{\boldsymbol{n}}(\underline{\boldsymbol{x}};t) = \underline{\boldsymbol{t}}_{n,0}(\underline{\boldsymbol{x}};t) \qquad \forall(\underline{\boldsymbol{x}};t) \in \Gamma_T \times \mathbb{I}_t \tag{A.16}$$

with $\Gamma_T \subseteq \partial\Omega$ the surface where the Neumann's conditions are applied. For the sake of simplicity, $\Gamma_T = \partial\Omega$ and a free-surface is assumed (i.e. $\underline{\boldsymbol{t}}_{n,0} = \underline{\boldsymbol{0}}$).

A.4 Variational formulation of the elasto-dynamic problem

The solution of the Euler-Lagrange equation, supplied by complex boundary conditions, rarely has a closed form. However, $\underline{\boldsymbol{u}}(\underline{\boldsymbol{x}};t)$ may be sought in the functional space of the kinematic-admissible fields $\mathcal{S}^t$ defined as follows:

$$\begin{aligned} \mathcal{S}^t := \{&\underline{\boldsymbol{u}}(\underline{\boldsymbol{x}};t) : \Omega \times \mathbb{I}_t \rightarrow \mathbb{R}^d | \underline{\boldsymbol{u}} \in H^1(\Omega)^d, \forall t \in \mathbb{I}_t; \\ &\underline{\boldsymbol{u}}(\underline{\boldsymbol{x}};t) = \underline{\boldsymbol{g}}(\underline{\boldsymbol{x}};t), \forall(\underline{\boldsymbol{x}};t) \in \Gamma_D \times \mathbb{I}_t\} \end{aligned} \tag{A.17}$$

where $H^1(\Omega)$ represents the Sobolev's space of the functions in $L^2(\Omega) = H^0(\Omega)$ with their gradient (in a distributional sense) in $[L^2(\Omega)]^d$. $\underline{\boldsymbol{g}}$ represents the eventual displacement imposed as Dirichlet's condition onto the boundary $\Gamma_D \subseteq \partial\Omega$. Furthermore, the space of admissible displacements $\delta\mathcal{S}$ is expressed as:

$$\begin{aligned} \delta\mathcal{S} := \{&\underline{\boldsymbol{w}}(\underline{\boldsymbol{x}}) : \Omega \rightarrow \mathbb{R}^d | \underline{\boldsymbol{w}} \in H^1(\Omega)^d; \\ &\underline{\boldsymbol{w}}(\underline{\boldsymbol{x}}) = \underline{\boldsymbol{0}}, \forall \underline{\boldsymbol{x}} \in \Gamma_D\} \end{aligned} \tag{A.18}$$

At this point, the variational formulation consists in finding the couple $(\underline{\boldsymbol{u}}, \underline{\boldsymbol{v}}) \in \mathcal{S}^t \times \mathcal{S}^t$ that solves, for all test functions $\underline{\boldsymbol{w}} \in \delta\mathcal{S}$ and $\forall t \in \mathbb{I}_t$, the following equations, obtained by multiplying left-

and right-hand sides of Equations A.11, A.15 and A.16 by the kinematic admissible field $\underline{\boldsymbol{w}}\left(\underline{\boldsymbol{x}}\right)$ and integrating over the domain volume Ω (Komatitsch and Vilotte, 1998):

$$\begin{cases} \left(\underline{\boldsymbol{w}}\left(\underline{\boldsymbol{x}}\right), \rho\left(\underline{\boldsymbol{x}}\right)\underline{\dot{\boldsymbol{v}}}\left(\underline{\boldsymbol{x}};t\right)\right)_{\Omega} = \left(\underline{\boldsymbol{w}}\left(\underline{\boldsymbol{x}}\right), \underline{\boldsymbol{b}}\left(\underline{\boldsymbol{x}};t\right)\right)_{\Omega} - \mathbb{A}_{\Omega}\left(\underline{\boldsymbol{w}}\left(\underline{\boldsymbol{x}}\right), \underline{\boldsymbol{u}}\left(\underline{\boldsymbol{x}};t\right)\right) + \left(\underline{\boldsymbol{w}}\left(\underline{\boldsymbol{x}}\right), \underline{\boldsymbol{t}}_{n,0}\left(\underline{\boldsymbol{x}};t\right)\right)_{\Gamma_T} \\ \left(\underline{\boldsymbol{w}}\left(\underline{\boldsymbol{x}}\right), \rho\left(\underline{\boldsymbol{x}}\right)\underline{\boldsymbol{v}}\left(\underline{\boldsymbol{x}};t\right)\right)_{\Omega} = \left(\underline{\boldsymbol{w}}\left(\underline{\boldsymbol{x}}\right), \underline{\dot{\boldsymbol{u}}}\left(\underline{\boldsymbol{x}};t\right)\right)_{\Omega} \end{cases} \tag{A.19}$$

(A.20)

with initial conditions:

$$\begin{cases} \left(\underline{\boldsymbol{w}}\left(\underline{\boldsymbol{x}}\right), \underline{\boldsymbol{u}}\left(\underline{\boldsymbol{x}};0\right)\right)_{\Omega} = \left(\underline{\boldsymbol{w}}\left(\underline{\boldsymbol{x}}\right), \underline{\boldsymbol{u}}_0\left(\underline{\boldsymbol{x}}\right)\right)_{\Omega} \\ \left(\underline{\boldsymbol{w}}\left(\underline{\boldsymbol{x}}\right), \underline{\boldsymbol{v}}\left(\underline{\boldsymbol{x}};0\right)\right)_{\Omega} = \left(\underline{\boldsymbol{w}}\left(\underline{\boldsymbol{x}}\right), \underline{\boldsymbol{v}}_0\left(\underline{\boldsymbol{x}}\right)\right)_{\Omega} \end{cases} \tag{A.21}$$

The inner products in Equations A.20 and A.21 are defined as :

- $\left(\underline{\boldsymbol{w}}, \underline{\boldsymbol{u}}\right)_{\Omega} = \int_{\Omega} \underline{\boldsymbol{w}}.\underline{\boldsymbol{u}} dV_x$
- $\left(\underline{\boldsymbol{w}}, \underline{\boldsymbol{t}}_n\right)_{\Gamma_T} = \int_{\Gamma_T} \underline{\boldsymbol{w}}.\underline{\boldsymbol{t}}_n dS_x$

and bilinear form $\mathbb{A}_{\Omega}(\underline{\boldsymbol{w}}, \underline{\boldsymbol{u}})$ is defined by:

$$\mathbb{A}_{\Omega}(\underline{\boldsymbol{w}}, \underline{\boldsymbol{u}}) = \int_{\Omega} \left(\underline{\boldsymbol{\nabla}}_x \otimes \underline{\boldsymbol{w}}\right) : \underline{\underline{\boldsymbol{\sigma}}}\left(\underline{\boldsymbol{u}}\right) dV_x \tag{A.22}$$

The bilinear form in Equation A.22 is symmetric, V-elliptic and continuous (Antonietti et al., 2012). The variational formulation may therefore be rewritten in a more generic way as:
Find the couple $\left(\underline{\boldsymbol{u}}; \underline{\boldsymbol{v}}\right) \in \mathcal{S}^t \times \mathcal{S}^t$ *that solves the equations:*

$$\begin{cases} \partial_t \left(\underline{\boldsymbol{w}}, \rho\underline{\boldsymbol{v}}\right)_{\Omega} + \mathbb{A}_{\Omega}\left(\underline{\boldsymbol{w}}, \underline{\boldsymbol{u}}\right)_{\Omega} = \mathcal{L}\left(\underline{\boldsymbol{w}}\right), \forall \underline{\boldsymbol{w}} \in \delta\mathcal{S} & \text{(A.23)} \\ \partial_t \left(\underline{\boldsymbol{w}}, \underline{\boldsymbol{u}}\right)_{\Omega} = \left(\underline{\boldsymbol{w}}, \underline{\boldsymbol{v}}\right)_{\Omega} & \text{(A.24)} \end{cases}$$

where ∂_t represent the time-derivative, and $\mathcal{L} : \delta\mathcal{S} \rightarrow \mathbb{R}^d$ represents a linear functional and is equal to $\left(\underline{\boldsymbol{w}}, \underline{\boldsymbol{b}}\right)_{\Omega} + \left(\underline{\boldsymbol{w}}, \underline{\boldsymbol{t}}_{n,0}\right)_{\Gamma_T}$. The solution of the variational formulation in Equation A.20 corresponds to the minimum of the energy associated to the Euler equation (Delavaud, 2007).

A.5 Spatial discretization

Semi-discrete approximation of the variational problem

The domain $\bar{\Omega}$ is discretized into N_e elements $\bar{\Omega}_e$ such that $\bar{\Omega} = \cup_{e=1,N_e} \bar{\Omega}_e$ and the intersection between two distinct elements $e^{'}$ and e $\bar{\Omega}_{e'} \cap \bar{\Omega}_e$ is an element's corner, edge or face. In turns, the semi-discretized problem reads:

$$\begin{aligned} &\sum_{e=1}^{N_e} \left(\underline{\boldsymbol{w}}_e\left(\underline{\boldsymbol{x}}_e\right), \rho\underline{\dot{\boldsymbol{v}}}_e\left(\underline{\boldsymbol{x}}_e;t\right)\right)_{\Omega_e} = \sum_{e=1}^{N_e} \left(\underline{\boldsymbol{w}}_e\left(\underline{\boldsymbol{x}}_e\right), \underline{\boldsymbol{b}}_e\left(\underline{\boldsymbol{x}}_e;t\right)\right)_{\Omega_e} - \\ &- \sum_{e=1}^{N_e} \mathbb{A}_{\Omega_e}\left(\underline{\boldsymbol{w}}_e\left(\underline{\boldsymbol{x}}_e\right), \underline{\boldsymbol{u}}_e\left(\underline{\boldsymbol{x}}_e;t\right)\right) + \sum_{e=1}^{N_e} \left(\underline{\boldsymbol{w}}_e\left(\underline{\boldsymbol{x}}_e\right), \underline{\boldsymbol{t}}_e; t\left(\underline{\boldsymbol{x}}_e\right)\right)_{\bar{\Omega}_e \cap \Gamma_T} \end{aligned} \tag{A.25}$$

Equation A.25 represents the semi-discrete approximation of the variational formulation expressed in Equation A.20, with each of the terms approximated by the all the single element contributions,

according to:

$$\begin{cases} \left(\underline{\boldsymbol{w}}\left(\underline{\boldsymbol{x}}\right), \rho\left(\underline{\boldsymbol{x}}\right)\underline{\dot{\boldsymbol{v}}}\left(\underline{\boldsymbol{x}};t\right)\right)_{\Omega} = \sum_{e=1}^{N_e}\left(\underline{\boldsymbol{w}}_e\left(\underline{\boldsymbol{x}}_e\right), \rho\underline{\dot{\boldsymbol{v}}}_e\left(\underline{\boldsymbol{x}}_e;t\right)\right)_{\Omega_e} & \text{(A.26)} \\ \left(\underline{\boldsymbol{w}}\left(\underline{\boldsymbol{x}}\right), \underline{\boldsymbol{b}}\left(\underline{\boldsymbol{x}};t\right)\right)_{\Omega} = \sum_{e=1}^{N_e}\left(\underline{\boldsymbol{w}}_e\left(\underline{\boldsymbol{x}}_e\right), \underline{\boldsymbol{b}}_e\left(\underline{\boldsymbol{x}}_e;t\right)\right)_{\Omega_e} & \text{(A.27)} \\ \mathbb{A}_{\Omega}\left(\underline{\boldsymbol{w}}\left(\underline{\boldsymbol{x}}\right), \underline{\boldsymbol{u}}\left(\underline{\boldsymbol{x}};t\right)\right) = \sum_{e=1}^{N_e}\mathbb{A}_{\Omega_e}\left(\underline{\boldsymbol{w}}_e\left(\underline{\boldsymbol{x}}_e\right), \underline{\boldsymbol{u}}_e\left(\underline{\boldsymbol{x}}_e;t\right)\right)_{\Omega_e} & \text{(A.28)} \\ \left(\underline{\boldsymbol{w}}\left(\underline{\boldsymbol{x}}\right), \underline{\boldsymbol{t}}\left(\underline{\boldsymbol{x}};t\right)\right)_{\Gamma_T} = \sum_{e=1}^{N_e}\left(\underline{\boldsymbol{w}}_e\left(\underline{\boldsymbol{x}}_e\right), \underline{\boldsymbol{t}}_e;t\left(\underline{\boldsymbol{x}}_e\right)\right)_{\bar{\Omega}_e\cap\Gamma_T} & \text{(A.29)} \end{cases}$$

where the footnote e represents the restriction of the Cartesian system of physical spatial coordinates $\underline{\boldsymbol{x}}$ to $\bar{\Omega}_e$. The latter discretization of the physical domain defines a quadrangulation $\mathcal{I}^h\left(\bar{\Omega}\right)$, h referring to the scale of the characteristic dimension that parametrizes the geometric discretization.

Geometrical mapping

In the spectral element geometrical computations (which are performed before entering the time loop for the transient solution), as well as in many other models, the following problem is encountered: given a point P and a geometrical figure (e.g., an element or an element face), determine whether or not the point lies within the figure. Sometimes, in the case that the point lies inside, it is also required to determine the normalized coordinates of the point with respect to the figure. This problem can be viewed as the inverse of the mapping transformations often used in Finite Element formulations. Therefore, on each element the quadrature formulas (see integrals above) are defined over a Cartesian hyper-cubic reference domain $\square_{\Omega} = [-1;1]^d$ (see Figure A.1). In this sense, each spectral element

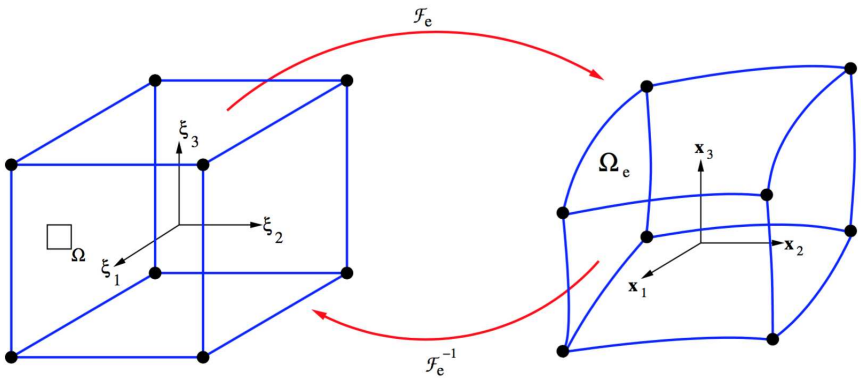

Figure A.1: 8-node hexahedral reference element and the mapping function

$\bar{\Omega}_e$ represents the image of $\square_{\Omega}$ by means of the regular diffeomorphism $\mathcal{F}_e$, i.e. the invertible function which maps the smooth manifold $\square_{\Omega}$ to another $\bar{\Omega}_e$, such that both $\mathcal{F}_e$ and its inverse $\mathcal{F}_e^{-1}$ are smooth (i.e. their derivatives of all orders are defined everywhere in their respective domains). This map can be expressed as follows:

$$\mathcal{F}_e : \square_{\Omega} \rightarrow \bar{\Omega}_e| \quad \underline{\boldsymbol{x}}_e = \underline{\boldsymbol{x}}|_e = \mathcal{F}_e\left(\underline{\boldsymbol{\xi}}\right), \underline{\boldsymbol{\xi}} = (\xi_1, ..., \xi_d) \in \square_{\Omega} \tag{A.30}$$

where $\underline{\boldsymbol{\xi}}$ is the Cartesian system of coordinates defined over the reference element $\square_{\Omega}$. A suitable and regular map $\mathcal{F}_e$ can be defined by means of the linear combination of the $\mathcal{N} = (N+1)^d$[2] multi-

[2] $\mathcal{N}$ represents the total number of control point on the element $\bar{\Omega}_e$

dimensional shape functions $\underline{\boldsymbol{\Psi}}^L\left(\underline{\boldsymbol{\xi}}\right)$, derived from the tensorization of 1D Lagrange polynomials (one per direction) of order N. A sample of position of GLL points on a 2D element of 9th order is shown in Figure A.2a, and an example of the 9th order Lagrange polynomials is shown in Figure A.2b. The k^{th} component of $\underline{\boldsymbol{x}}_e$ can be expressed as:

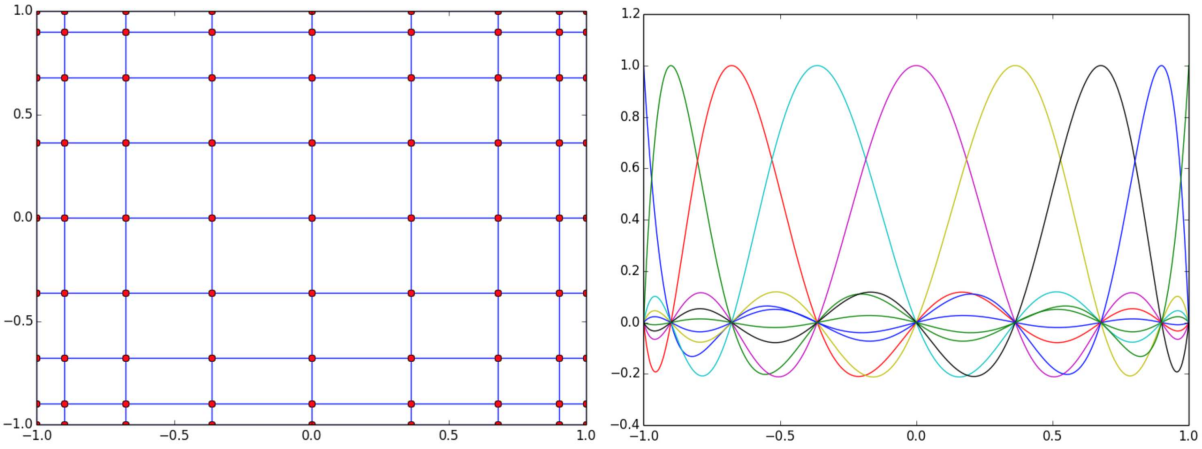

(a) (b)

Figure A.2: (a) Positions of GLL points on a 2D element of order 9. (b) Lagrange polynomial of order 9 (Delavaud, 2007)

$$x_{e_k} = \sum_{L=1}^{\mathcal{N}} \Psi_k^L\left(\underline{\boldsymbol{\xi}}\right) x_{e_k}^L \tag{A.31}$$

$$\underline{\boldsymbol{\Psi}}^L\left(\underline{\boldsymbol{\xi}}\right) = \sum_{k=1}^{d} \Psi_k^L\left(\underline{\boldsymbol{\xi}}\right) \underline{\boldsymbol{e}}_k \tag{A.32}$$

where $x_{e_k}^L$ is the k^{th} component of $\underline{\boldsymbol{x}}_e^L$, set of physical coordinates of *control points* indexed as L within the element e (i.e. whose coordinates are $\underline{\boldsymbol{x}}_e^L = \underline{\boldsymbol{x}}_e\left(\underline{\boldsymbol{\xi}}^L\right)$). $\Psi_k^L\left(\underline{\boldsymbol{\xi}}\right)$ represents the k^{th} component of the d-dimensional shape function $\underline{\boldsymbol{\Psi}}^L\left(\underline{\boldsymbol{\xi}}\right)$ and $\underline{\boldsymbol{e}}_k$ is the k^{th} Cartesian unit vector. The vectorial index L (useful for efficient numerical implementation) is expressed as a function $\mathcal{I}_d$ of the d dimensional multi-index $(i_1, ..., i_d)$:

$$\mathcal{I}_d : \mathbb{N}^d \to \mathbb{N} \tag{A.33}$$

$$L = \mathcal{I}_d\left(i_1, ..., i_d\right), \quad 0 \leq i_p \leq N, p = 1, ..., d \tag{A.34}$$

The GLL coordinates $\left(\xi_{i_1}^N, ..., \xi_{i_d}^N\right)$ associated to the multi-index $(i_1, ..., i_d)$ belong to the tensorial product $\otimes_{i=1}^d \Xi_i^{N+1}$. For instance, for $d = 2$ (see Figure) and considering the same number of nodes N along the two directions, one gets $L = \mathcal{I}_2\left(i, j\right) = N\left(j - 1\right) + i$.
Each of the $\Psi_k^L\left(\underline{\boldsymbol{\xi}}\right)$ function can be referred as the tensor product between d Lagrange polynomials (one per each Cartesian direction) of the type $\psi_N^{L_j}\left(\xi_j\right), 1 \leq j \leq d$ of degree N (see Equation A.5):

$$\Psi_k^L\left(\underline{\boldsymbol{\xi}}\right) = \otimes_{j=1}^d \psi_N^{L_j}\left(\xi_j\right) \tag{A.35}$$

where $L = \mathcal{I}_d\left(\{L_j\}_{j=1}^d\right)$ represents the generic computational node on the master domain $\square_\Omega$, and $\{L_j\}$ the ensemble of GLL points defined on the master element edge $[-1; 1]$ (Figure A.3). Equa-

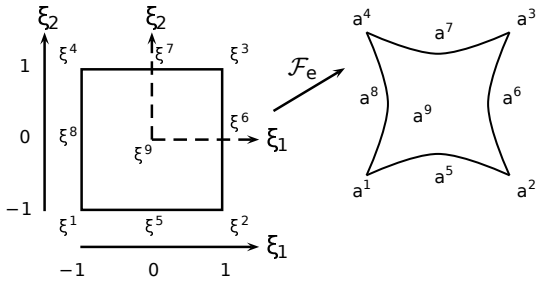

Figure A.3: Example of the diffeomorphism employed in the SEM.

tion A.35 stresses the isotropic nature of the set of shape functions, implying that:

$$\underline{\boldsymbol{x}}_e = \sum_{L=1}^{N_P} \Psi^L \left(\underline{\boldsymbol{\xi}}\right) \underline{\boldsymbol{x}}_e^L \tag{A.36}$$

One needs 4 and 8 or 9 control points for $d = 2$ and 8 and 20 or 27 control points for $d = 3$ to obtain linear and quadratic geometry discretization. Note that, in general, the linear (or quadratic) shape functions $N^L\left(\underline{\boldsymbol{\xi}}\right)$=$\Psi_1^L\left(\underline{\boldsymbol{\xi}}\right)$ (routinely employed in Finite Element) are used herein to map the geometry. The high-order spectral functions are instead employed to interpolate the displacements $\underline{\boldsymbol{u}}$. The analytical expressions of those shape functions and their derivatives may be found in Dhatt et al. (2012). This formulation assures the geometric continuity along the element's edges and faces, by means of element-to-element interface coincidence. The described geometric discretization holds its effectiveness even in case of distorted 3D elements, yet assuring non-zero determinant of the Jacobian matrix. This is because the element geometry is defined (in a linear way) by the nodes of the so called *macro-element*, not by those of the micro elements (i.e. defined by the ensemble of GLL within a macro-element). In other words, the present spectral elements can be viewed as *non-isoparametric* finite elements. The index L in Equation A.36 spans only the corner nodes (formally belonging to the macro-element). A further difference from classical finite elements is that the Jacobian, and thus the terms $\frac{\partial x_i}{\partial \xi_j}$, are to be evaluated at the GLL points, and not at ordinary Gauss points.

Non-linear geometric mapping: a deeper insight

In this context, to invert the diffeomorphism $\mathcal{F}_e$, one needs to compute the Jacobian matrix $\underline{\underline{\boldsymbol{J}}}$ of the transformation and its determinant J. Assuming, for the sake of simplicity, $d = 2$, $\underline{\underline{\boldsymbol{J}}}$ can be expressed as:

$$\underline{\underline{\boldsymbol{J}}} = \begin{bmatrix} \frac{\partial x}{\partial \xi} & \frac{\partial x}{\partial \eta} \\ \frac{\partial y}{\partial \xi} & \frac{\partial y}{\partial \eta} \end{bmatrix} \tag{A.37}$$

and its determinant J reads:

$$J = \frac{\partial x}{\partial \xi}\frac{\partial y}{\partial \eta} - \frac{\partial y}{\partial \xi}\frac{\partial x}{\partial \eta} \tag{A.38}$$

The inverse of the Jacobian matrix can be expressed as:

$$\underline{\underline{\boldsymbol{J}}}^{-1} = \begin{bmatrix} \frac{\partial \xi}{\partial x} & \frac{\partial \xi}{\partial y} \\ \frac{\partial \eta}{\partial x} & \frac{\partial \eta}{\partial y} \end{bmatrix} = \frac{1}{J}\begin{bmatrix} \frac{\partial y}{\partial \eta} & -\frac{\partial x}{\partial \eta} \\ -\frac{\partial y}{\partial \xi} & \frac{\partial x}{\partial \xi} \end{bmatrix} \tag{A.39}$$

If one considers $d = 3$, the Jacobian matrix is expressed by the following expression:

$$\underline{\underline{\boldsymbol{J}}} = \begin{bmatrix} \frac{\partial x}{\partial \xi} & \frac{\partial x}{\partial \eta} & \frac{\partial x}{\partial \zeta} \\ \frac{\partial y}{\partial \xi} & \frac{\partial y}{\partial \eta} & \frac{\partial y}{\partial \zeta} \\ \frac{\partial z}{\partial \xi} & \frac{\partial z}{\partial \eta} & \frac{\partial z}{\partial \zeta} \end{bmatrix} \tag{A.40}$$

The determinant of the Jacobian matrix in 3D reads instead:

$$J = \frac{\partial x}{\partial \xi} A_{11} + \frac{\partial y}{\partial \eta} A_{22} + \frac{\partial z}{\partial \zeta} A_{33} \tag{A.41}$$

$$A_{11} = \frac{\partial y}{\partial \eta}\frac{\partial z}{\partial \zeta} - \frac{\partial z}{\partial \eta}\frac{\partial y}{\partial \zeta}, A_{22} = \frac{\partial x}{\partial \xi}\frac{\partial z}{\partial \zeta} - \frac{\partial z}{\partial \xi}\frac{\partial x}{\partial \zeta}, A_{33} = \frac{\partial x}{\partial \xi}\frac{\partial y}{\partial \eta} - \frac{\partial x}{\partial \eta}\frac{\partial y}{\partial \xi} \tag{A.42}$$

Finally, the inverse of the Jacobian matrix reads:

$$\underline{\underline{\boldsymbol{J}}}^{-1} = \begin{bmatrix} \frac{\partial \xi}{\partial x} & \frac{\partial \xi}{\partial y} & \frac{\partial \xi}{\partial z} \\ \frac{\partial \eta}{\partial x} & \frac{\partial \eta}{\partial y} & \frac{\partial \eta}{\partial z} \\ \frac{\partial \zeta}{\partial x} & \frac{\partial \zeta}{\partial y} & \frac{\partial \zeta}{\partial z} \end{bmatrix} = \frac{1}{J} \begin{bmatrix} A_{11} & A_{21} & A_{31} \\ A_{12} & A_{22} & A_{32} \\ A_{13} & A_{23} & A_{33} \end{bmatrix} \tag{A.43}$$

with the coefficient $A_{ij,i\neq j}$ defined as:

$$A_{12} = \frac{\partial y}{\partial \zeta}\frac{\partial z}{\partial \xi} - \frac{\partial y}{\partial \xi}\frac{\partial z}{\partial \zeta}, A_{21} = \frac{\partial x}{\partial \zeta}\frac{\partial z}{\partial \eta} - \frac{\partial x}{\partial \eta}\frac{\partial z}{\partial \zeta} \tag{A.44}$$

$$A_{13} = \frac{\partial y}{\partial \xi}\frac{\partial z}{\partial \eta} - \frac{\partial z}{\partial \xi}\frac{\partial y}{\partial \eta}, A_{31} = \frac{\partial x}{\partial \eta}\frac{\partial y}{\partial \zeta} - \frac{\partial x}{\partial \zeta}\frac{\partial y}{\partial \eta} \tag{A.45}$$

When the spatial derivatives of shape functions have to be computed, the rule of chain derivative applies:

$$\frac{\partial \Psi_L^N}{\partial \xi_j} = \sum_{k=1}^{d} \frac{\partial \Psi_N^L}{\partial x_k}\frac{\partial x_k}{\partial \xi_j} \tag{A.46}$$

Equation A.46 represents a linear system which has to be solved for the unknowns $\frac{\partial \Psi_N^L}{\partial x_k}$, whose solution may be written as:

$$\frac{\partial \Psi_N^L}{\partial x_k}\left(\underline{\boldsymbol{\xi}}\right) = \sum_{j=1}^{d} \frac{\partial \Psi_N^L}{\partial \xi_j}\left(\underline{\boldsymbol{\xi}}\right)\frac{\partial \xi_j}{\partial x_k} \tag{A.47}$$

Specifying Equation A.47 for $d = 2$, one obtains:

$$\frac{\partial \Psi_N^L}{\partial x} = \frac{\partial \Psi_N^L}{\partial \xi}\frac{\partial \xi}{\partial x} + \frac{\partial \Psi_N^L}{\partial \eta}\frac{\partial \eta}{\partial x} = \frac{1}{J}\left(\frac{\partial \Psi_N^L}{\partial \xi}\frac{\partial y}{\partial \eta} - \frac{\partial \Psi_N^L}{\partial \eta}\frac{\partial y}{\partial \xi}\right)$$

$$\frac{\partial \Psi_N^L}{\partial y} = \frac{\partial \Psi_N^L}{\partial \xi}\frac{\partial \xi}{\partial y} + \frac{\partial \Psi_N^L}{\partial \eta}\frac{\partial \eta}{\partial y} = \frac{1}{J}\left(-\frac{\partial \Psi_N^L}{\partial \xi}\frac{\partial x}{\partial \eta} + \frac{\partial \Psi_N^L}{\partial \eta}\frac{\partial x}{\partial \xi}\right)$$

For $d = 3$ Equations A.47 becomes instead:

$$\frac{\partial \Psi_N^L}{\partial x} = \frac{1}{J}\left[\frac{\partial y}{\partial \xi}\left(\frac{\partial z}{\partial \eta}\frac{\partial \Psi_N^L}{\partial \zeta} - \frac{\partial z}{\partial \zeta}\frac{\partial \Psi_N^L}{\partial \eta}\right) - \frac{\partial y}{\partial \eta}\left(\frac{\partial z}{\partial \xi}\frac{\partial \Psi_N^L}{\partial \zeta} - \frac{\partial z}{\partial \zeta}\frac{\partial \Psi_N^L}{\partial \xi}\right) + \frac{\partial y}{\partial \zeta}\left(\frac{\partial z}{\partial \xi}\frac{\partial \Psi_N^L}{\partial \eta} - \frac{\partial z}{\partial \eta}\frac{\partial \Psi_N^L}{\partial \xi}\right)\right]$$

$$\frac{\partial \Psi_N^L}{\partial y} = \frac{1}{J}\left[\frac{\partial z}{\partial \xi}\left(\frac{\partial x}{\partial \eta}\frac{\partial \Psi_N^L}{\partial \zeta} - \frac{\partial x}{\partial \zeta}\frac{\partial \Psi_N^L}{\partial \eta}\right) - \frac{\partial z}{\partial \eta}\left(\frac{\partial x}{\partial \xi}\frac{\partial \Psi_N^L}{\partial \zeta} - \frac{\partial x}{\partial \zeta}\frac{\partial \Psi_N^L}{\partial \xi}\right) + \frac{\partial z}{\partial \zeta}\left(\frac{\partial x}{\partial \xi}\frac{\partial \Psi_N^L}{\partial \eta} - \frac{\partial x}{\partial \eta}\frac{\partial \Psi_N^L}{\partial \xi}\right)\right]$$

$$\frac{\partial \Psi_N^L}{\partial z} = \frac{1}{J}\left[\frac{\partial x}{\partial \xi}\left(\frac{\partial y}{\partial \eta}\frac{\partial \Psi_N^L}{\partial \zeta} - \frac{\partial y}{\partial \zeta}\frac{\partial \Psi_N^L}{\partial \eta}\right) - \frac{\partial x}{\partial \eta}\left(\frac{\partial y}{\partial \xi}\frac{\partial \Psi_N^L}{\partial \zeta} - \frac{\partial y}{\partial \zeta}\frac{\partial \Psi_N^L}{\partial \xi}\right) + \frac{\partial x}{\partial \zeta}\left(\frac{\partial y}{\partial \xi}\frac{\partial \Psi_N^L}{\partial \eta} - \frac{\partial y}{\partial \eta}\frac{\partial \Psi_N^L}{\partial \xi}\right)\right]$$

Substituting Equation A.35 in Equation A.47 and considering Equation A.6, the derivatives $\frac{\partial \Psi_N^L}{\partial \xi_j}$ read for $d = 2$:

$$\left.\frac{\partial \Psi_N^L}{\partial \xi}\right|_{\xi^r,\eta^s} = \left.\frac{\partial \psi_N^i}{\partial \xi}\right|_{\xi^r} \psi_N^j\left(\eta^s\right) = \left.\frac{\partial \psi_N^i}{\partial \xi}\right|_{\xi^r} \delta^{js} \tag{A.48}$$

$$\left.\frac{\partial \Psi_N^L}{\partial \eta}\right|_{\xi^r,\eta^s} = \psi_N^i\left(\xi^r\right)\left.\frac{\partial \psi_N^j}{\partial \eta}\right|_{\eta^s} = \delta^{ir}\left.\frac{\partial \psi_N^j}{\partial \eta}\right|_{\eta^s} \tag{A.49}$$

$$\tag{A.50}$$

with $L = \mathcal{I}_2(i,j)$. For $d = 3$, Equation A.50 becomes:

$$\begin{aligned}
\left.\frac{\partial \Psi_N^L}{\partial \xi}\right|_{\xi^r,\eta^s,\zeta^t} &= \left.\frac{\partial \psi_N^i}{\partial \xi}\right|_{\xi^r} \psi_N^j(\eta^s)\,\psi_N^j\left(\zeta^t\right) = \left.\frac{\partial \psi_N^i}{\partial \xi}\right|_{\xi^r} \delta^{js}\delta^{kt} \\
\left.\frac{\partial \Psi_N^L}{\partial \eta}\right|_{\xi^r,\eta^s,\zeta^t} &= \psi_N^i(\xi^r)\left.\frac{\partial \psi_N^j}{\partial \eta}\right|_{\eta^s} \psi_N^k\left(\zeta^t\right) = \delta^{ir}\left.\frac{\partial \psi_N^j}{\partial \eta}\right|_{\eta^s} \delta^{kt} \\
\left.\frac{\partial \Psi_N^L}{\partial \zeta}\right|_{\xi^r,\eta^s,\zeta^t} &= \psi_N^i(\xi^r)\,\psi_N^j(\eta^s)\left.\frac{\partial \psi_N^k}{\partial \zeta}\right|_{\zeta^t} = \delta^{ir}\delta^{js}\left.\frac{\partial \psi_N^k}{\partial \zeta}\right|_{\zeta^t}
\end{aligned}$$

with $L = \mathcal{I}_3(i,j,k)$.

A.6 Galerkin approximation of the solution

The semi-discretized problem in Equation A.25 is issued from the quadrangulation $\mathcal{I}^h\left(\bar{\Omega}\right)$. Such a discretization is preserved by replacing the infinite dimensional spaces $\mathcal{S}^t, \delta\mathcal{S}$ (Equations A.17-A.18) by the finite-dimensional subspaces $\mathcal{S}^{t,h} \subset \mathcal{S}^t$, $\delta\mathcal{S}^h \subset \delta\mathcal{S}$, based on the polynomial approximation:

$$\mathcal{S}^{t,h} := \{\underline{\boldsymbol{u}}^h \in \mathcal{S}^t, \underline{\boldsymbol{u}}_e^h = \underline{\boldsymbol{u}}^h|_{\bar{\Omega}_e} \circ \mathcal{F}_e \in \otimes_{i=1}^d \left[\mathbb{P}_N(\xi_i)\right]\} \tag{A.51}$$

$$\delta\mathcal{S}^h := \{\underline{\boldsymbol{w}}^h \in \delta\mathcal{S}, \underline{\boldsymbol{w}}_e^h = \underline{\boldsymbol{w}}^h|_{\bar{\Omega}_e} \circ \mathcal{F}_e \in \otimes_{i=1}^d \left[\mathbb{P}_N(\xi_i)\right]\} \tag{A.52}$$

with $\mathbb{P}_N(\xi_i)$ representing the space of generic polynomials of order $n \leq N$, defined over $[-1;1]$ and employed in the non-linear mapping $\mathcal{F}_e$ [3]. Taking into consideration the *non-isoparametric* mapping described in paragraphs A.5-A.5, the sought element-wise polynomial approximation of the displacement vector field $\underline{\boldsymbol{u}}_e^h = \underline{\boldsymbol{u}}^h|_{\bar{\Omega}_e}$ reads:

$$u_k^h|_{\bar{\Omega}_e} = I_N u_k|_{\bar{\Omega}_e}(\underline{\boldsymbol{x}}) = \sum_{r,s,t=0}^{N} u_{e_k}^h\left(\xi_r^N, \xi_s^N, \xi_t^N\right)\phi_k^r(\xi_1)\,\phi_k^s(\xi_2)\,\phi_k^t(\xi_3) \tag{A.53}$$

with $\underline{\boldsymbol{x}} = \mathcal{F}_e\left(\underline{\boldsymbol{\xi}}\right) = \mathcal{F}_e(\xi_1,\xi_2,\xi_3)$, I_N the Lagrange interpolation operator that ensures the $\mathcal{C}^0$ continuity between elements, since the restriction $\underline{\boldsymbol{u}}^h|_{\bar{\Omega}_e}$ is the unique polynomial in $\otimes_{i=1}^d \mathbb{P}_N(\xi_i)$ coincident with $\underline{\boldsymbol{u}}|_{\bar{\Omega}_e}$ on the $(N+1)^d$ GLL points.
Therefore, taking into consideration the Gauss quadrature rule in Equation A.9, the generic inner product of the semi-discretized formulation of the Euler-Lagrange Equation A.25 can be approximated on the tensorial grid $\otimes_{i=1}^d \Xi_i^{N+1}$ as follows:

$$\left(\underline{\boldsymbol{w}}_e^h, \underline{\boldsymbol{u}}_e^h\right)_{\Omega_e}^h = \int_{\Omega_e} \underline{\boldsymbol{w}}_e^h(\underline{\boldsymbol{x}}) \,.\, \underline{\boldsymbol{u}}_e^h(\underline{\boldsymbol{x}})\, dV_x \simeq \sum_{\alpha,\beta,\gamma=0}^{N} \left[\underline{\boldsymbol{w}}_e^h \,.\, \underline{\boldsymbol{u}}_e^h\right]\left(\xi_\alpha^N, \xi_\beta^N, \xi_\gamma^N\right) J_e\left(\xi_\alpha^N, \xi_\beta^N, \xi_\gamma^N\right)\omega_{\alpha\beta\gamma} \tag{A.54}$$

where $J_e\left(\xi_\alpha^N, \xi_\beta^N, \xi_\gamma^N\right)$ represents the determinant of the Jacobian matrix $\underline{\underline{\boldsymbol{J}}}_e = \underline{\boldsymbol{\nabla}}_\xi \mathcal{F}_e$ (i.e. the gradient of the non-linear geometrical mapping between master and physical elements) evaluated at the GLL point $\left(\xi_\alpha^N, \xi_\beta^N, \xi_\gamma^N\right)$ and $\omega_{\alpha\beta\gamma} = \omega_\alpha\omega_\beta\omega_\gamma$. The approximation in Equation A.54 is not always exact, since the product $\left[\underline{\boldsymbol{w}}_e^h \,.\, \underline{\boldsymbol{u}}_e^h\right] \in \mathbb{P}_{2N}$

[3] in this case $\mathbb{P}_N(\xi_i)$ correspond to the space of the Lagrange polynomials $l_N(\xi)$

In turns, the Galerkin's formulation of the semi-discrete variational problem consists into searching for the couple $\left(\underline{\boldsymbol{u}}^h, \underline{\boldsymbol{v}}^h\right) \in \mathcal{S}^{t,h} \times \mathcal{S}^{t,h}$ for which the equation:

$$\begin{cases} \left(\underline{\boldsymbol{w}}^h, \rho^h \dot{\underline{\boldsymbol{v}}}^h\right)^h = \left(\underline{\boldsymbol{w}}^h, \underline{\boldsymbol{b}}^h\right)^h - \mathbb{A}_\Omega^h\left(\underline{\boldsymbol{w}}^h, \underline{\boldsymbol{u}}^h\right) + \left(\underline{\boldsymbol{w}}^h, \underline{\boldsymbol{t}}_n^h\right)_{\Gamma_T}^h & \text{(A.55)} \\ \left(\underline{\boldsymbol{w}}^h, \rho^h \dot{\underline{\boldsymbol{u}}}^h\right)^h = \left(\underline{\boldsymbol{w}}^h, \rho^h \underline{\boldsymbol{v}}^h\right)^h & \text{(A.56)} \end{cases}$$

Efficient vectorized formulation of the Galerkin's formulation

The Galerkin's formulation of the Euler-Lagrange equation expressed in Equation A.56, along with the GLL spectral discretization and quadrature formulas, represents an algebraic system of equations, whose Degrees Of Freedom (DOF, i.e. the unknowns of the system) are represented by the ensemble of 3D displacement and velocity vector fields evaluated at the GLL points, i.e. $u_{e_k}^h|_{rst} = u_{e_k}^h\left(\xi_r^N, \xi_s^N, \xi_t^N\right)$, $v_{e_k}^h|_{rst} = v_{e_k}^h\left(\xi_r^N, \xi_s^N, \xi_t^N\right)$ respectively. The latter are element-wise indexed (along with their corresponding local GLL points). To solve the problem along across the whole computational domain, an efficient vectorization was proposed by Deville et al. (2002) (see Figure A.4). The

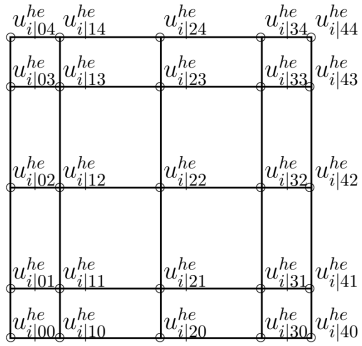

Figure A.4: 2D indexation of the unknown field $u_{e_i}^h$ at the 4×4 GLL grid points within the reference element. Reprinted from Delavaud (2007)

vectorization scheme proposed by Deville et al. (2002) is based on the vectorial index $\mathcal{I}_d$ defined in Equation A.34 and it consists into casting the k^{th} vector component of the unknown fields into vectors $\underline{\hat{\boldsymbol{u}}}_{e_k}^h$ as follows:

$$\begin{aligned} &\hat{u}_{e_k}^h|_{L=\mathcal{I}_d(rst)} = u_{e_k}^h|_{rst} \\ &\underline{\hat{\boldsymbol{u}}}_{e_k}^h = \left(u_{e_k}|_1, ..., u_{e_k}|_L, ..., u_{e_k}|_{\mathcal{N}}\right)^T = \\ &\qquad = \left(u_{e_k}|_{000}, ..., u_{e_k}|_{rst}, ..., u_{e_k}|_{NNN}\right)^T \end{aligned} \qquad \text{(A.57)}$$

with $\mathcal{N} = (N+1)^3$ and $L = 1 + r + (N+1)\, s + (N+1)^2\, t$. At this points, the vector containing all the element-wise unknowns (all the direction considered) is defined as $\underline{\hat{\boldsymbol{u}}}_e^h = \left(\underline{\hat{\boldsymbol{u}}}_{e_1}^h, \underline{\hat{\boldsymbol{u}}}_{e_2}^h, \underline{\hat{\boldsymbol{u}}}_{e_3}^h\right)^T$. Finally, all the element-wise unknown vectors are grouped into the vector of global unknowns $\underline{\hat{\boldsymbol{U}}}_L^h = \left(\underline{\hat{\boldsymbol{u}}}_1^h, ..., \underline{\hat{\boldsymbol{u}}}_e^h, ..., \underline{\hat{\boldsymbol{u}}}_{N_e}^h\right)^T \in \mathbb{R}^{N_e.d.\mathcal{N}}$. $\underline{\hat{\boldsymbol{U}}}_L^h$ is the concatenation of all the DOFs (Delavaud, 2007; Deville et al., 2002). The Lagrangian interpolation assures the element-to-element continuity across their shared faces/edges/corners, which implies the existence of a connectivity matrix $\underline{\underline{\boldsymbol{Q}}}_L^G$, to pass from a local (L) to a global (G) indexation, so to uniquely identify each of the $\mathcal{N}_G$ computational node (GLL)

and the vector of distinct DOFs on the entire mesh $\underline{\hat{\boldsymbol{U}}}_G^h \in \mathbb{R}^{d.\mathcal{N}_G}$:

$$\underline{\hat{\boldsymbol{U}}}_L^h = \underline{\underline{\boldsymbol{Q}}}_L^G \underline{\hat{\boldsymbol{U}}}_G^h \tag{A.58}$$

$\underline{\underline{\boldsymbol{Q}}}_L^G$ allows to pass from a global to a local indexation of each node and DOF, by means of copying common values from a vector one to another. $\underline{\underline{\boldsymbol{Q}}}_L^G$ is not invertible. However, its transpose is solely employed $\underline{\underline{\boldsymbol{Q}}}_G^L = \left(\underline{\underline{\boldsymbol{Q}}}_L^G\right)^T$, as an assemblage operator, to sum correctly all the contributions coming from each element. $\underline{\underline{\boldsymbol{Q}}}_L^G$ is never computed/stored directly, yet its action is addressed indirectly.

Galerkin's formulation: a deeper insight

The application of the quadrature rule to the inner product $\mathbb{A}_\Omega^e$ appear more complex, due to the presence of the gradient $\underline{\boldsymbol{\nabla}}_x \otimes \underline{\boldsymbol{w}}_e^h$. The latter can be unraveled by first applying the chain's rule to the partial derivative of the k^{th} component of the function $\underline{\boldsymbol{w}}_e^h$ with respect to the m^{th} spatial coordinate x_m, evaluated at GLL point corresponding to $\left(\xi_\alpha^N, \xi_\beta^N, \xi_\gamma^N\right) \in \otimes_{i=1}^d \Xi_i^{N+1}$:

$$\frac{\partial w_{e_k}^h}{\partial x_m}\left(\underline{\boldsymbol{x}}\left(\xi_\alpha^N, \xi_\beta^{N\,N}, \xi_\gamma^N\right)\right) = \sum_{i=1}^d \frac{\partial w_{e_k}^h}{\partial \xi_i} \frac{\partial \xi_i}{\partial x_m}\left(\xi_\alpha^N, \xi_\beta^{N\,N}, \xi_\gamma^N\right) \tag{A.59}$$

In Equation A.59, the terms $\frac{\partial \xi_i}{\partial x_m}$ express the non-linear geometrical mapping, described in paragraph A.5 and unravelled in paragraph A.5 in the 2D and 3D case. Therefore, the terms to be further characterized are the derivatives $\frac{\partial w_{e_k}^h}{\partial \xi_i}$. To this end, let us take, for the sake of simplicity, the derivative $\frac{\partial w_{e_k}^h}{\partial \xi_1}$ and the polynomial approximation of $\underline{\boldsymbol{w}}_e$ (Equation A.53):

$$\begin{aligned}
\frac{\partial w_{e_k}^h}{\partial \xi_1}\left(\xi_\alpha^N, \xi_\beta^N, \xi_\gamma^N\right) &= \sum_{r,s,t=0}^N u_{e_k}^h\left(\xi_r^N, \xi_s^N, \xi_t^N\right) \frac{\partial \psi_k^r}{\partial \xi_1}\left(\xi_\alpha^N\right) \phi_k^s\left(\xi_\beta^N\right) \phi_k^t\left(\xi_\gamma^N\right) = \\
&= \sum_{r,s,t=0}^N u_{e_k}^h\left(\xi_r^N, \xi_s^N, \xi_t^N\right) \frac{\partial \psi_k^r}{\partial \xi_1}\left(\xi_\alpha^N\right) \delta^{s\beta}\delta^{t\gamma} = \sum_{r=0}^N u_{e_k}^h\left(\xi_r^N, \xi_\beta^N, \xi_\gamma^N\right) \frac{\partial \psi_k^r}{\partial \xi_1}\left(\xi_\alpha^N\right) = \\
&= \sum_{r=0}^N u_{e_k}^h\left(\xi_r^N, \xi_\beta^N, \xi_\gamma^N\right) D_{r\alpha}^N
\end{aligned} \tag{A.60}$$

Therefore, the 1D-derivative matrix $\underline{\underline{\boldsymbol{D}}}^N$ has $(N+1)^2$ elements (associated to the $N+1$ GLLs) and it can be defined in its entirety as follows (Delavaud, 2007):

$$D_{ij}^N \equiv \begin{cases}
\dfrac{L_N\left(\xi_i^N\right)}{L_N\left(\xi_j^N\right)} \dfrac{1}{\left(\xi_i^N - \xi_j^N\right)}, & i \neq j & \text{(A.61)} \\
-\dfrac{N\left(N+1\right)}{4}, & i = j = 0 & \text{(A.62)} \\
\dfrac{N\left(N+1\right)}{4}, & i = j = N & \text{(A.63)} \\
0, & \text{otherwise} & \text{(A.64)}
\end{cases}$$

In turns, if one employs the vectorization proposed by Deville et al. (2002) and expressed in Equation A.57, the vector field $\frac{\partial \underline{\hat{\boldsymbol{w}}}_{e_k}^h}{\partial \xi_j}\left(\xi_\alpha^N, \xi_\beta^N, \xi_\gamma^N\right)$ can be written as:

$$\frac{\partial \underline{\hat{\boldsymbol{w}}}_{e_k}^h}{\partial \xi_j}\left(\xi_\alpha^N, \xi_\beta^N, \xi_\gamma^N\right) = \left.\frac{\partial \underline{\hat{\boldsymbol{w}}}_{e_k}^h}{\partial \xi_j}\right|_{\alpha,\beta,\gamma} = \left.\mathbb{D}_j \underline{\hat{\boldsymbol{w}}}_{e_k}^h\right|_{\alpha,\beta,\gamma} \tag{A.65}$$

with the algebraic operator $\mathbb{D}_j$, defined as the tensorial product:

$$\mathbb{D}_j \equiv \begin{cases} \mathbb{D}_1 = \underline{\underline{\boldsymbol{I}}}^{N+1} \otimes \underline{\underline{\boldsymbol{I}}}^{N+1} \otimes \underline{\underline{\boldsymbol{D}}}^{N} & \text{(A.66)} \\ \mathbb{D}_2 = \underline{\underline{\boldsymbol{I}}}^{N+1} \otimes \underline{\underline{\boldsymbol{D}}}^{N} \otimes \underline{\underline{\boldsymbol{I}}}^{N+1} & \text{(A.67)} \\ \mathbb{D}_3 = \underline{\underline{\boldsymbol{D}}}^{N} \otimes \underline{\underline{\boldsymbol{I}}}^{N+1} \otimes \underline{\underline{\boldsymbol{I}}}^{N+1} & \text{(A.68)} \end{cases}$$

with $\underline{\underline{\boldsymbol{I}}}^{N+1}$ being the $(N+1)^2$ identity matrix and $\otimes$ the tensorial product. The operator $\mathbb{D}_j$ employs $(N+1)(N+1)^3$ coefficients to store $(N+1)^2$ values. Following the latter developments, the derivative in the physical domain (Equation A.59) simplifies to:

$$\begin{aligned} &\left.\frac{\partial \underline{\hat{\boldsymbol{u}}}^h_{e_k}}{\partial x_m}\right|_{\alpha,\beta,\gamma} = \sum_{i=1}^{d} \left[\frac{\partial \underline{\hat{\boldsymbol{u}}}^h_{e_k}}{\partial \xi_i}\frac{\partial \xi_i}{\partial x_m}\right]_{\alpha,\beta,\gamma} = \sum_{i=1}^{d} \left[\mathbb{D}_i \underline{\hat{\boldsymbol{u}}}^h_{e_k}\frac{\partial \xi_i}{\partial x_m}\right]_{\alpha,\beta,\gamma} = \\ &\left(\left.\underline{\hat{\boldsymbol{u}}}^h_{e_k}\right|_{\alpha,\beta,\gamma}\right)^T \sum_{i=1}^{d} \left[\mathbb{D}_i^T \frac{\partial \xi_i}{\partial x_m}\right]_{\alpha,\beta,\gamma} = \left[\underline{\hat{\boldsymbol{u}}}^{hT}_{e_k}\tilde{\mathbb{D}}^T_m\right]_{\alpha,\beta,\gamma} = \left[\tilde{\mathbb{D}}_m \underline{\hat{\boldsymbol{u}}}^h_{e_k}\right]_{\alpha,\beta,\gamma} \end{aligned} \tag{A.69}$$

When the vectorization proposed by Deville et al. (2002) is applied, and all the field components are considered, its gradient becomes:

$$\left[\mathcal{D}_m \underline{\hat{\boldsymbol{u}}}^h_e\right]_{\alpha,\beta,\gamma} = \left(\left[\tilde{\mathbb{D}}_m \underline{\hat{\boldsymbol{u}}}^h_{e_1}\right]_{\alpha,\beta,\gamma}, \left[\tilde{\mathbb{D}}_m \underline{\hat{\boldsymbol{u}}}^h_{e_2}\right]_{\alpha,\beta,\gamma}, \left[\tilde{\mathbb{D}}_m \underline{\hat{\boldsymbol{u}}}^h_{e_3}\right]_{\alpha,\beta,\gamma}\right)^T \tag{A.70}$$

With the interpolated version of the gradient field being defined, the approximate expression of $\mathbb{A}_{\Omega_e}$ (under its vectorized version, at the GLL node $L = \mathcal{I}_d(r,s,t)$) can be easily written, by keeping in mind the as:

$$\begin{aligned} &\mathbb{A}_{\Omega_e}\left(\underline{\boldsymbol{w}}^h_e, \underline{\boldsymbol{u}}^h_e\right) = \int_{\square_\Omega} \left(\sum_{m,k=1}^{d} \underline{\boldsymbol{e}}_m \otimes \frac{\partial \underline{\boldsymbol{w}}^h_{e_k}}{\partial x_m}\right)\left(\underline{\boldsymbol{\xi}}\right) : \underline{\underline{\boldsymbol{\sigma}}}\left(\underline{\boldsymbol{u}}^h_e; \underline{\boldsymbol{v}}^h_e\right)\left(\underline{\boldsymbol{\xi}}\right) dV_\xi \\ &\mathbb{A}_{\Omega_e}\left(\underline{\boldsymbol{w}}^h_e, \underline{\boldsymbol{u}}^h_e\right)\Big|_{\mathcal{I}_d(r,s,t)} \simeq \mathbb{A}^h_{\Omega_e}\left(\underline{\hat{\boldsymbol{w}}}^h_e, \underline{\hat{\boldsymbol{u}}}^h_e\right)\Big|_{\mathcal{I}_d(r,s,t)} = \\ &= \sum_{m,k=1}^{d} \left[\underline{\hat{\boldsymbol{u}}}^{hT}_{e_k}\tilde{\mathbb{D}}^T_m\right]_{r,s,t} : \underline{\underline{\boldsymbol{\sigma}}}\left(\left.\underline{\hat{\boldsymbol{u}}}^h_e\right|_{\alpha,\beta,\gamma}; \left.\underline{\hat{\boldsymbol{v}}}^h_e\right|_{\alpha,\beta,\gamma}\right) J_e|_{r,s,t}\omega_{rst} \end{aligned} \tag{A.71}$$

Again, the stress operator $\underline{\underline{\boldsymbol{\sigma}}}(\cdot)$ depends on the rheology. Equation A.71 represent the internal force member in the semi-discretized dynamic balance equation.

A.7 Spectral Element discretized dynamic balance equations

The employment of the semi-discretized Galerkin's formulation of the Euler-Lagrange equation, along with the Lagrangian interpolation and the Gauss-Lobatto-Legendre quadrature formulas, led to a system of ordinary differential equations, governing the time-evolution of the nodal global (G) positions and vector fields, which can be written as follows:

$$\begin{cases} \mathbb{M}\dot{\underline{\hat{\boldsymbol{V}}}}^h_G = \mathbb{F}^{ext} - \mathbb{F}^{int}\left(\underline{\hat{\boldsymbol{U}}}^h_G; \underline{\hat{\boldsymbol{V}}}^h_G\right) + \mathbb{F}^{trac}\left(\underline{\boldsymbol{\mathcal{T}}}^h_G\right) & \text{(A.72)} \\ \dot{\underline{\hat{\boldsymbol{U}}}}^h_G = \underline{\hat{\boldsymbol{V}}}^h_G & \text{(A.73)} \end{cases}$$

with[4]:

[4] $\biguplus_{e=1}^{N_e}$ represents, in the following, the assemblage operator

- the $(d.\mathbb{N}_G) \times (d.\mathbb{N}_G)$ mass matrix $\mathbb{M}$, defined as:

$$\mathbb{M} = \biguplus_{e=1}^{N_e} \mathbb{M}_e \tag{A.74}$$

with $\mathbb{M}_e$ being defined as the elemental mass matrix:

$$\mathbb{M}_e = \underline{\underline{\boldsymbol{I}}}_d \otimes \underline{\underline{\hat{\boldsymbol{M}}}}_e \tag{A.75}$$

$\underline{\underline{\boldsymbol{I}}}_d$ is the identity matrix and $\underline{\underline{\hat{\boldsymbol{M}}}}_e$ is defined as:

$$\hat{M}_{ij} = \int_{\square_\Omega} \rho_e \left(\underline{\boldsymbol{\xi}}\right) \Psi_k^i \left(\underline{\boldsymbol{\xi}}\right) \Psi_k^j \left(\underline{\boldsymbol{\xi}}\right) J_e \left(\underline{\boldsymbol{\xi}}\right) dV_\xi = \sum_{\alpha,\beta,\gamma=1}^{N} \rho|_{\alpha,\beta,\gamma} J_e|_{\alpha,\beta,\gamma} \omega_{\alpha\beta\gamma} \tag{A.76}$$

The local mass matrix $\underline{\underline{\hat{\boldsymbol{M}}}}_e$ has an interesting property, being naturally diagonal, due to the intrinsic orthogonality of the Lagrange polynomials at the GLL points. From a computational point of view, this turns into an extremely convenient formulation, since no matrix inversion is required in the solving process: the solution of the system is obtained node-wise, since the nodal masses are naturally lumped.

- the $(d.\mathbb{N}_G) \times 1$ external force vector $\mathbb{F}^{ext}$, defined as:

$$\mathbb{F}^{ext} = \biguplus_{e=1}^{N_e} \mathbb{F}_e^{ext} \tag{A.77}$$

where $\mathbb{F}_e^{ext}$ represents the local element-wise external force contribution. In computational seismology, the external forces are commonly generated by either point-wise forces, double-couple (see Section D.2.5) or extended kinematic fault planes (Aki and Richards, 1980). For the first two cases, the analytical expression of point-wise force/couple placed at point $\underline{\boldsymbol{x}}_0$ reads (Faccioli et al., 1997; Madariaga, 1989):

$$\underline{\boldsymbol{b}}\left(\underline{\boldsymbol{x}};t\right) \equiv \begin{cases} \sum_{i=1}^{d} A_i \delta\left(\underline{\boldsymbol{x}} - \underline{\boldsymbol{x}}_S\right) f\left(t\right) \underline{\boldsymbol{e}}_i, & \text{point-wise force} \quad \text{(A.78)} \\ -\underline{\boldsymbol{\nabla}}_x \cdot \underline{\underline{\boldsymbol{m}}}\left(\underline{\boldsymbol{x}};\underline{\boldsymbol{x}}_S\right) f\left(t\right), & \text{point-wise double couple} \quad \text{(A.79)} \end{cases}$$

with A_i is the amplitude of the point-wise force along the i^{th} direction, δ the Dirac's delta, $\underline{\boldsymbol{x}}_S$ the source point and $\underline{\underline{\boldsymbol{m}}}\left(\underline{\boldsymbol{x}};t\right)$ the seismic moment tensor density and $\underline{\underline{\boldsymbol{m}}}\left(\underline{\boldsymbol{x}}\right) = \underline{\underline{\boldsymbol{m}}}_0 \delta\left(\underline{\boldsymbol{x}} - \underline{\boldsymbol{x}}_S\right)$. To translate the analytical formulation of the point-wise forces, let first $\underline{\boldsymbol{x}}_S$ coincide for simplicity with one of the GLL nodes. Then the body force numerical counterparts $\underline{\boldsymbol{b}}^N\left(\underline{\boldsymbol{x}};t\right)$ may be written as:

$$\underline{\boldsymbol{b}}^N\left(\underline{\boldsymbol{x}};t\right) \equiv \begin{cases} \sum_{i=1}^{d} A_i \delta^N\left(\underline{\boldsymbol{x}} - \underline{\boldsymbol{x}}_S\right) f\left(t\right) \underline{\boldsymbol{e}}_i, & \text{point-wise force} \quad \text{(A.80)} \\ -\underline{\boldsymbol{\nabla}}_x \cdot \left[\underline{\underline{\boldsymbol{m}}}_0 \delta^N\left(\underline{\boldsymbol{x}} - \underline{\boldsymbol{x}}_S\right)\right] f\left(t\right), & \text{point-wise double couple} \quad \text{(A.81)} \end{cases}$$

δ^N is the numerical counterpart of the Dirac's delta. According to the quadrature formulas and Lagrangian interpolation employed in the SE discretization, δ^N is the N^{th} order Lagrangian shape function Ψ^L/ω_L (with $L = \mathcal{I}_d\left(r,s,t\right)$ the multi-index corresponding to the GLL point coordinated by the indexes r,s,t on a 3D master element) that vanishes at all GLL points $I \neq L$ within the element, except at $\underline{\boldsymbol{x}}_S\left(\underline{\boldsymbol{\xi}}^L\right)$, where it is equal to $1/\omega_L$ (the GLL weight associated to

$\underline{\boldsymbol{\xi}}^L$ in quadrature formula on Ω_e). Note that the integral $\int_{\Omega_e} \delta^N dV_x = 1$ according to the GLL quadrature formulas employed. Therefore, the Galerkin's formulation of the external force on an element e (and according to the local reference system $\underline{\boldsymbol{x}}_e$) reads:

$$\left(\underline{\boldsymbol{w}}_e^h\left(\underline{\boldsymbol{x}}_e\right), \sum_{i=1}^{d} A_i \delta^N\left(\underline{\boldsymbol{x}}_e - \underline{\boldsymbol{x}}_{eS}\right) f\left(t\right) \underline{\boldsymbol{e}}_i\right)_{\Omega_e}^h = f\left(t\right) \sum_{i=1}^{d} A_i w_{e_i}\left(\underline{\boldsymbol{x}}_{eS}\right) \tag{A.82}$$

for a point-wise force. Concerning the double-coupe source, a convenient representation of the seismic moment tensor density was originally formulated by Aki and Richards (1980), in the following fashion:

$$\underline{\underline{\boldsymbol{m}}}\left(\underline{\boldsymbol{x}}; \underline{\boldsymbol{x}}_S\right) = \underline{\underline{\boldsymbol{m}}}_0 \delta\left(\underline{\boldsymbol{x}} - \underline{\boldsymbol{x}}_S\right) = \frac{M_0}{V}\left(\underline{\boldsymbol{d}}_\Sigma \otimes_S \underline{\boldsymbol{n}}_\Sigma\right) \delta\left(\underline{\boldsymbol{x}} - \underline{\boldsymbol{x}}_S\right) \tag{A.83}$$

with $\underline{\boldsymbol{d}}_\Sigma$ and $\underline{\boldsymbol{n}}_\Sigma$ the slip and normal vector defining the spatial disposition of the fault offset; M_0 is the total seismic moment (see Section 3.9.2) and V the source elementary volume (Faccioli et al., 1997). The seismic moment[5] translates into the equivalent body force distribution proposed in Equation A.79. Hence, the application of the divergence theorem to the variational formulation of Equation A.81, gives:

$$\begin{aligned}
&\left(\underline{\boldsymbol{w}}_e^h\left(\underline{\boldsymbol{x}}_e\right), -\underline{\boldsymbol{\nabla}}_x \cdot \left[\underline{\underline{\boldsymbol{m}}}_0 \delta^N\left(\underline{\boldsymbol{x}} - \underline{\boldsymbol{x}}_S\right)\right] f\left(t\right)\right)_{\Omega_e}^h = \\
&= \left(\underline{\underline{\boldsymbol{m}}}_0 \delta^N\left(\underline{\boldsymbol{x}} - \underline{\boldsymbol{x}}_S\right) f\left(t\right), \underline{\boldsymbol{w}}_e^h \otimes_S \underline{\boldsymbol{\nabla}}_x\right)_{\Omega_e}^h = \\
&= \frac{1}{2} \sum_{i,j=1}^{d} f\left(t\right) m_{0_{ij}} \left(\frac{\partial w_{e_i}^h}{\partial x_j} + \frac{\partial w_{e_j}^h}{\partial x_i}\right) \omega_L = \\
&\frac{1}{2} \sum_{i,j=1}^{d} f\left(t\right) m_{0_{ij}} \left(\frac{\partial \Phi_i^L}{\partial x_j} + \frac{\partial \Phi_j^L}{\partial x_i}\right)
\end{aligned} \tag{A.84}$$

From Equation A.84, it appears that the right-hand member vanishes if L is associated to any of the nodes outside the sub-domain e containing the source, whereas it is different from zero for those L associated to each of the nodes inside e (except at $\underline{\boldsymbol{x}}_S$). Thus, due to the discretization into subdomains of finite size, the virtual internal work associated to the source is spread over e . As a consequence, the numerical method can accurately portray a double couple point source provided the size (Faccioli et al., 1997).

- the $(d.\mathbb{N}_G) \times 1$ traction force vector $\mathbb{F}^{trac}\left(\underline{\boldsymbol{\mathcal{T}}}_G^h\right)$, defined as:

$$\mathbb{F}^{trac}\left(\underline{\boldsymbol{\mathcal{T}}}_G^h\right) = \biguplus_{e=1}^{N_e} \underline{\boldsymbol{F}}_e^{trac}\left(\hat{\underline{\boldsymbol{t}}}_{ne}^h\right) \tag{A.85}$$

with $\underline{\boldsymbol{\mathcal{T}}}_G^h$ being the global traction vector (defined onto Γ_T) and $\underline{\boldsymbol{\mathcal{T}}}_L^h$ its local counterpart on each element.

- the $(d.\mathbb{N}_G) \times 1$ internal force vector $\mathbb{F}^{int}\left(\hat{\underline{\boldsymbol{U}}}_G^h; \underline{\boldsymbol{V}}_G^h\right)$, defined as:

$$\mathbb{F}^{int}\left(\hat{\underline{\boldsymbol{U}}}_G^h; \underline{\boldsymbol{V}}_G^h\right) = \biguplus_{e=1}^{N_e} \underline{\boldsymbol{F}}_e^{int}\left(\hat{\underline{\boldsymbol{U}}}_L^h; \underline{\boldsymbol{V}}_L^h\right) \tag{A.86}$$

[5]The seismic moment tensor is symmetric. Its traces vanishes for pure slip condition, i.e. when $\underline{\boldsymbol{d}}_\Sigma . \underline{\boldsymbol{n}}_\Sigma = 0$.

The internal forces, as mentioned above, depend on the local rheology, being it either elastic (which implies the internal forces to solely depend on the displacement field), viscous-elastic (which, in turns, implies the dependency on the velocity vector field) or elastic-plastic (which implies the dependency on evolution of the stress field). As a matter of fact, the rheology determines the way the stress operator $\underline{\underline{\boldsymbol{\sigma}}}(\cdot)$ transforms the local displacement field (and strain rate) into local stress state and in turns to local internal forces.

Time discretization

Generally, the Equation A.73 should be solved numerically at each time step. The time interval $\mathbb{I}_t$ is descretized into short intervals $\Delta t : t_0, t_1, t_2 ....$ with $t_n = t_{n-1} + \Delta t$. Denote with $\hat{\underline{\boldsymbol{U}}}_G^{h,n}$, $\hat{\underline{\boldsymbol{V}}}_G^{h,n}$ and $\hat{\underline{\boldsymbol{A}}}_G^{h,n}$ the displacement, velocity and acceleration global DOF vectors respectively, evaluated at the time step t_n. The time solution of the discretized dynamic balance equation can be inscribed into the general time-marching Newmark's solution scheme for dynamic problems (Chan and Newmark, 1952; Hughes, 1987; Simo, 1992). Consider, therefore, three integration parameters $\alpha, \beta, \gamma \in [0, 1]$. The Equation A.73 can be written, at time step $t_{n+\alpha}$, as (Komatitsch, 1997; Komatitsch and Tromp, 1999) :

$$\begin{cases} \mathbb{M}\hat{\underline{\boldsymbol{A}}}_G^{h,n+1} = \mathbb{F}^{ext,n+1} - \mathbb{F}^{int}\left(\hat{\underline{\boldsymbol{U}}}_G^{h,n+1}; \hat{\underline{\boldsymbol{V}}}_G^{h,n+1}\right) & \text{(A.87)} \\ \hat{\underline{\boldsymbol{U}}}_G^{h,n+1} = \hat{\underline{\boldsymbol{U}}}_G^{h,n} + \Delta t_n \hat{\underline{\boldsymbol{V}}}_G^{h,n} + \Delta t_n^2 \left[\left(\frac{1}{2} - \beta\right)\hat{\underline{\boldsymbol{A}}}_G^{h,n} + \beta \hat{\underline{\boldsymbol{A}}}_G^{h,n+1}\right] & \text{(A.88)} \\ \hat{\underline{\boldsymbol{V}}}_G^{h,n+1} = \hat{\underline{\boldsymbol{V}}}_G^{h,n} + \Delta t_n \left[(1-\gamma)\hat{\underline{\boldsymbol{A}}}_G^{h,n} + \gamma \hat{\underline{\boldsymbol{A}}}_G^{h,n+1}\right] & \text{(A.89)} \end{cases}$$

The general Newmark's scheme has the following stability properties, according to the values of the coefficients α, β, γ (Hughes, 1987):

- $\beta \geq \gamma \geq 1/2$: the system is unconditionally stable
- $\beta < 1/2$ and $\gamma \geq 1/2$: the system is conditionally stable
- $\gamma = 1/2$: the system has a 2^{nd} order approximation in time
- $\beta = 0$ and $\gamma = 1/2$: the angular momentum conservation is ensured
- $\gamma = 1/2$ and $\beta = 1/4$ (trapezoidal rule): the angular moment is not preserved, but the linear momentum is preserved. This numerical integration scheme depends on the acceleration field, which is always polluted by numerical noise (Komatitsch, 1997).

The time-marching scheme proposed in Equation A.89 solves the set of second-order ordinary differential equations (e.g. the equation expressing the conservation of the linear momentum), of the type:

$$\frac{d^2x}{dt^2} = F(x) \tag{A.90}$$

The second-order differential equation may be rewritten and decoupled into the dynamic system below, which unveil the unknown velocity field dx/dt:

$$\begin{cases} \dfrac{dv}{dt} = F(x) & \text{(A.91)} \\ \dfrac{dx}{dt} = v(x,t) & \text{(A.92)} \end{cases}$$

In analogy with Equation A.92, the system of Equations A.89 the can be rewritten as a function of the velocity field:

$$\begin{cases} \frac{1}{\Delta t}\mathbb{M}\left[\hat{\underline{\boldsymbol{V}}}_G^{h,n+1} - \hat{\underline{\boldsymbol{V}}}_G^{h,n}\right] = \mathbb{F}^{ext,n+\alpha} - \mathbb{F}^{int}\left(\hat{\underline{\boldsymbol{U}}}_G^{h,n+\alpha}; \hat{\underline{\boldsymbol{V}}}_G^{h,n+\alpha}\right) & \text{(A.93)} \\ \hat{\underline{\boldsymbol{U}}}_G^{h,n+1} = \hat{\underline{\boldsymbol{U}}}_G^{h,n} + \Delta t\left[\left(1-\frac{\beta}{\gamma}\right)\hat{\underline{\boldsymbol{V}}}_G^{h,n} + \frac{\beta}{\gamma}\hat{\underline{\boldsymbol{V}}}_G^{h,n+1}\right] + \Delta t^2\left(\frac{1}{2}-\frac{\beta}{\gamma}\right)\hat{\underline{\boldsymbol{A}}}_G^{h,n} & \text{(A.94)} \\ \hat{\underline{\boldsymbol{A}}}_G^{h,n+1} = \frac{1}{\gamma\Delta t}\left[\hat{\underline{\boldsymbol{V}}}_G^{h,n+1} - \hat{\underline{\boldsymbol{V}}}_G^{h,n}\right] + \left(1-\frac{1}{\gamma}\right)\hat{\underline{\boldsymbol{A}}}_G^{h,n} & \text{(A.95)} \end{cases}$$

along with the Crank-Nicolson approximations:

$$\hat{\underline{\boldsymbol{U}}}_G^{h,n+\alpha} = \alpha\hat{\underline{\boldsymbol{U}}}_G^{h,n+1} + (1-\alpha)\,\hat{\underline{\boldsymbol{U}}}_G^{h,n} \tag{A.96}$$

$$\mathbb{F}^{ext,n+\alpha} = \alpha\mathbb{F}^{ext,n+1} + (1-\alpha)\,\mathbb{F}^{ext,n} \tag{A.97}$$

Some interesting properties may be mentioned for this velocity scheme: if the coefficients are set to $\alpha = \beta/\gamma = 1/2$, i.e. a conservative *leapfrog* scheme, independent on the acceleration field and with a second order accuracy if $\beta = 1/2$ and $\gamma = 1$ (Simo, 1992; Simo et al., 1992). The acceleration is estimated *a posteriori* as:

$$\hat{\underline{\boldsymbol{A}}}_G^{h,n+1} = \frac{\hat{\underline{\boldsymbol{V}}}_G^{h,n+1} - \hat{\underline{\boldsymbol{V}}}_G^{h,n}}{\Delta t} \tag{A.98}$$

See Hughes (1987); Simo (1992) for major details on the stability of the leap-frog scheme. In mathematics, leapfrog integration methods are employed to numerically integrate differential equations of the form of Equation A.90 (or, equivalently, of the form of Equation A.92). The name itself of the numerical scheme suggests that the leapfrog integration is equivalent to updating positions $x\,(t)$ and velocities $v\,(x,t) = dx/dt$ at interleaved time points, *staggered* in such a way that they *leapfrog* over each other. In contrast to Euler integration methods (i.e. forward/backward finite difference), which is only first-order, the leapfrog integration has second-order accuracy, yet implying the same number of function evaluations per step and it is conditionally stable (see Section A.8). In detail, the time-marching scheme may be written in the following manner:

$$\begin{cases} x_{t=\boldsymbol{t_i}} = x_{t=\boldsymbol{t_{i-1}}} + v|_{t=\boldsymbol{t_i}-\frac{1}{2}\boldsymbol{\Delta t}}\Delta t & \text{(A.99)} \\ a|_{t=\boldsymbol{t_i}} = \left(\frac{d^2x}{dt^2}\right)\Big|_{t=\boldsymbol{t_i}} = F\left(x|_{t=\boldsymbol{t_i}}\right) & \text{(A.100)} \\ v|_{t=\boldsymbol{t_i}+\frac{1}{2}\boldsymbol{\Delta t}} = v|_{t=\boldsymbol{t_i}-\frac{1}{2}\boldsymbol{\Delta t}} + a|_{t=\boldsymbol{t_i}}\Delta t & \text{(A.101)} \end{cases}$$

The separation of the acceleration calculation onto the beginning and end of a step means that if time resolution is increased by a factor of two ($\Delta t \to \Delta t/2$). There are two primary strengths to leapfrog integration, namely: (1) the time-reversibility (i.e. one can integrate forward n steps, and then integrate backwards n steps to arrive at the same starting position) and (2) its *symplectic* nature (i.e. the conservation of the energy related to the dynamical system).

At this point, by employing the *leapfrog* scheme, the nature of the Newmark's scheme is unravelled into its intrinsic phases: a *prediction*, the solution of the system and the final *correction*. The prediction $()^p$ reads:

$$\begin{cases} \hat{\underline{\boldsymbol{U}}}_G^{h,p} = \hat{\underline{\boldsymbol{U}}}_G^{h,n} & \text{(A.102)} \\ \hat{\underline{\boldsymbol{V}}}_G^{h,p} = \hat{\underline{\boldsymbol{U}}}_G^{h,n} & \text{(A.103)} \end{cases}$$

The system is then solved as:

$$\frac{1}{\Delta t}\mathbb{M}\Delta\underline{\hat{\boldsymbol{V}}}_G^{h,n} = \Delta\mathbb{F}^{ext,n+1/2} - \mathbb{F}^{int}\left(\underline{\hat{\boldsymbol{U}}}_G^{h,n+1/2}; \underline{\hat{\boldsymbol{V}}}_G^{h,n+1/2}\right) \tag{A.104}$$

and finally the correction $()^c$ is applied:

$$\underline{\hat{\boldsymbol{V}}}_G^{h,n+1} = \underline{\hat{\boldsymbol{V}}}_G^{h,n} + \Delta\underline{\hat{\boldsymbol{V}}}_G^{h,n} \tag{A.105}$$

$$\underline{\hat{\boldsymbol{U}}}_G^{h,n+1} = \underline{\hat{\boldsymbol{U}}}_G^{h,n} + \Delta t\Delta\underline{\hat{\boldsymbol{V}}}_G^{h,n} \tag{A.106}$$

$$\underline{\hat{\boldsymbol{A}}}_G^{h,n+1} = \underline{\hat{\boldsymbol{A}}}_G^{h,n} + \frac{\Delta\underline{\hat{\boldsymbol{V}}}_G^{h,n}}{\Delta t} \tag{A.107}$$

A.8 Courant-Friedrichs-Lewy (CFL) condition

The leapfrog integrator applied to the dynamic system of equation is conditionally stable and it requires a constant time step Δt. According to several authors (Komatitsch and Vilotte, 1998; Komatitsch et al., 2005; Festa and Vilotte, 2005; Cupillard et al., 2012, among others), the accuracy and stability of the numerical method is ensured when:

$$\Delta t \leq \Delta t_{min} = \frac{2}{\omega_{max}} \tag{A.108}$$

where ω_{max} represents an estimation of the higher frequency of the system, roughly estimated as $\left(\frac{\Delta x}{C_p}\right)_{min}$, with Δx being the characteristic element size and C_p is the P-wave velocity. The stability condition translate the need to sample a transient wave field at a higher rate than the wave speed and avoid aliasing. As a corollary, when the grid point separation is reduced, the upper limit for the time step also decreases. To ensure the stability to be preserved against the numerical spurious errors, the *Courant-Friedrichs-Lewy condition* (CFL) (Courant et al., 1956) kicks in and reduces the minimum time step to:

$$\Delta t \leq C\Delta t_{min} = C\left(\frac{d}{c_p}\right)_{min} \tag{A.109}$$

where d is the size of an element, n is the order of the polynomial, λ is the minimum wavelength and C is the Courant number which is generally considered to be 0.4 for a 3D modelling.

$$d \leq \frac{n}{5}\lambda_{min} \sim \frac{n}{10}\lambda_{min} \tag{A.110}$$

A.9 Absorbing boundary conditions

To be able to model the wave-propagation problem in a full/half space, some absorbing boundary conditions are routinely employed. As a matter of fact, a dichotomy arises between the necessity to model infinitely extended domains and the necessity to truncate the computational domain due to computational limits. As observed by several authors (Claerbout, 1970; Clayton and Engquist, 1977, ,among others), the standard boundary conditions used at the sides of seismic section in wave-equation migration generate artificial reflections. These reflections from the edges of the computational grid appear as artifacts in the final section. Clayton and Engquist (1977) observed tht padding the section with zero traces on either side adds to the computational cost and simply delays the inevitable reflections. Several stable absorbing boundary conditions have been analytically derived in the past (e.g., Clayton and Engquist, 1977; Engquist and Majda, 1977). More recently, an efficient absorbing boundary

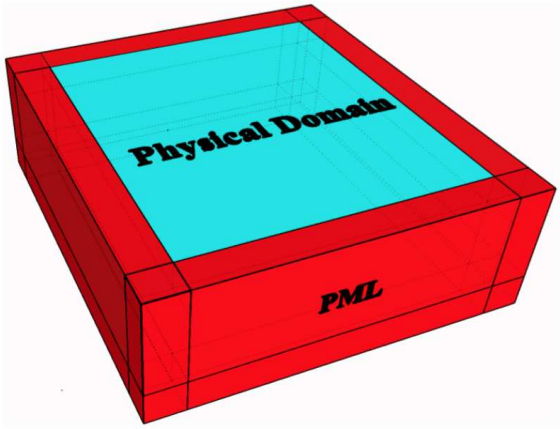

Figure A.5: A half space domain surrounded by PML materials

condition has been mediated from electro-magnetism (Berenger, 1994) and applied to computational seismology (Festa and Vilotte, 2005): the Perfect Matched Layers (PML) is herein applied to the SE formulation. PML is an absorbing medium that envelopes the computational domain so to absorb the wave-field impinging the domain truncation surface (see Figure A.5). In a wider sense, a PML corresponds to an imaginary extension of the real physical space. This extension of the spatial coordinates to the complex space is obtained by the following coordinate change Festa and Vilotte (2005) :

$$\tilde{x} = x + \frac{\Sigma(x)}{i\omega} \tag{A.111}$$

where ω is the circular frequency and $\Sigma(x)$ is an arbitrary function of x which increases regularly from the interface of the domain of interest to the external border of the PML. In turns, for a plane-wave written in the form of:

$$\mathbf{\Phi}(x, z, t) = \mathbf{A}e^{i(\omega t - k_x x - k_z z)} \tag{A.112}$$

where A is the amplitude and k_x and k_z are respectively the wave numbers in x and z directions, will be transformed in the PML in x direction as:

$$\tilde{\mathbf{\Phi}}(x, z, t) = \mathbf{\Phi}(x, z, t)e^{-\frac{k_x}{\omega}\Sigma} \tag{A.113}$$

which decreases exponentially independently of frequencies because of the ratio $\frac{k_x}{\omega}$. Consider the decomposition in plane-wave of an Rayleigh wave propagating along the free surface ($z = z_{max}$). The dependence along x direction of that wave will have the same characteristics as those of volume waves: they respect the same decreasing properties when they enter into the PML in x direction. Additionally, they preserve the characteristics of a surface wave, i.e. the movement is characterised by an exponential decreasing with the depth and an elliptic retrograde polarisation in the propagation plane on the surface, and prograde in the depth. The classical choice of transformation in PML domain, as indicated in A.111 allows for a uniform decay, independent of frequencies inside the absorbing layer PML and a simplified description of the motions. More sophisticated expressions can lead to just as simple representations in the time domain, with interesting properties inside the PML. If a real part is added to the frequency term, the pole of the stretching is moved away from the origin of the reference frame, into the imaginary axis, and the transformation can be written as:

$$\tilde{x} = x + \frac{\Sigma(x)}{i\omega + \omega_c} \tag{A.114}$$

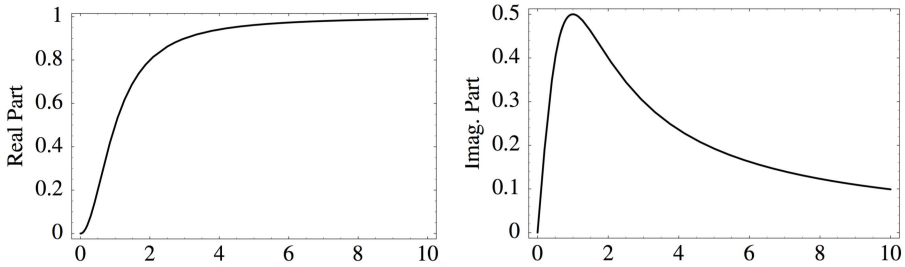

Figure A.6: Real and imaginary parts of the decay factor. The real parts controls the attenuation inside the absorbing layer and it is an increasing function reaching assymptotically the value 1. The imaginary part represents a phase shift, maximum at $\omega = \omega_c$ and decreasing to zero for both $\omega = 0$ and $\omega \to \infty$ Festa and Vilotte (2005)

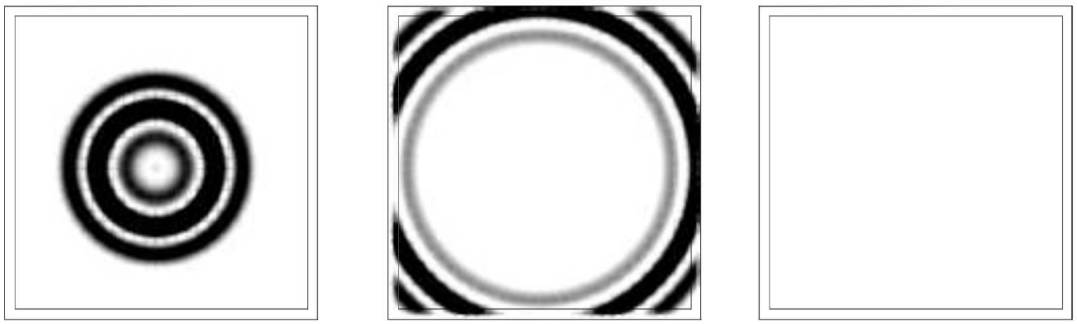

Figure A.7: Modulus of the velocity at three different instants Festa and Vilotte (2005) to show about the absorbing properties of PML

With this transformation, the compressional waves decrease in the PML following :

$$\tilde{\mathbf{\Phi}}(x,z,t) = \mathbf{\Phi}(x,z,t) e^{-\frac{k_x}{\omega}\frac{\omega^2 - i\omega\omega_c}{\omega^2+\omega_c^2}\Sigma} \tag{A.115}$$

where ω_c is for instance, the circular cut-off frequency. The transformation is finally dependent of frequencies through the factor $\frac{\omega^2 - i\omega\omega_c}{\omega^2+\omega_c^2}$. Its real part contributes to the changes of the amplitude of decay, while its imaginary part is responsible of a phase shift. An example of the real part and imaginary part of the decay factor, plotted as functions of ω/ω_c is presented in Figure A.6 Festa and Vilotte (2005). For the case of ($\omega = 0$ and k_x/ω finite), the real and imaginary parts tend to zero conducting to an elastic regime. When ($\omega \to \infty$), the real part tends tend to 1, while the imaginary part vanishes. In this case, a PML standard is asymptotically found. Regarding the real part, the PML medium is like an elastic medium at low frequencies and a dissipative layer in high-range, the transition being described by a low pass filtering with a cut off frequency ω_c. On the other hand, the imaginary part has a maximum for $\omega = \omega_c$, which corresponds to a phase shift. Figure A.7 (Festa and Vilotte, 2005) presents the modulus of velocity at three different instants : when waves propagate in the domain of interest, when waves arrive at the PML, and when waves are absorbed by PML. The source is simply an explosive Ricker at the center of the domain. It is shown that there is no visible reflections is seen to come back into the elastic medium.

A.10 Solid-Fluid interaction

The wave-field in the acoustic, inviscid fluid is governed by the system of conservation and dynamics equations (Landau and Lifshitz, 1959; Komatitsch et al., 2000):

$$\begin{cases} \dot{u}_W\left(\underline{\boldsymbol{x}};t\right)+\rho_W\left(\underline{\boldsymbol{x}};t\right)c_W^2\underline{\boldsymbol{\nabla}}_x.\underline{\boldsymbol{v}}=0, & \text{(conservation of mass)} \quad \text{(A.116)} \\ \underline{\boldsymbol{\nabla}}_x u_W+\rho_W\left(\underline{\boldsymbol{x}};t\right)\underline{\dot{\boldsymbol{v}}}=\underline{\mathbf{0}}, & \text{(conservation of linear momentum)} \quad \text{(A.117)} \end{cases}$$

with ρ_W being the water density, u_W the water pressure (defined as $u_W=-\underline{\underline{\boldsymbol{\sigma}}}:\underline{\underline{\boldsymbol{I}}}_3$), c_W the water pressure-wave velocity (defined as $c_W=\sqrt{\kappa_W/\rho_W}$, with κ_W the water bulk modulus). In SEM3D, the gravity was neglected, the water density ρ_W was considered homogeneous field, and the fluid is considered *irrotational* (i.e. $\underline{\boldsymbol{\nabla}}_x\wedge\underline{\boldsymbol{v}}=\underline{\mathbf{0}}$). At this point the velocity can be rewritten as the gradient of its scalar potential $\underline{\boldsymbol{v}}=\underline{\boldsymbol{\nabla}}_x\phi$ thus allowing to drop the pressure term in Equations A.117, and condense them into the following wave-equation:

$$\Delta_x\phi=c_W^{-2}\ddot{\phi} \quad \text{(A.118)}$$

To couple the two media at a fluid-solid interface, we have to ensure the continuity of traction $\underline{\boldsymbol{t}}_n\left(\underline{\boldsymbol{x}};t\right)=\underline{\underline{\boldsymbol{\sigma}}}\left(\underline{\boldsymbol{x}};t\right).\underline{\boldsymbol{n}}_{SF}\left(\underline{\boldsymbol{x}}\right)$, where $\underline{\boldsymbol{n}}_{SF}\left(\underline{\boldsymbol{x}}\right)$ denotes the unit normal to the solid-fluid interface. Due to the fact that the fluid is assumed inviscid, the traction vector takes the form:

$$\underline{\boldsymbol{t}}_n\left(\underline{\boldsymbol{x}};t\right)=-u_W\left(\underline{\boldsymbol{x}};t\right)\underline{\boldsymbol{n}}_{SF}\left(\underline{\boldsymbol{x}}\right)=\rho\dot{\phi}\left(\underline{\boldsymbol{x}};t\right) \quad \text{(A.119)}$$

On the other hand, the kinematic condition reads:

$$\underline{\boldsymbol{\nabla}}_x\phi\left(\underline{\boldsymbol{x}};t\right).\underline{\boldsymbol{n}}_{SF}\left(\underline{\boldsymbol{x}}\right)=\underline{\dot{\boldsymbol{u}}}\left(\underline{\boldsymbol{x}};t\right).\underline{\boldsymbol{n}}_{SF}\left(\underline{\boldsymbol{x}}\right) \quad \text{(A.120)}$$

Appendix B

Non-linear material modelling in explicit dynamics

B.1 Basic rheological assumptions

The *rheology* is properly defined as the study of the mathematical relationship between stresses and strain velocities in a deformable body. Those *constitutive relationships* are not unique but arbitrary, since they cannot directly be inferred form the fundamental equations of motion (i.e. the conservation of the linear and angular momentum). However, whichever constitutive relationship must satisfy the the fundamental laws of thermodynamics.
Roughly speaking, two classes of models are commonly employed for soil mechanics (Zienkiewicz et al., 1999), namely (1) *micro-mechanical* or *physical* models, developed for materials whose behaviour is highly influenced by its micro-structure (at smaller scale) and (2) *macro-mechanical* or *phenomenological* models for materials. Although the description of a material behaviour becomes more accurate (yet complex) by increasing the number of spanned scales, many materials (e.g., concrete and geo-materials) can be idealized as *equivalent continua*, rather than assemblages of particles. This *phenomenological* approach relies on the concept of *Representative Elementary Volume* (REV). The latter has a characteristic size much greater than the smaller scale heterogeneity, whose impact on the mechanical properties measured at the upper scale becomes statistically homogeneous. At this scale, the phenomenological model do not require any specific knowledge of the micro-structure and the mathematical model is validated upon experimental findings at the REV scale. The inferred properties will be ideally *attached* to the material point in common boundary problems. Therefore, the REV represents an infinitesimal volume dV in the Euclidean affine physical space, characterized by the fact that all the particles in it at time t_0 remain in it at all time t, despite the deformation the REV undergoes. In this sense, the REV centroid $\underline{\boldsymbol{x}}\,(t)$ represents the position of the abstract particle defined as *material point*. For granular materials, it can be possible to geometrically define the underlying micro-structure within the REV, provided that it contains a sufficient and representative number of grains. The material is called *homogeneous* (or more precisely *statistically homogeneous* whether all $dV s$ are statistically indistinguishable (i.e. same number of grains, same shapes and other morphological characteristics). No observable fluctuations of the material and physical quantities is observed at the phenomenological scale and the following inequalities must hold when considering an *continuum-equivalent* approach:

$$d \ll L_{REV} \ll L \tag{B.1}$$

where d, L_{REV} and L are the characteristic dimension of the micro-structural heterogeneities, of the REV and of the physical domain respectively.
In the following, a generic boundary problem is considered: a $d-$dimensional solid medium occupy-

ing an Euclidean open domain $\Omega \subset \mathbb{R}^d$, bounded by a smooth boundary $\partial\Omega$ with $\bar{Omega} = \Omega \bigcup \partial\Omega$ and a time interval of interest $\mathbb{I}_t = [0, T] \subset \mathbb{R}^+$. The position of any material point is defined by the space-coordinate $\underline{\boldsymbol{x}}$ (Euclidean description).
The problem of defining a material constitutive relationship can be as the definition of an admissible Cauchy's stress tensor $\underline{\underline{\boldsymbol{\sigma}}} : \Omega \times \mathbb{I}_t \to \mathbb{S} \subset \mathbb{R}^{d \times d}$ (in *small strain* approximation), being $\mathbb{S}$ the symmetric tensor subspace of order $d\,(d+1)\,/2$. This local stress state refers to the considered REV. Experimental evidence showed that stress state is affected by several variables (e.g. the temperature field) but primarily it depends on the body deformation pattern. The latter is fully determined at each time t_n by knowing the local velocity field $\underline{\boldsymbol{v}}_n(\underline{\boldsymbol{x}}; t)$. More specifically, it depends on the motion mapping $\underline{\boldsymbol{\chi}}$ between reference and actual configuration (at time t), defined as:

$$\underline{\boldsymbol{\chi}} : \Omega_0 \to \Omega_t, \quad \underline{\boldsymbol{x}}\,(t) = \underline{\boldsymbol{\chi}}\,(\underline{\boldsymbol{X}}; t) \tag{B.2}$$

where Ω_0 and Ω_t represent the initial and actual open physical domains, $\underline{\boldsymbol{X}}, \underline{\boldsymbol{x}}\,(\underline{\boldsymbol{X}}; t)$ the position vectors in the initial and actual configuration respectively.
Disregarding from now on the effect of the temperature in the material description (it might be added afterwards by changing material properties accordingly, based on the results of mechanical tests performed at different temperatures), a general constitutive relationship can be formulated by means of the *memory functional* $\mathcal{F}$:

$$\underline{\underline{\boldsymbol{\sigma}}}\,(\underline{\boldsymbol{x}}; t) = \mathcal{F}_{s\in[0,t];\underline{\boldsymbol{Y}}\in\Omega_0}\left(\underline{\boldsymbol{\chi}}\,(\underline{\boldsymbol{Y}}, s)\right) \tag{B.3}$$

The latter expression states that the Cauchy's stress tensor in actual configuration $\underline{\underline{\boldsymbol{\sigma}}}(\underline{\boldsymbol{x}}; t)$depends on the past and present motion history ($s \in [0, t]$) and on each point position $\underline{\boldsymbol{Y}}$ within the domain Ω_0 (in reference configuration). EquationB.3 respects the *causality principle*, i.e. the Cauchy's stress tensor does not depend on the future history.
The general constitutive relationship in EquationB.3 can be refined by making the so called assumption of *local action*: the spatial dependency of the memory function $\mathcal{F}$ is restricted to the infinitesimal neighbourhood of $\underline{\boldsymbol{X}} \in \Omega_0$, thus assuming that the local stress state depends on the local motion. Under this assumption furthermore, the motion mapping can be approximated by its n^{th}-order Taylor's series expansion and EquationB.3 reduces to:

$$\underline{\underline{\boldsymbol{\sigma}}}\,(\underline{\boldsymbol{x}}; t) = \mathcal{F}_{s\in[0,t];n>0}\left(\underline{\boldsymbol{\chi}}\,(\underline{\boldsymbol{X}}; s)\,; \frac{\partial^n \underline{\boldsymbol{\chi}}}{\partial \underline{\boldsymbol{X}}}^n\,(\underline{\boldsymbol{X}}; s)\right) \tag{B.4}$$

EquationB.4 further simplifies if one considers just the 1^{st}-order gradient $\underline{\underline{\boldsymbol{F}}}\,(\underline{\boldsymbol{X}}; t)$ (also called *deformation gradient*):

$$\underline{\underline{\boldsymbol{\sigma}}}\,(\underline{\boldsymbol{x}}; t) = \mathcal{F}_{s\in[0,t]}\left(\underline{\boldsymbol{\chi}}\,(\underline{\boldsymbol{X}}; s)\,; \underline{\underline{\boldsymbol{F}}}\,(\underline{\boldsymbol{X}}; s)\right) \tag{B.5}$$

A material that satisfies EquationB.5 is called *materially simple*. This kind of models neglects the strain second-order effects. This means that the motion mapping can be fully described by the linear tangent application $\underline{\underline{\boldsymbol{F}}}\,(\underline{\boldsymbol{X}}; t)$ that transforms the material fibre $\underline{\boldsymbol{dX}}$ into the current fibre $\underline{\boldsymbol{dx}}$ in the actual configuration. This assumption is most of the times confirmed by experimental results.

Material behaviour can be described according to different reference systems. Nevertheless Cauchy's stress should be evaluated independently on the adopted reference system. For a materially simple material, the Cauchy's stress in another reference system $\mathcal{R}^\star$ reads:

$$\underline{\underline{\boldsymbol{\sigma}}}^\star\,(\underline{\boldsymbol{x}}; t) = \mathcal{F}^\star{}_{s\in[0,t]}\left(\underline{\boldsymbol{\chi}}^\star\,(\underline{\boldsymbol{X}}; s)\,; \underline{\underline{\boldsymbol{F}}}^\star\,(\underline{\boldsymbol{X}}; s)\right) \tag{B.6}$$

where the change of reference system is fully defined by the linear mapping:

$$\begin{aligned} \underline{\boldsymbol{\chi}}^\star\,(\underline{\boldsymbol{X}}; t) &= \underline{\underline{\boldsymbol{R}}}\,(t)\,.\underline{\boldsymbol{\chi}}\,(\underline{\boldsymbol{X}}; s) + \underline{\boldsymbol{c}}\,(t)\,, \\ \underline{\underline{\boldsymbol{F}}}^\star\,(\underline{\boldsymbol{X}}; t) &= \underline{\underline{\boldsymbol{R}}}\,(t)\,.\underline{\underline{\boldsymbol{F}}}^\star\,(\underline{\boldsymbol{X}}; s)\,, \quad \forall \underline{\underline{\boldsymbol{R}}}\,(t) \in GO^+\left(\mathcal{R}^3\right) \end{aligned} \tag{B.7}$$

with $\underline{\underline{\boldsymbol{R}}}(t)$ and $\underline{\boldsymbol{c}}(t)$ are the orthogonal rotation tensor and the translation vector respectively. Cauchy's stress tensor is *by construction* an *objective* quantity, thus:

$$\underline{\underline{\boldsymbol{\sigma}}}^{\star}\left(\underline{\boldsymbol{x}};t\right)=\underline{\underline{\boldsymbol{R}}}\left(t\right).\underline{\underline{\boldsymbol{\sigma}}}\left(\underline{\boldsymbol{x}};t\right).\underline{\underline{\boldsymbol{R}}}^{T}\left(t\right),\quad\forall\underline{\underline{\boldsymbol{R}}}\left(t\right)\in GO^{+}\left(\mathcal{R}^{3}\right) \tag{B.8}$$

The deformation gradient is not objective instead, and it transforms as $\underline{\underline{\boldsymbol{F}}}^{\star}(\underline{\boldsymbol{X}};t)=\underline{\underline{\boldsymbol{R}}}(t).\underline{\underline{\boldsymbol{F}}}(\underline{\boldsymbol{X}};t)$. Therefore, by substituting EquationB.8 in EquationB.6 one gets the following relation for the memory functional $\mathcal{F}$:

$$\begin{aligned}&\underline{\underline{\boldsymbol{R}}}\left(t\right).\mathcal{F}_{s\in[0,t]}\left(\underline{\boldsymbol{\chi}}\left(\underline{\boldsymbol{X}};s\right);\underline{\underline{\boldsymbol{F}}}\left(\underline{\boldsymbol{X}};s\right)\right).\underline{\underline{\boldsymbol{R}}}^{T}\left(t\right)=\\&\mathcal{F}^{\star}\left(\underline{\underline{\boldsymbol{R}}}\left(s\right).\underline{\boldsymbol{\chi}}\left(\underline{\boldsymbol{X}};s\right)+\underline{\boldsymbol{c}}\left(s\right);\underline{\underline{\boldsymbol{R}}}\left(s\right).\underline{\underline{\boldsymbol{F}}}\left(\underline{\boldsymbol{X}};s\right)\right)\quad\forall\underline{\underline{\boldsymbol{R}}}\left(t\right)\in GO^{+}\left(\mathcal{R}^{3}\right)\end{aligned} \tag{B.9}$$

By considering the mentioned properties of the memory functional, a further step into the definition of the constitutive relationship maybe done considering the fundamental *material indifference principle* which states that memory functional $\mathcal{F}$ is insensitive to any euclidean transformation. The functional shape remains the same upon time-dependent roto-translation and time shifts. The latter kinds of transformations causes inertial effects which might be eventually taken into consideration as external forces. Centrifugal stress states are not disregarded herein, but they are not involved into the material law description. They are computed directly by enforcing the momentum balance equation on the body. As an example, the material indifference principle states that the stiffness of elastic materials does not depend on the chosen reference system.
Material indifference infers two corollary properties of the memory functional:

1. $\mathcal{F}$ does not explicitly depend on the position $\underline{\boldsymbol{x}}(\underline{\boldsymbol{X}};t)$

$$\begin{aligned}&\forall\underline{\boldsymbol{c}}\left(t\right)\in\mathbb{R}^{3},\underline{\underline{\boldsymbol{R}}}\left(t\right)=\underline{\underline{\boldsymbol{I}}},\\&\mathcal{F}'_{s\in[0,t]}\left(\underline{\boldsymbol{\chi}}\left(\underline{\boldsymbol{X}};s\right)+\underline{\boldsymbol{c}}\left(s\right);\underline{\underline{\boldsymbol{F}}}\left(\underline{\boldsymbol{X}};s\right)\right)=\\&\mathcal{F}_{s\in[0,t]}\left(\underline{\boldsymbol{\chi}}\left(\underline{\boldsymbol{X}};s\right);\underline{\underline{\boldsymbol{F}}}\left(\underline{\boldsymbol{X}};s\right)\right)\rightarrow\frac{\partial\mathcal{F}}{\partial\underline{\boldsymbol{x}}}=\underline{\boldsymbol{0}},\quad\underline{\underline{\boldsymbol{\sigma}}}\left(\underline{\boldsymbol{x}};t\right)=\mathcal{F}_{s\in[0,t]}\left(\underline{\underline{\boldsymbol{F}}}\left(\underline{\boldsymbol{X}};s\right)\right)\end{aligned} \tag{B.10}$$

2. $\mathcal{F}$ does not explicitly depend on the time

$$\begin{aligned}&\forall t_{0},\underline{\underline{\boldsymbol{R}}}\left(t\right)=\underline{\underline{\boldsymbol{I}}},\mathcal{F}'_{s\in[0,t]}\left(\underline{\underline{\boldsymbol{F}}}\left(\underline{\boldsymbol{X}};s\right),t-t_{0}\right)=\\&\mathcal{F}_{s\in[0,t]}\left(\underline{\underline{\boldsymbol{F}}}\left(\underline{\boldsymbol{X}};s\right),t\right)\rightarrow\frac{\partial\mathcal{F}}{\partial t}=\underline{\boldsymbol{0}}\end{aligned} \tag{B.11}$$

The first statement cannot be directly extended to the $\underline{\boldsymbol{X}}$. A material defined by a memory function $\mathcal{F}$ independent on the position in the reference configuration is called *homogeneous* material. Unless geo-materials are generally heterogeneous materials, only homogeneous materials will be considered for the sake of simplicity. Earth's crust and shallow geological deposits will be considered as the ensemble of different homogeneous parts. The second corollary property does not exclude at all the material dependence on time (i.e. irrecoverable effects due to the past stress path) and on the velocity of charge (i.e. stress relaxation due to viscous effects). Those phenomena are included by coupling the constitutive relationship with a set of equations that relate the stress evolution to the evolution of *hidden* or *internal* variables. Their evolution will be described by an time-incremental approach, that involves the time-derivatives of all those quantities. The memory function is *explicitly* independent on time by means that it is not affected by the selected observation time of the reference system. Those variables represent extra degrees of freedom of the model and they may describe the effect of the underlying micro-structure (e.g. in case of anisotropy) or keep track of the whole loading path.

B.2 Viscous-Elastic modelling: key concepts

The (hyper)elastic response of the material is described by postulating the existence of a *stored energy function* $\psi\left(\underline{\underline{\boldsymbol{\varepsilon}}}_x^{el}\right) : \mathbb{S} \rightarrow \mathbb{R}$, such that:

$$\underline{\underline{\boldsymbol{\sigma}}}\left(\underline{\boldsymbol{x}};t\right) = \underline{\underline{\boldsymbol{\nabla}}}_{\varepsilon^{el}} \psi\left(\underline{\boldsymbol{x}};t\right) \tag{B.12}$$

For an elastic isotropic material, the rheological model reads:

$$\underline{\underline{\boldsymbol{\sigma}}}\left(\underline{\boldsymbol{u}}\left(\underline{\boldsymbol{x}};t\right)\right) = \lambda\left(\underline{\boldsymbol{x}}\right) Tr\left(\underline{\underline{\boldsymbol{\varepsilon}}}_x\left(\underline{\boldsymbol{u}}\left(\underline{\boldsymbol{x}};t\right)\right)\right) + 2\mu\left(\underline{\boldsymbol{x}}\right)\underline{\underline{\boldsymbol{\varepsilon}}}_x\left(\underline{\boldsymbol{u}}\left(\underline{\boldsymbol{x}};t\right)\right) \tag{B.13}$$

with $\lambda\left(\underline{\boldsymbol{x}}\right)$, $\mu\left(\underline{\boldsymbol{x}}\right)$ are the so called Lamé coefficients, and the linear operator $\underline{\underline{\boldsymbol{\varepsilon}}}_x\left(\cdot\right)$ is the small strain tensor, defined as:

$$\underline{\underline{\boldsymbol{\varepsilon}}}_x\left(\underline{\boldsymbol{u}}\left(\underline{\boldsymbol{x}};t\right)\right) = \underline{\boldsymbol{u}} \otimes_s \underline{\boldsymbol{\nabla}}_x\left(\underline{\boldsymbol{x}};t\right) \tag{B.14}$$

being $\underline{\cdot} \otimes_s \underline{\boldsymbol{\nabla}}_x$ the symmetric gradient operator. The Lamé coefficients are usually casted into the so called *elasticity* 4^{th} *tensor* $\mathbb{D}^{el}$, that reads:

$$\mathbb{D}^{el}\left(\underline{\boldsymbol{x}}\right) = \lambda\left(\underline{\boldsymbol{x}}\right)\underline{\underline{\boldsymbol{I}}} \otimes \underline{\underline{\boldsymbol{I}}} + \mu\left(\underline{\boldsymbol{x}}\right)\mathbb{I}, \quad \underline{\underline{\boldsymbol{\sigma}}}\left(\underline{\boldsymbol{u}}\left(\underline{\boldsymbol{x}};t\right)\right) = \mathbb{D}^{el} : \underline{\underline{\boldsymbol{\varepsilon}}}_x\left(\underline{\boldsymbol{u}}\left(\underline{\boldsymbol{x}};t\right)\right) \tag{B.15}$$

with $\underline{\underline{\boldsymbol{I}}}$ the 2^{nd} order identity tensor and $\mathbb{I}$ the 4^{th} order tensor. When one considers an anisotropic elastic $\mathbb{D}^{el}\left(\underline{\boldsymbol{x}}\right)$ has 21 independent coefficients. The $\mathbb{D}^{el}\left(\underline{\boldsymbol{x}};t\right)$ is the fourth-order linearized elastic stiffness tensor, featured by minor and major symmetries, and positive definite, if restricted to $\mathbb{S}$ (the so called *Hadamard's condition* Festa and Vilotte, 2005):

$$\underline{\underline{\boldsymbol{A}}} : \mathbb{D}^{el}\left(\underline{\boldsymbol{x}};t\right) : \underline{\underline{\boldsymbol{A}}} \geq \alpha\left(\underline{\boldsymbol{x}}\right)\underline{\underline{\boldsymbol{A}}} : \underline{\underline{\boldsymbol{A}}} > 0 \tag{B.16}$$

In a more general sense, the stress state in attenuating media is determined by the functional:

$$\underline{\underline{\boldsymbol{\sigma}}}\left(\underline{\boldsymbol{x}};t\right) = \int_{-\infty}^{t} \mathbb{D}^{el}\left(\underline{\boldsymbol{x}};t-\tau\right)\underline{\underline{\boldsymbol{\varepsilon}}}_x\left(\underline{\boldsymbol{u}}\left(\underline{\boldsymbol{x}};\tau\right)\right)d\tau \tag{B.17}$$

In seismology, the quality factor Q is generally observed to be approximately constant over a wide range of frequencies. To approximate such an absorption-band solid, Liu and Archambeau (1976) introduced the idea of using a series of L standard linear solids (Moczo et al., 2007). It has been widely observed that the Earth's bulk quality factor is several hundred times larger than the shear quality factor, which means that attenuation mainly depends on the shear quality factor. To effectively model attenuation one can focus onto modelling the time evolution of the average isotropic shear modulus (Komatitsch et al., 2005), as proposed by Liu and Archambeau (1976):

$$\mu\left(\underline{\boldsymbol{x}};t\right) = \mu_R\left(\underline{\boldsymbol{x}}\right)\left[1 - \sum_{i=1}^{L}\left(1 - \frac{\tau_i^{\varepsilon}}{\tau_i^{\sigma}}\exp\left(-\frac{t}{\tau_i^{\sigma}}\right)\right)\right]H\left(t\right) \tag{B.18}$$

with $H\left(t\right)$ is the Heaviside's function and τ_i^{σ}, τ_i^{ε} denote the stress and strain relaxation times, respectively, of the i^{th} standard solid and $\mu_R\left(\underline{\boldsymbol{x}}\right)$ the relaxed shear modulus. The stress state reads therefore:

$$\underline{\underline{\boldsymbol{\sigma}}}\left(\underline{\boldsymbol{x}};t\right) = \mathbb{D}_U^{el}\left(\underline{\boldsymbol{x}}\right) : \underline{\underline{\boldsymbol{\varepsilon}}}_x\left(\underline{\boldsymbol{u}}\left(\underline{\boldsymbol{x}};t\right)\right) - \sum_{i=1}^{L}\underline{\underline{\boldsymbol{R}}}_i\left(\underline{\boldsymbol{x}};t\right) \tag{B.19}$$

with $\mathbb{D}_U^{el}$ the un-relaxed elastic tensor:

$$\mathbb{D}_U^{el}\left(\underline{\boldsymbol{x}}\right) = \mathbb{D}^{el}\left(\underline{\boldsymbol{x}}\right)\left(1 - \sum_{i=1}^{L}\left(1 - \frac{\tau_i^{\varepsilon}}{\tau_i^{\sigma}}\right)\right) \tag{B.20}$$

The memory variables $\underline{\underline{\boldsymbol{R}}}_i(\underline{\boldsymbol{x}};t)$[1] solve each one the following differential equation:

$$\partial_t \underline{\underline{\boldsymbol{R}}}_i(\underline{\boldsymbol{x}};t) = -\frac{\underline{\underline{\boldsymbol{R}}}_i(\underline{\boldsymbol{x}};t) - \delta\mu_i \underline{\underline{\boldsymbol{e}}}(\underline{\boldsymbol{x}};t)}{\tau_i^{\sigma}} \tag{B.21}$$

with $\underline{\underline{\boldsymbol{e}}}(\underline{\boldsymbol{x}};t)$ the deviatoric strain tensor. The modulus *defect* $\delta\mu_i$ associated with each individual standard linear solid determined as

$$\delta\mu_i(\underline{\boldsymbol{x}};t) = -\mu_R(\underline{\boldsymbol{x}})\left(1 - \frac{\tau_i^{\varepsilon}}{\tau_i^{\sigma}}\right) \tag{B.22}$$

B.3 Elastic-Plastic modelling: key concepts

B.3.1 The concept of elastic domain and yield locus

As confirmed by experimental evidence, non-linear modelling is based on the assumption that the total strain rate is the sum of a recoverable and an irrecoverable strain ones (*elastic-plastic split*):

$$\dot{\underline{\underline{\boldsymbol{\varepsilon}}}}_x(\underline{\boldsymbol{x}};t) = \dot{\underline{\underline{\boldsymbol{\varepsilon}}}}^{re}(\underline{\boldsymbol{x}};t) + \dot{\underline{\underline{\boldsymbol{\varepsilon}}}}^{ir}(\underline{\boldsymbol{x}};t) \tag{B.23}$$

where $\dot{\underline{\underline{\boldsymbol{\varepsilon}}}}_x(\underline{\boldsymbol{x}};t) \in \mathbb{S}$ represents the small-strain rate tensor for a generic REV positioned at point $\underline{\boldsymbol{x}}$ in space at time t; $\dot{\underline{\underline{\boldsymbol{\varepsilon}}}}^{re}(\underline{\boldsymbol{x}};t)$ and $\dot{\underline{\underline{\boldsymbol{\varepsilon}}}}^{ir}(\underline{\boldsymbol{x}};t)$ are the recoverable and irrecoverable strain rates respectively. In the elastic-plastic framework, the recoverable strain rate is called *elastic* one ($\dot{\underline{\underline{\boldsymbol{\varepsilon}}}}^{el}_x$), whereas the entire irrecoverable part is purely plastic ($\dot{\underline{\underline{\boldsymbol{\varepsilon}}}}^{pl}_x$). Irrecoverable strain increments take place *instantaneously*, coherently with the rate-independent plasticity theory. As mentioned in subsection B.1, the non-linear cyclic material behaviour is modelled by considering a set of *hidden internal variables*, noted as $\underset{\sim}{\boldsymbol{\chi}}(\underline{\boldsymbol{x}};t) \in \mathbb{K}$). The hidden variables keep track of the loading path, by influencing the stress response at each time. For instance, a typical stress-strain curve for a simple-shear test is shown in Figure B.1. The stress-strain relationship remains linear as long as the stress state does not exceed

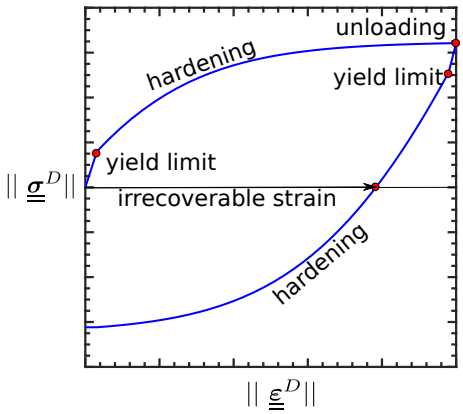

Figure B.1: Typical non-linear strain-stress curve.

a certain threshold (indicated as *yield limit* in Figure B.1). At this stage, all the strain cumulated is entirely recoverable and the set of hidden variables does not evolve since strain and stress states are directly related through the incremental linear (hyper-) elastic Hooke's law, which reads:

$$\dot{\underline{\underline{\boldsymbol{\sigma}}}}(\underline{\boldsymbol{x}};t) = \frac{\partial^2\psi}{\underline{\underline{\boldsymbol{\varepsilon}}}^{el}_x \otimes \underline{\underline{\boldsymbol{\varepsilon}}}^{el}_x} : \dot{\underline{\underline{\boldsymbol{\varepsilon}}}}^{el}_x(\underline{\boldsymbol{x}};t) = \mathbb{D}^{el}(\underline{\boldsymbol{x}};t) : \dot{\underline{\underline{\boldsymbol{\varepsilon}}}}^{el}_x(\underline{\boldsymbol{x}};t) = \mathbb{D}^{el}(\underline{\boldsymbol{x}};t) : \left(\dot{\underline{\underline{\boldsymbol{\varepsilon}}}}_x(\underline{\boldsymbol{x}};t) - \dot{\underline{\underline{\boldsymbol{\varepsilon}}}}^{pl}_x(\underline{\boldsymbol{x}};t)\right) \tag{B.24}$$

[1] $\underline{\underline{\boldsymbol{R}}}_i(\underline{\boldsymbol{x}};t)$ are symmetric and have zero trace

The Hooke's law is valid within the so called *initial elastic domain* (Simo and Hughes, 1998). As general assumption, the stress state and the set of hidden variables must lie at all the time within the an *admissible* domain referred as to the *instantaneous elastic range* $\mathbb{E}_{\sigma\chi}$ (that can be seen as a non-linear evolution of the initial one). Its boundary is called the *yield locus* $\partial\mathbb{E}_{\sigma\chi}$ (defined by means of a convex *yield function* $f\left(\underline{\underline{\boldsymbol{\sigma}}};\underset{\sim}{\boldsymbol{\chi}}\right)=0$): in an elastic-plastic framework, the stress-strain relationship is perfectly linear and elastic before crossing $\partial\mathbb{E}_{\sigma\chi}$, and $\underset{\sim}{\boldsymbol{\chi}}$ remains constant. The yield locus constrains the admissible stresses within a closed interval (i.e. the $\mathbb{E}_{\sigma\chi}$ is a closed convex set, Simo and Hughes, 1998). To sum up, the elastic-plastic material behaviour requires:

- an *instantaneous elastic range* (open set):

$$\text{int}\left(\mathbb{E}_{\sigma\chi}\right):=\{\left(\underline{\underline{\boldsymbol{\sigma}}};\underset{\sim}{\boldsymbol{\chi}}\right)\in\left(\mathbb{S}\times\mathbb{K}\right)|f\left(\underline{\underline{\boldsymbol{\sigma}}};\underset{\sim}{\boldsymbol{\chi}}\right)<0\} \tag{B.25}$$

- a *yield locus* (convex set):

$$\partial\mathbb{E}_{\sigma\chi}:=\{\left(\underline{\underline{\boldsymbol{\sigma}}};\underset{\sim}{\boldsymbol{\chi}}\right)\in\left(\mathbb{S}\times\mathbb{K}\right)|f\left(\underline{\underline{\boldsymbol{\sigma}}};\underset{\sim}{\boldsymbol{\chi}}\right)=0\} \tag{B.26}$$

- an incremental formulation to describe the path-dependent evolution of the irrecoverable (plastic) strains

This yield surface can be allowed to expand or contract (*isotropic behaviour*) or translate (*kinematic behaviour*) in the stress space. In principle, distortion of the surface can also be allowed.

B.3.2 Mathematical description of the elastic-plastic cyclic transition

Plastic flow develops as long as the the stress state is equal or exceeds the yield limit. The yield function evolves along with the plastic flow, according to the appropriate flow rule. The whole process of elastic loading and unloading or elastic-plastic loading and unloading naturally appears as constrained problem of evolution and it requires a careful mathematical description. The path-dependent stress evolution may be described by employing some non-linear programming conditions. As a matter of fact, the plastic flow activation and evolution are traditionally ruled by the manifold *Karush-Kuhn-Tucker condition* (KKT) (Simo and Hughes, 1998):

$$\mathcal{K}:\begin{cases} f\left(\underline{\underline{\boldsymbol{\sigma}}};\underset{\sim}{\boldsymbol{\chi}}\right)\leq 0, & \text{(B.27)}\\ p\geq 0, \qquad \forall\left(\underline{\underline{\boldsymbol{\sigma}}};\underset{\sim}{\boldsymbol{\chi}}\right)\in\mathbb{S}\times\mathbb{K} & \text{(B.28)}\\ \dot{p}f\left(\underline{\underline{\boldsymbol{\sigma}}};\underset{\sim}{\boldsymbol{\chi}}\right)=0 & \text{(B.29)}\end{cases}$$

where $\dot{p}$ is the so called plastic multiplier and embodies the magnitude of the plastic strain rate:

$$\dot{p}=\|\underline{\underline{\dot{\boldsymbol{\varepsilon}}}}_x^{pl}\|_{\mathcal{J}_2^\varepsilon}=\sqrt{\frac{2}{3}\underline{\underline{\dot{\boldsymbol{\varepsilon}}}}_x^{pl}:\underline{\underline{\dot{\boldsymbol{\varepsilon}}}}_x^{pl}} \tag{B.30}$$

The KKT conditions represent unilateral conditions for $\dot{p}$ and $\underline{\underline{\boldsymbol{\sigma}}}$ and they translate mathematically the experimental evidence that when the applied stress is less than the flow stress, no irrecoverable strain is developed and the instantaneous response of the device is elastic. The inadmissible stress state therefore lies outside the yield locus. The last condition of the set of Equations B.29 is called *consistency condition* and it enables to determine the actual value of $\dot{p}$ at any time during the loading

path (Simo and Hughes, 1998). The KKT approach generalizes the method of Lagrange multipliers (limited to equality constraints). The system of equations and inequalities is rarely solved directly (except for closed-form solutions). In general, many optimization algorithms can be interpreted as methods for numerically solving the KKT system of equations and inequalities. However, the consistency condition requires a complementary condition to ensure the *persistency* of the plastic flow, i.e.:

$$\dot{p}\dot{f}\left(\underline{\underline{\boldsymbol{\sigma}}};\underset{\sim}{\boldsymbol{\chi}}\right)=0, \qquad \forall\left(\underline{\underline{\boldsymbol{\sigma}}};\underset{\sim}{\boldsymbol{\chi}}\right)\in\mathbb{S}\times\mathbb{K} \tag{B.31}$$

where the $\dot{\square}$ represents the material derivative. The persistency condition B.31 assures the stress state to be confined within the evolving yield locus. For instance, if at time t a stress state attains the yield locus (i.e. $\underline{\underline{\boldsymbol{\sigma}}}(t)\in\partial\mathbb{E}_{\sigma\chi}$), the KKT must remain valid at the next time step $t+\Delta t$:

$$\begin{aligned}
&f\left(\underline{\underline{\boldsymbol{\sigma}}};\underset{\sim}{\boldsymbol{\chi}}\right)(t)=0\\
&f\left(\underline{\underline{\boldsymbol{\sigma}}};\underset{\sim}{\boldsymbol{\chi}}\right)(t+\Delta t)=f\left(\underline{\underline{\boldsymbol{\sigma}}};\underset{\sim}{\boldsymbol{\chi}}\right)(t)+\dot{f}\left(\underline{\underline{\boldsymbol{\sigma}}};\underset{\sim}{\boldsymbol{\chi}}\right)(t)\,\Delta t+o\left(\Delta t\right)\\
&\dot{p}\dot{f}\left(\underline{\underline{\boldsymbol{\sigma}}};\underset{\sim}{\boldsymbol{\chi}}\right)(t)=0,\forall\left(\underline{\underline{\boldsymbol{\sigma}}};\underset{\sim}{\boldsymbol{\chi}}\right)(t)\in\mathbb{S}\times\mathbb{K}
\end{aligned} \tag{B.32}$$

B.3.3 Flow rule and strain hardening plasticity

Once the elastic-plastic evolution has been ruled by the KKT conditions, a further feature to be addressed is the description of the plastic flow, whose evolution determines the non-linear stress-state relationship and the cumulation of irrecoverable plastic strains. From a general point of view, the *flow rule* reads:

$$\underline{\underline{\dot{\boldsymbol{\varepsilon}}}}_x^{pl}=\dot{p}\underline{\underline{\boldsymbol{\nabla}}}_\sigma g \tag{B.33}$$

where g is the so called *plastic potential*. The flow rule expressed in Equation B.33 expresses the relation between plastic multiplier and plastic strain rate: the former represents some sort of norm of the second. The plastic flow develops along the direction (in the stress space) of maximum increase of the plastic potential g. In case $g=f$, the flow rule is *associative*. Most of the models developed for soil mechanics bare on a non-associative flow rule though.
Following the same scheme, the evolution of the hidden variables is determined by the *hardening rule*, that reads:

$$\dot{\underset{\sim}{\boldsymbol{\eta}}}=-\dot{p}\underline{\underline{\boldsymbol{\nabla}}}_\chi g \tag{B.34}$$

where $\underset{\sim}{\boldsymbol{\eta}}$ is a set of *hidden kinematic variables* (in analogy with the plastic strain rate, which per se a kinematic quantity), whereas $\underset{\sim}{\boldsymbol{\chi}}$ is defined as the set of *static hidden variables*. $\underset{\sim}{\boldsymbol{\eta}}$ and $\underset{\sim}{\boldsymbol{\chi}}$ are meant to be conjugated variables.
What distinguish an elastic-plastic model from another is basically the different hardening rule adopted. A vast number of models of varying level of sophistication have been developed to model the elasto-plastic behavior of soils under cyclic conditions (Prevost, 1977, 1978; Aubry et al., 1982; Prevost, 1982, 1985; Hujeux, 1985; Dafalias, 1986, among others). The major difference among them resides in the hardening rules steering the movement of the yield surface (the *kinematic hardening*) and the change in the size (the *isotropic hardening*). From a general point of view, the two mechanisms are identified by dictating the non-linear evolution of the set of inner variables $\underset{\sim}{\boldsymbol{\chi}}=\left[\underline{\underline{\boldsymbol{X}}};R\right]$, being $\underline{\underline{\boldsymbol{X}}}$ the *backstress* (its center) and R the *yield strength* (its radius). Concerning the translation of the yield surface, Drucker and Prager (1952) and Ziegler (1959) initiated the fundamental frame-work for kinematic hardening rules. Mroz (1967) introduced successively the notion of a field of work-hardening moduli represented by a number of nested hypersurfaces, the so called *loading surfaces*.

In the generalization of his model to non-proportional loading, a new rule for kinematic hardening is proposed by Armstrong and Frederick (1966) with an evanescent strain-memory term (*dynamic recovery term*) for more accurate prediction of the multiaxial Bauschinger effect. The Armstrong and Frederick rule has been retrieved and improved extensively by Chaboche (1989) and Lemaitre and Chaboche (1990), that postulated an additive decomposition of the evolution equation of the back-stress into several components of the Armstrong-Frederick type. Another interesting approach for the translation rules is the so called *bounding surface* approach (Krieg, 1975; Dafalias and Popov, 1975, among others). It postulates the existence of a loading stress surface and an outer one (i.e. located outside the yield surface) *bounding* the evolution of the other. Expansion of the bounding surface represents the development of isotropic hardening, while translation of the yield surface inside the bounding surface describes the nonlinear kinematic hardening.

B.3.4 Solution of the elastic-plastic problem

The classical theory of rate-independent plasticity is effectively described by means of strain-stress rate (i.e. infinitesimal increments). The reason behind this approach is that it allows to follow the path-dependent material response at each step by solving a set of non-linear ordinary differential equations (ODEs). Within the context outlined above, the *incremental* integration of the rate-independent elastic-plastic model is regarded as a *strain-driven process* in which the total strain $\underline{\underline{\boldsymbol{\varepsilon}}}_x\left(\underline{\boldsymbol{u}}\left(\underline{\boldsymbol{x}};t\right)\right)$ is the basic independent variable. The set of ordinary differential equations can be casted into the following time-marching computational problem, arising by taking the sub-steps $\Delta t_n = \left(t_n; t_{n+1}\right)$ of the total time interval $\mathbb{I}_t = \cup_{n=0}^{N} \Delta t_n$:

Given the state of the material $\left(\underline{\underline{\boldsymbol{\sigma}}}_n, \underset{\sim}{\boldsymbol{\chi}}_n\right)$ *at* $t = t_n$*, and the evolution equations of the Elastic-Plastic model:*

$$\mathcal{EP}\left(\underline{\underline{\boldsymbol{\sigma}}}, \underset{\sim}{\boldsymbol{\chi}}\right): \begin{cases} \dot{\underline{\underline{\boldsymbol{\sigma}}}} = \mathbb{D}^{ep}\left(\underline{\underline{\boldsymbol{\sigma}}}; \underset{\sim}{\boldsymbol{\chi}}\right) : \dot{\underline{\underline{\boldsymbol{\varepsilon}}}}_x, & \text{elastoplastic CE} \quad \text{(B.35)} \\ \dot{\underset{\sim}{\boldsymbol{\chi}}} = \dot{p}\underset{\sim}{\boldsymbol{h}}\left(\underline{\underline{\boldsymbol{\sigma}}}; \underset{\sim}{\boldsymbol{\chi}}\right) = \mathbb{H}\left(\underline{\underline{\boldsymbol{\sigma}}}; \underset{\sim}{\boldsymbol{\chi}}\right) : \dot{\underline{\underline{\boldsymbol{\varepsilon}}}}_x, & \text{hardening law} \quad \text{(B.36)} \end{cases}$$

find:

$$\begin{cases} \underline{\underline{\boldsymbol{\sigma}}}_{n+1} = \underline{\underline{\boldsymbol{\sigma}}}_n + \int_{t_n}^{t_{n+1}} \mathbb{D}^{ep}\left(\underline{\underline{\boldsymbol{\sigma}}}; \underset{\sim}{\boldsymbol{\chi}}\right) : \dot{\underline{\underline{\boldsymbol{\varepsilon}}}}_x d\tau & \text{(B.37)} \\ \underset{\sim}{\boldsymbol{\chi}}_{n+1} = \underset{\sim}{\boldsymbol{\chi}}_n + \int_{t_n}^{t_{n+1}} \mathbb{H}\left(\underline{\underline{\boldsymbol{\sigma}}}; \underset{\sim}{\boldsymbol{\chi}}\right) : \dot{\underline{\underline{\boldsymbol{\varepsilon}}}}_x d\tau & \text{(B.38)} \end{cases}$$

and that respect the KKT conditons $\mathcal{K}$ *(Equation B.29).*

$\mathbb{D}^{ep}$ is the so called *elastic-plastic* tensor. The plastic multiplier, in a strain driven problem, can be found by replacing the stress definition B.24 in the material derivative of the yield locus (applying the chain rule), as follows:

$$\dot{f}\left(\underline{\underline{\boldsymbol{\sigma}}}, \underset{\sim}{\boldsymbol{\chi}}\right) = \underline{\underline{\boldsymbol{\nabla}}}_{\sigma} f : \dot{\underline{\underline{\boldsymbol{\sigma}}}} + \nabla_{\underset{\sim}{\chi}} f : \dot{\underset{\sim}{\boldsymbol{\chi}}} = 0 \quad \text{(B.39)}$$

$$\dot{f}\left(\underline{\underline{\boldsymbol{\sigma}}}, \underset{\sim}{\boldsymbol{\chi}}\right) = \underline{\underline{\boldsymbol{\nabla}}}_{\sigma} f : \mathbb{D}^{el} : \left(\dot{\underline{\underline{\boldsymbol{\varepsilon}}}}_x - \dot{p}\underline{\underline{\boldsymbol{\nabla}}}_{\sigma} g\right) + \nabla_{\underset{\sim}{\chi}} f : \underset{\sim}{\boldsymbol{h}}\dot{p} \quad \text{(B.40)}$$

$$\rightarrow \dot{p} = \left\langle \frac{\underline{\underline{\boldsymbol{\nabla}}}_{\sigma} f : \mathbb{D}^{el} : \dot{\underline{\underline{\boldsymbol{\varepsilon}}}}_x}{\underline{\underline{\boldsymbol{\nabla}}}_{\sigma} f : \mathbb{D}^{el} : \underline{\underline{\boldsymbol{\nabla}}}_{\sigma} g - \nabla_{\underset{\sim}{\chi}} f : \underset{\sim}{\boldsymbol{h}}} \right\rangle \quad \text{(B.41)}$$

with $\langle\cdot\rangle$ is the Macaulay brackets, with $\langle x\rangle = (x + |x|)/2$. The denominator in the right-hand side of Equation B.41 can be seen as an hardening scalar measure $\mathcal{H} = \underline{\underline{\boldsymbol{\nabla}}}_{\sigma} f : \mathbb{D}^{el} : \underline{\underline{\boldsymbol{\nabla}}}_{\sigma} g - \nabla_{\underset{\sim}{\chi}} f : \underset{\sim}{\boldsymbol{h}}$, with $\dot{f} = \underline{\underline{\boldsymbol{\nabla}}}_{\sigma} f : \underline{\underline{\dot{\boldsymbol{\sigma}}}} + \mathcal{H}\dot{p}$.Equation B.41 entails the definition of the elastic-plastic tensor:

$$\mathbb{D}^{ep}\left(\underline{\boldsymbol{x}}; t\right) = \mathbb{D}^{el} - \frac{\underline{\underline{\boldsymbol{\nabla}}}_{\sigma} f : \mathbb{D}^{el}}{\mathcal{H}} \tag{B.42}$$

It is worth noting that for rate-independent materials, the physical time t can be rescaled to the time step Δt as the following non-dimensional measure:

$$T = \frac{t - t_n}{t_{n+1} - t_n}, \qquad T\left(t_n\right) = 0; \qquad T\left(t_{n+1}\right) = 1 \tag{B.43}$$

Keeping this scaling in mind, all time-derivatives can be written in the form $\frac{d\cdot}{dt}$ can be rewritten as $= \frac{d\cdot}{dT}\Delta t_n$. Henceforth, for the sake of simplicity, The evolution equations $\mathcal{EP}$ transform into:

$$\mathcal{EP}\left(\underline{\underline{\boldsymbol{\sigma}}}, \underset{\sim}{\boldsymbol{\chi}}\right) : \begin{cases} \dfrac{d\underline{\underline{\boldsymbol{\sigma}}}}{dT} = \mathbb{D}^{ep}\left(\underline{\underline{\boldsymbol{\sigma}}}; \underset{\sim}{\boldsymbol{\chi}}\right) : \underline{\underline{\boldsymbol{\Delta\varepsilon}}}_n, & \text{elastoplastic CE} \quad \text{(B.44)} \\ \dfrac{d\underset{\sim}{\boldsymbol{\chi}}}{dT} = \mathbb{H}\left(\underline{\underline{\boldsymbol{\sigma}}}; \underset{\sim}{\boldsymbol{\chi}}\right) : \underline{\underline{\boldsymbol{\Delta\varepsilon}}}_n, & \text{hardening law} \quad \text{(B.45)} \end{cases}$$

In a strain driven problem, $\underline{\underline{\boldsymbol{\Delta\varepsilon}}}_n = \Delta t_n \underline{\underline{\dot{\boldsymbol{\varepsilon}}}}_x$ is a givena data (Sloan et al., 2001; Simo and Hughes, 1998), since it can be cmioputed from the velocity field $\underline{\boldsymbol{v}}_n\left(\underline{\boldsymbol{x}}; t\right)$:

$$\underline{\underline{\dot{\boldsymbol{\varepsilon}}}}_x = \underline{\boldsymbol{v}}_n^p\left(\underline{\boldsymbol{x}}; t\right) \otimes_S \underline{\boldsymbol{\nabla}}_x \tag{B.46}$$

with $\underline{\boldsymbol{v}}_n^p$ the velocity *prediction* in a general Newmark's prediction-multi-correction scheme (described in Section A.7) Looking at Equation B.45, one may notice that if the unknowns are casted in the general vector $x = \{\underline{\underline{\boldsymbol{\sigma}}}; \underset{\sim}{\boldsymbol{\chi}}\} \in (\mathbb{S} \times \mathbb{K})$, as well as the mapping $f\left(x\right) = \{\mathbb{D}^{ep}\left(\underline{\underline{\boldsymbol{\sigma}}}; \underset{\sim}{\boldsymbol{\chi}}\right) : \underline{\underline{\boldsymbol{\Delta\varepsilon}}}_n; \mathbb{H}\left(\underline{\underline{\boldsymbol{\sigma}}}; \underset{\sim}{\boldsymbol{\chi}}\right) : \underline{\underline{\boldsymbol{\Delta\varepsilon}}}_n\} : (\mathbb{S} \times \mathbb{K}) \rightarrow (\mathbb{S} \times \mathbb{K})$, it is re-written in the general form of:

$$\left.\begin{aligned} \frac{dx}{dT}\left(T\right) &= f\left(x\left(T\right)\right) \\ x(0) &= x_n \end{aligned}\right\} \forall T \in [0; 1] \tag{B.47, B.48}$$

An approximation of Equation B.38 (in its general form) is defined as:

$$\begin{cases} x_{n+1} = x_n + \Delta t_n f\left(x_{n+\theta}\right) & \text{(B.49)} \\ x_{n+\theta} = \theta x_{n+1} + (1 - \theta)\, x_n, \qquad \theta \in [0; 1] & \text{(B.50)} \end{cases}$$

Here, $x_{n+1} \cong x(1)$ represents the algorithmic approximation of the exact value $x(1)$ (Simo and Hughes, 1998). This family of algorithms contains well-known integrative schemes, in particular

$$\begin{cases} \theta = 0, & \text{forward (explicit) Euler} \quad \text{(B.51)} \\ \theta = 1/2, & \text{midpoint rule} \quad \text{(B.52)} \\ \theta = 1, & \text{backward (implicit) Euler} \quad \text{(B.53)} \end{cases}$$

The unconditional stability of the integration scheme proposed in Equation B.50 is assured for $\theta \geq 1/2$ (Simo and Hughes, 1998). However, the standard explicit methods can be used to integrate numerically the evolution equations, with the recurrence formulas in Equation B.55, become:

$$\begin{cases} \underline{\underline{\boldsymbol{\sigma}}}_{n+1} = \underline{\underline{\boldsymbol{\sigma}}}_n + \mathbb{D}^{ep}\left(\underline{\underline{\boldsymbol{\sigma}}}_n; \underset{\sim}{\boldsymbol{\chi}}_n\right) : \underline{\underline{\boldsymbol{\Delta\varepsilon}}}_n & \text{(B.54)} \\ \underset{\sim}{\boldsymbol{\chi}}_{n+1} = \underset{\sim}{\boldsymbol{\chi}}_n + \mathbb{H}\left(\underline{\underline{\boldsymbol{\sigma}}}_n; \underset{\sim}{\boldsymbol{\chi}}_n\right) : \underline{\underline{\boldsymbol{\Delta\varepsilon}}}_n & \text{(B.55)} \end{cases}$$

The update of the stress and of the state variables in its explicit form is first order accurate: the global discretization error is of the order of $O(\Delta t_n)$. Despite the conditional stability, some regularization techniques have been proposed in the literature, as for instance the family of Runge-Kutta (RK) pth-order recurrence formulas:

$$\begin{cases} x(1) = x_n + \Delta t_n \sum_{k=0}^{p} c'_k f_k = x_n + \sum_{k=0}^{p} c_k f_k & \text{(B.56)} \\ f_k = f\left(t_n + \alpha'_k \Delta t_n; x_n + \Delta t_n \sum_{i=1}^{p-1} \beta'_{ki} f_i\right) = f\left(\alpha_k; x_n + \sum_{i=1}^{p-1} \beta_{ki} f_i\right) & \text{(B.57)} \end{cases}$$

Sloan et al. (2001) proposed an adaptive procedure inspired from the RK algorithm and based on the pioneering work of Sloan (1987), so to improve the solution accuracy. The latter *sub-stepping algorithm* was implemented in SEM3D, due to the important enhancements to improve their accuracy, efficiency and robustness. The seminal idea behind this modified forward-Euler integrator $\mathcal{SI}$ resides in the fact that the time step Δt_n or ($\Delta T = 1$ equivalently) is subdivided in n_s sub-steps ΔT_k, with $\cup_{k=1}^{n_s}$, not necessarily of the same size. The size of each sub-step can be estimated adaptively based on a prescribed error tolerance. The sub-stepping algorithm (see the algorithm in (A1)) is unraveled by firstly update the current stress/state variables. Once the current strain increment is computed, the *trial stress increment* $\underline{\underline{\boldsymbol{\Delta\sigma}}}_n^{trial} = \mathbb{D}^{el} \underline{\underline{\boldsymbol{\Delta\varepsilon}}}_n$ is evaluated: the latter represents a purely elastic first guess of the current stress increment, as if the flow rule was not taking place. The total stress at the end of the step can be rewritten in terms of trial increment by rearranging Equation B.45 as:

$$\underline{\underline{\boldsymbol{\sigma}}}_{n+1} = \underline{\underline{\boldsymbol{\sigma}}}_n + \mathbb{D}^{el} : \underline{\underline{\boldsymbol{\Delta\varepsilon}}}_n - \Delta p \mathbb{D}^{el} : \underline{\underline{\boldsymbol{\nabla}}}_\sigma g = \underline{\underline{\boldsymbol{\sigma}}}_n^{trial} - \Delta p \mathbb{D}^{el} : \underline{\underline{\boldsymbol{\nabla}}}_\sigma g \quad \text{(B.58)}$$

Equation B.58 clearly show that the elastic-plastic step is composed by a trial elastic increment (blue) and an elastic-plastic correction (red). If the flow rule is associated (i.e. $f \equiv g$) the elastic-plastic correction is perpendicular to the yield locus.

The trial state $\left(\underline{\underline{\boldsymbol{\sigma}}}_n^{trial}; \underset{\sim}{\boldsymbol{\chi}}_n\right) = \left(\underline{\underline{\boldsymbol{\sigma}}}_n + \underline{\underline{\boldsymbol{\Delta\sigma}}}_n^{trial}; \underset{\sim}{\boldsymbol{\chi}}_n\right)$ is plugged into the yield locus to test the plastic consistency $\mathcal{K}$: if the trial stress resides (within a certain tolerance) inside the yield locus, the update is straight forward and the next step is started. On the contrary, if the trial stress exceeds the yield limit, the plastic correction takes place (see algorithm (A2)). As a matter of fact, the trial stress increment is linear. Therefore, it is possible to split it into two parts: the one lying inside the yield locus ($\alpha_{NL} \underline{\underline{\boldsymbol{\Delta\sigma}}}_n^{trial}$) and the part exceeding it ($(1 - \alpha_{NL}) \underline{\underline{\boldsymbol{\Delta\sigma}}}_n^{trial}$). The so called *modified Pegasus algorithm* $\mathcal{IP}$ (unravelled in)(A3-A4), Dowell and Jarratt, 1971) is employed at this stage to find the stress state $\underline{\underline{\boldsymbol{\sigma}}}_n^{int} = \underline{\underline{\boldsymbol{\sigma}}}_n + \alpha_{NL} \underline{\underline{\boldsymbol{\Delta\sigma}}}_n^{trial}$ that lies on the yield locus. The Pegasus algorithm is a modified *regula-falsi* method to find the zeros of an equation (i.e. $f\left(\underline{\underline{\boldsymbol{\sigma}}}_n^{int}; \underset{\sim}{\boldsymbol{\chi}}_n\right) = 0$) and therefore the value of α_{NL}. The original algorithm is modified so to effectively handle the elastic-to-plastic transition, even when an abrupt elastic-plastic unloading takes place when the initial stress state already lies on the yield locus (see Figure B.2). Once the intersection with the yield locus has been found, the stress and state variable states at the end of the step $T = 1$ are obtained by applying a multi-step procedure to the trial stress part that exceeds the yield criterion $(1 - \alpha_{NL}) \underline{\underline{\boldsymbol{\Delta\sigma}}}_n^{trial}$ (see Algorithm (A5)). For each sub-increment, the local error measure is found by taking the difference between a second order accurate modified Euler solution and a first order accurate Euler solution. The next time-step size is determined according to error of the previous one. This type of error control permits the size of each sub-increment to vary throughout the integration process, depending on the non-linearity of the constitutive relations. Moreover, the *drift correction* algorithm proposed by Potts and Gens (1985) kicks-in at each sub-increment to be sure the final stress state lies on the yield locus (Algorithm (A6)).

Modified Forward Euler scheme (A1)

function $\left(\underline{\underline{\boldsymbol{\sigma}}}_{n+1}; \underset{\sim}{\boldsymbol{\chi}}_{n+1}\right) = \mathcal{SI}\left(\underline{\underline{\boldsymbol{\varepsilon}}}_{n}; \underline{\underline{\boldsymbol{\sigma}}}_{n}; \underset{\sim}{\boldsymbol{\chi}}_{n}; \underline{\underline{\boldsymbol{\Delta\varepsilon}}}_{n}\right)$

0. Update current state variables:

$\rightarrow \left(\underline{\underline{\boldsymbol{\varepsilon}}}_{n}; \underline{\underline{\boldsymbol{\sigma}}}_{n}; \underset{\sim}{\boldsymbol{\chi}}_{n}\right) \leftarrow \left(\underline{\underline{\boldsymbol{\varepsilon}}}_{n+1}; \underline{\underline{\boldsymbol{\sigma}}}_{n+1}; \underset{\sim}{\boldsymbol{\chi}}_{n+1}\right)$

1. Compute strain increment:

$\rightarrow \underline{\underline{\boldsymbol{\Delta\varepsilon}}}_{n} = \underline{\boldsymbol{v}}_{n}^{p} \otimes_S \underline{\boldsymbol{\nabla}}_{x}$

2. Predict elastic trial stress:

$\rightarrow \underline{\underline{\boldsymbol{\Delta\sigma}}}_{n}^{trial} = \mathbb{D}^{el} : \underline{\underline{\boldsymbol{\Delta\varepsilon}}}_{n} (\underline{\underline{\boldsymbol{\Delta\varepsilon}}}^{pl} = \underline{\mathbf{0}})$

3. Check Plasticity[1]:

$\rightarrow (status; \alpha_{NL}) = \mathcal{CP}\left(\underline{\underline{\boldsymbol{\varepsilon}}}_{n}; \underline{\underline{\boldsymbol{\sigma}}}_{n}; \underset{\sim}{\boldsymbol{\chi}}_{n}; \underline{\underline{\boldsymbol{\Delta\sigma}}}_{n}^{trial}\right)$

$\underline{\underline{\boldsymbol{\sigma}}}_{n}^{int} = \underline{\underline{\boldsymbol{\sigma}}}_{n} + \alpha_{NL} \underline{\underline{\boldsymbol{\Delta\sigma}}}_{n}^{trial}$

4. Elasto-Plastic correction[2]

if $status == ELASTIC$ **then**

$\rightarrow$ *ELASTIC (UN-)LOADING* $\rightarrow \underline{\underline{\boldsymbol{\Delta\sigma}}}_{n} = \underline{\underline{\boldsymbol{\Delta\sigma}}}_{n}^{trial} (\underline{\underline{\boldsymbol{\Delta\varepsilon}}}^{pl} = \underline{\mathbf{0}})$

$\rightarrow$ EXIT

else if $status == PLASTIC$ **then**

$\rightarrow$ *(ELASTO-)PLASTIC LOADING* $\left(\underline{\underline{\boldsymbol{\Delta\sigma}}}_{n}^{\star}; \underset{\sim}{\boldsymbol{\Delta\chi}}_{n}^{\star}\right) = \mathcal{PC}\left(\alpha_{NL}; \underline{\underline{\boldsymbol{\Delta\varepsilon}}}_{n}; \underline{\underline{\boldsymbol{\Delta\sigma}}}_{n}^{trial}; \underline{\underline{\boldsymbol{\sigma}}}_{n}^{int}; \underset{\sim}{\boldsymbol{\chi}}_{n}\right)$

$\rightarrow \underline{\underline{\boldsymbol{\sigma}}}_{n+1} = \underline{\underline{\boldsymbol{\sigma}}}_{n}^{int} + \underline{\underline{\boldsymbol{\Delta\sigma}}}_{n}^{\star}$

$\rightarrow \underset{\sim}{\boldsymbol{\chi}}_{n+1} = \underset{\sim}{\boldsymbol{\chi}}_{n} + \underset{\sim}{\boldsymbol{\Delta\chi}}_{n}^{\star}$

end if

end function

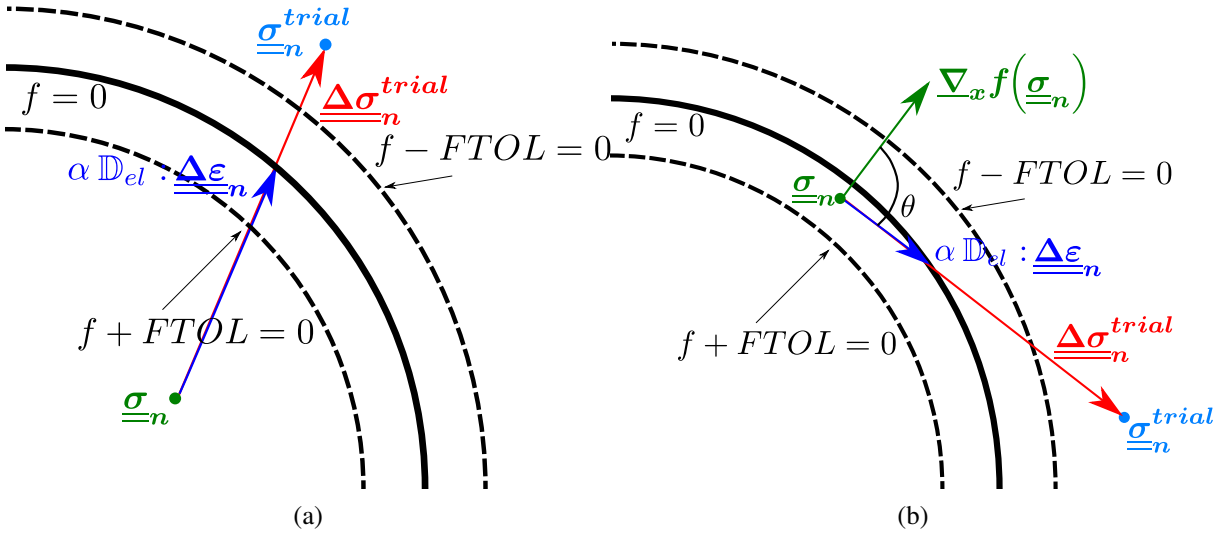

Figure B.2: Sketch of the trial stress and intersection check.

[1] See Algorithm (A2)
[2] See Algorithm (A5)

Check Plasticity (A2)

function $(status; \alpha_{NL}) = \mathcal{CP}\left(\underline{\underline{\boldsymbol{\varepsilon}}}_n; \underline{\underline{\boldsymbol{\sigma}}}_n; \underset{\sim}{\boldsymbol{\chi}}_n; \underline{\underline{\boldsymbol{\Delta\varepsilon}}}_n\right)$

3.1 Yield condition:

$\rightarrow f_S = f\left(\underline{\underline{\boldsymbol{\sigma}}}_n; \underset{\sim}{\boldsymbol{\chi}}_n\right); f_T = f\left(\underline{\underline{\boldsymbol{\sigma}}}_n + \underline{\underline{\boldsymbol{\Delta\sigma}}}_n^{trial}; \underset{\sim}{\boldsymbol{\chi}}_n\right)$

3.2 Evaluate loading condition:

if $f_S < -FTOL$[3] **then**
  if $f_T \leq FTOL$ **then**
    $\rightarrow (status; \alpha_{NL}) = (ELASTIC; 1) \rightarrow$ GO TO **(A2) - STEP 4**
  else
    $\rightarrow status = PLASTIC$
    $\rightarrow \alpha_{NL} = \mathcal{IP}\left(\underline{\underline{\boldsymbol{\sigma}}}_n; \underset{\sim}{\boldsymbol{\chi}}_n; \underline{\underline{\boldsymbol{\Delta\sigma}}}_n^{trial}; \cos(\theta)\right)$[4]
    $\rightarrow$ GO TO **(A2) - STEP 4**
  end if
else if $|f_S| < FTOL$ **then**
  $\cos(\theta) = \frac{\underline{\underline{\boldsymbol{\nabla}}}_\sigma f\left(\underline{\underline{\boldsymbol{\sigma}}}_n\right) : \underline{\underline{\boldsymbol{\Delta\sigma}}}_n^{trial}}{\|\underline{\underline{\boldsymbol{\nabla}}}_\sigma f\left(\underline{\underline{\boldsymbol{\sigma}}}_n\right)\| \|\underline{\underline{\boldsymbol{\Delta\sigma}}}_n^{trial}\|}$
  if $\cos(\theta) \geq -LTOL$ **then**
    $\rightarrow \alpha_{NL} = 0$
    $\rightarrow status = PLASTIC \rightarrow$ GO TO **(A2) - STEP 4**
  else
    if $f_T < -FTOL$ **then**
      $\rightarrow (status, \alpha_{NL}) = (ELASTIC, 1)$ (UNLOADING)
      $\rightarrow$ GO TO **(A2) - STEP 4**
    else
      $\rightarrow status = PLASTIC$
      $\rightarrow \alpha_{NL} = \mathcal{IP}\left(\underline{\underline{\boldsymbol{\sigma}}}_n; \underset{\sim}{\boldsymbol{\chi}}_n; \underline{\underline{\boldsymbol{\Delta\sigma}}}_n^{trial}; \cos(\theta)\right)$[4]
      $\rightarrow$ GO TO **(A2) - STEP 4**
    end if
  end if
else if $|f_S| > FTOL$ **then**
  $\rightarrow$ **ERROR**
end if

end function

[3] $FTOL$ is typically set to 10^{-3}
[4] See Algorithm (A3)

Find Intersection (Modified Pegasus algorithm) (A3)

function $\alpha_{NL} = \mathcal{IP}\left(\underline{\underline{\boldsymbol{\sigma}}}_n; \underset{\sim}{\boldsymbol{\chi}}_n; \underline{\underline{\boldsymbol{\Delta\sigma}}}_n^{trial}; \cos(\theta)\right)$

3.2.1 Set up trial values:

$\rightarrow \alpha_0^{trial} = 0$ and $\alpha_1^{trial} = 1$

3.2.2 Compute stress starting values:

$\rightarrow \underline{\underline{\boldsymbol{\sigma}}}_0 = \underline{\underline{\boldsymbol{\sigma}}}_n + \alpha_0^{trial}\underline{\underline{\boldsymbol{\Delta\sigma}}}_n^{trial} = \underline{\underline{\boldsymbol{\sigma}}}_n$

$\rightarrow \underline{\underline{\boldsymbol{\sigma}}}_1 = \underline{\underline{\boldsymbol{\sigma}}}_n + \alpha_1^{trial}\underline{\underline{\boldsymbol{\Delta\sigma}}}_n^{trial} = \underline{\underline{\boldsymbol{\sigma}}}_n + \underline{\underline{\boldsymbol{\Delta\sigma}}}_n^{trial}$

3.2.3 Compute yield locus:

$\rightarrow f_0 = f\left(\underline{\underline{\boldsymbol{\sigma}}}_0; \underset{\sim}{\boldsymbol{\chi}}_n\right)$

$\rightarrow f_1 = f\left(\underline{\underline{\boldsymbol{\sigma}}}_1; \underset{\sim}{\boldsymbol{\chi}}_n\right)$

3.2.4 Correct trial values (just for load reversal):

if $\cos(\theta) < -LTOL$[5] **then**

$\rightarrow (\alpha_0, \alpha_1) = \mathcal{UC}\left(\alpha_0^{trial}, \alpha_1^{trial}; f_0, f_1; \underline{\underline{\boldsymbol{\sigma}}}_n; \underset{\sim}{\boldsymbol{\chi}}_n; \underline{\underline{\boldsymbol{\Delta\varepsilon}}}_n\right)$[6]

$\rightarrow \underline{\underline{\boldsymbol{\sigma}}}_0 = \underline{\underline{\boldsymbol{\sigma}}}_n + \alpha_0\underline{\underline{\boldsymbol{\Delta\sigma}}}_n^{trial}$

$\rightarrow \underline{\underline{\boldsymbol{\sigma}}}_1 = \underline{\underline{\boldsymbol{\sigma}}}_n + \alpha_1\underline{\underline{\boldsymbol{\Delta\sigma}}}_n^{trial}$

else

(α_0, α_1)=$\left(\alpha_0^{trial}, \alpha_1^{trial}\right)$

end if

3.2.5 Find Intersection:

for $i = 1 : MAXITS$[7] **do**

$\rightarrow \alpha_t = \alpha_1 - \frac{(\alpha_1 - \alpha_0) f_1}{f_1 - f_0}$

$\rightarrow \underline{\underline{\boldsymbol{\sigma}}}_t = \underline{\underline{\boldsymbol{\sigma}}}_0 + \alpha_t\underline{\underline{\boldsymbol{\Delta\sigma}}}_n^{trial}$

$\rightarrow f_t = f\left(\underline{\underline{\boldsymbol{\sigma}}}_t; \underset{\sim}{\boldsymbol{\chi}}_n\right)$

if $|f_t| \leq FTOL$ **then**

INTERSECTION FOUND

$\rightarrow \alpha_{NL} = \alpha_t$

$\rightarrow$ EXIT LOOP OVER i

else

if $f_t f_0 < 0$ **then**

$\rightarrow \alpha_1 = \alpha_0$

$\rightarrow f_1 = f_0$

else

$\rightarrow f_1 = \frac{f_1 f_0}{f_0 + f_t}$

end if

$\rightarrow f_0 = f_t$

$\rightarrow \alpha_0 = \alpha_t$

end if

end for

if $f_t > FTOL$ **then**

ERROR

end if

end function

[5] $LTOL$ is typically set to 10^{-6}

[6] See Algorithm (A4)

[7] $MAXITS$ is typically set to 10

Find Intersection (Modified Pegasus algorithm for load reversal) - (A4)

function $(\alpha_0, \alpha_1) = \mathcal{UC}\left(\alpha_0^{trial}, \alpha_1^{trial}; f_0, f_1; \underline{\underline{\boldsymbol{\sigma}}}_n; \underset{\sim}{\boldsymbol{\chi}}_n; \underline{\underline{\underline{\underline{\boldsymbol{\Delta\varepsilon}}}}}_n\right)$

$\alpha_0 = \alpha_0^{trial}; \alpha_1 = \alpha_1^{trial}$
$f_{save} = f_0$
for $i = 1 : NSUB_0$[8] **do**

$\rightarrow \Delta\alpha = (\alpha_1 - \alpha_0)/NSUB_1$[8]
$\rightarrow FLAGEXIT =$`false`
for $j = 0 : NSUB_1$ **do**
$\rightarrow \alpha_t = \alpha_0 + \Delta\alpha$
$\rightarrow \underline{\underline{\boldsymbol{\sigma}}}_t = \underline{\underline{\boldsymbol{\sigma}}}_0 + \alpha_t \underline{\underline{\underline{\underline{\boldsymbol{\Delta\sigma}}}}}_n^{trial}$
$\rightarrow f_t = f\left(\underline{\underline{\boldsymbol{\sigma}}}_t; \underset{\sim}{\boldsymbol{\chi}}_n\right)$
if $f_t > FTOL$ **then**
$\rightarrow \alpha_1 = \alpha_t$
if $f_0 < -FTOL$ **then**
$\rightarrow f_1 = f_t$
$\rightarrow FLAGEXIT =$`true`
else
$\rightarrow \alpha_0 = 0$
$\rightarrow f_0 = f_{save}$
end if
$\rightarrow$ EXIT LOOP OVER j
else
$\rightarrow \alpha_0 = \alpha_t$
$\rightarrow f_0 = f_t$
$\rightarrow$ LOOP OVER j
end if

end for
end for
if $FLAGEXIT ==$`false` **then**
ERROR : NO INTERSECTION FOUND!

end if

end function

[8] $NSUB_0 = MAXITS, NSUB_1 = 10$

Elastic-Plastic Correction (A5)

function $\left(\underline{\underline{\boldsymbol{\Delta\sigma}}}_n^{\star}; \underset{\sim}{\boldsymbol{\Delta\chi}}_n^{\star}\right) = \mathcal{PC}\left(\alpha_{NL}; \underline{\underline{\boldsymbol{\Delta\varepsilon}}}_n; \underline{\underline{\boldsymbol{\Delta\sigma}}}_n^{trial}; \underline{\underline{\boldsymbol{\sigma}}}_n^{int}; \underset{\sim}{\boldsymbol{\chi}}_n\right)$

5.1 Initialize values

$\rightarrow T = 0; \Delta T = 1$

$\rightarrow \underline{\underline{\boldsymbol{\sigma}}}_T = \underline{\underline{\boldsymbol{\sigma}}}_n^{int}$

$\rightarrow \underset{\sim}{\boldsymbol{\chi}}_T = \underset{\sim}{\boldsymbol{\chi}}_n$

5.2 Correct by adaptive sub-increment

while $T < 1$ **do**

Increment (1)

$\rightarrow \underline{\underline{\Delta\boldsymbol{\sigma}}}_1 = \Delta T\,(1-\alpha_{NL})\,\mathbb{D}^{ep}\left(\underline{\underline{\boldsymbol{\sigma}}}_T; \underset{\sim}{\boldsymbol{\chi}}_T\right) : \underline{\underline{\boldsymbol{\Delta\varepsilon}}}_n ; \underset{\sim}{\Delta\boldsymbol{\chi}}_1 = \Delta T\,(1-\alpha_{NL})\,\mathbb{H}\left(\underline{\underline{\boldsymbol{\sigma}}}_T; \underset{\sim}{\boldsymbol{\chi}}_T\right) : \underline{\underline{\boldsymbol{\Delta\varepsilon}}}_n$

Update (1)

$\rightarrow \underline{\underline{\boldsymbol{\sigma}}}_1 = \underline{\underline{\boldsymbol{\sigma}}}_T + \underline{\underline{\Delta\boldsymbol{\sigma}}}_1 ; \underset{\sim}{\boldsymbol{\chi}}_1 = \underset{\sim}{\boldsymbol{\chi}}_T + \underset{\sim}{\Delta\boldsymbol{\chi}}_1$

Increment (2)

$\rightarrow \underline{\underline{\Delta\boldsymbol{\sigma}}}_2 = \Delta T\,(1-\alpha_{NL})\,\mathbb{D}^{ep}\left(\underline{\underline{\boldsymbol{\sigma}}}_1; \underset{\sim}{\boldsymbol{\chi}}_1\right) : \underline{\underline{\boldsymbol{\Delta\varepsilon}}}_n ; \underset{\sim}{\Delta\boldsymbol{\chi}}_2 = \Delta T\,(1-\alpha_{NL})\,\mathbb{H}\left(\underline{\underline{\boldsymbol{\sigma}}}_1; \underset{\sim}{\boldsymbol{\chi}}_1\right) : \underline{\underline{\boldsymbol{\Delta\varepsilon}}}_n$

Average

$\hat{\underline{\underline{\boldsymbol{\sigma}}}}_i = \underline{\underline{\boldsymbol{\sigma}}}_T + \frac{\underline{\underline{\Delta\boldsymbol{\sigma}}}_1 + \underline{\underline{\Delta\boldsymbol{\sigma}}}_2}{2} ; \hat{\underset{\sim}{\boldsymbol{\chi}}}_i = \underset{\sim}{\boldsymbol{\chi}}_T + \frac{\underset{\sim}{\Delta\boldsymbol{\chi}}_1 + \underset{\sim}{\Delta\boldsymbol{\chi}}_2}{2}$

Compute error

$R_{T+\Delta T} = \frac{1}{2}\max\left\{\frac{\left\|\underline{\underline{\Delta\boldsymbol{\sigma}}}_2 - \underline{\underline{\Delta\boldsymbol{\sigma}}}_1\right\|}{\left\|\hat{\underline{\underline{\boldsymbol{\sigma}}}}_i\right\|}; \frac{\left\|\underset{\sim}{\Delta\boldsymbol{\chi}}_2 - \underset{\sim}{\Delta\boldsymbol{\chi}}_1\right\|}{\left\|\hat{\underset{\sim}{\boldsymbol{\chi}}}_i\right\|}; macheps^{9}\right\}$

if $R_{T+\Delta T} > STOL$[10] - **STEP FAILED then**

Change time-step

$\Delta T \leftarrow \max\{q\Delta T; \Delta T_{min}\}$

$\rightarrow q = \max\{\sqrt{0.9STOL/R_{T+\Delta T}}; 0.1\}; \quad \Delta T_{min} = 10^{-4}$

Repeat step from **Increment (1)**

else if $R_{T+\Delta T} \leq STOL$ - **STEP SUCCESSFUL then**

Update time-step

$T = T + \Delta T$

$\Delta T \leftarrow q\Delta T$

$\rightarrow q = \min\{\sqrt{0.9STOL/R_{T+\Delta T}}; 1.1\}$

$\rightarrow \Delta T = \max\{\Delta T; \Delta T_{min}\}; \Delta T = \min\{\Delta T; 1-T\}$

Update stress/state variables

$\underline{\underline{\boldsymbol{\sigma}}}_T \xleftarrow{} \hat{\underline{\underline{\boldsymbol{\sigma}}}}_i ; \underset{\sim}{\boldsymbol{\chi}}_T \xleftarrow{} \hat{\underset{\sim}{\boldsymbol{\chi}}}_i$

if $\left|f\left(\underline{\underline{\boldsymbol{\sigma}}}_T; \underset{\sim}{\boldsymbol{\chi}}_T\right)\right| > FTOL$ **then**

Drift correction $\left(\underline{\underline{\boldsymbol{\sigma}}}_T; \underset{\sim}{\boldsymbol{\chi}}_T\right) = \mathcal{DC}\left(\underline{\underline{\boldsymbol{\sigma}}}_T; \underset{\sim}{\boldsymbol{\chi}}_T\right)$[10]

end if

end if

end while

5.3 Update finale state

$\underline{\underline{\boldsymbol{\Delta\sigma}}}_n^{\star} = \underline{\underline{\boldsymbol{\sigma}}}_T - \underline{\underline{\boldsymbol{\sigma}}}_n^{int}; \underset{\sim}{\boldsymbol{\Delta\chi}}_n^{\star} = \underset{\sim}{\boldsymbol{\chi}}_T - \underset{\sim}{\boldsymbol{\Delta\chi}}_n$

end function

[8] Machine Epsilon

[9] $STOL$ is typically set to 10^{-6}

[10] See Algorithm A6

Drift Correction (A6)

function $\left(\underline{\underline{\boldsymbol{\sigma}}}^{C}_{T+\Delta T};\underset{\sim}{\boldsymbol{\chi}}^{C}_{T+\Delta T}\right)=\mathcal{DC}\left(\underline{\underline{\boldsymbol{\sigma}}}_{T+\Delta T};\underset{\sim}{\boldsymbol{\chi}}_{T+\Delta T}\right)$

6.1 Initialize values

$\rightarrow \underline{\underline{\boldsymbol{\sigma}}}_0=\underline{\underline{\boldsymbol{\sigma}}}_T;\underset{\sim}{\boldsymbol{\chi}}_0=\underset{\sim}{\boldsymbol{\chi}}_T$

$\rightarrow f_0=f\left(\underline{\underline{\boldsymbol{\sigma}}}_0;\underset{\sim}{\boldsymbol{\chi}}_n\right)>FTOL;\mathcal{H}_0=\mathcal{H}\left(\underline{\underline{\boldsymbol{\sigma}}}_0;\underset{\sim}{\boldsymbol{\chi}}_n\right)$

6.2 Sub-stepping drift correction

for $i=1:MAXITS$ **do**

$\rightarrow \Delta p_t=\frac{f_0}{\mathcal{H}_0}$

$\rightarrow \underline{\underline{\boldsymbol{\sigma}}}_t=\underline{\underline{\boldsymbol{\sigma}}}_0-\Delta p_t\mathbb{D}^{el}:\underline{\underline{\boldsymbol{\nabla}}}_{\chi}g\left(\underline{\underline{\boldsymbol{\sigma}}}_0;\underset{\sim}{\boldsymbol{\chi}}_0\right)$

$\rightarrow \underset{\sim}{\boldsymbol{\chi}}_t=\underset{\sim}{\boldsymbol{\chi}}_0+\Delta p_t:\underset{\sim}{\boldsymbol{h}}_0$

if $\left|f\left(\underline{\underline{\boldsymbol{\sigma}}}_t;\underset{\sim}{\boldsymbol{\chi}}_t\right)\right|>\left|f_0\right|$ **then**

Radial correction $\rightarrow \Delta p_t=f_0\Big/\left[\underline{\underline{\boldsymbol{\nabla}}}_{\sigma}f:\underline{\underline{\boldsymbol{\nabla}}}_{\sigma}f\left(\underline{\underline{\boldsymbol{\sigma}}}_0;\underset{\sim}{\boldsymbol{\chi}}_0\right)\right]$

$\rightarrow \underline{\underline{\boldsymbol{\sigma}}}_t=\underline{\underline{\boldsymbol{\sigma}}}_0-\Delta p_t\underline{\underline{\boldsymbol{\nabla}}}_{\sigma}f\left(\underline{\underline{\boldsymbol{\sigma}}}_0;\underset{\sim}{\boldsymbol{\chi}}_0\right)$

$\rightarrow \underset{\sim}{\boldsymbol{\chi}}_t=\underset{\sim}{\boldsymbol{\chi}}_0$

end if

if $\left|f\left(\underline{\underline{\boldsymbol{\sigma}}}_t;\underset{\sim}{\boldsymbol{\chi}}_t\right)\right|\leq 0$ **then**

$\left(\underline{\underline{\boldsymbol{\sigma}}}^{C}_{T};\underset{\sim}{\boldsymbol{\chi}}^{C}_{T}\right)=\left(\underline{\underline{\boldsymbol{\sigma}}}_t;\underset{\sim}{\boldsymbol{\chi}}_t\right)$

EXIT

end if

end for

end function

B.3.5 The Armstrong-Frederick model

Armstrong and Frederick (1966) model (AF) stemmed from the classic Prager linear kinematic model (Drucker and Prager, 1952). In its simplest form, the AF model employs a non-linear kinematic hardening rule to describe a closed hysteresis loop, but without functions for cumulative plastic strain. In the framework of time-independent plasticity, using the yield surface concept and taking into account the plastic incompressibility though a von-Mises yield function, leads to:

$$f\left(\underline{\underline{\boldsymbol{\sigma}}};\underset{\sim}{\boldsymbol{\chi}}\right)=\sqrt{3\mathcal{J}_2^{\sigma}\left(\underline{\underline{\boldsymbol{S}}}^{\sigma}-\underline{\underline{\boldsymbol{X}}}\right)}-\sigma_{yld}-R \tag{B.59}$$

where $\mathcal{J}_2^{\sigma}\left(\underline{\underline{\boldsymbol{S}}}_{\sigma}-\underline{\underline{\boldsymbol{X}}}\right)$ is the second invariant of the deviatoric stress $\underline{\underline{\boldsymbol{S}}}_{\sigma}-\underline{\underline{\boldsymbol{X}}}$, $\underline{\underline{\boldsymbol{S}}}_{\sigma}$ is the deviatoric part of the Cauchy's stress state, $\underline{\underline{\boldsymbol{X}}}$ is the deviatoric back stress (or *rest stress*) (Chaboche, 1989), σ_{yld} the initial yield strength, R its evolution (increase or decrease).
$\underset{\sim}{\boldsymbol{\chi}}=\left[\underline{\underline{\boldsymbol{X}}};R\right]$ represent the set of *static hidden variables*. The flow and hardening rules are defined upon a plastic potential g in the form:

$$g\left(\underline{\underline{\boldsymbol{\sigma}}};\underset{\sim}{\boldsymbol{\chi}}\right)=\sqrt{3\mathcal{J}_2^{\sigma}\left(\underline{\underline{\boldsymbol{S}}}^{\sigma}-\underline{\underline{\boldsymbol{X}}}\right)}-\sigma_{yld}-R+\frac{3}{4}\frac{\kappa_{kin}}{C_{kin}}\underline{\underline{\boldsymbol{X}}}:\underline{\underline{\boldsymbol{X}}} \tag{B.60}$$

being C_{kin} and κ_{kin} two model constants. The term $\frac{3}{4}\frac{\kappa_{kin}}{C_{kin}}\underline{\underline{\boldsymbol{X}}}:\underline{\underline{\boldsymbol{X}}}$ represents a *fading memory*, that tends to be constant if the back-stress values saturates (typically at large plastic strain). Although a non-associative flow rule is employed ($f\neq g$), one may notice that $\underline{\underline{\boldsymbol{\nabla}}}_{\sigma}g=\underline{\underline{\boldsymbol{\nabla}}}_{\sigma}f$. With that respect, the plastic flow is not affected by the recall term, but the hardening rule is.
Armstrong and Frederick (1966) proposed the following relationship between $\underset{\sim}{\boldsymbol{\chi}}$ and the set of kinematic hidden variables $\underset{\sim}{\boldsymbol{\eta}}=\left[\underline{\underline{\boldsymbol{\alpha}}};r\right]$:

$$\underline{\underline{\boldsymbol{X}}}\left(\underline{\underline{\boldsymbol{\alpha}}}\right)=\frac{2}{3}C_{kin}\underline{\underline{\boldsymbol{\alpha}}} \tag{B.61}$$

$$R\left(r\right)=R_{iso}^{\infty}\left(1-\exp\left(-b_{iso}p\right)\right) \tag{B.62}$$

where R_{iso}^{∞} and b_{iso} are two model parameters for the isotropic model. From Equation B.62, one may notice the isotropic hardening evolution keeps track of the cumulated plastic strain. Once the relationship between conjugated variables has been defined, their rates are obtained by (1) taking the gradient of the plastic potential (Equation B.60), which reads :

$$\underline{\underline{\dot{\boldsymbol{\alpha}}}}=-\dot{p}\underline{\underline{\boldsymbol{\nabla}}}_{X}g=-\dot{p}\left(-\underline{\underline{\boldsymbol{\nabla}}}_{\sigma}f+\frac{3}{2}\frac{\kappa}{C}\underline{\underline{\boldsymbol{X}}}\right)=\underline{\underline{\dot{\boldsymbol{\varepsilon}}}}_{x}^{pl}-\dot{p}\frac{3}{2}\frac{\kappa}{C}\underline{\underline{\boldsymbol{X}}} \tag{B.63}$$

$$\dot{r}=-\frac{\partial g}{\partial R}\dot{p}=\dot{p}=\|\underline{\underline{\dot{\boldsymbol{\varepsilon}}}}_{x}^{pl}\|_{\mathcal{J}_2^{\varepsilon}} \tag{B.64}$$

and (2) by substituting Equations B.63 and B.64 in Equations B.61 and B.62 respectively:

$$\underline{\underline{\dot{\boldsymbol{X}}}}=\frac{2}{3}C_{kin}\underline{\underline{\dot{\boldsymbol{\varepsilon}}}}_{x}^{pl}-\kappa_{kin}\underline{\underline{\boldsymbol{X}}}\dot{p} \tag{B.65}$$

$$\underline{\underline{\dot{\boldsymbol{X}}}}=\frac{2}{3}C_{kin}\underline{\underline{\dot{\boldsymbol{\varepsilon}}}}_{x}^{pl}-\kappa_{kin}\underline{\underline{\boldsymbol{X}}}\dot{p} \tag{B.66}$$

has two distinct terms: a strain hardening term and a dynamic *recall* term that operates at all times.

Appendix C

The Elasto-Dynamic problem

Let us consider an physical space ε isomorphic to $\mathbb{R}^3$ (Euclidean space). Consider an open domain $\Omega \in \mathbb{R}^3$ and a point $p \in \Omega$. By associating an orthogonal base to ε the point p can be referenced by a coordinate set $\underline{\boldsymbol{x}}$. The classical equation of dynamic equilibrium of Ω (called *momentum balance equation*)takes the following form:

$$\int_{\partial\Omega} \underline{\boldsymbol{t}}_n \left(\underline{\boldsymbol{u}}\right)\left(\underline{\boldsymbol{x}};t\right) dS + \int_{\Omega} \underline{\boldsymbol{f}}_{ext}\left(\underline{\boldsymbol{u}}\right)\left(\underline{\boldsymbol{x}};t\right) dV = \int_{\Omega} \rho \partial_{tt}\underline{\boldsymbol{u}}\left(\underline{\boldsymbol{x}};t\right) dV \tag{C.1}$$

where $\underline{\boldsymbol{u}}\left(\underline{\boldsymbol{x}};t\right)$ represents the relative displacement field with the respect to a reference configuration; $\underline{\boldsymbol{t}}_n\left(\underline{\boldsymbol{u}}\right)\left(\underline{\boldsymbol{x}};t\right)$ is the traction vector onto the domain boundary; $\underline{\boldsymbol{f}}_{ext}\left(\underline{\boldsymbol{x}};t\right)$ the volume density of external forces and $\rho\left(\underline{\boldsymbol{x}}\right)$ the unit mass.
By taking the Cauchy's assumption, it exists a 2[nd]-order stress tensor $\underline{\underline{\boldsymbol{\sigma}}}\left(\underline{\boldsymbol{u}}\right)\left(\underline{\boldsymbol{x}};t\right)$ for which:

$$\int_{\partial\Omega} \underline{\boldsymbol{t}}_n \left(\underline{\boldsymbol{u}}\right)\left(\underline{\boldsymbol{x}};t\right) dS = \int_{\Omega} \underline{\underline{\boldsymbol{\sigma}}}\left(\underline{\boldsymbol{u}}\right)\underline{\boldsymbol{n}}\left(\underline{\boldsymbol{x}};t\right) dV \tag{C.2}$$

For small perturbations of the equilibrium configuration (thus assuming $\underline{\boldsymbol{u}}\left(\underline{\boldsymbol{x}};t\right)$ and $\partial_t\underline{\boldsymbol{u}}\left(\underline{\boldsymbol{x}};t\right)$ 1[st] order infinitesimals) and exploiting the Stoke's divergence theorem, Equation C.2 can be specified point-wise as:

$$\underline{\boldsymbol{\nabla}}_x.\underline{\underline{\boldsymbol{\sigma}}}\left(\underline{\boldsymbol{u}}\right)\left(\underline{\boldsymbol{x}};t\right) + \underline{\boldsymbol{f}}_{ext}\left(\underline{\boldsymbol{x}};t\right) = \rho\left(\underline{\boldsymbol{x}}\right)\partial_{tt}\underline{\boldsymbol{u}}\left(\underline{\boldsymbol{x}};t\right) \quad \left(\underline{\boldsymbol{x}};t\right) \in \left(\Omega,\mathbb{I}_t\right) \tag{C.3}$$

The strain tensor can be defined as:

$$\underline{\underline{\boldsymbol{\varepsilon}}}_x\left(\underline{\boldsymbol{u}}\right) = \underline{\boldsymbol{u}} \otimes_s \underline{\boldsymbol{\nabla}}_x \tag{C.4}$$

For the sake of simplicity, let us consider the solid material to be elastic, thus writing the linear constitutive relationship by means of the 4[th]-order elasticity tensor $\mathbb{D}^{el}\left(\underline{\boldsymbol{x}}\right)$:

$$\underline{\underline{\boldsymbol{\sigma}}}\left(\underline{\boldsymbol{u}}\right) = \mathbb{D}^{el} : \underline{\underline{\boldsymbol{\varepsilon}}}_x\left(\underline{\boldsymbol{u}}\right) \tag{C.5}$$

with the : defining tensor double contraction. Considering the symmetry of both $\mathbb{D}^{el}$and $\underline{\underline{\boldsymbol{\varepsilon}}}_x$, Equation C.3 becomes:

$$\underline{\boldsymbol{\nabla}}_x.\left(\mathbb{D}^{el} : \left(\underline{\boldsymbol{u}} \otimes_s \underline{\boldsymbol{\nabla}}_x\right)\right) + \underline{\boldsymbol{f}}_{ext} = \rho\left(\underline{\boldsymbol{x}}\right)\partial_{tt}\underline{\boldsymbol{u}} \quad \left(\underline{\boldsymbol{x}};t\right) \in \left(\Omega,\mathbb{I}_t\right) \tag{C.6}$$

If the solid material is considered homogeneous, $\mathbb{D}^{el}\left(\underline{\boldsymbol{x}}\right) = \mathbb{D}^{el}$ can be written by means of the two Lamé constants (λ,μ):

$$\mathbb{D}^{el} = \lambda\underline{\underline{\boldsymbol{I}}} \otimes \underline{\underline{\boldsymbol{I}}} + 2\mu\mathbb{I} \tag{C.7}$$

with $\underline{\underline{\boldsymbol{I}}} = \sum_j \underline{\boldsymbol{e}}_j \otimes \underline{\boldsymbol{e}}_j$ and $\mathbb{I} = \sum_{i,j} \underline{\boldsymbol{e}}_i \otimes \underline{\boldsymbol{e}}_j \otimes \underline{\boldsymbol{e}}_i \otimes \underline{\boldsymbol{e}}_j$ the 2nd- and 4th-order identity tensors respectively. From Equation C.6, the stress tensor can be written as:

$$\underline{\underline{\boldsymbol{\sigma}}}\left(\underline{\boldsymbol{u}}\right) = \lambda\left(\underline{\boldsymbol{\nabla}}_x.\underline{\boldsymbol{u}}\right)\underline{\underline{\boldsymbol{I}}} + 2\mu\underline{\underline{\boldsymbol{\varepsilon}}}_x\left(\underline{\boldsymbol{u}}\right) \tag{C.8}$$

Finally, Navier-Stokes equation C.6 becomes:

$$\left(\lambda+\mu\right)\underline{\boldsymbol{\nabla}}_x\left(\underline{\boldsymbol{\nabla}}_x.\underline{\boldsymbol{u}}\right) + \mu\Delta_x\underline{\boldsymbol{u}} + \underline{\boldsymbol{f}}_{ext} = \rho\partial_{tt}\underline{\boldsymbol{u}} \tag{C.9}$$

If we further consider the relation $\Delta_x\underline{\boldsymbol{u}} = \underline{\boldsymbol{\nabla}}_x\left(\underline{\boldsymbol{\nabla}}_x.\underline{\boldsymbol{u}}\right) - \underline{\boldsymbol{\nabla}}_x \wedge \left(\underline{\boldsymbol{\nabla}}_x \wedge \underline{\boldsymbol{u}}\right)$, the latter expression can be rewritten as:

$$\left(\lambda+2\mu\right)\underline{\boldsymbol{\nabla}}_x\left(\underline{\boldsymbol{\nabla}}_x.\underline{\boldsymbol{u}}\right) - \mu\underline{\boldsymbol{\nabla}}_x \wedge \left(\underline{\boldsymbol{\nabla}}_x \wedge \underline{\boldsymbol{u}}\right) + \underline{\boldsymbol{f}}_{ext} = \rho\partial_{tt}\underline{\boldsymbol{u}} \tag{C.10}$$

C.1 Helmholtz decomposition

For the sake of simplicity, let us first solve the homogeneous Navier-Stokes equation, i.e. by putting $\underline{\boldsymbol{f}}_{ext} = \underline{\boldsymbol{0}}$. The non-zero solutions of this set of equations represent the free-modes of the system and they belong to the kernel of the following differential operator:

$$\left(\Delta_x^\star - \rho\partial_{tt}\right)\left(\cdot\right) = \left(\left(\lambda+\mu\right)\underline{\boldsymbol{\nabla}}_x\left(\underline{\boldsymbol{\nabla}}_x.\left(\cdot\right)\right) + \mu\Delta_x\left(\cdot\right) - \rho\partial_{tt}\left(\cdot\right)\right) \tag{C.11}$$

$$\left(\Delta_x^\star - \rho\partial_{tt}\right)\left(\underline{\boldsymbol{u}}\right) = \underline{\boldsymbol{0}} \tag{C.12}$$

Suitable solutions of the rearranged Navier-Stokes equation are sought within the space of slow growing exponential functions, e.g. the space of tempered distributions. This choice eliminates from the solution space the functions exponential growing at infinite, which are not physically acceptable.
From now on, Fourier's transform defined on the functions belonging to the selected solution space are defined in a distribution sense.

Navier-Stokes equation can be easily solved by exploiting the so called *Helmholtz decomposition* of the displacement vector:

$$\underline{\boldsymbol{u}} = \underline{\boldsymbol{\nabla}}_x\Phi + \underline{\boldsymbol{\nabla}}_x \wedge \underline{\boldsymbol{\Psi}}, \quad \underline{\boldsymbol{\nabla}}_x.\underline{\boldsymbol{\Psi}} = 0 \tag{C.13}$$

The Helmholtz decomposition introduces a scalar potentials Φ and a solenoidal vector potential $\underline{\boldsymbol{\Psi}}$ that can be uniquely determined by solving two uncoupled Laplace equations of the form:

$$\Delta_x\Phi = \underline{\boldsymbol{\nabla}}_x.\underline{\boldsymbol{u}}, \quad \Delta_x\underline{\boldsymbol{\Psi}} = -\underline{\boldsymbol{\nabla}}_x \wedge \underline{\boldsymbol{u}} \tag{C.14}$$

Equation C.13substituted into Equation C.12), lead to the following couple of equations for Φ and $\underline{\boldsymbol{\Psi}}$:

$$\underline{\boldsymbol{\nabla}}_x\left(\left(\lambda+2\mu\right)\Delta_x\Phi - \rho\partial_{tt}\Phi\right) + \underline{\boldsymbol{\nabla}}_x \wedge \left(\mu\Delta_x\underline{\boldsymbol{\Psi}} - \rho\partial_{tt}\underline{\boldsymbol{\Psi}}\right) \tag{C.15}$$

The uniqueness of Helmholtz decomposition implies that Equation C.15 can be solved by the following system of equations:

$$\left(\lambda+2\mu\right)\Delta_x\Phi - \rho\partial_{tt}\Phi = 0 \tag{C.16}$$

$$\mu\Delta_x\underline{\boldsymbol{\Psi}} - \rho\partial_{tt}\underline{\boldsymbol{\Psi}} = \underline{\boldsymbol{0}} \tag{C.17}$$

The latter system of equations is based on the 1D wave equation structures, that can be expressed as:

$$c^2\Delta_x F - \partial_{tt}F = 0 \tag{C.18}$$

C.1.1 Plane wave solution

Equation C.18 can be solved either by separation of variables either throughout Fourier's transform. A suitable generic solution of this equation is called monochromatic plane wave function and it reads:

$$F\left(\underline{\boldsymbol{x}};t\right)=F_0e^{i\left(\underline{\boldsymbol{k}}.\underline{\boldsymbol{x}}-\omega t\right)},\quad \|\underline{\boldsymbol{k}}\|=\frac{\omega}{c} \tag{C.19}$$

Those functions are called *plane-waves* since all the points $\underline{\boldsymbol{x}}$ belonging to the plane $P\left(\underline{\boldsymbol{\xi}},\underline{\boldsymbol{x}}_o\right)$ passing by the point $\underline{\boldsymbol{x}}_0$ and of outward normal $\underline{\boldsymbol{\xi}}$ verify the following equation:

$$F_{\pm}\left(\underline{\boldsymbol{x}};t\right)=F_{\pm}\left(\underline{\boldsymbol{x}}_0;t\right) \tag{C.20}$$

The plane $P\left(\underline{\boldsymbol{\xi}},\underline{\boldsymbol{x}}_o\right)$ is called *wave-front* and wave motion is in phase along it. The wave-front propagates with velocity c along the $\underline{\boldsymbol{\xi}}$ direction, because:

$$F\left(\underline{\boldsymbol{x}}\pm ct'\underline{\boldsymbol{\xi}};t\pm t'\right)=F_{\pm}\left(\underline{\boldsymbol{x}}_0;t\right) \tag{C.21}$$

Using the expression $\underline{\boldsymbol{k}}=\omega\underline{\boldsymbol{\xi}}$ and considering F_0 as the Fourier transform of a generic function f, the inverse Fourier's transform of Equation C.19 with the respect to ωtakes the general form:

$$F_{\pm}\left(\underline{\boldsymbol{x}};t\right)=f\left(\underline{\boldsymbol{\xi}}.\underline{\boldsymbol{x}}\pm ct\right),\quad \|\underline{\boldsymbol{\xi}}\|=1 \tag{C.22}$$

This type of non-zero solution of the 1D wave equation are now exploited to solve Equation C.17. From now on, we further assume $f:\mathbb{R}\rightarrow\mathbb{R}$ belonging to the Sobolev's space $H_1\left(\mathbb{R}\right)$.

C.1.2 Elastic Plane waves

Considering Equations C.17 and the 1D wave equation solution C.22 the two Helmholtz potentials may be written as:

$$\Phi\left(\underline{\boldsymbol{x}};t\right)=\Phi_0e^{i\omega\left(\frac{\underline{\boldsymbol{\xi}}.\underline{\boldsymbol{x}}}{c_P}\pm\omega t\right)},c_P=\sqrt{\frac{\lambda+2\mu}{\rho}} \tag{C.23}$$

$$\underline{\boldsymbol{\Psi}}\left(\underline{\boldsymbol{x}};t\right)=\underline{\boldsymbol{\Psi}}_0e^{i\omega\left(\frac{\underline{\boldsymbol{\xi}}.\underline{\boldsymbol{x}}}{c_S}\pm\omega t\right)},c_S=\sqrt{\frac{\mu}{\rho}},\underline{\boldsymbol{\Psi}}_0.\underline{\boldsymbol{\xi}}=0 \tag{C.24}$$

c_P and c_S are the P-wave and S-wave velocities for isotropic homogeneous elastic material. Substituting the solutions in Equation C.24 into Equation C.13, the displacement field that solves the homogeneous wave equation composes of two terms $\underline{\boldsymbol{u}}_P$ and $\underline{\boldsymbol{u}}_S$:

$$\underline{\boldsymbol{u}}_P\left(\underline{\boldsymbol{x}};t\right)=\underline{\boldsymbol{\nabla}}_x.\underline{\boldsymbol{u}}=i\underline{\boldsymbol{k}}_P\Phi\left(\underline{\boldsymbol{x}};t\right) \tag{C.25}$$

$$\underline{\boldsymbol{u}}_S\left(\underline{\boldsymbol{x}};t\right)=\underline{\boldsymbol{\nabla}}_x\wedge\underline{\boldsymbol{u}}=i\underline{\boldsymbol{k}}_S\wedge\underline{\boldsymbol{\Psi}}\left(\underline{\boldsymbol{x}};t\right) \tag{C.26}$$

$\underline{\boldsymbol{k}}_P$ and $\underline{\boldsymbol{k}}_S$ are the wave-number vectors for P- and S-wave respectively.

Pressure waves

The wave field $\underline{\boldsymbol{u}}_P$, derived from the Φ potential and called *pressure wave field* propagates parallel to $\underline{\boldsymbol{\xi}}$, at velocity c_P. The associated traction vector, on a surface of outward unit vector $\underline{\boldsymbol{\xi}}$, reads (from Equation C.1):

$$\underline{\boldsymbol{t}}_n\left(\underline{\boldsymbol{u}}_P\right)\left(\underline{\boldsymbol{x}};t\right)=-\rho\omega^2\Phi\left(\underline{\boldsymbol{x}};t\right)\underline{\boldsymbol{\xi}}=i\rho\omega c_P\underline{\boldsymbol{u}}_P\left(\underline{\boldsymbol{x}};t\right) \tag{C.27}$$

$\underline{\boldsymbol{t}}_n\left(\underline{\boldsymbol{u}}_P\right)$ is also parallel to $\underline{\boldsymbol{\xi}}$ thus being the P-wave field longitudinal and compressional. Moreover, c_P is calculated from the *oedometric* modulus, since no tangential stress is induced on the wave front.

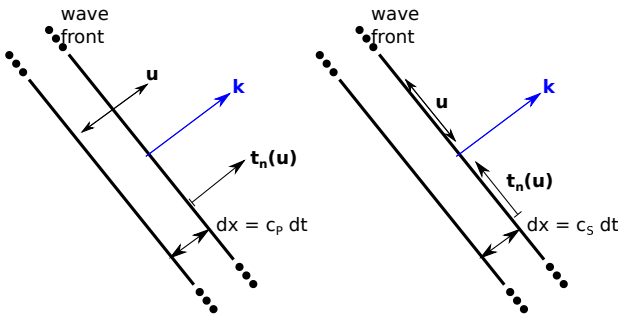

(a) (b)

Figure C.1: Displacement and traction vectors on plane-wave fronts. (a) P-wave front; (b) S-wave front

Shear waves

The wave field $\underline{\boldsymbol{u}}_S$, derived from the $\underline{\boldsymbol{\Psi}}$ potential and called *shear wave field* propagates perpendicular to $\underline{\boldsymbol{k}}_S$, at velocity c_S. The associated traction vector, on a surface of outward unit vector $\underline{\boldsymbol{\xi}}$, reads (from Equation C.1):

$$\underline{\boldsymbol{t}}_n\left(\underline{\boldsymbol{u}}_S\right)\left(\underline{\boldsymbol{x}};t\right) = -\rho\omega^2\left(\underline{\boldsymbol{\xi}} \wedge \underline{\boldsymbol{\Psi}}\left(\underline{\boldsymbol{x}};t\right)\right) = i\rho\omega c_S \underline{\boldsymbol{u}}_S\left(\underline{\boldsymbol{x}};t\right) \tag{C.28}$$

$\underline{\boldsymbol{t}}_n\left(\underline{\boldsymbol{u}}_S\right)$ is also perpendicular to $\underline{\boldsymbol{\xi}}$ thus being the S-wave field transversal and shearing. Moreover, being $c_P > c_S$, S-wave arrival are delayed with the respect to P-wave one, thus calling them primary (P) and secondary (S) waves.

C.1.3 Impedance and Radiation

From Equations C.27, C.28, we derived the general formula for traction vectors, called *impedance relation*:

$$\underline{\boldsymbol{t}}_n\left(\underline{\boldsymbol{u}}_\alpha\right)\left(\underline{\boldsymbol{x}};t\right) = i\omega c_\alpha \underline{\boldsymbol{u}}_\alpha \tag{C.29}$$

The latter expression is still valid for non-plane waves whose wave-front has small curvature, i.e. wave fields that locally behave as plane waves. From a numerical point of view, they are mainly exploited to express local boundary conditions, especially to enforce *non-reflection* condition. On the other hand, they are used to express the mathematical condition known as *Sommerfeld's radiation condition* that reads:

$$\lim_{R\to\infty}\int_{\|\underline{\boldsymbol{x}}\|=R} \|\underline{\boldsymbol{t}}_n - \underline{\boldsymbol{t}}_n\left(\underline{\boldsymbol{u}}_\alpha\right)\|^2 dS = 0 \tag{C.30}$$

$$\lim_{R\to\infty}\int_{\|\underline{\boldsymbol{x}}\|=R} \left(\sigma_{nn} - i\omega\rho c_P \underline{\boldsymbol{u}}.\underline{\boldsymbol{n}}\right)^2 dS = 0 \tag{C.31}$$

$$\lim_{R\to\infty}\int_{\|\underline{\boldsymbol{x}}\|=R} \|\underline{\boldsymbol{t}}_n^t - i\omega\rho c_S \underline{\boldsymbol{u}}^t\|^2 dS = 0 \tag{C.32}$$

with $\underline{\boldsymbol{n}} = \underline{\boldsymbol{x}}/R$ and ^{t} defining the direction perpendicular to $\underline{\boldsymbol{n}}$. The Sommerfeld radiation condition states non-plane waves vanishes at infinite. Moreover, Equation C.30 is necessary to assure the uniqueness of stationary solutions of the Navier's equation. As a matter of fact, plane waves represent the non-trivial solution of Equation C.12. Therefore, at each particular solution of Navier-Stokes equations can be superposed a any plan-wave. If no wave field is present for $t < t_0$ (i.e. homogeneous boundary conditions) those plane-waves have zero amplitude, whereas this is not valid for stationary solutions. In particular, plane-waves do not verify Sommerfeld's radiation condition C.30. Plane-wave verify impedance condition just along their propagation direction, i.e. not for all directions. Stein and Wysession (2003)

C.2 Wave-field induced by body forces

Given two displacement fields $\underline{\boldsymbol{u}}_1(\underline{\boldsymbol{x}};t)$and $\underline{\boldsymbol{u}}_2(\underline{\boldsymbol{x}};t)$, solution of two Elasto-Dynamic problems with external forces $\underline{\boldsymbol{f}}_1(\underline{\boldsymbol{x}};t)$and $\underline{\boldsymbol{f}}_2(\underline{\boldsymbol{x}};t)$respectively, the *Reciprocity Theorem* (also called *Betti's Theorem*) states the following integral identity:

$$\begin{aligned}
&\int_\Omega \left[\left(\underline{\boldsymbol{f}}_1\left(\underline{\boldsymbol{x}};t\right)-\rho\left(\underline{\boldsymbol{x}}\right)\partial_{tt}\underline{\boldsymbol{u}}_1\left(\underline{\boldsymbol{x}};t\right)\right).\underline{\boldsymbol{u}}_2\left(\underline{\boldsymbol{x}};t\right)\right]dV\left(\underline{\boldsymbol{x}}\right)+\int_{\partial\Omega}\underline{\boldsymbol{t}}_n\left(\underline{\boldsymbol{u}}_1\left(\underline{\boldsymbol{x}};t\right)\right).\underline{\boldsymbol{u}}_2\left(\underline{\boldsymbol{x}};t\right)dS\left(\underline{\boldsymbol{x}}\right)=\\
&\int_\Omega \left[\left(\underline{\boldsymbol{f}}_2\left(\underline{\boldsymbol{x}};t\right)-\rho\left(\underline{\boldsymbol{x}}\right)\partial_{tt}\underline{\boldsymbol{u}}_2\left(\underline{\boldsymbol{x}};t\right)\right).\underline{\boldsymbol{u}}_1\left(\underline{\boldsymbol{x}};t\right)\right]dV\left(\underline{\boldsymbol{x}}\right)+\int_{\partial\Omega}\underline{\boldsymbol{t}}_n\left(\underline{\boldsymbol{u}}_2\left(\underline{\boldsymbol{x}};t\right)\right).\underline{\boldsymbol{u}}_1\left(\underline{\boldsymbol{x}};t\right)dS\left(\underline{\boldsymbol{x}}\right)
\end{aligned} \tag{C.33}$$

$\underline{\boldsymbol{t}}_n(\underline{\boldsymbol{u}}_i)(\underline{\boldsymbol{x}};t)$represents the traction vector distribution per unit surface and it is related to the Cauchy's stress tensor $\underline{\underline{\boldsymbol{\sigma}}}(\underline{\boldsymbol{x}};t)$by the relation:

$$\underline{\boldsymbol{t}}_n\left(\underline{\boldsymbol{u}}_i\right)\left(\underline{\boldsymbol{x}};t\right)=\underline{\underline{\boldsymbol{\sigma}}}\left(\underline{\boldsymbol{u}}\right)\left(\underline{\boldsymbol{x}};t\right).\underline{\boldsymbol{n}}$$

Note that Betti's theorem does not depend on the initial conditions on $\underline{\boldsymbol{u}}_1$, $\underline{\boldsymbol{u}}_2$, $\partial_{tt}\underline{\boldsymbol{u}}_1$, $\partial_{tt}\underline{\boldsymbol{u}}_2$, $\underline{\boldsymbol{t}}_n(\underline{\boldsymbol{u}}_1)(\underline{\boldsymbol{x}};t)$and $\underline{\boldsymbol{t}}_n(\underline{\boldsymbol{u}}_2)(\underline{\boldsymbol{x}};t)$. Moreover, it is time invariant, i.e. it does not depend on the time steps t_1, t_2 at which the two solutions are evaluated. For instance, considering the couple $t_1=t$,$t_2=\tau-t$ and integrates Equation C.33 between 0 and τ, the acceleration terms reduce to the following expression:

$$\begin{aligned}
\rho\left(\underline{\boldsymbol{x}}\right)\int_0^\tau\left[-\partial_{tt}\underline{\boldsymbol{u}}_1\left(\underline{\boldsymbol{x}};t\right).\underline{\boldsymbol{u}}_2\left(\underline{\boldsymbol{x}};\tau-t\right)+\partial_{tt}\underline{\boldsymbol{u}}_2\left(\underline{\boldsymbol{x}};\tau-t\right).\underline{\boldsymbol{u}}_1\left(\underline{\boldsymbol{x}};t\right)\right]dt=\\
\rho\left(\underline{\boldsymbol{x}}\right)\int_0^\tau\partial_t\left[-\partial_t\underline{\boldsymbol{u}}_1\left(\underline{\boldsymbol{x}};t\right).\underline{\boldsymbol{u}}_2\left(\underline{\boldsymbol{x}};\tau-t\right)+\underline{\boldsymbol{u}}_1\left(\underline{\boldsymbol{x}};t\right).\partial_t\underline{\boldsymbol{u}}_2\left(\underline{\boldsymbol{x}};\tau-t\right)\right]dt=\\
\rho\left(\underline{\boldsymbol{x}}\right)\left[-\partial_t\underline{\boldsymbol{u}}_1\left(\underline{\boldsymbol{x}};\tau\right).\underline{\boldsymbol{u}}_2\left(\underline{\boldsymbol{x}};0\right)+\underline{\boldsymbol{u}}_1\left(\underline{\boldsymbol{x}};\tau\right).\partial_t\underline{\boldsymbol{u}}_2\left(\underline{\boldsymbol{x}};0\right)+\right.\\
\left.\partial_t\underline{\boldsymbol{u}}_1\left(\underline{\boldsymbol{x}};0\right).\underline{\boldsymbol{u}}_2\left(\underline{\boldsymbol{x}};\tau\right)-\underline{\boldsymbol{u}}_1\left(\underline{\boldsymbol{x}};0\right).\partial_t\underline{\boldsymbol{u}}_2\left(\underline{\boldsymbol{x}};\tau\right)\right]
\end{aligned} \tag{C.34}$$

Non-homogeneous Navier-Stokes equations C.3 can therefore be solved for each density of body forces $\underline{\boldsymbol{f}}_{ext}(\underline{\boldsymbol{x}};t)$in two steps: first finding the solution for a unit force applied in $\underline{\boldsymbol{y}}$, at time t', acting along direction $\underline{\boldsymbol{a}}$, called $\underline{\boldsymbol{u}}^G\left(\underline{\boldsymbol{y}},t',\underline{\boldsymbol{a}};\underline{\boldsymbol{x}},t\right)$ and then superposing the solutions obtained at each $\underline{\boldsymbol{y}}$, t'. $\underline{\boldsymbol{u}}^G\left(\underline{\boldsymbol{y}},t',\underline{\boldsymbol{a}};\underline{\boldsymbol{x}},t\right)$ represent the Green's function of Equation C.3, thus it solves:

$$\left(\lambda+\mu\right)\underline{\boldsymbol{\nabla}}_x\left(\underline{\boldsymbol{\nabla}}_x.\underline{\boldsymbol{u}}^G\right)+\mu\Delta_x\underline{\boldsymbol{u}}^G+\delta_{\underline{\boldsymbol{y}}}\delta_{t'}\underline{\boldsymbol{a}}=\rho\partial_{tt}\underline{\boldsymbol{u}}^G \tag{C.35}$$

where $\delta_{\underline{\boldsymbol{y}}}=\delta\left(\underline{\boldsymbol{x}}-\underline{\boldsymbol{y}}\right)$ and $\delta_{t'}=\delta\left(t-t'\right)$[1]. Due to the linearity of Equation C.35, the general solution of Equation C.3 can be written as:

$$\underline{\boldsymbol{u}}\left(\underline{\boldsymbol{x}};t\right)=\sum_k\int_{\mathbb{R}^4}\underline{\boldsymbol{u}}^G\left(\underline{\boldsymbol{y}},t',\underline{\boldsymbol{e}}_k;\underline{\boldsymbol{x}},t\right)f_k\left(\underline{\boldsymbol{y}},\underline{\boldsymbol{t}}'\right)dV\left(\underline{\boldsymbol{y}}\right)dt' \tag{C.36}$$

with $(\underline{\boldsymbol{e}}_1,\underline{\boldsymbol{e}}_2,\underline{\boldsymbol{e}}_3)$ is the selected $\mathbb{R}^3$ orthonormal basis and $f_k=\underline{\boldsymbol{f}}.\underline{\boldsymbol{e}}_k$.

The convolution integral in Equation C.34 vanishes whether it exist an instant in time τ_0 before which both $\underline{\boldsymbol{u}}$ and $\underline{\boldsymbol{v}}$ are zero (and hence $\partial_t\underline{\boldsymbol{u}}$ and $\partial_t\underline{\boldsymbol{v}}=0$). This *quiescent past condition* can be applied to the Reciprocity Theorem, by integrating the two members of the expression in time, namely:

$$\begin{aligned}
&\int_{-\infty}^{+\infty}\int_\Omega\left(\underline{\boldsymbol{f}}_1\left(\underline{\boldsymbol{x}};t\right).\underline{\boldsymbol{u}}_2\left(\underline{\boldsymbol{x}},\tau-t\right)-\underline{\boldsymbol{f}}_2\left(\underline{\boldsymbol{x}},\tau-t\right).\underline{\boldsymbol{u}}_1\left(\underline{\boldsymbol{x}};t\right)\right)dV\left(\underline{\boldsymbol{x}}\right)dt=\\
&\int_{-\infty}^{+\infty}\int_{\partial\Omega}\left(\underline{\boldsymbol{t}}_n\left(\underline{\boldsymbol{u}}_2\left(\underline{\boldsymbol{x}},\tau-t\right)\right).\underline{\boldsymbol{u}}_1\left(\underline{\boldsymbol{x}};t\right)-\underline{\boldsymbol{t}}_n\left(\underline{\boldsymbol{u}}_1\left(\underline{\boldsymbol{x}};t\right)\right).\underline{\boldsymbol{u}}_2\left(\underline{\boldsymbol{x}},\tau-t\right)\right)dtdS\left(\underline{\boldsymbol{x}}\right)
\end{aligned} \tag{C.37}$$

[1] δ_x is a distribution defined for each continuous function ϕ, such that (ϕ,δ_x)=$\phi\left(x\right)$

To fully specify a Green's function, boundary condition on $\partial\Omega$ must be specified. If one considers $\partial\Omega$ as a rigid surface (homogeneous boundary conditions), $\underline{\boldsymbol{u}}^G$ depends on the time lag $t-\tau$, and the time origin can be shifted at will. Hence:

$$\underline{\boldsymbol{u}}^G\left(\underline{\boldsymbol{y}},t',\underline{\boldsymbol{a}};\underline{\boldsymbol{x}},t\right)=\underline{\boldsymbol{u}}^G\left(\underline{\boldsymbol{y}},0,\underline{\boldsymbol{a}};\underline{\boldsymbol{x}},t-t'\right)=\underline{\boldsymbol{u}}^G\left(\underline{\boldsymbol{y}},-t,\underline{\boldsymbol{a}};\underline{\boldsymbol{x}},-t'\right)\underline{\mathbf{0}},\quad\forall\underline{\boldsymbol{x}}\neq\underline{\boldsymbol{y}},\forall t\leq\tau, \tag{C.38}$$

Equation C.38 represents the *reciprocity condition between source and receiver* in time, for homogeneous boundary conditions.

C.2.1 Green's function in homogeneous space

In homogeneous space, the Green's function in Equation C.35 has the following property:

$$\underline{\boldsymbol{u}}^G\left(\underline{\boldsymbol{y}},t',\underline{\boldsymbol{a}};\underline{\boldsymbol{x}},t\right)=\underline{\boldsymbol{u}}^G\left(\underline{\mathbf{0}},0,\underline{\boldsymbol{a}};\underline{\boldsymbol{x}}-\underline{\boldsymbol{y}},t-t'\right) \tag{C.39}$$

For the sake of simplicity, from now on the unit force will be considered as applied in the origin and at time 0 and parameters $\underline{\boldsymbol{y}}$ and t' will be omitted. Equation C.35 becomes:

$$(\lambda+\mu)\,\underline{\boldsymbol{\nabla}}_x\left(\underline{\boldsymbol{\nabla}}_x.\underline{\boldsymbol{u}}^G\right)+\mu\Delta_x\underline{\boldsymbol{u}}^G+\delta\left(\underline{\boldsymbol{x}}\right)\delta\left(t\right)\underline{\boldsymbol{a}}=\rho\partial_{tt}\underline{\boldsymbol{u}}^G \tag{C.40}$$

with initial conditions $\underline{\boldsymbol{u}}^G\left(\underline{\boldsymbol{x}},t,\underline{\boldsymbol{a}}\right)=\partial_t\underline{\boldsymbol{u}}^G\left(\underline{\boldsymbol{x}},t,\underline{\boldsymbol{a}}\right)=\underline{\mathbf{0}}$, for $t<0$. The solution is sought by applying Fourier transform in space and time to Equation C.40.

Fourier transform in time

The Fourier transform with respect to time can be expressed as:

$$\widehat{\underline{\boldsymbol{u}}^G}\left(\underline{\boldsymbol{x}},\omega,\underline{\boldsymbol{a}}\right)=\int_{\mathbb{R}}\underline{\boldsymbol{u}}^G\left(\underline{\boldsymbol{x}},t,\underline{\boldsymbol{a}}\right)\exp\left(-i\omega t\right)dt \tag{C.41}$$

Equation C.40 becomes:

$$(\lambda+\mu)\,\underline{\boldsymbol{\nabla}}_x\left(\underline{\boldsymbol{\nabla}}_x.\widehat{\underline{\boldsymbol{u}}^G}\right)+\mu\Delta_x\widehat{\underline{\boldsymbol{u}}^G}+\delta\left(\underline{\boldsymbol{x}}\right)\underline{\boldsymbol{a}}=-\omega^2\rho\widehat{\underline{\boldsymbol{u}}^G} \tag{C.42}$$

For ω fixed, we are going to solve C.42 for harmonic functions in time.

Fourier transform in space

The Fourier transform with respect to time can be expressed as:

$$\widehat{\widehat{\underline{\boldsymbol{u}}^G}}\left(\underline{\boldsymbol{\xi}},\omega,\underline{\boldsymbol{a}}\right)=\int_{\mathbb{R}^3}\widehat{\underline{\boldsymbol{u}}^G}\left(\underline{\boldsymbol{x}},\omega,\underline{\boldsymbol{a}}\right)\exp\left(-i\left(\underline{\boldsymbol{\xi}}.\underline{\boldsymbol{x}}\right)\right)dV\left(\underline{\boldsymbol{x}}\right) \tag{C.43}$$

Before substituting C.43 in Equation C.42, it is worth recalling the following relations:

$$\widehat{\left(\partial_j\underline{\boldsymbol{u}}\right)}=-i\xi_j\widehat{\underline{\boldsymbol{u}}} \tag{C.44}$$

$$\widehat{\left(\underline{\boldsymbol{u}}\otimes\underline{\boldsymbol{\nabla}}_x\right)}=-i\widehat{\underline{\boldsymbol{u}}}\otimes\underline{\boldsymbol{\xi}} \tag{C.45}$$

$$\widehat{\left(\underline{\boldsymbol{\nabla}}_x.\underline{\boldsymbol{u}}\right)}=-i\underline{\boldsymbol{\xi}}.\widehat{\underline{\boldsymbol{u}}} \tag{C.46}$$

$$\widehat{\left(\Delta_x\underline{\boldsymbol{u}}\right)}=-\|\underline{\boldsymbol{\xi}}\|^2\widehat{\underline{\boldsymbol{u}}} \tag{C.47}$$

$$\widehat{\left(\underline{\boldsymbol{\nabla}}_x\left(\underline{\boldsymbol{\nabla}}_x.\underline{\boldsymbol{u}}\right)\right)}=-\left(\underline{\boldsymbol{\xi}}.\widehat{\underline{\boldsymbol{u}}}\right)\underline{\boldsymbol{\xi}} \tag{C.48}$$

Equation C.40 becomes:

$$(\lambda+\mu)\left(\underline{\boldsymbol{\xi}}.\widehat{\widehat{\underline{\boldsymbol{u}}^G}}\right)\underline{\boldsymbol{\xi}}+\left(\mu\|\underline{\boldsymbol{\xi}}\|^2-\rho\omega^2\right)\widehat{\widehat{\underline{\boldsymbol{u}}^G}}-\hat{\hat{\underline{\boldsymbol{f}}}}\left(\underline{\boldsymbol{\xi}};\omega\right)=\underline{\mathbf{0}} \tag{C.49}$$

where $\widehat{\widehat{\underline{\boldsymbol{f}}_{ext}}}=\underline{\boldsymbol{a}}$ is constant in $\left(\underline{\boldsymbol{\xi}};\omega\right)\in\mathbb{R}^3\times\mathbb{R}$. The solution of the problem will be computed once Equation C.49 is solved and it is the inverse Fourier transform of its solution:

$$\underline{\boldsymbol{u}}^G\left(\underline{\boldsymbol{x}};t\right)=\frac{1}{(2\pi)^4}\int_{\mathbb{R}^4}\widehat{\underline{\boldsymbol{u}}^G}\left(\underline{\boldsymbol{x}},\omega,\underline{\boldsymbol{a}}\right)\exp\left(-i\left(\underline{\boldsymbol{\xi}}.\underline{\boldsymbol{x}}\right)\right)dV\left(\underline{\boldsymbol{x}}\right)d\omega \tag{C.50}$$

The solution resulted as the contribution of a series of harmonic plane-waves of pulsation ω and wave-vector $\underline{\boldsymbol{\xi}}$, being the two apparently not linked. Due to the latter, those plane-waves are not of the same kind of those constituting the homogeneous solution. The constant external force $\widehat{\widehat{\underline{\boldsymbol{f}}_{ext}}}$ creates plane-waves at all frequencies and propagating in all the directions.

Resolution in the transformed domain

Let us take the take the scalar product of $\underline{\boldsymbol{\xi}}$ and all the members of Equation C.49:

$$\left(\underline{\boldsymbol{\xi}}.\widehat{\widehat{\underline{\boldsymbol{u}}^G}}\right)=\frac{\left(\underline{\boldsymbol{\xi}}.\underline{\boldsymbol{a}}\right)}{\rho\left(c_P^2\|\underline{\boldsymbol{\xi}}\|^2-\omega^2\right)} \tag{C.51}$$

By substituting the latter expression[2] in Equation C.49, one obtains the solution in transformed space:

$$\rho c_S^2\widehat{\widehat{\underline{\boldsymbol{u}}^G}}\left(\underline{\boldsymbol{\xi}};\omega\right)=\frac{\underline{\boldsymbol{a}}}{\|\underline{\boldsymbol{\xi}}\|^2-k_S^2}+\frac{\left(\underline{\boldsymbol{\xi}}.\underline{\boldsymbol{a}}\right)\underline{\boldsymbol{\xi}}}{k_S^2}\left(\frac{1}{\|\underline{\boldsymbol{\xi}}\|^2-k_S^2}-\frac{1}{\|\underline{\boldsymbol{\xi}}\|^2-k_P^2}\right) \tag{C.52}$$

with $k_\alpha=\omega/c_\alpha$.
In the usual sense, Equation C.52 has no meaning (yet it does in a distributional sense[3]) for either $\|\underline{\boldsymbol{\xi}}\|=\pm k_P$ and $\|\underline{\boldsymbol{\xi}}\|=\pm k_S$, i.e. for plane-wave solutions freely propagating in the homogeneous elastic space. For those values, $\widehat{\widehat{\underline{\boldsymbol{u}}^G}}$ is not defined.

[2]The scalar product in Equation C.51 refers to longitudinal waves since the scalar product of by $i\underline{\boldsymbol{\xi}}$ in the Fourier transformed space corresponds to take the gradient

[3]In a distributional sense, Equation C.52 is not meaningless. Let us consider a distribution T and a function f that have zero-values on the set of points x_i. With those assumptions, the equation $Tf=1$ has the following solution:

$$T=\frac{1}{f}+\sum_i\alpha_i\delta_{x_i} \tag{C.53}$$

with $1/f$ a pseudo-function and α_i any set of constants. To explain the role of the constants α_i one must consider the fact that dividing a function by $i\xi$ in the Fourier's transform domain, translates into a function integration in the physical domain, i.e.:

$$i\xi\hat{f}\left(\xi\right)=C \tag{C.54}$$

$$f\left(x\right)=\frac{1}{2\pi}\int_{\mathbb{R}}\frac{C}{i\xi}\exp\left(i\xi x\right)d\xi+\alpha_0=Cx+\alpha_0 \tag{C.55}$$

In Equation C.52, the denominator function has zero values onto the hypercones with spherical base defined by: $\|\underline{\boldsymbol{\xi}}\|^2=k_S^2$ and $\|\underline{\boldsymbol{\xi}}\|^2=k_P^2$. The latter expressions correspond to monochromatic plane-waves, adding to the Green's function solution two plane-waves (initial boundary conditions enforce their amplitudes nil).

C.2.2 Stationary Green's function

Let us consider the orthonormal base of $\mathbb{R}^3$, $(\underline{\boldsymbol{e}}_1, \underline{\boldsymbol{e}}_2, \underline{\boldsymbol{e}}_3)$, with $\underline{\boldsymbol{e}}_3$=$\underline{\boldsymbol{x}}/\|\underline{\boldsymbol{x}}\|$. The generic vector $\underline{\boldsymbol{\xi}}$ may be defined in spherical coordinates, $\underline{\boldsymbol{\xi}}$=$(\rho \sin\theta \sin\phi, \rho \cos\theta \sin\phi, \rho \cos\phi)^T$. Les us define $g\left(\underline{\boldsymbol{x}}\right)$ and $\hat{g}\left(\underline{\boldsymbol{\xi}}\right)$ a function and its Fourier's transform, defined as:

$$\hat{g}\left(\underline{\boldsymbol{\xi}}\right) = \frac{1}{\rho\left(\underline{\boldsymbol{\xi}}\right)^2 - k^2}, \quad g\left(\underline{\boldsymbol{x}}\right) = \frac{1}{(2\pi)^3}\int_{\mathbb{R}^3} \frac{\exp\left(i\underline{\boldsymbol{\xi}}.\underline{\boldsymbol{x}}\right)}{\rho\left(\underline{\boldsymbol{\xi}}\right)^2 - k^2} dV\left(\underline{\boldsymbol{\xi}}\right) \tag{C.56}$$

Thanks to the defined reference system, one can take $\underline{\boldsymbol{x}} = (0,0,r)^T$, leading to:

$$g\left(\underline{\boldsymbol{x}}\right) = \frac{1}{(2\pi)^2}\int_0^{+\infty} \frac{1}{\rho^2 - k^2}\int_0^{\pi} e^{ir\rho\cos\phi}\sin\phi d\phi \rho^2 d\rho \tag{C.57}$$

Integrating over ϕ, one obtains:

$$g\left(\underline{\boldsymbol{x}}\right) = \frac{1}{(2\pi)^2}\int_0^{+\infty} \frac{e^{-ir\rho} - e^{ir\rho}}{ir\left(\rho^2 - k^2\right)}\rho d\rho = -\frac{1}{ir\,(2\pi)^2}\int_{-\infty}^{+\infty} \frac{e^{ir\rho}}{\left(\rho^2 - k^2\right)}\rho d\rho \tag{C.58}$$

The latter integral in Equation C.58 is computed by considering ρ varying on a closed contour in the complex plane. This choice provides for positive k a pole in $-k$. The selected contour eliminates physically inadmissible solutions, i.e. plane waves ($k = \omega/c$) coming from infinite. Therefore, the integration finally leads to the following expression of $g\left(\underline{\boldsymbol{x}}\right)$:

$$g\left(\underline{\boldsymbol{x}}\right) = \frac{e^{ikr}}{4\pi r} \tag{C.59}$$

Furthermore, recalling the relation in Equations C.48, the following equation holds:

$$\hat{g}\left(\underline{\boldsymbol{\xi}}\right)\left(\underline{\boldsymbol{\xi}}.\underline{\boldsymbol{a}}\right)\underline{\boldsymbol{\xi}} = -(\underline{\boldsymbol{\nabla}}_x\,(\widehat{\underline{\boldsymbol{\nabla}}_x.\,(g\left(\underline{\boldsymbol{x}}\right)\underline{\boldsymbol{a}})})) \tag{C.60}$$

Finally, the integration (in the transformed domain) of Equation C.49 one gets the time Fourier's transform of the Green's function $\widehat{\underline{\boldsymbol{u}}^G}$:

$$\mu\widehat{\underline{\boldsymbol{u}}^G}\left(\underline{\boldsymbol{x}};\omega\right) = G_S\left(r\right)\underline{\boldsymbol{a}} + \left(\frac{1}{k_S}^2\right)\underline{\boldsymbol{\nabla}}_x\left(\underline{\boldsymbol{\nabla}}_x.\left(\left(G_S\left(r\right) - G_P\left(r\right)\right)\underline{\boldsymbol{a}}\right)\right) \tag{C.61}$$

with

$$G_\alpha = \frac{e^{ik_\alpha r}}{4\pi r}, \quad \alpha = p, s \tag{C.62}$$

Further interesting expressions can be obtained if one considers that for all functions $g\left(r\right)$ of this type, the following equations hold:

$$\begin{aligned} \underline{\boldsymbol{\nabla}}_x.\left(g\left(r\right)\underline{\boldsymbol{a}}\right) &= \left(\underline{\boldsymbol{a}}, \underline{\boldsymbol{e}}_r\right) g'\left(r\right) \\ \underline{\boldsymbol{\nabla}}_x\left(\underline{\boldsymbol{\nabla}}_x.\left(g\left(r\right)\underline{\boldsymbol{a}}\right)\right) &= \frac{1}{r}\left[\left(\underline{\boldsymbol{a}} - \left(\underline{\boldsymbol{a}}, \underline{\boldsymbol{e}}_r\right)\underline{\boldsymbol{e}}_r\right) g'\left(r\right) + r\left(\underline{\boldsymbol{a}}, \underline{\boldsymbol{e}}_r\right)\underline{\boldsymbol{e}}_r g''\left(r\right)\right] \end{aligned} \tag{C.63}$$

Equation C.61 becomes:

$$\begin{aligned} \mu\widehat{\underline{\boldsymbol{u}}^G}\left(\underline{\boldsymbol{x}};\omega\right) = G_S\left(r\right)\underline{\boldsymbol{a}} + \frac{1}{r}\left(\frac{c_s}{\omega}^2\right)\left[\underline{\boldsymbol{a}}\left(G'_S\left(r\right) - G'_P\left(r\right)\right) + \right. \\ \left. + \left(\underline{\boldsymbol{a}}, \underline{\boldsymbol{e}}_r\right)\underline{\boldsymbol{e}}_r\left(rG''_S\left(r\right) - G'_S\left(r\right) - rG''_P\left(r\right) + G'_P\left(r\right)\right)\right] \end{aligned} \tag{C.64}$$

with:

$$\begin{aligned} G'_{\alpha}(r) &= \left(\frac{ir\omega}{c_{\alpha}-1}\right)\frac{g_{\alpha}(r)}{r} \\ G''_{\alpha}(r) &= \left(2-\frac{2ir\omega}{c_{\alpha}-1}-\left(\frac{r\omega}{c_{\alpha}}\right)^{2}\right)\frac{g_{\alpha}(r)}{r^{2}} \end{aligned} \tag{C.65}$$

The final result fully developed is:

$$\begin{aligned} \mu\widehat{\underline{\boldsymbol{u}}^{G}}(\underline{\boldsymbol{x}};\omega) = G_S(r)\,\underline{\boldsymbol{a}} + \frac{1}{(k_S r)^2}\left[\left(G_P(r)\left(1-ik_P r\right)-G_S(r)\left(1-ik_S r\right)\right)\underline{\boldsymbol{a}} + \right. \\ \left. + \left(\left(3\left(1-ik_S r\right)-\left(k_S r\right)^2\right)G_S(r)-\left(3\left(1-ik_P r\right)-\left(k_P r\right)^2\right)G_P(r)\right)\left(\underline{\boldsymbol{a}},\underline{\boldsymbol{e}}_r\right)\underline{\boldsymbol{e}}_r\right] \end{aligned} \tag{C.66}$$

The stationary version of the latter Green's function can be attained by developing Equation C.66 in Taylor's series on $\frac{1}{\omega}$:

$$\mu\widehat{\underline{\boldsymbol{u}}^{G}}(\underline{\boldsymbol{x}};0) = \frac{1}{r}\left(\underline{\boldsymbol{a}}+\left(\left(\frac{c_S}{c_P}\right)^2-1\right)\left(\underline{\boldsymbol{a}}-\left(\underline{\boldsymbol{a}},\underline{\boldsymbol{e}}_r\right)\underline{\boldsymbol{e}}_r\right)\right) \tag{C.67}$$

C.2.3 Transient Green's function

To obtain the full expression of Green's function in space-time, one must perform the inverse Fourier's transform of Equation C.66. Let us first consider the following function (in the transformed domain) $\hat{f}(\omega)$ and $\hat{h}(\omega)$ in the form:

$$\begin{aligned} \hat{f}(\omega) &= e^{-i\omega\alpha} \\ \hat{h}(\omega) &= \left(\frac{1}{\omega^2}-\frac{i\alpha}{\omega}\right)\hat{f}(\omega) \end{aligned} \tag{C.68}$$

By denoting δ and H as the Dirac's delta and Heaviside functions[4] it is possible to prove[5] that their inverse Fourier's transforms read:

$$f(t) = \frac{1}{2\pi}\int_{-\infty}^{+\infty} e^{i\omega(t-\alpha)}d\omega = \delta(t-\alpha) \tag{C.74}$$

[4] $\delta(t)$ is defined for all test functions $\phi \in \mathcal{C}^{\infty}(\mathbb{R})$ as: $(\delta,\phi)=\phi(0)$. The Heaviside function $H(t)$ is defined as:

$$\begin{aligned} H(t) &= 1, \quad t \geq 0 \\ H(t) &= 0, \quad t < 0 \end{aligned} \tag{C.69}$$

and it verifies the relation $H' = \delta$ in a distributional sense.

[5] Let us compute the Fourier's transform of the function $g(t)$ defined as follows:

$$\begin{aligned} g(t) &= t, \quad t \geq 0 \\ g(t) &= 0, \quad t < 0 \end{aligned} \tag{C.70}$$

The latter admits Fourier's transform in a distributional sense, i.e. for all ϕ rapidly decreasing $\mathcal{C}^{\infty}(\mathbb{R})$ test functions:

$$\begin{aligned} (g'',\phi) = (g,\phi'') = \int_0^{+\infty} t\phi''(t)\,dt = -\int_0^{+\infty}\phi'(t)\,dt = \phi(0) = (\delta,\phi) \\ = \left(\hat{\delta},\hat{\phi}\right) = \left(\hat{g},\hat{\phi}''\right) = -\omega^2\left(\hat{g},\hat{\phi}\right) \end{aligned}$$

from which one can write:

$$\hat{g}(\omega) = -\frac{1}{\omega^2} \tag{C.71}$$

Following the same logic, one can obtain the Fourier's transform of the Heaviside function:

$$\hat{H}(\omega) = -\frac{i}{\omega} \tag{C.72}$$

$$h(t) = tH(t-\alpha) \tag{C.75}$$

from where one can derive the general expression of the transient Green's function:

$$\begin{aligned} 4\pi\underline{\boldsymbol{u}}^G(\underline{\boldsymbol{x}};t) = {} & \frac{1}{r^3}\left(3\left(\left(\underline{\boldsymbol{a}},\underline{\boldsymbol{e}}_r\right)\underline{\boldsymbol{e}}_r - \underline{\boldsymbol{a}}\right)t\left(H\left(t-\frac{r}{c_P}\right) - H\left(t-\frac{r}{c_S}\right)\right)\right) + \\ & \frac{1}{rc_S^2}\left(\left(\underline{\boldsymbol{a}},\underline{\boldsymbol{e}}_r\right)\underline{\boldsymbol{e}}_r - \underline{\boldsymbol{a}}\right)\delta\left(t-\frac{r}{c_S}\right) + \\ & \frac{1}{rc_P^2}\left(\left(\underline{\boldsymbol{a}},\underline{\boldsymbol{e}}_r\right)\underline{\boldsymbol{e}}_r\right)\delta\left(t-\frac{r}{c_P}\right) \end{aligned} \tag{C.76}$$

Finally, combining the equations above, one gets the inverse Fourier's transform of $h(\omega)$:

$$h(t) = \left(g(t) + \alpha H(t)\right) * \delta(t-\alpha) = tH(t-\alpha) \tag{C.73}$$

Appendix D

Mechanics of earthquake sources

D.1 Failure mechanism

As many other materials, rocks can bare a limited amount of shear stress before failure. The corresponding yield shear stress τ_m is often related to the normal stress σ_{nn} by mean of the Mohr-Coulomb law. Therefore, the yield stress of a fault discontinuity depends both on depth and on the regional stress field. Once the yield stress reached the material shows plastic deformations until a new shear stress is attained and plastic flow stops. A new yield stress $\tau_0 < \tau_m$ is reached at this point. The assumption of elasto-plastic constitutive behaviour implies that the plastic flow localizes along shear bands, i.e. the seismic fault and the relative slippage of its two edges. The surrounding rock material is softened along those shear bands the plastic deformation will always occur along these bands. In a time range of a few tenths of thousands of years, earthquakes always occur along existing faults. Depending on regional tectonic context, the stress drop $\Delta\tau = \tau_m - \tau_0$ ranges from 3 to 10 MPa. Since the plastic deformation is localized on the fault it can be characterized by the resulting relative

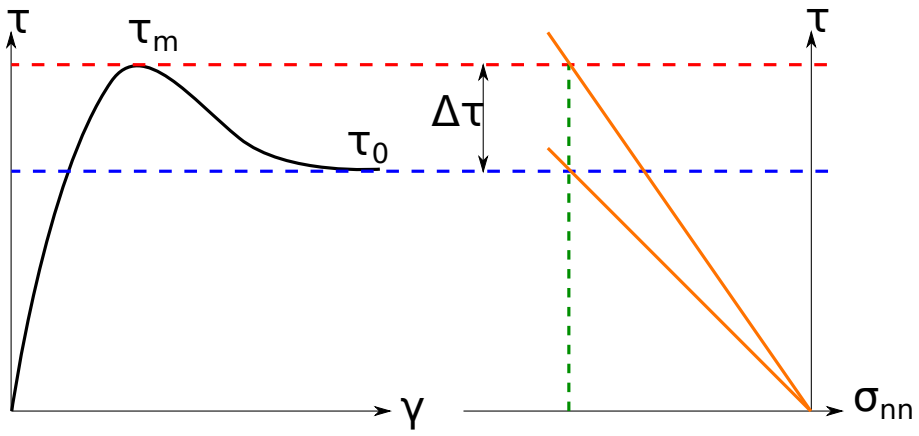

Figure D.1: Shear stress-strain behaviour along softened shear-bands (i.e. fault discontinuities). Peak shear stress τ_m reduces to its residual value τ_0 upon monotonic shearing (Clouteau, 2008)

displacement along it and denoted by $\underline{\boldsymbol{\Delta u}}$ (i.e. slippage). It satisfies $\underline{\boldsymbol{\Delta u}}.\underline{\boldsymbol{n}} = 0$ with $\underline{\boldsymbol{n}}$ the normal vector of the fault. The amplitude of this displacement depends both on the stress drop $\Delta\tau$ and on the elastic properties of the surrounding soil. In this analogical model, $\|\underline{\boldsymbol{\Delta u}}\|$ represents the total average slip $\langle\Delta u\rangle$ developed by the event along the fault surface (Bizzarri, 2014).

The simplest possible model of seismic source is that of a point source buried in an elastic half-space. The development of a proper model took a few years in the making. Nakano (1923) made the first

efforts, by modelling the earthquakes as explosions. After some years, Honda (1962) observed that the P-waves spatial distribution is well reproduced by a couple of forces, whereas this approach does not replicate the S-wave distribution. To solve the problem of the seismic radiation generated by a shear crack that starts from a point and grows radially with either a circular or an elliptical rupture front has been studied for a long time by application of the representation theorem of Burridge and Knopoff (1964). The problem was firstly solved for far-field body waves and a finite kinematic crack with an elliptical rupture front propagating at a constant velocity (Savage, 1966) and more realistic source models were proposed later on, based on dynamical models of the rupture propagation (i.e. self-similar crack growing indefinitely, taking into account the dynamic friction (Richards, 1976)). The dynamic problem was solved numerically for a finite circular crack by Madariaga (1976); Virieux and Madariaga (1982). However, concerning the seismic radiation itself, these latter authors only paid attention to the far-field body-wave terms. Very little attention was paid to the near-field terms of the seismic radiation problem in these early studies. With the exception

D.2 Kinematic source model

D.2.1 The Elasto-Dynamic Green's function

The Elasto-Dynamic problem is ruled by a non-homogeneous Navier-Stokes equation (see appendix C):

$$\underline{\boldsymbol{\nabla}}_x \cdot \underline{\underline{\boldsymbol{\sigma}}}\left(\underline{\boldsymbol{u}}\right)\left(\underline{\boldsymbol{x}};t\right) + \underline{\boldsymbol{f}}\left(\underline{\boldsymbol{x}};t\right) = \rho\left(\underline{\boldsymbol{x}}\right)\left(\underline{\boldsymbol{x}}\right)\partial_{tt}\underline{\boldsymbol{u}}\left(\underline{\boldsymbol{x}};t\right) \quad \left(\underline{\boldsymbol{x}};t\right) \in \left(\Omega, \mathbb{I}_t\right) \tag{D.1}$$

where $\Omega \subseteq \mathbb{R}^3$ is an open set representing the ensemble of point belonging to the body in the current configuration, $\mathbb{I}_t \subseteq \mathbb{R}$ is the time interval considered, $\rho\left(x\right)$ the material's density. $\underline{\underline{\boldsymbol{\sigma}}}(\underline{\boldsymbol{u}})(\underline{\boldsymbol{x}};t)$represents the Cauchy's stress tensor and $\underline{\boldsymbol{f}}(\underline{\boldsymbol{x}};t)$is the external force distribution per unit-weight. In small strain regime and in case of elastic material, the stress tensor can be written as:

$$\underline{\underline{\boldsymbol{\sigma}}}\left(\underline{\boldsymbol{u}}\left(\underline{\boldsymbol{x}};t\right)\right) = \mathbb{D}^{el}\left(\underline{\boldsymbol{x}}\right) : \underline{\underline{\boldsymbol{\varepsilon}}}_x\left(\underline{\boldsymbol{u}}\left(\underline{\boldsymbol{x}};t\right)\right), \quad \underline{\underline{\boldsymbol{\varepsilon}}}_x\left(\underline{\boldsymbol{u}}\left(\underline{\boldsymbol{x}};t\right)\right) = \underline{\boldsymbol{u}} \otimes_s \underline{\boldsymbol{\nabla}}_x\left(\underline{\boldsymbol{x}};t\right)$$

with $\underline{\underline{\boldsymbol{\varepsilon}}}_x(\underline{\boldsymbol{u}}\left(\underline{\boldsymbol{x}};t\right))$ called the *small strain tensor*. The *Uniqueness Theorem* proves that the displacement field $\underline{\boldsymbol{u}}(\underline{\boldsymbol{x}};t)$is a unique solution of Equation D.1 (Aki and Richards, 1980).
Assuming the linear elastic stress-strain relationship, $\underline{\boldsymbol{u}}^G\left(\underline{\boldsymbol{y}},t',\underline{\boldsymbol{a}};\underline{\boldsymbol{x}},t\right)$ represent the Green's function of Equation D.1, thus it solves:

$$\underline{\boldsymbol{\nabla}}_x \cdot \left(\mathbb{D}^{el} : \underline{\boldsymbol{u}}^G \otimes_s \underline{\boldsymbol{\nabla}}_x\right)\left(\underline{\boldsymbol{x}};t\right) + \delta_{\underline{\boldsymbol{y}}}\delta_{t'}\underline{\boldsymbol{a}} = \rho\partial_{tt}\underline{\boldsymbol{u}}^G \quad \left(\underline{\boldsymbol{x}};t\right) \in \left(\mathbb{R}^3, \mathbb{R}\right) \tag{D.2}$$

where $\underline{\bullet} \otimes_s \underline{\boldsymbol{\nabla}}_x$ represent the symmetric gradient operator and $\delta_{\underline{\boldsymbol{y}}}$, $\delta_{t'}$ are the Dirac's delta centered on $\underline{\boldsymbol{y}}$ and on t'.
Green's function has a tensor nature since it depends on both receiver and source's coordinates. The quiescent past conditions may be applied invariably in the form:

$$\underline{\boldsymbol{u}}^G\left(\underline{\boldsymbol{y}},t',\underline{\boldsymbol{a}};\underline{\boldsymbol{x}},t\right), \partial_t\underline{\boldsymbol{u}}^G\left(\underline{\boldsymbol{y}},t',\underline{\boldsymbol{a}};\underline{\boldsymbol{x}},t\right) = \underline{\boldsymbol{0}}, \quad \forall\underline{\boldsymbol{x}} \neq \underline{\boldsymbol{y}}, \forall t \leq \tau, \tag{D.3}$$

D.2.2 The Representation Theorem

Equation D.1 can be solved for whichever density of body forces $\underline{\boldsymbol{f}}(\underline{\boldsymbol{x}};t)$in two steps: first finding the solution for a unit force applied in $\underline{\boldsymbol{y}}$, at time t', acting along direction $\underline{\boldsymbol{a}}$, called $\underline{\boldsymbol{u}}^G\left(\underline{\boldsymbol{y}},t',\underline{\boldsymbol{a}};\underline{\boldsymbol{x}},t\right)$ and then superposing the solutions obtained at each $\underline{\boldsymbol{y}}$, t' as:

$$\underline{\boldsymbol{u}}\left(\underline{\boldsymbol{x}};t\right) = \sum_k \int_{\mathbb{R}^4} \underline{\boldsymbol{u}}^G\left(\underline{\boldsymbol{y}},t',\underline{\boldsymbol{e}}_k;\underline{\boldsymbol{x}},t\right) f_k\left(\underline{\boldsymbol{y}},\underline{\boldsymbol{t}}'\right) dV\left(\underline{\boldsymbol{y}}\right) dt' \tag{D.4}$$

with $(\underline{\boldsymbol{e}}_1, \underline{\boldsymbol{e}}_2, \underline{\boldsymbol{e}}_3)$ is the selected $\mathbb{R}^3$ orthonormal basis and $f_k = \underline{\boldsymbol{f}}.\underline{\boldsymbol{e}}_k$. Consider the domain depicted in Figure D.2 with inner discontinuity Σ. By substituting $\underline{\boldsymbol{u}}_1$=$\underline{\boldsymbol{u}}(\underline{\boldsymbol{x}};t)$, $\underline{\boldsymbol{u}}_2 = \underline{\boldsymbol{u}}^G\left(\underline{\boldsymbol{y}}, 0, \underline{\boldsymbol{e}}_k; \underline{\boldsymbol{x}}, t\right)$, $\underline{\boldsymbol{f}}_1$=$\underline{\boldsymbol{f}}$ and $\underline{\boldsymbol{f}}_2 = \delta_{\underline{\boldsymbol{y}}}\delta_0\underline{\boldsymbol{e}}_k$ in Reciprocity Theorem (in the form of Equation C.37), one gets the *First Representation theorem* (Burridge and Knopoff, 1964; Aki and Richards, 1980):

$$\begin{aligned}\underline{\boldsymbol{u}}\left(\underline{\boldsymbol{x}};t\right) = &\sum_k \int_{-\infty}^{+\infty}\int_\Omega \left[\underline{\boldsymbol{f}}.\underline{\boldsymbol{u}}^G\left(\underline{\boldsymbol{y}}, 0, \underline{\boldsymbol{e}}_k; \underline{\boldsymbol{x}}, t-\tau\right)\right]\underline{\boldsymbol{e}}_k dV\left(\underline{\boldsymbol{y}}\right)d\tau \\ &+\sum_k \int_{-\infty}^{+\infty}\int_\Sigma \left[\underline{\boldsymbol{t}}_n\left(\underline{\boldsymbol{u}}^G\left(\underline{\boldsymbol{y}}, 0, \underline{\boldsymbol{e}}_k; \underline{\boldsymbol{x}}, t-\tau\right)\right).\underline{\boldsymbol{u}}\right]\underline{\boldsymbol{e}}_k dS\left(\underline{\boldsymbol{y}}\right)d\tau \\ &-\sum_k \int_{-\infty}^{+\infty}\int_\Sigma \left[\underline{\boldsymbol{t}}_n\left(\underline{\boldsymbol{u}}\left(\underline{\boldsymbol{x}};t\right)\right).\underline{\boldsymbol{u}}^G\left(\underline{\boldsymbol{y}}, 0, \underline{\boldsymbol{e}}_k; \underline{\boldsymbol{x}}, t-\tau\right)\right]\underline{\boldsymbol{e}}_k dS\left(\underline{\boldsymbol{y}}\right)d\tau\end{aligned} \tag{D.5}$$

If elasticity holds, the traction vector issued from the Green's function can be written as:

$$\underline{\boldsymbol{t}}_n\left(\underline{\boldsymbol{u}}^G\left(\underline{\boldsymbol{y}}, 0, \underline{\boldsymbol{e}}_k; \underline{\boldsymbol{x}}, t-\tau\right)\right) = \left[\mathbb{D}^{el} : \left(\underline{\boldsymbol{u}}^G\left(\underline{\boldsymbol{y}}, 0, \underline{\boldsymbol{e}}_k; \underline{\boldsymbol{x}}, t-\tau\right) \otimes_S \nabla_x\right)\right].\underline{\boldsymbol{n}} \tag{D.6}$$

D.2.3 Equivalent body forces generated by fault slippage

The Earth's crust can be seen as an elastic domain Ω, bounded by the regular surface $\partial\Omega = \Gamma$, as a first approximation. According to Aki and Richards (1980), the seismic source may be conceptually described as displacement discontinuities $[\underline{\boldsymbol{u}}]\left(\underline{\boldsymbol{x}};t\right) = \Delta u\left(\underline{\boldsymbol{x}};t\right)\underline{\boldsymbol{d}}_\Sigma\left(\underline{\boldsymbol{x}};t\right)$ across a given surface Σ. The latter represents a buried active fault and it resides within Ω. Σ has two adjacent surfaces Σ^+ and Σ^- that *spontaneously* slip one with the respect to each other, radiating the earthquake wave-field. $\underline{\boldsymbol{d}}(\underline{\boldsymbol{x}};t)$is the *slip vector* ($\|\underline{\boldsymbol{d}}_\Sigma\| = 1$) representing the direction along which the relative displacement occurs. The displacement jump $[\underline{\boldsymbol{u}}](\underline{\boldsymbol{x}};t)$across Σ is expressed as:

$$[\underline{\boldsymbol{u}}]\left(\underline{\boldsymbol{x}};t\right) = \underline{\boldsymbol{u}}|_{\Sigma^+}\left(\underline{\boldsymbol{x}};t\right) - \underline{\boldsymbol{u}}|_{\Sigma^-}\left(\underline{\boldsymbol{x}};t\right) \tag{D.7}$$

In general, a similar discontinuity may be formed by traction vectors, due to external forces on Σ, but for spontaneous rupture the traction should be continuous $[\underline{\boldsymbol{t}}_n](\underline{\boldsymbol{x}};t)$=$\underline{\boldsymbol{0}}$. $[\underline{\boldsymbol{u}}](\underline{\boldsymbol{x}};t)$does not satisfy the elasto-dynamic equation in $int\left(\Omega\right)$, unless one extend its boundary to the discontinuity, i.e. $\partial\Omega^\star = \Gamma \cup \Sigma^+ \cup \Sigma^-$. At this point, Γ is no longer of direct interest (it may be the surface of the Earth), thus admitting homogeneous boundary conditions on it. Σ may be parametrized by a local reference system defined by $\underline{\boldsymbol{d}}$ and the outward normal unit vector $\underline{\boldsymbol{n}}_\Sigma(\underline{\boldsymbol{x}};t)$vector ($\underline{\boldsymbol{d}}_\Sigma.\underline{\boldsymbol{n}}_\Sigma = 0$) (Burridge and Knopoff, 1964; Aki and Richards, 1980). Let us consider a fault of thickness h in the direction of $\underline{\boldsymbol{n}}_\Sigma$ and let us denote by $\underline{\boldsymbol{x}}_O$ any point along the mean surface of the fault ($\underline{\boldsymbol{x}}_O \in \Sigma$). Assuming a linear variation of the displacement along $\underline{\boldsymbol{n}}_\Sigma$ leads to:

$$\begin{aligned}\underline{\boldsymbol{u}}\left(\underline{\boldsymbol{x}}_O + \zeta\underline{\boldsymbol{n}}_\Sigma;t\right) = \underline{\boldsymbol{u}}\left(\underline{\boldsymbol{x}}_O;t\right) + \frac{\zeta}{h}\Delta u\left(\underline{\boldsymbol{x}};t\right)\underline{\boldsymbol{d}}_\Sigma\left(\underline{\boldsymbol{x}}_O;t\right) + o\left(\zeta\right)\underline{\boldsymbol{n}}_\Sigma, \\ \zeta = \left(\underline{\boldsymbol{x}} - \underline{\boldsymbol{x}}_O\right).\underline{\boldsymbol{n}}_\Sigma\end{aligned} \tag{D.8}$$

The derived strain tensor (first order truncation) reads:

$$\underline{\underline{\boldsymbol{\varepsilon}}}_x\left(\underline{\boldsymbol{u}}\left(\underline{\boldsymbol{x}};t\right)\right) = [\underline{\boldsymbol{u}}] \otimes_s \underline{\boldsymbol{\nabla}}_x = \frac{\Delta u\left(\underline{\boldsymbol{x}};t\right)}{h}\underline{\boldsymbol{d}}_\Sigma \otimes_s \underline{\boldsymbol{n}}_\Sigma + o(\underline{\underline{\boldsymbol{I}}}) \tag{D.9}$$

where $\underline{\underline{\boldsymbol{I}}}$ represents the 2$^{\text{nd}}$-order identity tensor and $\otimes_s$ the symmetric tensor-product.
Taking the limit of the strain tensor in Equation D.9 for $h \to 0$ the generalized strain tensor (in a distribution sense) associated to the displacement jump reads:

$$\underline{\underline{\boldsymbol{\varepsilon}}}_x\left(\underline{\boldsymbol{u}}\left(\underline{\boldsymbol{x}};t\right)\right) = [\underline{\boldsymbol{u}}] \otimes_s \underline{\boldsymbol{\nabla}}_x = \Delta u\left(\underline{\boldsymbol{x}};t\right)\delta_\Sigma\left(\underline{\boldsymbol{x}}\right)\underline{\boldsymbol{d}}_\Sigma \otimes_s \underline{\boldsymbol{n}}_\Sigma \tag{D.10}$$

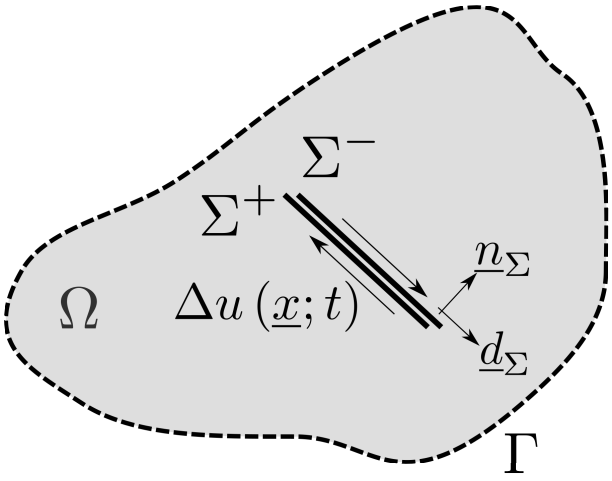

Figure D.2: A finite elastic body Ω with external surface Γ and internal surface Σ (representing the surface across which the discontinuous displacement field may arise, i.e. the buried fault). The two sides Σ^+ and Σ^- may slip one to each other, with a displacement discontinuity Δu. The normal vector to Σ points from Σ^- towards Σ^+ (Aki and Richards, 1980).

where $\delta_\Sigma\left(\underline{\boldsymbol{x}}\right)$ represents the Dirac's delta centered on the fault surface.
Assuming the Earth's crust as an elastic material, the equivalent traction forces associated to the displacement jump reads:

$$\underline{\boldsymbol{f}}_\Sigma\left(\underline{\boldsymbol{x}};t\right)=\underline{\boldsymbol{\nabla}}_x.\left(\mathbb{D}^{el}\left(\underline{\boldsymbol{x}}\right):\underline{\underline{\boldsymbol{\varepsilon}}}_x\left(\underline{\boldsymbol{u}}\left(\underline{\boldsymbol{x}};t\right)\right)\right)=\underline{\boldsymbol{\nabla}}_x.\left(\mathbb{D}^{el}\left(\underline{\boldsymbol{x}}\right):\Delta u\left(\underline{\boldsymbol{x}};t\right)\delta_\Sigma\left(\underline{\boldsymbol{x}}\right)\underline{\boldsymbol{d}}_\Sigma\otimes_s\underline{\boldsymbol{n}}_\Sigma\right) \tag{D.11}$$

where $\underline{\boldsymbol{\nabla}}_x.\left(\bullet\right)$ is the divergence operator, $\bullet:\bullet$ the double-contraction operator and $\mathbb{D}^{el}(\underline{\boldsymbol{x}})$ the 4^{th}-order elastic stiffness tensor.
It must be noted that the equivalent forces expressed in Equation D.11 have a double interpretation: on one side they represent the traction forces at the fault surface, on the other side they might be seen as concentrated body forces within the elastic domain Ω.

D.2.4 Displacement field generated by seismic sources

The first Representation TheoremD.5 is valid regardless the boundary conditions that $\underline{\boldsymbol{u}}^G$ mus satisfies. Therefore, a convenient choice of $\underline{\boldsymbol{u}}^G$ is done. The inner discontinuity surface can be seen as a fictitious surface across which the Green's function first derivatives are continuous (i.e. $\left[\underline{\boldsymbol{t}}_n\right]\left(\underline{\boldsymbol{u}}^G\left(\underline{\boldsymbol{x}};t\right)\right)=\underline{\boldsymbol{0}}$) so $\underline{\boldsymbol{u}}^G$ satisfies the equation of motion even on Σ. Thus, in absence of body forces $\underline{\boldsymbol{f}}=\underline{\boldsymbol{0}}$, Equation D.5 can be rewritten as follows:

$$\begin{aligned}\underline{\boldsymbol{u}}\left(\underline{\boldsymbol{x}};t\right)=\sum_k\int_{-\infty}^{+\infty}\int_\Sigma\left(\Delta u\left(\underline{\boldsymbol{y}};\tau\right)\delta_\Sigma\left(\underline{\boldsymbol{y}}\right)\underline{\boldsymbol{d}}_\Sigma\otimes_s\underline{\boldsymbol{n}}_\Sigma\right):\\ :\left(\mathbb{D}^{el}:\left(\underline{\boldsymbol{u}}^G\left(\underline{\boldsymbol{y}},0,\underline{\boldsymbol{e}}_k;\underline{\boldsymbol{x}},t-\tau\right)\otimes_S\nabla_y\right)\right)\underline{\boldsymbol{e}}_k dS\left(\underline{\boldsymbol{y}}\right)d\tau\end{aligned} \tag{D.12}$$

The same expression may be obtained by substituting $\underline{\boldsymbol{f}}_\Sigma$ in Equation D.13

$$\underline{\boldsymbol{u}}\left(\underline{\boldsymbol{x}};t\right)=\sum_k\int_{\mathbb{R}^4}\underline{\boldsymbol{u}}^G\left(\underline{\boldsymbol{y}},0,\underline{\boldsymbol{e}}_k;\underline{\boldsymbol{x}},t-\tau\right)\otimes\underline{\boldsymbol{f}}_\Sigma\left(\underline{\boldsymbol{y}};\tau\right).\underline{\boldsymbol{e}}_k dV\left(\underline{\boldsymbol{y}}\right)d\tau \tag{D.13}$$

and then by integrating by parts.

D.2.5 Double-Couple simplified solution

For an elastic isotropic and homogeneous medium, Equation D.11 reduces to:

$$\underline{\boldsymbol{f}}_{\Sigma}\left(\underline{\boldsymbol{x}};t\right)=2\mu\underline{\boldsymbol{\nabla}}_{x}.\left(\Delta u\left(\underline{\boldsymbol{x}};t\right)\delta_{\Sigma}\left(\underline{\boldsymbol{x}}\right)\underline{\boldsymbol{d}}_{\Sigma}\otimes_{s}\underline{\boldsymbol{n}}_{\Sigma}\right) \tag{D.14}$$

with μ the shear modulus of the crustal material.
By assuming a constant slip along the fault plane ($\Delta u\left(\underline{\boldsymbol{x}};t\right)=\Delta u\left(t\right)$), the equivalent force vector can be expressed as:

$$\underline{\boldsymbol{f}}_{\Sigma}\left(\underline{\boldsymbol{x}};t\right)=\underline{\underline{\boldsymbol{m}}}_{O}.\underline{\boldsymbol{\nabla}}_{x}\delta_{\Sigma}\left(\underline{\boldsymbol{x}}\right) \tag{D.15}$$

where $\underline{\underline{\boldsymbol{m}}}_{O}=2\mu\Delta u\left(t\right)\left(\underline{\boldsymbol{d}}_{\Sigma}\otimes_{s}\underline{\boldsymbol{n}}_{\Sigma}\right)$ represents the surface density of *moment tensor*. When observed far enough the fault surface can be approximated as a point, thus leading to approximate $\delta_{\Sigma}\left(\underline{\boldsymbol{x}};t\right)$ as $\delta_{o}|\Sigma|$ (being $\delta_{o}=\delta\left(\underline{\boldsymbol{x}}_{O};t\right)$ and $|\Sigma|$ the total fault surface). The resulting localized equivalent force vector reads:

$$\begin{aligned}\underline{\boldsymbol{f}}_{\Sigma}=\underline{\underline{\boldsymbol{M}}}_{O}.\underline{\boldsymbol{\nabla}}_{x}\delta_{O}=&M_{O}\lim_{h\to0}\frac{1}{h}\left(\underline{\boldsymbol{d}}_{\Sigma}\delta\left(\frac{h}{2}\underline{\boldsymbol{n}}_{\Sigma}\right)-\underline{\boldsymbol{d}}_{\Sigma}\delta\left(-\frac{h}{2}\underline{\boldsymbol{n}}_{\Sigma}\right)+\right.\\&\left.+\underline{\boldsymbol{n}}_{\Sigma}\delta\left(\frac{h}{2}\underline{\boldsymbol{d}}_{\Sigma}\right)-\underline{\boldsymbol{n}}_{\Sigma}\delta\left(-\frac{h}{2}\underline{\boldsymbol{d}}_{\Sigma}\right)\right)\end{aligned} \tag{D.16}$$

with $|\Sigma|=\int_{\Sigma}dS\left(\underline{\boldsymbol{y}}\right)$ being the area of the fault and $\underline{\underline{\boldsymbol{M}}}_{0}=2\mu|\Sigma|\Delta u\left(\underline{\boldsymbol{d}}_{\Sigma}\otimes_{s}\underline{\boldsymbol{n}}_{\Sigma}\right)$ the moment tensor generated by the point-discontinuity and consisting of four forces (two couples) applied around the hypocenter: two opposite shear forces on both side of the fault (Figure D.3(a)) and two forces on both side edge of the fault to balance the moment induced by the two first (Figure D.3(b)). This model is useful to understand the shear wave pattern induced by the fault rupture. Moreover, those four forces can also be seen as two couples of extension-compression forces, giving some insight on the induced P wave pattern. For a heterogeneous slip distribution $\Delta u\left(\underline{\boldsymbol{x}};t\right)$ in an heterogeneous medium, the

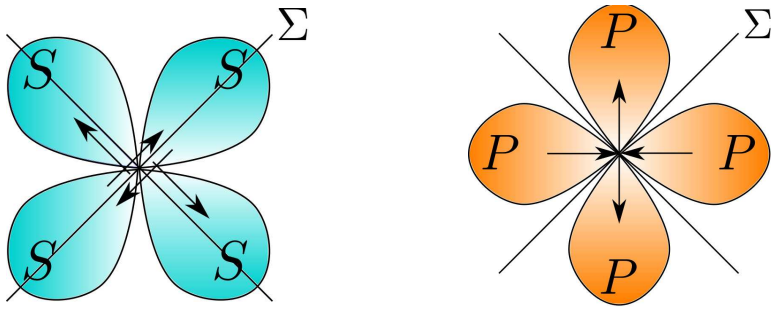

Figure D.3: Set of equivalent forces generated by spontaneous slippage along the active fault surface. (a) compressive and tensile traction forces; (b) shear traction forces.

moment tensor $\underline{\underline{\boldsymbol{M}}}_{O}\left(\underline{\boldsymbol{x}};t\right)$ represents the product average $2\int_{\Sigma}\mu\left(\underline{\boldsymbol{y}}\right)\Delta u\left(\underline{\boldsymbol{y}};t\right)\left(\underline{\boldsymbol{d}}_{\Sigma}\otimes_{S}\underline{\boldsymbol{n}}_{\Sigma}\right)dS\left(\underline{\boldsymbol{y}}\right)$. The solution of the elasto-dynamic problem for an elastic isotropic and homogeneous material and a point source $\underline{\boldsymbol{f}}=\delta\left(\underline{\boldsymbol{x}}-\underline{\boldsymbol{x}}_{O}\right)\underline{\boldsymbol{a}}$ reads (see sectionC.2):

$$\underline{\boldsymbol{u}}^{G}\left(\underline{\boldsymbol{x}},\underline{\boldsymbol{x}}_{O},\underline{\boldsymbol{a}};t\right)=\frac{\left(\underline{\boldsymbol{e}}_{r}.\underline{\boldsymbol{a}}\right)\underline{\boldsymbol{e}}_{r}}{4\pi\rho c_{P}^{2}r}\delta\left(t-\frac{r}{c_{P}}\right)+\frac{\underline{\boldsymbol{a}}-\left(\underline{\boldsymbol{e}}_{r}.\underline{\boldsymbol{a}}\right)\underline{\boldsymbol{e}}_{r}}{4\pi\rho c_{S}^{2}r}\delta\left(t-\frac{r}{c_{S}}\right) \tag{D.17}$$

being c_P,c_S the P-wave and S-wave velocities, ρ the crust density and with $r=\|\underline{\boldsymbol{x}}-\underline{\boldsymbol{x}}_{O}\|$, and $\underline{\boldsymbol{e}}_{r}=\left(\underline{\boldsymbol{x}}-\underline{\boldsymbol{x}}_{O}\right)/r$ the radial unit vector (in spherical coordinates).

Different expression of the seismic moment tensor

Although moment tensors provide a general theoretical framework to describe seismic sources based on generalized force couples, their description is not restricted to earthquake sources, but it can be extended to other types of seismic sources such as explosions, implosions, rock falls, landslides, meteorite terminal explosions (e.g. atmospheric), and mixed mode ruptures driven by fluid and gas injections. Moment tensor inversion techniques provide more accurate estimations of the earthquake focal mechanism (Dahm and Kruger, 2014). The coordinate system should always be published together with the moment tensor solution, since a wrong association may lead to misinterpretation of components and fault directions. The moment tensor is symmetric: the diagonal elements represent linear vector dipoles, whereas the off-diagonal terms can be schematized as the force-by-arm couples (see Figure D.4). The moment tensor has components M_{ij} where $i, j = 1, 2, 3$. Often, three local

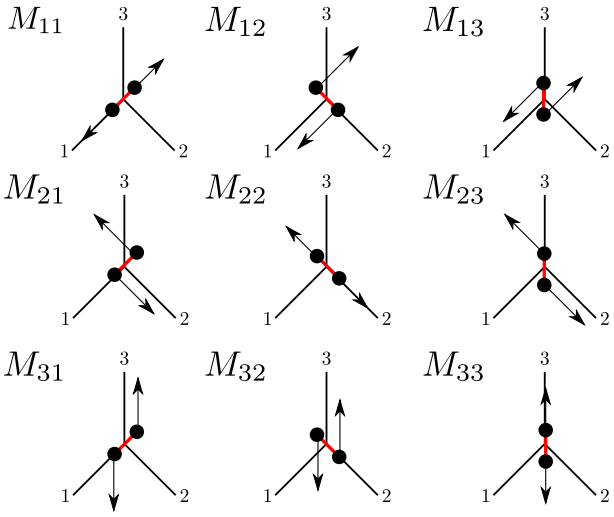

Figure D.4: The system of force couples representing the components of a Cartesian moment tensor. Diagonal elements of the moment tensor represent linear vector dipoles, while off-diagonal elements represent force couples with moment.

geographic coordinate system are used to define a Cartesian system tensor:

- *ENU*: with coordinate coordinate x_1 pointing Eastward (E), coordinate x_2 pointing to the real North (N) and positive x_3 pointing upward (U). It coincides with the UTM (*Universal Transverse Mercator*) reference system.
- *NED*: with coordinate x_1 pointing to the real North (N), coordinate x_2 pointing Eastward (E), and positive x_3 pointing downward (D).
- *USE* with coordinate x_1 pointing upward (U), coordinate x_2 pointing Southward (S), and positive x_3 pointing downward Eastward (E). This system is commonly reported in Global Centroid Moment tensors (Global CMT, formerly Harvard CMT). It is represented by the $r - \theta - \phi$-system, with r, θ, ϕ pointing upward, southward, and eastward (USE), respectively.

Tensor moment components can be easily converted from a reference system to another. If one considers the principal USE coordinate system as reference (i.e. $x_1 \equiv r$, $x_2 \equiv \theta$, $x_3 \equiv \phi$), the conversion from a reference system to another is easily performed according to the following rules:

- *USE* $\rightarrow$ *ENU*

$$\begin{aligned} M_{rr} &= +M_{UU}, \quad & M_{\theta\theta} &= +M_{EE}, \quad & M_{\phi\phi} &= +M_{NN} \\ M_{r\theta} &= -M_{EU}, \quad & M_{r\phi} &= +M_{NU}, \quad & M_{\theta\phi} &= -M_{EN} \end{aligned} \tag{D.18}$$

- *USE* $\rightarrow$ *NED*

$$\begin{aligned} M_{rr} &= +M_{DD}, \quad M_{\theta\theta} = +M_{NN}, \quad M_{\phi\phi} = +M_{EE} \\ M_{r\theta} &= +M_{ND}, \quad M_{r\phi} = -M_{ED}, \quad M_{\theta\phi} = -M_{EN} \end{aligned} \tag{D.19}$$

It is helpful at this point to realize that the moment tensor is simply a spatial integral of a stress tensor that is applied to the medium. Like any stress tensor, it can be decomposed into an isotropic (sometimes called hydrostatic stress) and a deviatoric part. Now, if an earthquake is composed of unidirectional slip on a plane, then the shear strain and stress necessary to simulate that slip provide a pure deviatoric moment tensor (i.e. $\underline{\underline{\boldsymbol{M}}}_0 = M_{ij}\underline{\boldsymbol{e}}_i \otimes_S \underline{\boldsymbol{e}}_j$, $i \neq j$). A point source of this type is commonly called a *double-couple source*. Unfortunately, the word non-double-couple source is common in geophysical literature, and it is often taken to mean sources that are not well described as slip on a plane (e.g., an explosion). For instance, explosive sources correspond to equal diagonal elements and vanishing non-diagonal elements of the moment tensor. The moment tensor representation is useful to represent compensated linear vector dipole source as well (Bizzarri, 2014). However, the word non-double-couple source technically means a source that is not fit with a simple shear at a point. The implementation of the moment-tensor source can be done either by particle velocity (Yomogida and Etgen, 1993; Graves, 1996, among other) or by stress (Virieux, 1986).

D.2.6 Seismic source time evolution

The time-evolution of the displacement jump is modelled with the so called the *Source Time Function* STF is employed. First of all, the quiescent past assumption (i.e. the fact, before the fault rupture initiation, the offset is zero) implies that a suitable STF should be zero $\forall t \leq 0$. Moreover, the STF has to remain constant after the earthquake (slip weakening is neglected in this study). Finally, at any time t, the STF and its first time-derivative (the so called Slip Velocity Function (SVF)) must be positive (so to fulfil the requirement of a positive moment tensor, since the SVF represents the L^2-norm of the vector slip velocity on the fault area (Bizzarri, 2014)):

$$\begin{cases} u_S(t) \geq 0 & t \geq 0 \\ \partial_t u_S(t) \geq 0 & t \geq 0 \end{cases} \tag{D.20}$$

Within the framework of a point-wise approximation of the seismic source, the choice of an *adequate* STF is not trivial. Since real recordings usually show the well-know ω^{-2} spectral decay (originally observed and theorized by Aki, 1967; Brune, 1970, , assuming a constant stress-drop model), a suitable STF can be selected accordingly. Indeed, the ω^{-2} model has been extensively used in source models (Boore, 2003, 2009, among others). However, the ω^{-2} spectral decay is not unique (Bizzarri, 2014): there is no universal theoretical or empirical evidence that favours one STF over another. In this sense, some mono-parametric STFs are described in the following.
The simplest STF model is the step or *Heaviside* function, vanishing for negative times and equal to one for positive times, namely:

$$u_S^{HVS}(t) = \begin{cases} 0, & t < t_S \\ A, & t \geq t_S \end{cases} \tag{D.21}$$

A the amplitude of the final displacement and t_S the time shift the function is centred on. Due to its abrupt increase from 0 to the unit slip ($u_S^{HVS}(t)$ is not C^1 at $t = t_S$), the Heaviside STF can create spurious numerical oscillations. Therefore, another simple model used to describe the slip rise along

the fault plane is the so called *ramp-function* (Cara and Bour, 1995, among others):

$$u_S^{RMP}(t) = \begin{cases} 0, & t < t_S \\ A\frac{t-t_S}{\tau}, & t_S \leq t \leq t_S + \tau \\ A, & t \geq \tau \end{cases} \tag{D.22}$$

τ is called *rise-time* and it represents the time-lag required to the whole local slip to take its maximum value (assumed constant). Again, due to its uneasy mathematical manipulation, $u_S^{RMP}(t)$ is often replaced by a *smoothed ramp function* $u_S^{TNH}(t)$ (initially proposed by Bouchon, 1981), that writes:

$$u_S^{TNH}(t) = \frac{A}{2}\left[1 + \tanh\left(\frac{t-t_S}{\tau}\right)\right] \tag{D.23}$$

In the literature, the smoothed ramp function is sometimes expressed in terms of another free-parameter f_C, referred as the *characteristic frequency* and being equivalent to $f_C = \frac{1}{4\tau}$. One of the major advantages of using $u_S^{TNH}(t)$ is that its third derivative is of the form of the well-known Ricker of order 2 function. Its principal advantage is not to create high frequencies due to its smoothed cut-off frequency (Bard and Bouchon, 1980). Alternatively, Brune (1970) proposed the following STF:

$$u_S^{EXP}(t) = \begin{cases} 0, & t < t_S \\ A\left[1 - \left(1 + \frac{t-t_S}{\tau}\right)\exp\left(-\frac{(t-t_S)}{\tau}\right)\right], & t \geq t_S \end{cases} \tag{D.24}$$

The associated slip rate is expressed as:

$$\partial_t u_S^{EXP}(t) = \begin{cases} 0, & t < t_S \\ -A\frac{t-t_S}{\tau^2}\exp\left(-\frac{(t-t_S)}{\tau}\right), & t \geq t_S \end{cases} \tag{D.25}$$

The free parameter τ can be considered either as the slip duration (Brune, 1970; Bizzarri, 2014) either as $\frac{\tau_R}{4}$ (Dreger et al., 2007, where τ_R is inferred from statistical regression, as in). Equation (D.24) recalls the slip rate proposed by Brune (1970):

$$\dot{s}(t) = \begin{cases} 0, & t < t_S \\ \frac{c_S \Delta\tau_b}{\mu}\exp\left(-\frac{(t-t_S)}{t_C}\right), & t \geq t_S \end{cases} \tag{D.26}$$

where $\Delta\tau_b$ is the *breakdown stress-drop* Bizzarri (2014). In Brune's model, the slip duration t_C is controlled by the propagation speed and by the dimension of the rupture. Moreover, the analytical form of has been also used by to describe the moment release function (Imperatori and Mai, 2013). However, Brune's model has a smooth spectrum and a ω^{-2} high frequency decay rate, where ω is the angular frequency.
Figure D.5 compares the mentioned STF in terms of fault offset u_S (displacement), slip velocity $\partial_t u_S$ and acceleration $\partial_{tt} u_S$ Further comparisons between different STF can be found in Bizzarri (2014). The resulting moment tensor can be therefore modelled as:

$$\underline{\underline{\boldsymbol{M}}}(t) = \underline{\underline{\boldsymbol{M}}}_0 \bar{u}_S(t) \tag{D.27}$$

being $\bar{u}_S(t)$ the normalized slippage time-history $u_S(t)/A$.
As proved by many authors (e.g., Tinti, 2005; Bizzarri, 2014), the choice of such a temporal evolution is not straightforward. The STF parametrization represent a delicate tuning exercise in wave propagation problems, either considering an point-source approximation, either for extended rupture models based on the kinematic approach.

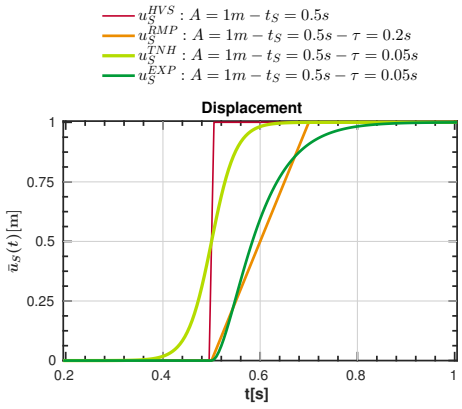

(a)

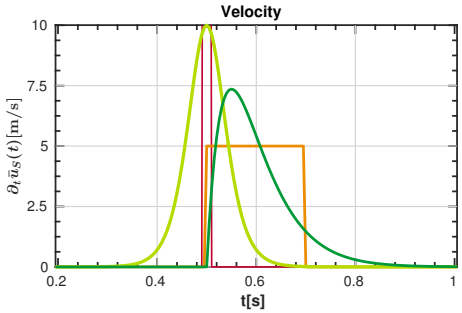

(b)

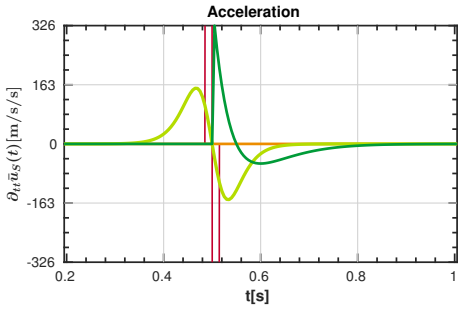

(c)

Figure D.5: Different source functions $\bar{u}_S(t)$ compared. (a) Displacement source functions; (b) Velocity source functions; (c) Acceleration source functions.

D.2.7 Full elasto-dynamic solution

Generally, at point $\underline{\boldsymbol{x}}$ and time t, the complete seismic motion $\underline{\boldsymbol{u}}(\underline{\boldsymbol{x}};t)$radiated by an arbitrary fault surface Σ with a dislocation vector field $\underline{\boldsymbol{\Delta u}}(\underline{\boldsymbol{x}};t)$over Σ can be written as the sum of three main contributions (near-, intermediate- and far-field) (Madariaga, 1989).

$$\underline{\boldsymbol{u}}(\underline{\boldsymbol{x}};t) = \underline{\boldsymbol{u}}^{NF}(\underline{\boldsymbol{x}};t) + \underline{\boldsymbol{u}}^{IF}(\underline{\boldsymbol{x}};t) + \underline{\boldsymbol{u}}^{FF}(\underline{\boldsymbol{x}};t) \tag{D.28}$$

The NED coordinate system is used below to derive relations between the angles of a ruptured fault (strike and dip angle) and the dislocation direction on the rupture plane (rake angle). In Figure D.6a and Figure D.6b $\underline{\boldsymbol{u}}$ is represented as a function of $\underline{\boldsymbol{n}}_\Sigma$, $\underline{\boldsymbol{e}}_r$, of the strike angle ϕ_S, the dip angle δ, the rake angle λ, the take-off angle i_ξ and the azimuth angle ϕ. By substituting Equation D.17 in Equation D.12, the displacement field is obtained and it writes (Aki and Richards, 1980):

$$\underline{\boldsymbol{u}}(\underline{\boldsymbol{x}};t) = \underline{\boldsymbol{u}}^{NF}(\underline{\boldsymbol{x}};t) + \underline{\boldsymbol{u}}^{IF-P}(\underline{\boldsymbol{x}};t) + \underline{\boldsymbol{u}}^{IF-S}(\underline{\boldsymbol{x}};t) + \underline{\boldsymbol{u}}^{FF-P}(\underline{\boldsymbol{x}};t) + \underline{\boldsymbol{u}}^{FF-S}(\underline{\boldsymbol{x}};t) \tag{D.29}$$

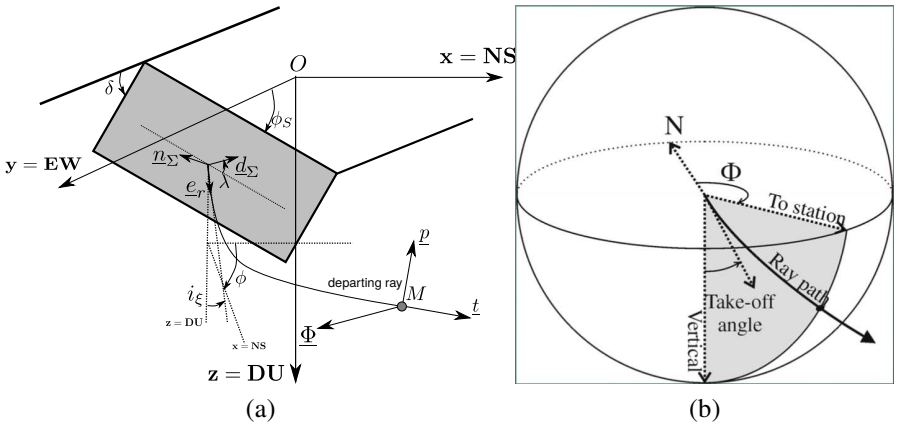

Figure D.6: Definition of the Cartesian coordinate system (x, y, z).

with:

- *Near-Field* displacement field:

$$\underline{\boldsymbol{u}}^{NF}\left(\underline{\boldsymbol{x}};t\right)=\frac{30\mu|\Sigma|A\left(\underline{\boldsymbol{e}}_r.\underline{\boldsymbol{n}}_\Sigma\right)\left(\underline{\boldsymbol{e}}_r.\int_{r/c_P}^{r/c_S}\tau\bar{u}_S\left(t-\tau\right)\underline{\boldsymbol{d}}_\Sigma d\tau\right)\underline{\boldsymbol{e}}_r}{4\pi\rho r^4}- \\ -\frac{6\mu|\Sigma|A\left(\underline{\boldsymbol{e}}_r.\int_{r/c_P}^{r/c_S}\tau\bar{u}_S\left(t-\tau\right)\underline{\boldsymbol{d}}_\Sigma d\tau\right)\underline{\boldsymbol{n}}_\Sigma}{4\pi\rho r^4}- \\ -\frac{6\mu|\Sigma|A\left(\underline{\boldsymbol{e}}_r.\underline{\boldsymbol{n}}_\Sigma\right)\int_{r/c_P}^{r/c_S}\tau\bar{u}_S\left(t-\tau\right)\underline{\boldsymbol{d}}_\Sigma d\tau}{4\pi\rho r^4} \tag{D.30}$$

  $\underline{\boldsymbol{u}}^{NF}(\underline{\boldsymbol{x}};t)$is composed of both P- and S-waves. It is therefore neither irrotational (i.e., having zero curl), nor solenoidal (i.e., having zero divergence), and this indicates that it is not always fruitful to decompose an elastic displacement field into its P- and S-wave components. The near-field attenuates as $\frac{1}{r^4}$.

- *Intermediate-Field* displacement field (P-waves):

$$\underline{\boldsymbol{u}}^{IF-P}\left(\underline{\boldsymbol{x}};t\right)=\frac{12\mu|\Sigma|A\left(\underline{\boldsymbol{e}}_r.\underline{\boldsymbol{n}}_\Sigma\right)\left(\underline{\boldsymbol{e}}_r.\bar{u}_S\left(t-\frac{r}{c_P}\right)\underline{\boldsymbol{d}}_\Sigma\right)\underline{\boldsymbol{e}}_r}{4\pi\rho c_P^2 r^2}- \\ -\frac{2\mu|\Sigma|A\left(\underline{\boldsymbol{e}}_r.\bar{u}_S\left(t-\frac{r}{c_P}\right)\underline{\boldsymbol{d}}_\Sigma\right)\underline{\boldsymbol{n}}_\Sigma}{4\pi\rho c_P^2 r^2}- \\ -\frac{2\mu|\Sigma|A\left(\underline{\boldsymbol{e}}_r.\underline{\boldsymbol{n}}_\Sigma\right)\bar{u}_S\left(t-\frac{r}{c_P}\right)\underline{\boldsymbol{d}}_\Sigma}{4\pi\rho c_P^2 r^2} \tag{D.31}$$

  The P-wave intermediate-field attenuates as $\frac{1}{r^2}$.

- *Intermediate-Field* displacement field (S-waves):

$$\underline{\boldsymbol{u}}^{IF-S}(\underline{\boldsymbol{x}};t) = -\frac{12\mu|\Sigma|A\left(\underline{\boldsymbol{e}}_r.\underline{\boldsymbol{n}}_\Sigma\right)\left(\underline{\boldsymbol{e}}_r.\bar{u}_S\left(t-\frac{r}{c_S}\right)\underline{\boldsymbol{d}}_\Sigma\right)\underline{\boldsymbol{e}}_r}{4\pi\rho c_S^2 r^2} + \\ + \frac{3\mu|\Sigma|A\left(\underline{\boldsymbol{e}}_r.\bar{u}_S\left(t-\frac{r}{c_S}\right)\underline{\boldsymbol{d}}_\Sigma\right)\underline{\boldsymbol{n}}_\Sigma}{4\pi\rho c_S^2 r^2} + \\ + \frac{3\mu|\Sigma|A\left(\underline{\boldsymbol{e}}_r.\underline{\boldsymbol{n}}_\Sigma\right)\bar{u}_S\left(t-\frac{r}{c_S}\right)\underline{\boldsymbol{d}}_\Sigma}{4\pi\rho c_S^2 r^2} \tag{D.32}$$

The S-wave intermediate-field attenuates as $\frac{1}{r^2}$.

- *Far-Field* displacement field (P-waves):

$$\underline{\boldsymbol{u}}^{FF-P}(\underline{\boldsymbol{x}};t) = \frac{2\mu|\Sigma|A\underline{\boldsymbol{e}}_r\left(\underline{\boldsymbol{e}}_r.\underline{\boldsymbol{d}}_\Sigma\right)\left(\underline{\boldsymbol{e}}_r.\underline{\boldsymbol{n}}_\Sigma\right)}{4\pi\rho c_P^3 r}\partial_t\bar{u}_S\left(t-\frac{r}{c_P}\right) \tag{D.33}$$

The P-wave far-field attenuates as $\frac{1}{r}$.

- *Far-Field* displacement field (S-waves):

$$\underline{\boldsymbol{u}}^{FF-S}(\underline{\boldsymbol{x}};t) = -\frac{2\mu|\Sigma|A\left(\underline{\boldsymbol{e}}_r.\underline{\boldsymbol{d}}_\Sigma\right)\left(\underline{\boldsymbol{e}}_r.\underline{\boldsymbol{n}}_\Sigma\right)}{4\pi\rho c_S^3 r}\partial_t\bar{u}_S\left(t-\frac{r}{c_S}\right)\underline{\boldsymbol{e}}_r + \\ + \frac{\mu|\Sigma|A\left(\underline{\boldsymbol{e}}_r.\underline{\boldsymbol{d}}_\Sigma\right)}{4\pi\rho c_S^3 r}\partial_t\bar{u}_S\left(t-\frac{r}{c_S}\right)\underline{\boldsymbol{n}}_\Sigma + \\ + \frac{\mu|\Sigma|A\left(\underline{\boldsymbol{e}}_r.\underline{\boldsymbol{n}}_\Sigma\right)}{4\pi\rho c_S^3 r}\partial_t\bar{u}_S\left(t-\frac{r}{c_S}\right)\underline{\boldsymbol{d}}_\Sigma + \tag{D.34}$$

The S-wave far-field attenuates as $\frac{1}{r}$.

Figure D.7 shows the *geometric attenuation* of the different components of the radiated wave-fields, at two stations place right above embedded in an horizontal fault plane and slipping in along it. All

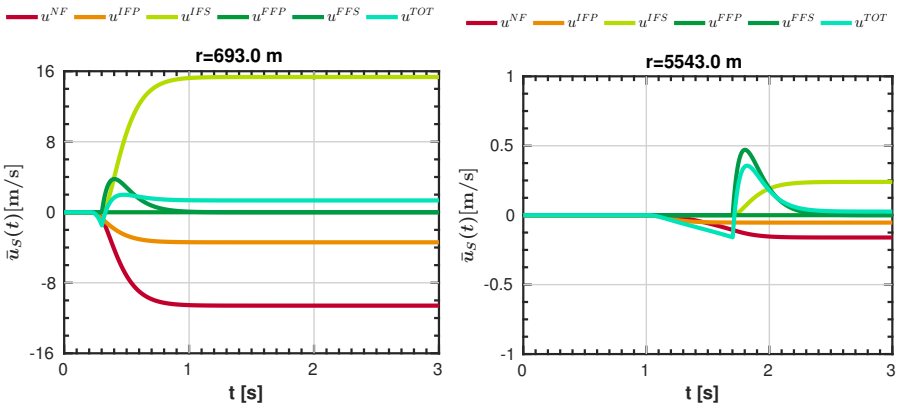

(a) (b)

Figure D.7: Near-,Intermediate- and Far-Field contribution to the total displacement radiated by an horizontal fault ($\phi_S = 0°$, $\lambda = 0°$, $\delta = 0°$) at an azimuth $\phi = 0°$ and take-off angle $i_\xi = 180°$. (a) Displacement fields at a distance $r = 800$ m from the point source; (b) displacement fields at a distance $r = 1000$ m from the point source.

the terms in Equation D.29 vanishes as power of $\frac{1}{r}$. Much of the practical work of seismology is done in the far field, at distances of several wavelengths from the source. When the distance r is large only the last two terms of Equation D.29 are important, i.e. in that region it is not necessary to use the complete elastic field. Thus, at large distances, the following *far-field* approximation holds:

$$\begin{aligned}\underline{\boldsymbol{u}}\left(\underline{\boldsymbol{x}};t\right) \approx & M_O\left(\frac{2\underline{\boldsymbol{e}}_r\left(\underline{\boldsymbol{e}}_r.\underline{\boldsymbol{d}}_\Sigma\right)\left(\underline{\boldsymbol{e}}_r.\underline{\boldsymbol{n}}_\Sigma\right)}{4\pi\rho c_P^3 r}H^{'}\left(t-\frac{r}{c_P}\right)+\right.\\ & \left.\frac{\underline{\boldsymbol{n}}_\Sigma\left(\underline{\boldsymbol{e}}_r.\underline{\boldsymbol{d}}_\Sigma\right)+\underline{\boldsymbol{d}}_\Sigma\left(\underline{\boldsymbol{e}}_r.\underline{\boldsymbol{n}}_\Sigma\right)-2\underline{\boldsymbol{e}}_r\left(\underline{\boldsymbol{e}}_r.\underline{\boldsymbol{d}}_\Sigma\right)\left(\underline{\boldsymbol{e}}_r.\underline{\boldsymbol{n}}_\Sigma\right)}{4\pi\rho c_S^3 r}H^{'}\left(t-\frac{r}{c_S}\right)\right)\end{aligned} \tag{D.35}$$

If it is considered that there is roughly a factor of 2 between c_P and c_S, one can assume that the second term in Equation D.35 is predominant, leading to the final approximate:

$$\underline{\boldsymbol{u}}\left(\underline{\boldsymbol{x}};t\right)=\underline{\boldsymbol{u}}_O\left(\underline{\boldsymbol{x}}\right)H^{'}\left(t-\frac{r}{c_S}\right) \tag{D.36}$$

$$\underline{\boldsymbol{u}}_O\left(\underline{\boldsymbol{x}}\right)=M_O\frac{\underline{\boldsymbol{n}}_\Sigma\left(\underline{\boldsymbol{e}}_r.\underline{\boldsymbol{d}}_\Sigma\right)+\underline{\boldsymbol{d}}_\Sigma\left(\underline{\boldsymbol{e}}_r.\underline{\boldsymbol{n}}_\Sigma\right)-2\underline{\boldsymbol{e}}_r\left(\underline{\boldsymbol{e}}_r.\underline{\boldsymbol{d}}_\Sigma\right)\left(\underline{\boldsymbol{e}}_r.\underline{\boldsymbol{n}}_\Sigma\right)}{4\pi\rho c_S^3 r} \tag{D.37}$$

As far as earthquake resistance of structure is concerned, the main quantity of interest is the acceleration. Equation D.37 shows that this acceleration is rather difficult to predict since it is given by the third derivative of the time evolution of the seismic moment, i.e. the third derivative of the slippage time-history. The approximate $H^{'}\approx\delta$ is too crude for this purpose.

The concept of *near-field*

There has been always been some confusion in the seismological literature with respect to the exact meaning of the term *far-field*, since a point force has zero length-scale, by definition. This problem has important practical consequences for the numerical solution of the wave equation, for the computation of *near-source* accelerograms, etc (Madariaga, 1989). In order to clarify this, one should examine the frequency domain expression for the Green function D.3, expressed in Equation

D.2.8 Finite size effect and corner frequency

Even if the detailed time-history of the seismic motion seems difficult to be predicted, some global tendency of the frequency content of the seismic motion can be sought by taking into account the fault size. Indeed, considering a planar rectangular fault Σ of size $H\times L$ in the $(\underline{\boldsymbol{e}}_1,\underline{\boldsymbol{e}}_2)$ plane and centered on the reference frame and accounting just for shear waves, one has:

$$\underline{\boldsymbol{u}}\left(\underline{\boldsymbol{x}};t\right)\approx\frac{1}{|\Sigma|}\int_\Sigma\underline{\boldsymbol{u}}_0\left(\underline{\boldsymbol{x}}-\underline{\boldsymbol{y}}\right)H^{'}\left(t-\frac{r}{c_S}\right)dS\left(\underline{\boldsymbol{y}}\right) \tag{D.38}$$

Since a far field approximate is sought, the first term in Equation D.38 is approximated by taking its value for $\underline{\boldsymbol{y}}=\underline{\boldsymbol{0}}$. Moreover, within the limits of this assumption, one can take $r\approx r_O-\underline{\boldsymbol{e}}_O.\underline{\boldsymbol{y}}$, being $r_O=\|\underline{\boldsymbol{x}}\|$ and $\underline{\boldsymbol{e}}_O=\frac{\underline{\boldsymbol{x}}}{r_O}$. Taking the Fourier transform of the last term of Equation D.38 leads to:

$$\hat{\underline{\boldsymbol{u}}}\left(\underline{\boldsymbol{x}};\omega\right)=\hat{\underline{\boldsymbol{u}}}_O\left(\omega\right)\frac{1}{|\Sigma|}\int_\Sigma\exp\left(i\omega\frac{\underline{\boldsymbol{e}}_O.\underline{\boldsymbol{y}}}{c_S}\right)dS\left(\underline{\boldsymbol{y}}\right) \tag{D.39}$$

with $\hat{\underline{\boldsymbol{u}}}_O(\omega)$ frequency response for a localized seismic moment. Finally, one gets:

$$\hat{\underline{\boldsymbol{u}}}\left(\omega\right)=\hat{\underline{\boldsymbol{u}}}_O\left(\omega\right)sinc\left(\omega T_1\right)sinc\left(\omega T_2\right) \tag{D.40}$$

where $T_\alpha = L_\alpha \frac{\underline{\boldsymbol{e}}_O \cdot \underline{\boldsymbol{e}}_\alpha}{2c_S}$ and $sinc\,(x) = \frac{\sin x}{x}$.
As a consequence, the finite size of the source has a low-pass filtering effect. The proposed model accounts only for a ω^{-1} decay at high-frequencies whereas experimental results usually show a ω^{-2} decay. The latter can be modelled using a more complex slip time-history. As a conclusion one can take the following expression for the Fourier amplitude of the far-field response:

$$|\underline{\hat{\boldsymbol{u}}}\,(\omega)\,| = \frac{|\underline{\hat{\boldsymbol{u}}}_O\,(\omega)\,|}{1 + (\omega \setminus \omega_C)^2} \tag{D.41}$$

with ω_C the corner circular frequency defined as :

$$\omega_C \approx \frac{2c_S}{3\sqrt{|\Sigma|}} \tag{D.42}$$

Using simple source models we have been able to explain and to quantify basic relationships between wave amplitudes, fault length, slippage, seismic moment, energy, frequency spectrum. However these expressions are not always consistent with the original Richter scale. Moreover the proposed models do not seem able to predict the maximum acceleration. At last, the propagation medium has been considered as homogeneous whereas the seismic wave experience large velocity contrasts when reaching the free surface. As a consequence more detailed studies have to be conducted in order to quantify the local seismic filed in the vicinity of structure to be designed (Clouteau, 2008).

D.2.9 From point to extended seismic source

The earthquake source signal is the *source time function* produced by the faulting. In the simplest case of a short fault that slips instantaneously, the seismic moment function is a step function whose derivative (i.e. a delta-function) is the source time function. However, real faults give rise to more complicated source time functions. For instance, consider a simple case in which the rupture at each point on a rectangular fault radiates an impulse (Figure D.8) The total radiated signal is not impulsive because of the progressive rupture along the fault plane. Waves arrive first from initial point of rupture and later from points further along the fault. Assume a rupture propagating along the fault plane at a *rupture velocity* V_R along the fault of length L and a receiver at distance r_0 and azimuth θ from the *nucleation point* N. The first seismic arrival is at time $T_0 = \frac{r_0}{c}$, where c represents the wave P-S wave velocity respectively. The far end point of the fault E ruptures at time $\frac{L}{V_R}$ later than the nucleation point, giving a seismic arrival time $T_E = \frac{L}{V_R} + \frac{r}{c}$, where r is the distance from between E and the receiver S. Simple trigonometry states that:

$$r^2 = r_0^2 + L^2 - 2r_0 \cos\theta \tag{D.43}$$

which can be simplified in far-field as:

$$r \approx r_0 - L\cos\theta \tag{D.44}$$

Thus, the time pulse generated by a finite fault is a *boxcar* of duration:

$$T_R = \frac{L}{c}\left(\frac{c}{V_R} - \cos\theta\right) \tag{D.45}$$

T_R is commonly known as *rupture time*. If one typically assumes $V_R \approx 0.7 - 0.8c$, the ratio $\frac{c}{V_R}$ equals 1.2 for S-waves and 2.2 for P-waves. The maximum duration occurs at $\theta = 180°$ (Stein and Wysession, 2003). A second effect lightening the time function is that, even at a single location on

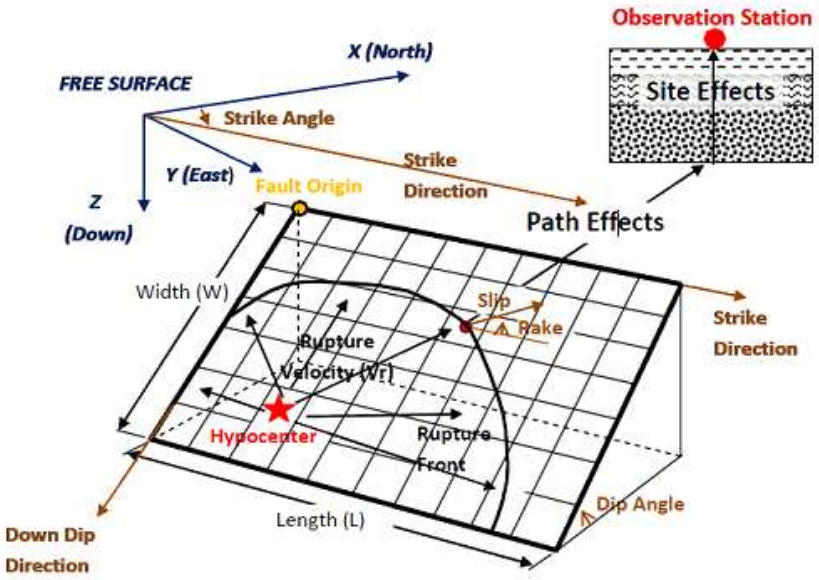

Figure D.8: Schematic fault plane and parameters required to perform numerical simulations (inner, outer and extra parameters). Reprinted from Yin-Tung (2012).

the fault, slip does not occur instantaneously,yet a slip history should be modelled instead. The latter is often assumed as a ramp function beginning at time zero and ending at the so called *rise time* τ. The source time function depends on the derivative of the slip history. For a ramp, this derivative is a *boxcar*. Convolving the finiteness of and rise time effects yields a trapezoid whose length is the sum of the rise and rupture.

$$r\left(t\right)\begin{cases}1, T_N \leq t \leq T_E & \text{(D.46)}\\ 0, t < T_N, t > T_E & \text{(D.47)}\end{cases}$$

$$s\left(t\right)\begin{cases}\bar{s}, 0 \leq t \leq \tau & \text{(D.48)}\\ 0, t < 0, t > \tau & \text{(D.49)}\end{cases}$$

$$\begin{aligned} u_S\left(t\right) = \int_{-\infty}^{+\infty} r\left(t-\tau\right) s\left(\tau\right) d\tau = \int_{-\infty}^{+\infty} r\left(\tau\right) s\left(t-\tau\right) d\tau = \\ \int_{T_N}^{T_E} s\left(t-\tau\right) d\tau = \int_{t-T_E}^{t-T_N} s\left(\tau\right) d\tau = \\ \int_{t-T_E}^{0} s\left(\tau\right) d\tau + \int_{0}^{\tau} s\left(\tau\right) d\tau + \int_{\tau}^{t-T_N} s\left(\tau\right) d\tau = \\ \bar{s} + \int_{t-T_E}^{0} s\left(\tau\right) d\tau + \int_{\tau}^{t-T_N} s\left(\tau\right) d\tau = \end{aligned} \quad \text{(D.50)}$$

$$u_S(t) = 0, t < T_N \tag{D.51}$$

$$u_S(t) = \bar{s}\left(\frac{t - T_N}{\tau}\right), T_N \leq t \leq T_N + \tau \tag{D.52}$$

$$u_S(t) = \bar{s}, T_N + \tau < t < T_E \tag{D.53}$$

$$u_S(t) = \bar{s}\left(1 - \frac{t - T_E}{\tau}\right), T_E \leq t < T_E + \tau \tag{D.54}$$

$$u_S(t) = 0, t > T_E + \tau \tag{D.55}$$

Other source function shapes of comparable length are possible, like triangles or Gaussian functions. Seismograms are often insensitive to the details of the source time function itself (Stein and Wysession, 2003).

D.3 The Wave-Number Integration Method

The WNI is based upon an extension of the wave-propagation into elastic full space to a layered half-space. The equations of elastodynamics for the layered half-space in Figure 3.21, read (for all $j = 1, ..., N + 1$ layers):

$$\begin{cases} \left(\lambda^j + 2\mu^j\right) \underline{\boldsymbol{\nabla}}_x \left(\underline{\boldsymbol{\nabla}}_x . \underline{\boldsymbol{u}}^j\right) - \mu^j \underline{\boldsymbol{\nabla}}_x \wedge \left(\underline{\boldsymbol{\nabla}}_x \wedge \underline{\boldsymbol{u}}^j\right) + \underline{\boldsymbol{f}}^j_{ext} = \rho^j \partial_{tt} \underline{\boldsymbol{u}}^j & \text{(D.56)} \\ \underline{\underline{\boldsymbol{\sigma}}}^1 . \underline{\boldsymbol{i}}_z = \underline{\mathbf{0}}, \quad (x, y, z, t) \in (\mathbb{R}, \mathbb{R}, z = 0) \times [0, t] & \text{(D.57)} \end{cases}$$

At each layer-to-layer interface, the following extra-conditions add to the problem (displacement and traction continuity):

$$\begin{cases} \underline{\boldsymbol{u}}^{j+1}\left(x, y, z^{j+1} = 0, t\right) = \underline{\boldsymbol{u}}^j\left(x, y, z^j = h^j, t\right) & \text{(D.58)} \\ \underline{\underline{\boldsymbol{\sigma}}}^{j+1} . \underline{\boldsymbol{i}}_z \left(x, y, z^{j+1} = 0, t\right) = \underline{\underline{\boldsymbol{\sigma}}}^j . \underline{\boldsymbol{i}}_z \left(x, y, z^j = h^j, t\right) & \text{(D.59)} \end{cases}$$

Again, the Sommerfeld's radiation condition holds at the deepest layer:

$$\begin{cases} \lim_{R \to \infty} \int_{\|\underline{\boldsymbol{x}}\| = R} \left(\sigma^{N+1}_{nn} - i\omega\rho^{N+1} V_P^{N+1} \underline{\boldsymbol{u}}^{N+1} . \underline{\boldsymbol{n}}\right)^2 dS = 0 & \text{(D.60)} \\ \lim_{R \to \infty} \int_{\|\underline{\boldsymbol{x}}\| = R} \|\underline{\boldsymbol{t}}^{t(N+1)}_n - i\omega\rho^{N+1} V_S^{N+1} \underline{\boldsymbol{u}}^{t(N+1)}\|^2 dS = 0 & \text{(D.61)} \end{cases}$$

The *Huygen's principle* states that a 3D displacement wave-field can be expressed as superposition of spherical waves of radius R in the general form of $u^S(R; \omega) = \frac{1}{R} e^{i\frac{\omega}{c}R}$ Hisada (1994) (ω is the circular frequency and c the propagation speed). In the WNI, those spherical waves are decomposed into cylindrical waves by means of the so called *Sommerfeld's integral* in the wave-number domain (referred as to k) Aki and Richards (1980):

$$\frac{1}{R} e^{i\frac{\omega}{c}R} = \int_0^{+\infty} \left[\frac{k}{\nu} e^{-\nu|z-h|} J_0(kr)\right] dk \tag{D.62}$$

where $J_0(kr)$ represents the 0^{th}-order Bessel's function and $\nu^2 = k^2 - \left(\frac{\omega}{c}\right)^2, \quad Re(\nu) \geq 0$. z and h represent the receiver's and source's depths respectively and $R = \sqrt{r^2 + (z-h)^2}$ (see Figure 3.21). In order to obtain the radiated stress field, one needs to perform the derivative of u^S with the respect to

r and z. Following the same approach, the derivative $\frac{\partial u^S}{\partial r}(r,\omega)$ can be expressed in the Sommerfeld integral form, namely:

$$\left(\frac{1}{R}-i\frac{\omega}{c}\right)\frac{r}{R^2}e^{i\frac{\omega}{c}r}=\int_0^{+\infty}\left[\frac{k^2}{\nu}e^{-\nu|z-h|}J_1(kr)\right]dk \tag{D.63}$$

where $J_1(kr)$ represents the 1^{th}-order Bessel's function. The semi-infinite integrals in Equations D.62 and D.63 oscillates (i.e. decreasing/increasing amplitudes with k) when $z\approx h$, since the decaying exponential term $e^{-\nu|z-h|}$ disappears. Nevertheless, Luco and Apsel (1983a,b) proved that the dynamic Green's functions converge to static for large k:

$$\begin{cases} \lim\limits_{k\to\infty}\left(\frac{1}{R}e^{i\frac{\omega}{c}R}\right)=\frac{1}{R}=\int_0^{+\infty}\left[e^{-k|z-h|}J_0(kr)\right]dk & \text{(D.64)}\\ \lim\limits_{k\to\infty}\left[\left(\frac{1}{R}-i\frac{\omega}{c}\right)\frac{r}{R^2}e^{i\frac{\omega}{c}R}\right]=\frac{r}{R^3}=\int_0^{+\infty}\left[ke^{-k|z-h|}J_1(kr)\right]dk & \text{(D.65)}\end{cases}$$

Subtracting Equations D.65 from Equations D.62 andD.63 respectively, one gets a residuum that converges fast to zero with the wave-number, even for $z\approx h$:

$$\begin{cases} \frac{1}{R}e^{i\frac{\omega}{c}R}=\int_0^{+\infty}\left[\left(\frac{k}{\nu}e^{-\nu|z-h|}-e^{-k|z-h|}\right)J_0(kr)\right]dk+\frac{1}{R} & \text{(D.66)}\\ \left(\frac{1}{R}-i\frac{\omega}{c}\right)\frac{r}{R^2}e^{i\frac{\omega}{c}R}=\int_0^{+\infty}\left[\left(\frac{k}{\nu}e^{-\nu|z-h|}-e^{-k|z-h|}\right)kJ_1(kr)\right]dk+\frac{r}{R^3} & \text{(D.67)}\end{cases}$$

Due to the rapid convergence to zero with the horizontal wave-number of the integral in Equations D.67, their numerical integration ranges can be reduced compared to Equations D.62 andD.63, particularly when the source depth is the same or close to the receiver depth. Based on this analytical result, Hisada (1994, 1995, 2008) developed an efficient numerical method to compute the Green's functions due to point and dipole sources, via the generalized reflection/transmission (R/T) coefficients. The WNI semi-analytical solution was implemented in a FORTRAN 77 code. The FORTRAN codes for this method for both point and dipole sources are open to academic use through anonymous FTP (hisada@cc.kogakuin.ac.jp).

Nomenclature

α and β Coefficient of Nakagawa and Soga (1995) model

$\alpha^{PGA}_{(\xi=5\%)}$ Median spectral acceleration amplification factor

$\alpha^{PGV}_{(\xi=5\%)}$ Median spectral velocity amplification factor

$\bar{\theta}(\mathbf{x})$ Mean of random field

$\mathbb{D}^{el}$ Elasticity 4^{th}-order tensor

δ Dirac's function

$\mathbb{D}^{ep}$ Elastic-Plastic 4^{th}-order tensor

$\underline{\underline{\dot{\boldsymbol{\varepsilon}}}}^{el}_{x}$ Elastic strain increment

$\underline{\underline{\dot{\boldsymbol{\varepsilon}}}}^{pl}_{x}$ Plastic strain increment

$\underline{\underline{\boldsymbol{S}}}^{\sigma}$ Deviatoric stress tensor

$\dot{p}$ Plastic multiplier

$\ell_{c\theta}$ Heterogeneity correlation length

$\lambda(\underline{\boldsymbol{x}})$, $\mu(\underline{\boldsymbol{x}})$ Lame's coefficients

$\rho(\underline{\boldsymbol{x}})$ Volumetric mass density

γ Shear strain

$\gamma_{r,1}$, n, β_1 and β_2 regression coefficients from Yee et al. (2011)

γ_r pseudo-reference Shear Strain

$\underline{\cdot} \otimes_s \underline{\boldsymbol{\nabla}}_x$ Symmetric gradient operator

$\underset{\sim}{\boldsymbol{\chi}}(\underline{\boldsymbol{x}}; t)$ Hidden internal variable set

$\mathbf{k}$ Wave-number vector

λ_{min} Minimum wave-length

$\mathbb{E}_{\sigma\chi}$ Instantaneous elastic range

$\mathbb{F}^{ext}$ Global external force vector

$\mathbb{F}^{int}\left(\underline{\hat{\boldsymbol{U}}}_G^h; \underline{\hat{\boldsymbol{V}}}_G^h\right)$ Global internal force vector

$\mathbb{F}^{trac}\left(\underline{\boldsymbol{\mathcal{T}}}_G^h\right)$ Global traction force vector

$\mathbb{H}$ Plastic hardening

$\mathbb{I}$ 4^{th} order identity tensor

$\mathbb{M}$ Global mass matrix

$\mathcal{R}_\theta(\mathbf{x})$ Auto-covariance model for random field

μ_{sec} Secant shear modulus

$\partial\mathbb{E}_{\sigma\chi}$ Yield Locus

$\rho_{XY}(\theta_{XY})$ Cross-correlation coefficient

σ'_{V0} Effective overburden vertical stress

σ_{yld} First yield limit

$\underline{\underline{\boldsymbol{\sigma}}}(\underline{\boldsymbol{x}}; t)$ Cauchy's small strain stress tensor

$\underline{\underline{\dot{\boldsymbol{e}}}}^{pl}$ Deviatoric plastic strain tensor

$\underline{\underline{\boldsymbol{\varepsilon}}}_x(\cdot)$ Small strain tensor

$\underline{\underline{\boldsymbol{I}}}$ 2^{nd} order identity tensor

$\underline{\underline{\boldsymbol{X}}}$ Back-stress tensor

θ_C Horizontal azimuthal deviation for 0 cross-correlation

θ_C Horizontal azimuthal deviation for 0 cross-correlation

θ_{XY} Horizontal azimuthal deviation

θ_{XY} Horizontal azimuthal deviation

$\theta(\mathbf{x})$ Stationary random field

θ_{BB} Horizontal azimuthal deviation at borehole

θ_{NP} Horizontal azimuthal deviation corresponding to fault parallel/normal direction

$\underline{\hat{\boldsymbol{A}}}_G^{h,n}$ Global acceleration vector

$\underline{\hat{\boldsymbol{U}}}_G^h$ Global displacement vector

$\underline{\hat{\boldsymbol{V}}}_G^h$ Global velocity vector

$\underline{\boldsymbol{\mathcal{T}}}_G^h$ Global traction vector

$\underline{\boldsymbol{b}}(\underline{\boldsymbol{x}}; t)$ Body forces

$\underline{\boldsymbol{t}}_{n,0}$ Traction vector

$\underline{\boldsymbol{u}}\left(\underline{\boldsymbol{x}};t\right)$ Displacement field

$\underline{\boldsymbol{v}}\left(\underline{\boldsymbol{x}};t\right)$ Velocity field

ξ Critical damping ratio

C Courant-Friedrichs-Lewy number

c_P, c_S P-wave and S-wave velocities

C_{kin} and κ_{kin} AF kinematic hardening parameters

D Critical damping coefficient

D_{LS} Large Strain critical Damping coefficient

D_{SS} Small Strain critical damping coefficient

D_{SS} Small Strain critical damping coefficient

f frequency

$f\left(\underline{\underline{\boldsymbol{\sigma}}};\underset{\sim}{\boldsymbol{\chi}}\right)$ Yield function

G Shear modulus

g Plastic potential function

$G\left(\underline{\boldsymbol{x}}\right)$ Gaussian random field

G_{max} Maximum/Initial shear modulus

$J2$ Second invariant of deviatoric tensor

L Domain characteristic dimension

No Number of integration points per minimum wave-length

p'_0 Mean effective confining Pressure

p_{atm} Atmospheric Pressure

Q Quality factor

Sa Pseudo Spectral Acceleration

$Sa_{GM}\left(\theta\right)$ Geometric Mean Pseudo Spectral Acceleration

$T_{V\backslash A}$ Predominant harmonic period

V_S Shear Wave Velocity

EMP-GM Geometric Mean Empirical borehole spectral ratio

$\mathrm{M_{JMA}}$ Earthquake magnitude according to the Japanese Meteorological Agency

$\mathrm{M_w}$ Earthquake moment magnitude

PGA Peak Ground Acceleration

PGA_H Peak Ground Acceleration of Horizontal components

PGA_H Peak Ground Acceleration of Horizontal components

PGA_V Peak Ground Acceleration of the Vertical component

PGA_R Peak Ground Acceleration at borehole bedrock

PGV_H Peak Ground Velocity of Horizontal components

PGV_H Peak Ground Velocity of Horizontal components

PGV_V Peak Ground Velocity of the Vertical component

R source-to-site distance

R_{JB} Joyner-Boore distance

R_{rup} Closes source-to-site distance from the fault plane

Bibliography

Aagaard, B. T., Brocher, T. M., Dolenc, D., Dreger, D., Graves, R. W., Harmsen, S., Hartzell, S., Larsen, S., McCandless, K., Nilsson, S., Petersson, N. A., Rodgers, A., Sjögreen, B., and Zoback, M. L. (2008a). Ground-Motion Modeling of the 1906 San Francisco Earthquake, Part II: Ground-Motion Estimates for the 1906 Earthquake and Scenario Events. *Bulletin of the Seismological Society of America*, 98(2):1012–1046.

Aagaard, B. T., Brocher, T. M., Dolenc, D., Dreger, D., Graves, R. W., Harmsen, S., Hartzell, S., Larsen, S., and Zoback, M. L. (2008b). Ground-Motion Modeling of the 1906 San Francisco Earthquake, Part I: Validation Using the 1989 Loma Prieta Earthquake. *Bulletin of the Seismological Society of America*, 98(2):989–1011.

Aagaard, B. T., Graves, R. W., Rodgers, A., Brocher, T. M., Simpson, R. W., Dreger, D., Petersson, N. A., Larsen, S. C., Ma, S., and Jachens, R. C. (2010a). Ground-Motion Modeling of Hayward Fault Scenario Earthquakes, Part II: Simulation of Long-Period and Broadband Ground Motions. *Bulletin of the Seismological Society of America*, 100(6):2945–2977.

Aagaard, B. T., Graves, R. W., Schwartz, D. P., Ponce, D. A., and Graymer, R. W. (2010b). Ground-Motion Modeling of Hayward Fault Scenario Earthquakes, Part I: Construction of the Suite of Scenarios. *Bulletin of the Seismological Society of America*, 100(6):2927–2944.

Abrahamson, N. A., Schneider, J. F., and Stepp, J. C. (1991). Empirical Spatial Coherency Functions for Application to Soil-Structure Interaction Analyses. *Earthquake Spectra*, 7(1):1–27.

Abrahamson, N. A. and Silva, W. J. (2007). Abrahamson & Silva NGA Ground Motion Relations for the Geometric Mean Horizontal Component of Peak and Spectral Ground Motion Parameters. Peer report 200x/xx pacific earthquake engineering research center, Pacific Earthquake Engineering Research Center College of Engineering University of California, Berkeley.

Abrahamson, N. A., Silva, W. J., and Kamai, R. (2013). *Update of the AS08 ground-motion prediction equations based on the NGA-West2 data set*. Pacific Earthquake Engineering Research Center.

Aki, K. (1967). Scaling law of seismic spectrum. *Journal of Geophysical Research*, 72(4):1217–1231.

Aki, K. (1968). Seismic displacements near a fault. *Journal of Geophysical Research*, 73(16):5359–5376.

Aki, K. and Richards, P. (1980). *Quantitative Seismology-Theory and Methods*, volume I-II of *Books in Geology*. W.H Freeman and Company, San Francisco (USA).

Alterman, Z. and Karal, F. C. (1968). Propagation of elastic waves in layered media by finite difference methods. *Bulletin of the Seismological Society of America*, 58(1):367–398.

Anderson, J. G. (2004). Quantitative measure of the goodness-of-fit of synthetic seismograms. *13th World Conference on Earthquake Engineering*, (243):775–784.

Antonietti, P. F., Mazzieri, I., Quarteroni, a., and Rapetti, F. (2012). Non-conforming high order approximations of the elastodynamics equation. *Computer Methods in Applied Mechanics and Engineering*, 209-212:212–238.

Aochi, H., Ducellier, A., Dupros, F., Delatre, M., Ulrich, T., de Martin, F., and Yoshimi, M. (2013a). Finite difference simulations of seismic wave propagation for the 2007 Mw 6.6 Niigata-ken Chuetsu-Oki earthquake: Validity of models and reliable input ground motion in the near field. *Pure and Applied Geophysics*, 170((1-2)):43–64. Springer Verlag (Germany).

Aochi, H., Ulrich, T., Ducellier, A., Dupros, F., and Michea, D. (2013b). Finite difference simulations of seismic wave propagation for understanding earthquake physics and predicting ground motions: Advances and challenges. In *24th IUPAP Conference on Computational Physics (IUPAP-CPP 2012)*, volume 454 of *Journal of Physics*, pages 43–64. IOP.

Aochi, H. and Yoshimi, M. (2016). Seismological asperities from the point of view of dynamic rupture modeling: the 2007 Mw6. 6 Chuetsu-Oki, Japan, earthquake. *Journal of Seismology*, 20(4):1089–1105.

Aoi, S., Sekiguchi, H., Morikawa, N., and Kunugi, T. (2008). Source process of the 2007 Niigata-ken Chuetsu-oki earthquake derived from near-fault strong motion data. *Earth, Planets and Space*, 60(11):1131–1135.

Aoi, S., Sekiguchi, H., Morikawa, N., Kunugi, T., and Shirasaka, M. (2007). Source Process of the 2007 Niigata-ken Chuetsu-Oki Earthquake Derived from Near-fault Strong Motion Data. Technical report, National Research Institute for Earth Science and Disaster Prevention.

Armstrong, P. J. and Frederick, C. O. (1966). *A mathematical representation of the multiaxial Bauschinger effect*. Central Electricity Generating Board and Berkeley Nuclear Laboratories, Research & Development Department.

Aubry, D., Hujeux, J. C., Lassoudiere, F., and Meimon, Y. (1982). A double memory model with multiple mechanisms for cyclic soil behaviour. In *Proceedings of the Int. Symp. Num. Mod. Geomech*, pages 3–13.

Aubry, D. and Modaressi, H. (1992). Seismic wave propagation in soils including non-linear and pore pressure effects. *Recent Advances in Earthquake Engineering and Structural Dynamics, V. Davidovici (ed.), Ouest Editions*, pages 209–224.

Babuska, I., Szabo, B. A., and Katz, I. N. (1981). The p-Version of the Finite Element Method. *SIAM Journal on Numerical Analysis*, 18(3):515–545.

Baker, J. W. (2007). Quantitative Classification of Near-Fault Ground Motions Using Wavelet Analysis. *Bulletin of the Seismological Society of America*, 97(5):1486–1501.

Baker, J. W., Cornell, C. A., and Tothong, P. (2005). Disaggregation of seismic drift hazard.

Baker, J. W., Luco, N., Abrahamson, N. A., Graves, R. W., Maechling, P. J., and Olsen, K. B. (2014). Engineering uses of physics-based ground motion simulations. In *Proceedings of the Tenth US Conference on Earthquake Engineering*.

Bao, H., Bielak, J., Ghattas, O., Kallivokas, L., O'Hallaron, D., Shewchuk, J., and Xu, J. (1998). Large-scale simulation of elastic wave propagation in heterogeneous media on parallel computers. *Computer Methods in Applied Mechanics and Engineering*, 152(1):85 – 102.

Bard, P.-Y. and Bouchon, M. (1980). The seismic response of sediment-filled valleys. Part 1. The case of incident SH waves. *Bulletin of the Seismological Society of America*, 70(4):1263–1286.

Berenger, J.-P. (1994). A perfectly matched layer for the absorption of electromagnetic waves. *Journal of computational physics*, 114(2):185–200.

Beresnev, I. and Wen, K.-l. (1996). Nonlinear Soil Response-A Reality ? *Bulletin of the Seismological Society of America*, 86(6):1964–1978.

Beresnev, I. A. and Atkinson, G. M. (1997). Modeling finite-fault radiation from the ω^n spectrum. *Bulletin of the Seismological Society of America*, 87(1):67–84.

Bernardi, C., Debit, N., and Maday, Y. (1990). Coupling Finite Element and Spectral Methods: First Results. *Mathematics of Computation*, 54(189):21–39.

Bielak, J., Loukakis, K., Hisada, Y., Yoshimura, C., Chiaki, Y., Ferna, A., Bielak, J., Hisada, Y., and Ferna, A. (2003a). Domain Reduction Method for Three-Dimensional Earthquake Modeling in Localized Regions. Part 1: Theory. *Bulletin of the Seismological Society of America*, 93(2):817–840.

Bielak, J., Loukakis, K., Hisada, Y., Yoshimura, C., Chiaki, Y., Ferna, A., Bielak, J., Hisada, Y., and Ferna, A. (2003b). Domain Reduction Method for Three-Dimensional Earthquake Modeling in Localized Regions. Part 2: Verification and Applications. *Bulletin of the Seismological Society of America*, 93(2):825–840.

Bishop, C. (1995). *Neural Networks for Pattern Recognition*. Clarendon Press - Oxford.

Bishop, C. and Roach, C. (1992). Fast Curve Fitting using Neural Networks. *Review of Scientific Instruments*, 63(10).

Bizzarri, A. (2012). Analytical representation of the fault slip velocity from spontaneous dynamic earthquake models. *Journal of Geophysical Research: Solid Earth*, 117(B6):n/a–n/a. B06309.

Bizzarri, A. (2014). On the point-source approximation of earthquake dynamics. *Annals of Geophysics*, 57(3).

Bolt, B. A. (2004). Seismic Input Motions for Nonlinear Structural Analysis. *ISET Journal of Earthquake Technology*, 41(448):223–232.

Boore, D. M. (1972). *Finite difference methods for seismic wave propagation in heterogeneous materials*, volume 11, pages 1–37. Elsevier.

Boore, D. M. (1983). Stochastic Simulation of High-Frequency Ground Motions Based on Seismological Models of the Radiated Spectra. *Bulletin of the Seismological Society of America*, 73(6):1865–1894.

Boore, D. M. (2003). Simulation of Ground Motion Using the Stochastic Method. *Pure and Applied Geophysics*, 160(3):635–676.

Boore, D. M. (2009). Comparing stochastic point-source and finite-source ground-motion simulations: SMSIM and EXSIM. *Bulletin of the Seismological Society of America*, 99(6):3202–3216.

Boore, D. M. and Joyner, W. B. (1997). Site Amplifications for Generic Rock Sites. *Bulletin of the Seismological Society of America*, 87(2):327–341.

Boore, D. M., Stewart, J. P., Emel, S., and Atkinson, G. M. (2013). NGA-West2 equations for predicting response spectral accelerations for shallow crustal earthquakes. PEER report 2013/05, Pacific Earthquake Engineering Research (PEER) Center. University of California, Berkeley.

Boore, D. M., Watson-Lamprey, J., and Abrahamson, N. (2006). Orientation-Independent Measures of Ground Motion. *Bulletin of the Seismological Society of America*, 96(4A):1502–1511.

Bouchon, M. (1981). A simple method to calculate Green's functions for elastic layered media. *Bulletin of the Seismological Society of America*, 71(4):959–971.

Bradley, B. A., Pettinga, D., Baker, J. W., and Fraser, J. (2017). Guidance on the Utilization of Earthquake-Induced Ground Motion Simulations in Engineering Practice. *Earthquake Spectra*.

Brune, J. N. (1970). Tectonic stress and the spectra of seismic shear waves from earthquakes. *Journal of Geophysical Research*, 75(26):4997–5009.

Burdick, L. J. and Mellman, G. R. (1976). Inversion of the body waves from the Borrego Mountain earthquake to the source mechanism. *Bulletin of the Seismological Society of America*, 66(5):1485–1499.

Burridge, R. and Knopoff, L. (1964). Body force equivalents for seismic dislocations. *Bulletin of the Seismological Society of America*, 54(6A):1875–1888.

Camata, J. J. and Coutinho, A. (2013). Parallel implementation and performance analysis of a linear octree finite element mesh generation scheme. *Concurrency and Computation: Practice and Experience*, 25(6):826–842.

Campbell, K. (2008). New Empirical Attenuation Relationship for the Western U.S. and California. Final Technical Report 03HQGR0026, ABS Consulting, Inc. (EQECAT). Research supported by the U.S. Geological Survey (USGS).

Canuto, C., Hussaini, M., Quarteroni, A., and Zhang, T. (1988). *Spectral methods in fluid dynamics*. Springer Series in Computational Physics. Springer-Verlag Berlin Heidelberg.

Cara, M. and Bour, M. (1995). An analytical solution of the elastodynamic equations along the axis of a circular fault. *Geophysical Journal International*, 123:373–390.

Cardona, O.-D., van Aalst, M. K., Birkmann, J., Fordham, M., McGregor, G., and Mechler, R. (2012). *Managing the Risks of Extreme Events and Disasters to Advance Climate Change Adaptation*, chapter Determinants of risk: exposure and vulnerability, pages 65–108. Cambridge University Press. A Special Report of Working Groups I and II of the Intergovernmental Panel on Climate Change (IPCC).

Casadei, F. and Gabellini, E. (1997). Implementation of a 3D Coupled Spectral Element/Finite Element Solver for Wave Propagation and Soil-Structure Interaction Simulations Part I - Models. E.c. environment and climate project trisee, Centre for Advanced Studies, Research and Development in Sardinia (CRS4).

Chaboche, J. (1989). Constitutive equations for cyclic plasticity and cyclic viscoplasticity. *International Journal of Plasticity*, 5(3):247 – 302.

Chaljub, E., Maufroy, E., Moczo, P., Kristek, J., Hollender, F., Bard, P.-Y., Priolo, E., Klin, P., de Martin, F., Zhang, Z., Zhang, W., and Chen, X. (2015). 3-D numerical simulations of earthquake ground motion in sedimentary basins: testing accuracy through stringent models. *Geophysical Journal International*, 201(1):90–111.

Chan, S. and Newmark, N. (1952). A Comparison of Numerical Methods for Analyzing the Dynamic Response of Structures. Contract N6onr-71, Task Order VI 064-1 83, University of Illinois. to Office of Naval Research.

Ciarlet, P. G. (2002). *The finite element method for elliptic problems*. SIAM.

Cirella, A., Piatanesi, A., Tinti, E., and Cocco, M. (2008). Rupture process of the 2007 Niigataken Chuetsu-Oki earthquake by non-linear joint inversion of strong motion and GPS data. *Geophysical Research Letters*, 35(16):1–5.

Claerbout, J. F. (1970). COARSE GRID CALCULATIONS OF WAVES IN INHOMOGENEOUS MEDIA WITH APPLICATION TO DELINEATION OF COMPLICATED SEISMIC STRUCTURE. *GEOPHYSICS*, 35(3):407–418.

Clayton, R. and Engquist, B. (1977). Absorbing boundary conditions for acoustic and elastic wave equations. *Bulletin of the Seismological Society of America*, 67(6):1529–1540.

Clouteau, D. (2008). *Notes de cours Séismes et Ouvrages*. CentraleSupélec, Chatenay-Malabry (France). Polycopiés ECP.

Cotton, F., Pousse, G., Bonilla, F., and Scherbaum, F. (2008). On the discrepancy of recent European ground-motion observations and predictions from empirical models: Analysis of KiK-net accelerometric data and point-sources stochastic simulations. *Bulletin of the Seismological Society of America*, 98(5):2244–2261.

Courant, R., Friedrichs, K., and Lewy, H. (1956). *On the partial difference equations of mathematical physics*. Number March. AEC Computing and Applied Mathematics Center.

Courant, R., Friedrichs, K., and Lewy, H. (1967). On the partial difference equations of mathematical physics. *IBM Journal of Research and Development*.

Cox, K. E. and Ashford, S. A. (2002). Characterization of large velocity pulses for laboratory testing. Technical Report April, Pacific Earthquake Engineering Research Center.

Cupillard, P., Delavaud, E., Burgos, G., Festa, G., Vilotte, J.-P., Capdeville, Y., and Montagner, J.-P. (2012). RegSEM: a versatile code based on the spectral element method to compute seismic wave propagation at the regional scale. *Geophysical Journal International*, 188(3):1203–1220.

Curtis, a., Gerstoft, P., Sato, H., Snieder, R., and Wapenaar, K. (2006). Seismic interferometry - turning noise into signal. *The Leading Edge*, 25:1082–1092.

Cybenko, G. (1989). Approximation by superpositions of a sigmoidal function. *Mathematics of control, signals and systems*, 2(4):303–314.

Dafalias, Y. F. (1986). An anisotropic critical state soil plasticity model. *Mechanics Research Communications*, 13(6):341–347.

Dafalias, Y. F. and Popov, E. P. (1975). A model of nonlinearly hardening materials for complex loading. *Acta mechanica*, 21(3):173–192.

Dahm, T. and Kruger, F. (2014). Moment tensor inversion and moment tensor interpretation. Information sheet, Helmholtz Centre Potsdam GFZ German Research Centre.

Dalguer, L. A. and Mai, P. M. (2011). Near-Source Ground Motion Variability from M = 6.5 Dynamic Rupture Simulations. In *4th IASPEI-IAEE International Symposium-Effects of Surface Geology on Seismic Motion*.

Darendeli, M. B. (2001). *Development of a new family of normalized modulus reduction and material damping curves*. PhD thesis, The University of Texas at Austin.

Das, S. and Aki, K. (1977). Fault plane with barriers: A versatile earthquake model. *Journal of Geophysical Research*, 82(36):5658–5670.

Dave, J. and Armstrong, B. (1970). Computations of high-order associated Legendre polynomials. *Journal of Quantitative Spectroscopy and Radiative Transfer*, 10(6):557–562.

Day, S. M., Graves, R., Bielak, J., Dreger, D., Larsen, S., Olsen, K. B., Pitarka, A., and Ramirez-Guzman, L. (2008). Model for basin effects on long-period response spectra in southern California. *Earthquake Spectra*, 24(1):257–277.

De Martin, F. (2010). *Influence of the Nonlinear Beavior of Soft Soils on Strong Ground Motions*. phdthesis, École Centrale Paris.

De Martin, F. (2011). Verification of a Spectral-Element Method Code for the Southern California Earthquake Center LOH.3 Viscoelastic Case. *Bulletin of the Seismological Society of America*, 101(6):2855–2865.

De Martin, F., Aochi, H., and Foerster, E. (2007). Testing the Double-Couple Point Source Model in GEFDYN. Technical report, BRGM.

Delavaud, E. (2007). *Simulation numérique de la propagation d'ondes en milieu géologique complexe: application à l'évaluation de la réponse sismique du bassin de Caracas (Venezuela)*. phdthesis, Institut de Physique du Globe de Paris.

Deville, M., Fischer, P., and Mund, E. (2002). *High-Order Methods for Incompressible Fluid Flow*. Cambridge Monographs on Applie. Cambridge University Press.

Dhatt, G., Lefrançois, E., and Touzot, G. (2012). *Finite Element Method*. Numerical Method. ISTE Ltd and John Wiley & Sons, Inc.

di Prisco, C., Stupazzini, M., and Zambelli, C. (2007). Nonlinear SEM numerical analyses of dry dense sand specimens under rapid and dynamic loading. *International Journal for Numerical and Analytical Methods in Geomechanics*, 31(November 2006):757–788.

Dobry, R. (2013). Radiation damping in the context of one-dimensional wave propagation: A teaching perspective. *Soil Dynamics and Earthquake Engineering*, 47:51–61.

Douglas, J. (2011). Ground-motion prediction equations 1964-2010. PEER Report 102, Pacific Earthquake Engineering Research Center - Bureau de Recherches Géologiques et Miniéres.

Douglas, J., Akkar, S., Ameri, G., Bard, P.-Y., Bindi, D., Bommer, J. J., Bora, S. S., Cotton, F., Derras, B., Hermkes, M., et al. (2014). Comparisons among the five ground-motion models developed using RESORCE for the prediction of response spectral accelerations due to earthquakes in Europe and the Middle East. *Bulletin of earthquake engineering*, 12(1):341–358.

Dowell, M. and Jarratt, P. (1971). A Modified Regula Falsi Method for Computing the Root of an equation. *BIT*, 11:168–174.

Dreger, D., Hurtado, G., Chopra, A. K., and Larsen, S. (2007). Near-Fault Seismic Ground Motions. Technical Report 59A0435, California Department of Transportation.

Drucker, D. C. (1988). Conventional and unconventional plastic response and representation. *Appl. Mech. Rev*, 41(4):151–167.

Drucker, D. C. and Prager, W. (1952). Soil Mechanics and Plastic Analysis or Limit Design. *Quarterly of Applied Mathematics*, 10(2):157–165.

Ducellier, A. and Aochi, H. (2010). Numerical simulation of the Mw 6.6 Niigata, Japan, earthqhake: Reliable input ground motion for engineering purpose. In *14th European Conference on Earthquake Engineering*.

Dumbser, M. and Käser, M. (2006). An arbitrary high-order discontinuous Galerkin method for elastic waves on unstructured meshes - II. The three-dimensional isotropic case. *Geophysical Journal International*, 167(1):319–336.

Duputel, Z., Rivera, L., Kanamori, H., and Hayes, G. (2012). W phase source inversion for moderate to large earthquakes (1990-2010). *Geophysical Journal International*, 189(2):1125.

Duputel, Z., Tsai, V. C., Rivera, L., and Kanamori, H. (2013). Using centroid time-delays to characterize source durations and identify earthquakes with unique characteristics. *Earth and Planetary Science Letters*, 374:92–100.

Engquist, B. and Majda, A. (1977). Absorbing Boundary Conditions for the Numerical Simulation of Waves. *Mathematics of Computation*, 31(139):629–651.

Eshelby, J. D. (1957). The Determination of the Elastic Field of an Ellipsoidal Inclusion, and Related Problems. *Proceedings of the Royal Society of London A: Mathematical, Physical and Engineering Sciences*, 241(1226):376–396.

Faccioli, E., Maggio, F., Paolucci, R., and Quarteroni, A. (1997). 2D and 3D elastic wave propagation by a pseudo-spectral domain decomposition method. *Journal of Seismology*, 1(3):237–251.

Faccioli, E. and Vanini, M. (2003). Complex seismic site effects in sediment-filled valleys and implications on design spectra. *Progress in Structural Engineering and Materials*, 5(4):223–238.

Festa, G. and Vilotte, J.-P. (2005). The Newmark scheme as velocity-stress time-staggering: an efficient PML implementation for spectral element simulations of elastodynamics. *Geophysical Journal International*, 161(3):789–812.

Frankel, A. (2009). A Constant Stress-Drop Model for Producing Broadband Synthetic Seismograms: Comparison with the Next Generation Attenuation Relations. *Bulletin of the Seismological Society of America*, 99(2A):664–680.

Frederick, C. O. and Armstrong, P. J. (2007). A mathematical representation of the multiaxial Bauschinger effect. *Materials at High Temperatures*, 24(1):1–26.

Fujiwara, H., Kawai, S., Aoi, S., Morikawa, N., Senna, S., Kudo, N., Ooi, M., Hao, K. X.-S., Hayakawa, Y., Toyama, N., Matsuyama, H., I.-K., Suzuki, H., and Liu, Y. (2009). A study on subsurface structure model for deep sedimentary layers of Japan for strong-motion evaluation. *Technical Note of the National Research Institute for Earth Science and Disaster Prevention*, 337:260.

Fukushima, S. (2007). Seismic hazard analysis based on the joint probability density function of PGA and PGV. In *Transactions, SMiRT 19*, volume M03.

Gallovič, F. (2016). Modeling Velocity Recordings of the Mw 6.0 South Napa, California, Earthquake: Unilateral Event with Weak High-Frequency Directivity. *Seismol. Res. Lett.*, 87(1):2–14.

Gatti, F., Lopez-Caballero, F., and Clouteau, D. (2015). One-Dimensional Seismic Soil Response at the Nuclear Power Plant of Kashiwazaki-Kariwa during the 2007 Niigata-Chuetsu-Oki Earthquake. In Kruis, J., Tsompanakis, Y., and Topping, B., editors, *Proceedings of the Fifteenth International Conference on Civil, Structural and Environmental Engineering Computing*, number 157 in Computational, Engineering and Technology Conferences and Publications, pages 1–16, Stirlingshire, UK,. Civil-Comp Press.

Gatti, F., Lopez-Caballero, F., de Abreu Corrêa, L., Clouteau, D., and Paolucci, R. (2017). Physics-based Scenario of the 2007 Chuetsu-Oki Earthquake. In *6th International Conference on Computational Methods in Structural Dynamics and Earthquake Engineering. COMPDYN 2017. 15-17 June 2017, Rhodes Island, Greece*.

Geller, R. J. (1976). Scaling relations for earthquake source parameters and magnitudes. *Bulletin of the Seismological Society of America*, 66(5):1501–1523.

Göddeke, D., Komatitsch, D., and Möller, M. (2014). *Finite and Spectral Element Methods on Unstructured Grids for Flow and Wave Propagation Methods*, chapter 9, pages 183–206. Springer.

Goldsby, D. L., Tullis, T. E., Okazaka, K., Platt, J. D., and Mitchell, T. M. (2014). Experimental Studies of Dynamic Fault Weakening Due to Thermal Pore-Fluid Pressurization. In *AGU Fall Meeting Abstracts*.

Graves, R. W. (1996). Simulating seismic wave propagation in 3D elastic media using staggered-grid finite differences. *Bulletin of the Seismological Society of America*, 86(4):1091–1106.

Graves, R. W., Aagaard, B. T., Hudnut, K. W., Star, L. M., Stewart, J. P., and Jordan, T. H. (2008). Broadband simulations for Mw 7.8 southern San Andreas earthquakes: Ground motion sensitivity to rupture speed. *Geophysical Research Letters*, 35(22).

Graves, R. W. and Pitarka, A. (2004). Broadband time history simulation using a hybrid approach. In *13th World Conference on Earthquake Engineering, Vancouver, B.C., Canada*.

Graves, R. W. and Pitarka, A. (2010). Broadband Ground-Motion Simulation Using a Hybrid Approach. *Bulletin of the Seismological Society of America*, 100(5A):2095–2123.

Graves, R. W. and Wald, D. J. (2004). Observed and Simulated Ground Motions in the San Bernardino Basin Region for the Hector Mine, California, Earthquake. *Bulletin of the Seismological Society of America*, 94(1):131–146.

Green, R. and Cameron, W. I. (2003). The influence of ground motion characteristics on site response coefficients. In *PCEE 2003: 7th Pacific Conference on Earthquake Engineering*, pages 1–8. New Zealand Society for Earthquake Engineering.

Gürpinar, A., Serva, L., Livio, F., and Rizzo, P. C. (2017). Earthquake-induced crustal deformation and consequences for fault displacement hazard analysis of nuclear power plants. *Nuclear Engineering and Design*, 311:69 – 85.

Hagan, M. T., Demuth, H. B., Beale, M. H., and De Jesús, O. (1996). *Neural network design*, volume 20. PWS publishing company Boston, 2nd edition edition.

Hanks, T. C. and McGuire, R. K. (1981). The character of high frequency strong ground motion. *Bulletin of the Seismological Society of America*, 71:2071–2095.

Hartzell, S., Bonilla, L. F., and Williams, R. (2004). Prediction of nonlinear soil effects. *Bulletin of the Seismological Society of America*, 94(5):1609–1629.

Hartzell, S., Guatteri, M., Mai, P. M., Liu, P.-C., and Fisk, M. (2005). Calculation of Broadband Time Histories of Ground Motion, Part II: Kinematic and Dynamic Modeling Using Theoretical Green's Functions and Comparison with the 1994 Northridge Earthquake. *Bulletin of the Seismological Society of America*, 95(2):614–645.

Hartzell, S., Liu, P., and Mendoza, C. (1996). The 1994 Northridge, California, earthquake: Investigation of rupture velocity, risetime, and high-frequency radiation. *Journal of Geophysical Research*, 101(B9):20091–20108.

Hartzell, S. H. (1978). Earthquake aftershocks as Green's functions. *Geophysical Research Letters*, 5(1):1–4.

Harvey, D. and Choy, G. L. (1982). Broad-band deconvolution of GDSN data. *Geophysical Journal of the Royal Astronomical Society*, 69(3):659–668.

Hashash, Y. M. A. and Groholski, D. R. P. C. (2010). Recent advances in non-linear site response analysis. In *Recent Advances in Geotechnical Earthquake Engineering and Soil Dynamics and Symposium in Honor of Professor I.M. Idriss*, number OSP 4, pages 1–22.

Hashash, Y. M. a. and Park, D. (2001). Non-linear one-dimensional seismic ground motion propagation in the Mississippi embayment. *Engineering Geology*, 62(1-3):185–206.

Hashiguchi, K. (2015). Exact Formulation of Subloading Surface Model: Unified Constitutive Law for Irreversible Mechanical Phenomena in Solids. *Archives of Computational Methods in Engineering*.

Haskell, N. A. (1953). The dispersion of surface waves on multilayered media. *Bulletin of the seismological Society of America*, 43(1):17–34.

Haskell, N. A. (1964). Total energy and energy spectral density of elastic wave radiation from propagating faults. *Bulletin of the Seismological Society of America*, 54(6A):1811–1841.

Haskell, N. A. (1969). Elastic displacements in the near-field of a propagating fault. *Bulletin of the Seismological Society of America*, 59(2):865–908.

Hayakawa, T., Tsuda, K., Uetake, T., Hikima, K., Tokumitsu, R., and Nagumo, H. (2011). Modeling 3D velocity structure in the fault region of the 2007 Niigataken Chuetu-oki Earthquake-Incorporating the 3D fold geological structure beneath the Kashiwazaki-Kariwa nuclear power plant. In *Japan Geoscience Union meeting*, number SSS023, page 14.

Herrero, A. and Bernard, P. (1994). A kinematic self-similar rupture process for earthquakes. *Bulletin of the Seismological Society of America*, 84(4):1216–1228.

Hijikata, K., Nishimura, I.and Mizutani, H., Tokumitsu, R., Mashimo, M., and Tanaka, S. (2010). Ground motion characteristics of 2007 Niigata-ken Chuetsu-Oki earthquake. *Journal of Structural and Construction Engineering*, 75(653):1279–1288.

Hikima, K. (2007). Source process of the 2007 Chuetsu-Oki earthquake inferred from far field waveforms and strong motions. In *Seismological Society of Japan-Fall Meeting 2007*, Fall Meeting 2007, pages 1–85. Seismological Society of Japan.

Hikima, K. and Koketsu, K. (2005). Rupture processes of the 2004 Chuetsu (mid-Niigata prefecture) earthquake, Japan: A series of events in a complex fault system. *Geophysical Research Letters*, 32(18):1–5.

Hisada, Y. (1994). An efficient method for computing Green's Functions for layered half-space with sources and receivers at close depths. *Bulletin of the Seismological Society of America*, 84(5):1456–1472.

Hisada, Y. (1995). An efficient method for computing Green's functions for a layered half-space with sources and receivers at close depths (part 2). *Bulletin of the Seismological Society of America*, 85(4):1080–1093.

Hisada, Y. (2008). Broadband strong motion simulation in layered half-space using stochastic Green's function technique. *Journal of Seismology*, 12(2):265–279.

Hisada, Y., Nagano, M., Nozu, A., Miyakoshi, K., Asano, K., Matsumoto, T., and Nakagawa, T. (2012). Benchmark Tests for Strong Ground Motion Prediction Methods using Theoretical Methods. In *15th World Conference on Earthquake Engineering*.

Honda, H. (1962). Earthquake mechanism and seismic waves. *Journal of Physics of the Earth*, 10(2):1–97.

Hughes, T. J. R. (1987). *The finite element method: linear static and dynamic finite element analysis*. Prentice-Hall, Inc.

Hujeux, J. C. (1985). Une loi de comportement pour le chargement cyclique des sols. *Génie parasismique*, pages 287–302.

Hyodo, M. and Hirahara, K. (2003). A viscoelastic model of interseismic strain concentration in Niigata-Kobe Tectonic Zone of central Japan. *Earth, planets and space*, 55(11):667–675.

IAEA (2014). *Review of Seismic Evaluation Methodologies for Nuclear Power Plants Based on a Benchmark Exercise*. INTERNATIONAL ATOMIC ENERGY AGENCY, Vienna. IAEA-TECDOC-1722.

Ida, Y. (1972). Cohesive force across the tip of a longitudinal-shear crack and Griffith's specific surface energy. *Journal of Geophysical Research*, 77(20):3796–3805.

Imperatori, W. and Mai, P. M. (2013). Broad-band near-field ground motion simulations in 3-dimensional scattering media. *Geophysical Journal International*, 192(2):725.

Irikura, K. (1983). Semi-Empirical Estimation of Strong Ground Motions During. *Bulletin of the Disaster Prevention Research Institute*, 33(2):63–104.

Irikura, K. (1991). The physical basis of the empirical Green's function method and the prediction of strong ground motion for large earthquake. In CENAPRED, editor, *International Workshop on Seismology and Earthquake Engineering*, pages 89–112, Mexico City.

Irikura, K. and Kamae, K. (1994). Estimation of strong ground motion in broad-frequency band based on a seismic source scaling model and an empirical Green's function technique. *Annals of Geophysics*, 37(6).

Irikura, K. and Miyake, H. (2010). Recipe for Predicting Strong Ground Motion from Crustal Earthquake Scenarios. *Pure and Applied Geophysics*, 168(1-2):85–104.

Isbiliroglu, Y., Taborda, R., and Bielak, J. (2015). Coupled Soil-Structure Interaction Effects of Building Clusters During Earthquakes. *Earthquake Spectra*, 31(1):463–500.

Ishihara, K., Yoshida, N., and Tsujino, S. (1985). Modelling of stress-strain relations of soils in cyclic loading. In *Fifth International conference on numerical methods in geomechanics*, pages 523–530.

Iwan, W. (1967). On a class of models for the yielding behavior of continuous and composite systems. *Journal of Applied Mechanics*, 34(3):612–617.

Jeffries, M. and Been, K. (2006). *Soil liquefaction: a critical state approach*. Taylor & Francis.

JNES (2008). Construction of the subsurface structure around the source area of 2007 Niigata Ken Chuetsu-Oki earthquake. Technical report, Japanes Nuclear Energy Safety Organization.

Jordan, T. (2015). Annual Report: Year 4. Technical report, Southern California Earthquake Center (SCEC).

Joyner, W. B. (1975). A Method for Calculating Nonlinear Seismic Response in Two Dimensions. *Bulletin of the Seismological Society of America*, 65(5):1337–1357.

Kamae, K., Irikura, K., and Pitarka, A. (1998). A Technique for Simulating Strong Ground Motion Using Hybrid Green's Functions. *Bulletin of the Seismological Society of America*, 88(2):357–367.

Kanamori, H. and Anderson, D. L. (1975). Theoretical basis of some empirical relations in seismology. *Bulletin of the Seismological Society of America*, 65(5):1073–1095.

Karypis, G. and Kumar, V. (1995). METIS - Unstructured Graph Partitioning and Sparse Matrix Ordering System, Version 2.0. Technical report, University of Minnesota.

Käser, M. and Dumbser, M. (2006). An arbitrary high-order discontinuous Galerkin method for elastic waves on unstructured meshes - I. The two-dimensional isotropic case with external source terms. *Geophysical Journal International*, 166(2):855–877.

Kato, A., Kurashimo, E., Igarashi, T., Sakai, S., Iidaka, T., Shinohara, M., Kanazawa, T., Yamada, T., Hirata, N., and Iwasaki, T. (2009). Reactivation of ancient rift systems triggers devastating intraplate earthquakes. *Geophysical Research Letters*, 36(L05301):1–5.

Kato, A., Sakai, S., Kurashimo, E., Igarashi, T., Iidaka, T., Hirata, N., Iwasaki, T., and Kanazawa, T. (2008). Imaging heterogeneous velocity structures and complex aftershock distributions in the source region of the 2007 Niigataken Chuetsu-Oki Earthquake by a dense seismic observation. *Earth, Planets Space*, 60:1111–1116.

Kawabe, H. and Kamae, K. (2010). Source modelling and 3D ground motion simulation of the 2007 Niigataken Chuetsu-oki earthquake (Mj6.8). In *13th Japan Earthquake Engineering Symposium, Tsukuba Japan*.

Kawase, H. (2011). Strong Motion Characteristics and their Damage Impact to Structures during the off Pacific Coast of Tohoku Earthquake of March 11, 2011: How Extraordinary was this M9.0 Earthquake. In *4th IASPEI-IAEE International Symposium-Effects of Surface Geology on Seismic Motion*, volume 11, pages 1–13.

Kayen, R., Brandenberg, S. J., Collins, B. D., Dickenson, S., Ashford, S., Kawamata, Y., Tanaka, Y., Koumoto, H., Abrahamson, N., Cluff, L., Tokimatsu, K., and Johnson, L. (2009). Geoengineering and Seismological Aspects of the Niigata-Ken Chuetsu-Oki Earthquake of 16 July 2007. *Earthquake Spectra*, 25(4):777–802.

Kikuchi, M. and Kanamori, H. (1982). Inversion of complex body waves. *Bulletin of the Seismological Society of America*, 72(2):491–506.

Kobayashi, I., Tateishi, M., Yoshimura, T., Ueda, T., and Kato, T. (1995). Geology of the Kashiwazaki District. Geological Survey of Japan.

Kokusho, T. and Suzuki, T. (2008). Vertical Array Records during 2007 Niigata-Ken Chuetsu-Oki Earthquake and Incident Wave Energy. In *The 14th World Conference on Earthquake Engineering*.

Komatitsch, D. (1997). *Méthodes spectrales et éléments spectraux pour l'équation de l'élastodynamique 2D et 3D en milieu hétérogène (Spectral and spectral-element methods for the 2D and 3D elastodynamics equations in heterogeneous media)*. PhD thesis, Institut de Physique du Globe, Paris, France. 187 pages.

Komatitsch, D., Barnes, C., and Tromp, J. (2000). Wave propagation near a fluid-solid interface: A spectral-element approach. *GEOPHYSICS*, 65(2):623–631.

Komatitsch, D. and Tromp, J. (1999). Introduction to the spectral element method for three-dimensional seismic wave propagation. *Geophysical journal international*, 139(3):806–822.

Komatitsch, D. and Tromp, J. (2002a). Spectral-element simulations of global seismic wave propagation-I. Validation. *Geophysical Journal International*, 149(2):390–412.

Komatitsch, D. and Tromp, J. (2002b). Spectral-element simulations of global seismic wave propagation-II. Three-dimensional models, oceans, rotation and self-gravitation. *Geophysical Journal International*, 150(1):303–318.

Komatitsch, D., Tsuboi, S., and Tromp, J. (2005). The Spectral-Element Method in Seismology. In Levander, A. and Nolet, G., editors, *Seismic Earth: Array Analysis of Broadband Seismograms*, volume 157 of *Geophysical Monograph*, pages 205–228. American Geophysical Union.

Komatitsch, D. and Vilotte, J.-P. (1998). The Spectral Element Method: An Efficient Tool to Simulate the Seismic Response of 2D and 3D Geological Structures. *Bulletin of the Seismological Society of America*, 88(2):368–392.

Komatitsch, D., Vilotte, J. P., Vai, R., Castillo-Covarrubias, J. M., and Sánchez-Sesma, F. J. (1999). The Spectral Element method for elastic wave equations: Application to 2D and 3D seismic problems. *SEG Expanded Abstracts 17*, 45:1139–1164.

Korczak, K. Z. and Patera, A. T. (1986). An isoparametric spectral element method for solution of the Navier-Stokes equations in complex geometry. *Journal of Computational Physics*, 62(2):361 – 382.

Kramer, S. L. (1996). *Geotechnical Earthquake Engineering*, volume 6. Prentice-Hall.

Krieg, R. D. (1975). A practical two surface plasticity theory. *Journal of applied mechanics*, 42(3):641–646.

Lagrange, J. L. (1853). *Mécanique analytique*, volume 1. Mallet-Bachelier.

Landau, L. and Lifshitz, E. (1959). *Course Of Theoretical Physics Vol 7: Theory Of Elasticity*. Addison-Wesley physics books. London : Pergamon Press ; Reading, Mass. : Addison-Wesley Pub. Co.

Langston, C. A. (1976). A body wave inversion of the Koyna, India, earthquake of December 10, 1967, and some implications for body wave focal mechanisms. *Journal of Geophysical Research*, 81(14):2517–2529.

Lapusta, N., Rice, J. R., Ben-Zion, Y., and Zheng, G. (2000). Elastodynamic analysis for slow tectonic loading with spontaneous rupture episodes on faults with rate-and state-dependent friction. *Journal of Geophysical Research: Solid Earth*, 105(B10):23765–23789.

Lavell, A. (2003). Programme for Risk Management in Central America: Ideas and notions relating to concept and practices. In *United Nations Development Programme (UNDP)*.

Lee, E., Chen, P., Jordan, T. H., Maechling, P. B., Denolle, M. A. M., and Beroza, G. C. (2014). Full 3D tomography for crustal structure in Southern California based on the scattering integral and the adjoint wavefield methods. *Journal of Geophysical Research: Solid Earth*, 119(8):6421–6451.

Lee, S. C. and Han, S. W. (2002). Neural-network-based models for generating artificial earthquakes and response spectra . *Computers & Structures*, 80:1627–1638.

Lemaitre, J. and Chaboche, J. L. (1990). *Mechanics of solid materials*. Cambridge University Press.

Levenberg, K. (1944). A method for the solution of certain non-linear problems in least squares. *Quarterly of applied mathematics*, 2(2):164–168.

Lin, Y. K. and Yong, Y. (1987). Evolutionary Kanai-Tajimi earthquake models. *Journal of engineering mechanics*, 113(8):1119–1137.

Liner, C. L. (2004). *Elements of 3D Seismology*, volume 1. PennWell Books.

Liu, H.-P. and Archambeau, C. B. (1976). The effect of anelasticity on periods of the Earth's free oscillations (toroidal modes)-correction. *Geophysical Journal International*, 43(3):795–814.

Liu, P., Archuleta, R. J., and Hartzell, S. H. (2006). Prediction of Broadband Ground-Motion Time Histories: Hybrid Low/High- Frequency Method with Correlated Random Source Parameters. *Bulletin of the Seismological Society of America*, 96(6):2118–2130.

Liu, Q. (2006). *Spectral-Element Simulations of 3-D Seismic Wave Propagation and Applications to Source and Structural Inversions*. PhD thesis, California Institute of Technology.

Liu, S. C. (1970). Dynamics of correlated random pulse trains. *J. Engrg. Mech. Div.*, 96:455.

Lopez-Caballero, F. and Modaressi-Farahmand-Razavi, A. (2010). Assessment of variability and uncertainties effects on the seismic response of a liquefiable soil profile. *Soil Dynamics and Earthquake Engineering*, 30(7):600–613.

Lopez-Caballero, F., Razavi, A. M. F., and Modaressi, H. (2007). Nonlinear numerical method for earthquake site response analysis i - Elastoplastic cyclic model and parameter identification strategy. *Bulletin of Earthquake Engineering*, 5:303–323.

Luco, J. and Apsel, R. (1983a). On the Green's Functions for a Layered Half-Space. Part I. *Bulletin of the Seismological Society of America*, 73(4):909–929.

Luco, J. and Apsel, R. (1983b). On the Green's Functions for a Layered Half-Space. Part II. *Bulletin of the Seismological Society of America*, 73(4):931–951.

Luco, N. and Cornell, C. (2007). Structure-specific scalar intensity measures for near-source and ordinary earthquake ground motions. *Earthquake Spectra*, 23(2):357–392.

Lysmer, J. and Drake, L. A. (1972). A finite element method for seismology. *Methods in computational physics*, 11:181–216.

Madariaga, R. (1976). Dynamics of an expanding circular fault. *Bulletin of the Seismological Society of America*, 66(3):639–666.

Madariaga, R. (1977). Implications of Stress-Drop Models of Earthquakes for the Inversion of Stress Drop from Seismic Observations. *Pure and Applied Geophysics*, 115.

Madariaga, R. (1978). The dynamic field of Haskell's rectangular dislocation fault model. *Bulletin of the Seismological Society of America*, 68(4):869–887.

Madariaga, R. (1989). *Seismic source: Theory*, pages 1129–1133. Springer US, Boston, MA.

Madariaga, R., Ampuero, J. P., and Adda-Bedia, M. (2013). *Seismic Radiation from Simple Models of Earthquakes*, pages 223–236. American Geophysical Union.

Maday, Y., Patera, A. T., and Ronquist, E. M. (1987). A well-posed optimal spectral element approximation for the Stokes problem.

Mai, P. M. and Beroza, G. C. (2003). A hybrid method for calculating near-source, broadband seismograms: Application to strong motion prediction. *Physics of the Earth and Planetary Interiors*, 137(1):183–199.

Marfurt, K. J. (1984). Accuracy of finite-difference and finite-element modeling of the scalar and elastic wave equations. *GEOPHYSICS*, 49(5):533–549.

Marquardt, D. W. (1963). An algorithm for least-squares estimation of nonlinear parameters. *Journal of the society for Industrial and Applied Mathematics*, 11(2):431–441.

Masing, G. (1923). On Heyn's hardening theory of metals due to inner elastic stresses. *Wiss. Veröff. Siemens-Konzern*, 3:231–239.

Masing, G. (1926). Eigenspannungen und verfestigung beim messing. In *Proceedings of the 2nd international congress of applied mechanics*, volume 100, pages 332–5.

Matsumoto, T., Matsubayashi, H., and Kazakami, T. (2007). F-net Moment Tensor Solution on The Niigataken Chuetsu-Oki Earthquake in 2007. In *Seismological Society of Japan*, Fall Meeting 2007, pages 1–88.

Maufroy, E., Chaljub, E., Hollender, F., Kristek, J., Moczo, P., Klin, P., Priolo, E., Iwaki, A., Iwata, T., Etienne, V., De Martin, F., Theodoulidis, N. P., Manakou, M., Guyonnet-Benaize, C., Pitilakis, K., and Bard, P.-Y. (2015). Earthquake Ground Motion in the Mygdonian Basin, Greece: The E2VP Verification and Validation of 3D Numerical Simulation up to 4 Hz. *Bulletin of the Seismological Society of America*, 105(3):1398–1418.

Mavroeidis, G., Dong, G., and Papageorgiou, A. (2004). Near-fault ground motions, and the response of elastic and inelastic single-degree-of-freedom (SDOF) systems. *Earthquake Engineering & Structural Dynamics*, 33(9):1023–1049.

Mavroeidis, G. and Papageorgiou, A. (2003). A Mathematical Representation of Near-Fault Ground Motions. *Bulletin of the Seismological Society of America*, 93(3):1099–1131.

Mayday, Y., Patera, A., and Rønquist, E. (1989). Optimal Legendre spectral element methods for the multi-dimensional Stokes problem. *SIAM J. Num. Anal*.

Mazzieri, I., Stupazzini, M., Guidotti, R., and Smerzini, C. (2013). SPEED: SPectral Elements in Elastodynamics with Discontinuous Galerkin: a non-conforming approach for 3D multi-scale problems. *International Journal for Numerical Methods in Engineering*, 95(12):991–1010.

McClelland, J., Rumelhart, D., and Group, P. R. (1986). *Parallel distributed processing: Explorations in the microstructure of cognition*, volume 1 of *Computational Models of Cognitions and Perception*. MIT press Cambridge, MA.

Menq, F.-Y. (2003). *Dynamic Properties of Sandy and Gravelly Soils*. PhD thesis, The University of Texas at Austin.

Miura, K., Kobayashi, S., and Yoshida, N. (2000). Equivalent Linear Analysis Considering Large Strains and Frequency Dependent Characteristics. In *12^{th} WCEE*, pages 1–8.

Miyake, H., Iwata, T., and Irikura, K. (2003). Source characterization for broadband ground-motion simulation. Kinematic heterogeneous source model and strong motion generation area. *Bulletin of the Seismological Society of America*, 93(6):2531–2545.

Miyake, H., Koketsu, K., Hikima, K., Shinohara, M., and Kanazawa, T. (2010). Source Fault of the 2007 Chuetsu-Oki, Japan, Earthquake. *Bulletin of the Seismological Society of America*, 100(1):384–391.

Moczo, P., Kristek, J., Galis, M., Pazak, P., and Balazovjech, M. (2007). The finite-difference and finite-element modeling of seismic wave propagation and earthquake motion. *Acta physica slovaca*, 57(2):177–406.

Moczo, P., Kristek, J., Vavryčuk, V., Archuleta, R. J., and Halada, L. (2002). 3D heterogeneous staggered-grid finite-difference modeling of seismic motion with volume harmonic and arithmetic averaging of elastic moduli and densities. *Bulletin of the Seismological Society of America*, 92(8):3042–3066.

Mogi, H., Shrestha, S. M., H., Okamura, S., Kawakami, H., Okamura, S., H., H., Okamura, S., Kawakami, H., Okamura, S., H., H., and Okamura, S. (2010). Nonlinear Soil Behavior Observed at Vertical Array in the Kashiwazaki-Kariwa Nuclear Power Plant during the 2007 Niigata-ken Chuetsu-Oki Earthquake. *Bulletin of the Seismological Society of America*, 100(2):762–775.

Montoya-Noguera, S. (2016). *Assessment and mitigation of liquefaction seismic risk: Numerical modeling of their effects on SSI*. PhD thesis, CentraleSupélec-Université Paris Saclay.

Motazedian, D. and Atkinson, G. M. (2005). Stochastic finite-fault modeling based on a dynamic corner frequency. *Bulletin of the Seismological Society of America*, 95(3):995–1010.

Mroz, Z. (1967). On the description of anisotropic workhardening. *Journal of the Mechanics and Physics of Solids*, 15(3):163–175.

Nakagawa, K. and Soga, K. (1995). Nonlinear Cyclic Stress-Strain Relation for Soils. In *3th International Conference on Recent Advances in Geotechnical Earthquake Engineering and Soil Dynamics*.

Nakahigashi, K., Shinohara, M., Kurashimo, E., Yamada, T., Kato, A., Takanami, T., Uehira, K., Ito, Y., Iidaka, T., Igarashi, T., Sato, H., Hino, R., Obana, K., Kaneda, Y., Hirata, N., Iwasaki, T., and Kanawaza, T. (2012). Seismic structure of the source region of the 2007 Chuetsu-oki earthquake revealed by offshore-onshore seismic survey: Asperity zone in intraplate earthquake delimited by crustal inhomogeneity. *Tectonophysics*, 562-563:562–563.

Nakamura, T., Ishihara, Y., Yamanaka, Y., and Kaneda, Y. (2009). Source process for complex fault system of the 2007 Chuetsu-Oki, Niigata, Japan, earthquake. *Earth, Planets and Space*, 61(2):273–278.

Nakano, H. (1923). Notes on the nature of the forces which give rise to the earthquake motions. *Seismological Bulletin of Central METEOROLOGICAL Observatory of Japan*, 1:92–120.

Newmark, N. M. and Hall, W. (1982). Earthquake Design and Spectra. In Agbabian, M., editor, *Engineering Monographs on Earthquake Criteria, Structural Design, and Strong Motion Records*, page 103. The Earthquake Engineering Research Institute, Oakland, CA.

Noda, H. and Lapusta, N. (2013). Stable creeping fault segments can become destructive as a result of dynamic weakening. *Nature*, 493(7433):518–521.

Nozu, A. (2008). Rupture process of the 2007 Chuetsu-Oki, Niigata, Japan, earthquake - Waveform inversion using empirical Green's functions. *Earth, Planets Space*, 60:1169–1176.

Obara, K., Kasahara, K., Hori, S., and Okada, Y. (2005). A densely distributed high-sensitivity seismograph network in Japan: Hi-net by National Research Institute for Earth Science and Disaster Prevention. *Review of Scientific Instruments*, 76(2):1–12.

O'Connell, D. R., Ake, J.P. Bonilla, F., Liu, P., LaForge, R., and Ostenaa, D. (1984). *Strong Ground Motion Estimation*, chapter 1, pages 3–69. Number OPTIISBN: 978-953-307-840-3 in Earthquake Research and Analysis - New Frontiers in Seismology.

Okada, Y., Kasahara, K., Hori, S. Obara, K., Sekiguchi, S. Fujiwara, H., and Yamamoto, A. (2004). Recent progress of seismic observation networks in Japan -Hi-net, F-net, K-NET and KiK-net. *Earth, Planets and Space*, 56:xv–xxviii.

Olsen, K. B. (2000). Site amplification in the Los Angeles basin from three-dimensional modeling of ground motion. *Bulletin of the Seismological Society of America*, 90(6B):S77–S94.

Olson, A. H., Orcutt, J. A., and Frazier, G. A. (1984). The discrete wavenumber/finite element method for synthetic seismograms. *Geophysical Journal International*, 77(2):421–460.

Oral, E. (2016). *Multi-dimensional modeling of seismic wave propagation in linear and nonlinear media*. PhD thesis, Université Paris Est.

Ozawa, T. (2008). Coseismic deformation of the 2007 Chuetsu-Oki earthquake derived from PALSAR/InSAR and its fault model. *Earth, Planets and Space*, 60(11):1099–1104.

Paludo, L., Bouvier, V., Cottereau, R., and Clouteau, D. (2015). Efficient Parallel Generation of Random Field of Mechanical Properties for Geophysical Application. In *6th International Conference on Earthquake Geotechnical Engineering*.

Panza, G. F., Cazzaro, R., and Vaccari, F. (1997). Correlation between macroseismic intensities and seismic ground motion parameters. *Annali di Geofisica*, XL(5).

Paolucci, R., Mazzieri, I., and Smerzini, C. (2015). Anatomy of strong ground motion: near-source records and 3D physics-based numerical simulations of the Mw 6.0 May 29 2012 Po Plain earthquake, Italy. *Geophysical Journal International*, 203:2001–2020.

Paolucci, R., Mazzieri, I., Smerzini, C., and Stupazzini, M. (2014). Physics -Based Earthquake Ground Shaking Scenarios in Large Urban Areas. In Ansal, A., editor, *Perspectives on European Earthquake Engineering and Seismology*, volume 34 of *Geotechnical, Geological and Earthquake Engineering*, pages 331–359. Springer.

Papageorgiou, A. S. and Aki, K. (1983). A specific barrier model for the quantitative description of inhomogeneous faulting and the prediction of strong ground motion. I. Description of the model. *Bulletin of the Seismological Society of America*, 73(3):693–722.

Patera, A. (1984). A spectral element method for fluid dynamics: Laminar flow in a channel expansion. *Journal of Computational Physics*, 54(3):468 – 488.

Pavlenko, O. V. and Irikura, K. (2012). Nonlinear Soil Behavior at the Kashiwazaki-Kariwa Nuclear Power Plant During the Niigata Chuetsu-Oki Earthquake (July, 16, 2007). *Pure and Applied Geophysics*, 169(10):1777–1800.

Pecker, A. (2011). Ground Response Analysis-Kashiwazaki-Kariwa Nuclear Plant-Unit 7 R/B. Technical report, Geodynamique et Structures.

Penzien, J. and Watabe, M. (1975). Characteristics of 3-dimensional earthquake ground motions. *Earthquake Engineering and Structural Dynamics*, 3(1975):365–373.

Pisanò, F. and Jeremić, B. (2013). A Comparison of Two Elastic-Plastic Approaches To Cyclic Soil Modelling. In *COMPDYN 2013 4th ECCOMAS Thematic Conference on Computational Methods in Structural Dynamics and Earthquake Engineering M. Papadrakakis, N.D. Lagaros, V. Plevris (eds.) Kos Island, Greece, 12th June 2013*, number June, pages 12–14.

Pisanò, F. and Jeremić, B. (2014). Simulating stiffness degradation and damping in soils via a simple visco-elastic-plastic model. *Soil Dynamics and Earthquake Engineering*, 63:98–109.

Pitarka, A., Irikura, K., Iwata, T., and Sekiguchi, H. (1998). Three-dimensional simulation of the near-fault ground motion for the 1995 Hyogo-Ken Nanbu (Kobe), Japan, earthquake. *Bulletin of the Seismological Society of America*, 88(2):428–440.

Plesch, A., Shaw, J. H., Benson, C., Bryant, W. A., Carena, S., Cooke, M., Dolan, J., Fuis, G., Gath, E., Grant, L., et al. (2007). Community fault model (CFM) for southern California. *Bulletin of the Seismological Society of America*, 97(6):1793–1802.

Porter, K. A. (2003). An overview of PEER's performance-based earthquake engineering methodology. In *Proceedings of Ninth International Conference on Applications of Statistics and Probability in Civil Engineering*.

Potts, D. M. and Gens, A. (1985). A Critical Assessment of Methods of Correcting for Drift from the Yield Surface in Elasto-Plastic Finite Element Analysis. *International Journal for Numerical and Analytical Methods in Geomechanics*, 9:149–159.

Prevost, J. (1977). Mathematical modelling of monotonic and cyclic undrained clay behaviour. *International Journal for Numerical and Analytical Methods in Geomechanics*, 1(2):195–216.

Prevost, J. (1978). Plasticity theory for soil stress-strain behavior. *Journal of the Engineering Mechanics Division*, 104(5):1177–1194.

Prevost, J. H. (1982). Two-surface versus multi-surface plasticity theories: a critical assessment. *International Journal for Numerical & Analytical Methods in Geomechanics*, 6(3):323–338.

Prevost, J. H. (1985). A Simple Plasticity Theory for Cohesionless Frictional Soils. *Soil Dynamics and Earthquake Engineering*, 4(1):9–17.

Priolo, E., Carcione, J. M., and Seriani, G. (1994). Numerical simulation of interface waves by high-order spectral modeling techniques. *The Journal of the Acoustical Society of America*, 95(2):681–693.

Proctor, B. P., Mitchell, T. M., Hirth, G., Goldsby, D., Zorzi, F., Platt, J. D., and Toro, G. D. (2014). Dynamic weakening of serpentinite gouges and bare surfaces at seismic slip rates. *Journal of Geophysical Research: Solid Earth*, 119(11):8107–8131.

Pulido, N. and Dalguer, L. A. (2009). Estimation of the high-frequency radiation of the 2000 Tottori (Japan) earthquake based on a dynamic model of fault rupture: application to the strong ground motion simulation. *Bulletin of the Seismological Society of America*, 99(4):2305–2322.

Puzrin, A. (2012). *Constitutive modelling in geomechanics: introduction*. Springer Science & Business Media.

Quinay, P. E. B., Ichimura, T., Hori, M., Nishida, A., and Yoshimura, S. (2013). Seismic Structural Response Estimates of a Fault-Structure System Model with Fine Resolution Using Multiscale Analysis with Parallel Simulation of Seismic-Wave Propagation. *Bulletin of the Seismological Society of America*, 103(3):2094–2110.

Régnier, J., Bonilla, L. F., Bard, P.-Y., Bertrand, E., Hollender, F., Kawase, H., Sicilia, D., Arduino, P., Amorosi, A., Asimaki, D., Boldini, D., Chen, L., Chiaradonna, A., De Martin, F., Ebrille, M., Elgamal, A., Falcone, G., Foerster, E., Foti, S., Garini, E., Gazetas, G., Gélis, C., Ghofrani, A., Giannakou, A., Gingery, J., Glinsky, N., Harmon, J., Hashash, Y., Iai, S., Jeremić, B., Kramer, S., Kontoe, S., Kristek, J., Lanzo, G., di Lernia, A., Lopez-Caballero, F., Marot, M., McAllister,

G., Diego M., E., Moczo, P., Montoya-Noguera, S., Musgrove, M., Nieto-Ferro, A., Pagliaroli, A., Pisanó, F., Richterova, A., Sajana, S., Santisi d'Avila, M., Shi, J., Silvestri, F., Taiebat, M., Tropeano, G., Verrucci, L., and Watanabe, K. (2016). International Benchmark on Numerical Simulations for 1D, Nonlinear Site Response (PRENOLIN): Verification Phase Based on Canonical Cases. *Bulletin of the Seismological Society of America*, 106(5):2112–2135.

Regnier, J., Cadet, H., Bonilla, L. F., Bertrand, E., and Semblat, J.-F. (2013). Assessing Nonlinear Behavior of Soils in Seismic Site Response: Statistical Analysis on KiK-net Strong-Motion Data. *Bulletin of the Seismological Society of America*, 103(3):1750–1770.

Rezaeian, S. and Der Kiureghian, A. (2012). Simulation of orthogonal horizontal ground motion components for specified earthquake and site characteristics. *Earthquake Engineering and Structural Dynamics*, 41(2):335–353.

Richards, P. G. (1976). Dynamic motions near an earthquake fault a three-dimensional solution. *Bulletin of the Seismological Society of America*, 66(1):1–32.

Rosenblatt, M. (1952). Remarks on a multivariate transformation. *The annals of mathematical statistics*, 23(3):470–472.

Roten, D., Cui, Y., Olsen, K. B., Day, S. M., Withers, K., Savran, W. H., Wang, P., and Mu, D. (2016). High-Frequency Nonlinear Earthquake Simulations on Petascale Heterogeneous Supercomputers. In *SC16: International Conference for High Performance Computing, Networking, Storage and Analysis*, pages 957–968.

Ruiz, J. A., Baumont, D., Bernard, P., and Berge-Thierry, C. (2011). Modelling directivity of strong ground motion with a fractal, k-2, kinematic source model. *Geophysical Journal International*, 186(1):226.

Sabetta, F. and Pugliese, A. (1996). Estimation of Response Spectra and Simulation of Nonstationary Earthquake Ground Motions. *Bulletin of the Seismological Society of America*, 86(2):337–352.

Sagiya, T., Miyazaki, S., and Tada, T. (2000). Continuous GPS array and presentday crustal deformation of Japan. *Pure Applied Geophysics*, 157:2303–2322.

Saikia, C. K. and Somerville, P. G. (1997). Simulated hard-rock motions in Saint Louis, Missouri, from large New Madrid earthquakes (Mw ¿ 6.5). *Bulletin of the Seismological Society of America*, 87(1):123–139.

Sato, H. (1994). The relationship between late Cenozoic tectonic events and stress field and basin development in northeast Japan. *Journal of Geophysics Research*, 99:22261–22274.

Savage, J. C. (1966). Radiation from a realistic model of faulting. *Bulletin of the Seismological Society of America*, 56(2):577–592.

SCEC (2017). Southern California Earthquake Center: Research Program in Earthquake System Science, 2017-2022. online. Proposal to the National Science Foundation and U. S. Geological Survey.

Sekiguchi, H., Yoshimi, M., Horikawa, H., Yoshida, K., Suzuki, H., Matsuyama, H., Morino, M., Takizawa, F., and Ying, L. (2009). 3D subsurface structure model of the Niigata sedimentary basin. *Ann. Rep. Active Fault Paleoearthq. Res.*, 9:175–259.

Seriani, G. (1998). 3-D large-scale wave propagation modeling by spectral element method on Cray T3E multiprocessor. *Computer Methods in Applied Mechanics and Engineering*, 164(1):235–247.

Seriani, G. and Oliveira, S. P. (2008). Dispersion analysis of spectral element methods for elastic wave propagation. *Wave Motion*, 45(6):729–744.

Seriani, G., Priolo, E., and Pregarz, A. (1995). Modelling waves in anisotropic media by a spectral element method. In *Proceedings of the third international conference on mathematical and numerical aspects of wave propagation*, pages 289–298. SIAM.

Seyhan, E., Stewart, J. P., and Graves, R. W. (2013). Calibration of a Semi-Stochastic Procedure for Simulating High-Frequency Ground Motions. *Earthquake Spectra*, 29(4):1495–1519.

Shahbazian, A. and Pezeshk, S. (2010). Improved Velocity and Displacement Time Histories in Frequency Domain Spectral-Matching Procedures. *Bulletin of the Seismological Society of America*, 100(6).

Shaw, J. H., Plesch, A., Tape, C., Suess, M. P., Jordan, T. H., Ely, G., Hauksson, E., Tromp, J., Tanimoto, T., Graves, R., Olsen, K., Nicholson, C., Maechling, P. J., Rivero, C., Lovely, P., Brankman, C. M., and Munster, J. (2015). Unified Structural Representation of the southern California crust and upper mantle. *Earth and Planetary Science Letters*, 415:1 – 15.

Shiba, Y. (2008). Source process and broadband strong motions during the Niigata-ken Chuetsu-Oki earthquake in 2007. *Denryoku Chuo Kenkyusho Hokoku*, (N08007):1–4. Japanese with English Abstract.

Shiba, Y., Hikima, K., Uetake, T., Mizutani, H., Tsuda, H., Hayakawa, T., and Tanaka, S. (2011). Source model of the 2007 Chuetsu-Oki earthquake based on precise aftershock distribution and 3D velocity structure. In *Japan Geoscience Union meeting*.

Shinohara, M., Kanazawa, T., Yamada, T., Nakahigashi, K., Sakai, S., Hino, R., Murai, Y., Yamazaki, A., Obana, K., Ito, Y., et al. (2008). Precise aftershock distribution of the 2007 Chuetsu-Oki Earthquake obtained by using an ocean bottom seismometer network. *Earth, planets and space*, 60(11):1121–1126.

Shinozuka, M. and Deodatis, G. (1991). Simulation of stochastic processes by spectral representation. *Applied Mechanics Reviews*, 44(4):191–204.

Simo, J. (1992). Algorithms for static and dynamic multiplicative plasticity that preserve the classical return mapping schemes of the infinitesimal theory. *Computer Methods in Applied Mechanics and Engineering*, 99(1):61–112.

Simo, J. and Hughes, T. J. R. (1998). *Computational Inelasticity*, volume 7 of *Interdisciplinary applied mathematics*. Springer.

Simo, J., Tarnow, N., and Wong, K. (1992). Exact energy-momentum conserving algorithms and symplectic schemes for nonlinear dynamics. *Computer Methods in Applied Mechanics and Engineering*, 100(1):63–116.

Sloan, S., Abbo, A., and Sheng, D. (2001). Refined explicit integration of elastoplastic models with automatic error control. *Engineering Computations*, 18(1/2):121–154.

Sloan, S. W. (1987). Substepping schemes for the numerical integration of elastoplastic stress-strain relations. *International Journal for Numerical Methods in Engineering*, 24(5):893–911.

Smerzini, C., Galasso, C., Iervolino, I., and Paolucci, R. (2014). Ground motion record selection based on broadband spectral compatibility. *Earthquake Spectra*, 30(4):1427–1448.

Smerzini, C. and Villani, M. (2012). Broadband Numerical Simulations in Complex Near-Field Geological Configurations: The Case of the 2009 Mw 6.3 L'Aquila Earthquake. *Bulletin of the Seismological Society of America*, 102(6):2436–2451.

Somerville, P., Irikura, K., Abrahamson, N., Sawada, S., Kagawa, T., and Tatsumi, A. (1999). Characterizing earthquake slip models for the prediction of strong ground motion. *Seismological Research Letters*, 70:59–80.

Somerville, P., Sen, M., and Cohee, B. (1991). Simulation of strong ground motions recorded during the 1985 Michoacan, Mexico and Valparaiso, Chile earthquakes. *Bulletin of the Seismological Society of America*, 81(1):1–27.

Sørensen, M., Stromeyer, D., and Grünthal, G. (2010). Intensity attenuation in the Campania region, Southern Italy. *Journal of seismology*, 14(2):209–223.

Spudich, P. and Archuleta, R. (1987). *Seismic Strong Motion Synthesis*, chapter Techniques for earthquake ground-motion calculation with applications to source parameterization to finite faults, pages 205–265. Number 5 in Seismic Strong Motion Synthesis. Academic Press, Orlando, Florida.

Spudich, P., Bayless, J., Baker, J. W., Chiou, B., Rowshandel, B., Shahi, S., and Somerville, P. (2013). Final Report of the NGA-West2 Directivity Working Group. Technical Report 2013/09, Pacific Earthquake Engineering Research Center - College of Engineering - University of California.

Spudich, P. and Frazer, L. N. (1984). Use of ray theory to calculate high-frequency radiation from earthquake sources having spatially variable rupture velocity and stress drop. *Bulletin of the Seismological Society of America*, 74(6):2061–2082.

Spudich, P. and Xu, J. (2002). Software for calculating earthquake ground motions from finite faults in vertically varying media. In William H.K. Lee, Hiroo Kanamori, P. C. J. and Kisslinger, C., editors, *International Handbook of Earthquake and Engineering Seismology*, volume 2 of *International Geophysics*, pages xi – xv. Academic Press.

Stein, S. and Wysession, M. (2003). *An Introduction to Seismology, Earthquakes and Earth Structure*. Blackwell Publishing.

Stupazzini, M., Paolucci, R., and Igel, H. (2009). Near-Fault Earthquake Ground-Motion Simulation in the Grenoble Valley by a High-Performance Spectral Element Code. *Bulletin of the Seismological Society of America*, 99(1):286–301.

Stupazzini, M. and Zambelli, C. (2005). GeoELSEvp: a spectral element apprach for dynamic elasto-viscoplastic problems. *Rivista Italiana di Geotecnica*, 4:70–82.

Taborda, R. and Bielak, J. (2013). Ground-Motion Simulation and Validation of the 2008 Chino Hills, California, Earthquake. *Bulletin of the Seismological Society of America*, 103(1):131–156.

Takeuchi, C. S. and Fialko, Y. (2012). Dynamic models of interseismic deformation and stress transfer from plate motion to continental transform faults. *Journal of Geophysical Research: Solid Earth*, 117(B5).

Tanioka, Y., Ruff, L., and Satake, K. (1997). What controls the lateral variation of large earthquake occurrence along the Japan Trench? *Island Arc*, 6(3):261–266.

Tape, C., Liu, Q., Maggi, A., and Tromp, J. (2010). Seismic tomography of the southern California crust based on spectral-element and adjoint methods. *Geophysical Journal International*, 180(1):433.

Tarantola, A. (1988). Theoretical background for the inversion of seismic waveforms, including anelasticity and attenuation. *Pure and Applied Geophysics*, 128(1/2):365–399.

TEPCO (2007). The data analysis recorded at the Kashiwazaki Kariwa Nuclear Power Plant during the 2007 Niigata-ken Chuetsu-oki earthquake. Technical report, The Tokyo Electric Power Company, Inc. in Japanese.

Thompson, E. M., Baise, L. G., Kayen, R. E., and Guzina, B. B. (2009). Impediments to predicting site response: Seismic property estimation and modeling simplifications. *Bulletin of the Seismological Society of America*, 99(5):2927–2949.

Thomson, W. T. (1950). Transmission of elastic waves through a stratified soil medium. *Journal of Applied Physics*, 21:89–93.

Tinti, E. (2005). A Kinematic Source-Time Function Compatible with Earthquake Dynamics. *Bulletin of the Seismological Society of America*, 95(4):1211–1223.

Tokimatsu, K. and Arai, H. (2008). Nonlinear soil properties estimated from downhole array recordings at Kashiwazaki-Kariwa nuclear power plant in the Niigata-Ken Chuetsu-Oki earthquakes. In *The 14th World Conference on Earthquake Engineering*, World Conferences on Earthquake Engineering, pages 2–9, Beijing, China.

Tokumitsu, R., Kikuchi, M., Nishimura, I., Shiba, Y., and Tanaka, S. (2009). Analysis of the strong motion records obtained from the 2007 Niigataken Chuetsu-Oki earthquake and determination of the design basis ground motions at the Kashiwazaki Kariwa Nuclear Power Plant. Part 1. Outline of the strong motion records and estimation of factors in large amplification. Technical report.

Tromp, J., Komattisch, D., and Liu, Q. (2008). Spectral-element and adjoint methods in seismology. *Communications in Computational Physics*, 3(1):1–32.

Tsuda, K., Hayakawa, T., Uetake, T., Hikima, K., Tokimitsu, R., Nagumo, H., and Shiba, Y. (2011). Modeling 3D Velocity Structure in the Fault Region of the 2007 Niigataken Chuetu-Oki Earthquake with Folding Structure. In *4th IASPEI/IAEE International Symposium-Effects of Surface Geology on Seismic Motion*, pages 1–11.

Uetake, T., Nishimura, I., and Mizutani, H. (2008). Characteristics of Strong Motion Records In Kashiwazaki-Kariwa Nuclear Power Station during the Niigataken Chuetsu-Oki Earthquake in 2007. In *14th WCEE*.

Vardanega, P. J. and Bolton, M. D. (2013). Stiffness of Clays and Silts : Normalizing Shear Modulus and Shear Strain. *Journal of Geotechnical and Geoenvironmental Engineering*, 139(9):1575–1589.

Villani, M., Faccioli, E., Ordaz, M., and Stupazzini, M. (2014). High-Resolution Seismic Hazard Analysis in a Complex Geological Configuration: The Case of the Sulmona Basin in Central Italy. *Earthquake Spectra*, 3(4):1801–1824.

Virieux, J. (1986). P-SV wave propagation in heterogeneous media: Velocity-stress finite-difference method. *Geophysics*, 51(4):889–901.

Virieux, J. and Madariaga, R. (1982). Dynamic faulting studied by a finite difference method. *Bulletin of the Seismological Society of America*, 72(2):345–369.

Virieux, J. and Operto, S. (2009). An overview of full-waveform inversion in exploration geophysics. *Geophysics*, 74(6):WCC1–WCC26.

Vucetic, M. (1990). Normalized behavior of clay under irregular cyclic loading. *Canadian Geotechnical Journal*, 27(1):29–46.

Wald, D., Quitoriano, V., Heaton, T., and Kanamori, H. (1999). Relationship between Peak Ground Acceleration, Peak Ground Velocity, and Modified Mercalli Intensity in California. *Earthquake Spectra*, 15(3).

Wald, D. J. and Graves, R. W. (1998). The seismic response of the Los Angeles basin, California. *Bulletin of the Seismological Society of America*, 88(2):337–356.

Waldhauser, F. and Ellsworth, W. L. (2000). A Double-Difference Earthquake Location Algorithm: Method and Application to the Northern Hayward Fault, California. *Bulletin of the Seismological Society of America*, 90(6):1353–1368.

Watanabe, T., Moroi, T., Nagano, M., Tokumitsu, R., Kikuchi, M., and Nishimura, I. (2009). Analysis of the strong motion records obtained from the 2007 Niigataken Chuetsu-Oki earthquake and determination of the design basis ground motions at the Kashiwazaki Kariwa Nuclear Power Plant. Part 2. Difference of site amplification based on the 2D FEM analysis of the folded structure. Technical report.

Withers, K. B. (2016). *Ground motion and variability from 3-D deterministic broadband simulations*. PhD thesis, University of California, San Diego and San Diego State University.

Yee, E., Stewart, J., and Tokimatsu, K. (2011). Nonlinear Site Response and Seismic Compression at Vertical Array Strongly Shaken by the Niigata-ken Chuetsu-Oki Earthquake. Technical report, Pacific Earthquake Engineering Research Center-College of Engineering - University of California, Berkeley.

Yin-Tung, Y. (2012). Synthesis of high-frequency ground motion using Empirical Green's Function. In *Workshop on Seismic Hazard Assessment Issues in the island arc of Taiwan and Japan*, National Central University, Taiwan.

Yomogida, K. and Etgen, J. T. (1993). 3-D wave propagation in the Los Angeles basin for the Whittier-Narrows earthquake. *Bulletin of the Seismological Society of America*, 83(5):1325–1344.

Yukutake, Y., Takeda, T., and Obara, K. (2008). Well-resolved hypocenter distribution using the double-difference relocation method in the region of the 2007 Chuetsu-oki Earthquake. *Earth, Planets and Space*, 60(11):1131–1135.

Zeng, Y., Anderson, J. G., and Yu, G. (1994). A composite source model for computing realistic synthetic strong ground motions. *Geophysical Research Letters*, 21(8):725–728.

Zhu, L. and Rivera, L. A. (2002). A note on the dynamic and static displacements from a point source in multilayered media. *Geophysical Journal International*, 148(3):619.

Zienkiewicz, . C., Chan, A., Pastor, M., Schrefel, B., and Shiomi, T. (1999). *Computational Geomechanics with Special Reference to Earthquake Engineering*. John Wiley and Sons Ltd.